MECHANISMS LINKING MITOCHONDRIAL DYNAMICS, MICROTUBULE MOTORS, AND NEUROLOGICAL DISEASE

Adam Ray Fenton

A DISSERTATION

in

Cell and Molecular Biology

Presented to the Faculties of the University of Pennsylvania

in

Partial Fulfillment of the Requirements for the

Degree of Doctor of Philosophy

2024

Supervisor of Dissertation

Erika L.F. Holzbaur, PhD,

Professor of Physiology

Co-Supervisor of Dissertation

Thomas A. Jongens, PhD

Associate Professor of Genetics

Graduate Group Chairperson

Daniel S. Kessler, PhD

Associate Professor of Cell and Developmental Biology

Dissertation Committee

Melike Lakadamyali, PhD, Professor of Physiology

E. Michael Ostap, PhD, Professor of Physiology

Roberto Dominguez, PhD, Professor of Physiology

Greg J. Bashaw, PhD, Professor of Neuroscience

MECHANISMS LINKING MITOCHONDRIAL DYNAMICS, MICROTUBULE MOTORS, AND NEUROLOGICAL DISEASE

ACKNOWLEDGMENTS

There are so many people that I have to thank for making my experience in grad school both fun and productive. First and foremost, thank you Erika Holzbaur and Tom Jongens for being outstanding mentors. Thank you for believing in my abilities as a scientist and giving me the freedom to navigate a thesis project that bridges both labs. It's been incredible to work under such supportive and encouraging scientists. Your excitement and enthusiasm for science drives me to work harder and I have many wonderful memories of sharing the thrill of scientific discovery with you that I will never forget. I have learned much from your support and guidance over the years.

A huge thank you goes to Mariko Tokito and Karen Jahn for being the backbone of the Holzbaur lab and helping me in countless ways. Mariko's masterful cloning skills were essential for the bulk of my research and I would be nowhere without her. Karen's mouse expertise helped me transition smoothly into mouse work at a very late stage in grad school, which is not done easily. It's been a great pleasure to work with you both and get to know you. I owe you both so much for all your tireless work helping me.

Thank you so much to all the members of the Holzbaur and Jongens labs that I've worked with over the years. It has been amazing to work with such talented scientists and fun people. I don't have the space to mention everyone here, but I want to broadly acknowledge the support and friendship that has made me feel at home in two labs. Thank you to those who helped me learn how to do science, especially to Erin Masucci for teaching me TIRF and mentoring me at the beginning of grad school, Ellie Tarlow for teaching me how to work with flies and being great conversation during all the time spent in the fly room, and Sydney Cason for teaching me neuron culture and being my dynein buddy over the years. Thanks also to Stephen Coscia. You're my mito brother now and always will be.

There are many other great people that I've had the pleasure to work with over the years. Thank you as well to the members of my thesis committee, Melike Lakadamyali, Mike Ostap, Greg Bashaw, and Roberto Dominguez, for their helpful suggestions and constructive feedback throughout this process. I appreciate the time and energy that you've given me over the years. Thank you to the members of the Genetics Department, Physiology Department, and Pennsylvania Muscle Institute for all the fun

conversations and helpful insight on my projects. There's something truly special and unique about the supportive environment in all these groups that I will greatly miss.

I am also grateful for having many collaborators that are wonderful to work with. Thank you to the Dominquez and Landers labs for including me as a collaborator on your interesting and impactful projects. Thank you as well to the Chang and Lakadamyali labs, whose kindness and willingness to collaborate has elevated my science in ways I never could have anticipated.

Of course, I owe much to my friends and family that have been by my side through this journey. To my parents, I can't thank you enough for your never-ending love and for always believing in me. Thank you for instilling me with the curiosity and work ethic needed to become a scientist and for patiently supporting me through all stages of my life. Thank you to the rest of my family and friends for enriching my life and bringing so much joy outside of lab.

Lastly, thank you to my best friend and partner, Liz. The past five years have been the happiest of my life and I owe it to you. I'm so glad to have met you in grad school and that I get to spend my life with you. You are so kind and caring, and an amazing scientist as well! I would not have been able to accomplish any of this without your support.

ABSTRACT

MECHANISMS LINKING MITOCHONDRIAL DYNAMICS, MICROTUBULE MOTORS, AND NEUROLOGICAL DISEASE

Adam Ray Fenton

Erika L. F. Holzbaur

Thomas A. Jongens

Mitochondria are critical organelles that continually remodel to carry out their many cellular functions. This remodeling is particularly important in neurons due to the specialized shape and high energy demands inherent to these cells. Mitochondrial network remodeling is determined in part by kinesin-1 and dynein-dynactin, which drive mitochondrial transport in opposite directions along microtubules. Interestingly, mitochondrial dynamics and microtubule motors both have close causal links to neurodegenerative and neurodevelopmental diseases, such as Amyotrophic Lateral Sclerosis (ALS) and Fragile X Syndrome. In this work, we describe molecular mechanisms connecting these diseases to mitochondrial dynamics and microtubule motors, and dissect the regulation of microtubule-based mitochondrial transport by TRAK-MIRO motor-adaptor complexes. First, we utilize *in vitro* single-molecule imaging and biochemistry to demonstrate that TRAK2 activates kinesin-1 and dynein-dynactin, and show that TRAK2 scaffolds an interaction between these motors to link their function within a single complex. In Chapter 3, we collaborate with the Dominguez lab to characterize a direct interaction between TRAK1 and MIRO1 that facilitates recruitment of TRAK1 to mitochondria. In Chapter 4, we collaborate with the Landers lab to investigate the effects of ALS-associated mutations on the kinesin-1 isoform KIF5A. We find that multiple ALS-linked mutations result in skipping of exon 27, which produce a novel C-terminal sequence within KIF5A that impairs its autoinhibition, creating a hyperactive motor protein that is toxic to neurons. In Chapter 5, we characterize mitochondrial morphological and metabolic defects in a *Drosophila* model of Fragile X Syndrome and show phenotypic links between this model, insulin signaling, and circadian behavior. Last, we show that FMRP, the protein whose dysfunction causes Fragile X Syndrome, is central to a mechanism

by which protein synthesis is locally orchestrated to efficiently guide mitochondrial fission in neurons. We characterize the precise spatiotemporal dynamics underlying this process with spinning-disk confocal microscopy and collaborate with the Lakadamyali and Chang labs to describe the nanoscale architecture of FMRP-mitochondria interactions with DNA-PAINT super-resolution microscopy and cryo-electron tomography. Together, these studies provide detailed insight into mechanisms underlying mitochondrial network organization in neurons and connect this organization to the regulation of microtubule motors and human neurological disease.

TABLE OF CONTENTS

LIST OF TABLES

LIST OF FIGURES

CHAPTER 1

CHAPTER 2

CHAPTER 3

CHAPTER 4

CHAPTER 5

CHAPTER 6

CHAPTER 1: INTRODUCTION

Parts of this chapter have been adapted from:

Fenton, AR; Jongens, TA; Holzbaur, ELF. Mitochondrial dynamics: Shaping and remodeling an organelle network. *Current Opinion in Cell Biology*, 68, 28–36 (2021).

The contents of eukaryotic cells are highly dynamic, yet organized precisely in space and time. Accurate spatiotemporal organization of molecules and organelles is vital to cellular function, especially in neurons, which contain specialized axonal and dendritic compartments that can extend over 100,000 times the length of a cell body. The extreme size, morphological complexity, and long lifespan of neurons provides numerous challenges for proper maintenance of cellular organization, including for mitochondria, which play critical roles in neuronal function. The mitochondrial network continually changes shape to carry out its many functions in neurons, with a substantial proportion of this shaping determined by interactions with the microtubule cytoskeleton and microtubule motors. The fundamental nature of this remodeling is highlighted by the many neurological diseases caused by mutations in microtubule motors and other proteins that drive mitochondrial dynamics. In this chapter, I present overviews of microtubule-based transport and mitochondrial dynamics, and describe connections between these processes and multiple neurological diseases in humans.

I. Microtubule-based transport

Microtubules

Microtubules are filamentous protein polymers comprised of repeating α-tubulin and β-tubulin heterodimers (Fig. 1.1A) (Bryan & Wilson, 1971; Feit et al., 1971). Tubulins bind the nucleotide guanosine triphosphate (GTP) to polymerize in a head-to-tail manner and form polarized protofilaments, which associate laterally with other protofilaments to create hollow tubular structures (Nogales, 2000). The number of protofilaments present in each microtubule is variable, but most consist of 13 protofilaments and create a ~25 nm hole in the middle (Tilney et al., 1973). Microtubules are polarized, such that α-tubulin is exposed at one end, termed the minus-end, while β-tubulin is exposed at the other end, termed the “plus-end”. Structural differences between α- and β-tubulin dictate properties of the plus- and minus-ends such that tubulin incorporates more rapidly at the plus-end than the minus-end (Fig. 1.1A).

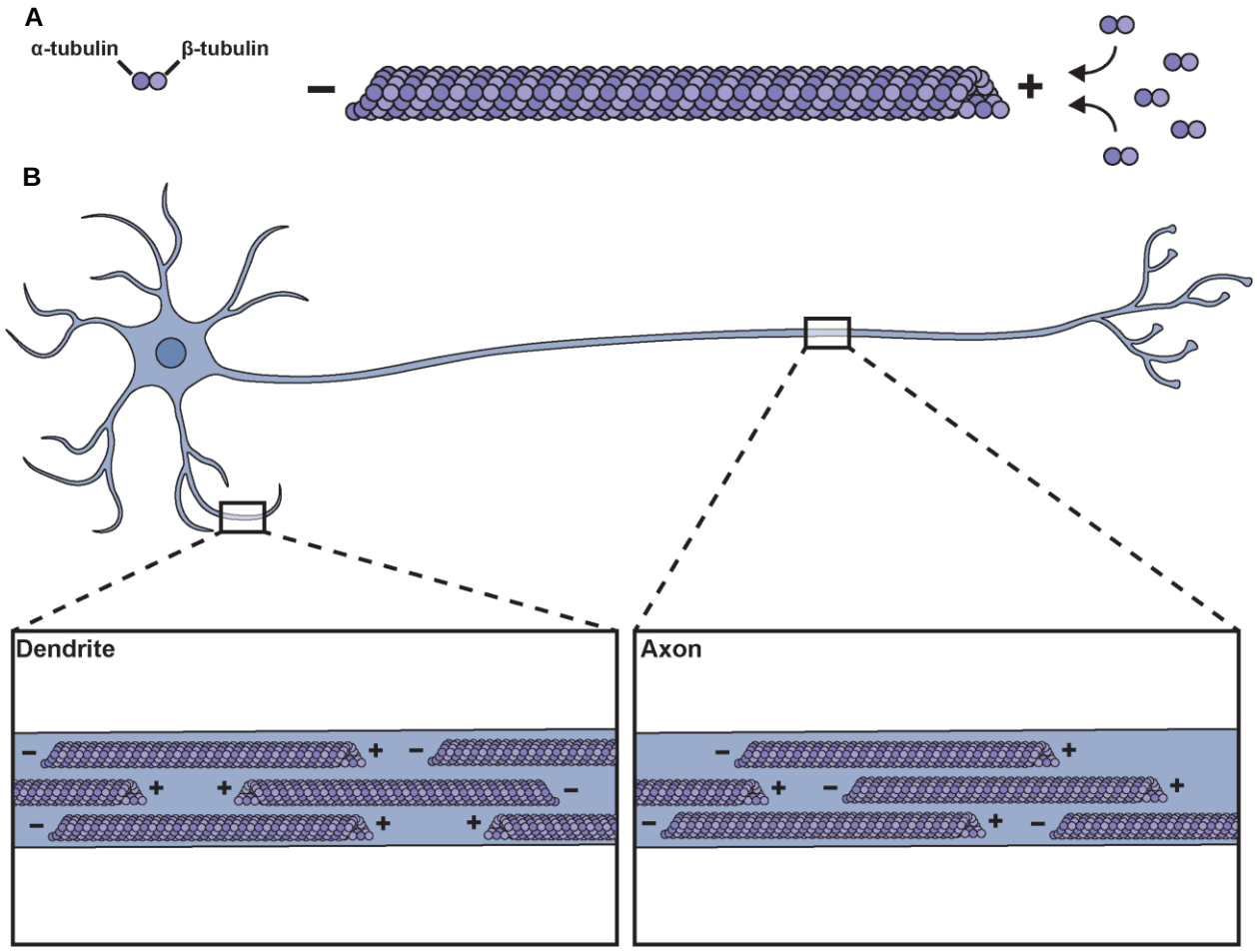

Figure 1.1: Microtubule structure and organization in neurons. A, Schematic showing α/β tubulin heterodimers and their preferential incorporation into the plus-end of the polarized microtubule filament. **B,** Organization of microtubules in mammalian neurons with mixed polarity in dendrites and uniform polarity in axons.

Microtubules are present throughout the cytoplasm, where they play central roles in many cellular functions, such as intracellular transport and cell division. The architecture of the microtubule network within cells allows for polarized trafficking of cargoes and greatly informs intracellular organization. In many cells, microtubules are oriented radially, with the minus-ends concentrated near the center of the cell, and plus-ends extended toward the cell periphery. Neurons also contain this radial microtubule orientation in the cell body, but also display specialized microtubule architecture in axons and dendrites (Fig. 1.1B). Axonal

microtubules are arranged into uniform, tiled arrays with their plus-ends directed outwards toward the growth cone (Baas et al., 1988; Heidemann et al., 1981). In contrast, dendritic microtubules display mixed polarity in mammalian neurons, with approximately 60% of microtubules oriented with their plus-ends away from the cell body (Baas et al., 1988).

Microtubule motors are classes of proteins that hydrolyze ATP to move along microtubules. These motor proteins can recognize the intrinsic polarity of microtubules to bias transport in one direction along the microtubule track. There are two classes of motor proteins that drive polarized transport along microtubules: kinesin and dynein. Kinesins typically move cargoes toward the microtubule plus-end while a single dynein is solely responsible for long-distance minus-end-directed cargo transport within cells.

Kinesin-1

The kinesin motor was first characterized as a protein in squid axoplasm capable of moving microtubules in an ATP-dependent manner, which is also responsible for cargo transport from the microtubule minus-end to the plus-end (Vale, Reese, et al., 1985; Vale, Schnapp, et al., 1985). This initial discovery led to the identification of a superfamily of 45 kinesin (KIF) genes that have been classified into 14 families based on sequence similarity (Hirokawa & Tanaka, 2015). Most kinesin families contain an N-terminal motor domain that binds microtubules and hydrolyzes ATP, a coiled-coil stalk region that facilitates dimerization, and a C-terminal tail that is involved in cargo association (Fig. 1.2A) (Verhey & Hammond, 2009). The structure and sequence of each kinesin allows for different kinesins to bind and transport different cargoes, allowing for specific control of transport. Conventional kinesin, otherwise known as kinesin-1 or KIF5, is responsible for the anterograde transport of many cargoes in neurons, including RNA granules, mitochondria, and lysosomes (Hirokawa & Takemura, 2005a).

Kinesin-1 is a homodimer comprised of two heavy chains (KHC) (DeBoer et al., 2008). In mammals, kinesin heavy chains are encoded by three different genes: *KIF5A*, *KIF5B*, and *KIF5C*, which are highly

conserved and differ mostly in the C-terminal tail. All three kinesin-1 isoforms are involved in cargo transport and are thought to have overlapping functions. However, the expression patterns differ between the kinesin-1 isoforms; KIF5B is expressed ubiquitously across cell-types while KIF5A and KIF5C are primarily expressed in neurons (Kanai et al., 2000). The KHC homodimer can also form a heterotetrametric complex by binding two copies of kinesin light chain (KLC) (DeBoer et al., 2008). KLCs play important roles in regulating the activity of the heavy chains and recruiting the complex to certain cargoes (Verhey & Hammond, 2009). However, kinesin-1 can also associate with some cargoes through a direct interaction with adaptor proteins, independent of the KLC interaction.

Kinesin-1 activity is tightly regulated by an autoinhibitory mechanism that prevents cargo association, microtubule binding, and ATP hydrolysis. The autoinhibited state of kinesin-1 is formed by folding of the coiled-coil stalk, which enables interaction between the motor and tail domains (Fig. 1.2B) (Coy et al., 1999; D. S. Friedman & Vale, 1999). A short, conserved patch of residues in the kinesin-1 tail, termed the isoleucine-alanine-lysine (IAK) motif, mediates this direction head-to-tail interaction to inhibit the motor domain.

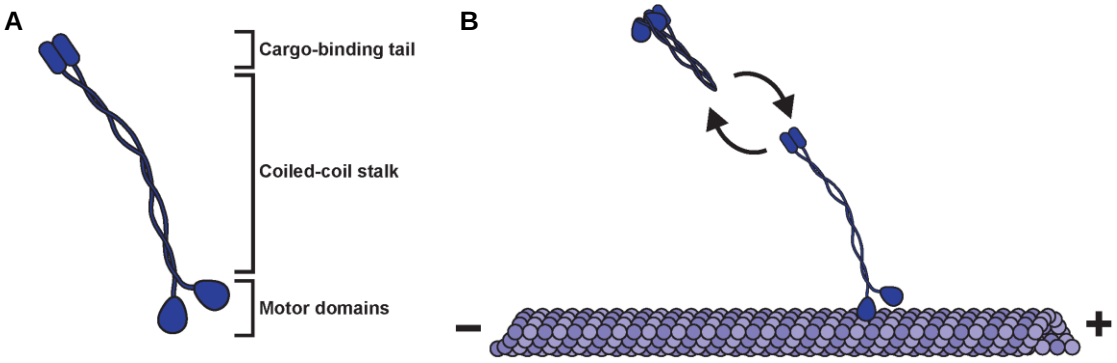

Figure 1.2: Structure and activation of kinesin-1. A, Architecture of kinesin-1. **B,** Schematic depiction of kinesin-1 autoinhibition and activation.

Dynein

Cytoplasmic dynein 1 (hence forth referred to as dynein) was originally identified as a protein that hydrolyzes ATP to produce force in the opposite direction to that observed for conventional kinesin, driving transport toward the microtubule minus-end (Paschal & Vallee, 1987). Within cells, dynein is the primary driver of organelle transport toward the microtubule minus-end. However, dynein plays many other roles in essential cellular processes, such as cell migration, nuclear positioning, and mitosis. The importance of dynein function is highlighted by the many diseases connected to mutations in dynein. Mutations in *DYNC1H1*, the gene encoding the largest subunit of dynein, are associated with a large spectrum of neuropathies, including Charcot-Marie-Tooth type 2 disease (CMT2), hereditary spastic paraplegia (HSP), spinal muscular atrophy, malformations of cortical development, intellectual disability, and epileptic spasms (Becker et al., 2020; Poirier et al., 2013; Su et al., 2022). The manifestation of *DYNC1H1* mutations as neurodegenerative and neurodevelopmental diseases involving both the peripheral and central nervous systems strongly suggests that dynein plays particularly critical roles in neurodevelopment and maintenance of the nervous system.

Dynein is a large, ~1.4 MDa complex comprised of many protein subunits that function together to bind cargo and convert the energy of ATP into movement. The largest subunit of dynein, dynein heavy chain (DHC), comprises an N-terminal tail domain that facilitate dimerization, six non-equivalent AAA+ ATPase domains that form a motor ring, and a stalk region that binds the microtubule (Fig. 1.3A). Within the AAA+ ring, AAA1 is the predominant site of ATP hydrolysis that drives motor translocation by conferring structural changes to the stalk, although this motility can also be controlled by the nucleotide state of AAA3. Several non-catalytic subunits are also present in the dynein complex, including intermediate chains (DIC), light intermediate chains (DLIC), and light chains (DLC). These subunits provide contact points with dynein accessory proteins that are necessary for cargo association and regulation of dynein activity.

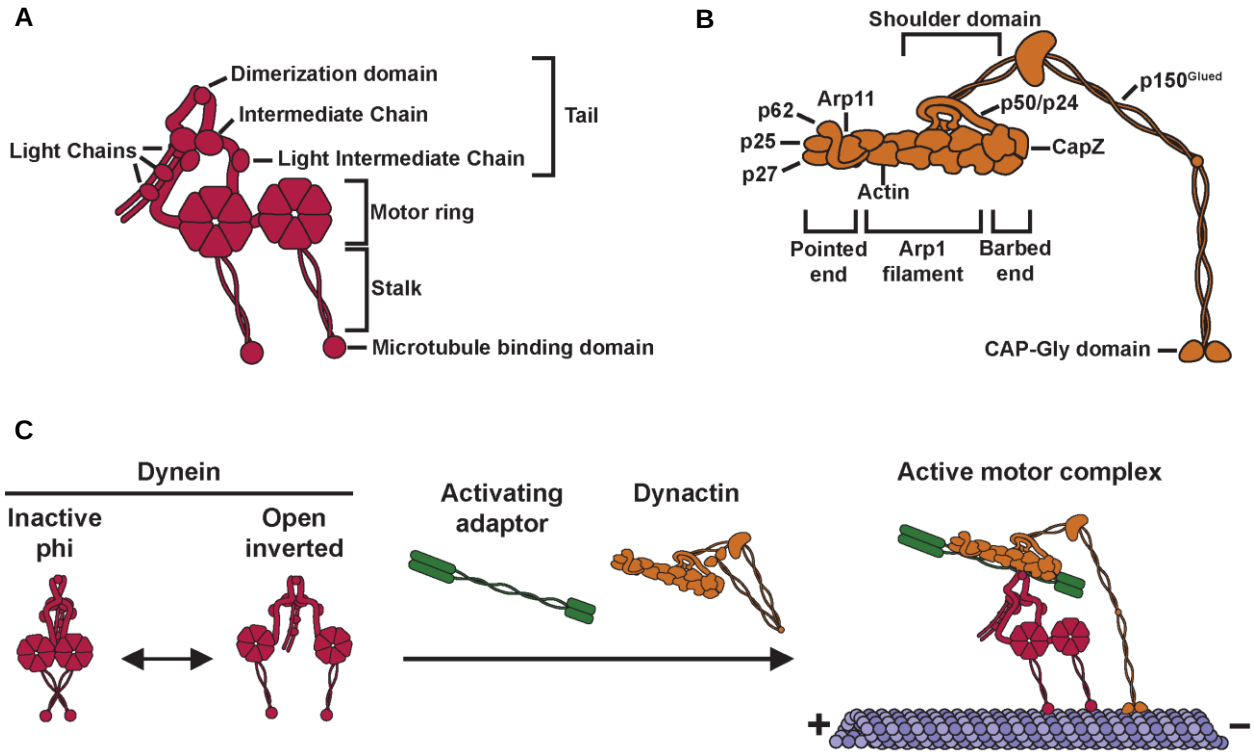

Figure 1.3: Structure and activation of dynein-dynactin. A-B, Architecture of dynein **(A)** and dynactin **(B)**. **C,** Schematic depiction of dynein autoinhibition and activation upon the addition of dynactin and an activating adaptor.

While initial studies of surface-attached dynein revealed robust microtubule translocation properties, it quickly became apparent that dynein activity is tightly regulated and requires additional cytoplasmic factors to drive transport along microtubules (Gill et al., 1991; Schroer & Sheetz, 1991). Without other binding partners, mammalian dynein typically forms an autoinhibited conformation in which the two motor domains and stalks dimerize to lock the complex in a weak microtubule binding state (K. Zhang et al., 2017). This state, termed the phi confirmation, does not move processively along microtubules. However, the presence of additional factors, later identified as dynactin and several classes of activating adaptor proteins allow for relief of the phi conformation to enable processive dynein motility.

Dynactin

Dynactin was initially identified as a protein complex that co-purified with dynein and enhanced the ability of dynein to transport vesicles along microtubules (Gill et al., 1991; Schroer & Sheetz, 1991). Further *in vitro* and cellular work has shown that dynactin affects dynein motility in multiple ways, including by aiding the recruitment of dynein to microtubule plus-ends and increasing the processivity of dynein stepping along microtubules (Ayloo et al., 2014; Q. Feng et al., 2020; Moughamian et al., 2013; Splinter et al., 2012). Moreover, complete activation of dynein for cargo transport within cells appears to depend on dynactin in most, if not all, instances of dynein function (Schroer, 2004).

The dynactin complex is composed of 23 subunits that form a ~1 MDa complex built around a filament of actin and actin-related proteins (Fig. 1.3B). This filament is comprised of eight actin-related protein (Arp1) subunits, one copy of β-actin, and another actin-related protein (Arp11) (Urnavicius et al., 2015). The ends of this filament are distinct and named according to the "pointed end" and "barbed end" nomenclature for the polarized ends of filamentous actin (F-actin). The pointed end of dynactin contains Arp11 bound to a complex of three proteins (p25, p27, and p62), while the barbed end of dynactin is capped by the F-actin capping protein, CapZ (Chowdhury et al., 2015; Urnavicius et al., 2015). Dynactin also contains a shoulder domain comprised of multiple copies of p24, p50, and $p150^{Glued}$ that binds along the Arp1 filament near the barbed end. The $p150^{Glued}$ subunit of dynactin contains multiple coiled-coil stretches which extend from the shoulder. These coiled-coil domains are highly flexible but can also fold back to stably dock against the Arp1 filament. Following these coiled-coils, $p150^{Glued}$ contains an N-terminal CAP-Gly domain, which directly binds microtubules to recruit dynein and increase dynein processivity (Ayloo et al., 2014; Q. Feng et al., 2020; Waterman-Storer et al., 1995). There is also an alternative splice form of $p150^{Glued}$ which lacks the CAP-Gly domain and thus cannot bind microtubules to aid dynein motility (McKenney et al., 2014; Tokito et al., 1996), although the specific functions of this isoform are not fully clear.

Dynein activation by adaptors

While dynactin interacts directly with dynein to increase dynein processivity, more recent work has revealed that a group of adaptor proteins enhance the interaction between dynein and dynactin to convert dynein into a fully active motor that moves processively along microtubules (McKenney et al., 2014; Schlager, Hoang, et al., 2014). The formation of a dynein–dynactin-adaptor complex reorients dynein such that the motor domains are oriented parallel to each other to facilitate directional stepping along the microtubule (Fig. 1.3C) (K. Zhang et al., 2017). Some dynein adaptors further increase the motility of dynein-dynactin by recruiting a second dynein dimer to dynactin, increasing the force production and velocity for a single motor complex (Chaaban & Carter, 2022; Grotjahn et al., 2018; Urnavicius et al., 2018).

The proteins that bridge dynein-dynactin to activate motility are known as activating adaptors. In addition to activating dynein motility, activating adaptors link dynein-dynactin to diverse cellular cargoes, allowing for specific activation of dynein on certain cellular structures (Olenick & Holzbaur, 2019; Reck-Peterson et al., 2018). The list of verified activating adaptors includes a set of evolutionarily distinct proteins that does not contain any single sequence common to all adaptors. However, the one common feature present across activating adaptors is a stretch of coiled-coil. Structural work on BICD2, BICDR1, and HOOK3 has revealed that each adaptor contains a long coiled-coil segment that extends along the length of dynactin's Arp1 filament and binds the dynein tails to stabilize the interaction between dynein and dynactin (Chaaban & Carter, 2022; Chowdhury et al., 2015; Urnavicius et al., 2015). All verified dynein activating adaptors, with two exceptions, are predicted to contain an extended coiled-coil that is sufficient to span dynactin in this manner (Olenick & Holzbaur, 2019; Reck-Peterson et al., 2018). Thus, the presence of a long coiled-coil is a hallmark feature used to identify candidate activating adaptors. The exceptions to this rule are JIP3 and JIP4, two closely related motor adaptors that facilitate the trafficking of lysosomes and autophagosomes in neurons (Cason et al., 2021; Cason & Holzbaur, 2023; Gowrishankar et al., 2017). Recent work has demonstrated that JIP3 and JIP4 are able to activate dynein motility *in vitro* despite having a much shorter coiled-coil that is not sufficient to span dynactin (Cason & Holzbaur, 2023; X. Fu et al., 2022; K. Singh et al., 2023). In fact, a short fragment of JIP3 that includes only the N-terminus and short coiled-

coil makes nearly no contact with dynactin, yet activates dynein motility (K. Singh et al., 2023). This JIP3 fragment still stabilizes the dynein heavy chain tails along dynactin's Arp1 filament, suggesting that the coiled-coil within activating adaptors primarily serves to orient dynein along dynactin.

Activating adaptors also contain binding sites for the flexible C-terminal helix of dynein light intermediate chain 1 (LIC1) and for dynactin's pointed end. These interaction interfaces are generally positioned with the LIC1 contact at the beginning of the coiled-coil and the pointed end contact at the end of the coiled-coil (Olenick & Holzbaur, 2019; Reck-Peterson et al., 2018). Different activating adaptors bind to LIC1 using distinct domains that have been classified into four subfamilies: the coiled-coil 1 box (CC1-Box), EF-hand, HOOK domain, and RILP Homology 1 (RH1) domain (Celestino et al., 2019, 2022; I.-G. Lee et al., 2018, 2020; K. Singh et al., 2023). For all four subfamilies, mutations in the LIC1-adaptor interface are sufficient to prevent dynein activation *in vitro* and disrupt adaptor function within cells, demonstrating the importance of this interaction. The Spindly motif is a short sequence (LΦXEΦ, where Φ is hydrophobic) that is present in nearly all activating adaptors and binds along the p25 subunit of dynactin's pointed end (Chaaban & Carter, 2022; Gama et al., 2017; K. Singh et al., 2023). Mutation of the Spindly motif disrupts the adaptor-dynactin interaction to impair adaptor function in cells (Gama et al., 2017). The Spindly motif also appears to be important for orienting activating adaptors along dynactin to efficiently place the adaptor's cargo-binding region in an optimal location for binding cargo, as seen for dynein-dynactin-JIP3 complexes (K. Singh et al., 2023).

II. Mitochondrial dynamics

Mitochondria are highly abundant double-membraned organelles that perform dozens of essential functions within eukaryotic cells (J. R. Friedman & Nunnari, 2014; Monzel et al., 2023). Typical mitochondria are comprised of an outer mitochondrial membrane (OMM), inner mitochondrial membrane (IMM), intermembrane space, and matrix within the IMM. The IMM forms many inward invaginations, termed cristae, which provide the optimal IMS geometry for electron transport chain complexes to produce energy

through oxidative phosphorylation. The mitochondrial matrix contains many components, such as mitochondrial ribosomes, mitochondrial DNA, and many metabolic enzymes.

The mitochondrial network morphologically adapts to fit cellular needs and changes in response to diverse cellular pathways, such as metabolism, intracellular calcium signaling, apoptosis, and mitosis. Despite the diversity of contexts that alter mitochondrial dynamics, the resultant effects on the mitochondrial network are largely dependent on a few processes. Fission, the division of a single mitochondrion into two mitochondria by cleavage of the OMM and IMM, and fusion, the joining of the OMM and IMM from two distinct mitochondria, are in equilibrium to determine network connectivity. Mitochondrial transport is mediated by the cytoskeleton and determines the intracellular placement of mitochondria. This section reviews recent work regarding the mechanisms and regulation of mitochondrial fission, fusion, and transport.

Mitochondrial fission

The key events of mitochondrial fission are constriction and scission of both the OMM and IMM. In most, if not all cases, outer membrane constriction is driven by dynamin-related protein 1 (DRP1), a GTPase that dynamically associates with the endoplasmic reticulum (ER) and mitochondria (Fig. 1.4A) (W. Ji et al., 2015; W.-K. Ji et al., 2017). DRP1 is recruited to mitochondria via interactions with receptors in the OMM: mitochondrial fission factor (MFF) and mitochondrial dynamics proteins 49 and 51 (MID49/51) (Osellame et al., 2016; Otera et al., 2010; Palmer et al., 2013; Yu et al., 2017). Some DRP1 is transferred to the OMM following MFF-dependent oligomerization on the ER; this transfer likely occurs at mitochondria-ER contact sites, which mark sites of mitochondrial division (Fig. 1.4B) (J. R. Friedman et al., 2011; W.-K. Ji et al., 2017). DRP1-dependent fission at mitochondria-ER contacts is facilitated by actin assembly, as inhibiting actin polymerization reduces fission frequency and DRP1 recruitment to mitochondria (De Vos et al., 2005; W. Ji et al., 2015; W.-K. Ji et al., 2017; Korobova et al., 2013). Actin assembly at mitochondria-ER contacts depends on two actin nucleating proteins, the formin INF2 and Spire1C, which reside on the ER and

mitochondria, respectively. These proteins interact to promote actin assembly and mitochondrial constriction (Fig. 1.4B) (Korobova et al., 2013; Manor et al., 2015). Actin filaments locally assemble in a wave-like manner around mitochondrial subpopulations to induce fission (Moore et al., 2016). Following actin disassembly, these mitochondrial subpopulations undergo fusion to locally remodel the mitochondrial network.

Recent advances in electron microscopy have revealed the three-dimensional ultrastructure of the actin cytoskeleton during mitochondrial constriction. Yang and Svitkina (2019) found dense arrays of filamentous actin with criss-cross orientation at mitochondrial constrictions (C. Yang & Svitkina, 2019). Many of these actin filaments extend from the nearby ER. This study also examined the positioning of non-muscle myosin II (NMII), as this motor has been implicated along with actin and INF2 in fission (W. Ji et al., 2015; Korobova et al., 2014). NMII is located near mitochondrial constrictions, primarily along the interstitial actin network (Fig. 1.4B-C), and is proposed to pull on the interstitial actin network to deform mitochondria upstream of DRP1, consistent with findings that NMII promotes DRP1 recruitment to mitochondria (Korobova et al., 2014).

Once recruited, DRP1 oligomerizes to wrap around the outer membrane (Fig. 1.5C). Upon GTP hydrolysis, DRP1 changes conformation, dissociating MID49/51 to shrink the oligomeric ring (Fig. 1.5D) (Kalia et al., 2018). While the DRP1 ring constricts the OMM, there is debate as to whether DRP1 carries out membrane scission. Initial studies found no evidence that DRP1 could drive membrane scission. Dynamin-2 (DNM2), another dynamin GTPase, was found at fission sites following DRP1 recruitment; DNM2 knockdown was also found to inhibit mitochondrial fission (J. E. Lee et al., 2016). However, several recent studies implicate DRP1 as the protein responsible for membrane scission. Fibroblasts lacking DNM2 or all three dynamin proteins display normal mitochondrial division, suggesting dynamins 1-3 are dispensable for fission (Fonseca et al., 2019; Kamerkar et al., 2018); in contrast, DRP1 is required for fission (De Vos et al., 2005; Fonseca et al., 2019; Kamerkar et al., 2018). Further, purified DRP1 can induce the fission of membrane tubules up to 250 nm in radius (Kamerkar et al., 2018). While these results

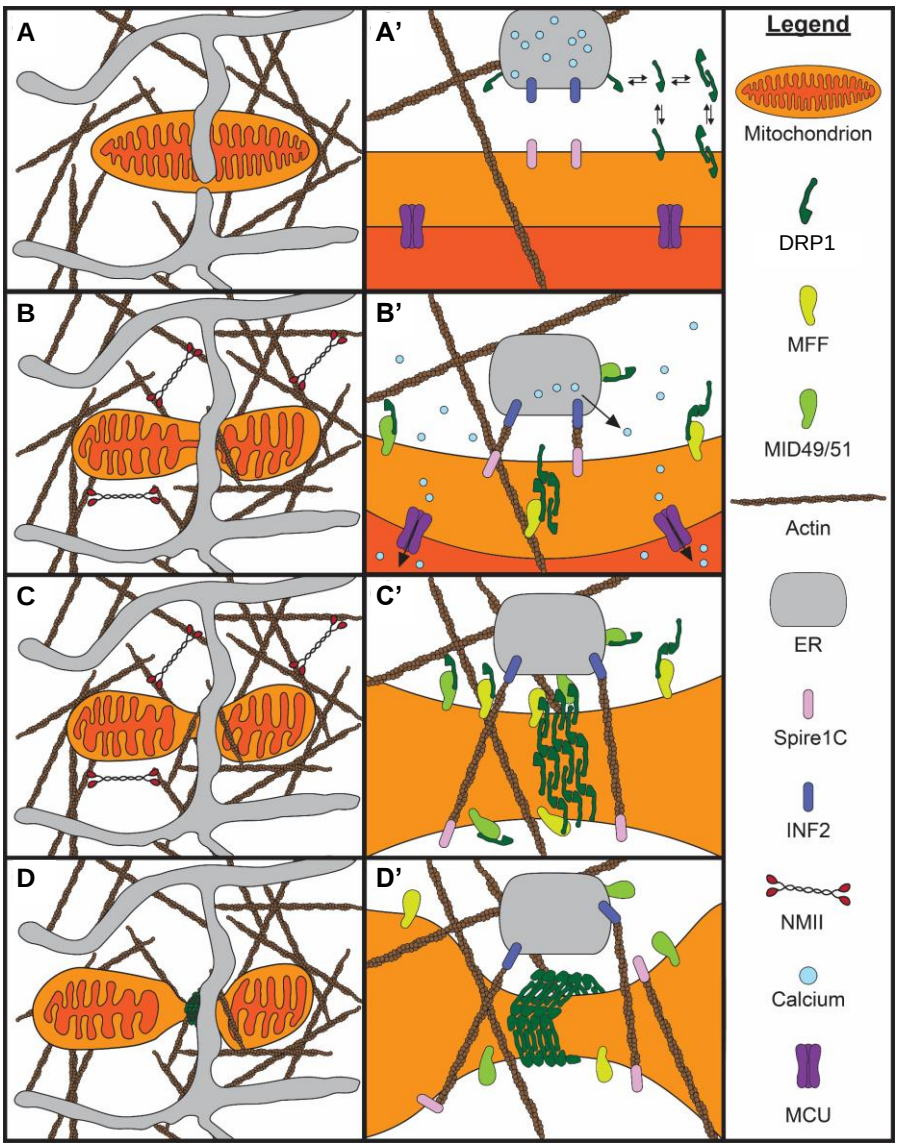

Figure 1.4: Mechanism of mitochondrial fission. (A) A mitochondrion is embedded in the interstitial actin network and closely associated with the ER. A closer view of the mitochondria–ER contact is shown in **(A')**. DRP1 dynamically associates with the cytosol, mitochondria, and ER before fission. **(B)** Peripheral NMII pulls on actin filaments to deform the mitochondrial membrane. Increased cytosolic calcium induces actin polymerization at mitochondria–ER contacts by INF2 on the ER and Spire1C on mitochondria. MFF and Mid49/51 begin recruiting DRP1 to the mitochondria–ER contact. Calcium is released from the ER and enters the mitochondria through the MCU, causing IMM constriction. **(C)** Elevated mitochondrial matrix calcium causes IMM division before OMM division. MFF and Mid49/51 continue recruiting DRP1 to the mitochondria–ER contact, with some DRP1 coming from the ER. DRP1 oligomerizes along the constricted OMM. **(D)** The DRP1 oligomer fully assembles around the OMM. DRP1 GTP hydrolysis dissociates Mid49/51, constricting the DRP1 ring. The DRP1 ring constricts the OMM and completes the process of fission. Abbreviations: ER, endoplasmic reticulum; IMM, inner mitochondrial membrane; OMM, outer mitochondrial membrane; MCU, mitochondrial calcium uniporter; MFF, mitochondrial fission factor; NMII, non-muscle myosin II.

implicate DRP1 as the protein responsible for scission, more work is required to confirm whether DRP1 drives the final step in fission.

Whereas outer membrane scission depends on DRP1 oligomerization and GTP hydrolysis, the mechanism of inner membrane scission is less clear. Recent studies have shown that the IMM constricts and divides at mitochondria-ER contacts prior to DRP1-dependent OMM fission (Chakrabarti et al., 2018; Cho et al., 2017). IMM constriction depends on INF2-mediated actin polymerization and NMII, similar to outer membrane constriction. Actin assembly at mitochondria-ER contacts stimulates calcium release from the ER and subsequent mitochondrial uptake through the mitochondrial calcium uniporter (MCU; Fig. 1.4B) (Chakrabarti et al., 2018). Elevated mitochondrial calcium then stimulates IMM constriction in a DRP1-independent manner, but the subsequent mechanism of IMM scission is a black box.

While it is clear that mitochondrial fission is largely coordinated by the ER, several other factors determine sites of fission. Fission relies on the dynamic recruitment of lysosomes and the lysosomal GTPase RAB7. GTP-bound RAB7 is recruited to mitochondria by the mitochondrial fission protein 1 (Fis1), an OMM protein with two tetratricopeptide repeat domains exposed to the cytosol (Suzuki et al., 2003). Once recruited, GTP-bound RAB7 promotes mitochondria-lysosome contact formation (Y. C. Wong et al., 2018). Mitochondria-lysosome contacts restrict mitochondrial motility, regulate inter-mitochondrial tethering, and mark sites of fission (Y. C. Wong et al., 2019). Fission is also modulated by the dynamic recruitment of the trans-Golgi network (TGN). The small GTPase ADP-ribosylation factor 1 (Arf1) and its effector, phosphatidylinositol 4-kinase-III-b [PI(4)KIIIb] are recruited to fission sites on TGN vesicles after DRP1 recruitment (Nagashima et al., 2020). Loss of Arf1 or PI(4)KIIIb produces a hyperfused and branched network, suggesting these proteins affect mitochondrial branching in addition to fission. Intriguingly, TGN vesicles converged with lysosomes and ER at fission sites. Each of these organelles is present at most, but not all mitochondrial fission sites. Further analysis of the temporal and spatial dynamics of these organelles and their effector proteins is necessary to understand how they are coordinated to promote fission.

Recently, it has become clear that there are two distinct types of mitochondrial fission with different mechanisms and outcomes. Some mitochondrial fission events occur at near the middle of the organelle; these “midzone” fission events occur in healthy mitochondria and frequently coincide with replication of mitochondrial DNA (Kleele et al., 2021). MFF, DRP1, actin, and the ER all coincide at midzone fission events to facilitate the even division of contents between the two daughter mitochondria. In contrast, other mitochondrial fission events occur near the tip of the organelle to produce a small mitochondrial fragment. Peripheral fission events occur within damaged mitochondria that have developed a loss of membrane potential and increase in levels of reactive oxygen species (Kleele et al., 2021). Peripheral fission events also require DRP1, but involve FIS1 and lysosomal contacts at the fission site, with minimal accumulation of MFF or contact with the ER (Kleele et al., 2021). The demonstration of multiple types of fission indicates that fission is more nuanced than previously anticipated. Given the large number of regulatory factors involved in fission, it will be interesting to examine possible variations on these mechanisms and determine further nuances in the multiple pathways that regulate mitochondrial fission.

Mitochondrial fusion

Mitochondrial fusion is mediated by the dynamin family GTPases mitofusin 1 (Mfn1), mitofusin 2 (Mfn2), and Opa1. Fusion begins with Mfn1/2-mediated OMM tethering and merging followed by Opa1-mediated joining of the IMM (Fig. 1.5A) (Cipolat et al., 2004; N. Ishihara, 2004). Opa1 has two isoforms: a long isoform (L-Opa1) containing a transmembrane domain, and a short isoform (S-Opa1) lacking the transmembrane domain. S-Opa1 is produced via proteolytic cleavage of L-Opa1 by one of two proteases, Yme1L or Oma1 (Mishra et al., 2014). Yme1L knockdown produces a fragmented mitochondrial network, suggesting that Opa1 processing promotes fusion (Mishra et al., 2014). A separate study found that L-Opa1 was sufficient for fusion in cells lacking Yme1L and Oma1; conversely, S-Opa1 overexpression in these cells resulted in mitochondrial fragmentation (Anand et al., 2014). These contrasting results raised the question of whether Opa1 processing promotes fission or fusion. Two recent studies used *in vitro*

membrane fusion assays to gain mechanistic insight into Opa1-mediated fusion (Ban et al., 2017; Ge et al., 2020). Both studies tested the sufficiency of Opa1 to facilitate membrane fusion of liposomes. In these assays, L-Opa1 is sufficient to drive fusion through a heterotypic interaction with cardiolipin (CL), a mitochondrial phospholipid, whereas S-Opa1 is unable to drive fusion (Ban et al., 2017; Ge et al., 2020). However, these studies found that S-Opa1 and L-Opa1 work synergistically to catalyze fusion. Ge *et al.* (2020) show that fusion efficiency peaks at an equimolar ratio of S-Opa1 to L-Opa1 (Fig. 1.6B) (Ge et al., 2020). Thus, Opa1 processing tightly regulates fusion, with insufficient or excess processing inhibiting fusion.

Additional insight into the control of fusion has come from reexamination of Fis1 and mitochondria-ER contact sites. Mammalian Fis1 was initially thought to promote fission since its yeast homolog recruits DRP1 to mitochondria and because Fis1 overexpression induces mitochondrial fragmentation (Yoon et al., 2003). However, human Fis1 does not function through DRP1 and is dispensable for fission (Osellame et al., 2016; Otera et al., 2010; Palmer et al., 2013). Fis1 has recently been shown to inhibit the activity of the fusion GTPases Opa1 and Mfn1/2 (Yu et al., 2019), suggesting that fusion inhibition is sufficient to fragment the mitochondrial network, mirroring fission activation (Fig. 1.5C). Mitochondrial fusion also occurs at mitochondria-ER contact sites, similar to fission (Abrisch et al., 2020; Y. Guo et al., 2018; Y. C. Wong et al., 2019). Fission and fusion proteins colocalize at mitochondria-ER contacts to form hotspots for membrane dynamics (Abrisch et al., 2020); these ER-associated dynamics also include contact untethering between mitochondria (Y. C. Wong et al., 2019). Thus, the ER regulates multiple aspects of mitochondrial dynamics at contact sites. The next challenge is to determine how these separate machineries are coordinated to promote a single process.

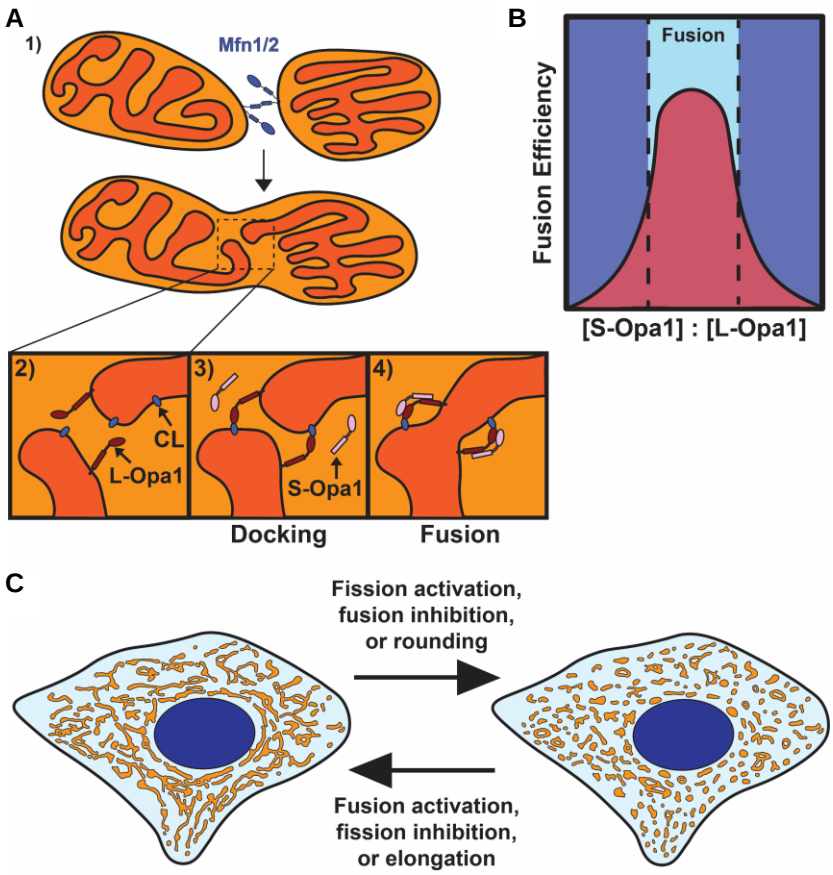

Figure 1.5: Mechanism and regulation of mitochondrial fusion. (A) The proposed model of mitochondrial fusion. 1) Mitochondrial fusion begins with Mfn1/2-mediated tethering of two mitochondrial outer membranes. 2) The inner membranes are positioned for fusion upon outer membrane fusion. 3) Interactions between L-Opa1 and CL dock the inner membranes, bringing them closer together. 4) S-Opa1 functions with L-Opa1 and CL to promote efficient inner membrane fusion. **(B)** Fusion efficiency at different S-Opa1:L-Opa1 ratios. Fusion efficiency peaks at an equimolar ratio of S-Opa1 to L-Opa1, with higher and lower ratios inhibiting fusion. **(C)** A diagram of a connected mitochondrial network (left) and fragmented mitochondrial network (right). The transition between these networks can occur through direct regulation of fission, fusion, or mitochondrial shape transition. Abbreviations: CL, cardiolipin.

Mitochondrial transport

Mitochondrial network morphology is also controlled by many additional interactions with the cytoskeleton. Mitochondrial transport is critical in highly polarized cells, such as neurons, where mitochondria undergo long-distance transport along the microtubule cytoskeleton (Misgeld & Schwarz, 2017). Most mitochondrial transport is microtubule-based, with transport toward the microtubule plus-end

mediated by kinesin-1 and transport toward the minus-end mediated by dynein and its partner complex, dynactin (Pilling et al., 2006; van Spronsen et al., 2013). In the canonical model of mitochondrial transport, these opposing motors are tethered to mitochondria through the TRAK/MIRO motor adaptor complex, which play a central role in the regulation of microtubule-based mitochondrial dynamics (Fig. 1.6).

Mammals contain two TRAK (trafficking and kinesin-binding) proteins, TRAK1 and TRAK2, which are orthologs of the *Drosophila* protein Milton. Milton was discovered in a screen for mutations that affect photoreceptor neurotransmission in *Drosophila* eyes (Stowers et al., 2002). Characterization of Milton mutant neurons revealed a lack of mitochondria at synapses and along the length of axons (Glater et al., 2006; Stowers et al., 2002). These studies further demonstrated that Milton binds kinesin-1 and recruits this motor to mitochondria, indicating that Milton facilitates anterograde mitochondrial transport by serving as an adaptor for kinesin-1 (Glater et al., 2006; Stowers et al., 2002). Similar to Milton, TRAK proteins are required for mitochondrial transport in a variety of mammalian cell types, including neurons (Loss & Stephenson, 2017; van Spronsen et al., 2013). In some cases, mitochondrial organization in neurons is dependent on isoform-specific functions of TRAK1 and TRAK2. Within rat hippocampal neurons, TRAK1 predominantly localizes to the axon and is required for anterograde mitochondrial motility into the axon while TRAK2 localizes more prominently to dendrites and is required for dendritic mitochondrial motility (van Spronsen et al., 2013). However, the extent of this compartment-specific phenotype decreased as neurons aged in culture, and this phenotype was not observed in rat cortical neurons, suggesting that the relative contribution of each TRAK to mitochondrial motility in the axon and dendrite is modulated in an age- and cell-type-dependent manner (Loss & Stephenson, 2017).

The importance of MIRO (Mitochondrial Rho GTPase) proteins for mitochondrial transport and neuronal homeostasis has been demonstrated in both *Drosophila* and mammalian neurons. MIRO was similarly identified in a *Drosophila* screen as a factor necessary for anterograde transport of mitochondria to synapses (X. Guo et al., 2005). *Drosophila* MIRO was shown to facilitate the recruitment of Milton to mitochondria leading to the model that MIRO proteins serve as essential receptors for Milton, which recruits microtubule motors enable mitochondrial transport in neurons (X. Guo et al., 2005). Further work on

mammalian MIRO proteins, MIRO1 and MIRO2 confirmed their role in promoting axonal and dendritic mitochondrial transport and demonstrated a similar role in the recruitment of TRAK proteins to mitochondria (Babic et al., 2015; MacAskill, Brickley, et al., 2009; Nguyen et al., 2014). However, MIRO knockout studies in mice revealed differences between MIRO1 and MIRO2, despite their high similarity. MIRO1 knockout is postnatally lethal in mice and conditional MIRO1 knockout causes neuronal degeneration, whereas knockout of MIRO2 has no obvious effects on viability or mitochondrial transport in neurons, suggesting that MIRO1 is the primary isoform responsible for mitochondrial transport in neurons (López-Doménech et al., 2016; Nguyen et al., 2014).

MIRO proteins are comprised of two Ca^{2+}-binding EF-hand domains, two GTPase domains, and a C-terminal transmembrane domain that localizes to the mitochondrial outer membrane (Birsa et al., 2013; X. Guo et al., 2005). The EF-hand domains of MIRO1 have been implicated in the regulation of mitochondrial transport, as local increases in Ca^{2+} concentrations halt mitochondrial transport in axons, but this phenomenon can be blocked by mutating the EF-hands of MIRO1. However, the role of MIRO1 in calcium-dependent mitochondrial arrest is not understood due to conflicting reports about the effects of Ca^{2+} on the interactions of MIRO1 with kinesin-1 and TRAK1 (Chang et al., 2011; MacAskill, Rinholm, et al., 2009; X. Wang & Schwarz, 2009). Other studies have suggested that mitochondrial trafficking can be modulated through the nucleotide state of the N-terminal GTPase of MIRO1. Unfortunately, the data as to whether GTP binding is important for the TRAK-MIRO interaction are conflicting, so there is no consensus mechanism from these studies (Babic et al., 2015; Davis et al., 2023; Fransson et al., 2006; MacAskill, Brickley, et al., 2009). Thus, further work is required to understand the sensitivity of MIRO1 and MIRO2 to changes in Ca^{2+} and nucleotide levels and how these factors influence the assembly of mitochondrial motor complexes.

Motors, TRAKs and MIRO proteins are required for mitochondrial transport, but the functional interactions among these components remain largely untested, and the molecular basis by which opposing kinesin and dynein motors are coordinated to produce directional transport of mitochondria is not understood. TRAK proteins bind to kinesin-1 and dynein/dynactin through an ~400 amino-acid region in

their N-terminus (Randall et al., 2013; M. J. Smith et al., 2006; van Spronsen et al., 2013). This motor-binding region contains a long stretch of predicted coiled-coil, as well as a CC1-Box and Spindly motif, all of which are common features present in known dynein activating adaptors. Thus, TRAKs were predicted to function as dynein activating adaptors, but this possibility was untested prior to the work presented in this thesis (Olenick & Holzbaur, 2019; Reck-Peterson et al., 2018). *In vitro* motility experiments with purified proteins have demonstrated that TRAK1 activates kinesin-1 for processive transport along microtubules (Henrichs et al., 2020). TRAK1 activates kinesin-1 independent of KLC, which is consistent with findings that *Drosophila* Milton does not recruit KLC to mitochondria (Glater et al., 2006). The high similarity and overlapping functions of TRAK1 and TRAK2 raises the question of whether TRAK2 similarly activates kinesin-1.

Motor regulation may also be adaptor-specific. For instance, TRAK2 has been proposed to predominantly interact with dynein-dynactin whereas TRAK1 interacts with both kinesin-1 and dynein-dynactin (van Spronsen et al., 2013). TRAK1 overexpression promotes plus-end directed mitochondrial transport in mouse embryonic fibroblasts (MEFs) while TRAK2 overexpression promotes minus-end directed mitochondrial transport. However, TRAK2 requires MIRO1, but not MIRO2, to promote dynein-dependent transport (López-Doménech et al., 2018). Combined, these results suggest that the direction of mitochondrial transport is determined by specific associations between TRAK and MIRO isoforms. Further studies are required to determine how individual TRAK and MIRO proteins interact with microtubule motors to selectively promote transport toward either microtubule end.

A recent study found that TRAKs localize to mitochondria and drive transport in MEFs lacking MIRO1 and MIRO2 (López-Doménech et al., 2018). While transport is reduced in MIRO1/2 knockout cells, this finding suggests that TRAKs can function independently of MIRO. Since TRAKs interact with other OMM proteins, such as MFN1 (C. A. Lee et al., 2018; Misko et al., 2010), another OMM protein may function as an alternate adaptor for TRAK1/2. MIRO proteins also serve as adaptors for myosin XIX (MYO19), a mitochondria-associated myosin motor, though MYO19 can also associate with the OMM independent of MIRO (Fig. 1.6) (Bocanegra et al., 2020; López-Doménech et al., 2018; Oeding et al., 2018). MYO19

overexpression increases mitochondrial motility in an actin-dependent manner (Quintero et al., 2009). Furthermore, TRAK overexpression reduces the association of MYO19 with mitochondria (Oeding et al., 2018), suggesting that MYO19 and TRAKs compete for MIRO binding to induce actin- or microtubule-based mitochondrial motility. Given the nature of MIRO proteins, it will be interesting to see how calcium binding and GTP hydrolysis affect the interaction of MIRO with TRAKs and MYO19.

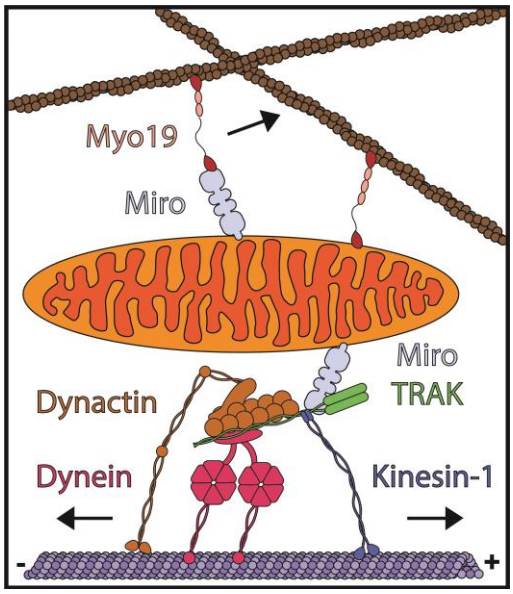

Figure 1.6: Mitochondrial transport on the cytoskeleton. TRAK and Miro proteins serve as adaptors for microtubule-based mitochondrial transport. Kinesin-1 drives transport to the microtubule plus-end while transport to the microtubule minus-end is mediated by dynein/dynactin. Myo19 associates with Miro proteins and directly with the mitochondrial outer membrane to drive mitochondrial transport along the actin cytoskeleton.

III. Mitochondria and microtubule motors defects in neurological disease

As our understanding of the molecular underpinnings of neuronal organization has grown, so has our understanding of the pathophysiology of neurological disease. The links between mechanistic neurobiology and neuropathology have largely been founded in human genetic studies and the identification of disease-

causing genetic variants (Claussnitzer et al., 2020). Many of the mutations that cause neurodegenerative and neurodevelopmental disease in humans are found in genes encoding proteins that drive transport along microtubules or mitochondrial dynamics. These genotype-phenotype relationships are further strengthened by observations of mitochondrial dysfunction in animal models of neurological disease and by evidence that disruption of mitochondrial dynamics or microtubule-based transport is sufficient to induce neuronal dysfunction and neurodegeneration. In fact, the connections between microtubule motors, mitochondrial dynamics, and neurological disease are too numerous to comprehensively cover here. For more thorough overviews of these topics, see the following reviews (Berth & Lloyd, 2023; Chevalier-Larsen & Holzbaur, 2006; Ortiz-González, 2021). Instead, the remainder of this chapter focuses on genotype-phenotype links connecting ALS to microtubule motor dysfunction and Fragile X Syndrome to mitochondrial network dysfunction.

Microtubule motors and ALS

Amyotrophic Lateral Sclerosis (ALS) is a neurodegenerative disease that is characterized by progressive degeneration of the motor cortex and motor neurons in the brainstem and spinal cord (Hardiman et al., 2017). As these neurons deteriorate, affected individuals experience muscle wasting, weakness, and paralysis; muscle atrophy occurs rapidly, frequently leading to death only a few years after symptom onset (Taylor et al., 2016). The onset of ALS can vary largely, but typically manifests between 50 and 65 years of age (Hardiman et al., 2017).

ALS is a complex disease with many genetic, environmental, and age-related factors. Approximately 10% of all ALS cases are transmitted through families, while the other ~90% of cases arise sporadically (Amin et al., 2020). Modern advances in genome sequencing have helped dissect the genetic etiology of both sporadic and familial ALS. Now, mutations in over 50 genes have been linked to ALS (Renton et al., 2014; Taylor et al., 2016). Many of these ALS-associated genes are related to similar biological pathways, suggesting that dysfunction of these pathways contributes to disease pathogenesis.

One major pathway that has been implicated in the pathophysiology of ALS is microtubule-based transport. There are two ALS-associated genes related to microtubule motor proteins: *DCTN1*, which encodes the p150^{Glued} subunit of dynactin, and *KIF5A*, a gene encoding one of the three kinesin-1 isoforms.

A single point mutation in *DCTN1* causes familial ALS and results in an amino acid substitution in the CAP-Gly domain of p150^{Glued} (Puls et al., 2003). This mutation disrupts the ability of the CAP-Gly domain to bind microtubules, reduces the association of dynactin with dynein, and impairs dynein-mediated transport throughout axons (Moughamian & Holzbaur, 2012; Puls et al., 2003). Of note, other nearby mutations in the p150^{Glued} CAP-Gly domain are associated with Perry syndrome, a distinct adult-onset neurodegenerative disease (Farrer et al., 2009). Perry syndrome mutations have a slightly different effect in neurons, where they specifically disrupt the initiation of retrograde transport in the distal axon (Moughamian & Holzbaur, 2012). Furthermore, targeted disruption of the dynactin complex is sufficient to disrupt retrograde axonal transport and induce late-onset progressive degeneration in mouse motor neurons (LaMonte et al., 2002). Together, these studies suggest that disruption of dynein-mediated axonal transport is involved in the pathogenesis of ALS and other forms of neurodegenerative disease.

Of the kinesin-1 isoforms, mutations in KIF5A are most frequently associated with disease, with over 90 reported mutations (Carrington et al., 2024). Mutations in KIF5A are causative for familial ALS, but are also associated with two other neurodegenerative diseases: HSP and CMT2 (Crimella et al., 2012; Y.-T. Liu et al., 2014; Nicolas et al., 2018). Interestingly, the vast majority of KIF5A mutations associated with HSP and CMT occur in the motor domain while ALS-associated mutations are more frequently present in the tail domain, suggesting a correlation between molecular function and disease pathogenesis. Very few mutations in KIF5B have been reported, and none seem to be linked to neurological disease. However, several mutations in KIF5C are associated with neurodevelopmental defects, including malformations of cortical development and microcephaly (Poirier et al., 2013). Ultimately, a more thorough characterization of the effects of each disease-associated KIF5 mutation on motor function and cellular homeostasis is needed to understand how and why these mutations manifest as a variety of neurological diseases.

Mitochondrial defects and Fragile X Syndrome

Fragile X Syndrome (FXS) is a severe neurodevelopmental disorder that has a variety of manifestations in humans. Typically, FXS is associated with intellectual disability, memory impairment, and autistic features, although severe cases also include increased risk of epileptic seizures (Hagerman et al., 2009). FXS is a dominant X-linked disorder and the most common genetic cause of intellectual impairment in humans (Crawford et al., 2001). The *fragile X messenger ribonucleoprotein 1* (*FMR1*) gene is the single causal gene in FXS (Pieretti et al., 1991; Verkerk et al., 1991). The majority of FXS cases are caused by a CGG-trinucleotide repeat expansion in the 5′ untranslated region of the *FMR1* gene, which results in transcriptional silencing of the gene locus (Pieretti et al., 1991; Verkerk et al., 1991). In general, the clinical severity of intellectual impairment in FXS correlates closely with the magnitude of the repeat expansion, and expression of the *FMR1* gene (Kaufmann et al., 1999). However, Fragile X Syndrome can also be caused by intragenic deletions, nonsense, and mis-sense mutations in the *FMR1* gene, indicating that FXS is primarily caused by a loss of function of the protein product of *FMR1*, termed the Fragile X Mesenger Ribonucleoprotein (FMRP) (De Boulle et al., 1993; Grønskov et al., 2011; Quan et al., 1995).

FMRP is an RNA-binding protein that is highly expressed in the nervous system, where it plays critical roles in RNA organization and translational control (Richter & Zhao, 2021). FMRP associates with mRNAs throughout neuronal sub-compartments, including the nucleus, axons, and dendrites, although FMRP is most prominently localized within the cell body and dendrites (Antar et al., 2005, 2006; Y. Feng et al., 1997). Further, FMRP promotes proper localization of associated mRNAs throughout neurons (Antar et al., 2005; Dictenberg et al., 2008; Goering et al., 2020). FMRP interacts with mRNAs through two heterogeneous nuclear ribonucleoprotein K homology (KH) domains and an arginine–glycine–glycine (RGG) box (Siomi et al., 1993). These domains are thought to facilitate preferential binding to specific RNAs, such as those containing G-quadruplex secondary structure (Brown et al., 2001; Darnell, 2005; Darnell et al., 2001; Goering et al., 2020). This notion of selective mRNA-binding is supported by observations that FMRP has highly variable affinities for different RNAs and that only a small fraction of all RNAs co-immunoprecipitate with FMRP in vitro and in cells (Ashley et al., 1993; Darnell et al., 2011).

However, the number and identity of RNAs that co-immunoprecipitate with FMRP is highly inconsistent across studies, including those with similar experimental setup (Ascano et al., 2012; Ashley et al., 1993; Darnell et al., 2011; Goering et al., 2020; Hale et al., 2021; Miyashiro et al., 2003; Sawicka et al., 2019). The inherent variability of FMRP-RNA interactions suggests that FMRP binding to any single mRNA is contextual and likely depends on the presence of many other cellular factors.

FMRP has also been shown to associate with ribosomes to regulate translation in neurons. Canonically, FMRP inhibits translation by stalling ribosome translocation on a set of target mRNAs, resulting in increased levels of proteins synthesis in brains of animals lacking FMRP (Ceman et al., 2003; Darnell et al., 2011; M. Qin et al., 2005; Shah et al., 2020). In some cases, however, FMRP has been shown to promote translation of select mRNAs (Bechara et al., 2009; Greenblatt & Spradling, 2018; Jung et al., 2023; Sawicka et al., 2019). These conflicting data on the role of FMRP in repressing or activating translation suggest that FMRP has a highly complex regulatory role for translation. FMRP likely modulates translation in a way that differs according to cell type, spatial localization, and cellular activity. Thus, further understanding of FMRP will require dissecting its function in a manner that is both spatiotemporally and pathway specific.

Recent work has demonstrated a close link between FMRP and mitochondrial form and function in many contexts. Our lab previously showed that Drosophila mutants lacking FMRP have a significantly decreased redox ratio for the mitochondrial cofactor nicotinate adenine dinucleotide (NAD+/NADH), increased maximum capacity of the electron transport chain, and reduced levels of carbohydrates and lipids (Weisz et al., 2018). Mitochondria present in the flight muscles of these FMRP mutants were fragmented and irregularly spaced compared to controls (Weisz et al., 2018). Further work examining mitochondria present at synaptic regions in the brains of *Fmr1* knockout (KO) mice demonstrated similar observations of increased respiratory capacity and changes to mitochondrial ultrastructure (Kuzniewska et al., 2020; Licznerski et al., 2020). These mouse studies also found irregularities in the formation of ATP synthase complexes, resulting in a “leak” of protons across the IMM that leads to dysregulation of mitochondrial metabolism in *Fmr1* KO mice (Licznerski et al., 2020). More recent studies have demonstrated that

hippocampal neurons cultured from *Fmr1* KO mice and iPSC-derived neurons from FXS patients both display mitochondrial networks that are shortened and sparse compared to controls (Geng et al., 2023; M. Shen et al., 2019). The commonality of mitochondrial metabolic and morphological phenotypes across multiple cell types and species lacking FMRP suggests that FMRP serves a central role in the regulation of eukaryotic mitochondrial biology.

FMRP regulates mitochondrial homeostasis through the translational control of mRNAs that affect mitochondrial dynamics and function. Multiple mechanisms have been proposed to explain the variety of mitochondrial alterations observed in animal models of Fragile X Syndrome. Specifically, loss of FMRP is proposed to dysregulate the expression of the ATP synthase β-subunit, resulting in a leak in the ATP synthase that accounts for altered mitochondrial respiration (Licznerski et al., 2020). This FMRP-dependent control of ATP synthase is thought to occur by FMRP directly binding the mRNA for the ATP synthase β-subunit (ATP5F1B). FMRP is also thought to regulate the expression of Mitofusin 2 (MFN2), as FMRP-deficient mouse neurons display significantly reduced expression of the *Mfn2* mRNA (M. Shen et al., 2019). This change in the expression of MFN2 is thought to account for the mitochondrial network abnormalities that occur upon loss of FMRP (M. Shen et al., 2019). However, neurons from *Fmr1* KO mice display alterations in the abundance and localization of many nuclear-encoded mitochondrial mRNAs (Jung et al., 2023; M. Shen et al., 2019). *Fmr1* KO mouse neurons also display substantial changes to the mitochondrial proteome in response to neuronal firing (Bülow, Zlatic, et al., 2021). Further, FMRP has been proposed to associate directly with mitochondria, where it plays a role in regulating mitochondria-ER contacts and mitochondrial calcium signaling by directly interacting with the voltage-dependent anion channel (VDAC) (Geng et al., 2023). Despite this extensive evidence for the involvement of FMRP in the regulation of mitochondrial homeostasis, it is still unclear how FMRP precisely directs the transport and translation of RNAs to control the expression of myriad mitochondrial proteins.

IV. Thesis overview

Throughout my thesis work, I examined multiple biological questions central to the regulation of microtubule motors and mitochondrial dynamics in neurons, and their connection to multiple neurological diseases (Fig. 1.7). I investigated the regulation of microtubule-based mitochondrial transport by TRAK-MIRO motor adaptor complexes at multiple levels. First, I studied how TRAK2 functions as a motor adaptor for mitochondrial transport. It was previously unclear whether TRAK2 could activate kinesin-1 and dynein-dynactin, or how TRAK2 could function as an adaptor for two motors that move in opposite directions along microtubules. To address these possibilities, I utilized *in vitro* single-molecule imaging and biochemistry to characterize the functional interactions of TRAK2 with kinesin-1 and dynein-dynactin (Chapter 2). Second, I focused on understanding the interaction between TRAK1 and MIRO1, as this interaction is critical for mitochondrial transport, but had not been precisely characterized. In Chapter 3, I worked with the Dominguez lab to biochemically characterize an interaction between TRAK1 and MIRO1 that facilitates recruitment of TRAK1 to mitochondria.

The later chapters of this work focus on mechanistic links connecting neurological disease to the regulation of microtubule motors and mitochondrial organization. Mutations in KIF5A were previously shown to cause familial ALS, but the effects of these mutations on KIF5A motility and function within cells were not understood. In Chapter 4, I collaborated with the Landers lab to demonstrate how multiple ALS-associated mutations in KIF5A result in the creation of a novel C-terminus that impairs motor autoinhibition and reduces neuronal viability. I also studied multiple relationships between neuronal mitochondrial dynamics and Fragile X Syndrome. In Chapter 5, I worked with other members of the Jongens lab to describe how mitochondrial and behavioral defects in a *Drosophila* model of Fragile X Syndrome share genetic links to insulin signaling. Lastly, I studied the mechanism by which FMRP supports mitochondrial homeostasis in neurons. I specifically focused on the interplay between FMRP granules and mitochondria in neurons, as the relationship between these organelles in not understood. I used advance microscopy techniques in collaboration with the Lakadamyali and Chang labs to demonstrate that that FMRP granules

dynamically interact with neuronal mitochondria to locally guide mitochondrial fission in neurons (Chapter 6). Together, these studies provide multiple new insights into the mechanisms underlying spatiotemporal control of mitochondrial organization in neurons, and show how dysregulation of these precise mechanisms is connected to multiple neurological diseases. I conclude with discussion of additional questions and future directions that stem from these findings.

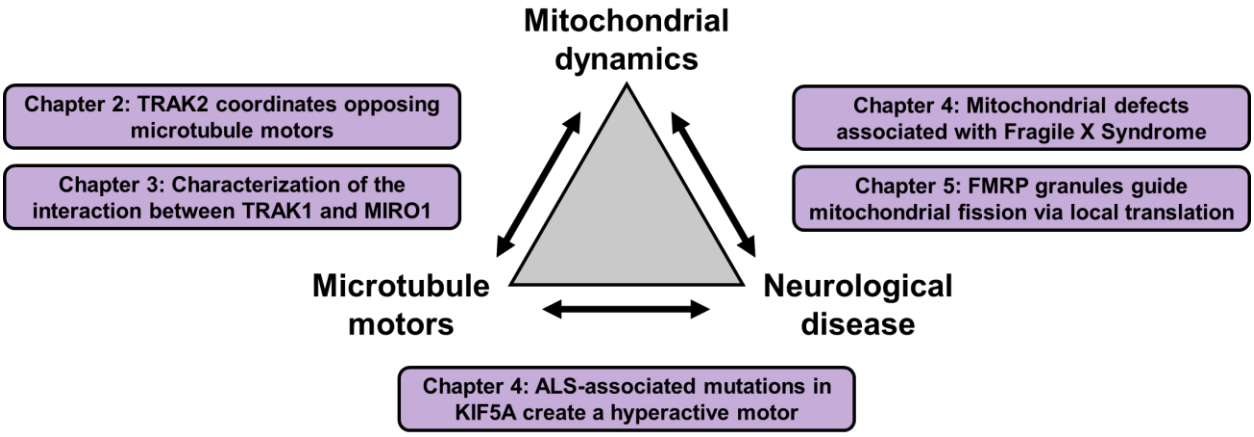

Figure 1.7: Thesis overview. Diagram depicting where each research chapter fits at the intersection of mitochondrial dynamics, microtubule motors, and neurological disease.

CHAPTER 2: MITOCHONDRIAL ADAPTOR TRAK2 ACTIVATES AND FUNCTIONALLY LINKS OPPOSING KINESIN AND DYNEIN MOTORS

This chapter is adapted from:

Fenton, AR; Jongens, TA; Holzbaur, ELF. Mitochondrial adaptor TRAK2 activates and functionally links opposing kinesin and dynein motors. Nature Communications, 12, 4578 (2021).

Contribution: ARF performed all experimental procedures, data analysis, writing, and figure design.

I. Summary

Mitochondria are transported along microtubules by opposing kinesin and dynein motors. Kinesin-1 and dynein-dynactin are linked to mitochondria by TRAK proteins, but it is unclear how TRAKs coordinate these motors. We used single-molecule imaging of cell lysates to show that TRAK2 robustly activates kinesin-1 for transport toward the microtubule plus-end. TRAK2 is also a novel dynein activating adaptor that utilizes a conserved coiled-coil motif to interact with dynein to promote motility toward the microtubule minus-end. However, dynein-mediated TRAK2 transport is minimal unless the dynein-binding protein LIS1 is present at a sufficient level. Using co-immunoprecipitation and co-localization experiments, we demonstrate that TRAK2 forms a complex containing both kinesin-1 and dynein-dynactin. These motors are functionally linked by TRAK2 as knockdown of either kinesin-1 or dynein-dynactin reduces the initiation of TRAK2 transport toward either microtubule end. We propose that TRAK2 coordinates kinesin-1 and dynein-dynactin as an interdependent motor complex, providing integrated control of opposing motors for the proper transport of mitochondria.

II. Introduction

Microtubule motors drive the transport of many organelles within the cell. Cargoes are transported to the microtubule plus-end by kinesin motors or to the microtubule minus-end by cytoplasmic dynein 1 (dynein). Whereas individual motors move unidirectionally along microtubules, many cellular cargoes move bidirectionally. For these cargoes, the activities of bound kinesin and dynein motors must be precisely coordinated to ensure proper transport and localization. Despite progress in understanding motor regulation, the mechanisms coordinating opposing motors for organelle transport remain unclear (Hancock, 2014).

Mitochondria are actively shuttled along the microtubule cytoskeleton to meet local energy needs. This transport is critical in highly extended cells, such as neurons, whose axons can grow to lengths on the meter scale. Within neurons, mitochondria undergo long-range transport to meet local energy demands and maintain neuronal homeostasis (Misgeld & Schwarz, 2017). Loss of mitochondrial transport results in defective neurotransmission and neurodegeneration, highlighting the importance of proper mitochondrial transport for neuronal function (Babic et al., 2015; X. Guo et al., 2005; López-Doménech et al., 2016; G. J. Russo et al., 2009; Stowers et al., 2002). Consistently, defective mitochondrial transport and function are implicated in the pathogenesis of neurological diseases, such as Alzheimer's disease (X. Wang et al., 2010; X.-L. Zhao et al., 2010), Parkinson's disease (X. Wang et al., 2011; Y. C. Wong & Holzbaur, 2015), and Amyotrophic Lateral Sclerosis (Baldwin et al., 2016). In cells, mitochondria exhibit bidirectional motility, in which transport to either the microtubule plus- or minus-end is punctuated by directional switching or periods of stationary docking. Mitochondrial transport to the microtubule plus-end is mediated primarily by the kinesin-1 (KIF5) family of motors whereas transport to the minus-end is mediated by dynein and its partner complex, dynactin (Pilling et al., 2006; van Spronsen et al., 2013). These motor proteins are linked to mitochondria by a conserved complex of motor adaptor proteins. The TRAK/Milton family of proteins act as mitochondrial motor adaptors that connect kinesin-1 and dynein-dynactin to the mitochondrial outer membrane protein Miro (Brickley & Stephenson, 2011; Glater et al., 2006; MacAskill, Brickley, et al., 2009; van Spronsen et al., 2013). This motor-adaptor function is conserved from *Drosophila* Milton to its

mammalian orthologs, TRAK1 and TRAK2. Both TRAK and Miro motor adaptor proteins are essential for proper mitochondrial distribution and transport in neurons (Babic et al., 2015; X. Guo et al., 2005; G. J. Russo et al., 2009; Stowers et al., 2002; van Spronsen et al., 2013).

Despite the essential role for TRAK proteins in mitochondrial transport, little is known about the molecular basis by which TRAKs interact with microtubule motors. Mass spectrometry and coimmunoprecipitation experiments indicate that TRAK1 and TRAK2 interact with kinesin-1 and dynein-dynactin (MacAskill, Rinholm, et al., 2009; Pekkurnaz et al., 2014; M. J. Smith et al., 2006; van Spronsen et al., 2013; X. Wang & Schwarz, 2009). However, endogenous KIF5B shows higher binding to TRAK1 than TRAK2, suggesting that TRAK2 has a weaker interaction with kinesin-1 (van Spronsen et al., 2013). These TRAK-specific interactions with kinesin-1 are thought to account for differences in the localization and function of TRAKs in the axon and dendrites of neurons (van Spronsen et al., 2013). Overexpressed TRAK1 promotes plus-end-directed mitochondrial transport whereas overexpressed TRAK2 promotes minus-end-directed mitochondrial transport in mouse embryonic fibroblasts (López-Doménech et al., 2018). As a result, TRAK2 has been proposed to preferentially promote dynein-mediated transport toward the microtubule minus-end (López-Doménech et al., 2018; van Spronsen et al., 2013).

Activation of mammalian dynein requires dynactin and an activating adaptor (McKenney et al., 2014; Schlager, Hoang, et al., 2014). The formation of a dynein-dynactin-adaptor complex aligns the dynein motor domains for processive transport (K. Zhang et al., 2017). Activating adaptors enhance the stability of the dynein-dynactin complex and allow for cargo-specific recruitment of dynein, enabling cargo transport toward the microtubule minus-end (Olenick & Holzbaur, 2019; Reck-Peterson et al., 2018). Although activating adaptors can vary greatly in structure and function, many activating adaptors have similar interactions with dynein and dynactin. Structural work on dynein-dynactin in complex with BICD2, BICDR1, or HOOK3 showed that each activating adaptor contains an extended coiled-coil domain that binds along the length of dynactin's 37 nm Arp1 filament (Urnavicius et al., 2015, 2018). All verified activating adaptors contain an extended coiled-coil domain that is sufficient to span this distance (Olenick & Holzbaur, 2019). Many of these adaptors have conserved features flanking this coiled-coil domain: a coiled-coil 1 box (CC1-

Box) at the N-terminus and a Spindly motif at the C-terminus. Structural studies on BICD2 and Spindly indicate that the CC1-Box binds to dynein light intermediate chain (LIC1) and the Spindly motif binds to the dynactin pointed end complex (Gama et al., 2017; I.-G. Lee et al., 2020). Both the CC1-Box and Spindly motif are conserved in TRAKs, where they flank a ~300 amino acid region predicted to form two coiled-coil domains (Fig. 2.1A). The conservation of these elements within TRAKs suggests that this coiled-coil region scaffolds the dynein-dynactin complex and thus activates dynein. However, the proposed role of TRAK proteins as dynein activating adaptors has yet to be experimentally validated.

The mechanism by which TRAKs coordinate opposing kinesin and dynein motors for mitochondrial transport has remained a perplexing topic. Previous studies have mapped the binding of kinesin-1 to the N-terminal coiled-coil region of TRAK2 (aa 124-283) (M. J. Smith et al., 2006; van Spronsen et al., 2013). This region lies within the predicted dynein-dynactin interface of TRAK2 (Fig. 2.1A). The overlap of the kinesin-1 and dynein-dynactin interfaces on TRAK2 raises the question of whether these opposing motors can simultaneously bind to TRAK2. Further, investigations of mitochondrial transport in neurons demonstrated that knockdown or inhibition of kinesin-1, dynein, or dynactin individually was sufficient to inhibit mitochondrial motility in both directions, suggesting the activity of one motor is required for the activity of the other (Martin et al., 1999; Moughamian et al., 2013; Pilling et al., 2006; Sainath & Gallo, 2015; van Spronsen et al., 2013). This paradox of motor co-dependence has been a major challenge for understanding the control of bidirectional mitochondrial transport, as the activities of these motors are difficult to uncouple (Hancock, 2014).

In light of these observations, we sought to develop a system to examine the functional interactions of TRAK2 with kinesin-1 and dynein-dynactin. We found that TRAK2 robustly activates kinesin-1 for processive transport toward the microtubule plus-end in single molecule assays using cellular extracts. TRAK2 minimally activates dynein under these same conditions, but expression of exogenous Lissencephaly-1 (LIS1) induces highly processive dynein motility, resulting in significantly more frequent minus-end-directed movement with longer run lengths and higher velocities. Dynein motility is dependent on the conserved CC1-Box dynein adaptor motif within TRAK2, which facilitates an interaction between

TRAK2 and dynein. We used co-immunoprecipitation and co-localization experiments to provide evidence for the formation of a complex containing TRAK2, kinesin-1, and dynein-dynactin. Knockdown studies indicate that TRAK2 initiates transport toward either microtubule end more frequently if the opposing motor is present. Together, these results indicate that kinesin-1 and dynein-dynactin are functionally interdependent when in complex with TRAK2, providing mechanistic insight into the coordinated motility of mitochondria within the cell.

III. Results

TRAK2 activates kinesin-1

To study the functional effects of TRAK2 on kinesin-1 and dynein, we utilized an *in vitro* single-molecule approach using total internal reflection fluorescence (TIRF) microscopy of cell extracts to characterize microtubule-based motility of individual TRAK2-motor complexes (Fig. 2.1B) (Ayloo et al., 2014; I.-G. Lee et al., 2018; Olenick et al., 2016). We expressed Halo-tagged TRAK2 in COS-7 cells and labeled cells with TMR-HaloTag ligand prior to generation of cell lysates; the endogenous kinesin, dynein, and dynactin present in COS-7 lysate allowed us to examine the interaction of Halo-TRAK2 with these proteins. Cell lysates were flowed together with fluorescently labeled tubulin heterodimers into chambers containing immobilized GMPCPP-stabilized microtubule seeds. Chambers were incubated at 37°C to visualize the movement of TRAK2 on dynamic microtubules. Use of dynamic microtubules more closely models the *in vivo* environment, and allows for the direct assessment of transport direction due to the greater growth and catastrophe rates of the microtubule plus-end (Baumbach et al., 2017; Guedes-Dias et al., 2019; Nirschl et al., 2016). We verified our ability to unambiguously identify plus- and minus-end-directed motility in control experiments using either purified KIF5B motor head domain (aa 1-560) or the KIF5C motor head expressed in COS-7 cells, both of which exhibited unidirectional transport toward the microtubule plus-end, while a truncated N-terminal construct of the dynein activator HOOK1 (aa 1-554) expressed in COS-7 cells exhibited unidirectional transport toward the microtubule minus-end (Fig. S2.1).

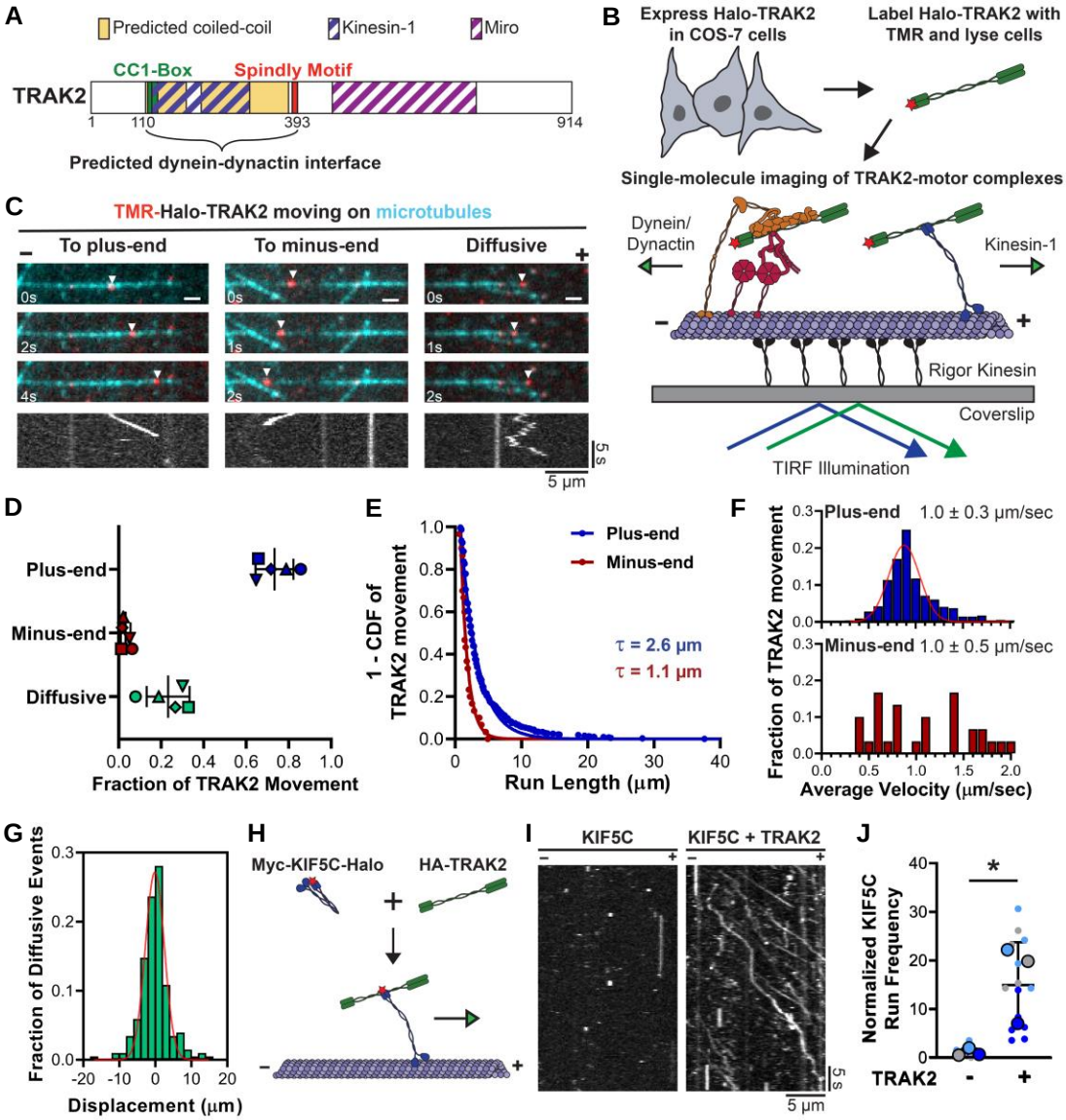

Figure 2.1: TRAK2 activates kinesin-1. A, Diagram of TRAK2 with binding regions for kinesin-1 and Miro, conserved dynein adaptor motifs, and predicted coiled-coil domains. **B,** Schematic depiction of the experimental design with an illustration of TMR labeled Halo-TRAK2 in complex with dynein-dynactin or kinesin-1. **C,** Time series and corresponding kymographs showing single Halo-TRAK2 particles (arrow) moving to the plus end, minus end, and bidirectionally along dynamic microtubules. White scale bars = 2 µm. **D,** Fraction of occurrence for each type of TRAK2 movement. Data points are shaped according to experimental replicate. The center line and bars are the mean ± s.d. from 5 independent experiments. **E-F,** Inverse cumulative distribution functions (CDF) of run length and histogram distributions of velocity for TRAK2 transport to either microtubule end (n = 758 plus-end events and 30 minus-end events). The curves in **(E)** represent a single exponential decay fit, with decay constant indicated above. In **(F)**, the red curve represents Gaussian distribution fit. In **(F)**, the mean ± s.d. is shown. **G,** Distribution of run displacement of TRAK2 diffusive movement (n = 203 events). Negative displacement indicates movement to the microtubule minus-end. The red line represents a Gaussian distribution fit. **H,** Schematic of KIF5C activation experiment. **I,** Representative kymographs showing

activation of KIF5C upon co-expression of TRAK2. **J,** Normalized frequency of KIF5C motility with and without exogenous TRAK2. Data points are color-coded according to experimental replicate, with smaller points representing KIF5C frequency per video. The center line and bars are the mean ± s.d. from 3 independent experiments (n = 14 videos without TRAK2 and 11 videos with TRAK2) *, p = 0.0320 (two-tailed t-test).

Using this system, we observed three distinct kinds of motility for individual TRAK2-motor complexes: unidirectional transport to the microtubule plus-end, unidirectional transport to the microtubule minus-end, and short back-and-forth movements (Fig. 2.1C and Fig. S2.2). Unidirectional TRAK2 transport toward either microtubule end was processive, as determined by the parabolic fit from mean-squared displacement (MSD) analysis of these runs (Fig. S3A, B). These processive movements are consistent with motor-based transport by kinesin-1 and dynein. The majority of TRAK2 movement was toward the microtubule plus-end (Fig. 2.1D and Video S2.1). Plus-end-directed TRAK2 transport was highly processive, with runs up to 38 µm and a mean velocity of 1 µm/s (Fig. 2.1E, F).

TRAK2 transport toward the microtubule minus-end was far less robust than transport toward the plus-end, with only ~3% of TRAK2 runs directed toward the minus-end (Fig. 2.1D). These minus-end-directed runs were short, with no runs greater than 5 µm, and displayed variable velocities up to 2 µm/s (Fig. 2.1E, F). These observations suggest that TRAK2 strongly activates kinesin and minimally activates dynein under the conditions of this assay.

The remaining ~23% of TRAK2 motility was bidirectional and characterized by frequent directional switches. These movements could displace TRAK2 up to 20 µm in either direction, but typically resulted in minor positional changes with no bias toward either microtubule end (Fig. 2.1G). This bidirectional motility is consistent with diffusion of TRAK2 along the microtubule, as shown by the linear fit from MSD analysis of these movements (Fig. S2.3C). Diffusive movements were motor-independent as neither the frequency nor the displacement of these events were affected by knockdown of endogenous KIF5B, dynein heavy chain (DHC), or $p150^{Glued}$ (Fig. S2.3D-G). TRAK1 was recently shown to contain a microtubule-binding domain within its C-terminus that allows for diffusion along microtubules *in vitro* (Henrichs et al., 2020).

Given the high similarity between TRAK1 and TRAK2, the motor-independent diffusion of TRAK2 along microtubules is likely facilitated by a direct interaction between TRAK2 and the microtubule.

Our finding that TRAK2 induces processive transport toward the microtubule plus-end suggests that TRAK2 activates kinesin-1, similar to how TRAK1 activates the kinesin-1 isoform KIF5B for processive transport along microtubules *in vitro* (Henrichs et al., 2020). To directly test if TRAK2 activates kinesin-1 for processive transport toward the microtubule plus-end, we transfected COS-7 cells with Halo- and Myc-tagged KIF5C and HA-tagged TRAK2. We then labeled cells with TMR-HaloTag ligand and performed our single-molecule motility assay on dynamic microtubules in the presence or absence of exogenous HA-TRAK2 (Fig. 2.1H). When expressed alone, KIF5C rarely displayed movement along microtubules, consistent with the autoinhibitory head-to-tail folding of inactive kinesin-1 (Fig. 2.1I) (Verhey & Hammond, 2009). Occasional movements toward the microtubule plus-end were observed, likely due to stochastic activation by endogenous adaptors present at low levels in the lysate (Video S2.2) (M. Fu & Holzbaur, 2013). When TRAK2 was co-expressed, the frequency of KIF5C runs increased by more than 10-fold (Fig. 2.1I-J and Video S2.3). Further, the presence of exogenous TRAK2 promoted longer KIF5C runs toward the microtubule plus-end with slightly increased velocities (Fig. S2.4). Thus, TRAK2 activates kinesin-1 to increase this molecular motor's processivity toward the microtubule plus-end.

LIS1 promotes processive dynein-mediated TRAK2 movement.

Because we rarely observed minus-end-directed TRAK2 transport under the conditions of this assay, we hypothesized that we might be lacking a component necessary for activation of dynein. One candidate regulator is Lissencephaly-1 (LIS1), which binds directly to the dynein motor domain (DeSantis et al., 2017; Htet et al., 2020; Huang et al., 2012). LIS1 has been reported to either antagonize or to activate processive dynein motility (Markus et al., 2020). However, recent studies found that LIS1 enhances dynein activity by stabilizing an open, uninhibited dynein conformation, promoting the assembly of the motile dynein-dynactin-adaptor complex, and favoring the recruitment of a second dynein motor to the same

complex (Elshenawy et al., 2020; Htet et al., 2020; Marzo et al., 2020; Qiu et al., 2019). Recruitment of a second dynein motor increases the velocity and force production of individual dynein-dynactin-adaptor complexes (Elshenawy et al., 2020; Htet et al., 2020; Urnavicius et al., 2018). This activating property of LIS1 is found across dynein-dynactin-adaptor complexes, including both CC1-Box-containing adaptors (BICD2 and BICDR1) and structurally unrelated adaptors (Hook3 and Ninl) (Elshenawy et al., 2020; Htet et al., 2020)., suggesting that LIS1 might similarly activate dynein-dynactin in complex with TRAK2.

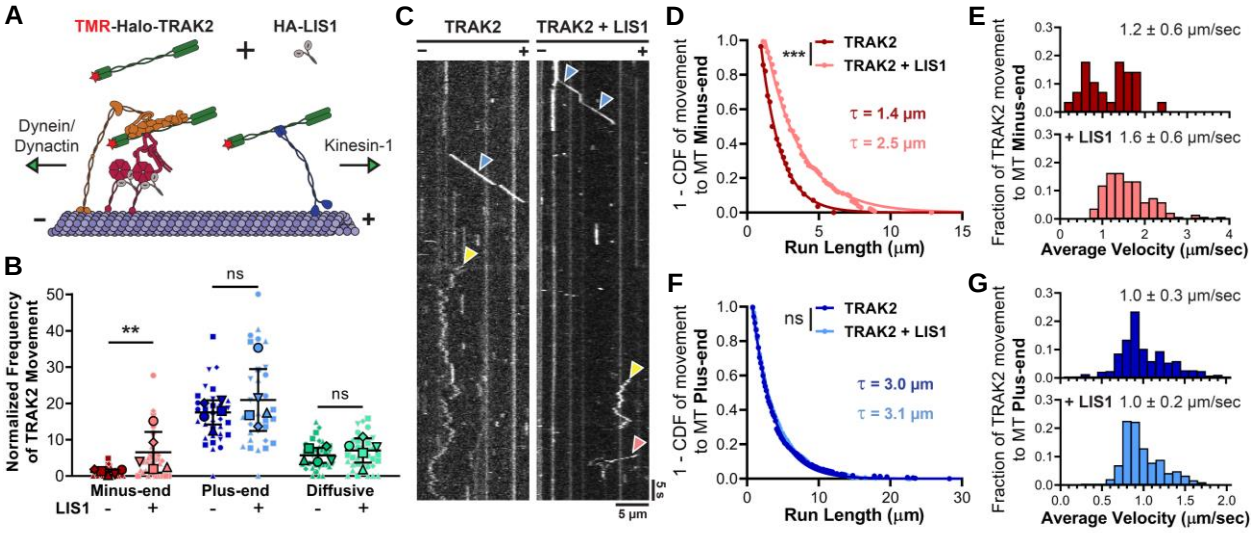

Figure 2.2: LIS1 enhances processive TRAK2 transport to the microtubule minus-end. A, Schematic illustration of experimental design, with LIS1 shown binding the dynein motor domain. **B,** Normalized frequency of TRAK2 motile events with and without exogenous HA-LIS1. Data points are shaped according to experimental replicate, with smaller points representing TRAK2 frequency per video. The center line and bars represent the mean ± s.d., (n = 34 videos per condition, 5 independent experiments). **, $p < 0.01$; ns, not significant (two-tailed Mann-Whitney U test). p-values: Minus-end, $p = 0.0079$; Plus-end, $p = 0.6905$; Diffusive, $p = 0.4206$. **C,** Representative kymographs showing that LIS1 induces minus-end-directed TRAK2 motility. Red, blue, and yellow arrows indicate minus-end, plus-end, and diffusive TRAK2 movement, respectively. **D-G,** Inverse cumulative distribution functions (CDF) of run length and histogram distributions of velocity for TRAK2 transport to either microtubule end with or without HA-LIS1 (n = 28 minus-end events without LIS1, 135 minus-end events with LIS1, 369 plus-end events without LIS1, and 570 plus-end events with LIS1) ***, $p = 0.0002$; ns, not significant, $p = 0.5265$ (two-tailed Mann-Whitney U test). In **(D, F)** single exponential decay curve fits are shown with decay constants indicated above. The values in **(E, G)** are mean ± s.d.

To determine the effect of LIS1 on the motility of TRAK2-motor complexes, we expressed Halo-TRAK2 with or without HA-tagged LIS1 in COS-7 cells and examined the motility of individual TRAK2 motor-complexes moving along dynamic microtubules with TIRF microscopy (Fig. 2.2A). Expression of HA-LIS1

raised LIS1 protein levels 4- to 8-fold above endogenous levels present in cell extracts (Fig. S2.5). We found that increased expression of LIS1 promoted robust TRAK2 transport toward the microtubule minus-end, causing a ~7-fold increase in the frequency of minus-end motility (Fig. 2.2B, C; Fig. S2.2; Video S2.4). This increase in minus-end run frequency coincided with increased processivity of minus-end-directed TRAK2 motility. Minus-end runs were longer with exogenous LIS1 present, with 24% of runs over 5 µm (Fig. 2.2D). Exogenous LIS1 also caused a significant increase in the velocity of minus-end-directed TRAK2 transport ($p=0.0008$, two-tailed Mann-Whitney U test), with 23% of runs displaying velocities over 2 µm/s (Fig. 2.2E). The observation of fast, sustained movements toward the microtubule minus-end upon the addition of LIS1 is consistent with recent reports that LIS1 promotes the formation of dynein-dynactin-adaptor complexes (Elshenawy et al., 2020; Htet et al., 2020; Qiu et al., 2019). We conclude that LIS1 promotes the activation of dynein-dynactin-TRAK2 complexes for processive transport.

Although LIS1 robustly increased the frequency of dynein-mediated TRAK2 transport, we did not observe any effect of LIS1 on the frequency of plus-end-directed or diffusive TRAK2 events (Fig. 2.2B). Similarly, the run length and velocity of plus-end runs were unaffected by the addition of LIS1, indicating that LIS1 does not affect the processivity of kinesin-1 when in complex with TRAK2 (Fig. 2.2F, G). These results indicate that LIS1 functions as a dynein-specific activator of TRAK2 transport.

While LIS1 had no effect on plus-end TRAK2 movement, these events still comprised the majority of TRAK2 movement, regardless of whether exogenous LIS1 was present. This bias for kinesin-based motility was surprising given the reported preference of TRAK2 for promoting dynein-based mitochondrial transport within cells (López-Doménech et al., 2018; van Spronsen et al., 2013). In contrast to TRAK2, TRAK1 has been shown to preferentially promote kinesin-based transport of mitochondria (López-Doménech et al., 2018; van Spronsen et al., 2013). As a result, we hypothesized that the observed plus-end bias of TRAK2 in our system might be caused by the presence of endogenous TRAK1 in complex with Halo-TRAK2. To test this possibility, we first examined if TRAK2 interacts with TRAK1 by expressing Halo-TRAK2 with HA-tagged TRAK1 in COS-7 cells. Using an antibody for the Halo tag, we immunoprecipitated Halo-TRAK2 and pulled down HA-TRAK1, confirming that TRAK2 binds TRAK1 (Fig. S2.6A, B).

We next examined whether knockdown of TRAK1 affects TRAK2 transport in our lysate-based single-molecule assay. Knockdown of TRAK1 by siRNA resulted in an ~70% reduction in the level of TRAK1 protein in COS-7 cells (Fig. S2.6C, D). Characterization of Halo-TRAK2 transport along microtubules in lysates prepared from these cells showed no marked changes in the frequency, run length, or velocity of runs toward either microtubule end (Fig. S6F-J). Since TRAK2 displays minimal transport toward the microtubule minus-end under these conditions, we performed the same experiment with HA-LIS1 expressed to promote processive TRAK2 transport toward the microtubule minus-end. Even with exogenous LIS1 present, we did not observe any effect of TRAK1 knockdown on the frequency, run length, or velocity of TRAK2 runs toward either microtubule end (Fig. 2.6K-P). In all conditions examined TRAK2 preferentially promoted transport toward the microtubule plus-end, indicating that the plus-end bias of TRAK2 in this system is not due to the presence of TRAK1 in these motor-adaptor complexes.

The TRAK2 CC1-Box is required for processive motility to the microtubule minus-end

The CC1-Box of the TRAK proteins is conserved among many dynein activating adaptors, such as Spindly and BICD2 (Fig. 2.3A), where it facilitates a direct interaction with dynein Light Intermediate Chain 1 (LIC1) (Cason et al., 2021; Gama et al., 2017; I.-G. Lee et al., 2018, 2020). Structural work on the BICD2 dimer indicates that the CC1-Box forms a hydrophobic pocket that binds LIC1 (I.-G. Lee et al., 2020). This LIC1-adaptor interaction is necessary for processive dynein motility in CC1-Box-containing adaptors and in the Hook family of adaptors, which bind LIC1 through an analogous coiled-coil segment (I.-G. Lee et al., 2018). Within the CC1-Box, multiple residues are essential for the adaptor interaction with dynein. Mutating two conserved alanine residues to valine residues in the CC1-Box of Spindly or BICD2 reduces the interaction with dynein and dynactin (Gama et al., 2017; Schlager, Serra-Marques, et al., 2014) while mutating a nearby tyrosine residue to aspartic acid in BICD2 disrupts the adaptor interaction with LIC1 (I.-G. Lee et al., 2020). Mutating the analogous isoleucine to aspartic acid in HAP1 is sufficient to disrupt dynein-dependent HAP1 motility in neurons (Cason et al., 2021).

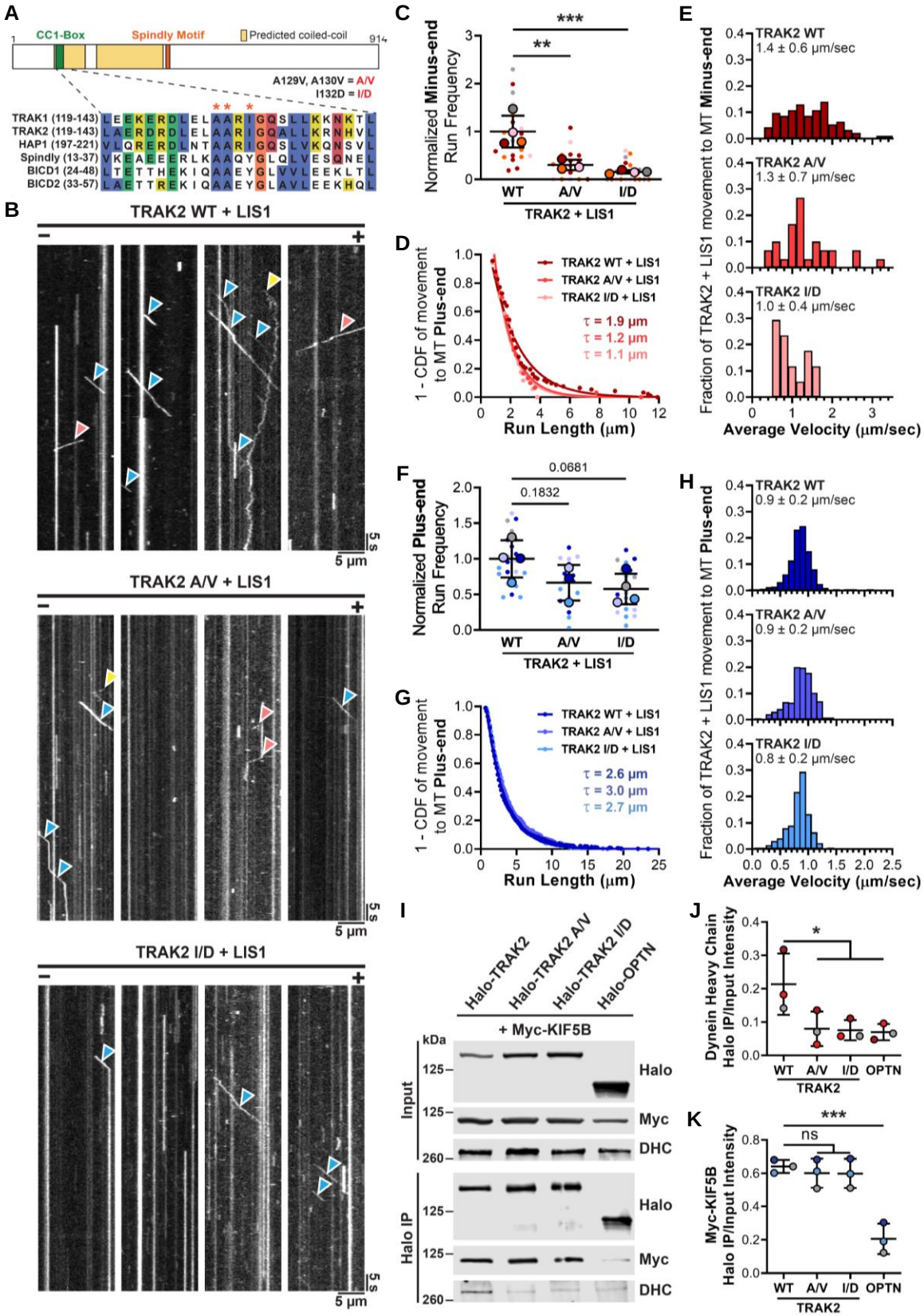
A
CC1-Box
Spindly Motif
Predicted coiled-coil
914
A129V, A130V = A/V
I132D = I/D
TRAK1 (119-143) LEEKERDLELAARIGQSLLKKNKTL
TRAK2 (119-143) LAERDRDLELAARIGQALLKRNHVL
HAP1 (197-221) VLQRERDLNTAARIGQSLVKQNSVL
Spindly (13-37) VKEAEEERLKAAQYGLQLVESQNEL
BICD1 (24-48) LTETTHEKIQAAEYGLVVLEEKLTL
BICD2 (33-57) LAETTREKIQAAEYGLAVLEEKHQL
B
TRAK2 WT + LIS1
TRAK2 A/V + LIS1
TRAK2 I/D + LIS1
5 µm
5 s
C
Normalized Minus-end Run Frequency
***
**
WT
A/V
I/D
TRAK2 + LIS1
D
1 - CDF of movement to MT Plus-end
TRAK2 WT + LIS1
TRAK2 A/V + LIS1
TRAK2 I/D + LIS1
τ = 1.9 µm
τ = 1.2 µm
τ = 1.1 µm
Run Length (µm)
E
Fraction of TRAK2 + LIS1 movement to MT Minus-end
TRAK2 WT
1.4 ± 0.6 µm/sec
TRAK2 A/V
1.3 ± 0.7 µm/sec
TRAK2 I/D
1.0 ± 0.4 µm/sec
Average Velocity (µm/sec)
F
Normalized Plus-end Run Frequency
0.0681
0.1832
WT
A/V
I/D
TRAK2 + LIS1
G
1 - CDF of movement to MT Plus-end
TRAK2 WT + LIS1
TRAK2 A/V + LIS1
TRAK2 I/D + LIS1
τ = 2.6 µm
τ = 3.0 µm
τ = 2.7 µm
Run Length (µm)
H
Fraction of TRAK2 + LIS1 movement to MT Plus-end
TRAK2 WT
0.9 ± 0.2 µm/sec
TRAK2 A/V
0.9 ± 0.2 µm/sec
TRAK2 I/D
0.8 ± 0.2 µm/sec
Average Velocity (µm/sec)
I
Halo-TRAK2
Halo-TRAK2 A/V
Halo-TRAK2 I/D
Halo-OPTN
+ Myc-KIF5B
kDa
Input
Halo IP
Halo
Myc
DHC
125
260
J
Dynein Heavy Chain Halo IP/Input Intensity
*
WT
A/V
I/D
OPTN
TRAK2
K
Myc-KIF5B Halo IP/Input Intensity
***
ns
WT
A/V
I/D
OPTN
TRAK2

Figure 2.3: The TRAK2 CC1-Box is important for processive motility and binding to dynein, but not kinesin-1. **A,** Schematic overview of TRAK2 with sequence alignment showing conservation of the CC1-Box. The red stars and text indicate the mutations introduced to TRAK2. **B,** Representative kymographs showing the effect of A/V and I/D mutations on TRAK2 motility along MTs when LIS1 is also expressed. Red, blue, and yellow arrows indicate minus-end, plus-end, and diffusive TRAK2 movement, respectively. **C,** Normalized frequency of TRAK2 transport to the microtubule minus-end with exogenous LIS1. Data points are color-coded to experimental replicate, with smaller points representing TRAK2 frequency per video. The center line and bars represent the mean ± s.d. from independent experiments (n = 22 videos from 4 experiments for WT, 18 videos from 3 experiments for A/V, and 21 videos from 4 experiments for I/D). **, p = 0.0047; ***, p = 0.0009 (one-way ANOVA with Dunnett's multiple comparisons test). **D-E,** Inverse cumulative distribution functions (CDF) of run length and histogram distributions of velocity for TRAK2 transport to the microtubule minus-end with exogenous LIS1 present (n = 92 events for TRAK2 WT, 30 events for TRAK2 A/V, and 17 events for TRAK2 I/D). The curves in **(D)** represent single exponential decay fits with decay constants indicated above. The values in **(E)** are mean ± s.d. **F,** Same as **(C)** but for TRAK2 transport to the microtubule plus-end. Exact p-values from one-way ANOVA with Dunnett's multiple comparisons test are shown. **G-H,** Same as **(D-E)** but for TRAK2 transport to the microtubule plus-end (n = 693 events for TRAK2 WT, 369 events for TRAK2 A/V, and 391 events for TRAK2 I/D). **I**, Immunoprecipitation using a Halo antibody of extracts from COS-7 cells transfected with Myc-KIF5B and Halo-tagged TRAK2, TRAK2 A/V, TRAK2 I/D, or negative control Optineurin (OPTN). **J,** Quantification of co-immunoprecipitation of endogenous dynein heavy chain (DHC) with Halo-tagged constructs. Data points are color-coded according to experimental replicate. The center line and bars represent the mean ± s.d. from 3 independent experiments. *, p < 0.05 (one-way ANOVA with Dunnett's multiple comparisons test). p-values: WT vs. A/V, p = 0.0475; WT vs. I/D, p = 0.0416; WT vs. OPTN, p = 0.0346. **K,** Same as **(J)** but for co-immunoprecipitation of Myc-KIF5B. ***, p < 0.001; ns, not significant (one-way ANOVA with Dunnett's multiple comparisons test). p-values: WT vs. A/V, p = 0.8697; WT vs. I/D, p = 0.8513; WT vs. OPTN, p = 0.0004.

To test if the TRAK2 CC1-Box is necessary for processive dynein-dependent transport to the microtubule minus-end, we introduced point mutations predicted to disrupt the interaction of TRAK2 with dynein: two alanine to valine (A129V, A130V) mutations and an isoleucine to aspartic acid (I132D) mutation. Isoleucine residue 132 is analogous to the tyrosine residue that is required for BICD2 to interact with LIC1, suggesting it facilitates an interaction with LIC1 (I.-G. Lee et al., 2020). We then compared the motility of Halo-TRAK2 with A/V or I/D mutations to wild type (WT) in TIRF; we co-expressed HA-LIS1 with Halo-TRAK2 to promote transport to the microtubule minus-end. Both CC1-Box mutations caused a marked reduction in the frequency of processive runs towards the microtubule minus-end (Fig. 2.3B, C). TRAK2 I/D displayed reduced run lengths and velocities when moving to the minus-end (Fig. 2.3D, E). These impaired minus-end runs resembled those of TRAK2 without activation by exogenous LIS1, indicating that the TRAK2 CC1-Box is required to activate dynein for robust transport to the microtubule minus-end. Surprisingly, these CC1-Box mutations also caused a slight reduction (33% for A/V and 42% for I/D) in the frequency of TRAK2 runs toward the microtubule plus-end (Fig. 2.3F). However, neither CC1-Box mutation

altered the run length or velocity of plus-end-directed TRAK2 motility, indicating that the CC1-Box is not required to activate kinesin-1 for processive transport to the microtubule plus-end. (Fig. 2.3G, H).

To determine whether the CC1-Box affects binding of TRAK2 to dynein and kinesin-1, we expressed WT, A/V, or I/D versions of Halo-TRAK2 with Myc-tagged KIF5B in COS-7 cells and immunoprecipitated with an anti-Halo antibody. We observed that both CC1-Box mutations reduced TRAK2 binding to endogenous dynein heavy chain (Fig. 2.3I-J), consistent with the low number of dynein runs initiated by TRAK2 A/V and I/D. In contrast, neither mutation had any effect on the interaction between TRAK2 and kinesin-1 (Fig. 2.3I, K). Combined, these results indicate that the TRAK2 CC1-Box specifically facilitates an interaction with dynein to promote dynein-mediated transport.

Kinesin-1 and dynein-dynactin promote TRAK2 transport by the opposing motor

We next sought to determine the relationship between kinesin-1 and dynein-dynactin within single TRAK2-motor complexes. We used siRNAs against KIF5B, DHC, or $p150^{Glued}$ to knock down endogenous kinesin-1, dynein, or dynactin, respectively, within COS-7 cells expressing Halo-TRAK2. We then used these cell lysates to study the microtubule-based transport of TRAK2 in TIRF; this experiment was performed with either cells expressing just Halo-TRAK2 or cells co-expressing HA-LIS1 as a way to promote transport to the microtubule minus-end. Using this system, we found that knockdown of KIF5B significantly reduced the frequency of plus-end-directed TRAK2 transport by 94% and 85%, with and without LIS1, respectively (Fig. 2.4A-B; Fig. S7A, B). This result confirms that the observed plus-end motility of TRAK2 is driven by kinesin-1 and supports previous reports that kinesin-1 is the primary motor driving mitochondrial transport to the microtubule plus-end (Pilling et al., 2006; van Spronsen et al., 2013). Surprisingly, knockdown of dynein or dynactin, with LIS1 present, reduced the frequency of TRAK2 transport toward the plus-end by 44 and 51%, respectively (Fig. 2.4A-B). Knockdown of dynein or dynactin also caused a slight increase in the run length of TRAK2 transport toward the microtubule plus-end, but had no effect on the velocity of these plus-end runs (Fig. 2.4C-D). Knockdown of dynein and dynactin had similar effects on the

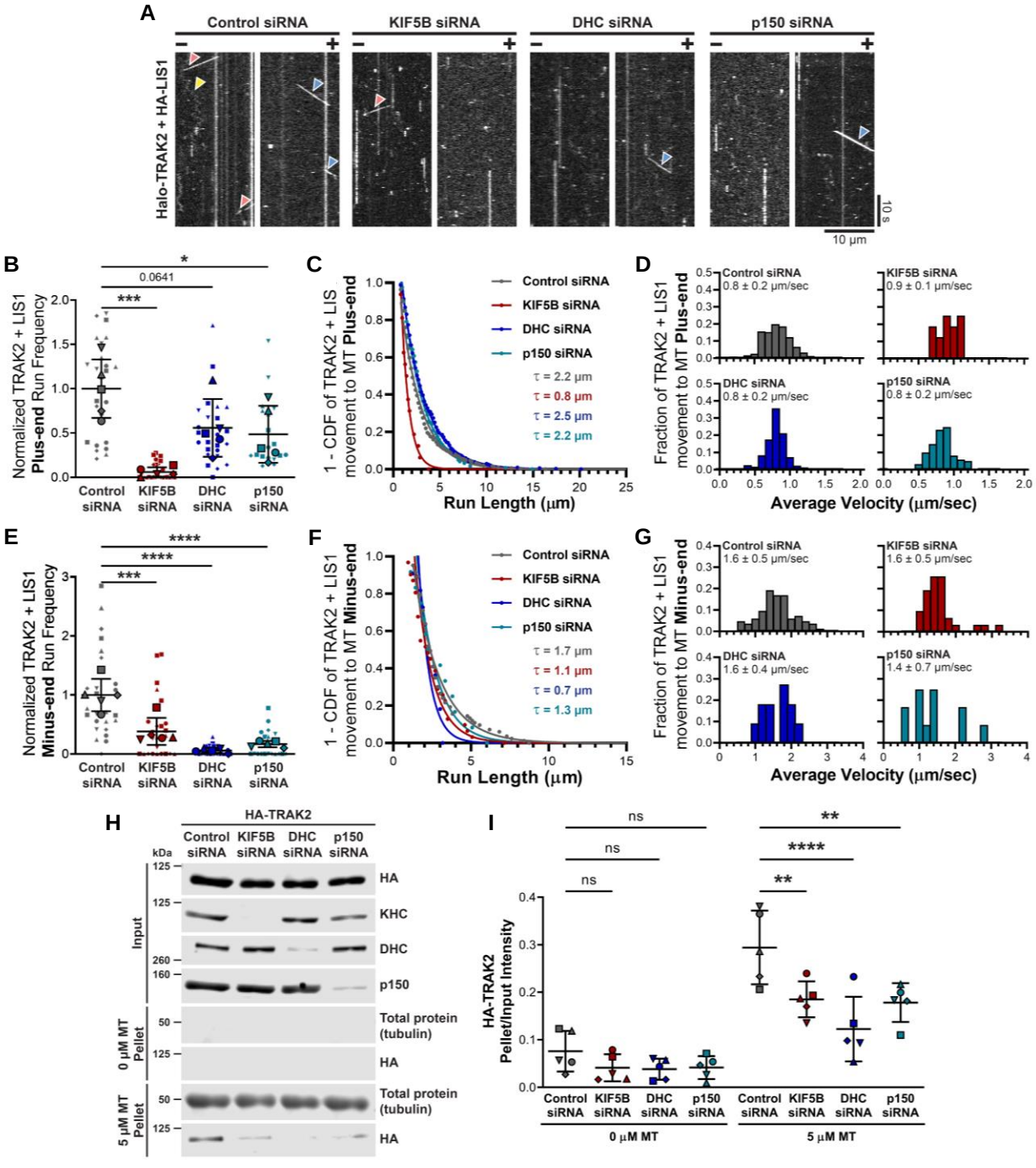

Figure 2.4: Kinesin-1 and dynein-dynactin promote TRAK2 transport by the opposing motor. A, Representative kymographs showing how siRNA knockdown of KIF5B, dynein heavy chain (DHC), or p150^{Glued} (p150) affects TRAK2 motility along MTs when LIS1 is expressed. Red, blue, and yellow arrows indicate minus-end, plus-end, and diffusive TRAK2 movement, respectively. **B,** Normalized frequency of TRAK2 transport to the MT plus-end upon motor knockdown when LIS1 is expressed. Data points represent the frequency of TRAK2 motility per video normalized to the average frequency of control siRNA events. The center line and bars represent mean ± s.d., (n = 26 for control

siRNA, 26 for KIF5B siRNA, 25 for DHC siRNA, and 21 for p150 siRNA, 5 independent experiments). Exact p-values are shown when p > 0.05; *, p = 0.029; ***, p = 0.0002 (one-way ANOVA with Dunnett's multiple comparisons test). **C-D,** Inverse cumulative distribution functions (CDF) of run length and histogram distributions of velocity for TRAK2 transport to the microtubule plus-end with exogenous LIS1 present (n = 301 events for control siRNA, 16 events for KIF5B siRNA, 302 events for DHC siRNA, and 121 events for p150 siRNA). The curves in **(C)** represent single exponential decay fits with decay constants indicated above. The values in **(D)** are mean ± s.d. **E,** Same as **(B)** but for TRAK2 transport to the microtubule minus-end. ***, p = 0.0002; ****, p < 0.0001 (one-way ANOVA with Dunnett's multiple comparisons test). **F-G,** Same as **(C-D)**, but for TRAK2 transport to the microtubule minus-end (n = 83 events for control siRNA, 31 events for KIF5B siRNA, 11 events for DHC siRNA, and 12 events for p150 siRNA). **H,** Microtubule binding assays were performed using cell lysates from HA-TRAK2 transfected COS-7 cells with siRNA knockdown of KIF5B, DHC, p150, or a control siRNA. Lysates were probed for HA, kinesin heavy chain (KHC), dynein heavy chain (DHC), and $p150^{Glued}$ (p150). Lysates were incubated with microtubules, spun down, and the resulting microtubule pellets were probed for total protein (tubulin) and HA. **I,** Quantification of relative HA-TRAK2 in 0 and 5 µM microtubule pellets from (**H**). The center line and bars represent mean ± s.d. from 5 independent experiments. ns, not significant; **, p < 0.01; ****, p < 0.0001 (one-way ANOVA with Dunnett's multiple comparisons test). p-values for 0 µM MT conditions: Control siRNA vs. KIF5B siRNA, p = 0.7476; Control siRNA vs. DHC siRNA, p = 0.6789; Control siRNA vs. p150 siRNA, p = 0.7551. p-values for 5 µM MT conditions: Control siRNA vs. KIF5B siRNA, p = 0.0049; Control siRNA vs. DHC siRNA, p < 0.0001; Control siRNA vs. p150 siRNA, p = 0.0026.

frequency, run length, and velocity of plus-end plus-end-directed TRAK2 transport without exogenous LIS1 present (Fig. S7A-D). Thus, the initiation of kinesin-dependent TRAK2 transport to the microtubule plus-end is enhanced by dynein and dynactin, independent of dynein activation via LIS1.

We also examined the effect of motor knockdown on TRAK2 transport toward the microtubule minus-end. This assessment of minus-end transport was done with and without expression of exogenous LIS1, but the rarity of minus-end-directed TRAK2 transport without LIS1 precluded meaningful comparison between conditions (Fig. S7E-G). With exogenous LIS1 present, knockdown of dynein or dynactin reduced the frequency of minus-end motility by 94% and 82% respectively (Fig. 2.4E), as expected for dynein-mediated motility. However, KIF5B knockdown also reduced the frequency of minus-end-directed TRAK2 events by 58% (Fig. 2.4E). Despite this large decrease in dynein motility upon knockdown of KIF5B, we observed only a small decrease in run length and no change in velocity of minus-end-directed TRAK2 transport upon KIF5B knockdown (Fig. 2.4F-G). Thus, kinesin-1 specifically enhances the initiation of TRAK2 dynein motility.

We wondered if the reduction in TRAK2 transport upon motor knockdown was due to reduced association of TRAK2 with microtubules. To test this, we expressed HA-TRAK2 in COS-7 cells, knocked

down endogenous KIF5B, DHC, or p150^{Glued}, and examined the ability of HA-TRAK2 to pellet with GMPCPP-stabilized microtubules. Under control conditions, TRAK2 pellets with microtubules (Fig. 2.4H-I). Knockdown of KIF5B, DHC, or p150^{Glued} was sufficient to reduce the ability of TRAK2 to pellet with microtubules, indicating that each component contributes to the association of TRAK2 with microtubules. Combined, these data show that kinesin-1, dynein, and dynactin promote the association of TRAK2 with microtubules and promote initiation of processive TRAK2 transport toward either microtubule end.

TRAK2 facilitates an interaction between kinesin-1 and dynein-dynactin

Our finding that kinesin-1 and dynein-dynactin promote the initiation of TRAK2 transport by the opposing motor raised the question of whether TRAK2 concurrently interacts with these motors. It is unclear whether TRAK2 interacts with these motors alternately or simultaneously, but our knockdown studies suggest that these motors cooperate within single TRAK2-motor complexes to initiate processive movement. In line with these findings, we observed instances of TRAK2 switching directions during a run while examining TRAK2 transport in the presence of LIS1. These events consisted of processive movement with a single immediate change in direction and were typically accompanied by a change in velocity upon directional switch (Fig. 2.5A and Video S2.5). Switches could occur in either direction, but the majority (85%) of switches were in the plus-to-minus direction. We interpret these plus-to-minus directional switches in the presence of LIS1 as transient activation of dynein in TRAK2-motor complexes containing kinesin-1. To further test the possibility that LIS1 activates dynein to promote minus-end-directed transport of motor complexes containing TRAK2 and kinesin-1, we expressed Myc-KIF5C-Halo and HA-TRAK2 with or without HA-LIS1 in COS-7 cells and used TIRF microscopy to track the movement of activated KIF5C along dynamic microtubules. Without exogenous LIS1 present, KIF5C moved unidirectionally toward the microtubule plus-end, as expected. In the presence of LIS1, we found several instances of KIF5C moving processively toward the microtubule minus-end (Fig. S2.8). Together, these data suggest that both kinesin-

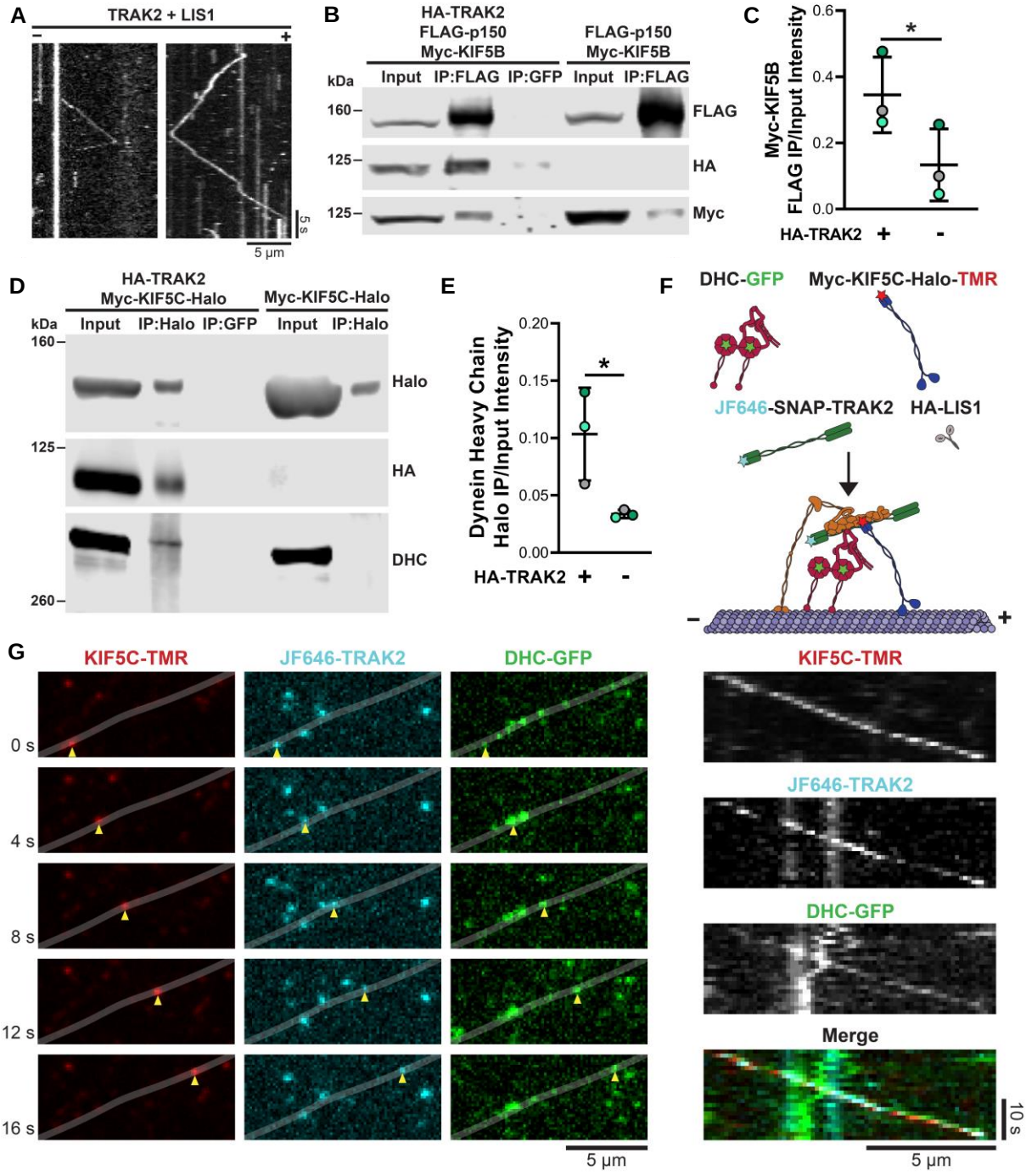

Figure 2.5: TRAK2 forms a complex with kinesin-1, dynein, and dynactin. **A,** Representative kymographs show TRAK2-motor complexes switching direction during a run. **B,** Lysates from COS-7 cells transfected with HA-TRAK2, FLAG-p150^{Glued}, and Myc-KIF5B were immunoprecipitated with a FLAG antibody or negative control GFP antibody. Lysates from COS-7 cells expressing just FLAG-p150^{Glued} and Myc-KIF5B were immunoprecipitated with a FLAG antibody in parallel. **C,** Quantification of the difference in Myc-KIF5B co-immunoprecipitation with FLAG-p150^{Glued} upon

addition of HA-TRAK2. Data points are colored according to experimental replicate. Bars represent mean ± s.d. from 3 independent experiments. *, p = 0.0405 (two-tailed t-test). **D,** Lysates from COS-7 cells transfected with HA-TRAK2 and Myc-KIF5C-Halo were immunoprecipitated with a Halo antibody or negative control GFP antibody. Lysates from COS-7 cells expressing just Myc-KIF5C-Halo were immunoprecipitated with a Halo antibody in parallel. **E,** Quantification of the difference in dynein heavy chain co-immunoprecipitation with Myc-KIF5C-Halo upon addition of HA-TRAK2. Data points are colored according to experimental replicate. Bars represent mean ± s.d. from 3 independent experiments. *, p = 0.0410 (two-tailed t-test). **F,** Schematic illustration for three-color single-molecule imaging of GFP-dynein heavy chain, Myc-KIF5C-Halo labeled with TMR, and SNAP-TRAK2 labeled with Janelia Fluor 646. HA-LIS1 is also present in this experiment. **G,** Time series showing a processive complex containing KIF5C, TRAK2, and dynein heavy chain. The gray line indicates microtubule position, as inferred from the max projection of KIF5C. Right: corresponding kymographs.

1 and dynein-dynactin can form a complex with TRAK2 and that the activities of these motors are coordinately regulated to achieve changes in direction.

To directly test if TRAK2 can simultaneously bind kinesin-1 and dynein-dynactin, we performed two immunoprecipitation experiments. We first tested if TRAK2 can form a complex with kinesin-1 and dynactin by expressing HA-tagged TRAK2 alongside Myc-tagged KIF5B and a FLAG-tagged p150 subunit of dynactin in COS-7 cells. Using an antibody for the FLAG tag, we immunoprecipitated FLAG-p150 and pulled down both HA-TRAK2 and Myc-KIF5B, confirming the formation of a TRAK2/kinesin-1/dynactin motor complex (Fig. 2.5B). When the same immunoprecipitation was performed in cells expressing just FLAG-p150 and Myc-KIF5B, less Myc-KIF5B was pulled down, indicating that TRAK2 enhances the association between kinesin-1 and dynactin (Fig. 2.5B-C). Next, we tested if TRAK2 can form a complex with kinesin-1 and dynein by expressing HA-tagged TRAK2 alongside Myc- and Halo-tagged KIF5C in COS-7 cells. Using a Halo antibody, we immunoprecipitated KIF5C and pulled down both HA-TRAK2 and endogenous dynein heavy chain, confirming the formation of a TRAK2/kinesin-1/dynein motor complex (Fig. 2.5D). When the same immunoprecipitation was performed in cells expressing Myc-KIF5C-Halo alone, significantly less dynein heavy chain coimmunoprecipitated with KIF5C, indicating that TRAK2 enhances the association between kinesin-1 and dynein (Fig. 2.5E).

To further verify that TRAK2 can concurrently bind kinesin-1 and dynein-dynactin we used TIRF microscopy to perform co-localization experiments. We first tested whether TRAK2 can form a motile complex with kinesin and dynactin present by expressing Halo-TRAK2 alongside a GFP-tagged p25 subunit

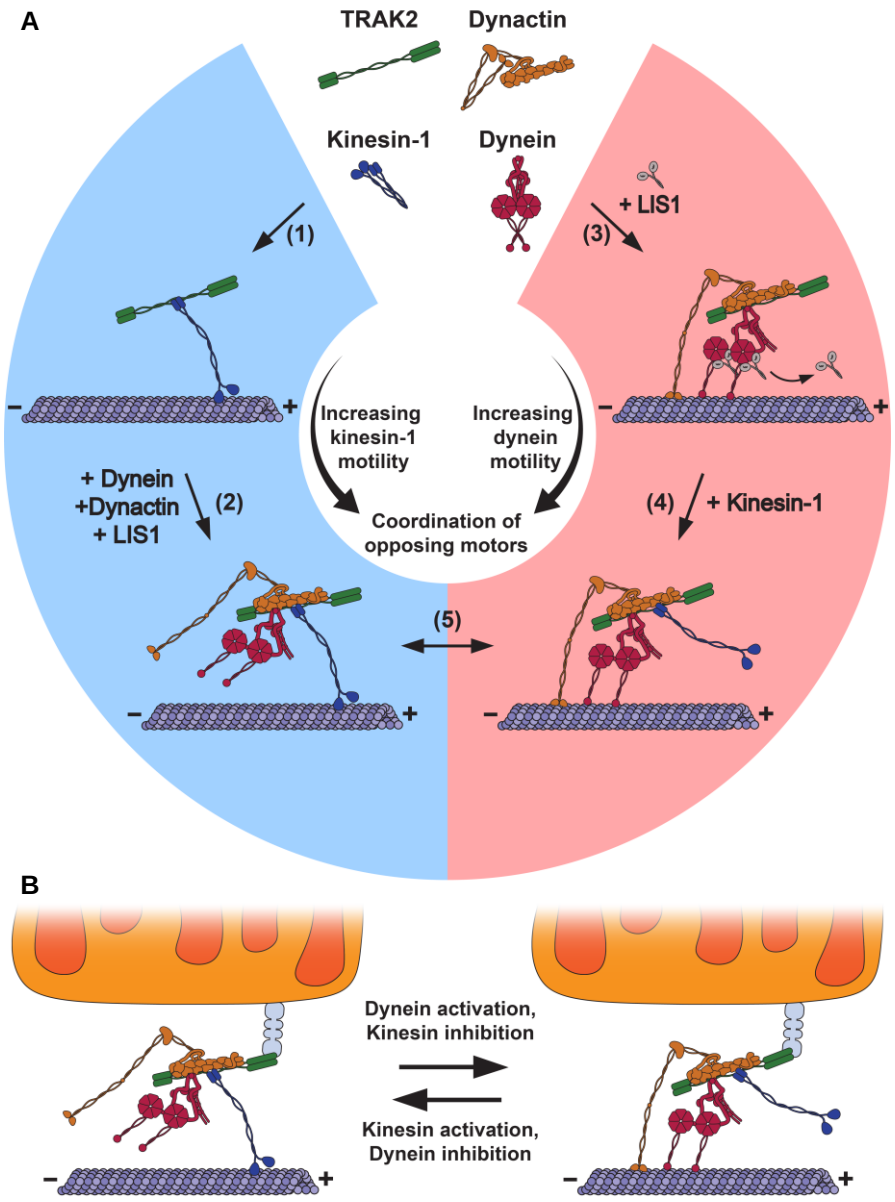

Figure 2.6: TRAK2 functionally links opposing microtubule motors. **A,** A model for TRAK2 transport by microtubule motors. Blue indicates active kinesin-1 and red indicates active dynein. (1) TRAK2 binds to kinesin-1 to form a motor complex that moves processively toward the microtubule plus-end. (2) Although TRAK2 activates kinesin-1 in the absence of dynein/dynactin, the formation of a TRAK2/kinesin-1/dynein/dynactin complex further enhances the frequency of transport toward the plus-end. (3) TRAK2 binds dynein and dynactin to form a motor complex that moves processively toward the microtubule minus-end in the presence of LIS1. LIS1 transiently activates dynein before dissociating from the motor complex. (4) Kinesin-1 binding to TRAK2 further enhances TRAK2 motility toward the minus-end. (5) TRAK2 coordinates the activities of kinesin-1 and dynein-dynactin within the TRAK2/kinesin-1/dynein/dynactin complex to allow for processive transport in a single direction. **B,** A model for mitochondrial transport by multi-motor TRAK2 complexes. The TRAK2/kinesin-1/dynein/dynactin complex associates with mitochondria via a Miro protein (gray). Kinesin and dynein are selectively activated or inhibited by cellular factors to promote mitochondrial transport toward the microtubule plus- or minus-end.

of the dynactin pointed-end complex in COS-7 cells. We then performed dual-color TIRF imaging of TMR-labeled Halo-TRAK2 and GFP-p25 to track the motility of co-complexes on dynamic microtubules. As expected, we observed colocalization and co-migration of TRAK2-dynactin complexes (Fig. S2.9A-B). These co-complexes displayed both processive and diffusive movements along the microtubule, as seen previously for TRAK2. Moreover, we observed TRAK2-dynactin complexes moving processively toward the microtubule plus-end, indicating that kinesin-1 was present and active in these complexes (Fig. S2.9C). The movement of these co-complexes closely resembled that of TRAK2 alone, as most TRAK2-p25 motility consisted of processive transport toward the microtubule plus-end. This bias toward the microtubule plus-end suggests TRAK2 preferentially promotes kinesin-based motility under the conditions of this assay, even when dynactin is bound to TRAK2. Next, we performed three-color single-molecule imaging of TRAK2, kinesin-1, and dynein (Fig. 2.5F). For this experiment, we expressed SNAP-tagged TRAK2, Myc-KIF5C-Halo, and HA-LIS1 in HeLa cells stably expressing GFP-tagged dynein heavy chain (DHC-GFP)(Poser et al., 2008; Splinter et al., 2012). We then labeled cells with JF646-SNAP ligand and TMR-HaloTag ligand prior to generation of cell lysates and flowed lysates into chambers containing unlabeled microtubules. We observed TRAK2, KIF5C, and dynein heavy chain move processively along microtubules as a single complex (Fig. 2.5G and Video S2.6). Surprisingly, we found that TRAK2-KIF5C-DHC co-complexes exclusively exhibited transport toward the microtubule plus-end (41 of 41 runs containing all three components; Fig. S2.10), providing additional evidence that kinesin-1 functions as the dominant motor when in complex with TRAK2, under the conditions of our assay, regardless of the association of dynein–dynactin. Combined, these results demonstrate that TRAK2 promotes an interaction between kinesin-1 and dynein–dynactin that allows these opposing motors to be transported together as a multi-motor complex.

IV. Discussion

TRAK proteins play an essential role as motor adaptors in the transport of mitochondria along microtubules (Fenton et al., 2021b; Schwarz, 2013). Although specific roles have been proposed for TRAK1 and TRAK2 in the control of mitochondrial transport, our understanding of the molecular mechanisms by which TRAK

proteins function is largely unknown. Previous studies of mitochondrial transport in the axons and dendrites of rat hippocampal and cortical neurons identified TRAK1 as the motor adaptor primarily responsible for axonal mitochondrial transport, while dendritic transport depends on the motor adaptor TRAK2 (Loss & Stephenson, 2017; van Spronsen et al., 2013). It was proposed that these compartmental differences were the result of differential interactions of TRAK1 and TRAK2 with microtubule motors; TRAK1 was proposed to interact with kinesin-1 and dynein-dynactin whereas TRAK2 was thought to primarily interact with dynein-dynactin (van Spronsen et al., 2013). However, in our functional studies of single TRAK2-motor complexes, we found that TRAK2 strongly activates kinesin-1 over dynein. Such a bias against dynein motility could either be due to the absence of dynein from these complexes or insufficient activation of the dynein motor under these assay conditions. We show that TRAK2 robustly activates kinesin-1 irrespective of whether dynein or dynactin is present in the complex, ruling out the possibility that the absence of dynein-dynactin drives this bias. Thus, the reported preference of TRAK2 for binding dynein-dynactin and promoting minus-end-directed transport is likely contextual and dependent on additional factors that regulate motor binding and activity. TRAK2 requires Miro1, but not Miro2, to promote mitochondrial transport toward the microtubule minus-end, suggesting that the Miro isoform bound to TRAK2 may regulate the directional preference of TRAK2-motor complexes (López-Doménech et al., 2018).

TRAK2 has been predicted to function as an activating adaptor that increases dynein processivity because of its known interaction with dynein-dynactin and the identification of conserved motifs present in well-characterized activating adaptors (Canty & Yildiz, 2020; Olenick & Holzbaur, 2019). Interestingly, we found that LIS1 enhances the frequency, run length, and velocity of TRAK2 transport toward the microtubule minus-end, which closely resembles the effect of LIS1 on other dynein activating adaptors: BICD2, Hook3, and Ninl (Elshenawy et al., 2020; Htet et al., 2020). For these dynein activating adaptors, LIS1 transiently binds dynein to promote the formation of activated dynein-dynactin-adaptor complexes. Binding of LIS1 increases the force production and velocity of individual dynein-dynactin-adaptor complexes by recruiting a second dynein dimer. Thus, the fast and sustained minus-end-directed TRAK2 motility induced by LIS1 overexpression is likely due to both the enhanced formation of a dynein-dynactin-adaptor complex and the

recruitment of a second dynein dimer. Perhaps the addition of a second dynein dimer allows for dynein to more efficiently initiate processive TRAK2 transport toward the microtubule minus end.

The processive minus-end directed motility of TRAK2 induced by LIS1 also depends on the TRAK2 CC1-Box. We find that both the A/V and I/D mutations drastically reduced the frequency of minus-end runs and reduced the interaction between TRAK2 and dynein (Fig. 2.3). Since these CC1-Box mutations disrupt the interaction between BICD2 and LIC1, we propose that the TRAK2 CC1-Box facilitates a similar interaction with dynein light intermediate chain. Our findings substantiate the role of TRAK2 as a dynein activating adaptor, since minus-end-directed TRAK2 motility is dependent on dynein and dynactin, enhanced by the addition of LIS1, and requires the TRAK2 CC1-Box.

Intriguingly, the predicted dynein-dynactin interface encompasses the proposed kinesin-1-binding region on TRAK2 (Fig. 2.1A). A similar overlap of kinesin-1 and dynactin-binding regions is present in JIP1, a motor adaptor that regulates the transport of autophagosomes (Cason et al., 2021; M. Fu et al., 2014). JIP1 is thought to regulate motor activity by switching between mutually exclusive complexes containing either kinesin-1 or dynein-dynactin (M. Fu & Holzbaur, 2013), raising the possibility that TRAK2-motor complexes are mutually exclusive as well. However, we demonstrate here that kinesin-1 and dynein-dynactin can concurrently interact with TRAK2 and that TRAK2 promotes the joining of these opposing motor components (Fig. 2.5). The ability of TRAK2 to form a motor-adaptor complex with kinesin and dynein may represent a more general feature of bidirectional motor adaptors as the dynein activating adaptor HOOK3 has been shown to scaffold an interaction between dynein-dynactin and the kinesin-3 motor KIF1C for processive transport toward either microtubule end (Kendrick et al., 2019). While both TRAK2 and HOOK3 scaffold kinesin and dynein motors, the relationship between these opposing motors on TRAK2 is unique. We found that genetic depletion of KIF5B, dynein heavy chain, or the $p150^{Glued}$ subunit of dynactin reduced the association of TRAK2 with microtubules and the frequency of TRAK2 transport to both microtubule ends, demonstrating that the functions of these motors are coordinated to promote processive TRAK2 transport along the microtubule (Fig. 2.4). The frequency of kinesin-based TRAK2 transport was reduced by targeted CC1-Box mutations that specifically disrupt TRAK2 binding to dynein without affecting

its interaction with kinesin-1 (Fig. 2.3F-K), further supporting the notion of a functional linkage between these motors on TRAK2. Moreover, we found that TRAK2-motor complexes could quickly switch from processive transport by one motor to processive transport by the opposing motor. Such immediate directional switches suggest that the activities of kinesin and dynein are tightly regulated within multi-motor TRAK2 complexes to achieve directed transport. Combined, our data support a model in which TRAK2 coordinates kinesin-1 and dynein-dynactin as an interdependent motor complex, providing integrated control of opposing motors (Fig. 2.6).

Our findings provide new insights into the control of microtubule-based bidirectional mitochondrial transport. We show that single TRAK2-motor complexes display distinct modes of bidirectional transport that closely resemble the transport of mitochondria in cells. First, we consistently observed motor-independent diffusion of TRAK2 that is characterized by frequent directional switches and no net displacement along the microtubule. These bidirectional movements resemble the short, back-and-forth movements displayed by neuronal mitochondria, which have often been interpreted as an unregulated tug-of-war between opposing motors (Hancock, 2014). Although the exact nature of the bidirectional movement seen *in vivo* remains uncertain, our findings for single TRAK2-motor complexes are not consistent with a tug-of-war between kinesin and dynein motors, as this bidirectional diffusive motility is largely unaffected by loss of kinesin-1, dynein, or dynactin. Instead, we propose that these short bidirectional movements are the result of one-dimensional diffusion along the microtubule that is likely mediated by TRAK2 itself.

In contrast to this diffusive motility, neuronal mitochondria display a distinct kind of bidirectional transport in which they rapidly reverse their direction of transport during processive movement. The immediate nature of these reversals suggests that kinesin and dynein are simultaneously bound and coordinately regulated on a single mitochondrion. Our observation of immediate directional switching during the processive movement of a TRAK2-motor complex mirrors this behavior of neuronal mitochondria. We propose that mitochondrial transport is facilitated by multi-motor TRAK2 complexes, which allow for integrated control of opposing kinesin and dynein motors (Fig. 2.6B). The direction of mitochondrial transport could then be regulated by specifically modulating the activities of kinesin and dynein within this

multi-motor TRAK complex. One potential direction-specific transport effector is Disrupted-In-Schizophrenia 1 (DISC1). DISC1 interacts with the TRAK/Miro complex to promote kinesin-1-dependent anterograde axonal mitochondrial transport in mouse hippocampal neurons (Ogawa et al., 2014). Another transport effector, NudE neurodevelopmental protein 1 (NDE1), associates with the TRAK/Miro complex to selectively promote retrograde mitochondrial transport (Ogawa et al., 2016; Shao et al., 2013). The association of these transport effectors, combined with the specific TRAK and Miro isoforms in complex with microtubule motors on mitochondria could then allow for local regulation of motor activity in response to cellular signals.

Our finding that kinesin-1 and dynein-dynactin are functionally linked when in complex with TRAK2 provides insight into the coordination of these motors for mitochondrial transport. It has been apparent that specific disruptions of kinesin-1, dynein, or dynactin cause bidirectional transport defects since the discovery that these motors are essential for fast axonal transport (Martin et al., 1999). Initial observations of bidirectional mitochondrial transport in axons similarly found that transport in both directions was affected by mutations in kinesin-1, dynein, or dynactin (Pilling et al., 2006). This finding that disrupting one motor leads to diminished mitochondrial motility in both directions has been observed across systems (Moughamian et al., 2013; Sainath & Gallo, 2015; Vagnoni & Bullock, 2016; van Spronsen et al., 2013), raising the question of how opposing microtubule motors are interdependent for mitochondrial transport. We observed a similar interdependence of opposing motors in our single-molecule studies of TRAK2 (Fig. 2.4), indicating that motor co-dependence is inherent to the TRAK2-motor complex. This observation suggests that the paradox of motor co-dependence for mitochondrial transport stems from molecular interactions within individual TRAK-motor complexes. Loss or inhibition of kinesin-1 or dynein-dynactin might reduce the frequency of transport by the opposing motor within each TRAK-motor complex, reducing mitochondrial transport in both directions. Kinesin-1, dynein, and dynactin each contain a microtubule-binding domain that may facilitate increased association of the TRAK-motor complex with the microtubule, resulting in more frequent transport in either direction. However, an alternative mechanism may account for the paradox of motor co-dependence. TRAK2 is known to undergo conformational changes that control motor binding (van Spronsen et al., 2013). These conformational changes may facilitate specific

interactions between kinesin-1 and dynein-dynactin that result in a functionally interdependent motor complex. Moreover, the presence of additional factors may be required to functionally link these opposing motors. Our lysate-based approach may include cellular factors that facilitate such an interaction. Future studies of TRAK-motor complexes using purified proteins and *in vitro* reconstitution of mitochondrial transport will help to elucidate the precise interactions between microtubule motors and TRAK proteins that allow for proper transport and positioning of mitochondria within a cell.

V. Methods

Cell culture and transfections

COS-7 cells (ATCC, CRL-1651) and HeLa cells stably expressing GFP-tagged dynein heavy chain (gift from A. Hyman, Max Planck Institute for Molecular Cell Biology and Genetics) were cultured in DMEM with 2 mM glutamax (GIBCO) and 10% fetal bovine serum. Cells were transiently transfected with Fugene 6 (Roche) according to manufacturer's instructions and harvested 18–24 hours post transfection. The following DNA constructs were used: HA-TRAK2 (gift from C. Hoogenraad, Utrecht University), Halo-TRAK2 (subcloned from HA-TRAK2 into pFN21A-HaloTag-CMV vector from Promega), Halo-TRAK2 AA129-130VV and Halo-TRAK2 I132D (generated from Halo-TRAK2), HA-LIS1 (gift from D. Smith, University of South Carolina), Myc-KIF5B (full-length mouse KIF5B in pRK5-Myc vector, gift from J. Kittler, University College London), Myc-KIF5C-Halo (full-length mouse KIF5C in pRK5-Myc vector, gift from J. Kittler, University College London, with a HaloTag subcloned into the C-terminus), KIF5C(1-560)-Halo (original KIF5C 1-560 construct, gift from Y. Konishi, Hamamatsu University, was subcloned into pEGFP-N1 plasmid backbone with eGFP removed), KIF5B(1-560)-Halo (original KIF5B 1-560 construct, gift from R. Vale, UCSF, was subcloned into the pHTC-HaloTag-CMV neo Vector from Promega), FLAG-p150^{Glued} (gift from T. Schwarz, Boston Children's Hospital), eGFP-P25 (gift from T. Schroer, Johns Hopkins University), and Halo-HOOK1(1-554) (first 554 aa of human HOOK1 were generated from the human

HOOK1 sequence and subcloned into pFN21A-HaloTag-CMV vector from Promega). All constructs were verified by DNA sequencing.

For RNAi transfection in knockdown experiments, Lipofectamine RNAiMax (Invitrogen) was used for transfection of siRNA duplexes at 50 nM. The 5' to 3' sequence of each siRNA is as follows: control non-targeting – UGGUUUACAUGUCGACUAA, KIF5B – GAACUGGCAUGAUAGAUGA, Dynein Heavy Chain – GAUCAAACAUGACGGAAUU, $p150^{Glued}$ – CUGGAGCGCUGUAUCGUAA, TRAK1 – GGAAACGAUGAGCGGAGUA.

Protein expression and purification

KIF5C(1-560)-Halo and rigor kinesin-1_{E236A} proteins were purified as described in Masucci et al., 2021(Masucci et al., 2021). Briefly, the plasmids were transformed into BL21(DE3)pLysE bacteria (Sigma, CMC0015-20X40UL) and grown in Terrific Broth media at 37 °C then at 18 °C for 18 hours in the presence of 0.15 mM IPTG. Cells were pelleted, flash frozen in liquid nitrogen, and stored at −80 °C. On the day of purification, cells were lysed by microfluidizer and clarified through centrifugation. The proteins were purified through a Co^{2+} agarose bead column (GoldBio, H-310-25) according to the manufacturer's protocol. KIF5C(1-560)-Halo was then bound to newly polymerized microtubules with AMPPNP and pelleted via centrifugation. The bound motors were then released from microtubules with ATP and centrifuged to remove the microtubules.

Immunoprecipitation assays

COS-7 cells were harvested 20-24 hours after transfection in 300 µL of lysis buffer containing 50 mM HEPES (pH 7.4), 25 mM NaCl, 1 mM EDTA, 1 mM MgCl2, 0.5% Triton X-100, and protease inhibitors (1 mM PMSF, 0.01 mg/ml Nα-p-tosyl-L-arginine methyl ester [TAME], 0.01 mg/ml leupeptin, 0.001 mg/ml pepstatin A, 1 mM DTT). Cell lysates were clarified at 17,000 x g for 10 min before use. 50 µL of Protein G Dynabeads (Promega) were resuspended in 200 µL of PBS + 0.02% Tween 20. The beads were incubated with 5 µg of anti-FLAG (Sigma, F4042), anti-GFP (Abcam, ab1218), or anti-HaloTag (Promega, G9281) for

15 minutes at room temperature. Beads were then washed once with 200 µL PBS + 0.02% Tween 20, once with 200 µL lysis buffer, and incubated with 300 µL lysate for 30 minutes at room temperature. Beads were then washed 3 times with 300 µL PBS, eluted in 60 µL SDS sample buffer, and analyzed by Western blot.

Microtubule pelleting assays

COS-7 cells were transfected with siRNAs against KIF5B, dynein heavy chain, p150, or a control non-targeting siRNA for 40-48 hours and transfected with Halo-TRAK2 for 20-24 hours. Cells were then lysed in BRB80 buffer (80 mM PIPES, 1 mM EGTA, and 1 mM MgCl2 (pH 6.8)) with 0.5% Triton X-100 and protease inhibitors (as described above) and clarified with two centrifugation steps at 17,000 and 32,000 x g. An input sample was taken from the clarified cell lysate. Unlabeled tubulin was clarified at 352,000 x g for 10 minutes at 4°C to pellet potential tubulin aggregates then polymerized at 5 mg/ml in BRB80 and stabilized with 1 mM GMPCPP. Equal volumes of cell lysate were then incubated with 0 or 5 µM of GMPCPP-stabilized microtubules at 37°C for 20 min. Samples were then centrifuged at 38,400 x g at 25 °C for 20 min. The resulting supernatant and pellet were then separated and denatured. The denatured inputs and pellets were then analyzed by Western blot.

Immunoblotting

Samples were analyzed by SDS-PAGE and transferred onto PDVF Immobilon FL membranes (Millipore). Membranes were dried for 1 hr, rehydrated in methanol, and stained for total protein (LI-COR REVERT Total Protein Stain). Following imaging of the total protein, membranes were destained, blocked for 1 hour in Odyssey Blocking Buffer TBS (LI-COR), and incubated overnight at 4°C with primary antibodies diluted in Blocking Buffer with 0.2% Tween-20. Membranes were washed four times for 5 min in 1xTBS Washing Solution (50 mM Tris-HCl pH 7.4, 274 mM NaCl, 9 mM KCl, 0.1% Tween-20), incubated in secondary antibodies diluted in Odyssey Blocking Buffer TBS (LI-COR) with 0.2% Tween-20% and 0.01% SDS for 1 hour, and again washed four times for 5 min in the washing solution. Membranes were immediately imaged using an Odyssey CLx Infrared Imaging System (LI-COR). Band intensities were measured in the Licor

Image Studio application. Primary antibodies used for Western blots included the following: HaloTag (Promega, G9281) at 1:1000, $p150^{Glued}$ (BD Transduction Laboratories, 610474) at 1:5000, Kinesin Heavy Chain (Millipore, MAB 1614) at 1:1000, Dynein Heavy Chain (Santa Cruz Biotechnology, R-325) at 1:500, FLAG (Sigma, F4042) at 1:1000, Myc (Sigma, R950-25) at 1:1000, HA (Covance, 16B12) at 1:1000, LIS1 (Abcam, ab109630) at 1:1000, and TRAK1 (Thermo PA5-44180) at 1:1,000. Secondary antibodies used for Western blots at a 1:20,000 dilution included the following: IRDye 800CW donkey anti-rabbit IgG (LI-COR, 926-32213), IRDye 680RD donkey anti-rabbit IgG (LI-COR, 926-68073), and IRDye 800CW donkey anti-mouse IgG (LI-COR, 926-32212).

Single-molecule motility assays

COS-7 cells expressing Halo-tagged constructs for 20-24 hours were labeled with 2.5 µM tetramethylrhodamine (TMR)-Halo ligand (Promega) for 15 minutes, washed twice with Ca2+- and Mg2+-free Dulbecco PBS (dPBS; GIBCO), returned to culture medium and left in the incubator for 30 minutes. For 3-color imaging experiments, GFP-DHC HeLa cells were labeled with TMR-Halo ligand and washed as described then labeled with 375 nM JF646-SNAP (provided by Luke Lavis, Janelia Farms) for 30 minutes, washed twice with dPBS, returned to culture medium and left in the incubator for 15 minutes. Cells were then washed twice with dPBS and collected in dPBS and pelleted at 5,000 x g for 5 min. The cell pellet was then lysed in 40 mM HEPES, 1 mM EDTA, 120 mM NaCl, 0.1% Triton X-100, and 1 mM magnesium ATP (pH 7.4) supplemented with protease inhibitors (as described above). The lysate was left on ice for 10 minutes and clarified at 17,000 x g for 10 minutes at 4°C.

GMPCPP-stabilized microtubule seeds were prepared by combining unlabeled tubulin and 2.5 or 5% HiLyte647-labeled or HiLyte488-labeled tubulin (Cytoskeleton) to a final concentration of 50 µM. This mix was clarified, polymerized, and stabilized as described above. A soluble tubulin mix was prepared by combining unlabeled tubulin and 2.5 or 5% labeled tubulin of the same color to a final concentration of 50 µM. This mix was clarified at 352,000 x g for 10 minutes at 4°C and kept on ice. In all experiments, the labeling of the microtubule seeds and free tubulin are the same.

Flow-chambers were prepared using silanized #1.5 glass coverslips (Warner) attached to glass slides (FisherScientific) using double-sided tape. To reduce non-specific binding, coverslips were cleaned through rounds of sonication in acetone, potassium hydroxide and ethanol, dried, plasma cleaned and silanized with PlusOne Repel-Silane (GE Healthcare). Flow-chambers were coated with 0.5 µM rigor kinesin-1_{E236A}, washed and blocked with 5% Pluronic F-127 (Sigma). After washing, 25 nM labeled GMPCPP-stabilized microtubules were flowed in and left to attach to the coverslip for 1 minute. Unbound microtubules were washed out with P12 (12 mM PIPES, 1 mM EGTA, 2 mM MgCl2). A final solution with 1:20 cell lysate, 10 µM tubulin mix, 1 mM Mg-GTP, 1 mM Mg-ATP in Dynamic Assay Buffer (P12, 0.3 mg/mL BSA, 0.3 mg/mL casein, 10 mM DTT, 15 mg/mL glucose, 0.05% methylcellulose) and an oxygen scavenging system (0.5 mg/mL glucose oxidase, 470 U/mL catalase; Sigma) was then flowed-in and let to equilibrate for approximately 5 minutes at 37°C before time lapse acquisition was initialized. 3 to 5 videos lasting 3 minutes were acquired at 37°C for each chamber. The microtubule channel was acquired at 1 frame each 10 seconds and the motor/adaptor channel was acquired at 4 frames per second in experiments examining a single motor or adaptor moving along dynamic microtubules. In dual-color co-migration experiments, the microtubule channel was acquired at 1 frame each 10 seconds and the other channels were acquired at 1 frame per second. In three-color co-migration experiments, all channels were imaged at 1 frame per second. Imaging was performed on a Nikon Eclipse Ti Inverted Microscope equipped with an Ultraview Vox spinning disk TIRF system and 100x 1.49 NA oil immersion objective (Nikon). Signals were collected using a Hamamatsu EMCCD C9100-13 camera, with a pixel size of 158 nm, controlled by Volocity software (PerkinElmer).

Analysis of motility on dynamic microtubules

Kymographs of the Halo-TRAK2 or Myc-KIF5C-Halo channel were generated for each microtubule at its maximum length by plotting a segmented line and using the Multi Kymograph macro for ImageJ. Microtubules were randomly selected from the field of view, but only microtubules with clearly defined polarity were analyzed. The microtubule plus-end was identified as the end with higher rates of growth and catastrophe through the 3-minute video. In 3-color co-migration experiments, the polarity of unlabeled

microtubules was defined by the transport of KIF5C toward the plus-end. Individual runs were then scored as processive to the MT plus-end, processive to the MT minus-end, or bidirectional/diffusive. Each processive run was manually tracked to determine run length, and velocity. Processive motility to either microtubule end was defined as unidirectional transport for a minimum of 4 pixels (632 nm) lasting at least 1 second (4 frames) without switching direction. In unidirectional trajectories that exhibited pauses of at least 1 second between processive segments, each segment was analyzed as a separate run. Bidirectional/diffusive motility was defined as any run lasting at least 2 seconds (8 frames) that traveled at least 4 pixels (632 nm) and switched direction during transport. Diffusive events were manually tracked to determine the net displacement from the position where the run initiated to the position where the run terminated. Run frequency was calculated on a per-video basis by dividing the total number of runs of each kind of motility by the total MT length. The number of runs per micron MT in each video was then divided by the TRAK2 or KIF5C concentration in each cell lysate. The relative concentration of TMR-labeled TRAK2 or KIF5C in each lysate was calculated by interpolating the fluorescence intensity value on a standard curve of TMR at known concentrations obtained from a Cytation 5 Imaging Reader (BioTek) using 554 ± 5 nm excitation band and 580 ± 5 nm emission band. TMR-normalized run frequencies were then averaged across videos to determine the run frequency per cell lysate. A final normalization was performed by scaling all data so the average frequency across biological replicates of the control condition is 1.

Mean-squared displacement analysis was performed by manually tracking the position of a single TRAK2 particle every frame during a run. The mean-squared displacement was then calculated from the run trajectory in R version 4.0.3.

Statistics and reproducibility

Statistical analyses were performed using GraphPad Prism version 9.1.0. Two-tailed unpaired student's t test, one-way ANOVA with Dunnett's multiple comparisons test, or two-tailed Mann-Whitney U test were used to calculate p values. * $p < 0.05$, ** $p < 0.01$, *** $p < 0.001$, and **** $p < 0.0001$ are considered significant. The types of the statistical tests, sample size, and statistical significance are reported in the

figures and corresponding figure legends. Data in column graphs are shown as individual data points with mean ± standard deviation (s.d.) from biologically independent experimental replicates. Individual data points from technical replicates within experiments are plotted whenever possible. All statistical analysis is conducted on data from at least three biologically independent experimental replicates. Kymographs and western blot images shown in the figures are representative of three or more independent experiments with similar results unless otherwise noted. The source data for statistical analyses can be found in the Source data file.

VI. Acknowledgements

We thank Mariko Tokito and Erin Masucci for technical assistance. We thank Elizabeth Gallagher, Stephen Coscia, and Sydney Cason for helpful feedback and discussion. This work was supported by National Institutes of Health Grants T32 GM008216 to A.R.F., AG064618 to T.A.J., and R35 GM126950 and RM1 GM136511 to E.L.F.H.

Author contributions

A.R.F., T.A.J., and E.L.F.H. designed the experiments and wrote the manuscript. A.R.F. performed the experiments and analysis. All the authors reviewed the figures and manuscript and approved its final version.

CHAPTER 3: INTERACTION BETWEEN THE MITOCHONDRIAL ADAPTOR MIRO AND THE MOTOR ADAPTOR TRAK

This chapter is adapted from:

Baltrusaitis, EE*; Ravitch, EE*; **Fenton, AR**; Perez, TA; Holzbaur; ELF; Dominquez, R. Interaction between the mitochondrial adaptor MIRO and the motor adaptor TRAK. *Journal of Biological Chemistry*. 299, 105441 (2023).

(***** equal contribution)

Contribution: ARF performed experimental procedures, data analysis, writing, and figure design related to cellular experiments in Fig. 3.6.

I. Summary

MIRO (mitochondrial Rho GTPase) consists of two GTPase domains flanking two Ca2+-binding EF-hand domains. A C-terminal transmembrane helix anchors MIRO to the outer mitochondrial membrane, where it functions as a general adaptor for the recruitment of cytoskeletal proteins that control mitochondrial dynamics. One protein recruited by MIRO is TRAK (trafficking kinesin-binding protein), which in turn recruits the microtubule-based motors kinesin-1 and dynein-dynactin. The mechanism by which MIRO interacts with TRAK is not well understood. Here, we map and quantitatively characterize the interaction of human MIRO1 and TRAK1 and test its potential regulation by Ca^{2+} and/or GTP binding. TRAK1 binds MIRO1 with low micromolar affinity. The interaction was mapped to a fragment comprising MIRO1's EF-hands and C-terminal GTPase domain and to a conserved sequence motif within TRAK1 residues 394 to 431, immediately C-terminal to the Spindly motif. This sequence is sufficient for MIRO1 binding in vitro and is necessary for MIRO1- dependent localization of TRAK1 to mitochondria in cells. MIRO1's EF-hands bind Ca^{2+} with dissociation constants (KD) of 3.9 μM and 300 nM. This suggests that under cellular conditions one EF-hand may be constitutively bound to Ca^{2+} whereas the other EF-hand binds Ca^{2+} in a regulated manner, depending on its local concentration. Yet, the MIRO1-TRAK1 interaction is independent of Ca^{2+} binding to the EF-hands and of the nucleotide state (GDP or GTP) of the C-terminal GTPase. The interaction is also independent of TRAK1 dimerization, such that a TRAK1 dimer can be expected to bind two MIRO1 molecules on the mitochondrial surface.

II. Introduction

Mitochondrial Rho GTPase (MIRO, isoforms 1 and 2; 60% sequence identity) acts as a general Ca^{2+}- and GTP-regulated adaptor on the outer mitochondrial membrane. MIRO is implicated in mitochondrial transport, morphogenesis, inheritance, homoeostasis, degradation, and contacts with the endoplasmic reticulum (Birsa et al., 2013; Eberhardt et al., 2020; Fransson et al., 2003, 2006; Kanfer et al., 2015; Modi et al., 2019; Saotome et al., 2008; Weihofen et al., 2009). MIRO consists of N- and C-terminal GTPase domains (nGTPase, residues 1-168 and cGTPase, residues 416-579; numbering is for human MIRO1) that surround two pairs of EF-hands. Each EF-hand pair consists of a canonical Ca^{2+}-binding EF-hand and a "hidden" EF-hand that does not bind Ca^{2+}, and hosts in its hydrophobic pocket a ligand-mimic helix (Klosowiak et al., 2013; Stathopulos et al., 2008). Together, the EF-hand pair with its bound ligand-mimic helix is referred to as the ELM domain (ELM1, residues 183-274; ELM2, residues 303-384) (Fig. 3.1A) (Klosowiak et al., 2013). Additionally, MIRO has a C-terminal transmembrane helix (residues 590-618) that inserts into the outer mitochondrial membrane (OMM), where MIRO is predominantly localized (Fransson et al., 2003).

One of the proteins MIRO recruits to mitochondria is trafficking kinesin protein (TRAK, isoforms 1 and 2; 49% sequence identity), which in turn recruits the microtubule-based motors kinesin-1 and dynein-dynactin (Brickley & Stephenson, 2011). Sequence identity among TRAK isoforms is somewhat higher (53%) for the N-terminal ~400-amino acid region, which harbors the dynein-dynactin and kinesin-1-binding sites (Canty et al., 2023; Fenton et al., 2021a; Glater et al., 2006; Randall et al., 2013; M. J. Smith et al., 2006; Tan et al., 2023; van Spronsen et al., 2013). TRAK belongs to a family of activating adaptors that, while generally unrelated, share long regions of coiled-coil and are capable of recruiting and activating dynein and dynactin for long-range processive motility (McKenney et al., 2014; Schlager, Hoang, et al., 2014). By analogy with known cryo-electron microscopy (cryo-EM) structures of other activating adaptors in complex with dynein and dynactin (Urnavicius et al., 2015, 2018), the region of TRAK involved in binding dynein-dynactin consists of amino acids 118-392 (numbering is for human TRAK1). This region is predicted to form a long coiled-coil along the F-actin-like dynactin minifilament that forms the core of the dynactin

complex and includes the CC1-box (residues 125-139) and Spindly (residues 373-379) motifs at its N- and C-terminal ends, respectively. The CC1-box interacts with the dynein light intermediate chain, and this interaction is important for processive dynein motility (Celestino et al., 2019; Gama et al., 2017; I.-G. Lee et al., 2018, 2020). While the binding site of kinesin-1 has not been precisely mapped, several studies converge on a fragment comprising TRAK residues 1-360 (Canty et al., 2023; Glater et al., 2006; Randall et al., 2013; M. J. Smith et al., 2006; Tan et al., 2023; van Spronsen et al., 2013). Thus, the binding sites of kinesin-1 and dynein-dynactin may overlap. Yet, both motors have been localized to a single TRAK adaptor, which suggests the existence of regulatory mechanisms that avoid a futile tug-of-war between the two motors during mitochondrial transport toward the opposite ends of the microtubule (Canty et al., 2023; Fenton et al., 2021a). Moreover, knockdown or inhibition of either motor impairs mitochondrial motility in both microtubule directions, suggesting functional interdependence of the two motor systems (Pilling et al., 2006; van Spronsen et al., 2013).

TRAK (Brickley & Stephenson, 2011; Stowers et al., 2002; van Spronsen et al., 2013) and MIRO (Babic et al., 2015; X. Guo et al., 2005; López-Doménech et al., 2016; MacAskill, Rinholm, et al., 2009; G. J. Russo et al., 2009) are both essential for mitochondrial motility and distribution in neurons. Knockout studies in mice identify MIRO1, and not MIRO2, as the main isoform associated with mitochondrial transport in axons and dendrites (López-Doménech et al., 2016). Similarly, TRAK1 appears to play a predominant role compared to TRAK2 in mitochondrial motility in mature neurons (Brickley & Stephenson, 2011). Perhaps for this reason, most studies have focused on isoforms MIRO1 and TRAK1. Yet, given a relatively high sequence identity among the isoforms of each protein, our underlying hypothesis is that they interact through a conserved mechanism, which nevertheless remains poorly understood due in part to conflicting evidence in the literature.

Some studies have implicated MIRO's nGTPase in the interaction with TRAK, while specifically excluding the EF-hands and cGTPase (Babic et al., 2015; Davis et al., 2023; Fransson et al., 2006; MacAskill, Rinholm, et al., 2009). These studies, however, disagree as to whether the nucleotide state of the nGTPase (GTP or GDP) is important (Babic et al., 2015; Davis et al., 2023; MacAskill, Rinholm, et al.,

2009) or not (Fransson et al., 2006) for this interaction. On the other hand, elevated local Ca^{2+} concentrations arrest mitochondrial trafficking in different cell types (Brough et al., 2005; Quintana et al., 2006; Yi et al., 2004), and this effect is suppressed by mutations in the EF-hands of MIRO1 (Chang et al., 2011; MacAskill, Rinholm, et al., 2009; Saotome et al., 2008; X. Wang & Schwarz, 2009). While these studies appear to directly implicate the EF-hands in interactions with either kinesin-1 or TRAK1 (MacAskill, Rinholm, et al., 2009; Saotome et al., 2008; X. Wang & Schwarz, 2009), another study suggests that the effect of the EF-hand mutations is indirect, by reducing Ca^{2+} entry into mitochondria, which in turn acts as a signal to control mitochondrial motility (Chang et al., 2011). A recent study finds that MIRO1 and TRAK1/2 interact and comigrate in the absence or the presence of Ca^{2+} (Canty et al., 2023). It is therefore unclear which MIRO domain(s) bind TRAK and whether the interaction is regulated by Ca^{2+} and/or nucleotide.

Here, we map and quantitatively characterize the interaction of MIRO1 with TRAK1 and explore its potential regulation by Ca2+ and the nucleotide state (GTP or GDP) of MIRO1. MIRO1 binds TRAK1 through a fragment comprising the EF-hands and cGTPase. The interaction is independent of Ca^{2+} binding to the EF-hands and is unaffected by the nucleotide state of the cGTPase. On TRAK1, the interaction was mapped to a conserved motif (residues 394–431) C terminal to the Spindly motif. This sequence is necessary for MIRO1- dependent localization of TRAK1 to mitochondria in cells. The interaction is independent of TRAK1 dimerization, such that a TRAK1 dimer can be expected to bind to two MIRO1 molecules on the mitochondrial membrane.

III. Results

MIRO1 binds TRAK1 through a fragment comprising the EF-hands and cGTPase

Using pull-down experiments, a recent study found that MIRO1 forms a quaternary complex with kinesin-1 (KIF5B), dynein-dynactin, and a TRAK1 fragment comprising residues 1-532 ($TRAK1_{1-532}$), but not with a shorter fragment consisting of residues 1-360 ($TRAK1_{1-360}$) (Canty et al., 2023). These results suggested that the MIRO1-binding site is located within TRAK1 residues 360-532. Moreover, these authors

found that the association and comigration of MIRO1 with TRAK1$_{1-532}$, dynein-dynactin, and KIF5B was independent of the nucleotide state or the presence of Ca^{2+}. Based on these results, we designed MIRO1 and TRAK1 constructs to specifically map their interaction using glycerol gradient cosedimentation. Experiments were initially performed in the presence of 1 mM $CaCl_2$, 1 mM $MgCl_2$, 0.1 mM GTP. The longest TRAK1 construct analyzed consisted of residues 99-532 (TRAK1$_{99-532}$), comprising the previously identified MIRO1-binding region (Canty et al., 2023), but avoiding the less conserved N-terminal sequence that precedes the coiled-coil that binds dynein-dynactin (Fig. 3.1A and Fig. S3.1). Crystal structures have been determined of human MIRO1's nGTPase (K. P. Smith et al., 2020) and a fragment comprising the EF-hands and cGTPase (Klosowiak et al., 2016). These structures and AlphaFold (Jumper et al., 2021) suggest that the nGTPase is detached from the EF-hands and cGTPase, with the latter two being more tightly packed against one another. These considerations informed the design of three MIRO1 constructs: MIRO1$_{1-591}$, a near full-length construct lacking the C-terminal transmembrane helix that reduces solubility; MBP-MIRO1$_{1-180}$, corresponding to MIRO1's nGTPase and fused to MBP (maltose-binding protein) for enhanced purity and solubility; and MIRO1$_{177-591}$, comprising the EF-hands and cGTPase.

MIRO1$_{1-591}$ comigrated with TRAK1$_{99-532}$ in the glycerol gradient, as indicated by a rightward (higher mass) shift of the main peak of TRAK1$_{99-532}$ when ran together with MIRO1$_{1-591}$ as compared to control (TRAK1$_{99-532}$ ran alone) (Fig. 3.1B and Fig S3.2A). The migration profile of TRAK1$_{99-532}$ did not change with or without MBP-MIRO1$_{1-180}$ (Fig. 3.1C and Fig S3.2B). This result suggests a lack of interaction and disagrees with previous reports that mapped this interaction to the nGTPase using cellular pulldowns and point mutations in the catalytic site of the nGTPase (Babic et al., 2015; Davis et al., 2023; Fransson et al., 2006; MacAskill, Brickley, et al., 2009). In contrast, TRAK1$_{99-532}$ comigrated with MIRO1$_{177-591}$, suggesting that the TRAK1-binding site is contained within the EF-hands and/or cGTPase (Fig. 3.1D and Fig S3.2C).

In the sedimentation assays, MIRO1$_{1-591}$ and TRAK1$_{99-532}$ migrated over a broad range of glycerol concentrations, both alone and together (Fig. 3.1A-C), which suggests these proteins are extended, assume multiple conformations, or form higher molecular weight oligomers. Mass photometry was used to explore the oligomerization state of the three MIRO1 constructs used above, which by SDS-PAGE migrate

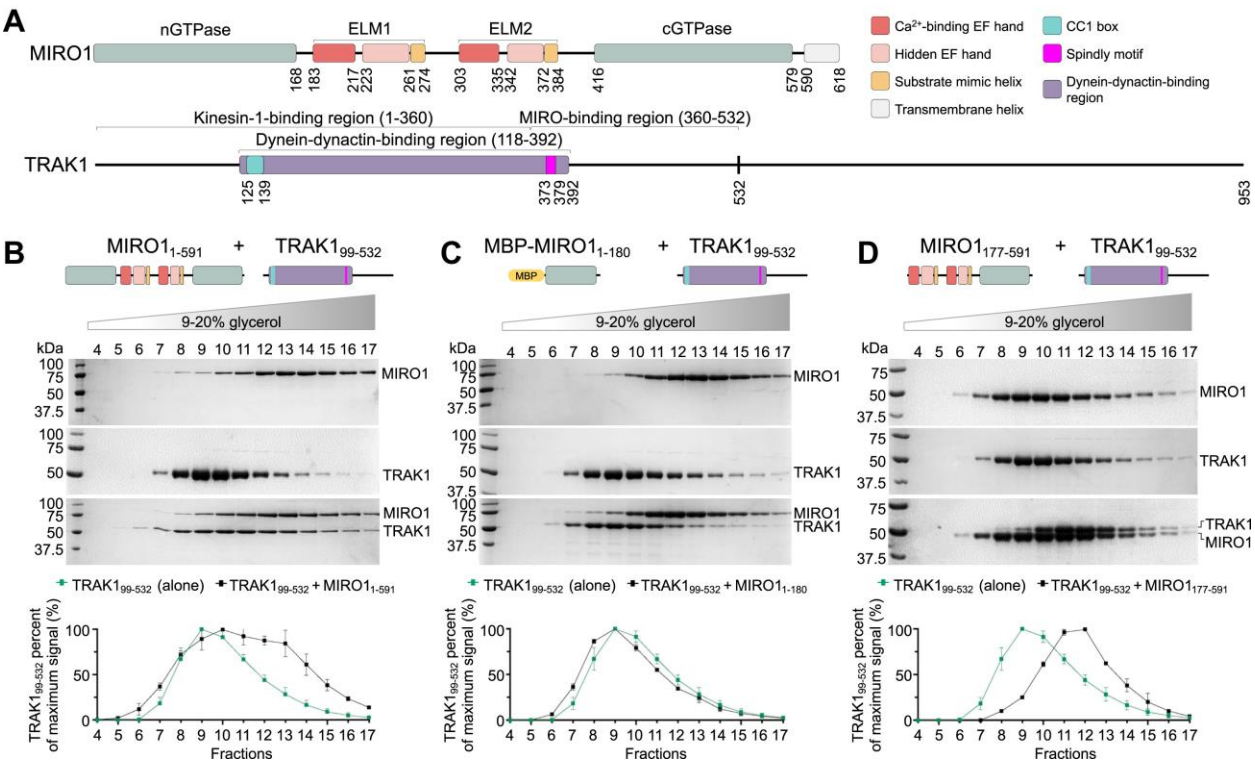

Figure 3.1: MIRO1 binds TRAK1 through a fragment comprising the EF-hands and cGTPase. A, Domain diagrams of MIRO1 and TRAK1 (nGTPase and cGTPase, N- and C-terminal GTPase domains; ELM 1 and 2, EF-hand pair ligand mimic 1 and 2; CC1 box, coiled-coil 1 box). Each ELM domain consists of a Ca^{2+}-binding EF-hand (red), a hidden EF-hand that does not bind Ca^{2+} (pink), and a ligand mimic helix (orange). By analogy with other dynein-dynactin adaptors (Urnavicius et al., 2015, 2018), the dynein-dynactin-binding region of TRAK1 can be mapped to residues 118-392 (purple) and comprises the CC1 box (cyan) and the Spindly motif (magenta). The binding sites of kinesin-1 and MIRO1 have been approximately mapped to residues 1-360 (Canty et al., 2023; Fenton et al., 2021a; M. J. Smith et al., 2006; Tan et al., 2023; van Spronsen et al., 2013) and 360-532 (Canty et al., 2023), respectively. **B-D,** Migration of $MIRO1_{1-591}$, $MBP\text{-}MIRO1_{1-180}$, $MIRO1_{177-591}$ alone and together with $TRAK1_{99-532}$ in a 5-30% glycerol gradient. The figures show representative SDS-PAGE analyses of the fractions 4-17 (9-20% glycerol) containing these proteins. Densitometric analysis of the gels is shown at the bottom. For each fraction, the average TRAK1 signal (alone, green or with MIRO1 constructs, black) from N=3 independent experiments (Fig. S3.2) is reported as the percentage of the average signal for the TRAK1 fraction with the maximum intensity.

as single bands (Fig. S3.3A). Of note, this method uses low protein concentrations (~20-150 nM), such that weakly interacting species tend to dissociate. Moreover, mass measurement become less accurate for proteins with molecular weights <100 kDa (Young et al., 2018). It is nevertheless a useful technique to study large proteins and protein complexes or to assess sample homogeneity (Sonn-Segev et al., 2020), which is our purpose here. With $MIRO1_{1-591}$, we observed multiple species, and the distribution profile was

very similar in the presence of 100 mM $CaCl_2$ or 1 mM ethylene glycol tetraacetic acid (EGTA), which chelates Ca^{2+} (Fig. S3.3B). This result indicates that $MIRO1_{1-591}$ tends to oligomerize and that Ca^{2+} binding to the EF-hands is unlikely to produce a substantial conformational change. MBP-$MIRO1_{1-180}$, which does not include the EF-hands, was only analyzed in 1 mM EGTA and also showed multiple species (Fig. S3.3C). Therefore, the nGTPase may be at least in part responsible for MIRO1's tendency to oligomerize, consistent with structural studies showing that the nGTPase forms dimers (K. P. Smith et al., 2020). In contrast, at this low concentration (150 nM) $MIRO1_{177-591}$ displayed a single peak, both in the presence or the absence of Ca^{2+}, suggesting a rather stable conformation independent of Ca^{2+} binding (Fig. S3.3D). This result is also consistent with crystal structures of this fragment showing fundamentally the same conformation independent of the bound cation or nucleotide (Klosowiak et al., 2013, 2016). $MIRO1_{177-591}$ is thus used in most experiments below, as it comprises the TRAK1-binding site (Fig. 3.1D) and appears homogeneous (Fig. S3.3D).

With $TRAK1_{99-532}$ we observed two peaks (Fig. S.33E), with measured masses 66 ± 4.8 kDa and 91 ± 9 kDa (theoretical mass of monomer: 53.5 kDa). While these mass measurements are not accurate, this result suggests that by itself and at low concentration (125 nM) the TRAK1 coiled-coil dimer is unstable, and the protein may exist in monomer-dimer equilibrium. The coiled-coil is likely stabilized in the complex with dynein-dynactin, as observed in the cryo-EM structures of other adaptors (Urnavicius et al., 2015, 2018).

TRAK1 binds MIRO1 through a conserved sequence C-terminal of the Spindly motif

Having identified the region of MIRO1 implicated in TRAK1 binding, we set out to map the binding site on TRAK1. As mentioned above, the MIRO1-binding site is expected to be located within TRAK1 residues 360-532 (Canty et al., 2023), which is also consistent with our cosedimentation analysis (Fig. 3.1B,D). We focused on this area and designed TRAK1 constructs taking into consideration sequence conservation and coiled-coil prediction (Fig. 3.2A), two factors which may be important for the interaction

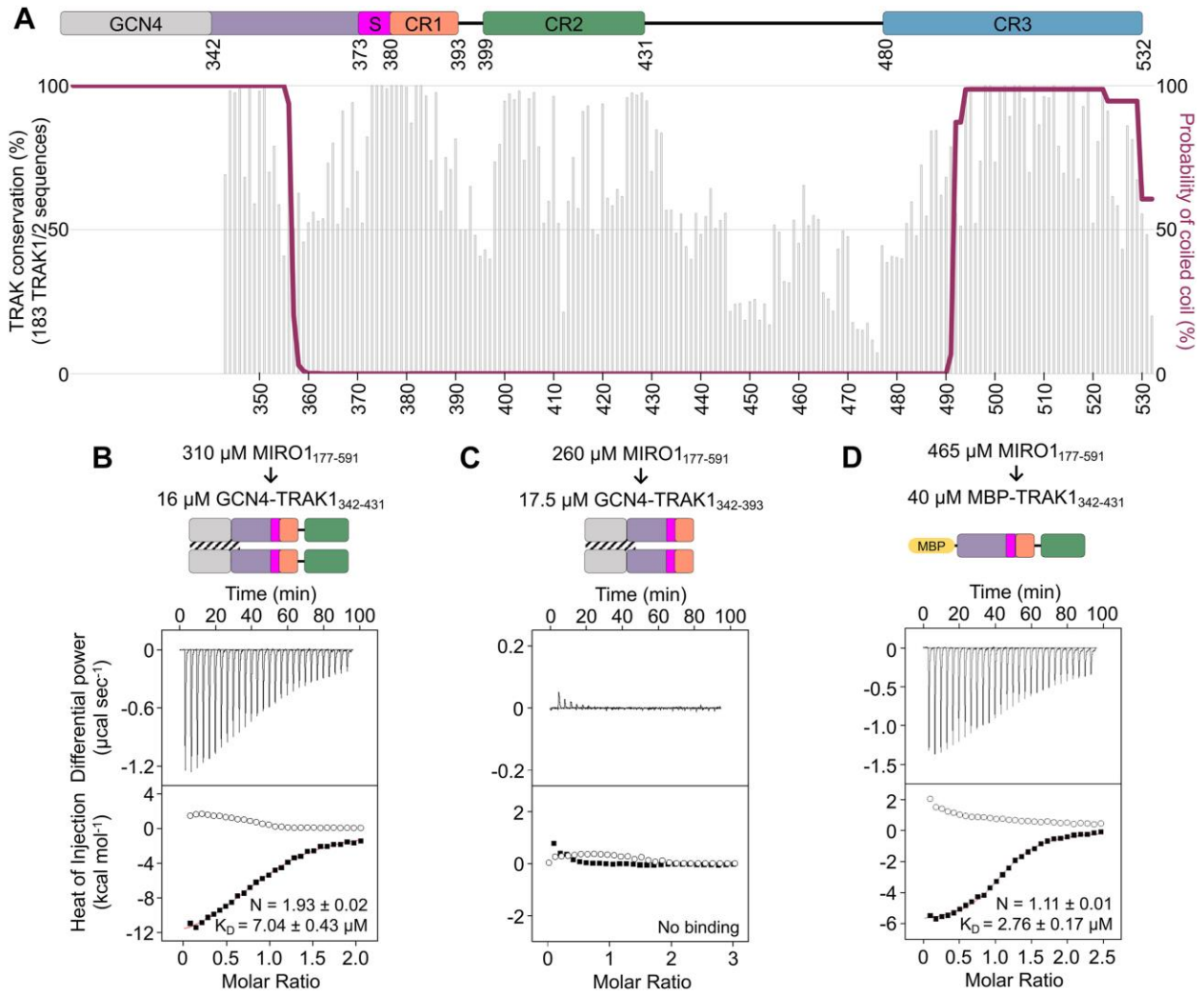

Figure 3.2: TRAK1 binds MIRO1 through a conserved sequence C-terminal of the Spindly motif. A, Domain diagram (top), sequence conservation (bottom, gray bars), and coiled-coil prediction (bottom, maroon trace) of construct GCN4-TRAK1$_{342-431}$ (see also Fig. S3.1). Per-residue conservation scores were calculated with the program Scorecons (Valdar, 2002) from an alignment of 183 vertebrate TRAK sequences, including 93 TRAK1 and 90 TRAK2 sequences. The coiled-coil prediction used a 28-amino acid window. Three conserved regions (CR1, CR2, and CR3) identified C-terminally to the Spindly motif are highlighted. **B-D,** Representative ITC titrations of MIRO1$_{177-591}$ into the indicated TRAK1 constructs from N = 3 independent experiments (Table 3.1). Prior to each titration, the proteins in the syringe (top) and in the cell (bottom) were co-dialyzed for three days in ITC buffer with 50 μM $CaCl_2$. Listed with each titration are the concentrations of the protein in the syringe and in the cell and, for interacting proteins, the parameters of the fit (stoichiometry N and dissociation constant K_D) to a binding isotherm (red line). Errors correspond to the s.d. of the fits. Open symbols correspond to control titrations into buffer.

with MIRO1. Because the coiled-coil prediction drops around residue 352 (Fig. S3.1), the TRAK1 constructs analyzed here start with residue E342, within the region of high coiled coil probability. To further stabilize

the coiled-coil, a 30-amino acid GCN4 leucine-zipper (O'Shea et al., 1991) was added N-terminally to E342, ensuring that the heptad repeats of the leucine-zipper and TRAK1 matched at the point of fusion (Fig. S3.4).

The MIRO-TRAK interaction is likely conserved among TRAK species and isoforms and should therefore involve a region of high sequence conservation. Other than the Spindly motif, three regions of high sequence conservation can be identified within TRAK1 residues 360-532 (Fig. 3.2A): CR1 (380-393), CR2 (399-431), and CR3 (480-532). Isothermal titration calorimetry (ITC) was used to quantitatively test the interaction of $MIRO1_{177-591}$ with TRAK1 constructs lacking either CR3 (GCN4-$TRAK1_{342-431}$) or CR2 and CR3 (GCN4-$TRAK1_{342-393}$) (Fig. S3.5). Experiments were performed in 50 mM $CaCl_2$, 1 mM $MgCl_2$, 0.1 mM GTP (higher Ca^{2+} concentrations precipitated the GCN4 hybrid constructs). $MIRO1_{177-591}$ bound GCN4-$TRAK1_{342-431}$ with K_D = 7.04 mM and stoichiometry N = 1.93 (Fig. 3.2B, Table 3.1) but did not bind GCN4-$TRAK1_{342-393}$ (Fig. 3.2C, Table 3.1). This finding suggests the MIRO1 binding site lies within the 33-residue CR2 region. $MIRO1_{177-591}$ also bound the monomeric construct MBP-$TRAK1_{342-431}$, in which GCN4 was replaced with MBP, with similar affinity (K_D = 2.76 mM) as for GCN4-$TRAK1_{342-431}$ but with stoichiometry N = 1.11 (Fig. 3.2D, Table 3.1). This result suggests that a TRAK1 dimer can potentially bind to two MIRO1 molecules on the mitochondrial surface.

In these ITC experiments, the control titrations of $MIRO1_{177-591}$ into buffer (open symbols) displayed a small amount of dissociation heat (endothermic), which was subtracted from the heats of binding to TRAK1 constructs (exothermic). Dissociation is not observed when monomeric TRAK1 constructs are injected into $MIRO1_{177-591}$ (see below).

The MIRO1-TRAK1 interaction is independent of Ca^{2+} binding to the EF-hand domains

Models diverge as to whether the MIRO-TRAK interaction is regulated by Ca^{2+} binding to MIRO's EF-hands (Saotome et al., 2008) or not (Canty et al., 2023; Fransson et al., 2006; MacAskill, Rinholm, et al., 2009). This question is addressed here using quantitative ITC experiments and mutagenesis. The experiments

described above were performed in the presence of 50 mM $CaCl_2$. The titration of 800 mM $CaCl_2$ into this protein did not reveal additional Ca^{2+} binding (Table 3.1), demonstrating that the EF-hands are saturated at 50 mM $CaCl_2$. Lowering the $CaCl_2$ concentration of the protein 10-fold further produced the same result (Fig. 3.3A), indicating that the K_D for Ca^{2+} binding to both EF-hands is below 5 mM. To fully remove the Ca^{2+} from the EF-hands, $MIRO1_{177-591}$ was dialyzed against 5 mM EGTA, 1 mM $MgCl_2$, and 0.1 mM GTP. Most of the EGTA was then removed in a stepwise manner, to a final concentration of 0.08 mM, to ensure that only a small amount of the Ca^{2+} was chelated in subsequent experiments. The titration of 800 mM $CaCl_2$ into this protein revealed two Ca^{2+}-binding sites, with affinities differing by >10-fold (K_D = 0.3 mM and 3.94 mM) (Fig. 3.3C and Table 3.1). The intracellular concentration of free Ca^{2+} fluctuates between 0.1 mM at rest and 10 mM during activation (Berridge et al., 1998, 2000), suggesting that one of the Ca^{2+}-binding sites of MIRO1 may be constitutively occupied by Ca^{2+} whereas the other site could play a regulatory role, binding Ca^{2+} only when its local concentration increases.

These experiments showed that in the presence of 5 mM EGTA the EF-hands of $MIRO1_{177-591}$ are free of Ca^{2+}. Under these conditions, $MIRO1_{177-591}$ bound dimeric GCN4-$TRAK1_{342-431}$ (K_D = 5.13 mM, N= 1.84) and monomeric MBP-$TRAK1_{342-431}$ (K_D = 8.77 mM, N= 1.09) with similar affinities and stoichiometries as observed above in the presence of Ca^{2+} (compare Figs. 3.2B-C and 3.3C-D). This result provides direct evidence that the interaction of MIRO1 with TRAK1 is independent of Ca^{2+} binding to MIRO1, which is consistent with some of the previous findings (Canty et al., 2023; Fransson et al., 2006; MacAskill, Rinholm, et al., 2009).

The experiments described above were all performed in the presence of 1 mM $MgCl_2$. Therefore, it must be considered whether Mg^{2+} occupies the EF-hands of MIRO1 under these conditions, as previously observed in crystal structures (Klosowiak et al., 2013, 2016). The binding of Mg^{2+} to MIRO1's EF-hands likely has physiological importance, since the free concentration of Mg^{2+} in cells ranges from 0.5 to 1.0 mM (Romani & Scarpa, 1992). Therefore, at resting free Ca^{2+} concentrations, Mg^{2+} may saturate most EF-hands, including those of MIRO1, which has led to the proposal that the Ca^{2+}-dependent activation of EF-hand proteins must take into account the displacement of Mg^{2+} (and other divalent cations) from EF-hands

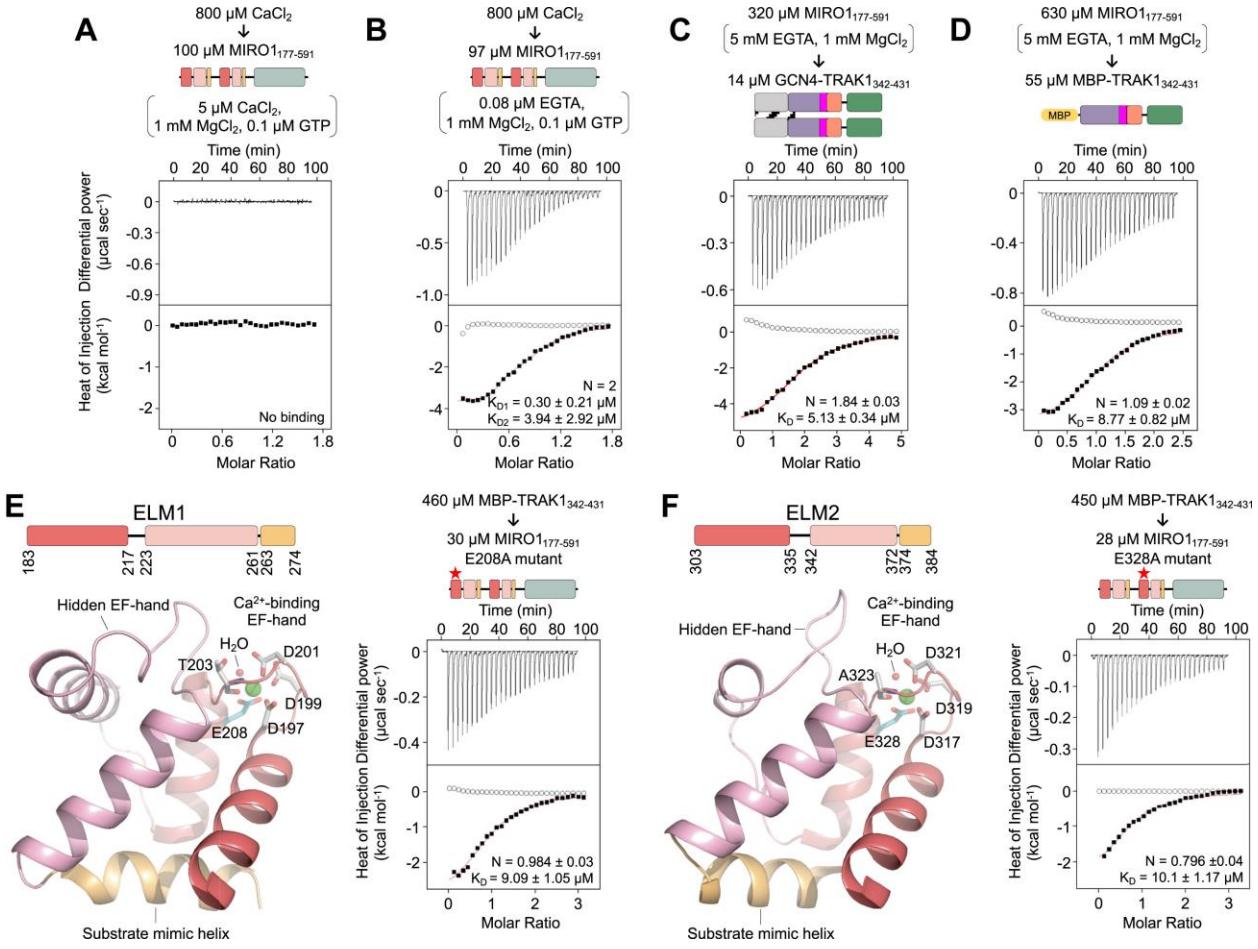

Figure 3.3: The MIRO1-TRAK1 interaction is independent of Ca^{2+} binding to the EF-hand domains. A-B, Representative ITC titrations (see also Table 3.1) of 800 µM $CaCl_2$ into $MIRO1_{177-591}$. Prior to the titrations, $MIRO1_{177-591}$ was dialyzed for three days in ITC buffer with either 5 µM $CaCl_2$ **(A)** or 5 mM EGTA followed by stepwise removal of EGTA to a final concentration of 0.08 µM **(B)**. The titrated $CaCl_2$ was dissolved in the dialysis buffer. **C-D,** Representative ITC titrations from N = 3 independent experiments (Table 3.1) of $MIRO1_{177-591}$ into the indicated TRAK1 constructs. Proteins were dialyzed in ITC buffer with 5 mM EGTA. **E-F,** Representative ITC titrations from N = 3 independent experiments (Table 3.1) of MBP-$TRAK1_{342-431}$ into $MIRO1_{177-591}$ mutants E208A **(E)** and E328A **(F)**. Proteins were dialyzed in ITC buffer with 5 mM EGTA. Ribbon diagrams (left, color coded as in Fig. 3.1A, Ca^{2+} ions in green) highlight the location of the mutated amino acid (cyan Cα) within the Ca^{2+}-binding loop of each ELM domain(Klosowiak et al., 2016). Shown with each ITC titration in this figure are the concentrations of the protein (or $CaCl_2$) in the syringe and in the cell and the parameters of the fit (stoichiometry N and dissociation constant K_D) to a binding isotherm (red line). Errors correspond to the s.d. of the fits. Open symbols correspond to control titrations into buffer.

(Grabarek, 2011; Senguen & Grabarek, 2012). Because Mg^{2+} coordinates the nucleotide in the catalytic site of the cGTPase, $MgCl_2$ cannot be removed in experiments with $MIRO1_{177-591}$, which precipitates in its absence. Therefore, to specifically disrupt the binding of cations to the EF-hands, the bidentate cation-

coordinating residues E208 and E328 were independently mutated to alanine within the first or second Ca^{2+}-binding EF-hands, respectively (Fig. 3E-F, left). These mutants bound monomeric MBP-TRAK1$_{342-431}$ with similar affinity and stoichiometry as observed above in the presence or the absence of Ca^{2+}, indicating that the MIRO1-TRAK1 interaction is independent of cation binding to the EF-hands (Fig. 3E-F, right).

Note that the order of the titrations has been deliberately inverted among the various experiments described in this work (i.e., MIRO1 and TRAK1 constructs are found sometimes in the syringe and sometimes in the cell) and each ITC experiment was repeated multiple times with similar results (Table 3.1). Of note, the slight endothermic heats of dissociation observed in control titrations into buffer when MIRO1$_{177-591}$ is in the syringe (i.e., Figs. 3.2D and 3.3D, open symbols) are not observed when MBP-TRAK1$_{342-431}$ is in the syringe (Fig. 3E, F, open symbols).

The MIRO1-TRAK1 interaction is independent of the nucleotide state of the cGTPase

Both GTPase domains of yeast MIRO (Gem1) (Koshiba et al., 2011) and the nGTPase of *Drosophila* MIRO (S. Lee et al., 2016) have been shown to be catalytically active, but whether mammalian MIRO hydrolyzes GTP is controversial. While biochemical studies suggest that mammalian MIRO hydrolyses GTP (Peters et al., 2018; Suzuki et al., 2014), key catalytic residues present in Ras-family GTPases are missing in the GTPase domains of MIRO(Peters et al., 2018). Moreover, a crystal structure of the nGTPase of MIRO1 reveals a lack of nucleotide hydrolysis in the crystals and a non-catalytic configuration of the GTP-binding site (K. P. Smith et al., 2020). Therefore, it is unclear whether the nucleotide state of MIRO1, and particularly that of the cGTPase, plays a role in target recognition. To determine the nucleotide state of MIRO1$_{177-591}$ and its potential role in TRAK1 binding we used reverse-phase analytical HPLC and ITC.

First, the nucleotide state of *E. coli*-expressed MIRO1$_{177-591}$ was determined using as reference analytical-grade commercial GDP and GTP. By reverse-phase analytical HPLC, the commercial GDP

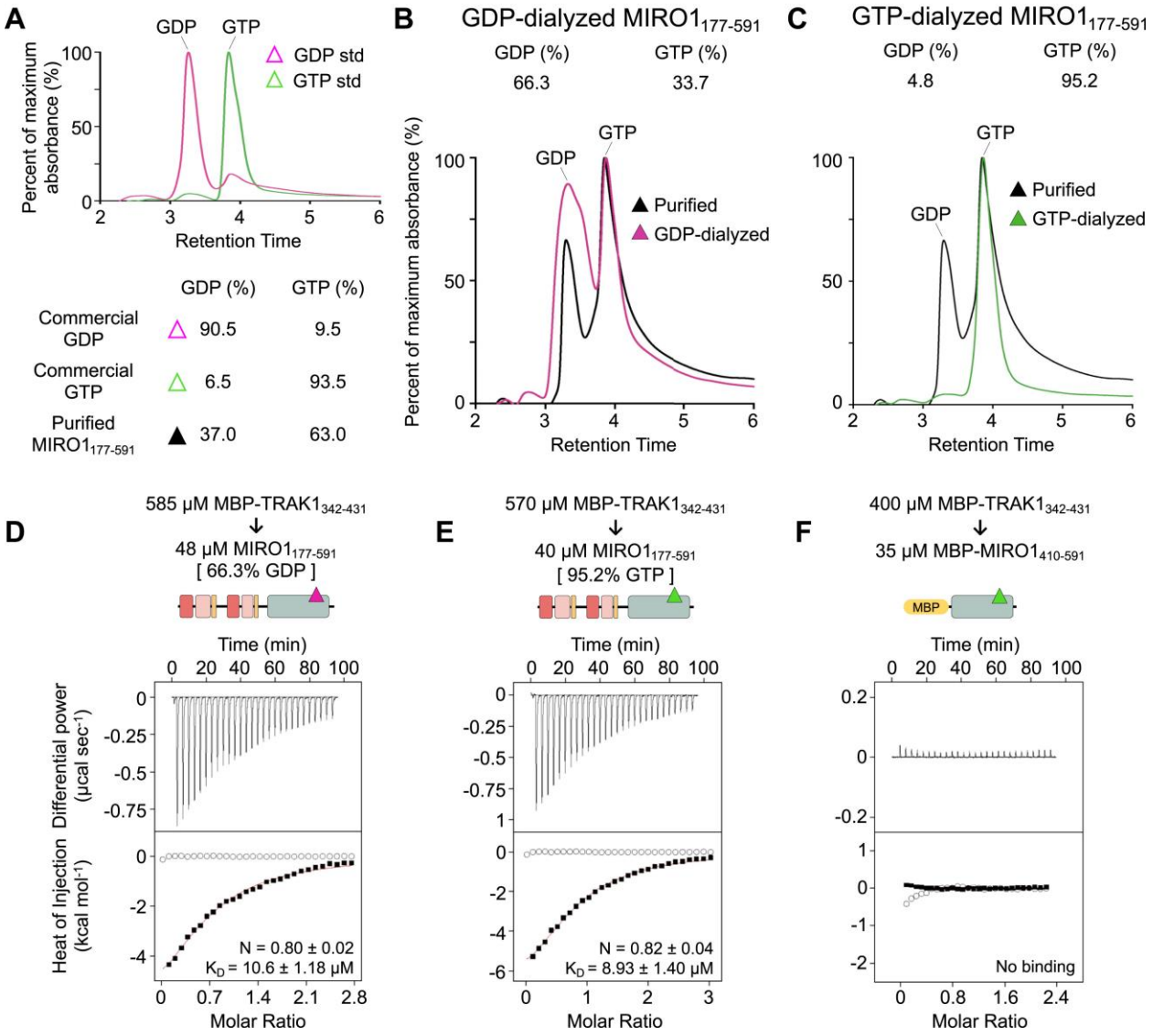

Figure 3.4: The MIRO1-TRAK1 interaction is independent of the nucleotide state of the cGTPase. A, HPLC analysis of analytical-grade commercial GDP (pink) and GTP (green) standards (left) and quantifications (right). The normalized maximum absorbance at 256 nm (y-axis) is plotted as a function of the retention time. **B-C,** HPLC analysis of *E. coli*-expressed MIRO1$_{177-591}$ before (black trace) and after addition of 35-molar excess of commercial nucleotide (GDP, pink trace; GTP, green trace) followed by 3-day dialysis into ITC buffer with 5 mM EGTA and no extra nucleotide added (left). Quantifications based on absorbance at 256 nm are shown above each graph and in part A (right). **D-F,** Representative ITC titrations from N = 3 independent experiments (Table 3.1) of MBP-TRAK1$_{342-431}$ into the nucleotide-exchanged MIRO1$_{177-591}$ samples (GDP, part **B** and **D**; GTP, part **C** and **E**) or MIRO1$_{410-591}$ (same dialysis as GTP-dialyzed MIRO1$_{177-591}$). Listed with each titration are the concentrations of the protein in the syringe and in the cell and the parameters of the fit (stoichiometry N and dissociation constant K_D) to a binding isotherm (red line). Errors correspond to the s.d. of the fits. Open symbols correspond to control titrations into buffer.

sample contains 90.5% GDP and 9.5% GTP whereas the commercial GTP sample contains 6.5% GDP and 93.5% GTP (Fig. 3.4A). Using the HPLC elution profile of these two samples as reference, *E. coli*-expressed MIRO1$_{177-591}$ was found to contain 37.0% GDP and 63.0% GTP. To exchange the nucleotide on MIRO1$_{177-591}$, a 35-molar excess of commercial nucleotide (GDP or GTP) was added and incubated for one hour on ice, followed by 3-day dialysis into a buffer with no extra nucleotide added. After dialysis and passage through a PD10 column (see Methods), the sample pre-incubated with GDP had 66.3% GDP and 33.7% GTP (Fig. 3.4B), whereas the sample pre-incubated with GTP had 4.8% GDP and 95.2% GTP (Fig. 3.4C). The inefficient incorporation of GDP contrasts with the nearly complete incorporation of GTP and suggests that the cGTPase has a marked preference for GTP, analogous to other Ras-family GTPases (Lenzen et al., 1998). Moreover, because the cellular concentration of GTP is ~10-fold higher than that of GDP (Traut, 1994), purified MIRO1$_{177-591}$ could have been expected to be have mostly GTP bound. That it had 37% GDP bound suggests that GTP was being slowly hydrolyzed during purification, as suggested by studies that show that the MIRO1 GTPases are catalytically active (Peters et al., 2018; Suzuki et al., 2014). MBP-TRAK1$_{342-431}$ bound the MIRO1$_{177-591}$ samples pre-incubated with GDP or GTP with similar affinities and stoichiometries (Fig. 3.4D-E), which were also similar to those observed in other experiments performed here (Figs. 3.2D, 3.3D-F). From these results, we conclude that the interaction with TRAK1 is independent of the nucleotide state of the cGTPase, consistent with studies showing that mutations of the cGTPase have little effect on mitochondrial trafficking and TRAK recruitment to mitochondria (Davis et al., 2023; Fransson et al., 2006).

MIRO1$_{177-591}$ contains both the EF hands and cGTPase. We asked whether the TRAK1-binding site was fully contained within one of these domains or whether the two domains contributed together toward the interaction. Therefore, constructs MBP-MIRO1$_{177-404}$ (EF hands) and MBP-MIRO1$_{410-591}$ (cGTPase) were expressed to test binding to TRAK1 by ITC. However, while MBP-MIRO1$_{410-591}$ was well-behaved, MBP-MIRO1$_{177-404}$ could not be used as it was poorly expressed and prone to aggregation. By ITC, MBP-MIRO1$_{410-591}$ did not bind MBP-TRAK1$_{342-431}$ (Fig. 3.4F). This result shows that the presence of the EF-hands is required for TRAK1 binding, but we cannot rule out participation of the cGTPase in the interaction via a combined interface with the EF-hands.

A conserved motif in TRAK1 mediates the interaction with MIRO1 in vitro and in cells

The interaction with MIRO1 was mapped above to CR2 of TRAK1 (Fig. 3.2). Using site directed mutagenesis, we tested the role of conserved residues within CR2 in the interaction. Among 183 TRAK sequences from different species and isoforms, two segments of high sequence conservation are observed toward the N- and C-terminal ends of CR2: ^{399}QKRVFETV^{406} and ^{425}IPGSN^{429} (Fig. 3.5A). Two MBP-TRAK1$_{342-431}$ mutants, ^{400}KR^{401} to AA and ^{425}IPG^{427} to AAA, were made to test the role of these conserved

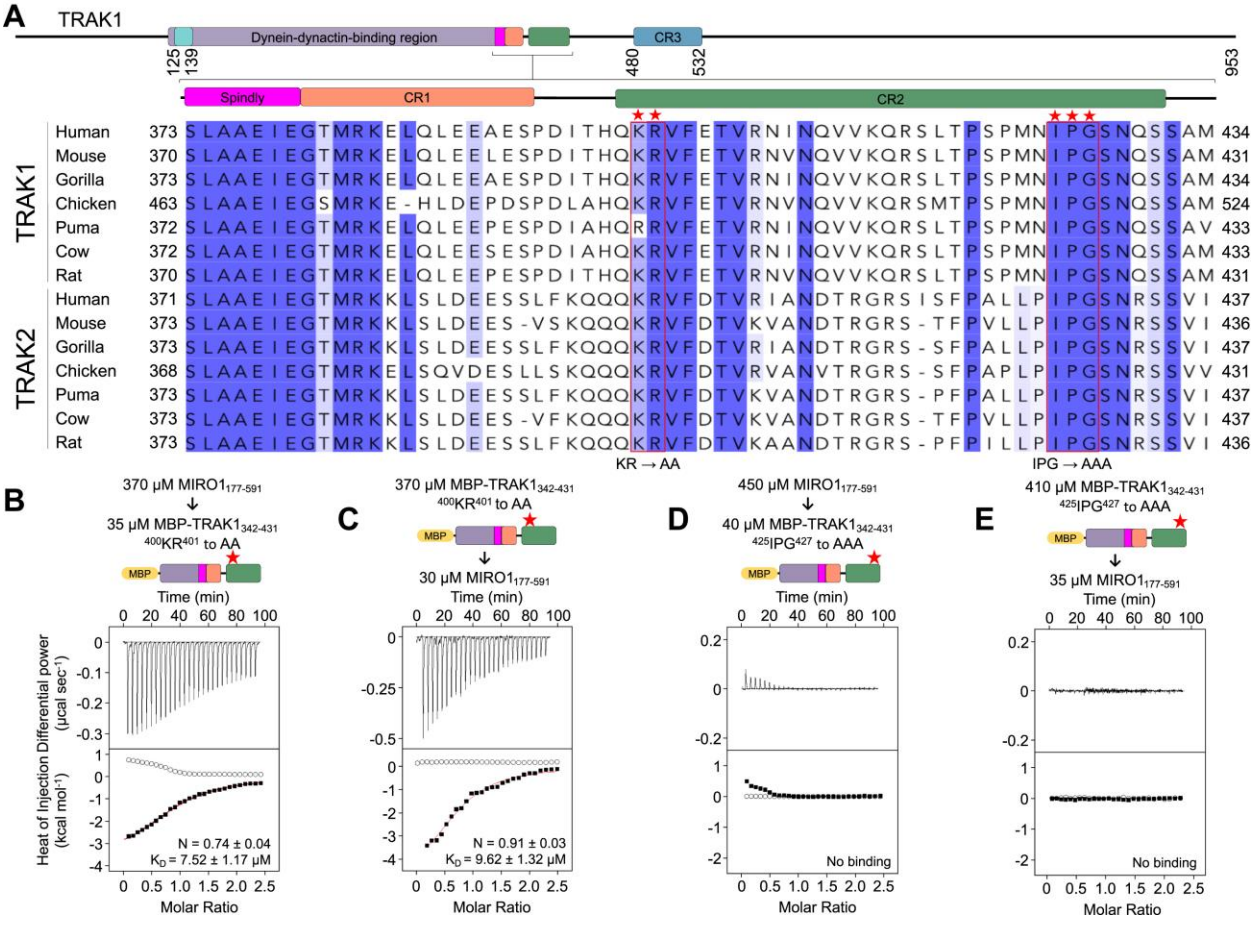

Figure 3.5: A conserved motif in TRAK1 mediates the interaction with MIRO1. A, Subgroup of TRAK1/2 sequences extracted from an alignment of 183 TRAK sequences (Fig. S3.1) and showing residues 373-434, including the CR2 region that binds MIRO1 (Fig. 3.2B, C). Amino acids conserved in >50% and >85% of the 183 sequences are highlighted light and dark blue, respectively. Stars highlight residues ^{400}KR^{401} and ^{425}IPG^{427} (boxed red) mutated to alanine. **B-E,** Representative ITC titrations of MIRO1$_{177-591}$ into the MBP-TRAK1$_{342-431}$ mutants **(B, D)** and inverted titrations **(C, E)** from N = 3 independent experiments (Table 3.1). Prior to each titration, the proteins in the syringe (top) and in the cell (bottom) were co-dialyzed for three days in ITC buffer with 5 mM EGTA. Listed with each titration are the concentrations of the protein in the syringe and in the cell and the parameters of the fit (stoichiometry N and dissociation constant K_D) to a binding isotherm (red line). Errors correspond to the s.d. of the fits. Open symbols correspond to control titrations into buffer.

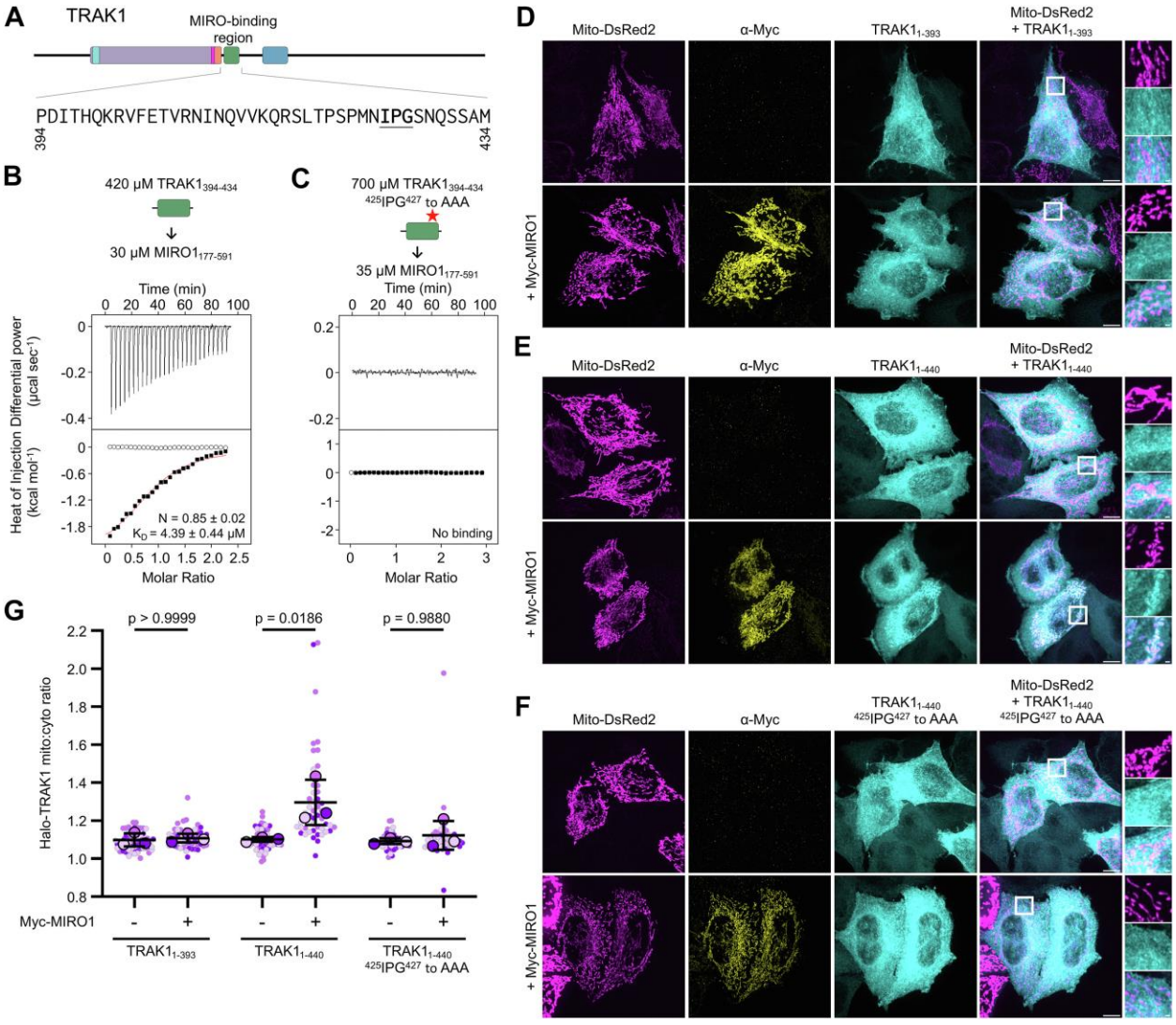

Figure 3.6: The CR2 region of TRAK1 is sufficient to bind MIRO1 *in vitro* and in cells. A, Schematic and sequence representation of the MIRO1-binding region of TRAK1. **B-C,** Representative ITC titrations of TRAK1$_{394-434}$ into MIRO1$_{177-591}$ WT **(B)** and mutant ^{425}IPG^{427} to AAA **(C)** from N = 3 independent experiments (Table 3.1). Proteins were dialyzed in ITC buffer with 5 mM EGTA and 0.1 μM GTP. Listed with each titration are the concentrations of the protein in the syringe and in the cell and, for interacting proteins, the parameters of the fit (stoichiometry N and dissociation constant K_D) to a binding isotherm (red line). Errors correspond to the s.d. of the fits. Open symbols correspond to control titrations into buffer. **D-F,** Representative maximum-intensity projections of Halo-TRAK1$_{1-393}$ **(D)**, Halo-TRAK1$_{1-440}$ **(E)**, or Halo-TRAK1$_{1-440}$ ^{425}IPG^{427} to AAA **(F)** and Mito-DsRed2 in HeLa cells, with or without Myc-MIRO1 co-expression. **G,** Ratio of mitochondrial to cytoplasmic intensity for Halo-TRAK1 constructs, with or without Myc-MIRO1 co-expression. Data points are color-coded by experimental replicate, with smaller points representing individual cells. N=3 independent experiments, with 48-63 cells per condition. The center line and bars represent the mean ± s.d. from independent experiments. P-values from one-way ANOVA with the Tukey's multiple comparisons test are shown. Scale bars: 10 μm **(D-F)**, 1 μm **(D-F insets)**.

segments in the interaction with MIRO1$_{177-591}$. Because the interaction is independent of Ca^{2+} (Fig. 3.3), experiments were performed in the presence of 5 mM EGTA, which we have found favors MIRO1$_{177-591}$ solubility. Binding of MIRO1$_{177-591}$ to MBP-TRAK1$_{342-431}$ was unaffected by the ^{400}KR^{401} to AA mutation, independent of which protein was in the syringe and the cell (Fig. 3.5B-C). In contrast, the ^{425}IPG^{427} to AAA mutation eliminated binding of MIRO1$_{177-591}$ to MBP-TRAK1$_{342-431}$ (Fig. 3.5D), and the same result was obtained when the titration was inverted (Fig. 3.5E).

Based on these results, we made a shorter TRAK1 peptide narrowly encompassing CR2 (TRAK1$_{394-434}$) (Fig. 3.6A). TRAK1$_{394-434}$ bound MIRO1$_{177-591}$ with stoichiometry and affinity consistent with other experiments described here (Fig. 3.6B), and the interaction was abolished when the ^{425}IPG^{427} to AAA mutation was introduced into this peptide (Fig. 3.6C).

Next, we assessed the physiological importance of this interaction for TRAK1 recruitment to mitochondria in cells. Two N terminally Halo-tagged constructs, one lacking (TRAK1$_{1-393}$) and one containing (TRAK1$_{1-440}$) the CR2 region necessary for MIRO1 binding *in vitro*, were individually expressed in HeLa cells and visualized using confocal microscopy. Mitochondria were labeled with Mito-DSRed2, and the overlap of each TRAK1 construct with mitochondria was quantified in the presence or the absence of Myc-MIRO1, whose overexpression is known to be required for efficient mitochondrial recruitment of exogenously expressed TRAK1 (MacAskill, Brickley, et al., 2009). TRAK1$_{1-440}$ but not TRAK1$_{1-393}$ colocalized with mitochondria and only with Myc-MIRO1 coexpression (Fig. 3.6D, E, and G). Moreover, TRAK1$_{1-440}$ recruitment to mitochondria was abolished by the ^{425}IPG^{427} to AAA mutation (Fig. 3.6 F-G). These results suggest that the CR2 of TRAK1 is necessary for MIRO1-dependent recruitment of TRAK1 to mitochondria.

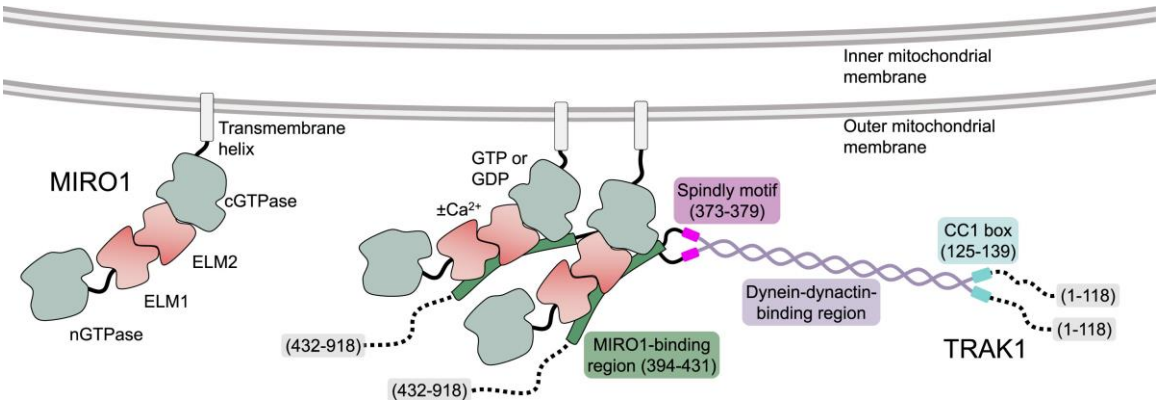

Figure 3.7: Two MIRO1 molecules bind one TRAK1 dimer on the mitochondrial surface. One TRAK1 dimer binds to two MIRO1 molecules on the mitochondrial surface, independent of Ca^{2+}-binding to the EF-hands or the cGTPase nucleotide state of MIRO1. The interaction is mediated by a conserved motif C terminal to the Spindly motif of TRAK1 and directly implicates MIRO1's EF-hands. MIRO, mitochondrial Rho GTPase; TRAK, trafficking kinesin-binding protein.

IV. Discussion

MIRO plays a central role in mitochondrial trafficking by recruiting TRAK, which in turn coordinates anterograde and retrograde motility along microtubules by kinesin-1 and dynein-dynactin (Eberhardt et al., 2020). It is, however, poorly understood and often debated how mitochondrial trafficking is regulated and specifically whether the MIRO-TRAK interaction is responsible for this regulation. Here, we have mapped the MIRO1-TRAK1 interaction and analyzed the effect of MIRO1-binding cofactors (Ca^{2+}, Mg^{2+}, GTP, and GDP) on TRAK1 binding. While this work focused on isoforms MIRO1 and TRAK1, the findings can likely be extended to MIRO2 and TRAK2, since sequence conservation was used as a guiding principle in mapping the interaction of the two proteins. The main findings of this study are: a) MIRO1 binds to a conserved motif on TRAK1, located C-terminal to the Spindly motif and consisting of TRAK1 residues 394-431, b) mutations in this sequence disrupt MIRO1 binding *in vitro* and mitochondrial localization of TRAK1 in cells, c) TRAK1 binds to a fragment containing MIRO1's EF-hands and cGTPase, d) deleting MIRO1's EF-hands abolishes the interaction, pointing to their direct involvement in TRAK1 binding either alone or

together with the cGTPase, e) the MIRO1-TRAK1 interaction is independent of the nucleotide state of the cGTPase, f) the interaction is also independent of Ca^{2+} or Mg^{2+} binding to MIRO1's EF-hands, g) the interaction has 1:1 stoichiometry, such that one TRAK1 dimer has the potential to bind two MIRO1 molecules on the mitochondrial surface (Fig. 3.7). Therefore, this interaction may be further enhanced through avidity via the formation of MIRO clusters on the mitochondrial membrane (Modi et al., 2019). These findings rule out models that have implicated MIRO's nGTPase in TRAK binding (Fransson et al., 2006; MacAskill, Brickley, et al., 2009) but are consistent with studies that have found that the MIRO-TRAK interaction is independent of Ca^{2+} binding to MIRO's EF-hands (Canty et al., 2023; MacAskill, Rinholm, et al., 2009; X. Wang & Schwarz, 2009).

Local increases in Ca^{2+} concentration stop mitochondrial trafficking (Brough et al., 2005; Quintana et al., 2006; Yi et al., 2004), and this effect is suppressed by mutations in MIRO's EF-hands (Chang et al., 2011; MacAskill, Rinholm, et al., 2009; Saotome et al., 2008; X. Wang & Schwarz, 2009). Because TRAK acts as an intermediate scaffold between MIRO and the microtubule-based motors that drive mitochondrial trafficking (Fransson et al., 2006; van Spronsen et al., 2013), it is reasonable to think that the effect of Ca^{2+} on mitochondrial motility could be through regulation of the MIRO-TRAK interaction (Saotome et al., 2008). However, our finding that the MIRO1-TRAK1 interaction is independent of Ca^{2+} binding to MIRO1 suggests that a different mechanism is responsible for the Ca^{2+}-dependent arrest of mitochondria. For instance, some evidence has suggested that kinesin-1 binds MIRO1 directly and that this interaction is regulated by Ca^{2+} (MacAskill, Rinholm, et al., 2009; X. Wang & Schwarz, 2009). The binding of kinesin-1 presumably implicates the EF-hands of MIRO1 and is thought to be independent of the MIRO1-TRAK1 interaction demonstrated here. While our data cannot rule out this possibility, we note that this model cannot explain why retrograde motility by dynein-dynactin is also arrested by increases in Ca^{2+}. Moreover, recent results negate the existence of a direct MIRO1-kinesin-1 interaction (Canty et al., 2023). Other models propose that Ca^{2+} regulates MIRO's interactions with other proteins, which in turn control mitochondrial trafficking and dynamics, such as syntaphilin (Canty et al., 2023), Armcx (Cartoni et al., 2016; López-Doménech et al., 2012), and MFN (Fatiga et al., 2021). This may explain why mutations in MIRO's EF-hands impair Ca^{2+} regulation.

Our work implicates the EF-hands of MIRO1 in TRAK1 binding. Most EF-hand proteins undergo major conformational changes upon Ca^{2+} binding, with Ca^{2+} acting as an on/off switch for target recognition (Kawasaki & Kretsinger, 2017). Thus, it may appear surprising that Ca^{2+} (or Mg^{2+}) binding to MIRO1's EF-hands has little effect on the interaction with TRAK1. Indeed, our data suggests that MIRO1 acts as a Ca^{2+} sensor, but probably not through a major conformational change. Under resting conditions, when the intracellular free Ca^{2+} concentration is ~0.1 mM, one of the EF-hands of MIRO1 is occupied by Ca^{2+} whereas the other EF-hand may bind Ca^{2+} only upon activation, when the free Ca^{2+} concentration can reach ~10 mM (Berridge et al., 1998, 2000). In other words, the two pairs of EF-hands of MIRO1 can be separated into constitutively-bound and regulatory Ca^{2+}-binding pairs. At rest, the regulatory pair (which our data does not assign) is likely occupied by Mg^{2+}, whose free intercellular concentration ranges from 0.5 to 1.0 mM (Romani & Scarpa, 1992), such that Ca^{2+} binding may proceed through the displacement of Mg^{2+}, as proposed for other EF-hand proteins (Grabarek, 2011; Senguen & Grabarek, 2012). While MIRO1 may share some of these features with other EF-hand-containing proteins, other characteristics make it unique. For instance, MIRO's EF-hands differ substantially from those of the prototypical Ca^{2+}-sensing protein calmodulin (Chin & Means, 2000). In calmodulin, all four EF-hands bind Ca^{2+}, which induces a conformational change that exposes hydrophobic pockets in the two pairs of EF-hands for the binding of calmodulin's cellular targets (Chin & Means, 2000). In MIRO1, only one EF-hand of each pair binds Ca^{2+}. Moreover, in calmodulin, the two pairs of EF-hands are separated by a long and flexible linker, allowing them to move with relative independence of one another to grab the target protein (Chin & Means, 2000). In MIRO, however, the two pairs of EF-hands are rigidly packed against one another (Klosowiak et al., 2013, 2016). Finally, unlike calmodulin, MIRO already has target peptides bound intramolecularly to the hydrophobic pockets of the two pairs of EF-hands, i.e. the ligand-mimic helices (Fig. 3.1A and Fig. 3.3E-F) (Klosowiak et al., 2013). These differences suggest that, while in calmodulin the EF-hands are used as a Ca^{2+}-dependent switch for target recognition, in MIRO the EF-hands play a structural role, acting as a rigid domain. This may explain why MIRO1's EF-hands show fundamentally the same conformation in crystal structures determined under different conditions (apo, Ca^{2+}- or Mg^{2+}-bound) (Klosowiak et al., 2013, 2016).

In summary, MIRO seems to function as a Ca^{2+}-dependent sensor, but not a Ca^{2+}-dependent conformational switch.

V. Methods

Proteins

Primers used in this study are listed in Table 3.2. The cDNA coding for human MIRO1 (UniProt ID: Q81X12) was purchased from Addgene (Plasmid: 127613). The cDNA coding for human TRAK1 (Uniprot ID: Q9UPV9) and GCN4-TRAK1$_{342-431}$ were synthesized with codon optimization for *E. coli* expression by GenScript (Piscataway, NJ). MIRO1$_{1-591}$ and TRAK1$_{99-532}$ were cloned into vector pRSFDuet-1 and MIRO1$_{177-591}$, GCN4-TRAK1$_{342-393}$, and GCN4-TRAK1$_{342-431}$ were cloned into vector pETDuet-1 (Novagen, Darmstadt, Germany). MBP-MIRO1$_{1-180}$, MBP-MIRO1$_{410-591}$, MBP-TRAK1$_{342-431}$, and TRAK1$_{394-434}$ (WT and ^{425}IPG^{427} to AAA) and were cloned into vector pMAL-c6T (NEB, Ipswich, MA). Point mutations in MIRO1$_{177-591}$ (E208A and E328A) and MBP-TRAK1$_{342-431}$ (^{400}KR^{401} to AA and ^{425}IPG^{427} to AAA) were introduced using the QuikChange mutagenesis kit (Agilent Technologies, Wilmington, DE). The Myc-MIRO1 construct was obtained from Addgene (Plasmid: 47888). Halo-TRAK1 1-393 and Halo-TRAK1 1-440 (WT and mutant ^{425}IPG^{427} to AAA) were cloned from HA-TRAK1 (a gift from C. Hoogenraad, Utrecht University) into pFN21A-HaloTag-CMV vector (Promega, Madison, WI). Affinity tags used in purification (see below) are either part of the vectors or were added during cloning.

All the proteins were expressed in *E. coli* ArcticExpress(DE3) cells (Agilent Technologies), grown in Terrific Broth medium at 37 °C to an OD_{600} of 1.5–2, followed by 24 hours at 9 °C with the addition of 0.35 mM isopropyl-β-D-thiogalactoside (IPTG). Cells were pelleted by centrifugation, resuspended in TRAK1 or MIRO1 buffers (see below) supplemented with 1 mM phenylmethylsulfonyl fluoride (PMSF) and lysed using a Microfluidizer (Microfluidics, Newton, MA). Lysates were clarified by centrifugation and supernatants were loaded onto their corresponding affinity columns according to protocols from the manufactures (see below).

All the TRAK1-derived proteins were prepared in TRAK1 buffer (20 mM HEPES pH 7.5 and 200 mM NaCl). TRAK1$_{99-532}$ and GCN4-TRAK1 constructs were affinity-purified on a Strep-Tactin Sepharose column (IBA Lifesciences, Göttingen, Germany) and eluted with 40 mM Biotin pH 8.0 (dissolved in TRAK1 buffer), followed by purification on a Ni-NTA column (G-Biosciences, St. Louis, MO). MBP-TRAK1$_{342-431}$ constructs (WT and mutants) were affinity-purified on an amylose column (NEB), and further purified through a Strep-Tactin column. MBP-TRAK1$_{394-434}$ peptides (WT and mutant) were purified through an amylose affinity column (NEB). The MBP tag was removed by incubation with TEV protease for 48 hours at 4 °C. The cleaved peptides were separated from 6xHis-MBP and 6xHis-TEV on a Ni-NTA column. After tag removal, the peptides were further purified on an SD75HL 16/60 column (GE Healthcare, Little Chalfont, UK) in 20 mM HEPES pH 7.5 and 50 mM NaCl. The peptides were loaded onto a SourceQ anion exchange column (Cytiva, Marlborough, MA) and eluted in the flowthrough in 20 mM HEPES pH 7.5.

All the MIRO1-derived proteins were prepared in MIRO1 buffer (20 mM HEPES pH 7.5, 300 mM NaCl, 1 mM $CaCl_2$, 1 mM $MgCl_2$, 5% w/v sucrose, and 0.1 µM GTP). MIRO1$_{1-591}$ was prepared in MIRO1 buffer containing 500 mM NaCl, 30 mM imidazole pH 7.3, and 5% glycerol. The protein was affinity-purified on a Ni-NTA column and then on a Strep-Tactin Sepharose column and eluted with 40 mM Biotin pH 8.0 (dissolved in the same buffer). MBP-MIRO1$_{1-180}$ (in MIRO1 buffer lacking $CaCl_2$) was purified through a Strep-Tactin column and eluted with 40 mM Biotin pH 8.0 and diluted to a NaCl concentration of 50 mM. The protein was further purified on a MonoQ anion exchange column (Cytiva) with Buffer A (20 mM HEPES pH 7.5, 50 mM NaCl, 1 mM $MgCl_2$, 5% w/v sucrose) and eluted using a stepwise gradient of Buffer B (Buffer A + 1 M NaCl). MIRO1$_{177-591}$ (WT and mutants) were purified on a Ni-NTA column in MIRO1 buffer supplemented with 30 mM imidazole pH 7.3. Aggregates were removed by centrifugation at 372,000 x g for 20 minutes. The protein was diluted to a NaCl concentration of 75 mM, loaded onto a SourceQ column, and eluted in the flowthrough in MIRO1 buffer lacking NaCl (contaminants remain bound to the column under these conditions). MBP-MIRO1$_{410-591}$ (in MIRO1 buffer lacking $CaCl_2$) was affinity purified on an amylose column (NEB).

Glycerol gradient cosedimentation

Proteins were mixed at a final concentration of 4 µM in Starting buffer (20 mM HEPES pH 7.5, 500 mM NaCl, 1 mM $MgCl_2$, 1 mM $CaCl_2$, 1 mM DTT, and 0.1 µM GTP). A 5%–30% glycerol gradient was prepared by layering 2 mL of Light solution (Starting buffer + 5% glycerol) on top of 2 mL of Heavy solution (Starting buffer + 30% glycerol) and mixing the solutions using a BioComp Gradient Master 107 (Biocomp Instruments, Fredericton, Canada) set to rotate for 94 seconds at 86 degrees. Proteins (250 µL) were pipetted on top of the gradient and spun using a SW-60 rotor at 165,000 g for 16 hours at 4 °C. Samples were fractionated and analyzed by SDS-PAGE. Gels were Coomassie blue-stained, captured with the program GENESys V1.5.6.0 (Genesys Limited, Langhorne, PA) set to capture a Visible Protein Gel stained with Coomassie Blue, and band intensities were quantified using ImageLab (Bio-Rad, Hercules, CA).

Isothermal titration calorimetry

ITC measurements were carried out on a VP-ITC instrument (MicroCal, Northampton, MA). Protein samples were dialyzed against ITC buffer (20 mM HEPES pH 7.5, 400 mM NaCl, 1 mM $MgCl_2$, 5% w/v sucrose, 0.125 mM TCEP, and 0.1 µM GTP) with the addition of experiment-specific cofactors ($CaCl_2$, GDP, EGTA) for at least 3 days. Protein concentrations were determined using the Bradford method. Peptide concentrations were measured using fluorescence after labeling with fluorescamine. Proteins in the syringe were titrated at a concentration 8- to 15-fold higher than that of proteins in the cell of volume 1.44 mL. Experiments were carried out at 25 °C. Titrations consisted of 10 µl injections, lasting for 10 s, with an interval of 200 s between injections. Heats of binding were determined from the point-by-point subtraction of the heats of injection into buffer (control) from the heats of injection into protein. Experiments were repeated (see Table 3.1). The program Origin (OriginLab, Northampton, MA) was used to analyze the data and fit binding curves. The experiment-specific cofactors and parameters of the fits are listed in the figures and Table 3.1.

Analysis of bound nucleotide

Proteins were loaded onto a Sephadex G-25 PD10 column (Global Life Science Solutions, Sheffield, UK) with 20 mM Tris pH 7.5 to remove unbound nucleotide, and fractions (500 µL each) were collected. Peak fractions were denatured with the addition of 2.5 µL of 10% perchloric acid followed by 2.5 µL of 4 M sodium acetate pH 4.0. Denatured proteins were pelleted by centrifugation. The supernatants (200 µL), containing the nucleotides, were mixed with 100 µL of HPLC Loading buffer (100 mM KH_2PO_4, 100 mM K_2HPO_4, 10 mM tetrabutylammonium bromide pH 6.5). Commercial nucleotides were solubilized in 20 mM Tris pH 7.5 to a final concentration of 10 µM. A 200 µL volume was mixed with 100 µL of HPLC Loading buffer, and 250 µL were run isocratically through a Vydac 208MS C_8 reverse phase HPLC column (VWR, Radnor, PA) with Loading buffer supplemented with 8.5% acetonitrile. To exchange the nucleotide on $MIRO1_{177-591}$, a 35-molar excess of commercial nucleotide (GDP or GTP) was added and incubated for one hour on ice, followed by 3-day dialysis into a buffer with no extra nucleotide added.

Mass photometry

Mass photometry experiments were performed on a Refeyn TwoMP-0220 instrument using programs AcquireMP v2022 R1 and DiscoverMP v2022 R1 for analysis. Proteins were dialyzed for 24 hours against 20 mM HEPES pH 7.5, 300 mM NaCl, 1 mM $CaCl_2$, and 1 mM $MgCl_2$. Two hours before the experiments, proteins were diluted to a concentration of 600 nM (i.e., a >12-fold dilution) in a buffer containing 100 mM NaCl, 50 µM $MgCl_2$, 50 µM GTP and either 1 mM EGTA or 100 µM $CaCl_2$. The instrument was calibrated with the corresponding buffer and proteins were applied to a final concentration of 125-150 nM. Movies were acquired for 60 seconds using default parameters. Ratiometric contrasts were converted to molecular weights using a mass calibration curve generated from three proteins: 75 nM bovine serum albumin (MW: 66.43 kDa), 75 nM beta-amylase (MW: 112 kDa dimer and 224 kDa tetramer), and 22.5 nM thyroglobulin (MW: 670 kDa). Gaussian curves were fit to each histogram distribution, and the masses and normalized counts were determined. For each fit, the bin width was set to 1 kDa, and the data is reported as the percent relative to the bin with the highest number of counts.

Sequence analysis

Vertebrate TRAK and MIRO sequences were aligned with the program Clustal Omega (Sievers & Higgins, 2021) and sequence conservation scores were calculated with the program Scorecons using the valdar01 method (Fig. S3.1A, B and Fig. 3.2A) (Valdar, 2002). Coiled-coil predictions were performed with the program prabi (Fig. S3.1A and Fig. 3.2A) (Combet et al., 2000). The program Waggawagga was used for prediction of coiled-coil heptads (Simm et al., 2015).

TRAK localization to mitochondria

HeLa-M cells (A. Peden, Cambridge Institute for Medical Research, Cambridge, England) were maintained in DMEM (Corning, 10-017-CM, Corning, NY) supplemented with 1% GlutaMAX (ThermoFisher, 35050061, Waltham, MA) and 10% Fetal Bovine Serum (HyClone, SH30071.03, Logan, UT). Cells were maintained at 37 °C in a 5% CO_2 incubator. Cells tested negative for mycoplasma contamination and were authenticated by STR profiling at the DNA Sequencing Facility of the University of Pennsylvania. For imaging experiments, cells were plated on 35 mm glass-bottom dishes (MatTek, P35G-1.5-20-C, Ashland, MA) and transfected using FuGENE 6 transection reagent (Promega, E269A).

Twenty-four hours after transfection, HeLa cells were fixed for 10 minutes using warm PBS with 4% paraformaldehyde and 4% sucrose and washed three times with PBS. Cells were labelled with 100 nM Janelia Fluor 646-Halo ligand (Promega, GA1121) in PBS for 20 minutes at 37 °C, followed by a 30-minute wash with PBS at 37 °C. Cells were then permeabilized with 0.2% Triton X-100 in PBS for 15 minutes, and washed three times with PBS. Cells were blocked for 1 hour in blocking solution (5% goat serum and 1% BSA in PBS) and incubated overnight at 4 °C with anti-Myc antibody (Invitrogen, R950-25, Waltham, MA) diluted 1:1000 in blocking solution. Cells were then washed three times with PBS, incubated for 1 hour with Alexa Fluor 488 goat anti-mouse IgG (H + L) (Invitrogen, A11029) diluted 1:1000 in blocking solution, and washed three more times with PBS.

HeLa cells were imaged using a V3 spinning disk confocal on a Nikon Eclipse Ti Microscope with an Apochromat 100×1.49 numerical aperture oil immersion objective (Nikon, Melville, NY). Images were acquired with a Hamamatsu CMOS ORCA-Fusion (C11440-20UP) driven by VisiView software (Visitron, Puchheim, Germany). Z-stacks spanning the height of transfected cells were collected at 200-nm step-size.

Maximum-intensity projections were generated for the Halo-TRAK1 and Mito-DsRed2 channels in ImageJ (NIH, Bethesda, MD). The area of the Mito-DsRed2 channel was then converted to a binary mask using the Pixel classification module of Ilastik, a machine-learning based image segmentation program (Berg et al., 2019). The binarized image was used to make two regions of interest for each cell, one encompassing the mitochondria and one encompassing everything except the mitochondria. The mean fluorescence intensity of Halo-TRAK1 was measured in each region to determine the ratio of mitochondrial to cytoplasmic signal.

VI. Acknowledgements

The authors thank Grzegorz Rebowski for help with the analysis of the ITC data, Malgorzata Boczkowska for help with data analysis, and David Kast for helpful discussions about the nucleotide exchange of MIRO1.

Author contributions

E. E. B., E. E. R., and R. D. conceptualization; E. E. B., E. E. R., and R. D. visualization; E. E. B., E. E. R., A. R. F., and T. A. P. investigation; E. E. B., E. E. R., and T. A. P. formal analysis; E. E. B., E. E. R., and A. R. F. methodology; E. E. B. and E. E. R. writing-original draft; E. E. B., E. E. R., A. R. F., E. L. F. H., and R. D. writing-review and editing; E. L. F. H. and R. D. funding acquisition; E. L. F. H. and R. D. resources; R. D. project administration; E. L. F. H. and R. D. supervision.

Funding and additional information

Supported by National Institutes of Health (NIH) grant RM1 GM136511 (R. D. and E. L. F. H.) and training grant T32 GM132039 (E. E. B.). The content is solely the responsibility of the authors and does not necessarily represent the official views of the NIH.

Table 3.1: ITC experiments, experimental conditions, and fitting parameters

Buffer	ITC titration (syringe → cell)	Experiment	Conc. syringe (μM)	Conc. cell (μM)	*N*	K_d (μM)	Representative experiment
50 μM $CaCl_2$, 1 mM $MgCl_2$, 0.1 μM GTP	$MIRO1_{177-591}$ → GCN4-$TRAK1_{342-431}$	1	300	15	1.56 ± 0.07	9.35 ± 1.29	Fig. 2B
		2	310	16	1.93 ± 0.02	7.04 ± 0.43	
		3	300	15	1.59 ± 0.05	9.35 ± 0.96	
50 μM $CaCl_2$, 1 mM $MgCl_2$, 0.1 μM GTP	$MIRO1_{177-591}$ → GCN4-$TRAK1_{342-393}$	1	260	17.5	No binding		Fig. 2C
		2	260	17.5	No binding		
		3	260	17.5	No binding		
50 μM $CaCl_2$, 1 mM $MgCl_2$, 0.1 μM GTP	$MIRO1_{177-591}$ → MBP-$TRAK1_{342-431}$	1	465	40	1.11 ± 0.01	2.76 ± 0.17	Fig. 2D
		2	465	40	1.03 ± 0.02	5.38 ± 0.73	
		3	465	40	0.97 ± 0.03	5.95 ± 0.99	
5 (1) or 50 (2) μM $CaCl_2$, 1 mM $MgCl_2$, 0.1 μM GTP	$CaCl_2$ → $MIRO1_{177-591}$	1	800	105	No binding		Fig. 3A
		2	800	100	No binding		
5 mM to 0.08 μM EGTA, 1 mM $MgCl_2$, 0.1 μM GTP	$CaCl_2$ → $MIRO1_{177-591}$	1	800	97	2	K_{d1} = 0.30 ± 0.21 K_{d2} = 3.94 ± 2.92	Fig. 3B
		2	800	97	2	K_{d1} = 0.15 ± 0.08 K_{d2} = 6.80 ± 1.29	
		3	800	97	2	K_{d1} = 0.29 ± 0.16 K_{d2} = 7.58 ± 1.94	
5 mM EGTA, 1 mM $MgCl_2$, 0.1 μM GTP	$MIRO1_{177-591}$ → GCN4-$TRAK1_{342-431}$	1	320	14	1.84 ± 0.03	4.81 ± 0.44	Fig. 3C
		2	320	14	1.73 ± 0.04	3.52 ± 0.40	
		3	320	14	1.84 ± 0.03	5.13 ± 0.34	
5 mM EGTA, 1 mM $MgCl_2$, 0.1 μM GTP	$MIRO1_{177-591}$ → MBP-$TRAK1_{342-431}$	1	630	50	0.94 ± 0.002	6.02 ± 0.80	Fig. 3D
		2	630	55	0.97 ± 0.02	8.00 ± 0.94	
		3	630	55	1.09 ± 0.02	8.85 ± 1.09	
5 mM EGTA, 1 mM $MgCl_2$, 0.1 μM GTP	MBP-$TRAK1_{342-431}$ → $MIRO1_{177-591}$ E208A	1	460	30	0.90 ± 0.03	8.85 ± 1.10	Fig. 3E
		2	460	30	0.98 ± 0.03	9.09 ± 1.05	
		3	460	30	1.32 ± 0.02	3.86 ± 0.35	
5 mM EGTA, 1 mM $MgCl_2$, 0.1 μM GTP	MBP-$TRAK1_{342-431}$ → $MIRO1_{177-591}$ E328A	1	450	28	0.77 ± 0.05	9.17 ± 1.42	Fig. 3F
		2	450	28	0.80 ± 0.04	10.1 ± 1.17	
		3	450	28	0.82 ± 0.06	10.3 ± 1.60	
5 mM EGTA, 1 mM $MgCl_2$, 50 μM GDP	MBP-$TRAK1_{342-431}$ → $MIRO1_{177-591}$	1	585	48	0.80 ± 0.02	10.6 ± 1.18	Fig. 4D
		2	585	48	0.82 ± 0.02	24.8 ± 1.42	
		3	585	48	0.89 ± 0.07	20.9 ± 2.40	
5 mM EGTA, 1 mM $MgCl_2$, 50 μM GTP	MBP-$TRAK1_{342-431}$ → $MIRO1_{177-591}$	1	570	40	0.82 ± 0.04	8.93 ± 1.40	Fig. 4E
		2	570	40	0.83 ± 0.03	18.5 ± 1.27	
		3	570	40	0.99 ± 0.03	15.7 ± 1.19	
1 mM $MgCl_2$, 50 μM GTP	MBP-$TRAK1_{342-431}$ → $MIRO1_{410-591}$	1	400	35	No binding		Fig. 4F
		2	400	35	No binding		
		3	400	35	No binding		
5 mM EGTA, 1 mM $MgCl_2$, 0.1 μM GTP	$MIRO1_{177-591}$ → MBP-$TRAK1_{342-431}$ $^{400}KR^{401}$ to AA	1	370	35	0.85 ± 0.02	4.39 ± 0.40	Fig. 5B
		2	370	35	1.03 ± 0.02	2.98 ± 0.36	
		3	370	35	0.95 ± 0.03	3.98 ± 0.66	
5 mM EGTA, 1 mM $MgCl_2$, 0.1 μM GTP	MBP-$TRAK1_{342-431}$ $^{400}KR^{401}$ to AA → $MIRO1_{177-591}$	1	370	30	0.74 ± 0.04	7.52 ± 1.17	Fig. 5C
		2	370	30	0.58 ± 0.05	11.3 ± 1.78	
		3	370	30	0.63 ± 0.04	8.55 ± 1.30	
5 mM EGTA, 1 mM $MgCl_2$, 0.1 μM GTP	$MIRO1_{177-591}$ → MBP-$TRAK1_{342-431}$ $^{425}IPG^{427}$ to AAA	1	450	40	No binding		Fig. 5D
		2	450	40	No binding		
		3	450	40	No binding		
5 mM EGTA, 1 mM $MgCl_2$, 0.1 μM GTP	MBP-$TRAK1_{342-431}$ $^{425}IPG^{427}$ to AAA → $MIRO1_{177-591}$	1	410	35	No binding		Fig. 5E
		2	410	35	No binding		
		3	410	35	No binding		
5 mM EGTA, 1 mM $MgCl_2$, 0.1 μM GTP	$TRAK1_{394-434}$ → $MIRO1_{177-591}$	1	420	30	0.91 ± 0.03	9.62 ± 1.32	Fig. 6B
		2	420	25	0.78 ± 0.07	6.10 ± 1.49	
		3	420	30	0.90 ± 0.04	5.65 ± 1.13	
5 mM EGTA, 1 mM $MgCl_2$, 0.1 μM GTP	$TRAK1_{394-434}$ $^{425}IPG^{427}$ to AAA → $MIRO1_{177-591}$	1	700	50	No binding		Fig. 6C
		2	700	50	No binding		
		3	700	50	No binding		

Table 3.2: Primers used in Chapter 3

Construct	MW	Forward Primer (5' to 3')		Reverse Primer (5' to 3')		SDS-PAGE
$MIRO1_{1-591}$	67.7 kDa		TTCGAATTCATGAAGAAAGACGTGC GGATCCTG	Rev 1	AAACTGCGGGTGGCTCCAGAACGT GGAGCTCTTGAGGTCAGCTTG	Fig. 1B
				Rev 2	TTCGCGGCCGCTCACTTTTCAAACT GCGGGTGGCTCCAGAAC	
MBP-$MIRO1_{2-180}$	65.6 kDa		TTCGGTACCATGAAGAAAGACGTG CGGATCCTG		TTCGAATTCTCACTTTTCAAACTGC GGGTGGC	Fig. 1C
$MIRO1_{177-591}$	50.3 kDa		CTTGGATCCGAGGAGAAGGAGATG AAACCAGCTT		TTCGCGGCCGCTCACTTTTCAAACT GCGGGTGGCTCCAGAAC	Fig. 1D
$MIRO1_{177-591}$ E208A	50.3 kDa	QC	GTACTCTCAATGATGCTGCACTCAA CTTCTTTCAGAGG	QC	CCTCTGAAAGAAGTTGAGTGCAGC ATCATTGAGAGTAC	Fig. S5, Lane 1
$MIRO1_{177-591}$ E328A	50.3 kDa	QC	GAGACTGTGCTTTGTCACCTGATGC GCTTAAAGATTTATTTAAAG	QC	CTTTAAATAAATCTTTAAGCGCATCA GGTGACAAAGCACAGTCTC	Fig. S5, Lane 2
MBP-$MIRO1_{410-591}$	62.5 kDa		TTCGGATCCCAGAAAAAACAAACTC AAAGAAATGTGTTCAGATG		TTCGCGGCCGCTCACTTTTCAAACT GCGGGTGGCTCCAGAAC	Fig. S5, Lane 3
$TRAK1_{99-532}$	53.5 kDa		GGATCCTGCCGCAGAGAGGGTGG GACAGATGA	Rev 1	AAACTGCGGGTGGCTCCACTCTCC CTTCTCTGCCAGCTC	Fig. 1B-D
				Rev 2	TTCGCGGCCGCTCACTTTTCAAACT GCGGGTGGCTCCACTC	
GCN4-$TRAK1_{342-393}$	27.4 kDa (dimer)		TTCGAATTCATGAAACAGCTGGAGG ACAAAGTGGAAGAACTG	Rev 1	TTCCGGGTGGCTCCAGGACTCTGC CTCCTCCAGCTG	Fig. S5, Lane 4
GCN4-$TRAK1_{342-431}$	36.0 kDa (dimer)		TTCGAATTCATGAAACAGCTGGAGG ACAAAGTGGAAGAACTG	Rev 1	TTCCGGGTGGCTCCAGGACTCTGC CTCCTCCAGCTG	Fig. S5, Lane 5
				Rev 2	TTCGGTACCTCACTTTTCAAACTGC GGGTGGCTCCAGGACTCTG	
MBP-$TRAK1_{342-431}$	55.1 kDa (monomer)		TTCGGATCCGAGGCCCAGGAGGAG CTGAAG		TTCGGTACCTCACATGGCAGAGGA CTGATTGCTGC	Fig. S5, Lane 6
MBP-$TRAK1_{342-431}$ $^{400}KR^{401}$ to AA	55.0 kDa	QC 1	GACATCACACACCAGGCGAGGGTG TTCGAGACAGTGCGGAACATC	QC 1	GATGTTCCGCACTGTCTCGAACAC CCTCGCCTGGTGTGTGATGTC	Fig. S5, Lane 7
		QC 2	GACATCACACACCAGGCGGCGGTG TTCGAGACAGTGCGGAACATC	QC 2	GATGTTCCGCACTGTCTCGAACAC CGCCGCCTGGTGTGTGATGTC	
MBP-$TRAK1_{342-431}$ $^{425}IPG^{427}$ to AAA	55.1 kDa	QC 1	ACACCATCCCCCATGAACATCGCC GGCAGCAATCAGTCCTGGAGC	QC 1	GCTCCAGGACTGATTGCTGCCGGC GATGTTCATGGGGGATGGTGT	Fig. S5, Lane 8
		QC 2	ACACCATCCCCCATGAACATCGCC GCCAGCAATCAGTCCTGGAGC	QC 2	GCTCCAGGACTGATTGCTGGCGGC GATGTTCATGGGGGATGGTGT	
		QC 3	ACACCATCCCCCATGAACGCCGCC GCCAGCAATCAGTCCTGGAGC	QC 3	GCTCCAGGACTGATTGCTGGCGGC GGCGTTCATGGGGGATGGTGT	
$TRAK1_{394-434}$ WT and $^{425}IPG^{427}$ to AAA	4.8 kDa (peptide)		TTCGGATCCCCCGACATCACACAC CAGAAGAG	Rev 1	TTCGGTACCTCACATGGCAGAGGA CTGATTGCTGC	Fig. S5, Lanes 9 and 10
				Rev 2	TCACATGGCGGACTGATTGCTGGC GGCG	
				Rev 3	GGTACCTCACATGGCGGACTGATT GCTG	

CHAPTER 4: ALS-ASSOCIATED KIF5A MUTATIONS ABOLISH AUTOINHIBITION RESULTING IN A TOXIC GAIN OF FUNCTION

This chapter is adapted from:

Baron, DM*; **Fenton, AR***; Saez-Atienzar, S*; Giampetruzzi, A*; Sreeram, A; Shankaracharya; Keagle, PJ; Doocy, VR; Smith, NJ; Danielson, EW; Andresano, M; McCormack, MC; Garcia, J; Bercier, V; Van Den Bosch, L; Brent, JR; Fallini, C; Traynor, BJ; Holzbaur, ELF; Landers, JE. ALS-associated KIF5A mutations abolish autoinhibition resulting in a toxic gain of function. Cell Reports, 39, 110598 (2022).

(* equal contribution)

Contribution: ARF performed experimental procedures, data analysis, writing, and figure design related to single-molecule imaging experiments in Fig. 4.3.

I. Summary

Understanding the pathogenic mechanisms of disease mutations is critical to advancing treatments. ALS-associated mutations in the gene encoding the microtubule motor KIF5A result in skipping of exon 27 (KIF5A$^{\Delta Exon27}$) and the encoding of a protein with a novel 39 amino acid residue C-terminal sequence. Here, we report that expression of ALS-linked mutant KIF5A results in dysregulated motor activity, cellular mislocalization, altered axonal transport, and decreased neuronal survival. Single-molecule analysis revealed that the altered C terminus of mutant KIF5A results in a constitutively active state. Furthermore, mutant KIF5A possesses altered protein and RNA interactions and its expression results in altered gene expression/splicing. Taken together, our data support the hypothesis that causative ALS mutations result in a toxic gain of function in the intracellular motor KIF5A that disrupts intracellular trafficking and neuronal homeostasis.

II. Introduction

Amyotrophic lateral sclerosis (ALS) is a neurodegenerative disorder characterized by the progressive loss of brain and spinal cord motor neurons (MNs). As the disease progresses, patients experience impairment in mobility, speech, and respiration, ultimately leading to death, typically 2–5 years after initial symptom onset. Although ALS is classified as a rare neurological disorder, it is the most common motor neuron disease in its class, accounting for about 70% of all the cases in the United States. Approximately 5,000 people are diagnosed with ALS each year and approximately 5 per 100,000 die annually in the United States (Hirtz et al., 2007; Mehta et al., 2018). Over the past decade, tremendous advances have been made in defining the genetic factors contributing to ALS. To date, causative mutations for familial ALS have been identified in over 30 genes. Most importantly, the function and classification of these mutant genes have established the primary pathways contributing to ALS pathogenesis. Cytoskeletal disturbances and axonal transport deficits are among these primary pathways (Chevalier-Larsen & Holzbaur, 2006; Eira et al., 2016; W. Guo et al., 2020; McMurray, 2000). Furthermore, cytoskeletal/axonal transport defects extend to several other neurodegenerative diseases including Alzheimer's disease (AD), Parkinson's disease (PD), and Huntington's disease (HD). Supporting the contribution of these defects to neurodegeneration, we have previously reported mutations within the kinesin family member 5A (KIF5A) gene as a cause of familial ALS (Nicolas et al., 2018).

Kinesins are a superfamily of microtubule (MT) motor proteins essential for many cellular functions, including intracellular trafficking and cell division(Hirokawa & Tanaka, 2015). Kinesin-1 (also known as KIF5) is required for neuronal development and function (Aiken & Holzbaur, 2021). The kinesin-1 core is a dimer of heavy chains (KHCs), each with an N-terminal motor domain, a hinged coiled-coil stalk, and a globular C-terminal tail domain. The motor domain binds MTs in an ATP-dependent manner, and the coiled-coil domain mediates heavy chain dimerization and conformational changes within the dimer. The C-terminal domain serves several functions: (1) cargo binding, (2) autoinhibition, and (3) MT sliding/bundling (del Castillo et al., 2015). This region regulates cargo binding via binding of kinesin light chains (KLC) and adaptor proteins. KLCs 1 and 2 may also associate with the motor to further regulate cargo binding and

autoinhibition (Yip et al., 2016). The alternate ATP-dependent stepping of the motor domains drives cargo movement toward the plus ends of MTs (Skowronek et al., 2007). There are three kinesin-1 isoforms in mammals: KIF5A, KIF5B, and KIF5C. KIF5B is ubiquitously expressed in most mammalian cells, whereas KIF5A and KIF5C are neuron specific (Kanai et al., 2000; Miki et al., 2001). Kinesin-1 is responsible for the anterograde axonal transport of diverse cargos in neurons including mitochondria, lysosomes, RNA granules, and neurofilaments (Hirokawa & Takemura, 2005b). Most cellular kinesin-1 is autoinhibited and unable to bind either cargo or MTs(Hackney et al., 2009; Kaan et al., 2011; Yip et al., 2016). Autoinhibition is mediated by a direct intramolecular interaction of the motor domain with a short, charged region within the C-terminal region, called the isoleucine-alanine-lysine (IAK) motif. In contrast, binding to activators, such as JIP1 and FEZ1(Blasius et al., 2007), promotes dimer unfolding and relieves autoinhibition, allowing interaction with cargo and the MT track.

III. Results

The C-terminal sequence of mutant KIF5A confers a toxic gain of function

We previously reported that ALS-associated mutations alter the KIF5A tail domain(Nicolas et al., 2018). Point mutations located within the splice acceptor and splice donor region of exon 27 lead to the skipping of this exon (Fig. 4.1A) resulting in a protein where the C-terminal 34 amino acids (aa) of wild-type KIF5A ($KIF5A^{WT}$) are replaced with a novel 39 aa sequence ($KIF5A^{\Delta Exon27}$). Additional studies have similarly identified exon 27 splice site mutations within ALS and frontotemporal dementia (FTD) patients (Naruse et al., 2021; Saez-Atienzar et al., 2020). Furthermore, an additional three ALS-related single-base-pair deletions within exon 26 and 27 also predict transcripts with an identical mutant C terminus (Fig. 4.1B) (Nicolas et al., 2018). Given the number of charged residues in the C-terminal tail, we examined how the mutant sequence might alter the protein's charge. While the isoelectric point (pI) of the whole proteins showed only a modest change (5.65 in $KIF5A^{WT}$ versus 6.12 in $KIF5A^{\Delta Exon27}$), comparison of the C-terminal sequences revealed a dramatic difference in charge (4.14 in $KIF5A^{WT}$ versus 12.13 in $KIF5A^{\Delta Exon27}$; Fig.

4.1C). Based on these observations, we speculated that the mutant KIF5A protein contributes to pathogenesis through a toxic gain of function instead of haploinsufficiency.

To investigate the toxic properties of mutant KIF5A, we compared the survival of primary cortical neurons expressing either KIF5A^{WT} or KIF5A$^{\Delta Exon27}$ via automated longitudinal live-cell imaging (Arrasate & Finkbeiner, 2005; Linsley et al., 2019), where the individual lifetimes of large numbers of neurons are measured. Cox proportional hazards analysis is then used to generate a hazard ratio (HR) representing an

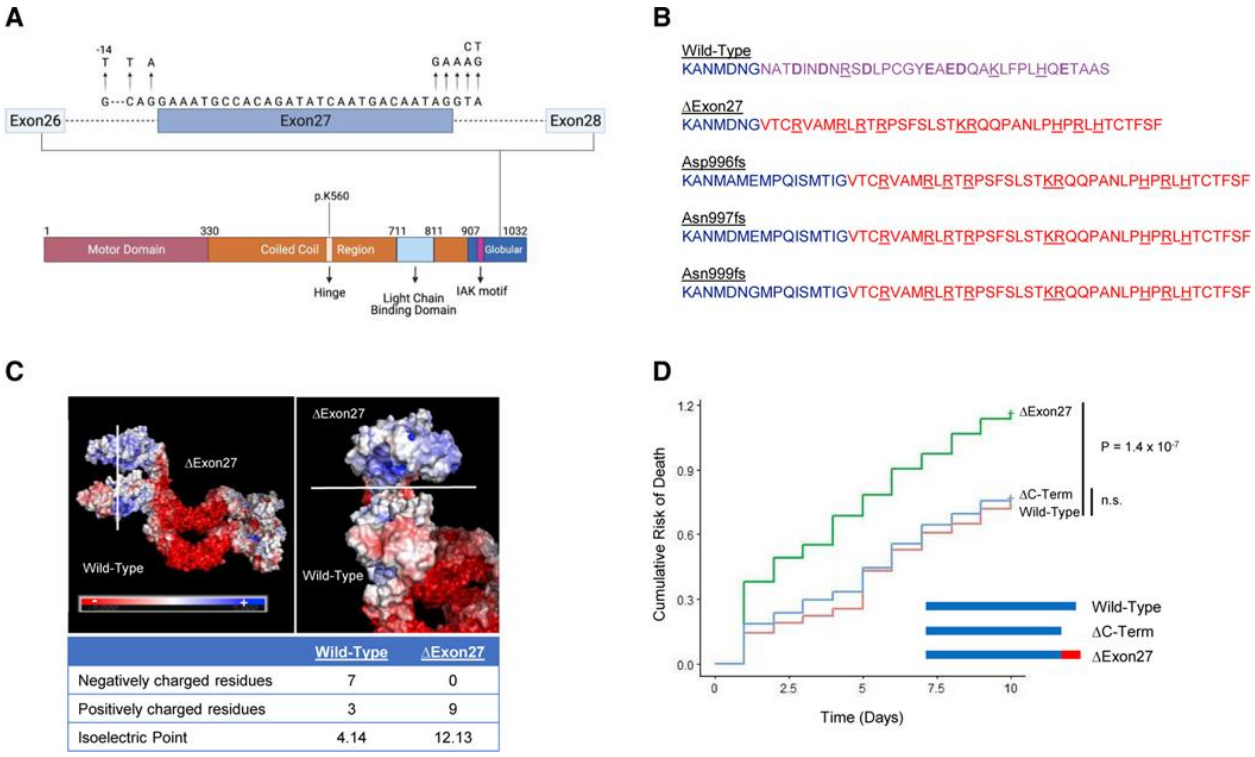

Figure 4.1: ALS-associated KIF5A mutations are clustered to exon 27 resulting in a common toxic C terminus mutation. A, KIF5A domain structure. The kinesin light chain domain, the hinge domain, and the regulatory IAK domain are indicated. Arrows in the expanded intron/exon diagram indicate the ALS-related mutations. A mutation denoted with −14, is positioned 14 bp upstream of exon 27, but still creates the same mutant C terminus. Image created with Biorender.com. **B,** ALS-associated mutations in KIF5A all lead to a common C-terminal tail as indicated in red. Positively and negatively charged amino acids are underlined and bolded, respectively. **C,** Electrostatic surface charge distribution images show that the novel mutant C-terminal tail reverses the protein charge density making the mutant tail highly positively charged. **D,** Expression of the KIF5A$^{\Delta Exon27}$ mutant, but not KIF5A$^{\Delta C\text{-}term}$, in primary mouse cortical neurons leads to increased risk of death compared with KIF5A^{WT}-expressing cells. A representative graph of three biological experiments is shown; n = 597 cells for KIF5A^{WT}, n = 212 cells for KIF5A$^{\Delta Exon27}$, and n = 475 cells for KIF5A$^{\Delta C\text{-}term}$ in the experiment shown. p = 1.4 x 10^{-7} by Cox hazard analysis.

estimate of the relative risk of death for each cohort of neurons. This methodology has been used extensively to study toxic properties of several proteins associated with ALS and other neurodegenerative diseases (Barmada et al., 2010, 2014, 2015; Bilican et al., 2012; Skibinski et al., 2014; The HD iPSC Consortium, 2012). Expression of KIF5A$^{\Delta Exon27}$ resulted in an increased HR compared with the wild-type protein (HR = 1.69, p = 1.4 × 10^{-7}; Figure 4.1D). This supports, in part, the hypothesis that KIF5A$^{\Delta Exon27}$ acts through a toxic gain of function. This toxicity could be due to either the addition of the mutant 39 aa C-terminal tail or the loss of the wild-type 34 aa from the tail. To distinguish these possibilities, we further evaluated the neuronal survival of a wild-type KIF5A protein truncated at aa 998 (KIF5A$^{\Delta C\text{-}term}$), where the wildtype and mutant tail sequences diverge. Our evaluation revealed that neurons expressing KIF5A$^{\Delta C\text{-}term}$ survived similarly to those expressing KIF5A^{WT} (HR = 1.04; p = 0.67; Fig. 4.1D). These results suggest that the toxic gain-of-function properties of KIF5A$^{\Delta Exon27}$ are conferred by the mutant C-terminal sequence.

Mutant KIF5A displays altered binding to MTs, distal accumulation, and a dominant-negative effect over wild-type KIF5A

Given the C-terminal charge changes and how that might affect inter- and intra-protein interactions, we sought to investigate how this mutation might affect KIF5A's basic function and localization. Usually, most KIF5A within cells is cytosolic, unbound from cargo, inhibited by a head-tail association (Cai et al., 2007; Dietrich et al., 2008; Hackney & Stock, 2000). While inhibited, KIF5A displays a decreased affinity for MTs, whereas activation causes a marked increase in the KIF5A-MT interaction (Cai et al., 2007; D. S. Friedman & Vale, 1999). We evaluated the ability of the motor to bind MTs by expressing KIF5A^{WT} and KIF5A$^{\Delta Exon27}$ in SKNAS cells and evaluated co-localization to MTs through cellular staining. KIF5A^{WT} displayed a diffuse staining pattern with little MT co-localization. In contrast, nearly 60% of KIF5A$^{\Delta Exon27}$-expressing cells showed a high degree of colocalization (Fig. 4.2A, B). These results suggest that the effect of the ALS-associated mutation is to attenuate autoinhibition of KIF5A$^{\Delta Exon27}$. Furthermore, we observed

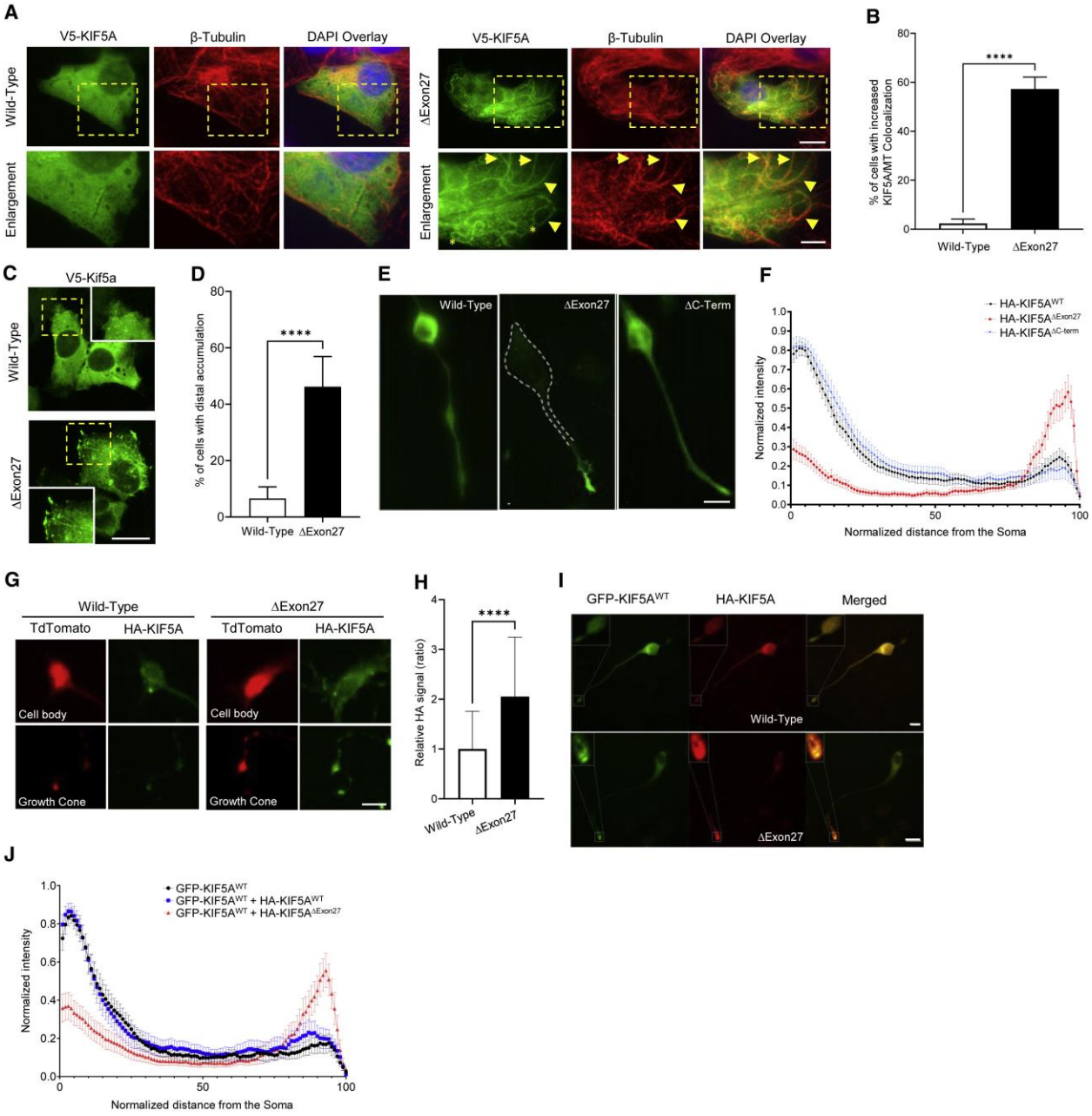

Figure 4.2: Mutant KIF5A associates more readily with microtubules, displays microtubule plus-end accumulation, and has a dominant-negative effect on wild-type KIF5A A, SKNAS cells expressing V5-tagged KIF5A$^{\Delta Exon27}$ show increased microtubule (MT) co-localization compared with KIF5A^{WT} as demonstrated by V5-KIF5A highlighting the MT tracks. Examples of KIF5A (V5; green) and β-tubulin (red) co-localization are indicated by arrowheads. Many cells have KIF5A$^{\Delta Exon27}$-associated MTs with a non-radial pattern (asterisks). Scale bars, 10 μm (wide view), 5 μm (enlargement). **B,** Quantification of the experiment in **(A)**. n = 5 biological replicates are shown with $p < 0.0001$. **C-G,** Expression of KIF5A$^{\Delta Exon27}$ results in distal/growth cone accumulation of tagged-KIF5A in transfected SKNAS **(C)**, differentiated N2A **(E)**, and PMN cells **(G)**. Scale bars, 20 μm **(C)**, 25 μm **(E)**, and 10 μm **(G)**. **D,** Quantification of the percentage of transfected SKNAS cells in **(C)** with distal accumulation. n = 5 biological replicates

are shown with $p < 0.0001$. **F,** HA intensity analysis of the experiment in **(E)**. n = 3 biological replicates are shown with n ≥ 60 cells per sample. **H,** Quantification of the HA signal intensity from the growth cone compared with that of the cell body for the PMNs in (**G**). n = 3 biological replicates are shown with $p < 0.0001$. **I,** Representative images of differentiated N2A cells transfected with GFP-KIF5A^{WT} and either HA-tagged KIF5A^{WT} or KIF5A$^{\Delta Exon27}$. Scale bar, 25 µm. Confirmation of this protein binding is shown in Figure S4.1B. **J,** Quantification of the GFP intensity along the length of the cells in **(I)** when different forms of HA-tagged KIF5A are present. n = 3 biological replicates with n≥51 cells analyzed per sample. Data in **(B)**, **(D)**, and **(H)** are represented as mean ± SD. Data in **(F)** and **(J)** are represented as mean ± 95% CI.

that the MT network within KIF5A$^{\Delta Exon27}$ cells specifically often displayed a non-radial pattern with numerous loops (Fig. 4.2A, asterisks). This pattern resembles the MT reorganization seen in cells exposed to kinesore, an inducer of kinesin-1 activation (Randall et al., 2017). Finally, we observed distal accumulation of KIF5A$^{\Delta Exon27}$ in a substantial percentage of cells relative to KIF5A^{WT}-expressing cells (50% versus 5%; Fig. 4.2C, D), a phenotype observed in vitro with activated forms of KIF5A (Guardia et al., 2016; R. Yang et al., 2016). This result was validated in both differentiated Neuro-2A (N2A) cells and primary mouse motor neurons (PMNs), where expression of KIF5A$^{\Delta Exon27}$ resulted in a ~2-fold increase in distally accumulated protein (Fig. 4.2E–H). As with the survival assays, the results of KIF5A$^{\Delta C\text{-}term}$ expression paralleled KIF5A^{WT} supporting that mislocalization was dependent on the mutant C terminus specifically (Fig. 4.2E, F).

Kinesin-1 is formed by the dimerization of two heavy chains. We find that KIF5A$^{\Delta Exon27}$ can homodimerize and heterodimerize with KIF5A^{WT} (Fig. S4.1A, B). Based on this, we asked whether KIF5A$^{\Delta Exon27}$ can have a dominant-negative effect on KIF5A^{WT} resulting in mislocalization of both proteins. We compared the localization of GFP-KIF5A^{WT} in differentiated N2A cells co-expressing either HA-tagged-KIF5A$^{\Delta Exon27}$ or -KIF5A^{WT}. GFP-KIF5A^{WT} displayed increased accumulation within distal neurites when co-expressed with HA-KIF5A$^{\Delta Exon27}$, but not when expressed with HA-KIF5A^{WT} (Fig. 4.2I, J). These results support the hypothesis that KIF5A$^{\Delta Exon27}$ can act in a dominant-negative fashion over KIF5A^{WT}.

Mutant KIF5A displays defective autoinhibition

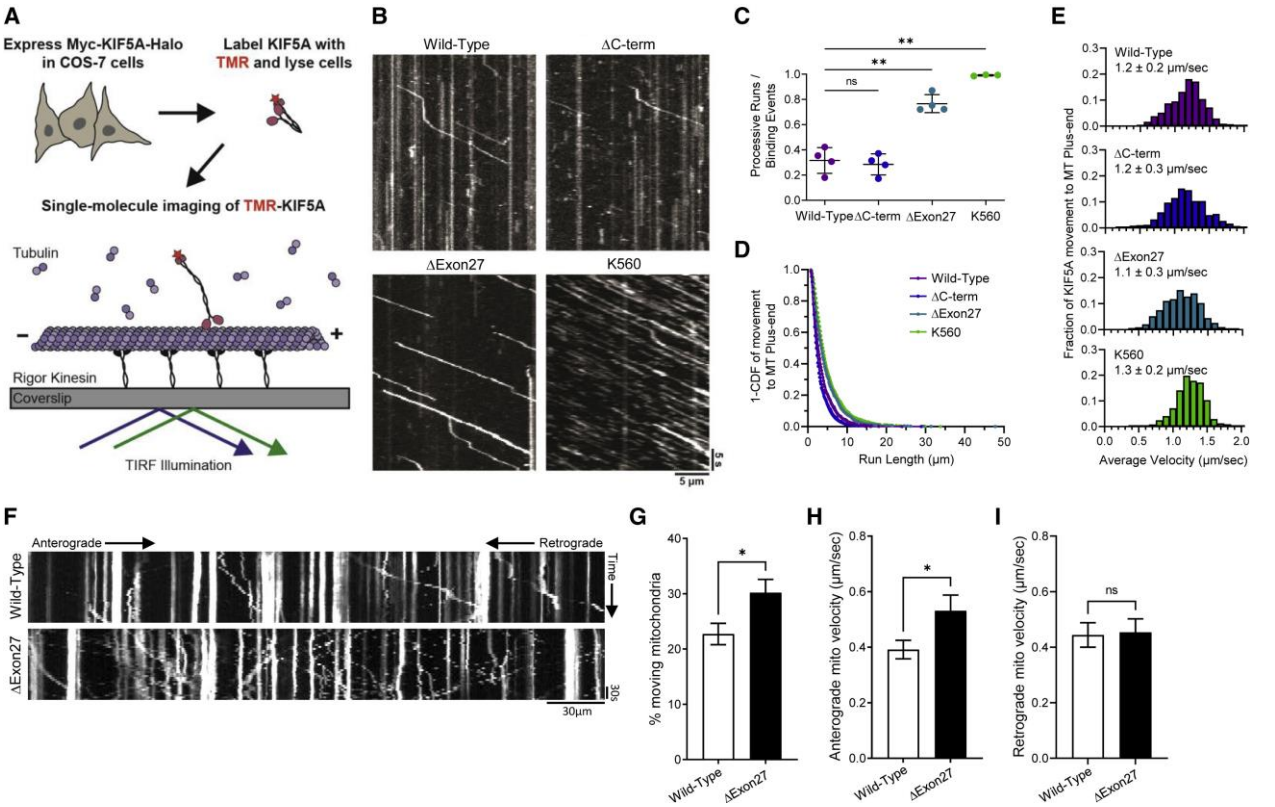

Figure 4.3: Mutant KIF5A displays qualities of a hyperactive kinesin in axonal transport. A, Schematic representation of the single-molecule labeling method used to track KIF5A movement. **B,** Representative kymographs showing the effect of KIF5A$^{\Delta C-Term}$, KIF5A$^{\Delta Exon27}$, and KIF5A^{K560} mutations on motility compared with KIF5A^{WT}. Scale bars, 5 µm (distance) and 5 s (time). **C,** Quantification of the ratio of processive runs to total binding events for KIF5A. n = 3–4 biological replicates with p = 0.0022 for K560 versus wild-type, p = 0.0021 for ΔExon27 versus wild-type and non-significant for ΔC-term versus wild-type as determined by the Brown-Forsythe ANOVA with Dunnett's multiple comparison test. **D-E,** Inverse cumulative distribution functions (CDF) of run length and histogram distributions of velocity for KIF5A transport to the MT plus end (n = 652 events for wild-type, 667 events for ΔC-term, 1,074 events for ΔExon27, and 660 events for K560 samples). The curves in **(D)** represent single exponential decay fits. The values in **(C, E)** are mean ± SD. **F,** Representative kymographs showing the effect of the KIF5A$^{\Delta Exon27}$ on mitochondrial transport. Scale bar, 30 µm (distance) and 30 s (time). **G–I,** Quantification of mitochondrial transport characteristics. The total number of moving mitochondria **(G)** are reported as well as anterograde mitochondrial velocity **(H)**, and retrograde velocity **(I)**. For each experiment n = 3 biological replicates p = 0.017 in **(G)**, 0.032 in **(H)**, and is non-significant (ns) in **(I)**. The data represented in **(G–I)** are mean ± SEM.

KIF5A is autoregulated through the direct intramolecular interaction of the C-terminal IAK motif with the N-terminal motor domain. In humans, the IAK domain consists of the amino acids QIAKPIR located at residues 917–923. This sequence is located upstream of the aberrant ALS-associated mutant tail, which diverges from the wild-type protein at aa 998. Altering this intramolecular interaction, through mutation or deletion of the IAK motif, for instance, results in a constitutively active kinesin (Cai et al., 2007). This, in

turn, results in increased MT binding (Hackney & Stock, 2000), altered MT dynamics (Randall et al., 2017), and accumulation in distal neurites (Seiler et al., 2000). Given the similarities between these observations and the KIF5A$^{\Delta Exon27}$ phenotypes, we hypothesize that KIF5A$^{\Delta Exon27}$ forms a constitutively active kinesin lacking autoinhibition.

To test this hypothesis, we utilized an in vitro assay to evaluate the MT-based motility of wild-type and mutant KIF5A (Fenton et al., 2021a). The transport of KIF5A along dynamic MTs was examined at single-molecule resolution using total internal reflection fluorescence (TIRF) microscopy (Fig. 4.3A). For this analysis, KIF5A$^{\Delta Exon27}$, KIF5A^{WT}, KIF5A$^{\Delta C\text{-}term}$, and a truncated, constitutively active construct corresponding to the first 560 aa residues of KIF5A (KIF5A^{K560}) were compared. All KIF5A constructs landed on MTs and exhibited processive transport toward the MT plus end (Fig. 4.3B). However, KIF5A$^{\Delta Exon27}$ displayed more frequent motile events (77% versus 31% of binding events) and longer run lengths (4.6 versus 3.6 μm on average) than KIF5A^{WT}. The motile properties of KIF5A$^{\Delta Exon27}$ were comparable with those observed for the constitutively active construct KIF5A^{K560} (Fig. 4.3C, D). In contrast, the KIF5A$^{\Delta C\text{-}term}$ displayed a frequency of motile events and run lengths comparable with KIF5A^{WT}, supporting that the mutant C terminus is necessary to disrupt autoinhibition. Of note, the velocity of moving KIF5A molecules did not differ among any of the expression constructs (Fig. 4.3E), indicating that the activity of the motor domain remains unaltered despite the loss in autoinhibition seen with KIF5A$^{\Delta Exon27}$. In summary, the properties of KIF5A$^{\Delta Exon27}$ are consistent with an inability to autoinhibit, resulting in a constitutively active motor.

Mutant KIF5A expression results in increased movement and velocity of mitochondria

To test how the loss of KIF5A autoinhibition affects neuronal cargo transport, we examined the effects of wild-type and mutant KIF5A on mitochondrial transport in PMNs via live-cell imaging. Mitochondrial axonal transport is a regulated process that is essential to maintain neuronal integrity.

Anterograde transport of mitochondria is primarily driven by kinesin-1 (Hollenbeck & Saxton, 2005; van Spronsen et al., 2013). Consistently, mitochondrial transport defects have been associated with neurodegenerative diseases, including AD, PD, and ALS (W. Guo et al., 2020; McLelland et al., 2014; Millecamps & Julien, 2013; E. F. Smith et al., 2019; Q. Wang et al., 2019). Expression of KIF5A$^{\Delta Exon27}$ resulted in a higher percentage of moving mitochondria with an increased anterograde, but not retrograde, velocity compared with PMNs expressing KIF5A^{WT} (Fig. 4.3F–I). Of note, velocities measured in the TIRF assay (Fig. 4.3E) corresponded to processive runs only, excluding pauses, while mitochondrial transport was measured as the average velocity over the course of the experiment and thus is affected by changes in either the frequency or durations of pauses. Thus, the increase in average anterograde velocity of mitochondria may reflect either an increase in instantaneous velocity or a decreased frequency or duration of pauses during transport. Together, these data indicate that expression of KIF5A$^{\Delta Exon27}$ alters axonal transport.

Mutant KIF5A displays altered interactions with proteins and RNA

KIF5A also functions to transport proteins and RNA. The C-terminal region of KIF5A contributes to the binding of cargo either directly or through adapters (Cross & Dodding, 2019). With the aforementioned structural changes present in mutant KIF5A, we hypothesized that the protein might also exhibit alterations in protein and RNA binding properties. To identify differentially interacting proteins, we transfected SKNAS cells with V5-tagged KIF5A^{WT} and KIF5A$^{\Delta Exon27}$ and immunoprecipitated the tagged proteins (Fig. 4.4A; Table S4.1). We identified 78 and 21 proteins displaying increased and decreased binding, respectively, to KIF5A$^{\Delta Exon27}$ relative to KIF5A^{WT}. Among the enriched KIF5A$^{\Delta Exon27}$ interactions were SQSTM1/p62, MOV10, and UPF1. SQSTM1/p62 functions in the autophagy pathway and mutations in this protein cause ALS/FTD and Paget disease (Duran et al., 2011; Falchetti et al., 2004; Hocking et al., 2004; Laurin et al., 2002). UPF1 is an RNA-dependent helicase required for nonsense-mediated decay(G. Singh et al., 2008). MOV10 is an RNA helicase required for miRNA-mediated cleavage of complementary mRNAs by RISC

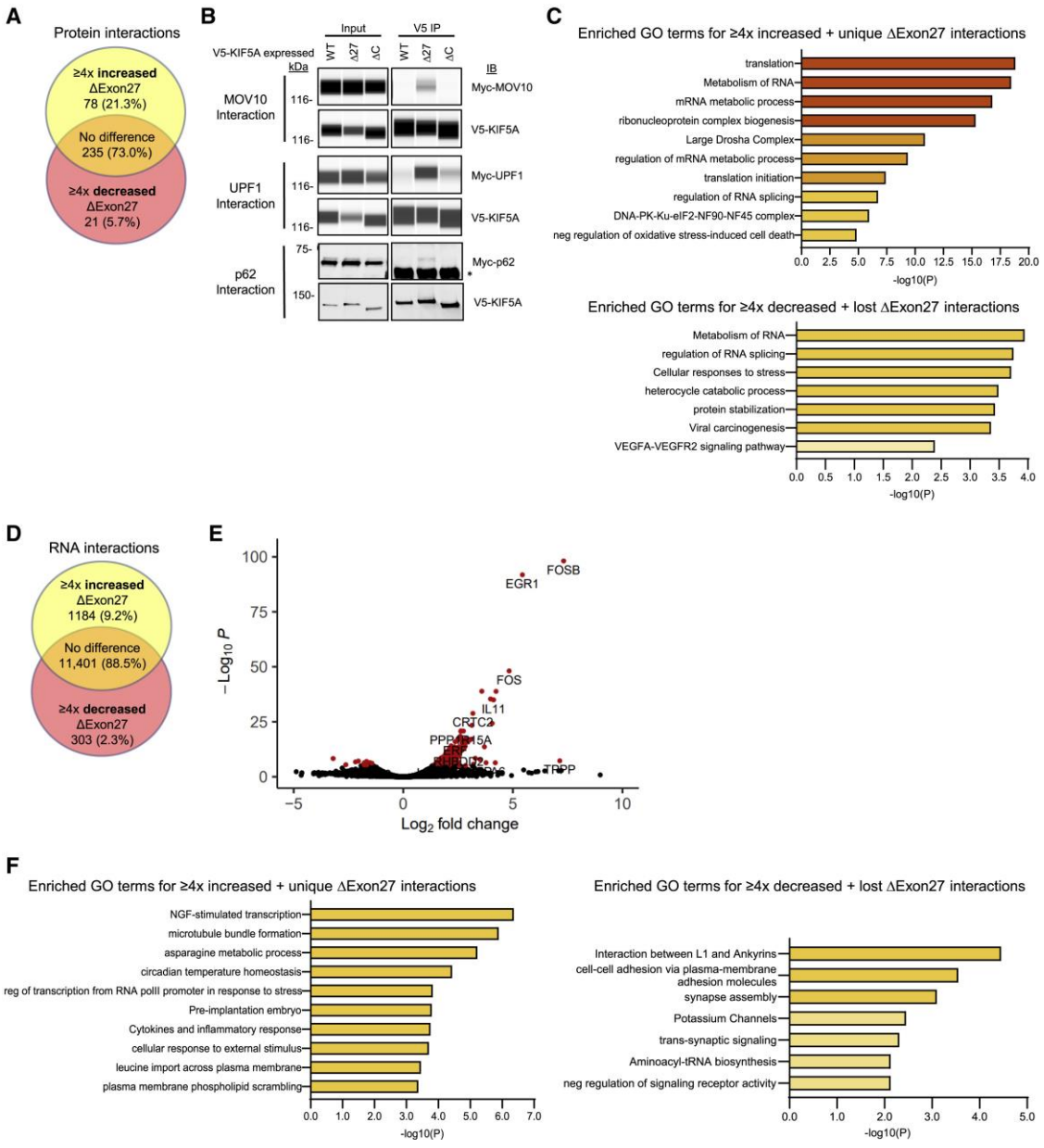

Figure 4.4: KIF5A binding partners are altered in cells expressing mutant KIF5A. A, Mass spectrometry analysis of V5-tagged KIF5A^{WT} and KIF5A$^{\Delta Exon27}$ bound proteins in SKNAS cells. Venn diagram indicates the number of protein binding partners altered in KIF5A$^{\Delta Exon27}$ mutant immunoprecipitations. Yellow region: proteins that are unique to, or have ≥4× increase in the amount bound to, KIF5A$^{\Delta Exon27}$. Red region: proteins that are absent from, or have ≥4× decrease in the amount bound to, KIF5A$^{\Delta Exon27}$. Orange region: proteins that show no binding preference to either form of KIF5A. **B,** Validation of several Myc-tagged mass spectrometry hits from **(A)** by western blotting. Capillary western blots of MOV10 (upper panel) and UPF-1 (middle panel) show the strong interaction of V5-KIF5A$^{\Delta Exon27}$, but not KIF5A^{WT}. Exposure settings for the capillary western blots were adjusted individually for each band of interest as needed for each sample set (samples of the same type; ex:. all of the input samples). A traditional western blot of p62 (lower panel) also shows a unique interaction with V5-KIF5A$^{\Delta Exon27}$. Asterisk: the antibody heavy chain pulled down in

the IP. The blot for MOV10, UPF1, and p62 is representative of n = 4, n = 1, and n = 4 biological replicates, respectively. **C,** Pathway analysis on the proteins enriched (upper) and diminished (lower) in the KIF5A$^{\Delta Exon27}$ mutant mass spectrometry sample. **D,** Analysis of RNAs associated with immunoprecipitated V5-tagged KIF5A^{WT} and KIF5A$^{\Delta Exon27}$ mutant containing complexes. The Venn diagram indicates how many RNAs had altered interactions with KIF5A$^{\Delta Exon27}$ mutant samples as described in **(A)**. **E,** A volcano plot of RNA immunoprecipitation results sowing significantly altered RNA interactors in red. Data are based on n = 2 biological replicates. **F,** Pathway analysis on the RNAs enriched (left) and diminished (right) in the KIF5A$^{\Delta Exon27}$ mutant sample. See expanded pathway analyses in Fig S4.2.

and a mediator of mRNA decay via interaction with UPF1 (Meister et al., 2005; Nawaz et al., 2022). While the interaction of KIF5A with these proteins was confirmed by co-immunoprecipitation/western blotting (Fig. 4.4B), it is interesting to note that all three of these proteins have been found in complex previously (Fritzsche et al., 2013; X. Li et al., 2015; Soria-Valles et al., 2016). Pathway analysis of the enriched KIF5A$^{\Delta Exon27}$ interactors (Fig. 4.4C and S4.2A) revealed several categories associated with RNA processing, a well-established process associated with ALS pathogenesis (Butti & Patten, 2019). Similarly, pathway analysis of proteins with reduced KIF5A$^{\Delta Exon27}$ interactions included ALS-associated categories of protein stabilization and cellular stress response (Parakh & Atkin, 2016), suggesting a downstream consequence of altered binding that leads to disruption of cellular homeostasis.

We next sought to identify differentially bound RNAs using RIP-seq (Fig. 4.4D, E; Table S4.1). Here, we identified 1,184 and 303 transcripts that displayed enriched and decreased binding, respectively, to KIF5A$^{\Delta Exon27}$ compared with KIF5A^{WT}. Pathway analysis again revealed several categories related to ALS pathogenesis (Fig. 4.4F and S4.2B). KIF5A$^{\Delta Exon27}$-enriched pathways included nerve growth factor (NGF)-stimulated transcription, which is related to neurite outgrowth (J. Liu et al., 2007). Pathways that were underrepresented in KIF5A$^{\Delta Exon27}$ samples included interactions between L1 and Ankyrins, synapse assembly, and potassium channels. Hyperexcitability is a hallmark of ALS primarily resulting from the dysfunction of ion channels (LoRusso et al., 2019). Together, our results demonstrate that KIF5A mutations can result in altered protein and RNA interactions associated with ALS-related pathways.

Mutant KIF5A expression contributes to altered gene expression and splicing

To circumvent overexpression effects, we created isogenic iPSC CRISPR lines with a p.Arg1007Lys (c.3020G>A) mutation (Fig. 4.1A and S4.3A-B). This mutation was chosen because it alters an essential splice site sequence and was observed in two distinct familial ALS cases (Nicolas et al., 2018). The wild-type parental line (Iso Control) and the heterozygous mutant line (KIF5A^{R1007K}) were differentiated into motor neurons (iMNs) and subject to RNA-seq. Evaluation of differentiation markers (Islet/Tuj1) revealed a >85% differentiation efficiency of iPSC to mature iMNs, which are ChAT and MAP2 positive by DIV15 (Fig. 4.5A–C). The mutant iMNs faithfully recapitulated the skipped exon 27 phenotype seen in patients (not shown) and appeared to have a similar level of total KIF5A between the two lines (Fig. S4.3C-D). Interestingly, the level of wild-type protein in the mutant line was ~65% that of the isogenic control (Fig. S3E-F), suggesting there is ~2× more wild-type than mutant protein present in this line.

While altered interactions, MT transport, and localization of KIF5A$^{\Delta Exon27}$ may be a direct result of constitutive activation, there are several secondary effects that could occur as well. As KIF5A$^{\Delta Exon27}$ had been found to have altered interactions with RNA metabolism-related proteins, we investigated the effects of KIF5A$^{\Delta Exon27}$ on global gene expression. RNA-seq analysis of the iMNs revealed 57 genes displaying altered expression (Fig. 4.5D, E; Table S4.2). We evaluated six of these genes by qPCR whose functions were related to enriched pathways seen in our protein and RNA studies, including NMJ function, mRNA processing, and neurite outgrowth. All tested genes recapitulated the results observed by RNA-seq (Fig. 4.5E). Pathway analysis of the altered genes (Fig. 4.5F) suggests that, similar to our studies in SKNAS cells, expression of ALS-related mutant KIF5A disrupts RNA metabolism within the cell. Because so many altered protein interactors are related to mRNA splicing (Fig. 4.4C), we extended our analysis to investigate whether splicing was altered between the isogenic iMNs. Differential splicing events were identified with the multivariate analysis of transcript splicing method(S. Shen et al., 2014). Using this tool, we identified 1,919 transcripts with altered splicing compared with the isogenic control iMNs (Fig. 4.6A; Table S4.3). Of these, 1,000 exons and 919 exons showed decreased and increased skipping, respectively, in KIF5A^{R1007K} lines. Pathway analysis of each of these groups (Fig. 4.6B and S4.4A, B) suggests that this group of altered

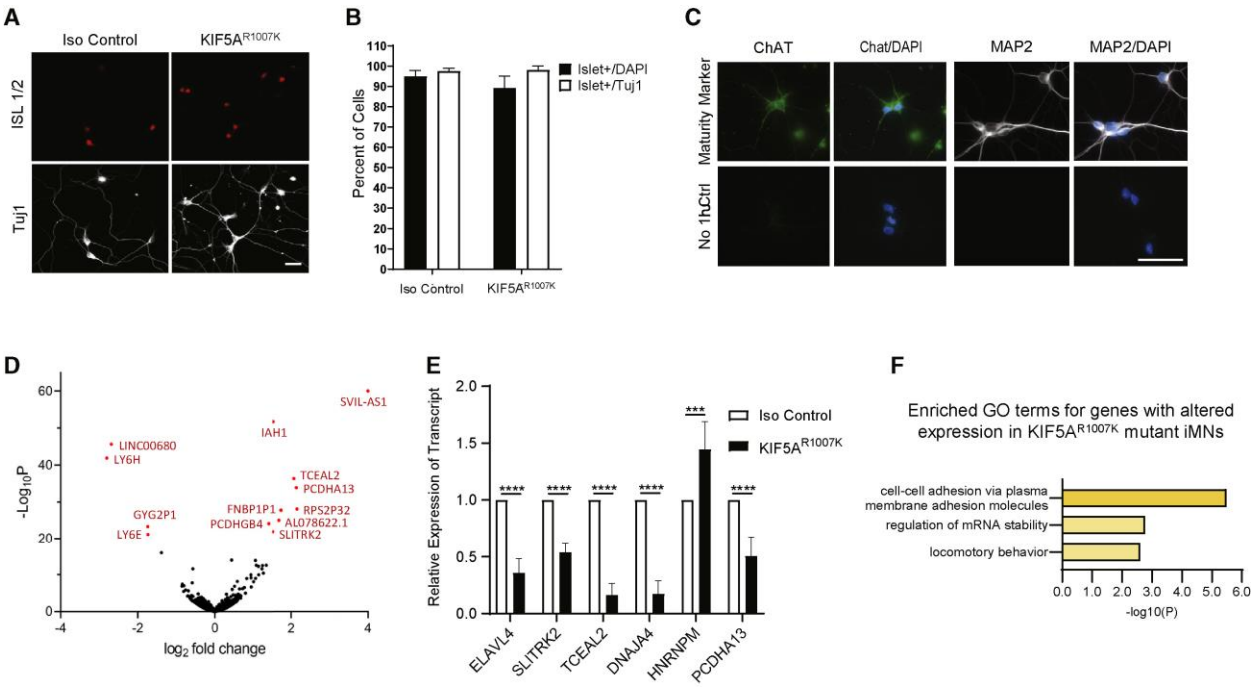

Figure 4.5: Isogenic iPSCs expressing mutant KIF5A display altered gene expression. A, Patient-derived Arg1007Lys mutant KIF5A iPSC line and isogenic control differentiated into motor neurons (iMNs) display the MN specific marker, Islet1/2 (red), and Tuj1 (white) at DIV15. Scale bar, 50 µm. **B,** The differentiation efficiency of KIF5A iMNs at DIV15. Data are representative of n = 3 biological replicates where n = 531 control cells and n = 624 KIF5A^{R1007K} cells were counted over all experiments. **C,** Staining for maturity markers in DIV15 control iMNs differentiated by this method. At least 100 cells were observed in each of n = 2 biological replicates. Scale bar, 50 µm. **D,** A volcano plot of RNA-seq analysis of the KIF5A^{R1007K} line and isogenic control showing several genes that are differentially expressed in the mutant. n = 4 biological replicates. **E,** Validation of several of the differentially expressed genes in **(D)** via qPCR. n = 3 biological replicates, each experiment run in triplicate with $p < 0.0001$ by two-way ANOVA. **F,** Pathway analysis of differentially expressed genes in **(D)**. Enriched GO terms recapitulate themes of mRNA processing from previous experiments. Data in **(B)** and **(E)** are represented as mean ± SD.

genes, as a whole, represents cytoskeletal and transport defects in the cell, both of which are hallmarks of neurodegenerative disease (Chevalier-Larsen & Holzbaur, 2006; Eira et al., 2016; W. Guo et al., 2020; McMurray, 2000).

To determine which RNA binding proteins (RBPs) could contribute to the splicing changes, we utilized rMAPS2 (Hwang et al., 2020), which evaluates enrichment of binding sites for over 100 RBPs in a position-dependent manner in differentially spliced genes. This analysis revealed an enrichment of the

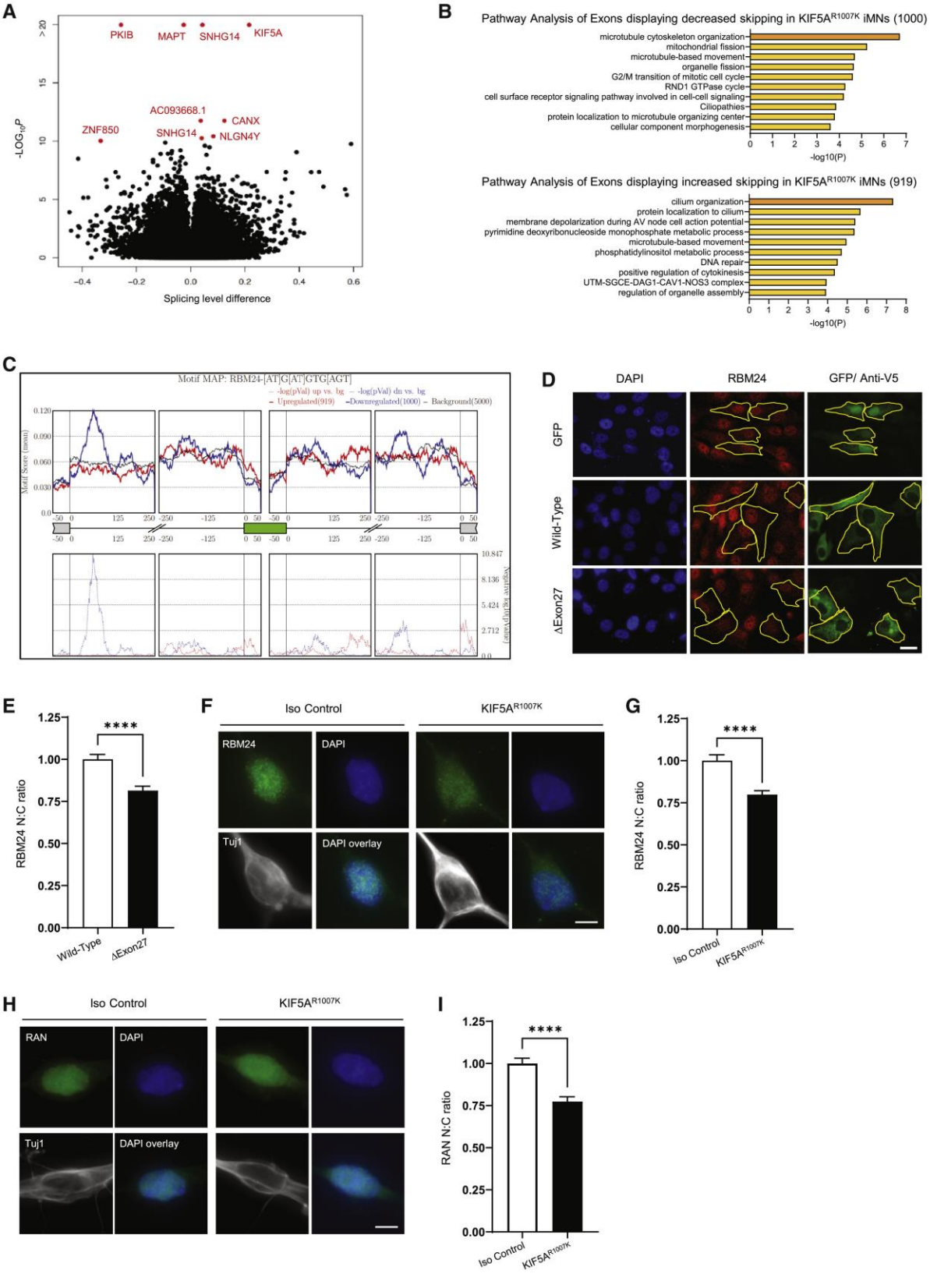
A
PKIB
MAPT
SNHG14
KIF5A
AC093668.1
CANX
ZNF850
SNHG14
NLGN4Y
-LOG10P
Splicing level difference
B
Pathway Analysis of Exons displaying decreased skipping in KIF5AR1007K iMNs (1000)
microtubule cytoskeleton organization
mitochondrial fission
microtubule-based movement
organelle fission
G2/M transition of mitotic cell cycle
RND1 GTPase cycle
cell surface receptor signaling pathway involved in cell-cell signaling
Ciliopathies
protein localization to microtubule organizing center
cellular component morphogenesis
-log10(P)
Pathway Analysis of Exons displaying increased skipping in KIF5AR1007K iMNs (919)
cilium organization
protein localization to cilium
membrane depolarization during AV node cell action potential
pyrimidine deoxyribonucleoside monophosphate metabolic process
microtubule-based movement
phosphatidylinositol metabolic process
DNA repair
positive regulation of cytokinesis
UTM-SGCE-DAG1-CAV1-NOS3 complex
regulation of organelle assembly
-log10(P)
C
Motif MAP: RBM24-[AT]G[AT]GTG[AGT]
Upregulated(919)
Downregulated(1000)
Background(5000)
Motif Score (mean)
Motif Score (Average)
D
DAPI
RBM24
GFP/ Anti-V5
GFP
Wild-Type
ΔExon27
E
RBM24 N:C ratio
****
Wild-Type
ΔExon27
F
Iso Control
KIF5AR1007K
RBM24
DAPI
Tuj1
DAPI overlay
G
RBM24 N:C ratio
****
Iso Control
KIF5AR1007K
H
Iso Control
KIF5AR1007K
RAN
DAPI
Tuj1
DAPI overlay
I
RAN N:C ratio
****
Iso Control
KIF5AR1007K

Figure 4.6: Nuclear-cytoplasmic transport is disrupted in mutant KIF5A-expressing cells. A, Volcano plot of splicing analysis results from RNA-seq experiments showing significantly altered genes in KIF5A$^{\Delta Exon27}$ iMNs. Red dots indicate values with $p < 10^{-10}$. Data are representative of n = 4 biological replicates. **B,** Pathway analysis of genes where decreased (top) or increased (bottom) exon skipping is observed. The number of affected exons in each group are listed in parentheses. See expanded pathway analyses in Figure S4.4. C, Motif mapping identifies enrichment of RBM24 binding sites in alternatively spliced genes ($p < 10^{-10}$). **D,** Micrographs of SKNAS cells transfected with either GFP alone or V5-tagged KIF5A^{WT} or KIF5A$^{\Delta Exon27}$ (green) and stained for RBM24 (red) show that RBM24 localization is altered in KIF5A$^{\Delta Exon27}$-expressing cells. Scale bar, 20 µm. Cells outlined with yellow dashed lines show examples of this phenomena. **E,** Quantification of the RBM24 staining intensity in the nucleus versus the cytoplasm (N:C) in SKNAS transfected cells represented in **(D)**. Graph represents data from 171 KIF5A^{WT} and 176 KIF5A$^{\Delta Exon27}$ cells collected over n = 4 biological replicates with $p < 0.0001$. **F,** Max projected micrographs of KIF5A^{R1007K} and isogenic control iMNs stained with RBM24 (green), DAPI (blue), and Tuj1 (white) confirm the N:C ratio dysregulation seen in SKNAS cells. Scale bar, 5 µm. **G,** Quantification of RBM24 localization in cells represented in **(F)**. Graph represents data from 116 isogenic control and 124 KIF5A^{R1007K} iMNs collected over n = 4 biological replicates with $p < 0.0001$. **H,** Max projected micrographs of KIF5A^{R1007K} and isogenic control iMNs stained with RAN (green), DAPI (blue), and Tuj1 (white) shows expression of KIF5A^{R1007K} in differentiated iMNs alters RAN localization in these cells Scale bar, 5 µm. **I,** Quantification of RAN localization in cells represented in **(H)**. Graph represents data from 89 isogenic controls and 92 KIF5A^{R1007K} iMNs collected over n = 3 biological replicates with $p < 0.0001$. Data in **(E)**, **(G)**, and **(I)** are represented as mean ± SEM.

binding motif for RBM24 (Fig. 4.6C), a multifunctional RNA binding protein involved with many aspects of mRNA processing and whose function is essential for cell fate decision and differentiation (Jin et al., 2010; Lin et al., 2018; Xu et al., 2014; M. Zhang et al., 2018). We speculate that the decrease in RBM24-mediated alternative splicing may be due to disruption of RBM24 nuclear: cytoplasmic localization in mutant KIF5A-expressing cells. This could be directly due to the expression of the mutant protein as we identified RBM24 RNA as a unique interactor of KIF5A$^{\Delta Exon27}$ in SKNAS (Table S4.1), and the redistribution of KIF5A$^{\Delta Exon27}$ with this RNA bound may result in altered localized translation of RBM24. Alternatively, sequestration of other altered protein/RNA binding partners may result in downstream deficits in global nucleocytoplasmic transport (NCT) for which RBM24 is a symptom. This hypothesis was evaluated by staining RBM24 in SKNAS cells expressing either KIF5A^{WT} or KIF5A$^{\Delta Exon27}$. Here, we observed that RBM24 has a greater cytoplasmic localization in KIF5A$^{\Delta Exon27}$-expressing cells supporting our position (Fig. 4.6D-E). This result was further validated in the KIF5A^{R1007K} iMNs (Fig. 4.6F-G).

This result could indicate a global NCT defect, so we extended our investigation to examine the RAN gradient in KIF5A isogenic iMNs. RAN (ras-related nuclear protein) is a GTP binding protein essential for transporting macromolecules through the nuclear pore complex (Matsuura, 2016; Steggerda & Paschal,

2002). The presence of RAN in the nucleus and cytoplasm of cells establishes a gradient by which the directionality of normal NCT function is determined (Görlich & Mattaj, 1996; Hutten & Dormann, 2020). Typically RAN is at a higher density in the nucleus, but compromised NCT can cause higher protein elevations in the cytoplasm (Görlich & Mattaj, 1996; Hutten & Dormann, 2020; Kodiha et al., 2004). We found that KIF5A^{R1007K} iMNs had more cytoplasmic RAN than the isogenic control (Fig. 6H-I), demonstrating that mutant KIF5A perturbs NCT. This is not surprising as dysregulation of NCT has been implicated in several neurodegenerative diseases, including ALS, FTD, AD, and HD (Ding & Sepehrimanesh, 2021; Hutten & Dormann, 2020).

IV. Discussion

Neurodegenerative diseases represent a complex set of disorders in which there is dire need for improved therapeutics. Increased comprehension of the mechanisms underlying these diseases is an essential step toward the development of effective therapies. To date, causative mutations in over 30 genes for ALS have been identified. Among these, we previously identified several mutations within KIF5A in familial ALS that result in a common aberrant C-terminal tail. How these ALS mutations in KIF5A lead to MN death and the molecular mechanisms that cause pathology in cells are not understood. We examined the pathogenic effects of ALS mutant KIF5A, showing that mutant KIF5A confers a toxic gain of function via its altered C-terminal tail. Specifically, this mutation causes KIF5A hyperactivity, likely due the negative charge of the KIF5A$^{\Delta Exon27}$ C-terminal tail. It is not understood how a charge reversal could impact the overall structure of mutant KIF5A; however, it is known that an adjacent region with a positive charge is essential in maintaining the stable tail-head association necessary for KIF5A inactivation (Y. L. Wong & Rice, 2010).

Defects in axonal transport have long been established as a hallmark feature in neurodegenerative diseases (Chevalier-Larsen & Holzbaur, 2006; W. Guo et al., 2020). Of particular interest, C9ORF72 repeat-expansion results in arginine-rich di-peptide repeats that directly impede dynein and kinesin-1 movement

through physical interaction with the axonal transport machinery (Fumagalli et al., 2021). The data supporting the distal accumulation of KIF5A and increased movement of cargo, raises the possibility that mutant KIF5A may lack re-cycling properties and that mitochondria and other cargo accumulate distally. Since mitochondria are an important cellular organelle for cell health and function, their abnormal neuronal location could possibly lead to cellular toxicity and death.

Mutant KIF5A displays aberrant binding to several proteins. Pathway analysis revealed that altered binding interactions influence RNA processing-related pathways. These pathways are well established as contributing to ALS pathogenesis. Among the proteins displaying increased binding to mutant KIF5A are UPF1 and MOV10. UPF-1 and MOV10 are RNA helicases that are important for non-sense-mediated decay. Interestingly, Barmada et al. (2015) showed that expression of either UPF-1 or MOV10 resulted in reduced cell death in mutant TDP-43-expressing primary neurons (Barmada et al., 2015). This suggests that UPF-1 and MOV10 might be critical proteins to maintain overall cell health and survival. Mutant KIF5A also displayed increased binding to p62/SQSTM1. Mutations in p62/SQSTM1 are a cause of familial ALS (Fecto et al., 2011). Knockout of p62/SQSTM1 in mice results in neurodegeneration (Ramesh Babu et al., 2008) and reduced levels of p62 in a zebrafish model cause ALS-like phenotypes (Lattante et al., 2015). These results suggest that the binding to mutant KIF5A inactivates these proteins from performing their normal function. However, further studies are needed to determine the mechanisms by which KIF5A binding leads to their inactivation.

Mutant KIF5A also displays altered interactions with RNA species. Pathways associated with RNAs displaying increased binding include NGF-transcription, supporting neuronal survival, MT assembly, and homeostatic processes. We further reported that EGR1 and FosB mRNA display a high level of enrichment of mutant KIF5A binding. EGR1 is highly expressed in the brain, regulates pathways involved in synaptic plasticity and maintains synaptic homeostasis at the neuromuscular junction (MacDonald et al., 2017). Interestingly, EGR1 knockout mice show decreased limb muscle strength affecting motor functions (Jones et al., 2001). FosB RNA has previously been shown to interact with UPF1 and this binding is enhanced in epileptic samples (Mooney et al., 2017). Intriguingly, FosB displays increased binding to mutant FUS.

Furthermore, increased axonal branching results from mutant FUS can be rescued by reducing the expression of FosB RNA (Akiyama et al., 2019).

Here, we have shown that ALS-associated mutations result in a loss of autoinhibition leading to disease pathogenesis. Remarkably, there are several examples of disease-causing pathogenic mutations within a kinesin gene that result in hyperactivation. Heterozygous KIF21A mutations, which heavily occur in its third coiled-coil domain with a few in the motor domain, result in the ocular motility disorder congenital fibrosis of the extraocular muscles type 1 (Yamada et al., 2003). Interestingly, autoregulation of KIF21A is accomplished through interaction of these domains and the pathogenic mutations within both domains relieve autoinhibition. Mutant KIF21A displays several characteristics of ALS-associated mutant KIF5A including increased binding to MTs, axonal growth cone accumulation, altered MT dynamics, and an increased frequency of movements upon MT binding. Missense mutations in the KIF21B gene result in neurodevelopmental delays and brain malformations. Pathogenic mutations within a region of the second coiled-coil domain regulate autoinhibition through the intramolecular binding to the motor domain (van Riel et al., 2017). Mutations in KIF21B relieve autoinhibition enhancing binding to MTs and motor activity resulting in impaired neuronal migration (Asselin et al., 2020). Numerous mutations in KIF1A are associated with various neuronal diseases and intellectual disabilities. At least 10 point mutations in KIF1A lead to hereditary spastic paraplegia and, in general, are thought to inhibit motor activity. Chiba et al. (2019) demonstrated that a subset of mutations results in hyperactive KIF1A, resulting in overactive transport of synaptic vesicle precursors (Chiba et al., 2019). The kinesin KIF22 contributes to the alignment of the chromosome during mitosis. Heterozygous mutations in KIF22 result in spondyloepimetaphyseal dysplasia with joint laxity, leptodactylic type (Boyden et al., 2011; Min et al., 2011). Pathogenic mutations in KIF22, observed in two adjacent amino acids in the motor domain or a single amino acid within the coiled-coil domain, disrupt chromosome segregation in anaphase. Expression of a constitutively active KIF22 displays similar properties, suggesting that these mutations attenuate the autoinhibition of KIF22. There is also suggestive evidence that mutations in KIF7 that relieve autoinhibition may contribute to human disease (Blasius et al., 2021). Taken together, mutations that attenuate or abolish the autoinhibition may represent a converging mechanism of pathogenesis for kinesin-associated diseases.

Limitations of the study

It should be noted that several of the experiments leading to the conclusion that ALS-related mutations in KIF5A attenuate autoinhibition and alter protein/RNA binding are based on the overexpression of mutant KIF5A within cell lines. Overexpression systems do have their shortcomings, although in some cases they are necessary to recapitulate a disease phenotype within the general limitations of experiments. Nonetheless, they do not necessarily reflect the true cellular environment with patients carrying KIF5A mutations. Here, we have supplemented our investigation with the development of isogenic iPSC lines harboring a KIF5A mutations. However, our investigation did not directly address whether several of the aberrant KIF5A functions observed in our cellular in vitro overexpression system are recapitulated within the mutant iMN lines. Further studies will be focused toward accomplishing this goal.

V. Methods

Immortalized and primary cell culture

SKNAS human neuroblastoma cells (ATCC) were maintained at 37C with 5% CO_2 in Dulbecco's modified Eagle's medium (DMEM, Invitrogen) supplemented with 10% (v/v) heat-inactivated fetal bovine serum (FBS) (MediaTech), 2 mM L-glutamine (Gibco) and 1% (v/v) penicillin and streptomycin solution (Gibco). COS-7 cells (ATCC, CRL-1651) were maintained in DMEM supplemented with 10% (v/v) FBS and 2 mM glutamax (GIBCO). N2A cells (ATCC) and HEK293FT cells were maintained at 37°C with 5% CO_2 in standard growth media DMEM (Sigma) supplemented with 10% (v/v) FBS (Corning) and 1% (v/v) penicillin and streptomycin solution (Fisher). All biological replicates were done on cells from the same passage and N2A cells were discarded after passage 30. For differentiation, N2A cells were maintained in differentiation media: DMEM supplemented with 1% FBS, 10 µm all trans Retinoic Acid (Sigma), and 1% (v/v) penicillin and streptomycin solution (Fisher). Primary mouse cortical neurons (E14–16) were isolated from C57BL/6 mice and cultured as described previously (Giampetruzzi et al., 2019). Briefly, primary cortical neurons were plated on poly-D-lysine (0.125 mg/mL, Sigma-Aldrich P7280–5X5MG) and natural mouse laminin

(5mg/mL, Corning 354232) coated 384-well plates at 300,000 cells/mL and grown at 37C and 5% CO_2 in Neurobasal medium (Gibco 12348–017) supplemented with 2% B27 (Gibco 17504–044) and 1% Glutamax (Gibco 35050061). PMNs from C57BL/6 mice were isolated and cultured as described previously(Fallini et al., 2010). Briefly, PMNs (E12.5) from C57BL/6 mice were plated on poly-D-L-Ornithine (Sigma) coated coverslips that were painted with laminin (Invitrogen) right before plating. Cells were grown at 37°C and 5% CO_2 in MN media (Neurobasal, 0.5 mM Glutamax, 2% horse serum, 2% B27, 10 ng/mL BDNF, CNTF, and GDNF, 0.04% β-mercaptoethanol) until the day of the experiment. All animal experiments were conducted in accordance with the guidelines of the Institutional Animal Care and Use Committee (IACUC) at UMASS Medical School (Protocol #PROTO201900275). Embryos from pregnant adult female mice were used for these experiments.

IPS cell culture and differentiation

iPSCs were maintained and differentiated into motor neurons using induction protocols described in a methods paper previously (Fernandopulle et al., 2018) with a few modifications. First the cells were replated after induction at lower densities than described, approximately 52,000/cm^2. Second, the induced cells were replated on a 1:1 mixture of 1X PDL:PLO, the latter being diluted from the described 10x stock in ultrapure water (Invitrogen). Third, the incubation in IM media + BrdU was extended to 72 h. Finally, the MN media was made with the Neurobasal Plus system components (Invitrogen) and was refreshed every 2–3 days with ½ volume media changes until the day of the experiment. The iPSC lines harboring the $KIF5A^{R1007K}$ heterozygous mutation were CRISPR engineered from the ASE9109 line (Isogenic control) by Applied Stem Cell (Milpitas, California). All iPSC lines used were confirmed to have a normal karyotype (Quest Diagnostics) prior to making inducible lines.

Creation and characterization of KIF5A NIL iPSC lines

The CYBL1 targeting NIL cassette used to create the inducible cell lines (a gift of Dr. Ward) (Fernandopulle et al., 2018) had been modified to contain a blasticidin selection marker. To transfect the cassette into IPS cells, the cells were grown to 80% confluency before dissociating them to single cells with accutase and plating 50,000 cells into a Matrigel (Corning) coated wells of a 24-well plate (one well for each line made)

in Stemflex media (Invitrogen) + 10uM ROCK inhibitor (RI, Selleck Chemicals). The next day, the media was refreshed and the cells were incubated at 37°C for 1h before transfection. The RNP complex solution was made by mixing the following per well to be transfected: 3 µl of 1 µM sgRNA (Synthego, ATGTTGGAAGGATGAGGAAA) + 3 µl of 1 µM Hifi Cas9 (IDT) + 19 µl of OptiMEM1 (Invitrogen) and incubating at RT for 5 min. After the incubation, 500 ng of the NIL cassette construct was added to the RNP complex solution and mixed by pipetting. In a second tube, 25 µL of OptiMEM1 (Invitrogen) + 1 µl Lipofectamine STEM (Invitrogen) was mixed by flicking the tube. The contents of the latter tube were added to the former tube, mixed by flicking the tube, and incubated at RT for 10 min. During the incubation, the Stemflex + RI media was removed from the wells and replaced with 0.5 mL of OptiMEM1+ RI. After the incubation, 50 ul of the transfection mix was added to each well to incubate at 37°C for 4 h until 0.5 mL of Stemflex media (Invitrogen) was added. At 1 day post-transfection (dpt) the cells were dissociated to single cells with accutase and plated in 3 wells of 6 well Matrigel-coated plate in 50% serial dilution series in Stemflex + RI. At 2 dpt, the Stemflex media (Invitrogen) was replaced with media containing 25ug/mL blasticidin (RPI international) to select for positive transductants. The selection media was refreshed every two days until the remaining cells established colonies. Blasticidin-resistant colonies were scored for the percentage of mApple + transformants present. Colonies that were ≥90% mApple+ were selected for expansion and further validation. DNA was collected from IPS cells using a 15% Chelex w/v (Sigma) in 10 mM Tris, 0.1 mM EDTA, pH 8.0 and heated at 100°C for 20 min. NIL-IPS lines were validated for integration of the NIL cassette as described previously(Fernandopulle et al., 2018), using AmpliTaq Gold 360 master mix (Thermo Fisher Scientific) and an annealing temperature of 55°C. Stem cell identity of the NIL lines was confirmed by immunofluorescence staining of the pluripotency markers Oct4 and Sox2 (see below) and normal Karyotype was confirmed thorough diagnostic testing (Quest Diagnostics).

Plasmids used for this study

The KIF5A^{WT}, KIF5A$^{\Delta Exon27}$, and KIF5A$^{\Delta C\text{-}term}$ constructs in the N-terminal GFP tagging plasmid, peGFP-C1, were used to make the other tagged versions of KIF5A. In each case, the GFP tag was removed and the V5 or HA tag was inserted via Gibson assembly. The pMyc-MOV10 plasmid was acquired from Addgene (#10977). The Myc-tagged UPF1 construct was made in a 2-step Hifi Assembly process. First, MOV10 was

removed from the aforementioned plasmid with SalI/NotI digest. Using the UPF1-GFP construct (Addgene, 17708) the UPF1 gene + 20 bp overhangs homologous to the digested pMyc plasmid were PCR amplified. The UPF1 PCR product was inserted into the pMyc plasmid using the Hifi Assembly kit (New England Biolabs) following the manufacturer's instructions. To correct a deletion of a GC-rich region in the N-terminal portion of UPF1 created by the PCR amplification, a second round of Hifi Assembly was done. The intermediate construct was digested with SalI to remove the mutated N-terminal portion of the gene and a gblock with the correct sequence was constructed (IDT) and inserted into the digested construct using a Hifi Assembly kit (New England Biolab). Myc-p62 was created by subcloning the p62 gene from a p62-HA construct (Addgene, 28027) into the pMyc plasmid. A SalI and NotI restriction site were PCR amplified onto the N- and C-terminus, respectively, of the p62 gene and then subcloned into a SalI/NotI digested pMyc plasmid backbone. All constructs were confirmed through sequencing and prepped with a Maxi prep kit (Qiagen) following the manufacturer's instructions. To generate pCDNA3.1 N-terminal GFP -tagged KIF5A constructs for N2A experiments, eGFP was first cloned by PCR and ligated into Nhe1/BamH1 sites. Subsequently, the CDS of human KIF5A was cloned from pWBC (Addgene clone #15239) and ligated in frame with eGFP into the BAMH1/Xba1 sites. To make N-terminal HA-tagged KIF5A^{WT}, KIF5A$^{\Delta Exon27}$, and KIF5A$^{\Delta C\text{-}term}$, HA sequence was added by inclusion into the forward primer for KIF5A variants by PCR and this sequence was ligated into the Nhe1/BamH1 sites of pCDNA 3.1 (+). A flexible linker (GGSGx2) was added to all constructs by addition to the forward primer for the KIF5A CDS. All constructs were sequenced and prepped with Invitrogen PureLink HiPure Plasmid Midiprep Kit. To generate Myc- and Halo-tagged KIF5A constructs, a C-terminal Halo tag was first cloned by PCR and ligated into HindIII/ AflII sites in the pRK5:Myc-KIF5A vector (Addgene clone #127616). The KIF5A^{WT}, KIF5A$^{\Delta Exon27}$, and KIF5A$^{\Delta C\text{-}term}$, and KIF5A^{K560} sequences were then subcloned into the pRK5 vector using EcoNI/AflII sites.

KIF5A survival experiments

On DIV5, immediately prior to transfection, all the conditioned neurobasal medium was removed, saved, and replaced with 25µL pre-warmed OptiMEM serum-free media (Invitrogen 11058021). Transfection was done with 0.05% Lipofectamine 2000 (Invitrogen 11668019) and 28 ng DNA for 3.5 h at 37°C. A ratio of 7:1 was used for KIF5A and tdTomato vectors. After incubation, cells were washed once with pre-warmed

neurobasal medium and a 1:3 mix of conditioned to fresh complete medium was added. Cells were imaged using the BioTek Cytation 5 multi-mode plate reader every 24 h. The plate was incubated at 37°C and 5% CO_2 between imaging runs with the BioTek BioSpa automated incubator. For the survival analysis, images were exported from the Cytostation 5 and aligned using Image J. Analysis was performed using custom python scripts and machine learning libraries from TensorFlow and Keras. Two different convolutional neural networks (CNN) were trained to perform the survival analysis. Cortical neurons were detected at the first timepoint using the YOLOv2 algorithm which was trained to identify primary cortical neurons. The health of the identified cells was examined at all other timepoints using DenseNet201 which was trained to classify cells as alive or dead. The results from the CNN analysis were exported to a CSV file and processed using R stats. All analysis was performed using Google Collaboratory.

Immunofluorescence

For KIF5A localization in SKNAS cells were grown to 75% confluency then media was removed and replaced with fresh media. After an 1 h incubation at 37°C, the cells were transfected with Lipofectamine 2000 (Invitrogen) using a DNA:Lipo ratio of 3 µg:8 ul per 6 well according to the manufacturer's instructions. Twenty-four hours after transfection, the cells were fixed in 4% PFA for 15 min at RT then gently rinsed with 1X PBS. After removing the PBS, the coverslips were blocked in PBSAT (1X PBS+ 1% BSA+ 0.5% Triton X-100) for at least 1hr. Subsequent antibody incubations on the coverslips were done for 1 h with the antibodies diluted in PBSAT. Between antibody incubations, the coverslips were washed with PBSAT. After the final antibody incubation, the coverslips were washed with PBSAT followed by 1X PBS. The coverslips were rinsed in water and mounted on slides using Prolong Gold + DAPI (Invitrogen). All steps were carried out at room temperature. For V5-tagged KIF5A localization experiments, 1:1000 mouse anti-V5 (Invitrogen) and 1:200 rabbit anti-β-tubulin (Cell Signaling, 9F3) antibody was used. Nucleocytoplasmic staining used the following antibodies: 1:200 rabbit anti-RBM24 (Thermo Fisher) and 1:200 rabbit anti-RAN (Bethyl Labs) antibody. IPS and I^3 MN were stained using the same method as the SKNAS cells with the following markers: 1:1000 mouse anti-Sox2 (R&D Systems), 1:1000 mouse anti-Oct4 (R&D Systems) and 1:500 mouse anti-Islet1/2 (Developmental Studies Hybridoma Bank). For I^3 maturity marker staining, the following primaries were incubated overnight at 4°C: 1:200 goat anti-ChAT (Millipore), and 1:2000 rabbit anti-MAP2.

All other primary antibodies were incubated with the cells for 1 h at RT. Host matched secondary antibodies (Jackson Immunoresearch) were diluted 1:1000 in PBSAT (1X PBS +1% BSA + 0.5% Triton X-100) and incubated for 1 h at room temperature. Cy5-conjugated Tuj1 (Biolegend) was applied to I^3 neurons at 1:400 for 1 h at ambient temperature following secondary antibody incubations. Cells were mounted in ProLong Gold anti-fade reagent with DAPI (Invitrogen).

For KIF5A localization in N2A cells, they were plated at a density of 4.5 x 10^5 cells in 35 mm dishes 24 h before transfection using Lipofectamine 3000 (Invitrogen) per manufacturer instructions. 2.5 micrograms of DNA was used for all experiments and for cotransfection of GFP-KIF5A^{WT} along with HA-KIF5A variants a 1:1 ratio was used. At 24 h after transfection, the cells were trypsinized and replated on Poly D-Lysine (Sigma) coated glass coverslips at a density of 1.5 x 10^5 cells in a 35 mm dish. The cells were grown in standard growth media for 24 h and differentiation was performed by switching the media to differentiation media for an additional 48 h. Cells were fixed in 4% Formaldehyde diluted in 1X PBS for 10 min at RT. Cell were blocked using 1% BSA in 1X TBS with 0.1% Triton X-100 for 1 h at RT. HA staining was performed using mouse monoclonal HA antibody CA 215 for 1 h at RT and anti-mouse secondary antibodies for 1 h at RT: for expression alone FITC (Jackson) and for co-expression experiments TRITC (Jackson). Coverslips were mounted onto a glass slide using mounting media (Calbiochem Mowiol Reagent added to Glycerol and diluted in PBS). For KIF5A localization staining in PMNs, DIV2 PMNs were transfected with HA-KIF5A plasmids and TdTomato plasmid using 1.75 µL NeuroMag reagent (OZ Biosciences) + 0.5 µg DNA. Complete growth medium was replaced with serum-free neurobasal medium 1 h prior and removed 1 h after transfection. At DIV6 cells were fixed with 4% PFA Fixed motor neurons were treated with hot 10 mM citrate buffer, pH 6 for 20 min before permeabilization with 0.25% Triton X-100 for 10 min. Cells were blocked with 5% BSA for 40 min and hybridized with the appropriate antibodies overnight at 4°C. Anti-mouse (Jackson, 488) and anti-rabbit (Jackson, 647) secondary antibodies were hybridized for 1 h at room temperature. Coverslips were mounted onto a glass slide using Prolong Gold mounting medium (Thermo Fisher).

KIF5A localization in SKNAS cells

Cells were imaged in stacks with a 0.3 mm step size using a Leica DMI6000 widefield microscope with a 63x lens. For KIF5A MT association and plus-end accumulation, the percentage of transfected cells (V5 positive) with these characteristics were counted in a blinded fashion by two separate observers. KIF5A localization in PMNs: Cells were imaged using a Nikon TiE widefield microscope with a cooled CMOS camera (Andor Zyla) using a 320 lens. Immunofluorescence images were deconvolved using an adaptative blind deconvolution algorithm (Autoquant X3, Media Cybernetics) before analysis. To measure fluorescence intensities, the signals were thresholded and the resulting integrated densities were normalized on the area of the selected region (e.g., growth cone, nucleus). The axon was identified as the longest neurite processing from the neuron, with the growth cone determined by morphology at the axon terminal of the axon, using the TdTomato signal. Thresholds were kept consistent for all images within experiments. For all experiments, values were normalized to HA-KIF5A^{WT}. KIF5A localization in N2A cells: Cells were imaged using a Nikon Eclipse Ti widefield microscope with an X-Cite LED1 light source and Photometrics Prism 95B camera. Images were taken the 40X lens at 1.5X magnification with stacks at a 0.3 µm step size. Exposure was kept consistent for all images within experiments. Analysis was performed in blinded fashion. FIJI was used to generate maximum intensity projections and plot profile analysis was performed as previously described (Lu et al., 2018, 2020). In brief, a segmented line (width 1) was drawn from the edge of the cell nucleus to the tip of the longest neurite and the plot profile command was entered. The data output containing mean gray value along various distances along the line is saved. A MATLAB script was used to normalize the distance from minimum 0 to maximum of 100 and intensity from minimum 0 to maximum 1 and is available upon request. Sub-analysis was performed by stratifying the data 0–50 (soma and proximal neurite), 51–100 (distal neurite) followed by identifying the maximum normalized intensity in each of these 2 segments using the max function. N:C ratio analysis: Cells were imaged using a 63x lens on a Leica DMI6000 widefield microscope. Cells were imaged in a stack with a 0.3 µm step size through the entire cell. Sum projections of the stacks were created and a 20 × 20-pixel ROI was used to capture mean intensity measurements. One ROI was placed in the center of the nucleus avoiding nucleoli (nuclear mean), one was placed in the cytoplasm adjacent to the nucleus (cytoplasmic mean), and one was

placed in a region of the field of view that lacked cells (for background subtraction). DAPI and Tuj1 staining was used to define the nuclear and cell body borders, respectively. The mean intensity of the background ROI was subtracted from the nuclear and cytoplasmic ROIs then a ratio of nuclear/cytoplasmic mean intensity was calculated.

Single-molecule KIF5A assay

Cells were transiently transfected with Fugene 6 (Roche) according to the manufacturer's instructions and harvested 20–24 h post-transfection. COS-7 cells expressing Halo-tagged KIF5A constructs were labeled with 2.5 µM TMR-Halo ligand (Promega) for 15 min in the culture medium. Cells were then washed 2x with Ca2+- and Mg2+-free Dulbecco PBS (GIBCO), returned to the culture medium, and left in the incubator for 30 min. The cells were then washed 2x with PBS, collected in PBS, and centrifuged at 5,000 x g for 5 min. The resulting cell pellet was resuspended in a solution containing 40 mM HEPES, 1 mM EDTA, 120 mM NaCl, 0.1% Triton X-100, 1 mM DTT, and 1 mM magnesium ATP (pH 7.4) supplemented with protease inhibitors (1 mM PMSF, 0.001 mg/mL pepstatin A, 0.01 mg/mL leupeptin, and 0.01 mg/mL Nα-p-tosyl-L-arginine methyl ester) and left on ice for 10 min. The lysate was then clarified at 17,000 × g at 4°C for 10 min. MT seeds were made by combining unlabeled tubulin with HiLyte488-labeled tubulin (Cytoskeleton) in BRB80 buffer (80 mM PIPES, 1 mM EGTA, and 1 mM $MgCl_2$ (pH 6.8)) at a 1:20 ratio of labeled to unlabeled tubulin and a final concentration of 50 µM. This tubulin mixture was clarified at 352,000 × g for 10 min at 4°C. The resulting supernatant was then incubated with 1 mM GMPCPP at 37°C for 30 min to polymerize and stabilize MTs. A mixture of soluble tubulin was prepared by combining a 1:20 ratio of unlabeled to HiLyte488-labeled tubulin as above. This tubulin mixture was clarified at 352,000 × g for 10 min at 4°C and left on ice. Flow chambers were constructed by attaching #1.5 glass coverslips (Warner) to glass slides (Fisher Scientific) with double-sided tape. Coverslips were cleaned via sonication in acetone, potassium hydroxide, and ethanol, plasma cleaned and silanized with PlusOne Repel-Silane (GE Healthcare) to reduce nonspecific binding. Flow chambers were first incubated with 0.5 µM rigor kinesin-1^{E236A} for 5 min, then washed and blocked with 5% Pluronic F-127 (Sigma) for 5 min. After blocking, a 1:200 dilution of GMPCPP-stabilized MTs was flowed into the chamber and allowed to incubate for 2 min. The chamber was then washed with P12 buffer (12 mM PIPES, 1 mM EGTA, 2 mM $MgCl_2$) to remove unbound

MTs. A final solution containing 1 mM Mg-ATP, 1 mM Mg-GTP, 10 μM soluble tubulin mixture, and 1:20 cell lysate in Dynamic Assay Buffer (P12, 0.3 mg/mL BSA, 0.3 mg/mL casein, 10 mM DTT, 15 mg/mL glucose, 0.05% methylcellulose) and an oxygen scavenging system (0.5 mg/mL glucose oxidase, 470 U/mL catalase; Sigma) was flowed into the chamber. The chamber was then moved to 37°C and allowed to thermally equilibrate for ~5 min before video acquisition. For each chamber, three to five videos lasting 3 min were acquired at 37°C. The KIF5A channel was acquired at 4 frames/second and the MT channel was acquired at 1 frame every 10 s. Imaging was performed on a Nikon Eclipse Ti Inverted Microscope equipped with an Ultraview Vox spinning disk TIRF system and 100 x 1.49 NA oil immersion objective (Nikon). Signals were collected using a Hamamatsu EMCCD C9100–13 camera, with a pixel size of 158 nm, controlled by Volocity software (PerkinElmer). Kymographs of the KIF5A channel were generated by plotting a segmented line along each MT at its maximum length using the Multi Kymograph macro in ImageJ. The plus-end of each MT was identified as the end with higher growth rates and catastrophe throughout the video. Kymographs were manually analyzed to determine the number of binding events and processive runs. Non-motile binding was defined as any particle that associates with the MT for at least 1 s (4 frames) and has a displacement of less than 4 pixels (632 nm). Processive motility was defined as any particle that associates with the MT for at least 1 s (4 frames) and displays unidirectional movement for a minimum of 4 pixels (632 nm). Each processive segment was analyzed as a separate run for particles that exhibited pauses of at least 1 s between processive movements.

Mitochondrial trafficking

Primary motor neurons (DIV2) were co-transfected using NeuroMag paramagnetic nanobeads (Oz Biosciences) with the dsRed-mito reporter (Clontech) and different untagged KIF5A constructs in a 1:2 ratio. Briefly, complete neuronal medium was removed 1hr prior to magnetofection and replaced with serum-free Neurobasal/B27 medium. 0.5mg plasmid DNA was added and incubated with 1.75 μl NeuroMag beads in 100μl minimum essential medium (MEM) for 15 min, then added drop wise to cultures. Cell plates were then placed on top of a magnetic plate (Oz Biosciences) for 15 min. After 1hr, complete Neurobasal medium was added back to cells. Twenty-four hours after transfection, cells were imaged using a widefield fluorescence microscope (Nikon) equipped with a 20x objective. Time lapses were acquired with a frame

rate of 1 frame/second for a duration of 2 min. Analysis of mitochondria movement was performed on a 100 mm proximal axonal fragment using the Image J plugin Mtrack J (Meijering et al., 2012).

Immunoprecipitations

For transfection of the IP constructs, SKNAS were handled as described under the immunofluorescence section. For co-transfections, the DNA amount was divided equally between the constructs. The constructs were allowed to express for 24 h before harvesting in DHL buffer(G. Singh et al., 2014) + protease inhibitors (Roche). The protein concentration of the lysates was determined by the Pierce BCA Protein Assay kit (Thermo Fisher) per the manufacturer's instructions. V5-antibody conjugated magnetic beads (MBL), were washed 3x with 1X PBS+0.1% Tween 20 (PBS-T) before combining it with lysate in a 1µL:2 µg ratio (ex. 100µl of beads for 200 µg of lysate). The IP was incubated overnight at 4°C before collecting the flow-through (FT) and washing the beads 3x with PBS-T. For immunoprecipitation confirmation proteins were eluted in 2X loading sample buffer (Boston Bio) by boiling. For mass spec identification of KIF5A binding partners, the proteins were eluted by incubating the beads twice in 30ul of soft elution buffer(Antrobus & Borner, 2011) for 10 min at 28°C in a thermomixer set to 1,000 rpm. Elution samples were sent to the UMASS Medical School Mass Spectrometry facility for preparation and mudpit analysis. To identify the RNA binding partners, 0.2 U/µL SUPERase In (Invitrogen) was added to DHL and PBS-T buffers before their use. During the final wash 10% of the bead/wash solution was set aside for QC analysis with input and FT samples. RNAs were isolated from the IP beads by incubation in DHL buffer + SUPERase In + 0.1% SDS + 0.3 µg/µL PCR grade Proteinase K (Fisher Scientific) for 30 min at 55°C in a thermomixer set to 300 rpm. The resulting supernatant was separated from the beads and the RNA extracted using Trizol reagent (ThermoFisher Scientific) according to the manufacturer's instructions. The final RNA sample was resuspended in 5ul of nuclease-free water and sent to the Yale Genomic Core, where 2 ng of each sample was used as input RNA for library construction and sequencing.

For the KIF5A interactions, V5- and HA-tagged KIF5A interactions were confirmed by immunoprecipitation as described above. For interaction of GFP-tagged KIF5A with HA-tagged KIF5A, transfection of HEK293FT cells was performed by calcium phosphate method. pCDNA 3.1 (+) GFP

KIF5A^{WT} was transfected either alone or in equal amounts with pCDNA 3.1 (+) HA-KIF5A^{WT}, HA-KIF5A$^{\Delta Exon27}$, or HA-LIC. Pulldown by GFP binder was performed as described previously(Lu et al., 2018). Briefly, HEK293FT cells were harvested 48 h post-transfection in 500µl of 10 mM Tris buffer, pH 7.4, containing 150 mM NaCl, 0.5 mM $MgCl_2$ and protease inhibitor cocktail. After homogenization, 1% Triton X-100 was added to the solution and was centrifuged at 5,000xg at 4°C. Soluble fractions were incubated for 4 h at 4°C along with 30µl single-chain GFP antibody conjugated Sepharose beads (Gift from Vladimir Gelfand Lab). Beads were washed in the same buffer as above, minus Triton X-100, and resuspended in 30–50µL Laemmli sample buffer. Samples were boiled for 5 min and subsequently analyzed by Western blotting.

Mass spec analysis

Immunoprecipitated elution samples were analyzed by LC-MS/MS at UMASS Mass Spectrophotometry Facility. Raw data was processed using Thermo Proteome Discoverer 2.1.1.21 (Thermo Fisher Scientific Inc.) pipeline. The database search was performed by Mascot Server 2.6.2 (Matrix Science Ltd) search engine using the following search parameters: Homo Sapiens Swiss-Prot database FASTA file (download 04/2019); trypsin digestion with 2 maximum missed cleavages; the precursor mass tolerance of 10 ppm for the monoisotopic mass, and the fragment mass tolerance of 0.05 Da; carbamidomethylation of cysteine specified as the fixed modification and peptide N-terminal acetylation, methionine oxidation, N-terminal glutamine to pyroglutamate conversion specified as a variable modifications. Peptide and protein validation and annotation was done in Scaffold 4.10.0 (Proteome Software Inc.) employing Peptide Prophet (Keller et al., 2002) and Protein Prophet (Nesvizhskii et al., 2003) algorithms. Peptides were filtered at a 1% FDR, while the protein identification threshold was set to greater than 99% probability and with a minimum of 2 identified peptides per protein. Normalized iBAQ (Schwanhäusser et al., 2011) values were assigned to identified proteins for the quantitative comparison. The mass spectrometry proteomics data have been deposited to the ProteomeXchange Consortium via the PRIDE (Perez-Riverol et al., 2022) partner repository with the dataset identifier PXD031012 and 10.6019/PXD031012. Pathway analysis was completed using Metascape (Zhou et al., 2019).

Differential gene expression and alternate splicing RNAseq analysis

RNA samples were extracted and sequenced on an Illumina HiSeq2000 instrument at the Yale Center for Genome Analysis. The sample sequences were checked for overall quality and possible adapter contamination using FastQC (available at https:// www.bioinformatics.babraham.ac.uk/projects/fastqc/) and MultiQC(Ewels et al., 2016) tools. The read length was 101 and 151 for KIF5A RNA-Seq and RIP-Seq data, respectively. FASTQ files were mapped to the GRCh38 genome using STAR aligner (2.7.0a) (Dobin et al., 2013) in two-pass mode with the splice aware option. In particular, -outSAMtype BAM SortedByCoordinate was used to produce sorted bam and –sdjbOverhang 100 for optimal splice junction overhang length. Read counts were computed for each transcript based on gencode version 33 annotation using HTSeq (Anders et al., 2015) tool in strand-specific mode. After generating HTSeq counts, Differential expression analysis was performed using the DESeq2 package to compare the gene expression profiles(Love et al., 2014). Further in the downstream analysis process, the transcripts with a sum of ≥20 reads in all samples were selected for further analysis to remove the transcript with low count reads from the study. To further process the RIP experiment, genes with ≥20 read counts were compared between experiments. Only those genes found overlapping between the experiments (in either or both of the samples) were further analyzed. The differential expression experiment between wild-type and mutant was performed using the Wald test to generate p values and Log2 fold changes. The STAR aligned RNA Sequence sample bam files were used to detect differential alternative splicing events with the Multivariate Analysis of Transcript Splicing (MATS) method (using rMATS version 4.0.2) with a threshold of FDR0.1. rMATS uses a hierarchical framework to model exon inclusion levels to detect differential splicing events(S. Shen et al., 2014). Pathway analysis was completed using Metascape (Zhou et al., 2019). Analysis of RNA-binding proteins binding sites with positional dependent functions was performed using rMAPS2 (Hwang et al., 2020) directly on the rMAPS2 webserver located at http://rmaps.cecsresearch.org/.

qPCR analysis

Total RNA was isolated from DIV15 iMNs using the Qiagen RNAeasy Mini KIT (74104). Using the High Capacity cDNA reverse transcription kit (Applied Biosystems, 436814), RNA was reverse transcribed. Quantitative real-time PCR was performed in the Bio Rad CFX384 Real Time System with C1000 Touch

Thermal Cycler using the TaqMan Fast Advanced Master Mix (ThermoFisher, 4444556) and TaqMan Gene Expression Assay KITS (FAM, Hs01028461_s1, Hs04194669_sH, Hs00259032_s1, Hs01115690_m1, Hs00388055_m1, Hs00956610_mH, Hs02786624_g1). For relative expression, ΔΔCq method was employed, using GAPDH as an internal control. For each differentiation, quantitative RT-PCR was measured in triplicate and the mean for each differentiation used for analysis. A two-way ANOVA followed by Sidak's multiple comparison test was performed to determine significance.

Western blotting

Western blot analyses were performed by running protein lysates 10% polyacrylamide gels or gradient gels Bio-Rad) as needed. Transfers onto nitrocellulose membranes (Bio-rad) were completed using a Trans-blot Turbo (BioRad) apparatus according to the manufactuer's instructions. Membranes were blocked in a 1:1 solution of blocking buffer (Licor) and 1X PBS-T (IX PBS+ 0.01% Tween) for at least 1hr on a rocker at room temperature. Primary antibodies were diluted in PBS-T and incubated with the membrane overnight at 4°C. After washing the membrane in PBS-T on the rocker at room temperature 3x for 5 min each, secondary antibodies were diluted in a 1:1 solution of blocking buffer + PBS-T and incubated with the membrane on a rocker for at least 1hr. The membrane was washed as before and imaged on the Odyssey Imager (Licor) according to the manufacturer's instructions. Primary antibodies were used as follows: 1:5,000 for mouse anti-V5 (Invitrogen), 1:1000 rabbit anti-V5 (Novus), and 1:1000 rabbit anti-HA (Sigma). Mouse anti-Hemagglutinin (HA) antibody (Invitrogen) and Rabbit anti-GFP antibody (Proteintech) were both used to probe GFP-pulldown lysate at 1:1000 dilution. Blots were visualized with an Odyssey Infrared Imager (LiCor, Model 9120). Capillary Western blot analyses were done using the WES system (Protein Simple) following the manufacturer's instructions. Protein samples were mixed with 5x FL mastermix, boiled, and loaded into the plate. Primary antibodies were used as follows: 1:5,000 for mouse anti-V5 (Invitrogen), 1:1,000 for mouse anti-Myc (Sigma), 1:60 for rabbit anti-pan-KIF5A (Genetex), 1:60 for rabbit anti-mutKIF5A (Genewiz). and 1:1,500 for rabbit anti-GAPDH (Novus Biologicals). For immunoblotting of GFP-binder pulldown equal amounts of lysate were diluted in Laemli buffer and loaded into handcast trisglycine-SDS gels. Separation was performed using the Idea Scientific Minislab. Wet transfers to nitrocellulose membrane was performed using classic wet tank transfer for 1hr (Biorad). All blocking and

antibody incubations were performed using 5% nonfat milk diluted in TBST. The membrane was blocked for 1 h at RT. Primary antibodies, 1:7,000 rabbit anti-GFP (Proteintech) and 1:1,000 mouse anti-HA CA-215 were incubated overnight at 4°C. Secondary antibody 1:5,000 goat anti mouse HRP (Jackson) or 1:5,000 goat anti rabbit HRP were incubated for 1 hr. Chemiluminescent detection was performed using Anvansta WesternBright quantum reagent and Licor Odyssey XF Imager. Structure modeling—I-TASSER was utilized to predict the structure of $KIF5A^{WT}$ and $KIF5A^{\Delta Exon27}$ and the strongest match was selected(Roy et al., 2010; J. Yang et al., 2015; Y. Zhang, 2008). All models were generated using PyMOL (Version 2.0, Schrodinger, LLC).

Quantification and statistical analysis

Statistical analyses were performed using GraphPad Prism (GraphPad v9, SanDiego, CA, USA) software. Samples were compared by Students t-test unless otherwise specified in the figure legends. The number of replicates and p values are described in the legends. For reference, * = $p < 0.05$; ** = $p < 0.01$; *** = $p < 0.001$; **** = $p < 0.0001$.

Table 4.1: Key Resources for Chapter 4

REAGENT or RESOURCE	SOURCE	IDENTIFIER
Antibodies		
V5 Tag Monoclonal Antibody	Invitrogen	Cat# R96025
Rabbit Anti-V5 Antibody	Novus	Cat# NB600-381
β-Tubulin (9F3) Rabbit mAb	Cell Signaling Technologies	Cat# 2128
Anti-c-Myc Antibody (Clone #9E10)	Sigma-Aldrich	Cat# M4439
Rabbit Anti-HA Antibody	Sigma-Aldrich	Cat# H6908
Anti-Tubulin Beta 3 (TUBB3) Antibody-Cy5 conjugated	Biolegend	Cat# 657406; RRID: AB_2563610
Anti-Isl ½ Antibody	Developmental Studies Hybridoma Bank	Cat# 39.4D5; RRID: AB_2314683
Anti AcetylCholine Transferase Antibody	Sigma-Aldrich	Cat# AB144P
MAP2 Polyclonal Antibody	Proteintech	Cat# 17490-1-AP
Human/Mouse/Rat Sox2 Antibody (Clone #245610)	R & D Systems	Cat# MAB2018
Human Oct4 Antibody (Clone #653108)	R & D Systems	Cat# MAB17591
Anti-Kif5A Antibody	Genetex	Cat# GTX113761; RRID: AB_2037309
RBM24 Polyclonal Antibody	Invitrogen	Cat# PA5-66881
Rabbit Anti-RAN Antibody	Bethyl Laboratories	Cat# A304-297A
Anti-mutKif5A Antibody	This paper, Genewiz	N/A
Anti-GAPDH Antibody	Novus Biologicals	Cat# NB300-327
Rabbit Anti-HA Tag Antibody	Sigma-Aldrich	Cat# H6908
Goat Anti-Horseradish Peroxidase Antibody	Jackson Immunoresearch	Cat# 123-165-021; RRID: AB_2338959
Donkey Anti-Mouse 488	Jackson Immunoresearch	RRID: AB_2340846
Donkey Anti-Rabbit IgG 647	Jackson Immunoresearch	RRID: AB_2492288
Donkey Anti-Rabbit IgG 594	Jackson Immunoresearch	RRID: AB_2340621
Donkey anti-Mouse 546	Invitrogen	Cat# A10036
Mouse anti-Hemagglutinin (HA) antibody (12CA5)	Invitrogen	Cat# MA1-12429; RRID: AB_1074049
Goat anti-Mouse FITC	Jackson Immunoresearch	Cat# 115-095-003; RRID: AB_2338589
Goat anti-Mouse TRITC	Jackson Immunoresearch	Cat#115-025-003; RRID: AB_2338478
Rabbit anti-GFP	Proteintech	Cat# 50430-2-AP
Goat anti-Mouse HRP	Jackson Immunoresearch	Cat# 115-035-003; RRID: AB_10015289
Goat anti-Rabbit HRP	Jackson Immunoresearch	Cat# 111-004-003; RRID: AB_2337913
Biological samples		
Patient Kif5A iPSC	Applied Stem Cell; This paper	N/A
Isogenic Control iPSC	Applied Stem Cell	ASE-9109
Chemicals, peptides, and recombinant proteins		
FuGENE6 transfection reagent	Promega	Cat# E269A
Tetramethylrhodamine (TMR) Halo ligand	Promega	Cat# G8251
Guanosine-5′-[(α,β)-methyleno] triphosphate, sodium salt (GMPCPP)	Jena Bioscience	Cat# NU-405

(*Continued on next page*)

Continued

REAGENT or RESOURCE	SOURCE	IDENTIFIER
Porcine brain tubulin	Cytoskeleton	Cat# T240
HiLyte488-labeled tubulin	Cytoskeleton	Cat# TL488M
Purified Rigor Kinesin	Masucci et al. (2021)	N/A
PlusOne Repel-Silane ES	Cytiva	Cat# 17133201
Pluronic F-127	Sigma-Aldrich	Cat# P2443
Methyl cellulose	Sigma-Aldrich	Cat# M0512
Adenosine 5′-triphosphate magnesium salt (ATP)	Sigma-Aldrich	Cat# A9187
Guanosine 5′-triphosphate sodium salt hydrate (GTP)	Sigma-Aldrich	Cat# G8877
0.05% Trypsin EDTA	Gibco	Cat# 25300054
Poly-D-Lysine	Sigma-Aldrich	Cat# P7280-5X5MG
Natural Mouse Laminin	Corning	Cat# 354232
Neurobasal Medium, Minus Phenol Red	Gibco	Cat# 12348–017
B27 Supplement	Gibco	Cat# 17504–044
Glutamax	Gibco	Cat# 35050061
Opti-MEM I Reduced Serum Medium, no phenol red	Gibco	Cat# 11058021
Lipofectamine 2000 Transfection Reagent	Invitrogen	Cat# 11668019
2-Mercaptoethanol, 99% pure	Fisher Scientific	Cat# AC125470100
Dulbecco's Modified Eagle Medium (DMEM)	Gibco	Cat# 11965118
Fetal Bovine Serum, Regular	MediaTech	Cat# 35-010-CV
L-glutamine (200 mM)	Gibco	Cat# 25030081
Penicillin/Streptomycin	Gibco	Cat# 15140122
NeuroMag Transfection Reagent	Oz Biosciences	Cat# NM50200
Minimum Essential Media (MEM)	Gibco	Cat# 11095098
BSA (heat shock fraction, protease free)	Sigma-Aldrich	Cat# A3294
Triton X-	Sigma-Aldrich	Cat# T9284
Antigen Retrieval Buffer	Abcam	Cat# 93678
Prolong Gold Antifade Mountant with DAPI	Invitrogen	Cat# P-36931
Hank's Balanced Salt Solution (HBSS)	Gibco	Cat# 14175095
SUPERaseIn RNase Inhibitor	Invitrogen	Cat# AM2694
TRIzol Reagent	Life Technologies	Cat# 15596026
Denaturing Hypotonic Lysis buffer (DHL)	Singh et al. (2014)	N/A
Alt-R S.p. HiFi Cas9 Nuclease v3	Integrated DNA Technologies	Cat# 1081060
Blasticidin S Hydrochloride Powder	Research Products International	Cat# B12200
Ultrapure DNase/RNase-Free Distilled Water	Invitrogen	Cat# 10977015
SalI Restriction Enzyme	New England Biolabs	Cat# R0138L
NotI Restriction Enzyme	New England Biolabs	Cat# R3198L
Proteinase K	Thermo Scientific	Cat# FEREO0491
Laemmli SDS-Sample Buffer	Boston BioProducts	Cat# BP-111R
'Soft Elution Buffer'	Antrobus and Borner (2011)	N/A
Dulbecco's Phosphate Buffered Saline	Corning	Cat# 20-031-CV
Tween 20	Fisher BioReagents	Cat# BP337-500
Dithiothrieitol Solution	Sigma-Aldrich	Cat# 43816
Trypsin-EDTA	Gibco	Cat# 15400054
Odyssey Blocking Buffer	Licor	Cat# 927–40010

(*Continued on next page*)

Continued

REAGENT or RESOURCE	SOURCE	IDENTIFIER
Dulbecco's Modified Eagle Medium	Sigma-Aldrich	Cat# D7777
Heat-Inactivated Fetal Bovine Serum	Corning	Cat# MT35011CV
All *trans* Retinoic Acid	Sigma-Aldrich	Cat# R2625
Lipofectamine 3000	Invitrogen	Cat# L3000015
Poly-DL-Lysine	Sigma-Aldrich	Cat# P9011
Formaldehyde	Fisher	Cat# BP531-500
BSA (lyophilized powder)	Sigma-Aldrich	Cat# A9418
Triton X-100	Sigma-Aldrich	Cat# X-100
Mowiol 4–88 Reagent	Calbiochem	Cat# 47-590-4100GM
Sepharose GFP-Binder Beads	Gift from Vladimir Gelfand Lab	N/A
Accutase Cell Detachment Solution	Corning	Cat# MT25058CI
Matrigel hESC-Qualified Matrix	Corning	Cat# 08-774-552
ROCK Inhibitor	Selleck Chemicals	Cat# S1049
Lipofectamine Stem Transfection Reagent	Invitrogen	Cat# STEM00001
Chelex 100 Sodium form	Sigma-Aldrich	Cat# C7901
Stemflex Medium	Gibco	Cat# A3349401
B27 Plus Neuronal Culture System	Gibco	Cat# A3653401
Poly D-L-Ornithine	Sigma	Cat# P3655 (3000–7000 kDa)
Laminin	Invitrogen	Cat# 23017–015
Neurobasal medium	Invitrogen	Cat# 21103–049
Glutamax 200mM	Invitrogen	Cat# 35050–061
B27	Invitrogen	Cat# 17504–044
hsBDNF	PeproTech	Cat# 450–02
rnCNTF	PeproTech	Cat# 450–50
mmGDNF	PeproTech	Cat# 450–44
Horse Serum	Sigma	Cat# H1138-100ML
BSA	Gold Biotechnology	Cat# A-421-50
4–20% Mini-PROTEAN® TGX™ Gel, 15 well, 15 μL	Bio-Rad	Cat# 456–1096
Nitrocellulose membrane/filter paper pack, pkg of 50	Bo-Rad	Cat# 1620213
Protease inhibitor tables	Roche	Cat# 11873580001
NeuroMag paramagnetic beads	Oz Biosciences	Cat# NM50200
Magnetic plate	Oz Biosciences	Cat# MF10000
Critical commercial assays		
Pierce BCA Protein Assay Kit	ThermoFisher Scientific	Cat# 23227
AmpliTaq Gold 360 Master Mix	Applied Biosystems	Cat# 4398876
High Capacity cDNA Reverse Transcription Kit	Applied Biosystems	Cat# 436814
TaqMan Fast Advanced Master Mix	Applied Biosystems	Cat# 4444556
Taqman Gene Expression Assay, SLITRK2	ThermoFisher Scientific	Hs01028461_s1
Taqman Gene Expression Assay, TCEAL2	ThermoFisher Scientific	Hs04194669_sH
Taqman Gene Expression Assay, PCDHA13	ThermoFisher Scientific	Hs00259032_s1
Taqman Gene Expression Assay, HNRNPM	ThermoFisher Scientific	Hs01115690_m1
Taqman Gene Expression Assay, DNAJA4	ThermoFisher Scientific	Hs00388055_m1
Taqman Gene Expression Assay, ELAVL4	ThermoFisher Scientific	Hs00956610_mH
Taqman Gene Expression Assay, GAPDH	ThermoFisher Scientific	Hs02786624_g1

(*Continued on next page*)

Continued

REAGENT or RESOURCE	SOURCE	IDENTIFIER
NEBuilder HiFi DNA Assembly Cloning Kit	New England Biolabs	Cat# E5520S
HiSpeed Plasmid Midi Kit	Qiagen	Cat# 12662
PureLink HiPure Plasmid Midiprep Kit	Invitrogen	Cat# K210005
Deposited data		
Sequence data, analyses, and resources related to the RIPseq of V5-KIF5AΔ and V5-KIF5A$^{\Delta Exon27}$ immunoprecipitation eluates	This paper	Gene Expression Omnibus GSE196539
Sequence data, analyses, and resources related to the RNA sequencing of KIF5A^{R1007K} and isogenic control iMNs	This paper	Gene Expression Omnibus GSE196539
Sequence data, analyses and resources related to the mass spectrometry analysis of V5-KIF5A^{WT} and V5-KIF5A$^{\Delta Exon27}$ immunoprecipitation eluates	This paper	ProteomeXchange; PXD031012
Experimental models: Cell lines		
COS-7	ATCC	CRL-1651; RRID:CVCL_0224
SKNAS	ATCC	CRL-2137; RRID:CVCL_1700
HEK293FT	Invitrogen	R70007
Neuro2A	ATCC	CCL-131; RRID:CVCL_0470
Experimental models: Organisms/strains		
C57BL/6 female mice (primary neuron preps)	Charles River Laboratories	Cat# 027
Oligonucleotides		
sgRNA targeting CYBL locus – ATGTTGGAAGGATGAGGAAA	Fernandopulle et al. (2018)	N/A
Primer for HA-KIF5A Forward – ACTGACGCTAGCCACCATGTACCCA TACGATGTTCCAGATTACGCTGGTG GTTCTGGTGGTGGTTCTGGTATGGC GGAGACCAACAACG	This Paper	N/A
Primer for HA-KIF5A WT Reverse – AGAATCGGATCCTGTGGGAGAT TAGCTGGCTG	This Paper	N/A
Primer for HA-KIF5A Del27 Reverse – AGATACGGATCCCGAAGTTATGG TACCTTAGAAACTGA	This Paper	N/A
Primer for HA-KIF5A C-Term Reverse – AGAATCGGATCCTTATCCATTGTCCAT GTTGGCCTT	This Paper	N/A
Primer for eGFP Forward – AGTCAGGCTAGCCACCATGGTGA GCAAGGGAGAGGAG	This Paper	N/A
Primer for eGFP Reverse – AGATACGGATCCCTTGTACAGCT CGTCCATGCC	This Paper	N/A
Primer for GFP-KIF5A Forward – AGTCAGGGATCCGGTGGTTC TGGTGGTGGTTCTGGTATGG CGGAGACCAACAACG	This Paper	N/A
Primer for GFP-KIF5A WT Reverse – AGATACTCTAGATGTGGGAGATT AGCTGGCTG	This Paper	N/A

(*Continued on next page*)

Continued

REAGENT or RESOURCE	SOURCE	IDENTIFIER
Recombinant DNA		
DsRed-Mito	Takara Bio	Cat# 632421
pRK5:Myc-KIF5A	Addgene	Clone# 127616
pRK5-Myc-KIF5AWT-Halo	This paper	N/A
pRK5-Myc- KIF5AΔExon27-Halo	This paper	N/A
pRK5-Myc-KIF5AΔC-term-Halo	This paper	N/A
pRK5-Myc-KIF5A1-560-Halo	This paper	N/A
pcDNA4TO-K560-E236A-24xGCN4_v1-IRES-Puro	Tanenbaum et al. (2014)	Addgene Clone #60909
pGW1-Kif5AWT	This paper	N/A
pGW1-Kif5AΔExon27	This paper	N/A
pGW1-Kif5AΔC-term	This paper	N/A
pGW1-tdTomato	This paper	N/A
V5-Kif5AΔExon27	This paper	Addgene Clone #15239
V5-Kif5AWT	This paper	Addgene Clone #15239
GFP-Kif5AWT	This paper	Addgene Clone #15239
HA-Kif5AWT	This paper	Addgene Clone #15239
Kif5AΔExon27	This paper	N/A
pCMV-beta-Rat Lic1.FL-HA	Tynan et al. (2000)	N/A
pMyc-MOV10	Addgene	Cat# 10977
RNT1-GFP	Addgene	Cat# 17708
HA-p62	Addgene	Cat# 28027
pCDNA 3.1 (+) HA- KIF5A WT	This Paper	N/A
pCDNA 3.1 (+) HA- KIF5A Del27	This Paper	N/A
pCDNA 3.1 (+) HA- KIF5A C-Term	This Paper	N/A
pCDNA 3.1 (+) GFP-KIF5A WT	This Paper	N/A
pCDNA 3.1 (+) GFP- KIF5A Del27	This Paper	N/A
Software and algorithms		
FastQC	Babraham Institute	http://www.bioinformatics.babraham.ac.uk/projects/fastqc/
MultiQC	Ewels et al. (2016)	https://github.com/ewels/MultiQC
STAR aligner (2.7.0a)	Dobin et al. (2013)	https://github.com/alexdobin/STAR
HTSeq	Anders et al. (2015)	https://htseq.readthedocs.io/en/master/overview.html
DESeq2	Love et al. (2014)	https://bioconductor.org/packages/release/bioc/html/DESeq2.html
rMATS version 4.0.2	Shen et al. (2014)	http://rnaseq-mats.sourceforge.net/
Metascape	Zhou et al. (2019)	https://metascape.org/gp/index.html#/main/step1
rMAPS2	Hwang et al. (2020)	http://rmaps.cecsresearch.org/
ImageJ	NIH	https://imagej.nih.gov/ij/
MTrackJ	NIH	https://imagescience.org/meijering/software/mtrackj/
Volocity	PerkinElmer	https://www.perkinelmer.com
Prism 9	GraphPad	https://www.graphpad.com/scientific-software/prism
Survival Analysis YOLO	This paper	https://drive.google.com/drive/folders/1V36q_9QjX_0SHbLS_IN2PPngOSLKYS1_?usp=sharing

(*Continued on next page*)

Continued

REAGENT or RESOURCE	SOURCE	IDENTIFIER
Biorender	Biorender	https://www.biorender.com
AutoQuant x3	Media Cybernetics	https://www.mediacy.com/79-products/autoquant-x3
Proteome Discoverer 2.1.1.21	Thermo Scientific	https://www.thermofisher.com/us/en/home/industrial/mass-spectrometry/liquid-chromatography-mass-spectrometry-lc-ms/lc-ms-software/multi-omics-data-analysis/proteome-discoverer-software.html
Mascot Server 2.6.2	Matrix Science Ltd.	http://www.matrixscience.com/
Scaffold 4.10.0	Proteome Software, Inc.	https://www.proteomesoftware.com/products/scaffold-5
Peptide Prophet	Keller et al. (2002); Nesvizhskii et al. (2003)	http://peptideprophet.sourceforge.net/
PyMOL	The PyMOL Molecular Graphics System, Version 2.0 Schrödinger, LLC	https://pymol.org/2/
I-TASSER	Yang et al. (2015)	https://zhanggroup.org/I-TASSER/
Other		
Cytation 5 Cell Imaging Multi Mode Reader	Agilent (BioTek)	https://www.biotek.com/products/imaging-microscopy-cell-imaging-multi-mode-readers/cytation-5-cell-imaging-multi-mode-reader/
BioSpa 8 Automated Incubator	Agilent (BioTek)	https://www.biotek.com/products/software-robotics-robotics/biospa-8-automated-incubator/
Nikon Ti Eclipse	Nikon	Ti Eclipse
Leica DMI6000 Widefield Microscope	Leica Microsystems	DMI6000
Anti-V5 Tagged Magnetic Beads	MBL International	Cat#M167-11
CFX 384 Real-Time PCR Detection System	BioRad	https://www.bio-rad.com/en-us/product/cfx384-touch-real-time-pcr-detection-system?ID=LJB22YE8Z
C1000 Touch Thermal Cycler	BioRad	https://www.bio-rad.com/en-us/sku/1851138-c1000-touch-thermal-cycler-with-384-well-reaction-module?ID=1851138
Trans-Blot Turbo Transfer System	BioRad	Cat# 1704150

CHAPTER 5: PGC-1α INTEGRATES INSULIN SIGNALING WITH MITOCHONDRIAL PHYSIOLOGY AND BEHAVIOR IN A *DROSOPHILA* MODEL OF FRAGLE X SYNDROME

This chapter is adapted from:

Weisz, ED; **Fenton, AR**; Jongens, TA. PGC-1α integrates insulin signaling with mitochondrial physiology and behavior in a *Drosophila* model of Fragile X Syndrome. *npj Metabolic Health and Disease*. 2, 2 (2024).

Contribution: ARF performed experimental procedures, data analysis, writing, and figure design related to mitochondria imaging experiments, ATP measurements, and NAD/NADH measurements in Fig. 5.1 and 5.2.

I. Summary

Fragile X Syndrome (FXS) is the most prevalent monogenetic form of intellectual disability and autism. Recently, dysregulation of insulin signaling (IS) and aberrations in mitochondrial function have emerged as robust, evolutionarily conserved components of FXS pathophysiology. However, the mechanisms by which altered IS and mitochondrial dysfunction impact behavior in the context of FXS remain elusive. Here, we show that normalization of IS improves mitochondrial volume and function in flies that lack expression of *dfmr1*, the *Drosophila* homolog of the causal gene of FXS in humans. Further, we demonstrate that dysregulation of IS underlies diminished expression of the mitochondrial master regulator PGC-1α/Spargel in *dfmr1* mutant flies. These results are behaviorally relevant, as we show that pan-neuronal augmentation of PGC-1α/Spargel improves circadian behavior in *dfmr1* mutants. Notably, we also show that modulation of PGC-1α/Spargel expression in wild-type flies phenocopies the *dfmr1* mutant circadian defect. Taken together, the results presented herein provide a mechanistic link between mitochondrial function and circadian behavior both in FXS pathogenesis as well as more broadly at the interface between metabolism and behavioral output.

II. Introduction

Fragile X Syndrome (FXS) is the most common monogenetic cause of intellectual disability and autism (Kaufmann et al., 2004, 2017). Affected individuals experience a variety of difficulties that generally preclude their ability to care for themselves and create many challenges for patients and caretakers alike (Bailey et al., 2010; Bardoni & Mandel, 2002; Chonchaiya et al., 2009; de Vries et al., 1998; Gould et al., 2000; Kidd et al., 2014). Currently, there is no cure for FXS. Rather, a better understanding of FXS pathogenesis is necessary to identify effective treatments that improve the capabilities and quality of life of FXS patients.

At the molecular level, FXS is caused by loss of function of the *FMR1* gene (Bell et al., 1991; Oberlé et al., 1991; Sutcliffe et al., 1992; Verkerk et al., 1991). The protein product of *FMR1*, termed FMRP, is an RNA binding protein. While FMRP was initially defined as a translational repressor, advancements in cell-type specific transcriptomic and proteomic approaches have enabled us to learn that FMRP can also promote the expression of many of its targets through multiple modes of gene regulation (Ashley et al., 1993; Darnell et al., 2011; Darnell & Klann, 2013; Laggerbauer et al., 2001; Z. Li et al., 2001; Richter & Zhao, 2021; Siomi et al., 1993).

Since the etiology of FXS is well characterized, researchers have been able to generate valuable preclinical disease models (Bakker & Oostra, 2003; Bardoni & Mandel, 2002; Bhogal & Jongens, 2010). With the advent of a wealth of genetic tools, *Drosophila melanogaster* has emerged as a highly tractable model for the study of FXS (Dockendorff et al., 2002; Inoue et al., 2002; Morales et al., 2002; Weisz et al., 2015; Y. Q. Zhang et al., 2001). The *Drosophila* genome encodes a single gene, *dfmr1*, that is the sole ortholog of the FMR protein family (Wan et al., 2000). The product of *dfmr1*, termed dFMRP, shares both sequence identity and biochemical properties with those of its mammalian ortholog(Wan et al., 2000). Importantly, flies that harbor loss-of-function mutations in the *dfmr1* gene recapitulate many characteristics of FXS. Specifically, *dfmr1* mutant flies have neuroanatomical defects as well as deficits in memory, social behavior, and circadian rhythms (Bolduc et al., 2008; Dockendorff et al., 2002; Inoue et al., 2002; McBride et al., 2005; Morales et al., 2002; A. Russo & DiAntonio, 2019; Tauber et al., 2011).

Studies in preclinical models of FXS have uncovered signaling molecules and pathways that are dysregulated in the disease state. Previously, we reported that several components of the insulin signaling (IS) pathway are elevated in the brains of *dfmr1* mutants (Monyak et al., 2017). These changes included increased levels of the major insulin-like peptide, elevated phosphoinositide 3-kinase (PI3K) activity, and accumulation of phosphorylated Akt at the plasma membrane (Monyak et al., 2017). Aberrant IS appears to be directly linked to behavioral and cognitive function, as genetic manipulations that reduced IS were sufficient to increase circadian rhythmicity and rescue memory deficits in our *Drosophila* FXS model (Monyak et al., 2017). Dysregulation of IS has also been identified as an evolutionarily conserved feature of FXS pathogenesis in murine and patient derived cell models (Callan et al., 2012; Gross, Chang, et al., 2015; Gross et al., 2010; Gross, Raj, et al., 2015; Gross & Bassell, 2014, 2012; Luhur et al., 2017; N. Raj et al., 2021). Moreover, a multitude of genetic and pharmacological approaches that normalize insulin signaling are sufficient to restore behavior and cognition in mammalian FXS models (Callan et al., 2012; Gross, Chang, et al., 2015; Gross et al., 2010; Gross, Raj, et al., 2015; Gross & Bassell, 2014, 2012; Luhur et al., 2017; Monyak et al., 2017). However, the mechanism by which altered IS impinges on behavioral and cognitive function in FXS remains elusive.

To better understand the mechanism by which dysregulation of IS impacts behavioral and cognitive outputs in the *dfmr1* mutants, we conducted an unbiased metabolomics analysis. Paradoxically, our metabolic studies revealed reduced levels of carbohydrate and lipid metabolites in the *dfmr1* mutants despite increased brain insulin signaling; hyperphagia; and normal body size and activity levels (Weisz et al., 2018). We also found a robust decrease in the redox ratio of the mitochondrial cofactor nicotinate adenine dinucleotide (NAD^+/NADH) and qualitative defects in mitochondrial ultrastructure(Weisz et al., 2018). In aggregate, these robust metabolic defects suggest that mitochondrial function is impaired in our *Drosophila* model of FXS.

The notion that mitochondrial dysfunction underlies behavioral and cognitive impairments in preclinical models of FXS is particularly compelling in light of recent studies that have implicated mitochondrial defects in the pathogenesis of intellectual disability related syndromes and autism (Valenti et

al., 2014; Wallace, 2011; Wallace et al., 2010). While the central nervous system (CNS) represents 2% of total body weight, it consumes around 20% of inspired oxygen at rest (Valenti et al., 2014). This high oxidative demand renders the CNS particularly sensitive to changes in mitochondrial metabolism (Valenti et al., 2014). Proper mitochondrial function is especially critical for the establishment of neuronal connectivity, neurogenesis, and synaptic plasticity (Mattson et al., 2008; Valenti et al., 2014).

In this study, we characterize alterations of mitochondrial morphology and function in *dfmr1* mutant flies and demonstrate the genetic reduction of insulin signaling is sufficient to alleviate these mitochondrial defects. Together, these findings suggest that restoration of mitochondrial function is a mechanism by which normalization of IS improves behavior and cognition in a preclinical model of FXS. Moreover, we present evidence that elevated IS underlies diminished expression of the mitochondrial master regulator, PGC-1α, in the heads of *dfmr1* mutants. We report that pan-neuronal augmentation of PGC-1α in *dfmr1* mutants is sufficient to restore circadian behavior. Beyond their translational relevance for the FXS field, our results indicate a novel role of PGC-1α in the regulation of circadian rhythmicity and thereby provide a mechanism by which metabolism and mitochondrial function inform behavioral output.

III. Results

Mitochondrial volume and function are diminished in the absence of dFMRP

Prompted by our previous discovery that mitochondria in the indirect flight muscle of *dfmr1* mutants appeared to be qualitatively smaller and irregularly shaped, we wanted to quantitatively examine mitochondrial morphology in behaviorally relevant tissues. To do so, we leveraged a genetically encoded chimeric GFP construct (*UAS-mitoGFP*) that allowed us to label mitochondria in specific subtypes of cells with the binary Gal4/UAS system (Rizzuto et al., 1996). We were particularly interested in visualizing mitochondria in the insulin producing cells (IPCs) of the brain, because we previously found that constitutive expression of the *UAS-dfmr1* transgene under the control of a *dilp2-Gal4* driver that is specific to the 14

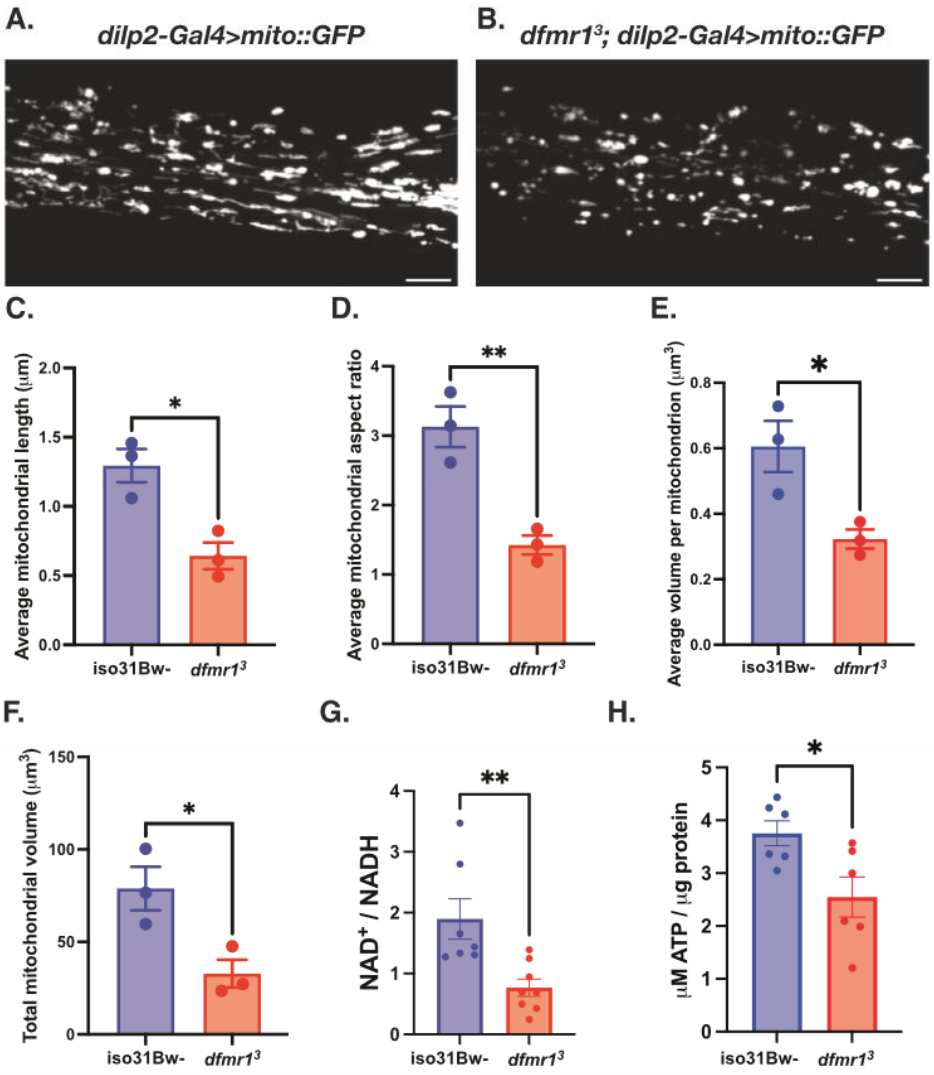

Figure 5.1: Mitochondrial volume and function are compromised in the absence of dFMRP. A-F, Mitochondria in the insulin producing cells (IPCs) of the brain were labeled by expressing a genetically encoded *UAS-mitoGFP* construct in conjunction with the *dilp2-Gal4* driver. Representative maximum-intensity projections of GFP-labeled mitochondria in the IPC processes of **(A)** *iso31Bw-* wild type and **(B)** *dfmr1* mutant flies. Scale bars: 5 μm. Images are oriented with the dorsal side on the left and the ventral side on the right. Quantification of **(C)** average mitochondrial length, **(D)** average mitochondrial aspect ratio, **(E)** average volume per mitochondrion, and **(F)** average total mitochondrial volume per brain. Sample number (N) per genotype= 3 brains. Unpaired t-tests indicated that the average length, aspect ratio, volume per mitochondrion, and total mitochondrial volume per brain were all significantly reduced in *dfmr1* mutants compared to *iso31Bw-* wild type controls. Values represent mean ± SEM. *p≤0.05, **p≤0.01. **G,** Quantification of the NAD^+/NADH ratio. Each sample contained 10 fly bodies. Sample number (N) per genotype: *iso31Bw-* = 7, *dfmr1*=8. An unpaired t-test indicated that the NAD^+/NADH ratio was significantly diminished in *dfmr1* mutants compared to *iso31Bw-* wild type controls (p=0.0059). Values represent mean ± SEM. **H,** Quantification of ATP levels relative to protein content. Each sample contained 5 fly bodies. Sample number (N) per genotype= 6. An unpaired t-test showed that ATP levels were significantly decreased in *dfmr1* mutants compared to *iso31Bw-* wild type controls (p=0.0224). Values represent mean ± SEM.

IPCs of the brain was sufficient to restore normal circadian behavior in *dfmr1* mutants (Monyak et al., 2017). Therefore, we expressed *the UAS-mitoGFP* transgene in conjunction with the *dilp2-Gal4* driver and used confocal microscopy to resolve GFP-labeled mitochondria in the IPC processes that extend ventrally through the brain. We observed that mitochondria in the IPCs of *dfmr1* mutants were shorter than controls, with decreased length and aspect ratio relative to *iso31Bw-* wild-type controls (Fig. 5.1A-D). Further, the average volume of individual mitochondria and total mitochondrial volume was decreased in *dfmr1* mutants' brains compared to controls (Fig. 5.1E-F). These findings match recent studies that revealed small mitochondria with decreased aspect ratios in the brains of $Fmr1^{-/y}$ mice during development and synaptic maturation (Licznerski et al., 2020; M. Shen et al., 2019).

Considering that mitochondrial network morphology and bioenergetic capacity are intimately intertwined, we next measured ATP levels in *dfmr1* mutants and wild type conspecifics as a direct physiologic readout of mitochondrial function. Consistent with the observed defects in mitochondrial morphology, we found that ATP levels were diminished in the *dfmr1* mutant flies compared to wild-type controls (Fig. 5.1H). Given that the ability of mitochondria to generate ATP is dependent on the redox state of the cofactor NAD^+, the diminution of ATP levels that we observed corresponds with our previous discovery (Weisz et al., 2018), which we have confirmed herein, that the NAD^+/NADH ratio is significantly decreased in *dfmr1* mutants (Fig. 5.1G). Our findings are also consistent with several reports of diminished cytosolic ATP levels in murine models of FXS (D'Antoni et al., 2020; Licznerski et al., 2020; M. Shen et al., 2019). Collectively, it appears that the mitochondria of *dfmr1* mutant flies are characterized by aberrant mitochondrial network morphology, decreased ATP levels, and a diminished NAD^+/NADH ratio.

Genetic reduction of insulin signaling ameliorates mitochondrial volume and function in dfmr1 mutants

Once we established that the dfmr1 mutants exhibit several robust hallmarks of mitochondrial dysfunction, we then sought to better understand the contribution of mitochondrial dysfunction to FXS pathophysiology.

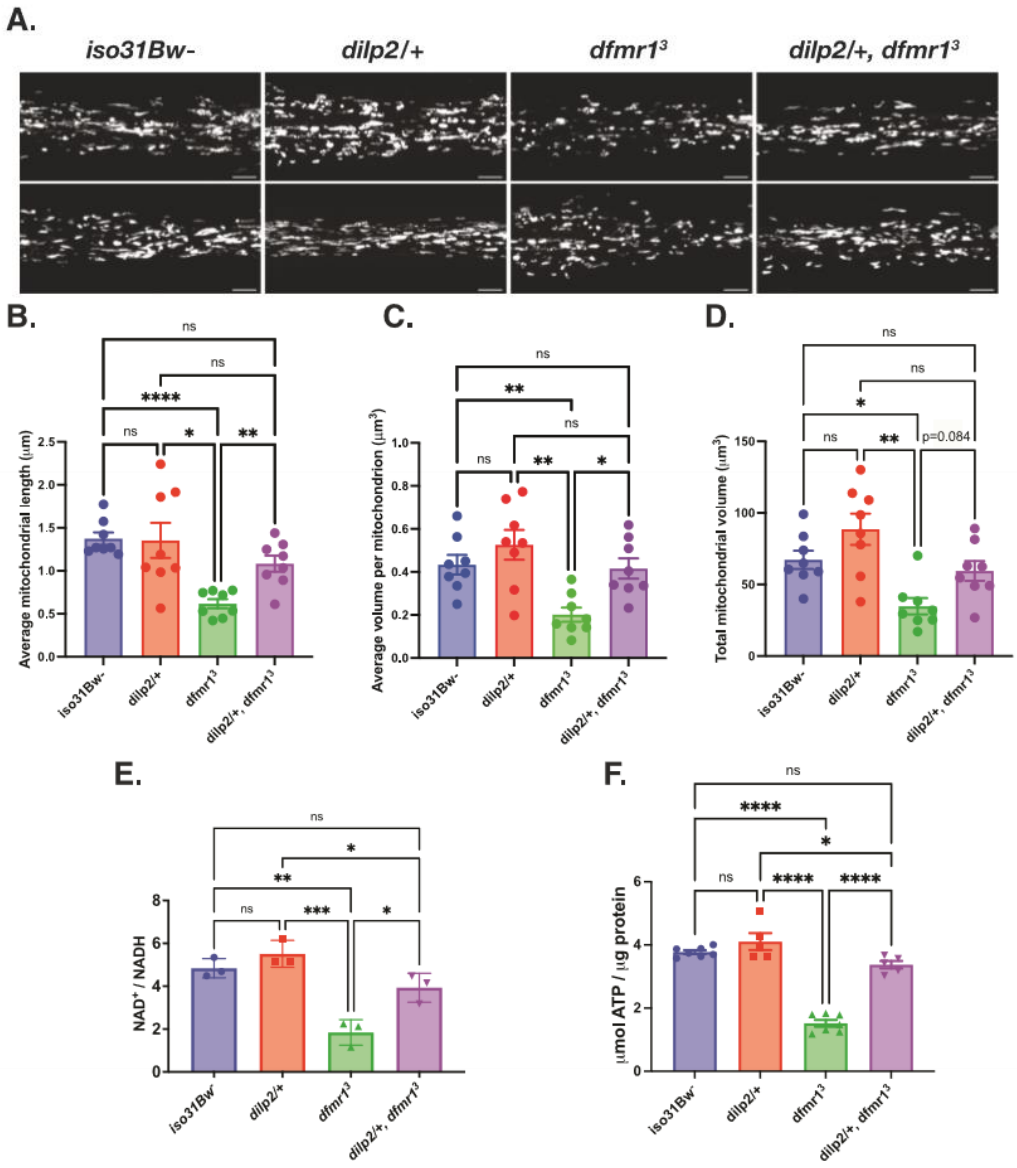

Figure 5.2: Genetic reduction of insulin signaling augments mitochondrial volume and function in *dfmr1* mutant flies. A-D, Mitochondria in the insulin producing cells (IPCs) of the brain were labeled by expressing a genetically encoded *UAS-mitoGFP* construct in conjunction with the *dilp2-Gal4* driver. **(A)** Two representative maximum-intensity projections of GFP-labeled mitochondria in the IPC processes of *iso31Bw-* wild type, *dilp2/+* heterozygous mutant, *dfmr1* homozygous mutant, and *dilp2/+, dfmr1* double mutant flies. Scale bars: 5 μm. Images are oriented with the dorsal side on the left and the ventral side on the right. Sample number (N) per genotype= 8 brains. Brown-Forsythe and Welch ANOVA with Dunnet's T3 multiple comparisons test revealed that genetic reduction of insulin signaling significantly improved **(B)** average mitochondrial length and **(C)** average volume per mitochondrion. **(D)** Total mitochondrial volume was not significantly increased in *dilp2/+, dfmr1* double mutants but showed a trend towards improvement (p=0.084). Values represent mean ± SEM. *p≤0.05, **p≤0.01, ***p≤0.001, ****p< 0.0001. **E,** Quantification of the NAD^+/NADH ratio. Each sample contained 10 fly bodies. Sample number (N) per genotype= 3. One-way ANOVAs revealed a significant group effect for the NAD^+/NADH ratio (p=0.0003). Post hoc Tukey tests

indicated while *dfmr1* mutant flies had a significantly lower NAD^+/NADH ratio than their *iso31Bw-* and *dilp2/+* heterozygous mutant conspecifics, *dilp2/+,dfmr1* double mutant flies had a significantly improved NAD^+/NADH ratio. Values represent mean ± SEM. *p≤0.05, **p≤0.01, ***p≤0.001. **F,** Quantification of ATP levels relative to protein content. Each sample contained 5 fly bodies. Sample number (N) per genotype: *iso31Bw-*=6, *dilp2/+*=5, *dfmr1*=6, *dilp2/+, dfmr1*=5. One-way ANOVAs revealed a significant group effect for the ATP levels (p<0.0001). Post hoc Tukey tests indicated while *dfmr1* mutant flies had a significantly lower ATP levels than their *iso31Bw-* and *dilp2/+* mutant conspecifics, *dilp2/+, dfmr1* double mutant flies had a significant boost in ATP levels. Values represent mean ± SEM. *p≤0.05, **** p≤0.0001.

For these experiments, we introduced one copy of a null allele of the dilp2 gene, which encodes the most abundant *Drosophila* insulin-like peptide, into the *dfmr1* mutant background. We were particularly interested in reduction of *dilp2* gene dosage because we have previously demonstrated that this precise genetic manipulation restores behavioral and cognitive function in the *dfmr1* mutants (Monyak et al., 2017). As an initial indication of mitochondrial health, we conducted TEM experiments on longitudinal sections of isolated thoraces to visualize the impact of genetic reduction of insulin signaling on mitochondrial ultrastructure in *dfmr1* mutant flies as well as wild-type controls. We selected the thorax for TEM analysis because this tissue has a distinctive structure of mitochondria aligned along myofibrils to support the high energy demand of flight (Clark et al., 2006). Encouragingly, we observed that in contrast to the small, irregularly shaped mitochondria present in micrographs from *dfmr1* mutants, elimination of one copy of the *dilp2* gene in *dfmr1* mutants restored mitochondrial ultrastructure (Fig. S5.1).

To quantitatively assess the impact of genetic reduction of IS on the mitochondrial network of *dfmr1* mutants, we generated *dilp2/+*, *dfmr1* double mutant flies in which mitochondria in the IPCs were labeled with GFP (*dilp2-Gal4>UAS-mitoGFP*). Congruent with our TEM findings, we observed that the average length and volume per mitochondrion in the IPCs of *dilp2/+*, *dfmr1* double mutant flies was significantly increased relative to *dfmr1* single mutants (Fig. 5.2A-C). Additionally, the total mitochondrial volume of *dilp2/+*, *dfmr1* double mutants was indistinguishable from that of *iso31Bw-* control flies (Fig. 5.2D). Taken together, the results of our TEM and confocal microscopy studies clearly demonstrate that genetic reduction of IS ameliorates brain and peripheral mitochondrial network morphology.

Given that normalization of IS substantially improved mitochondrial ultrastructure and network morphology in the *dfmr1* mutant flies, we postulated that constitutive elimination of one allele of the *dilp2* gene would also ameliorate mitochondrial function in *dfmr1* mutants. As predicted, we found that *dfmr1* mutants that carried one null allele of the *dilp2* gene had a significantly higher whole-body NAD^+/NADH ratio and ATP levels than their *dfmr1* mutant counterparts (Fig. 5.2E-F). The rescue of mitochondrial defects by a manipulation that restores circadian rhythmicity and memory in *dfmr1* mutant flies suggests that these processes are mechanistically linked. Thus, our results indicate that restoration of mitochondrial function is a potential mechanism by which normalization of insulin signaling improves behavior and cognition in the *Drosophila* model of FXS.

Elevated IS inhibits mitochondrial function by repression of Spargel/ PGC-1α expression in dfmr1 mutants

One intriguing candidate that integrates cellular energy metabolism with mitochondrial biomass and function is PGC-1α expression. Diminished PGC-1α expression is a compelling explanation for the bioenergetic defects in FXS because the PGC-1 family of proteins are transcriptional coactivators that strongly induce mitochondrial biogenesis and function (Merzetti & Staveley, 2015). Alignment of the *Drosophila* Srl protein with its three mammalian homologs revealed a high degree of sequence identity, particularly with respect to functional domains (Merzetti & Staveley, 2015). Similar to its mammalian counterpart, Srl is a transcriptional coactivator that has been shown to modulate mitochondrial biogenesis and energy metabolism (Merzetti & Staveley, 2015; Mukherjee et al., 2014). Thus, we can leverage the *Drosophila* model system to circumvent the functional redundancy present in mammalian models and identify possible roles of PGC-1α /Srl in FXS pathogenesis. Remarkably, flies with loss-of-function mutations in *Srl* have several phenotypic commonalities with *dfmr1* mutants including, similar deficits in energy stores; fragmented mitochondria; locomotor impairment; decreased female fecundity; and shortened lifespan (Mukherjee et al., 2014; Ng et al., 2017; Tiefenböck et al., 2010; Weisz et al., 2018; Y.

Q. Zhang et al., 2001). The robust phenotypic overlap between *dfmr1* and *Srl* loss-of-function suggests that these genes act in a common pathway to modulate mitochondrial function, behavior, and cognition.

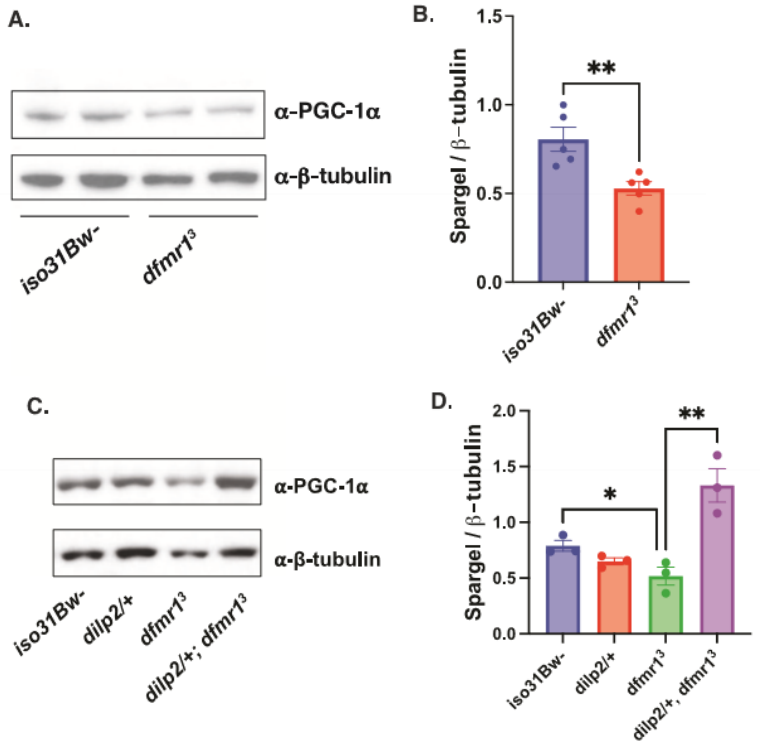

Figure 5.3: Diminished Spargel expression in the heads of *dfmr1* mutants is restored by normalization of IS. A, Western analysis of Spargel expression in extracts from *iso31Bw-* and *dfmr1* mutant fly heads. An antibody to PGC-1α was used to detect Spargel expression (top). β-Tubulin was used as a loading control (bottom). See Fig. S5.3 for full blots. **B,** Quantification of the intensity of Spargel relative to β-Tubulin. An unpaired t-test revealed that Spargel levels are diminished in dfmr1 mutant heads compared to *iso31Bw-* controls ($p = 0.0074$). Sample number (N) per genotype = 5. Each sample contained 10 fly heads. Values represent mean ± SEM. **$p \leq 0.01$. **C,** Western analysis of Spargel expression in extracts from *iso31Bw-* wild type, *dilp2/+* heterozygous mutant, *dfmr1* homozygous mutant, and *dilp2/+*, *dfmr1* double mutant fly heads. See Fig. S5.4 for full blots. **D,** An unpaired t-test indicated that *dilp2/+, dfmr1* double mutant flies have higher Spargel expression than dfmr1 single mutants ($p = 0.0088$). Sample number (N) per genotype = 3. Each sample contained 10 fly heads. Values represent mean ± SEM. **$p \leq 0.01$.

To measure Srl protein levels in the heads of *dfmr1* mutant and wild-type flies, we first validated that the mouse monoclonal antibody that specifically recognizes endogenous forms of PGC-1α cross-reacts with the *Drosophila* Srl protein (Fig. S5.2). As predicted by the convergence of loss-of-function phenotypes and the expected effects of known cellular signaling defects, we observed that Srl protein levels are diminished in the heads of *dfmr1* mutants compared to wild-type controls (Fig. 5.3A-B; Fig. S5.3). This

finding is congruent with a previous report that PGC-1α transcript levels are significantly down-regulated in an unbiased transcriptomic analysis of hippocampal neurons in Fmr1$^{-/y}$ mice (Sawicka et al., 2019).

To determine whether elevated IS contributes to decreased Srl expression, we measured Srl levels in the heads of *dfmr1* mutants that carried a null allele of *dilp2*. We observed that genetic reduction of IS restored Srl expression in the heads of *dfmr1* mutants to wild-type levels (Fig. 5.3C-D; Fig. S5.4). As another independent manipulation of IS, we acutely administered a highly specific PI3K inhibitor, LY294002, for 5 days post-eclosion and quantified Srl expression in the heads of *dfmr1* mutants and wild-type controls. Similar to our findings with genetic reduction of IS, we observed that pharmacologic reduction of IS boosts Srl expression in the heads *dfmr1* mutants (Fig. S5.5).

Pan-neuronal augmentation of Spargel expression rescues circadian rhythmicity in the dfmr1 mutants

Next, we queried whether elevation of Srl expression is sufficient to improve behavioral defects in the *dfmr1* mutant flies. To genetically boost Srl expression in *dfmr1* mutants, we used enhancer promoter (EP) induced overexpression of the *Srl* locus in the central nervous system. We obtained flies that contain a UAS element upstream of the endogenous *Srl* gene, termed *Srl*^{EY05931}, and made recombinants in the *dfmr1* mutant background. The resultant progeny were crossed to *dfmr1* mutants that expressed the *elav-Gal4* pan-neuronal driver to generate *dfmr1* mutant flies that expressed the *Srl*^{EY05931} transgene in conjunction with the *elav-Gal4* pan-neuronal driver. We then utilized the well-established Drosophila Activity Monitor (DAM) System to record the locomotor activity of these flies in free-running conditions.

Visual inspection of free-running rest:activity rhythms revealed that *dfmr1* mutant flies that contained the *elav-Gal4* driver in conjunction with the *Srl*^{EY05931} transgene had more rhythmic patterns of locomotor activity compared to *dfmr1* mutants that contained the *elav-Gal4* driver alone (Fig. 5.4A). To quantify circadian rhythmicity, we calculated fast Fourier transform (FFT) values for flies of each genotype. Conventionally, a fly with an FFT value that is above 0.04 is considered strongly rhythmic. In contrast, flies

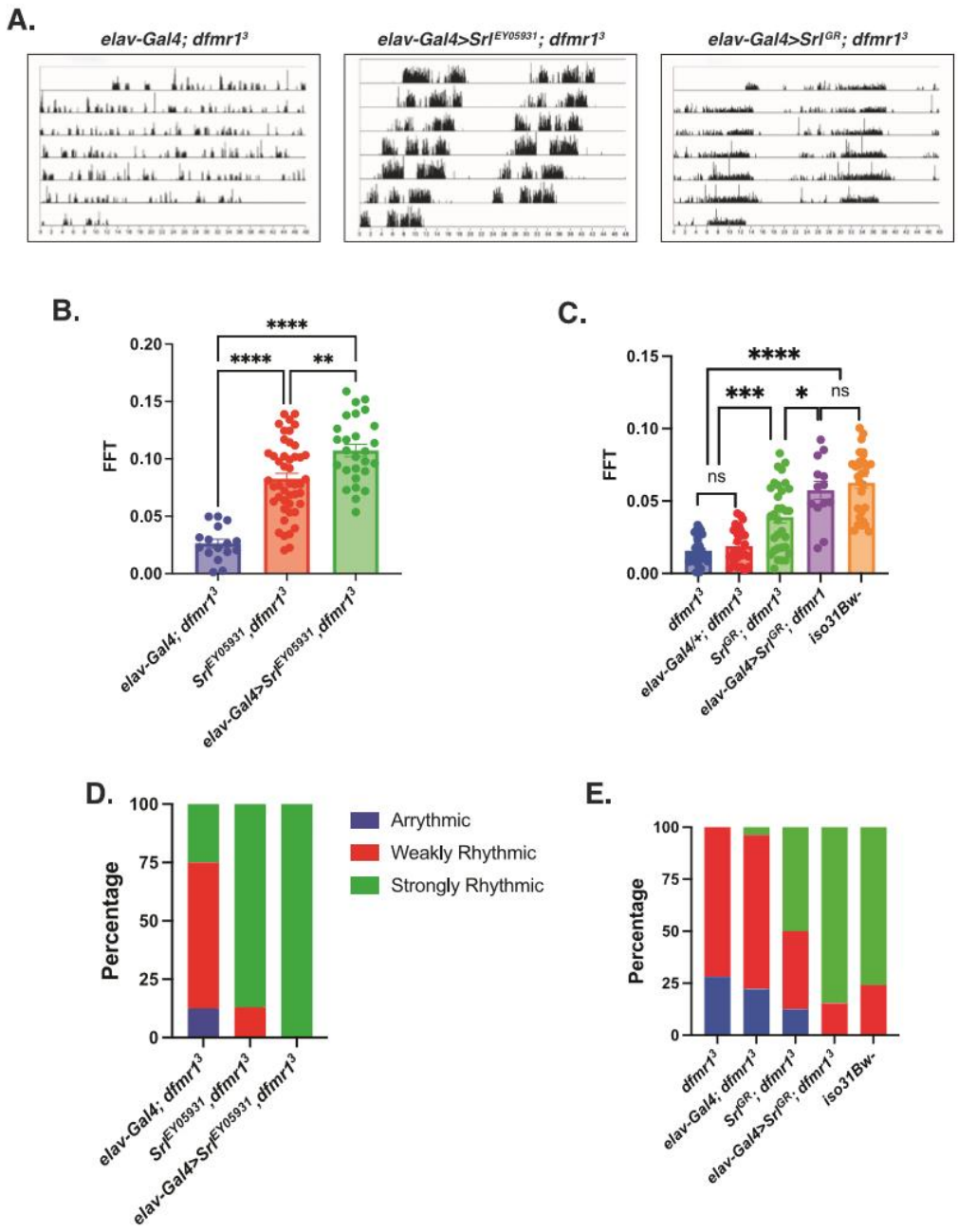

Figure 5.4: Pan-neuronal augmentation of *Spargel* rescues circadian rhythmicity in *dfmr1* mutant flies. A-E, Circadian behavior was evaluated by comparison of actogram appearance, the average fast Fourier transform (FFT) values, and percentage of rhythmic flies to ascertain whether augmentation of *Spargel* expression improves circadian behavior in *dfmr1* mutant flies. Sample number (N) per genotype: (*elav-Gal4; dfmr1*) = 16-27; (*Srl^{EY05931}, dfmr1*) = 46, (*elav-Gal4>Srl^{EY05931}, dfmr1*) = 27, *dfmr1* = 32, (*Srl^{GR}; dfmr1*) = 32, (*elav-Gal4>Srl^{GR}; dfmr1*) = 13, *iso31Bw-* = 29. **(A)** Representative actograms from flies of the genotypes indicated. In contrast to the free-running rest:activity rhythms of dfmr1 mutants that contain the *elav-Gal4* transgene alone, *dfmr1* mutants that contain the *Srl^{EY05931}* or *Srl^{GR}* transcript in conjunction with the *elav-Gal4* driver display consolidated, rhythmic behavior. **(B, C)** The average fast Fourier

transform (FFT) was calculated for genetic combinations. One-way ANOVAs revealed a significant group effect for FFT values ($p < 0.0001$). Post hoc Tukey tests indicated that *dfmr1* mutant flies that expressed the **(B)** $Srl^{EY05931}$ or **(C)** Srl^{GR} construct in conjunction with the *elav-Gal4* driver had significantly higher FFT values compared to *dfmr1* mutant flies that contained either transgene alone. Values represent mean ± SEM. *$p \leq 0.05$, **$p \leq 0.01$, ***$p \leq 0.001$, ****$p \leq 0.0001$. **(D, E)**. The percentages of strongly rhythmic (FFT ≥ 0.04), weakly rhythmic (0.04 > FFT ≥ 0.01), and arrhythmic (FFT < 0.01) flies of each genotype are shown in green, red, and blue, respectively. The percentage of strongly rhythmic flies is increased in dfmr1 mutants that contained the **(D)** $Srl^{EY05931}$ or **(E)** Srl^{GR} construct in conjunction with the *elav-Gal4* driver compared to either construct alone.

with FFT values between 0.01 and 0.04 are considered weakly rhythmic and those with FFT values below 0.01 are designated as arrhythmic. Congruent with their actogram appearance, on average, flies that pan-neuronally expressed the $Srl^{EY05931}$ transgene had higher FFT values than their *dfmr1* mutant counterparts that contained the *elav-Gal4* driver or $Srl^{EY05931}$ transgene alone (Fig. 5.4B). When we stratified the dataset into categories based on the percentage of rhythmic flies, we observed that in contrast to *dfmr1* mutants that expressed only the *elav-Gal4* driver or $Srl^{EY05931}$ construct, all *dfmr1* mutant flies that contained both the *elav-Gal4* driver and the $Srl^{EY05931}$ construct were strongly rhythmic (Fig. 5.4D).

To independently corroborate our findings, we obtained a UAS-Spargel genomic rescue fragment (Srl^{GR}) to elevate Srl expression in *dfmr1* mutants. Similar to what we observed with the $Srl^{EY05931}$ construct, pan-neuronal expression of Srl^{GR} in *dfmr1* mutants also resulted in more consolidated, rest: activity patterns than *dfmr1* mutant conspecifics that contained only the *elav-Gal4* driver alone (Fig. 5.4A). Moreover, pan-neuronal expression of Srl^{GR} in *dfmr1* mutants increased the average FFT value and percentage of strongly rhythmic flies relative to *dfmr1* mutant flies that contained either transgene alone (Fig. 5.4C,E). The ability of two distinct genetic manipulations that augment *Srl* expression to ameliorate circadian behavior in *dfmr1* mutants strongly suggests that elevation of *Srl* expression is sufficient to restore circadian rhythmicity. Notably, we did observe a significant increase in circadian rhythmicity for *dfmr1* mutant flies that contained the $Srl^{EY05931}$ or Srl^{GR} transgene alone compared to *dfmr1* mutants that contained only the *elav-Gal4* driver (Fig. 5.4). We believe that this is likely due to leaky expression of the UAS constructs whereby *Srl* expression is moderately increased, albeit not as highly as when the *elav-Gal4* driver is present. Therefore, the rescue of circadian rhythmicity by elevation of *Srl* expression in *dfmr1* mutants appears to occur in a dose-dependent manner.

Consistent with the known role of *Srl* as a modulator of mitochondrial biogenesis, in follow up TEM experiments, we observed that pan-neuronal expression of Srl^{GR} in *dfmr1* mutants substantially improved thoracic mitochondrial ultrastructure compared to *dfmr1* mutants that contained the *elav-Gal4* driver alone (Fig. S5.6). The ability of pan-neuronal expression of Srl^{GR} to restore mitochondrial ultrastructure in the thorax of *dfmr1* mutants suggests that this rescue occurs in a cell-non-autonomous manner. Much like our circadian results, the rescue of mitochondrial ultrastructure by augmentation of *Srl* expression appears to be dose-dependent, as mitochondrial ultrastructure was modestly improved in *dfmr1* mutants that caried the Srl^{GR} construct alone. Given that proper mitochondrial ultrastructure is essential to support energy production, we believe that elevation of *Srl* expression likely ameliorates mitochondrial function in *dfmr1* mutants and thereby restores circadian behavior.

Genetic manipulation of Spargel expression phenocopies the dfmr1 mutant circadian defect

As further confirmation that *Srl* is indeed a major contributor to FXS pathophysiology, particularly with respect to circadian behavior, we next tested whether *Srl* loss-of-function in a wild-type genetic background phenocopies *dfmr1* loss-of-function. For these experiments, we used the *daughterless-Gal4* (*da-Gal4*) driver to ubiquitously express a *UAS-*Srl^{RNAi} transgene in an otherwise wild-type genetic background. When we assayed circadian behavior, we observed that in contrast to the empty vector control (*UAS-*$Ctrl^{RNAi}$), ubiquitous knockdown of *Srl* expression in wild-type flies significantly disrupted free-running locomotor activity rhythms, diminished FFT values, and increased the percentage of flies that were arrhythmic or weakly rhythmic (Fig. 5.5A, B, E). Considering that pan-neuronal elevation of *Srl* expression was sufficient to rescue the circadian behavioral defect in *dfmr1* mutants, we hypothesized that *Srl* knockdown exclusively in the CNS would also mimic the *dfmr1* mutant phenotype. As expected, we observed that pan-neuronal knockdown of *Srl* expression in the wild-type genetic background recapitulated the circadian phenotype that we observed with the *da-Gal4* driver (Fig. 5.5A, C, F).

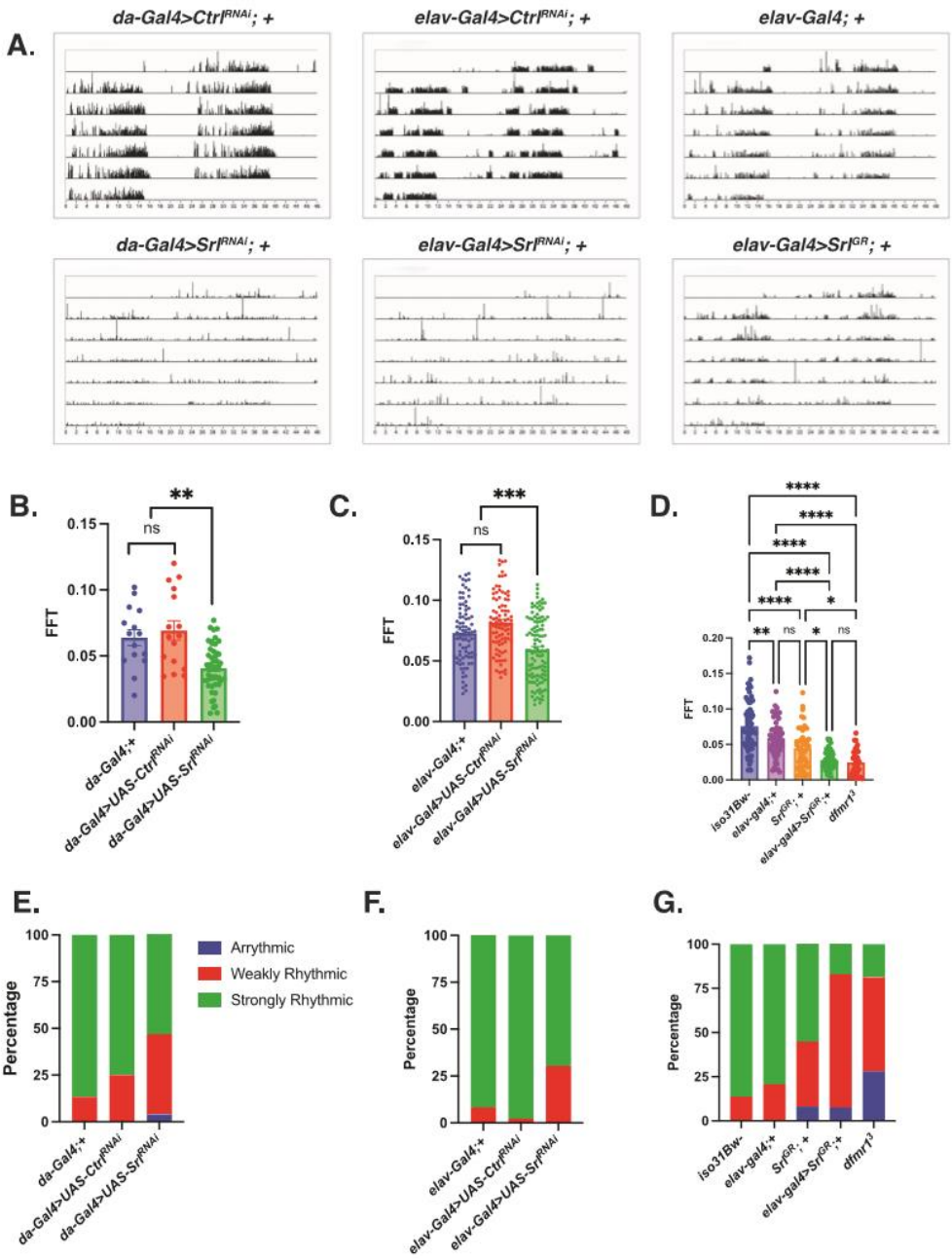

Figure 5.5: Modulation of *Spargel* expression in wild-type flies phenocopies the circadian defect observed in *dfmr1* mutant flies. A–G, Circadian behavior was evaluated by comparison of actogram appearance, the average fast Fourier transform (FFT) values, and percentage of rhythmic flies for genetic combinations to ascertain whether overexpression or knockdown of *Spargel* impacts circadian behavior in wild type flies. Sample number (N) per genotype: (*da-Gal4;*+) = 15, (*da-Gal4>UASCtrl*^{RNAi}) = 16, (*da-Gal4>UAS-Srl*^{RNAi}) = 49, (*elav-Gal4;*+) = 58-84, (*elav-Gal4>UAS-Ctrl*^{RNAi}) = 88, (*elav-Gal4>UAS-Srl*^{RNAi}) = 115, (*Srl*^{GR}*;* +) = 49, (*elav-Gal4>Srl*^{GR}) = 53, *iso31Bw-* = 73, *dfmr1* = 32. **(A)** Representative actograms from flies of the genotypes indicated. While control flies in the top row (*da-Gal4>UAS-Ctrl*^{RNAi}), (*elav-Gal4>UAS-Ctrl*^{RNAi}), and (*elav-Gal4;*+) display consolidated, rhythmic rest: activity patterns, both *Spargel* loss-of-function (*da-Gal4* or *elavGal4* > *UAS-Srl*^{RNAi}) and gain-of-function (*elav-Gal4>Srl*^{GR}) disrupt rest:activity patterns. **(B–D)** The average fast Fourier transform (FFT) was calculated for genetic combinations. One-

way ANOVAs revealed a significant group effect for FFT values ($p < 0.0001$). Post hoc Tukey tests indicated that wild-type flies that expressed a *UAS-Srl*^{RNAi} construct in conjunction with **(B)** *da-Gal4* or **(C)** *elav-Gal4* had significantly lower FFT values compared to wild-type flies that contained either *Gal4* driver alone or a *UAS-Ctrl*^{RNAi} fragment. Similarly, **(D)** wild-type flies that pan-neuronally expressed a *Srl*^{GR} over-expression construct (*elav-Gal4>Srl*^{GR}) had significantly lower FFT values than wild type flies that contained the *elav-Gal4* or *Srl*^{GR} transgene alone. There was no significant difference between the FFT values of the *elav-Gal4> Srl*^{GR} flies and those of *dfmr1* mutants. Values represent mean ± SEM. *$p \leq 0.05$, **$p \leq 0.01$, ***$p \leq 0.001$, ****$p \leq 0.0001$. **(E–G)** The percentages of strongly rhythmic (FFT ≥ 0.04), weakly rhythmic (0.04 > FFT ≥ 0.01), and arrhythmic (FFT < 0.01) flies of each genotype are shown in green, red, and blue, respectively. The percentage of weakly rhythmic and arrhythmic flies is increased in genetic combinations that result in **(E, F)** Spargel loss-of-function (*da-Gal4* or *elav-Gal4>UAS-Srl*^{RNAi}) and **(G)** gain-of-function (*elav-Gal4>Srl*^{GR}) compared to flies that contain each transgene alone.

The ability of *Srl* loss-of-function to phenocopy the circadian defect that we observe in the *dfmr1* mutants prompted us to conduct the inverse experiment to query whether pan-neuronal over-expression of *Srl* also impacts circadian behavior. Indeed, we observed that targeted over-expression of the *Srl*^{GR} in the CNS alone results in significantly altered rest:activity rhythms, diminished FFT values, and an increased percentage of weakly rhythmic and arrhythmic flies (Fig. 5.5A,D,G). While it is counterintuitive that both loss and gain of function manipulations of *Srl* expression have the same impact on circadian behavior, we postulate that the maintenance of circadian rhythmicity is particularly sensitive to *Srl* dosage. In this way, both too much and too little *Srl* expression are detrimental to circadian behavior. Taking the loss- and gain-of function experiments together, it is clear that we have identified a novel role for *Srl* as a modulator of circadian behavior. This finding is particularly exciting because it positions *Srl* at the intersection of metabolism, mitochondrial function, and behavior.

IV. Discussion

While the causal gene was first cloned and identified nearly three decades ago, there is still much to be learned about the molecular underpinnings of FXS. Our incomplete understanding of the precise mechanisms that underlie FXS pathogenesis has precluded the identification of effective therapeutic approaches to ameliorate the quality of life of affected individuals. Despite the advancement of several compounds to clinical trials, findings at the bench have had mixed success at the bedside. Rather, it has

become evident that the FXS field would benefit from the optimization of preclinical clinical strategies to identify therapeutic candidates and paradigms to predict their clinical efficacy.

One promising route to identify treatments for FXS has been the identification of conserved signaling pathway defects, such as IS, that can be targeted therapeutically (Weisz et al., 2015). Our studies in the *Drosophila* model of FXS pioneered the contribution of dysregulated IS to FXS pathogenesis (Monyak et al., 2017). In subsequent follow-up studies, we encountered a metabolic paradox whereby *dfmr1* mutant flies have decreased energy stores and are more sensitive to starvation despite elevated IS in the brain and hyperphagia (Weisz et al., 2018). Pursuit of an explanation for our discordant metabolic findings lead to our discovery that mitochondria in the *dfmr1* mutants have ultrastructural and functional defects (Weisz et al., 2018). Studies by other groups further support the notion that mitochondrial dysfunction is a robust, evolutionarily conserved component of FXS pathophysiology (D'Antoni et al., 2020; Griffiths et al., 2020; Licznerski et al., 2020; M. Shen et al., 2019).

The studies described herein integrate biochemical and physiologic methodologies with behavioral testing to provide a more comprehensive understanding of the contribution of mitochondrial dysfunction to FXS pathogenesis. We demonstrate that mitochondrial volume is diminished in the IPCs of *dfmr1* mutants and that ATP levels are decreased compared to wild-type conspecifics. Strikingly, we report that genetic reduction of IS is sufficient to correct morphologic defects in the mitochondria of *dfmr1* mutants as well as augment the NAD^+/NADH ratio and ATP levels. As such, our findings indicate that the defect in IS that modulates behavior and cognition in preclinical models of FXS is mechanistically linked to the observed mitochondrial defects. Further, we present evidence that dysregulated IS down-regulates the expression of the mitochondrial master regulator PGC-1α/Srl in the *dfmr1* mutants. This result led to the exciting discovery that pan-neuronal augmentation of *Srl* expression is sufficient to mitigate circadian behavior in *dfmr1* mutants. Moreover, genetic manipulation of *Srl* expression in wild-type flies is sufficient to disrupt circadian behavior. Thus, in addition to implicating *Srl* in FXS pathogenesis, our findings reveal novel role of *Srl* in the regulation of circadian behavior. Future studies will be necessary to elucidate the precise mechanisms

by which dysregulated IS impinges on PGC-1α expression in the brain. Additionally, it would be interesting to determine the extent to which mitochondrial phenotypes are present in female *dfmr1* mutants.

Notably, diminished PGC-1α expression has been reported in other syndromic forms of intellectual disability (ID) and autism, including Down Syndrome and Rett Syndrome (Valenti et al., 2014; Valenti & Vacca, 2023). The convergence of multiple distinct genetic forms of ID and autism on decreased PGC-1α expression suggests shared mechanistic underpinnings. Therefore, in a broader sense, further exploration of the precise mechanisms by which PGC-1α expression is compromised in ID and autism will expand our understanding of the contribution of reduced PGC-1α expression to behavioral pathology. Such studies have the potential to uncover novel treatments for FXS and other syndromic forms of ID and autism.

V. Methods

Fly genetics and husbandry

Fly strains that contain the *dfmr1*^{3} allele are described in Dockendorff *et al.* (Dockendorff et al., 2002). Fly strains that contain the *dilp2* mutation were obtained from the Bloomington Stock Center (stock number 30881). The *elav-Gal4* and *daughterless-Gal4* drivers were derived from the Bloomington Stock Center (stock numbers 8765 and 95282). Flies that contain the UAS-mitoGFP construct were obtained from the Bloomington Stock Center (stock number 8442). The *spargel-shRNA* and *shRNA* empty vector control lines were obtained from the Vienna Drosophila Resource Center (stock numbers 330271 and 60200). Stocks that contain the *srl*^{EY05931} allele were Bloomington Stock Center (stock number 20009). Stocks that contained the UAS-Spargel^{GR} were obtained from Hugo Stocker. All fly strains were outcrossed to *w1118* (*iso31Bw-*) flies as described in Monyak *et al.* (Monyak et al., 2017). Flies were cultured on a standard cornmeal-molasses medium and maintained in the presence of stringent 12 hours light: 12 hours dark (LD) cycles at 25°C.

Mitochondrial morphology in IPCs

We expressed the *UAS-mitoGFP* reagent described in Rizzuto et al. (Rizzuto et al., 1996) under the control of the *dilp2-Gal4* to directly visualize mitochondria in the insulin producing cells (IPCs). Brains were dissected from 4 to 8 days old male flies in 1x PBS and fixed with 4% paraformaldehyde (PFA) in PBS for 20 minutes at RT. Brains were then washed 3 times for 10 minutes in PBS-T (PBS +0.2% Triton-X 100) and mounted on slides in glycerol +2% N-Propyl gallate. Images were acquired with a Perkin Elmer UltraView Vox spinning disk confocal on a Nikon Eclipse Ti Microscope. Experiments were imaged on either a Hamamatsu EMCCD C9100-50 camera or a Hamamatsu CMOS ORCA-Fusion (C11440-20UP). The EMCCD camera was used with Volocity Software [Quorom Technologies/PerkinElmer] and the CMOS camera was used with VisiView (Visitron). Z-stacks encompassing mitoGFP signal were collected at 200-nm step-size. Images were analyzed using ImageJ (NIH). For each brain, a 50µm long region encompassing the IPCs was cropped for analysis. Mitochondria were manually measured to determine their number and size. Mitochondrial signal was converted to a binary mask using the Pixel classification module of Ilastik, a machine-learning based image segmentation program (Berg et al., 2019). We then used the 3D objects counter function in ImageJ to identify mitochondria and measure the volume per mitochondrion and total mitochondrial volume.

NAD^+/NADH quantification

The concentrations of nicotinamide nucleotides were measured using the NAD^+/NADH Quantification Colorimetric Kit (Abcam, Waltham, MA) as described in Balan et al. (Balan et al., 2008). Briefly, adult male flies aged 5 to 7 days were collected on dry ice. Fly heads were removed prior to homogenization and the decapitated fly bodies were pooled in groups of 10. The samples were homogenized in 400 µL of the NADH/NAD Extraction Buffer supplied in the kit and the homogenate was centrifuged at 18407 x g for 5 minutes at 25°C to remove debris. The cycling reaction was carried out as per the manufacturer's instructions for 2 hours and the nicotinamide nucleotide concentrations were determined in duplicate. The protein concentration of each sample was measured with the Pierce® BCA Protein Assay Kit (Thermo

Scientific, Rockford, IL). The concentration of nicotinamide nucleotide contained in each sample was then normalized to its respective protein content.

ATP measurement

ATP levels were measured using the ATP Determination Kit (Molecular Probes, Eugene, Oregon) as described in Tennessen et al.(Tennessen et al., 2014). Adult male flies aged 5 to 7 days were collected on dry ice. Fly heads were removed prior to homogenization and the decapitated fly bodies were pooled in groups of five. The samples were homogenized in 100μL of ATP homogenization buffer [6M guanidine HCL, 100 mM Tris (pH7.8), 4 mM EDTA]. An aliquot was boiled at 100°C for 5 minutes and centrifuged for 3 minutes at maximum speed at 4°C. 10 μL of the supernatant was transferred to a 1.5mL microfuge tube and diluted 1:10 with 90 μL dilution buffer [25mM Tris (pH 7.8, 100 μM EDTA]. Subsequently, 10 μL of the diluted supernatant was transferred to another 1.5 ml tube that contained 740 μL of dilution buffer such that the final dilution was 1:750. The diluted homogenate was centrifuged at 20,000 x g for 3 minutes. To prepare a series of low-concentration ATP standards, the 5mM ATP stock solution provided with the kit was diluted with ddH_2O to reach final concentrations of 0, 0.01, 0.05, 0.1, 0.5, and 1 μM. Next, 10 μL of each standard or sample was transferred in duplicate to a white, opaque 96 well plate. The reaction was started by adding 100μL of the reaction mixture with a multichannel pipette. Luminescence was measured three times sequentially using a plate reader and the values were averaged. The protein concentration of each sample was measured with the Pierce® BCA Protein Assay Kit (Thermo Scientific, Rockford, IL). The concentration of ATP contained in each sample was then normalized to its respective protein content.

Transmission electron microscopy

Tissues for electron microscopic examination were prepared as described in Weisz et al. (Weisz et al., 2018). Thora fixed with 2.5% glutaraldehyde, 2.0% paraformaldehyde in 0.1M sodium cacodylate buffer, pH 7.4, overnight at 4°C. After subsequent buffer washes, the samples were post-fixed in 2.0% osmium tetroxide for 1 hour at room temperature, and then washed again in buffer followed by dH_2O. After

dehydration through a graded ethanol series, the tissue was infiltrated and embedded in EMbed-812 (Electron Microscopy Sciences, Fort Washington, PA). Thin sections were stained with lead citrate and examined with a JEOL 1010 electron microscope fitted with a Hamamatsu digital camera and AMT Advantage image capture software.

Western blotting

Adult male flies aged 5-7 days were snap frozen and heads were separated into groups of 10 on dry ice. Protein extracts were prepared from the heads using extraction buffer (20 mM Hepes (pH 7.5), 100 mM KCl, 5% glycerol, 100 µM NA3VO4, 10 mM EDTA, 0.1% Triton X, 1 mM DTT, and (Phosphatase/protease inhibitors) 4X LDS (Invitrogen) and 10X Reducing Agent (Invitrogen) were added before samples were incubated at 70°C for 10 minutes to denature and reduce. Samples were separated on a 4-12% Bis-Tris gel (Invitrogen) and transferred to a PVDF membrane (Immobilon-P, Millipore, St. Louis, MO). Enhanced chemiluminescence (SuperSignal West Pico; Thermo Scientific) was used for antibody detection. The following primary antibodies were used: anti-PGC-1α 1:1000 (Millipore, St. Louis, MO), anti-β-tubulin E7 1:20,000 (Developmental Studies Hybridoma Bank, Iowa City, IA). The relative intensity of PGC-1α to β-tubulin was determined using ImageJ (NIH).

Circadian behavior

Circadian analysis was performed as described in Dockendorff et al., 2002. Male flies were collected 0-3 days post eclosion and entrained to a stringent 12 hours light: 12 hours dark cycle for three days at 25°C. Flies were then placed in individual tubes containing 5% sucrose, 2% agar, and loaded into monitors (Trikinetics, DAM2 system, Waltham, MA) that were placed in an incubator in constant darkness at 25°C. The activity of these flies, as indicated by beam breaks, was measured from days 2 to 6. Data were collected in 5-minute bins and analyzed with ClockLab software (Actimetrics, Wilmette, IL). Rhythmicity was determined by a fast fourier transform (FFT) analysis.

Statistics

The Prism software package (GraphPad Software, v9.5.1) was used to generate graphs and perform statistical analyses. Unpaired t-tests were used to evaluate pairwise comparisons. Multiple comparisons were investigated using one-way analysis of variance (ANOVA) with post hoc Tukey tests. Multiple comparisons were investigated for datasets with variable standard deviations using Brown-Forsythe and Welch ANOVA with Dunnett's T3 multiple comparisons test.

Acknowledgements

We thank Biao Zuo and Inna Martynyuk at the Electron Microscopy Resource Laboratory at the University of Pennsylvania for assistance with our electron microscopy experiments; Amita Sehgal, PhD at the University of Pennsylvania for use of her circadian facility; and Will Haury at the University of Pennsylvania for help with *Drosophila* husbandry. This work was supported by the National Institutes of Health (MH126257, NS129903) and the Autism Spectrum Program of Excellence at the University of Pennsylvania (https://aspe.med.upenn.edu).

Author contributions

Conceptualization, E.D.W., A.R.F., and T.A.J.; Methodology, E.D.W., A.R.F., and T.A.J.; Investigation E.D.W. and A.R.F.; Resources, T.A.J.; Writing – Original Draft, E.D.W; Writing – Review and Editing, E.D.W., A.R.F., and T.A.J.; Visualization, E.D.W. and A.R.F.; Supervision, T.A.J.; Funding Acquisition, T.A.J.

CHAPTER 6: FMRP GRANULES GUIDE MITOCHONDRIAL FISSION VIA LOCAL TRANSLATION IN NEURONS

This chapter is adapted from a manuscript currently in revision at *Nature Cell Biology*:

Fenton, AR; Peng, R; Bond, C; Hugelier, S; Lakadamyali, M; Chang, Y-W; Holzbaur, ELF; Jongens, TA. FMRP granules guide mitochondrial fission via local translation in neurons.

Contribution: ARF performed experimental procedures, data analysis, writing, and figure design related to all figures.

I. Summary

Mitochondrial homeostasis is maintained in neurons by network remodeling and local translation, but it is not understood how translation is coupled to mitochondrial dynamics. The Fragile X Messenger Ribonucleoprotein (FMRP) is a critical regulator of translation, whose absence causes Fragile X Syndrome. Loss of FMRP disrupts mitochondrial health in neurons, resulting in fragmented networks with impaired metabolism. However, the mechanism by which FMRP supports mitochondrial homeostasis in neurons is unknown. Here, we utilize super-resolution microscopy, cryo-electron tomography, and live-imaging in primary rodent neurons and human iPSC-derived neurons to describe how condensates of FMRP, ribosomes, and nuclear-encoded mRNAs remodel mitochondria by locally promoting mitochondrial fission. This process involves precise localization of FMRP granules along mitochondria and depends on contacts with endolysosomes and the activity of the GTPase Rab7. FMRP-associated fission depends on protein synthesis, coincides with local translation of Mitochondrial Fission Factor, and is spatially coordinated with the endoplasmic reticulum (ER) and mitochondrial DNA replication. Knockout or knockdown of FMRP dysregulates mitochondrial organization, resulting in the irregular distribution of mitochondrial nucleoids throughout neurons. Thus, FMRP-associated translation functions synergistically with endolysosomes, the ER, and mitochondrial DNA replication to locally direct mitochondrial fission, ensuring even distribution of DNA throughout mitochondrial networks in neurons.

II. Introduction

Neurons have extended axons and dendrites that rely on local protein synthesis to support cellular function. RNAs, RNA-binding proteins, and ribosomes form phase-separated granules that are transported to specific sub-cellular regions to enable local translation in neurons (Broix et al., 2021; Fernandopulle, 2021). The Fragile X Mesenger Ribonucleoprotein (FMRP) is a component of RNA granules known to play critical roles in RNA localization and translational control in neurons (Antar et al., 2005; Darnell et al., 2011; Dictenberg et al., 2008; Goering et al., 2020). FMRP loss-of-function mutations cause Fragile X Syndrome, a devastating neurodevelopmental disorder (De Boulle et al., 1993; Grønskov et al., 2011; Pieretti et al., 1991; Quan et al., 1995). Recent work has revealed that loss of FMRP function alters mitochondrial metabolism and network organization (Bülow, Wenner, et al., 2021; Geng et al., 2023; Kuzniewska et al., 2020; Licznerski et al., 2020; M. Shen et al., 2019; Weisz et al., 2018). Multiple mechanisms focusing on the bulk regulation of proteins affecting mitochondrial function or dynamics have been proposed to explain the variety of alterations observed in these models (Geng et al., 2023; Licznerski et al., 2020; M. Shen et al., 2019), but FMRP regulates neuronal RNA transport, translation, and mitochondrial function in a spatially controlled, compartment-specific manner (Bülow, Wenner, et al., 2021; Hale et al., 2021; Jung et al., 2023). Thus, the mechanisms by which FMRP granules locally promote mitochondrial network integrity in neurons are unclear.

III. Results

FMRP preferentially associates with the ends and midzone of mitochondria in mammalian neurons

We examined the spatial relationship between EGFP-tagged FMRP (EGFP-FMRP) and mitochondria with confocal microscopy in primary rat hippocampal neurons and mouse cortical neurons. EGFP-FMRP was densely packed in the cell body and overlapped with mitochondria, as previously reported

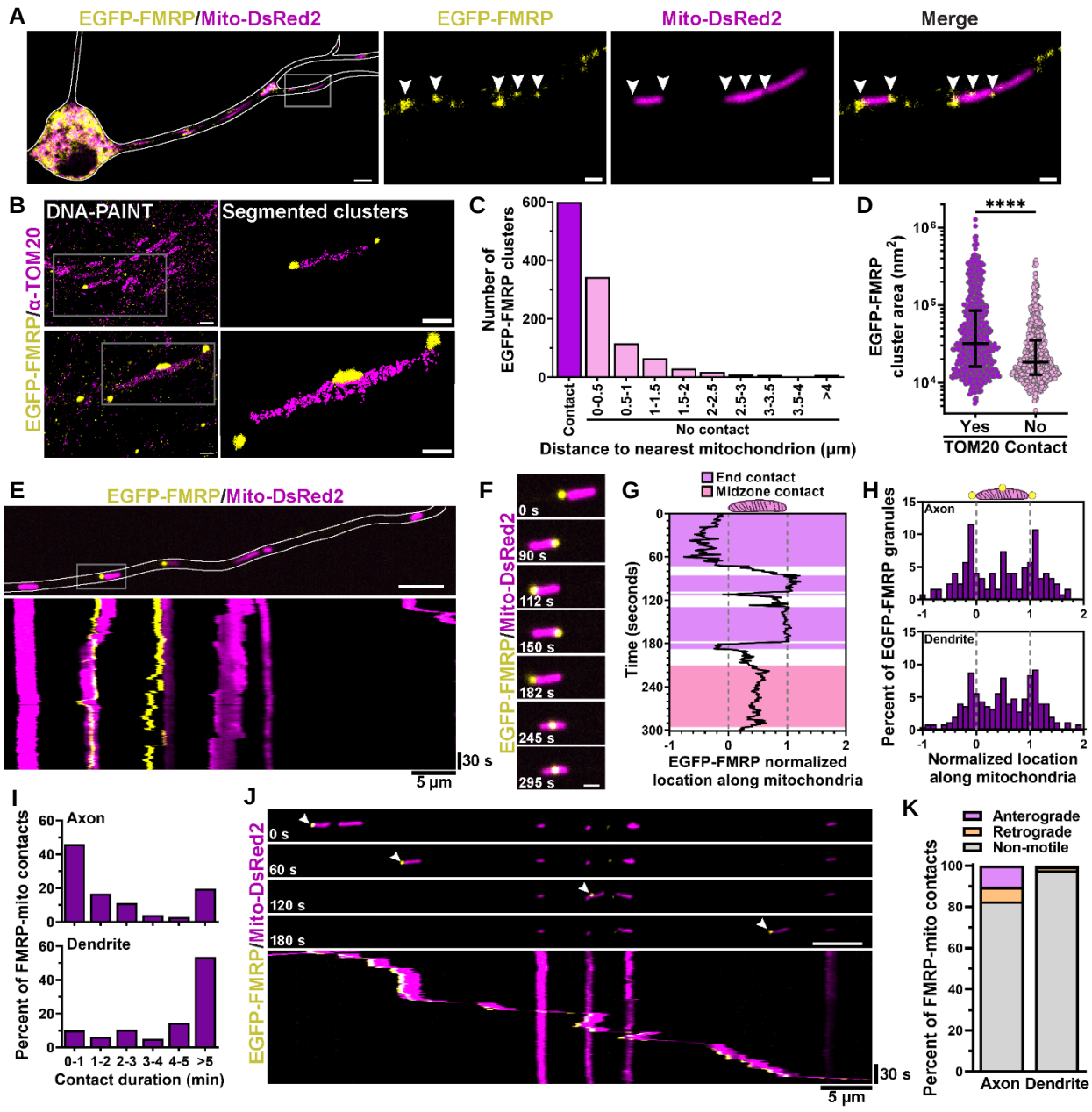

Figure 6.1: FMRP granules associate with the ends and midzone of mitochondria in neurons. A, Confocal image showing the association of EGFP-FMRP with mitochondria in a DIV8 rat hippocampal neuron. The EGFP-FMRP brightness is increased in the insets. Arrowheads indicate individual FMRP granules associated with mitochondria. **B,** DNA-PAINT images of EGFP-FMRP and TOM20-marked mitochondria in rat hippocampal neurons. Left: DNA-PAINT localizations. Right: example segmentation for individual mitochondria and nearby FMRP granules from high-density DNA-PAINT localizations. **C,** Histogram showing distance to nearest mitochondrion for EGFP-FMRP clusters. n=1199 clusters. **D,** EGFP-FMRP clusters from DNA-PAINT are larger when contacting mitochondria n=599 clusters with contact, 600 clusters without contact. Line and bars are median ± interquartile range. ****p < 0.0001, two-tailed Mann-Whitney test. **E,F,** Representative kymograph and time series depicting the localization of an EGFP-FMRP granule to

the ends and midzone of an axonal mitochondrion in a DIV7 mouse cortical neuron. **G,** Trajectory depicting EGFP-FMRP granule location along mitochondria over time for **(F)**, where mitochondrial length is normalized from 0 to 1. **H,** Histograms depicting the location of EGFP-FMRP granules along mitochondria in rat hippocampal neurons, where mitochondrial length is normalized from 0 to 1. n=121 granules from 24 axons and 250 granules from 30 dendrites. **I,** Duration of FMRP-mitochondria contacts in rat hippocampal neurons. n=72 contacts from 15 axons, 178 contacts from 14 dendrites. **J,** Time series and corresponding kymograph showing co-transport of FMRP with mitochondria in an axon of a DIV10 rat hippocampal neuron. **K,** Motility of FMRP when in contact with mitochondria. n=72 contacts from 15 axons, 178 contacts from 14 dendrites. Scale bars: 5 µm (**A**, **E**, **J**); 1 µm (**A** inset, **B**, **F**).

(Geng et al., 2023), but interactions between single mitochondria and FMRP granules could only be clearly resolved in neurites (Fig. 6.1A). To investigate the nanostructure of this interaction, we visualized EGFP-FMRP and TOM20-labelled mitochondria using multicolor DNA Point Accumulation in Nanoscale Topography (DNA-PAINT) super-resolution microscopy (Jungmann et al., 2014). EGFP-FMRP was found in circular clusters that frequently localized either at or adjacent to mitochondrial ends, or at the mitochondrial midzone (Fig. 6.1B). Approximately half of EGFP-FMRP clusters (599 of 1199) overlapped with mitochondria, mirroring the localization of endogenous FMRP in both rat hippocampal neurons and human iPSC-derived neurons (i^3Neurons; Extended Data Fig. 6.1A-E) (C. Wang et al., 2017). We measured the distance between EGFP-FMRP and mitochondria for clusters without mitochondrial overlap and found that most EGFP-FMRP clusters (~76%) were less than 1 µm from mitochondria (Fig. 6.1C), indicating that FMRP is spatially clustered in proximity to mitochondrial membranes, even without direct contact. EGFP-FMRP clusters in contact with mitochondria were significantly larger than those not in contact (32,166 nm^2 median area with contact vs. 18,175 nm^2; Fig. 6.1D). FMRP granules are known to form through liquid-liquid phase separation (Tsang et al., 2019), but mitochondrial contacts do not appear to alter the phase-separated condensate properties of FMRP granules, as we saw no significant difference in cluster circularity or in the rate of fluorescence recovery after photobleaching (FRAP) of EGFP-FMRP on or away from mitochondria (Extended Data Fig. 6.1F-I).

We tracked the movement of FMRP and mitochondria over time with live-cell imaging and observed a surprising behavior, in which FMRP granules quickly shuttle between the ends or midzone of mitochondria (Fig. 6.1E-G and Video S6.1). This dynamic association of FMRP with mitochondria was observed in both axons and dendrites, and was similar across observations in both rat hippocampal and mouse cortical

neurons (Fig. 6.1H, Fig. S6.2A-D, and Video S6.2). The duration of FMRP-mitochondria contacts was highly variable, with contacts lasting anywhere from a few seconds to longer than the 5-min recording period (Fig. 6.1I). Contacts were substantially longer in dendrites, where associations between FMRP and mitochondria could persist for over 30 mins (Fig. 1I, Fig. 6.2E). FMRP granules were also observed to undergo long-distance co-transport with mitochondria in neurons (Fig. 6.1J and Video S6.3). Co-transport was more frequent in axons than dendrites, but most FMRP-mitochondria interactions did not cause net displacement of FMRP in either compartment (Fig. 6.1K). The association of FMRP with mitochondria was not dependent on mitochondrial motility or interactions with the microtubule cytoskeleton, as nocodazole-induced microtubule depolymerization reduced mitochondrial transport without altering the frequency of FMRP-mitochondria contacts (Fig. S6.2F-G). Combined, these results reveal that FMRP granules dynamically associate with both mitochondrial ends and midzones, and traffic together throughout axons and dendrites.

FMRP marks sites of mitochondrial fission in neurons

Further tracking of FMRP-mitochondria dynamics in rat and mouse neurons revealed that FMRP granules mark sites of mitochondrial fission (Fig. 6.2A-E, Fig. S6.3A-B). FMRP granules were recruited to and retained at the mitochondrial midzone, where fission subsequently occurred within minutes (Fig. 6.2A-C and Video S6.4). These FMRP-associated fission events preferentially occurred near the mitochondrial midzone, although we noted a predominance of midzone fission in neurons, independent of FMRP association (Fig. 6.2F). EGFP-FMRP granules frequently overlapped with mitochondrial fission sites, although we also observed events in which FMRP granules were positioned sub-micron distances from the fission site, without direct contact (Fig. S6.3B). Upon completion of fission, most FMRP granules remained either in direct contact or adjacent to one of the newly formed mitochondrial ends for at least 1 min (Fig. 6.2D, Fig. S6.3C). These data suggest that the recruitment of FMRP granules to mitochondrial midzones

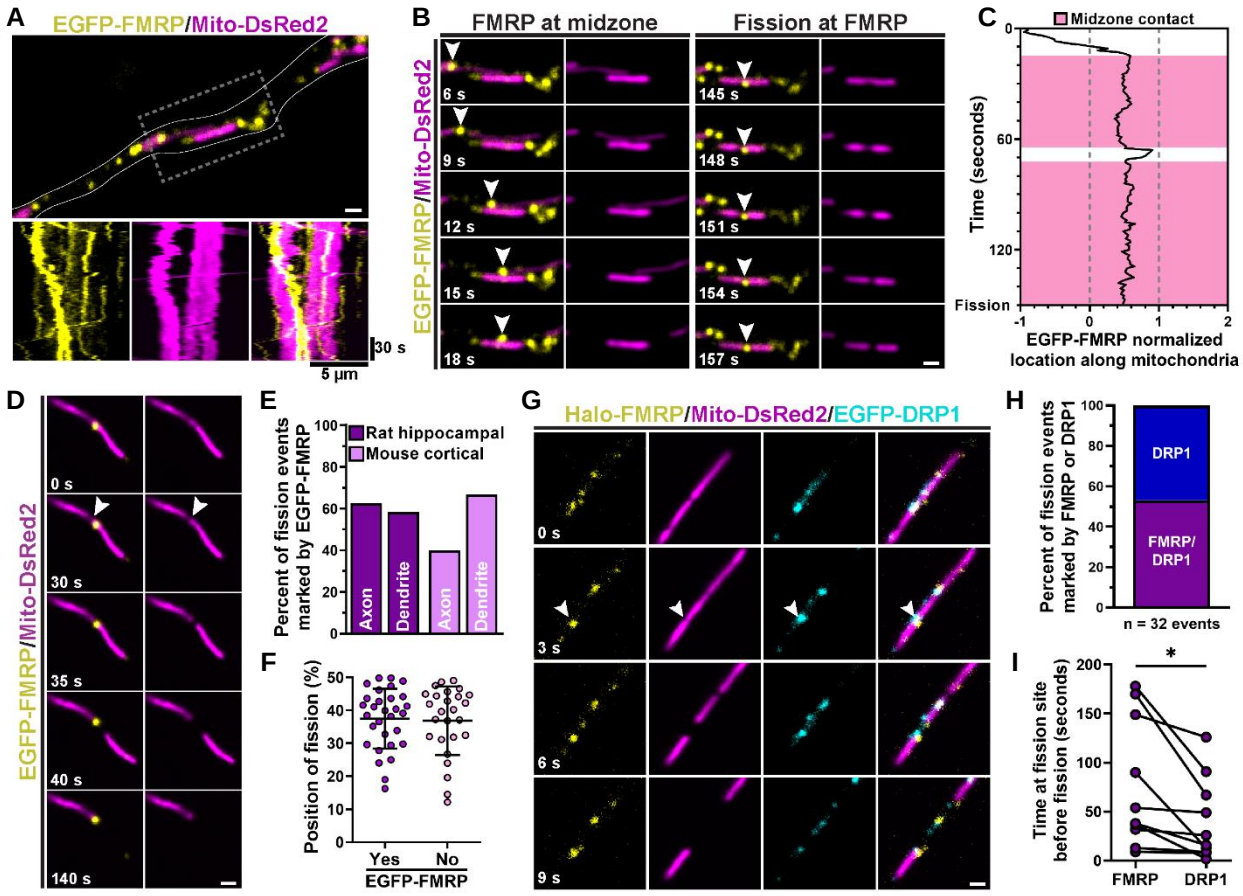

Figure 6.2: FMRP association with mitochondria precedes mitochondrial fission. A-B, Representative kymograph and time series from a DIV7 mouse cortical neuron depicting the localization of an EGFP-FMRP granule (arrowhead) to the mitochondrial midzone, followed by mitochondrial fission. **C,** Trajectory depicting EGFP-FMRP granule localization along mitochondria before fission for **(B)**, where mitochondrial length is normalized from 0 to 1. **D,** Representative time series from a DIV13 rat hippocampal neuron showing an EGFP-FMRP granule that marks a mitochondrial fission site and remains at the newly formed mitochondrial end. **E,** Percent of mitochondrial fission events marked by EGFP-FMRP in axons and dendrites of rat and mouse neurons. n=8 fission events from 36 rat axons, 98 fission events from 43 rat dendrites, 10 fission events from 17 mouse axons, and 18 fission events from 16 mouse dendrites. **F,** Position of fission relative to total mitochondrial length for events contacting or not contacting EGFP-FMRP. n=56 fission events from 17 hippocampal neurons. Line and bars are mean ± s.d. **G,** Representative time series showing Halo-FMRP and EGFP-DRP1 at a mitochondrial fission site in a DIV9 rat hippocampal neuron. **H,** Percent of mitochondrial fission events marked by Halo-FMRP and EGFP-DRP1. n=32 events from 9 rat hippocampal neurons. **I,** Halo-FMRP is recruited to fission sites before EGFP-DRP1. n=10 fission events. *$p < 0.05$, paired t-test. Scale bars: 1 µm.

may guide or initiate fission events while the persistent association of FMRP granules with mitochondrial ends may be the result of a previous fission event.

FMRP granules were found at 40-60% of mitochondrial fission sites in both axons and dendrites (Fig. 6.2E). In contrast, FMRP granules were not prominently localized to mitochondria in HeLa cells, and only 12% of fission events occurred in proximity to FMRP (Fig. S6.3D-F), suggesting that the correlation between FMRP granule association and mitochondrial fission might be neuron-specific. We confirmed the presence of FMRP at mitochondrial fission sites in neurons by co-localization with dynamin-related protein 1 (DRP1), a GTPase with a critical role in mitochondrial fission(Smirnova et al., 2001). Live-cell imaging of EGFP-tagged DRP1 and Halo-tagged FMRP revealed that all mitochondrial fission events with Halo-FMRP present also had EGFP-DRP1 (Fig. 6.2G-H), and that EGFP-DRP1 was recruited to fission sites after Halo-FMRP (Fig. 6.2I). These data suggest that FMRP granules dictate sites of mitochondrial fission upstream of DRP1, and in a neuron-specific manner.

Endolysosomal vesicles contribute to FMRP-mitochondria dynamics

We hypothesized that endolysosomal vesicles contribute to the dynamic interplay of FMRP and mitochondria. Early endosomes, late endosomes, and lysosomes recruit RNA granules to mitochondria to sustain mitochondrial function in the distal processes of neurons(Cioni et al., 2019; Liao et al., 2019; Schuhmacher et al., 2023). In other contexts, lysosomes closely regulate mitochondrial fission through Rab7 GTPase activity(Y. C. Wong et al., 2018). To test this hypothesis, we expressed fluorescently-tagged LAMP1 and Rab7 constructs to mark late endosomes/lysosomes and tagged Rab5 to mark early endosomes in rat hippocampal neurons. All three markers localized to vesicular structures that associated with FMRP granules at the ends of mitochondria (Fig. 6.3A-C). Strikingly, live-imaging revealed sustained contacts in which a LAMP1-positive vesicle was situated directly between an FMRP granule and a mitochondrial end (Fig. 6.3D and Video S6.5). The organization and persistence of these contacts suggest that endolysosomal vesicles tether FMRP granules to mitochondrial ends, filling the sub-micron gap observed between FMRP granules and mitochondria by DNA-PAINT (Fig. 6.1).

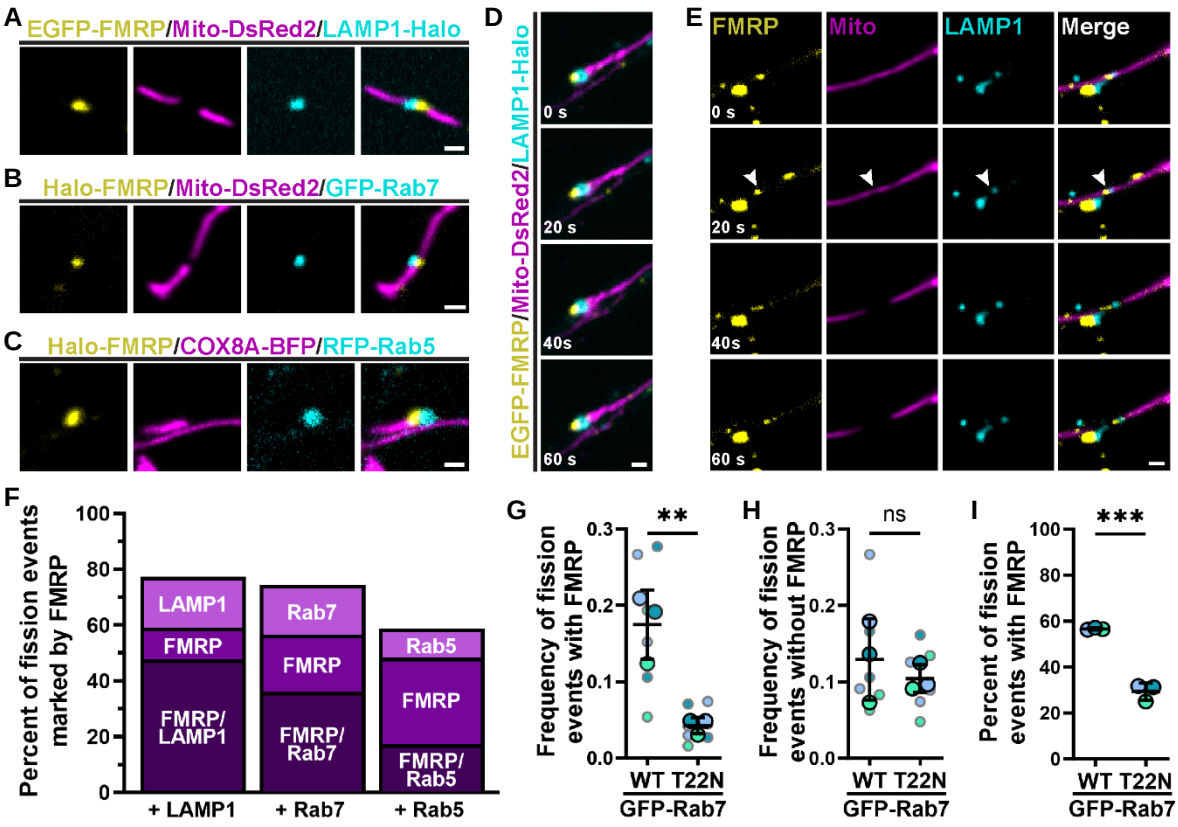

Figure 6.3: Endolysosomes contribute to FMRP-associated mitochondrial fission through Rab7 GTP hydrolysis. a-c) Examples of FMRP associating with endosomal markers (**a**) LAMP1, (**b**) Rab7, and (**c**) Rab5 at mitochondrial ends in DIV10 rat hippocampal neurons. **d,** Time series showing a LAMP1-positive vesicle tethering an FMRP granule to a mitochondrial end in a DIV10 rat hippocampal neuron. **e,** Time series showing a LAMP1-positive vesicle contacting an FMRP granule and mitochondria at a fission site in a DIV10 rat hippocampal neuron. The fission site is indicated by arrowheads. **f,** Percent of mitochondrial fission events marked by EGFP-FMRP and LAMP1-Halo, Halo-FMRP and GFP-Rab7, or Halo-FMRP and RFP-Rab5. n=44 fission events from 8 neurons, 39 fission events from 10 neurons, and 29 fission events from 17 neurons, respectively. **g-h,** Frequency of mitochondrial fission events with EGFP-FMRP (**g**) or without EGFP-FMRP (**h**) upon expression of wildtype (WT) or dominant negative (T22N) Rab7. n=6-7 neurons from 3 biological replicates. Line and bars are mean ± s.d. for biological replicates. **p < 0.01, two-tailed unpaired t-test. **i,** Percent of mitochondrial fission events marked by EGFP-FMRP upon expression of WT or T22N Rab7. n=3 biological replicates. Line and bars are mean ± s.d. ***p < 0.001, two-tailed unpaired t-test. Scale bars: 1 µm.

FMRP granules were also found to contact LAMP1 vesicles at sites of mitochondrial fission (Fig. 6.3E and Video S6.6). Approximately half of all fission events were co-positive for both LAMP1 and FMRP (Fig. 6.3F), indicating a preferential co-occurrence of lysosomes and FMRP granules at fission sites. We also investigated the association of Rab7 and Rab5 with FMRP granules at mitochondrial fission sites.

Rab7-positive vesicles associated with FMRP granules at 36% of fission sites, while Rab5-positive vesicles were only present with FMRP at 17% of fission sites (Fig. 6.3F). Thus, late endosomes/lysosomes likely play a greater role with FMRP at fission sites than early endosomes. As lysosomal Rab7 GTP hydrolysis regulates mitochondrial fission (Y. C. Wong et al., 2018), we tested whether fission at FMRP granules is also Rab7-dependent with a dominant-negative mutant Rab7 (T22N) construct. Expression of Rab7 T22N in rat hippocampal neurons significantly reduced the rate of mitochondrial fission at FMRP granules and resulted in a reduced fraction of FMRP-positive fission events (Fig. 6.3G-I), indicating that Rab7 activity is critical for mitochondrial fission associated with FMRP granules.

Mitochondria-associated FMRP granules are sites of protein synthesis

Next, we used correlative light and electron microscopy to identify EGFP-FMRP-positive target areas in rat hippocampal neurons and used cryo-electron tomography (cryo-ET) to reconstruct regions around mitochondria and EGFP-FMRP granules (Fig. S6.4). Tomographic reconstruction revealed two mitochondria with ends in close proximity to EGFP-FMRP fluorescence, with endoplasmic reticulum (ER) tubules wrapped around the region in between (Fig. 6.4A-B and Video S6.7). This orientation of mitochondria and the ER is consistent with the products of a fission event mediated by constriction of the ER (J. R. Friedman et al., 2011; Lewis et al., 2016).

We observed accumulations of electron-dense particles in the vicinity of this apparent fission event, which were identified as ribosomes by performing sub-tomogram averaging to a resolution of 27 Å (Fig. 6.4C). Ribosome structures with clearly resolved subunits were mapped back to the original tomogram, revealing large clusters alongside the mitochondria, with both the ER and vesicles nearby (Fig. 6.4D-E). The overlap of EGFP-FMRP fluorescence with many of the ribosomes supports previous findings indicating that ribosomes colocalize with FMRP granules in neurons (Antar et al., 2005; El Fatimy et al., 2016). Ribosomal arrangements observed within the granule include potential polysomes, with many ribosomes

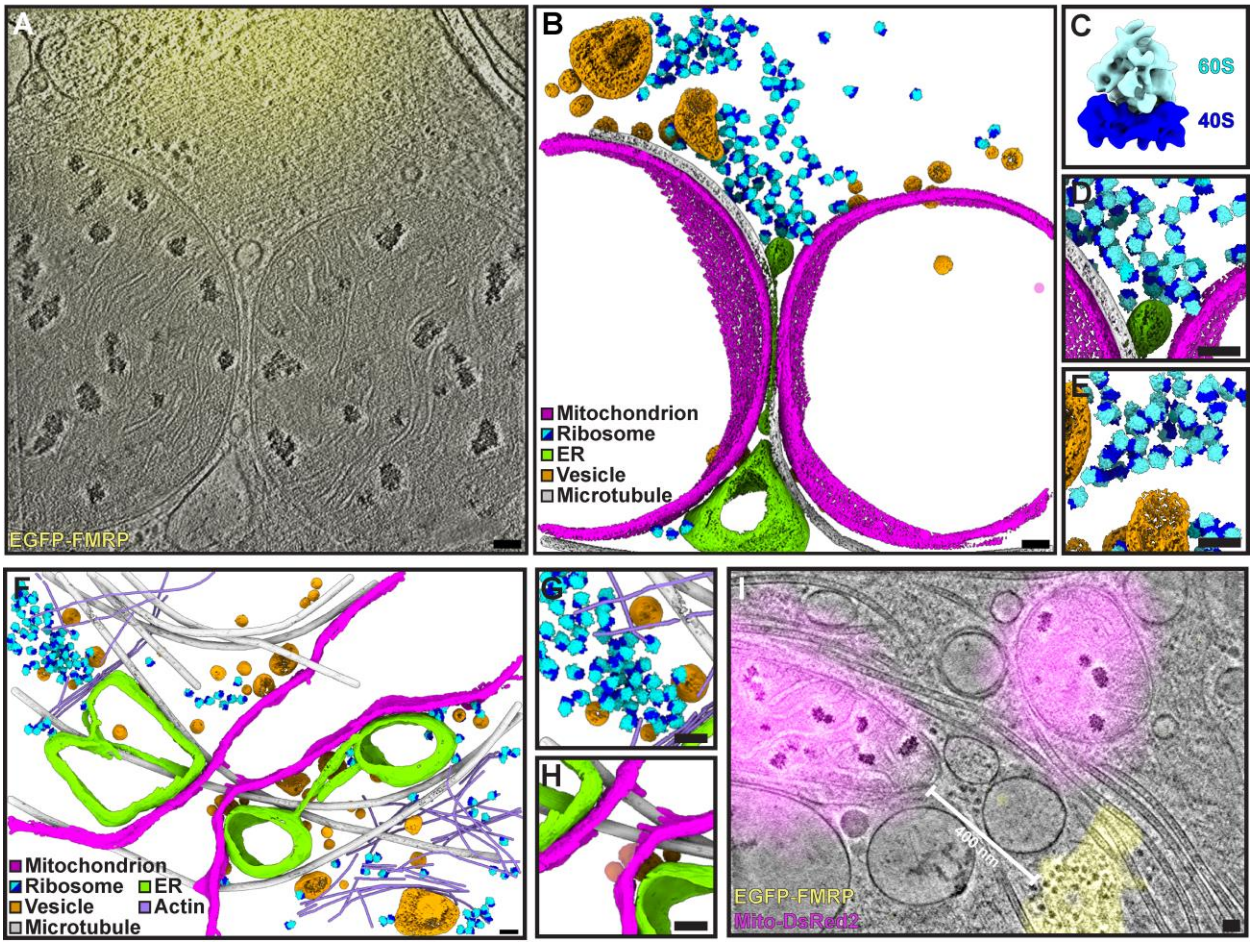

Figure 6.4: Correlative fluorescence microscopy and cryo-ET reveals ultrastructural features of EGFP-FMRP granules and mitochondria in neurons. A, A slice from a tomogram of two mitochondria in a DIV6 rat hippocampal neuron with EGFP-FMRP fluorescence overlaid. **B,** Segmentation of the tomogram from **(A)**. **C,** Reconstructed ribosome from sub-tomogram averaging. **D-E,** Zoomed-in views of **(B)** showing: ribosomes clustered near the ER and mitochondria **(D)** and ribosomes clustered near vesicles **(E)**. **F,** Segmentation of a tomogram showing a constricted mitochondrion in a DIV6 rat hippocampal neuron. **G-H,** Zoomed-in views of **(F)** showing: ribosomes clustered near the ER and vesicles **(G)** and the ER wrapping around a constricted mitochondrion with microtubules in the vicinity **(H)**. **I,** A slice from tomographic reconstruction of two mitochondria and a nearby FMRP granule in a DIV6 rat hippocampal neuron with Mito-DsRed2 (magenta) and EGFP-FMRP fluorescence (yellow) overlaid. For the full tomogram movies of (**B**) and (**F**), see Video S6.7 and Video S6.8, respectively. Scale bars: 50 nm.

held together along a single mRNA to sequentially synthesize a specific protein (Fig. S6.5A) (Brandt et al., 2010). We validated the overlap of mitochondria-associated FMRP granules with ribosomes and sites of active protein synthesis in rat hippocampal neurons via immunocytochemistry of ribosomal protein RPS3A and puromycin-labelled polypeptides (Fig. S6.5B-E). Enriched puromycin signal was present on ~50% of

mitochondria-associated FMRP granules and significantly attenuated upon treatment with the protein synthesis inhibitor cycloheximide (CHX; 50 µM for 30 minutes; Fig. S6.5F). Most FMRP granules overlapping RPS3A or puromycin-enrichment were found in close contact with mitochondria (Fig. S6.5C, E), indicating that protein synthesis at FMRP granules preferentially occurs in association with mitochondria. However, the association of FMRP with mitochondria did not require active protein synthesis, as treatment with cycloheximide or puromycin (50 µM for 30 minutes) had no effect on FMRP-mitochondria contacts (Fig. S6.5G-H). These results suggest that ribosomes are actively engaged in translation at or near FMRP granules, synthesizing proteins proximal to mitochondria.

Further analysis of our cryo-ET data-sets revealed several features of interest. In one tomogram, we noted a likely intermediate step of fission, with the ER wrapped around a constricted mitochondrion (Fig. 6.4F and Video S6.8). EGFP-FMRP fluorescence was less than 1 µm from the mitochondrial constriction site, but not directly covered by the tomogram (Fig. S6.4C). Ribosome clusters were localized near the mitochondrial constriction site, as were tubular ER and vesicles (Fig. 6.4G). Strikingly, several microtubules abutted the mitochondrion and the ER, running perpendicular to the site of mitochondrial constriction (Fig. 6.4H). Similarly, a single microtubule can be seen along the contour of both mitochondrial membranes in Fig. 6.4B, making close contacts with mitochondria and the ER. Previous work examining possible mitochondrial fission events at axon branch points has shown a similar orientation of microtubules at these sites (Nedozralova et al., 2022), suggesting that microtubules may scaffold mitochondrial fission events in neurons. In imaging experiments in which we co-expressed Mito-DsRed2 as a marker for mitochondria, we observed that EGFP-FMRP fluorescence overlapped a cluster of ribosomes near labelled mitochondria (Fig. 6.4I). In this tomogram, two vesicles can be seen in close contact with mitochondria and each other, filling the ~400 nm gap between a mitochondrion and the FMRP granule. This arrangement further suggests that vesicles facilitate contacts between FMRP granules and mitochondria, positioning ribosome-rich FMRP granules sub-micron distances from mitochondria.

MFF is translated at mitochondria-associated FMRP granules

Together, these observations suggest that local protein synthesis may facilitate FMRP-associated mitochondrial fission. To test this possibility, we treated rat hippocampal neurons with the protein synthesis inhibitor cycloheximide (50 µM for 30 minutes) and tracked mitochondrial dynamics over time in dendrites. We observed significantly fewer FMRP-positive mitochondrial fission events with CHX treatment, with no significant effect on the frequency of FMRP-negative fission events, resulting in decreased fraction of fission events marked by FMRP (Fig. 6.5A-C). This dependence of FMRP-associated mitochondrial fission on protein synthesis, and the observed ribosomal clustering, suggests that one or more proteins is translated at or near FMRP granules to drive fission.

Mitochondrial Fission Factor (MFF) is a fission adaptor that drives midzone fission in mammalian cells (Kleele et al., 2021; Otera et al., 2010). *Mff* mRNA is present in datasets for RNAs interacting with FMRP in mouse CA1 pyramidal neurons and cerebellar granule neurons (Sawicka et al., 2019). To explore whether MFF promotes fission at mitochondria-associated FMRP granules, we investigated the dynamics of MFF, mitochondria, and FMRP in hippocampal neurons. Both endogenous MFF and a GFP-tagged MFF (GFP-MFF) construct form puncta that are highly enriched at mitochondrial ends, marking the ends of nearly every mitochondrion in neurons (Fig. S6.7). All mitochondrial fission events observed were positive for GFP-MFF, with 56% co-positive for Halo-FMRP (Fig. 6.5D-E and Video S6.9). For these co-positive events, we found that FMRP was generally recruited to fission sites prior to the appearance of MFF (Fig. 6.5F), consistent with FMRP functioning upstream of MFF at fission sites.

Next, we performed single-molecule fluorescence *in situ* hybridization (FISH) (A. Raj et al., 2008) combined with immunocytochemistry for FMRP and mitochondria in i^{3}Neurons. We found that ~20% of *MFF* mRNA puncta colocalized with FMRP on mitochondria (Fig. 6.5G). For comparison, we also performed FISH for a select number of RNAs that encode proteins related to dynamic mitochondrial function and are present in datasets of RNAs that bind FMRP or RNAs that display altered transport in the absence of FMRP (Ascano et al., 2012; Darnell et al., 2011; Jung et al., 2023; Maurin et al., 2018; Sawicka et al., 2019).

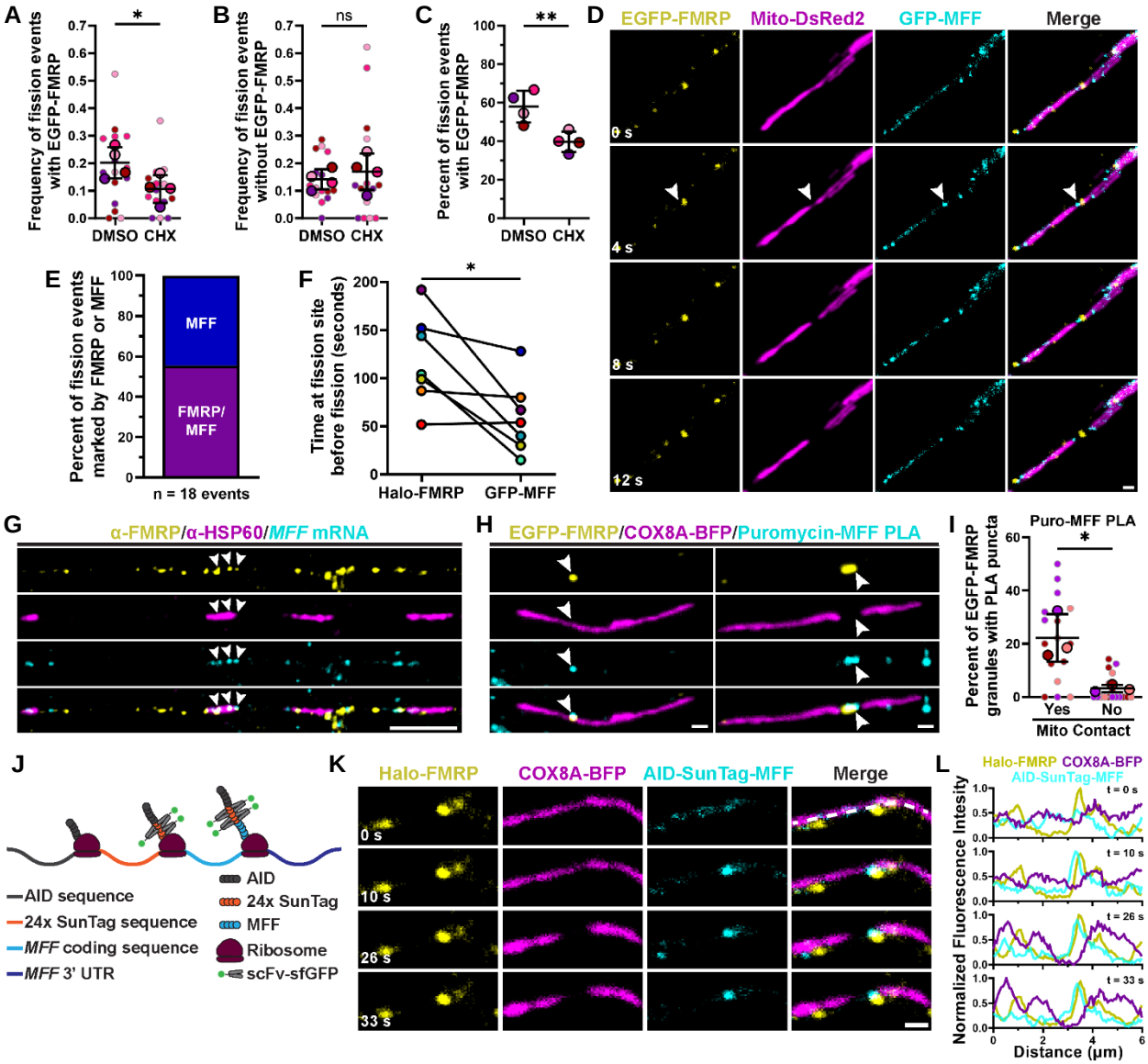

Figure 6.5: MFF is translated at FMRP granules to locally promote mitochondrial fission. A-B, Frequency of mitochondrial fission events with EGFP-FMRP **(A)** or without EGFP-FMRP **(B)** upon acute inhibition of protein synthesis with cycloheximide (CHX) in rat hippocampal neurons. n=4 biological replicates, 15 neurons. Line and bars are mean ± s.d. for biological replicates. *p < 0.05, two-tailed unpaired t-test. **C,** Percent of mitochondrial fission events marked by EGFP-FMRP upon treatment with DMSO or CHX. n=4 biological replicates. Line and bars are mean ± s.d. **p < 0.01, two-tailed unpaired t-test. **D,** Time series showing Halo-FMRP and GFP-MFF at a site of mitochondrial fission in a DIV10 rat hippocampal neuron. **E,** Percent of mitochondrial fission events marked by Halo-FMRP and GFP-MFF. n=18 events from 9 neurons. **F,** Quantification of how long Halo-FMRP and GFP-MFF puncta are present at fission sites before fission occurs. n=7 fission events. *p < 0.05, two-tailed paired t-test. **G,** Representative image showing co-localization between *MFF* mRNA and FMRP along mitochondria in DIV21 i^{3}Neurons. Arrows indicate *MFF* mRNA overlap with FMRP on mitochondria. **H,** Co-localization of signal from puromycin-MFF PLA with EGFP-FMRP along a mitochondrion and between the ends of two mitochondria in a DIV7 rat hippocampal neuron. **I,** Percent of EGFP-FMRP granules that contain puromycin-MFF PLA signal. n=17 neurons, 3 biological replicates. *p < 0.05, two-tailed unpaired t-test. Line and bars are mean ± s.d. for biological replicates. **J,** Schematic of SunTag-based nascent polypeptide labeling to visualize MFF synthesis. **K-L,** Time series and corresponding line scans showing that mitochondrial fission follows synthesis of AID-SunTag-MFF at a Halo-FMRP granule in a DIV10 rat hippocampal neuron. Scale bars: 5 μm (**G**); 1 μm (**D**, **H**, **K**).

Specifically, we chose RNAs for proteins that control mitochondrial fission, fusion, microtubule-based transport, ATP synthesis, and mitophagy (Fig. S6.6A-J). For most of these RNAs, we observed a similar extent of colocalization with mitochondria-associated FMRP as *MFF* (Extended Data Fig. 6.6K), indicating that a subset of RNAs is present in mitochondria-associated FMRP granules. We then treated rat hippocampal neurons with puromycin and carried out a proximity ligation assay (PLA) between MFF and puromycin to allow for detection of newly synthesized, puromycin-labelled MFF protein (tom Dieck et al., 2015; H. Yang et al., 2022). PLA signal for newly synthesized MFF overlapped with FMRP granules along mitochondria and immediately between mitochondria (Fig. 6.5H), which we interpret as representing FMRP granules pre- and post-fission, respectively. Overall, FMRP granules were ~7 times more likely to have signal for newly synthesized MFF when contacting mitochondria (Fig. 6.5I). To directly test if FMRP-associated translation of MFF coincides with mitochondrial fission, we used nascent polypeptide imaging based on the SunTag system to visualize MFF protein synthesis in real time (Tanenbaum et al., 2014; B. Wu et al., 2016). We designed a construct with 24 copies of the SunTag epitope fused to the MFF coding sequence and 3' UTR (Fig. 6.5J). As the protein is translated, single-chain antibody fragments fused to super-folder GFP (scFv-sfGFP) bind to the SunTag epitope and produce a fluorescent punctum. We included an N-terminal auxin induced degron (AID) as a means to degrade preexisting protein prior to imaging and reduce background fluorescence. The AID-SunTag-MFF construct was expressed in rat hippocampal neurons alongside COX8A-BFP to mark mitochondria and Halo-FMRP. AID-SunTag-MFF puncta appeared along mitochondria, where they colocalized with Halo-FMRP, providing further evidence that MFF is translated at mitochondria-associated FMRP granules (Fig. 6.5K, L). Following translation of AID-SunTag-MFF, mitochondrial fission occurred within the immediate vicinity (Fig. 6.5K, L), suggesting that MFF is translated in proximity to FMRP granules to locally promote mitochondrial fission in neurons.

FMRP plays an essential role in mtDNA organization in neurons

Our findings link FMRP-associated mitochondrial fission to local enrichment of MFF and to the ER. As MFF- and ER-dependent fission have both been linked to the replication of mitochondrial DNA (mtDNA) (Kleele et al., 2021; Lewis et al., 2016), we looked for a possible connection between FMRP granule localization and mtDNA. We expressed fluorescent constructs marking either all nucleoids (EGFP-TFAM) or replicating nucleoids (EGFP-TWINKLE and GFP-POLG2) in rat neurons. We observed close associations of FMRP granules with each nucleoid marker (Fig. 6.6A-C). Nucleoids remained associated with individual FMRP granules for several minutes, but could also associate with multiple, distinct FMRP granules during mitochondrial network remodeling (Fig. 6.6A). Overall, the spacing between nucleoids and FMRP granules was similar across markers, but POLG2 and TWINKLE were positioned slightly closer to FMRP granules than TFAM, suggesting a closer association of FMRP with replicating mtDNA (Fig. 6.6D). Further, we observed that FMRP granules were spatially linked to nucleoids during mitochondrial fission (Fig. 6.6E). Approximately half of FMRP-associated fission events were linked to nucleoids, regardless of marker (Fig. 6f; 48% for EGFP-TWINKLE vs 52% for GFP-POLG2 vs 57% for EGFP-TFAM). Thus, FMRP granules are spatially organized in proximity to mtDNA, including during mtDNA replication and mitochondrial fission.

We hypothesized that recruitment of FMRP granules to the mitochondrial midzone promotes localized control of mitochondrial fission, and that this in turn promotes the even distribution of mtDNA throughout mitochondria in neuronal processes. Thus, we would predict that loss of FMRP function would dysregulate mtDNA organization within neurons. To test this idea, we cultured cortical neurons from wild-type (WT) mice and *Fmr1* KO mice, which lack FMRP. Upon visualization of mitochondria with Mitotracker Deep Red and DNA with SYBR Green in WT neurons, we found a relatively uniform distribution of nucleoids within mitochondria, with the number of nucleoids per mitochondrion scaling linearly with mitochondrial length (Fig. 6.6G-H). In contrast, nucleoid density per mitochondrion was more variable and did not correlate as closely with mitochondrial length in *Fmr1* KO neurons (R^2 = 0.3397 for *Fmr1* KO vs 0.6166 for WT) due to the increased abundance of small mitochondria with multiple nucleoids and mitochondria with

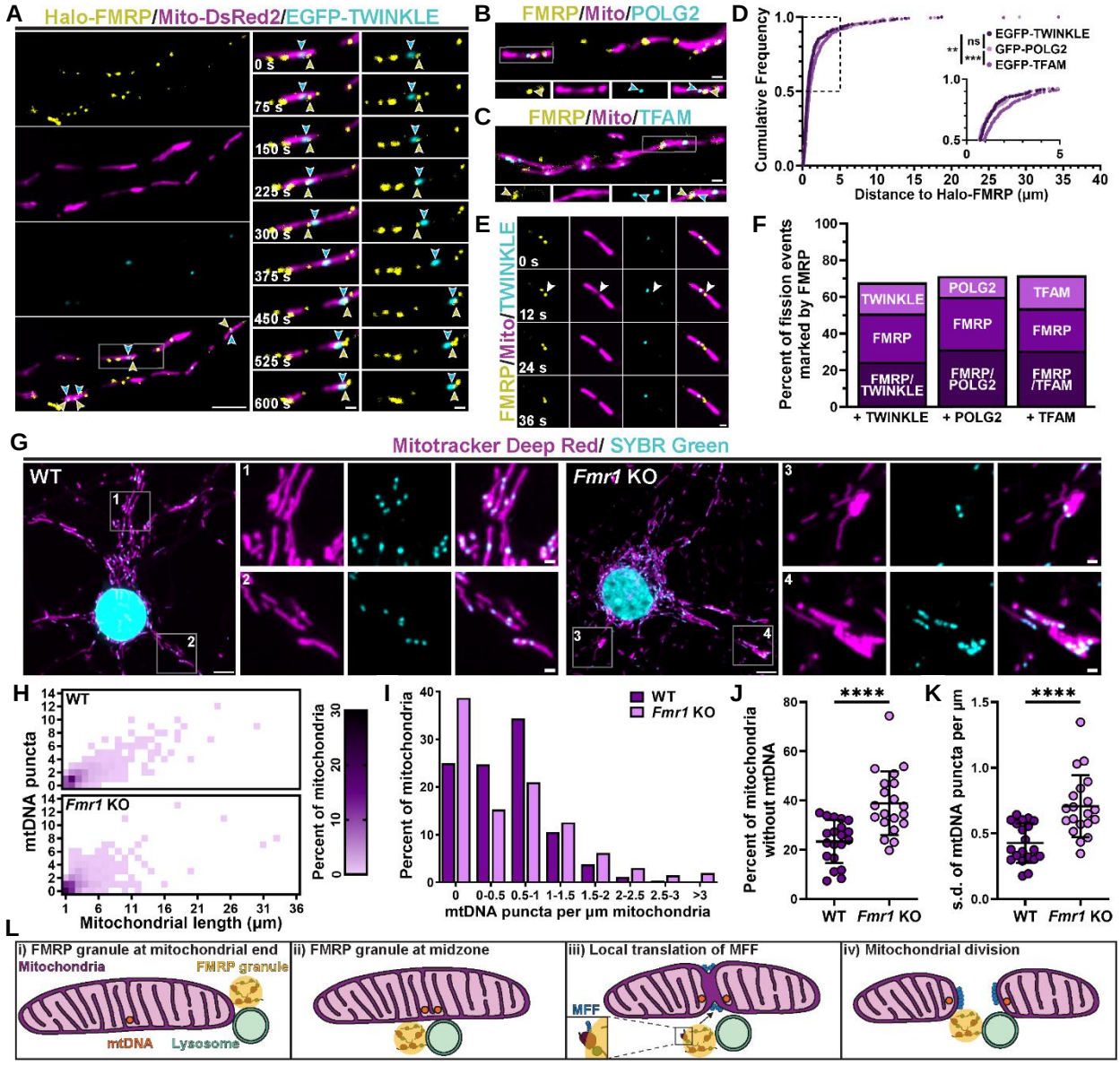

Fig. 6.6: FMRP promotes mitochondrial DNA homeostasis in neurons. A, Time series depicting associations between replicating nucleoids (EGFP-TWINKLE) and Halo-FMRP in a DIV9 rat hippocampal neuron. Nucleoids near FMRP are indicated with cyan (TWINKLE) and yellow (FMRP) arrowheads. **B-C,** DIV9 rat hippocampal neurons expressing Halo-FMRP, Mito-DsRed2, and GFP-POLG2 or EGFP-TFAM. Nucleoids near FMRP are indicated with cyan (POLG2/TFAM) and yellow (FMRP) arrowheads. **D,** Cumulative frequency of distance to nearest FMRP granule for TWINKLE, POLG2, and TFAM in rat hippocampal neurons. n=250 TWINKLE puncta from 15 neurons, 285 POLG2 puncta from 14 neurons, and 381 TFAM puncta from 15 neurons. **p < 0.01, ***p < 0.001, Kruskal-Wallis test with Dunn's multiple comparisons test. **E,** Time series from a DIV9 rat hippocampal neuron showing FMRP at a mitochondrial fission site that is linked to a TWINKLE-positive nucleoid. Arrowheads indicate the fission site. **F,** Percent of mitochondrial fission events marked by Halo-FMRP and EGFP-TWINKLE, Halo-FMRP and GFP-POLG2, or Halo-FMRP and TFAM-GFP. n=53 fission events from 11 neurons, 35 fission events from 7 neurons, and 39 fission events

from 7 neurons, respectively. **G,** Maximum-intensity projections of Mitotracker Deep Red-labelled mitochondria and SYBR Green-labelled DNA in DIV8 wild-type (WT) or *Fmr1* KO mouse cortical neurons. **H-I,** Heatmap of mitochondrial DNA (mtDNA) puncta per mitochondrion vs mitochondrial length **(H)** and distribution of mtDNA puncta density **(I)** in WT and *Fmr1* KO neurons. n=692 WT mitochondria and 1035 *Fmr1* KO mitochondria. **J-K,** Percent of mitochondria lacking mtDNA **(J)** and standard deviation of mtDNA puncta per micron mitochondria **(K)** for 20 WT and *Fmr1* KO neurons. Line and bars are mean ± s.d. ****p < 0.0001, two-tailed unpaired t-test (**j**) or two-tailed Mann–Whitney test **(K)**. **L,** Model for local control of mitochondrial fission by FMRP granules. i-ii, FMRP granules are localized to the mitochondrial ends or midzone, with endo-lysosomes contributing to this localization. iii, *MFF* mRNA within the FMRP granule is translated at the mitochondrial midzone. iv, Newly-synthesized MFF facilitates mitochondrial division, ensuring even segregation of mtDNA between daughter mitochondria. Scale bars: 5 µm (**A**, **G**); 1 µm (**A** inset, **B**, **C**, **E**, **G** inset).

few or no nucleoids (Fig. 6.6G-K). To examine whether FMRP maintains mtDNA organization in human neurons, we used CRISPR interference (CRISPRi) in i^{3}Neurons to knock down FMRP protein to 38% of its wild-type level (*FMR1* KD; Fig. S6.8A-B). *FMR1* KD i^{3}Neurons display fragmented mitochondrial networks, phenocopying FMRP loss-of-function in mouse neurons (Fig. S6.8C-E). *FMR1* KD neurons also exhibited a less uniform distribution of DNA throughout mitochondria than WT controls (Fig. S6.8F-J), and more variable nucleoid density per mitochondrion that did not correlate as strongly with mitochondrial length (R^2 = 0.2855 for *Fmr1* KO vs 0.6214 for WT).

IV. Discussion

Here we define a mechanism by which local protein synthesis at FMRP granules regulates mitochondrial fission dynamics in neurons. We propose that FMRP granules serve as platforms for local translation of MFF at the mitochondrial midzone to enable regulated control of mitochondrial fission (Fig. 6.6L). Synthesis of MFF at the mitochondrial midzone would provide the advantage of locally increasing protein concentration without affecting other nearby mitochondria, enabling organelle-specific control of mitochondrial fate throughout neurons. Our data indicate that multiple factors converge to orchestrate this highly precise, yet dynamic positioning of FMRP granules around mitochondria. Endolysosomal vesicles were frequently found juxtaposed with FMRP granules and mitochondria. Such vesicles influence the nanoscale spacing of ribosome-rich FMRP granules around mitochondria, and functionally contribute to

mitochondrial fission through Rab7 GTP hydrolysis. Thus, we propose that the roles for endolysosomes in RNA granule organization (Cioni et al., 2019; Liao et al., 2019; Schuhmacher et al., 2023) and mitochondrial fission (Y. C. Wong et al., 2018) are part of the same process that maintains mitochondrial form in neurons. We also find clusters of ribosomes in close association with FMRP, the ER, and mitochondrial structures that resemble fission intermediates, suggesting that local protein synthesis is coordinated with ER-mediated mitochondrial fission in neurons. Recent ultrastructural characterization of axon branches supports this idea by revealing that the ER, ribosomes, vesicles, and microtubules are locally concentrated at mitochondrial constrictions during fission (Nedozralova et al., 2022). Further, our live-imaging reveals that FMRP granules are spatially coordinated with mtDNA and dynamically enriched at sub-organellar regions of mitochondria on a timescale of seconds to minutes. We envision that FMRP granules, the ER, and vesicles form inter-organelle contacts with mitochondria that function synergistically with intramitochondrial factors to enable precise spatiotemporal control of translation and mitochondrial dynamics throughout axons and dendrites.

Studies investigating mitochondria in models of Fragile X Syndrome have repeatedly found that mitochondrial function and dynamics are compromised in neurons upon loss of FMRP, but it has been unclear how FMRP granules direct translation to promote mitochondrial homeostasis. We anticipate that a mitochondrion could carry or recruit an FMRP granule with mRNAs encoding multiple proteins, and locally synthesize those proteins when and where they are needed. This idea is supported by our observations that many nuclear-encoded transcripts related to mitochondrial form and function overlap with FMRP on mitochondria and that FMRP granules are actively transported with mitochondria. Disrupting this mechanism via FMRP loss-of-function would dysregulate many mitochondrial pathways, and differentially affect individual mitochondria depending on the local organization of RNAs and ribosomes. Our data demonstrate that mitochondrial DNA organization is disrupted upon loss or reduction of FMRP levels. We propose that translation at FMRP granules is locally orchestrated with mitochondrial DNA replication and mitochondrial fission to ensure that DNA is evenly distributed throughout the mitochondrial network. However, mitochondrial DNA homeostasis depends on efficient control of mitochondrial fusion (Silva Ramos et al., 2019), which is also regulated by FMRP (M. Shen et al., 2019), suggesting that FMRP granules regulate multiple aspects of mitochondrial dynamics to ensure proper mtDNA organization in

neurons. Since mtDNA encodes proteins critical for mitochondrial respiration, disrupting DNA organization could cause some of the known metabolic phenotypes in animals lacking FMRP. Therefore, our characterization of FMRP-mitochondria interactions provides a framework to understand the local regulation of mitochondrial function by FMRP and the diverse mitochondrial phenotypes observed in models of Fragile X Syndrome.

V. Methods

Plasmids

The following plasmids were used: mito-DsRed2 (gift from T. Schwarz, Harvard Medical School), EGFP-FMRP (gift from G. Bassell, Emory University), GFP-POLG2 (gift from W. Copeland, National Institutes of Health), Halo-FMRP (subcloned from EGFP-FMRP into pFN21A-HaloTag-CMV vector from Promega), COX8A-BFP (Goldsmith et al.(Goldsmith et al., 2022)), LAMP1-Halo (Gallagher and Holzbaur(Gallagher & Holzbaur, 2023)), GFP-MFF (Addgene, 49153), GFP-RAB7 (Addgene, 12605), GFP-RAB7 T22N (Addgene, 12660), RFP-RAB5 (Addgene, 14437), EGFP-DRP1 (subcloned from pcDNA 3.1-Drp1 [Addgene, 34706] into pEGFP-C1 vector), pCRISPRia-vs2 ((Horlbeck et al., 2016); Addgene 84832), PGK 4xMito-mEmerald (Addgene, 200430), pUbC-OsTIR1-myc-IRES-scFv-sfGFP (Addgene, 84563), AID-SunTag-MFF (subcloned from GFP-MFF, MFF cDNA clone [Transomic BC000797], and pUbC-FLAG-24xSuntagV4-oxEBFP-AID-baUTR1-24xMS2V5-Wpre [Addgene, 84561] into pEGFP-N1 vector with EGFP removed), EGFP-TWINKLE (subcloned from TWINKLE-APEX2-V5 [Addgene, 129705] into pEGFP-N1 vector), and EGFP-TFAM (subcloned from pCellFree_G03 TFAM into pEGFP-N1 vector).

Antibodies

The following antibodies were used for immunocytochemistry (ICC), western blot (WB), proximity ligation assay (PLA), and DNA-PAINT: anti-FMRP (Millipore, MAB2160) at 1:500 for ICC and WB, anti-HSP60 (Sigma-Aldrich, SAB4501464) at 1:100 for ICC, anti-puromycin (Millipore, MABE343) at 1:250 for PLA, anti-puromycin Alexa Fluor 647 conjugate (Millipore, MABE343-AF647) at 1:250 for ICC, anti-MFF (Proteintech, 17090-1-AP) at 1:1000 for ICC and PLA, anti-RPS3A (ThermoFisher, 14123-1-AP) at 1:500 for ICC, anti-

Neurofilament Heavy Chain (Aves Labs, NHF) at 1:2,000, anti-α/β tubulin (Cell Signaling, 2148S) at 1:1000 for WB, anti-TOM20 (Proteintech, 11802-1-AP) at 1:100 for DNA-PAINT. The following secondary antibodies were used: Alexa Fluor 488 goat anti-rabbit IgG (H + L) (Invitrogen, A11034) at 1:1000 for ICC, Alexa Fluor 594 goat anti-mouse IgG (H + L) (Invitrogen, A11032) at 1:1000 for ICC, Alexa Fluor Plus 647 goat anti-mouse IgG (H + L) (Invitrogen, A32728), at 1:1000 for ICC, IRDye 680RD donkey anti-rabbit IgG (LI-COR, 926-68073) at 1:20,000 for WB, IRDye 800CW donkey anti-mouse IgG (LI-COR, 926-32212) at 1:20,000 for WB, docking-strand-conjugated secondary anti-rabbit antibody (docking strand 2, Massive Photonics) at 1:100 for DNA-PAINT, and docking-strand conjugated GFP nanobody (docking strand 3, Massive Photonics, Germany) at 1:100 for DNA-PAINT.

Human iPSC and i³Neuron culture

Human WTC11 iPSCs that harbor a doxycycline-inducible NGN2 transgene at the AAVS1 locus and stably express dCas9-BFP-KRAB were a gift from M.Ward at the National Institutes of Health and have been previously described(Fernandopulle et al., 2018). iPSCs were cultured on dishes coated with hESC-qualified Matrigel (Corning) and fed daily with Essential 8 medium (ThermoFisher). iPSCs were differentiated into i³Neurons following a previously described protocol (Fernandopulle et al., 2018). Following differentiation, i³Neurons were cryo-preserved in i³Neuron media (BrainPhys Neuronal Medium [StemCell] supplemented with 2% B27 [Gibco], 10ng/mL NT-3 [PeproTech], 10ng/mL BDNF [PreproTech], and 1µg/mL Laminin [Corning]) with 10% DMSO added. i³Neurons (180,000 to 200,000 cells) were plated on 35-mm glass-bottom imaging dishes (MatTek, P35G-1.5-20-C) that were precoated with poly-L-ornithine (Sigma-Aldrich, P3655) overnight at 37°C. i³Neurons were cultured for 21-22 days in 5% CO_2 at 37°C prior to fixation or transfection. Every 3-4 days, 40% of the media was replaced with fresh culture media.

Generation of FMR1 CRISPRi iPSCs

Human iPSCs and i³Neurons with knockdown of FMRP via CRISPR interference (CRISPRi) were made using previously described methods for gene knockdown in this system (Aiken & Holzbaur, 2023; Tian et al., 2019). Briefly, the FMR1-targeting guide RNA sequence GGCGGGCCGACGGCGAGCGC was flanked with BlpI and BstXI cut sites and ligated into BlpI/BstXI-digested pCRISPRia-vs2 using NEB Quick

Ligase (New England Biolabs; M2200S). Guide incorporation was verified by sequencing. The sgRNA guide plasmid was then packaged into lentivirus and transduced into iPSCs. HEK293T cells were transfected with sgRNA plasmid, psPAX2 (HIV pol+gag), and pCMVVsv-g. Eight hours after transfection, media was replaced with fresh media supplemented with ViralBoost (Alstem; VB100). Forty hours later, HEK293T media was collected, filtered, and centrifuged with Lentivirus Precipitation Solution (Alstem; VC100) to isolate viral pellet. The virus-containing pellet was resuspended in E8 media with ROCK inhibitor, aliquoted, and frozen at -80C. Resuspended virus was then added to iPSCs and incubated together for two days. Virus-infected iPSCs were then selected for with puromycin (Takara; 631305) for four days, with fresh media added each day. iPSCs were then collected, cryo-preserved, and differentiated into i^3Neurons as described above.

Primary neuron culture

Embryonic day 18 Sprague Dawley rat hippocampal neurons were obtained from the Neurons R Us Culture Service Center at the University of Pennsylvania. Cells (live imaging, 220,000 cells on 20-mm glass; fixed imaging, 150,000 cells on 20-mm glass; proximity ligation assay, 110,000 cells on 7-mm glass) were plated in 35-mm glass-bottom dishes (MatTek, P35G-1.5-20-C or P35G-1.5-7-C) that were precoated with 0.5 mg/ml poly-L-lysine (Sigma-Aldrich, P1274). Cells were initially plated in Attachment Media (MEM supplemented with 10% horse serum, 33 mM D-glucose, and 1 mM sodium pyruvate). After 5 hours, Attachment Media was replaced with Maintenance Media (Neurobasal [Gibco] supplemented with 33 mM D-glucose, 2 mM GlutaMAX (Invitrogen), 100 units/ml penicillin, 100 mg/ml streptomycin, and 2% B-27 [ThermoFisher]). On the following day, cytosine arabinoside (1 µM) was added to the cultures to prevent proliferation of non-neuronal cells. Neurons were maintained at 37°C in a 5% CO_2 incubator for 6-12 days prior to transfection or fixation.

Fmr1 KO (Strain #003025) and C57BL/6J (Strain #000664) mice were obtained from The Jackson Laboratory. All experiments followed protocols approved by the Institutional Animal Care and Use Committee at the University of Pennsylvania. Mouse cortex from C57BL/6J (WT) embryos of either sex or a mixture of hemizygous male *Fmr1* KO and homozygous female *Fmr1* KO embryos was dissected in 1X

HBSS (Gibco) at day 15.5. Cortical neurons were isolated by digestion with 0.25% Trypsin and trituration through a pipette tip. Cells were plated and cultured as described for rat hippocampal neurons, except that Attachment Media and Maintenance Media were supplemented with 37.5 mM NaCl.

HeLa cell culture

HeLa-M (A. Peden, Cambridge Institute for Medical Research) cells were maintained in DMEM (Corning, 10- 017-CM) supplemented with 1% GlutaMAX (ThermoFisher, 35050061) and 10% Fetal Bovine Serum. Cells were maintained at 37°C in a 5% CO_2 incubator. Cells were routinely tested for mycoplasma contamination with a MycoAlert detection kit (Lonza, LT07). Cells were authenticated by STR profiling at the DNA Sequencing Facility at the University of Pennsylvania.

Transfection

Rat hippocampal neurons and mouse cortical neurons were transfected after 6-12 days *in vitro* (DIV). Neurons were transfected with 0.5–1.5 µg total of plasmid DNA using 4 µL Lipofectamine 2000 Transfection Reagent (ThermoFisher). Neurons were incubated with lipid:DNA complexes for 45 minutes before replacing with conditioned media. Primary rodent neurons were incubated for 18-24 hours before fixation or live imaging. i^3Neurons (DIV18) were transfected with 1 µg of plasmid DNA using 4 µL Lipofectamine Stem (ThermoFisher). Neurons were then incubated with lipid:DNA complexes for 90 minutes before replacing with conditioned media. i^3Neurons were incubated for 72 hours before fixation or live imaging. HeLa cells were plated on uncoated 35 mm glass-bottom dishes (MatTek, P35G-1.5-20-C), transfected with 1.5 µg total of plasmid DNA using FuGene 6 (Promega), and incubated for 24 hours before live imaging.

Live imaging

For experiments using live-cell imaging of rat and mouse neurons, cells were imaged at 37°C in Hibernate E medium (BrainBits) supplemented with 2% B27 and 33 mM D-glucose. Neurons expressing Halo-tagged constructs were labelled with 100 nM Janelia Fluor 646-Halo ligand (Promega, GA1121) for 15 minutes followed by a 30 min washout prior to imaging. For experiments involving translational inhibition with cycloheximide or puromycin, neurons were treated with 50 µM cycloheximide (Sigma-Aldrich, 01810),

50 µM puromycin, or equivalent volume DMSO for 30 minutes prior to imaging and during image acquisition. For experiments involving microtubule depolymerization with nocodazole, neurons were treated with 2 µM nocodazole (Sigma-Aldrich, M1404-10MG) or equivalent volume DMSO for 30 minutes prior to imaging and during image acquisition. For experiments examining mitochondrial DNA, neurons were treated with 1:10,000 MitoTracker Deep Red FM (Thermo Fisher Scientific, M22426) and 1:200,000 SYBR Green I (ThermoFisher, S7563) for 30 minutes prior to imaging. For live-cell imaging of HeLa cells, the culture media was replaced with Leibovitz's L-15 media (Gibco, 11415064) supplemented with 1% Glutamax and 10% fetal bovine serum. For live-cell imaging of i^3Neurons, cells were imaged in Hibernate A medium (Brain Bits) supplemented with 2% B27, 10 ng/mL BDNF and 10 ng/mL NT-3. For FRAP experiments, single EGFP-FMRP granules were photobleached in hippocampal neurons using the 488-nm laser line for 8 photobleaching cycles with 9 ms per pixel. One pre-FRAP timepoint was collected and images were captured every second post-bleaching for 240 seconds. For SunTag experiments, hippocampal neurons were transfected with AID-SunTag-MFF, pUbC-OsTIR1-myc-IRES-scFv-sfGFP, COX8A-BFP and Halo-FMRP following the above protocol. 3-Indoleacetic acid (Sigma, I2886) was diluted in ethanol and added to neuron cultures overnight at a final concentration of 500 µg/mL to degrade pre-existing proteins containing auxin-induced-degron.

All live-cell imaging experiments were performed using a Perkin Elmer UltraView Vox spinning disk confocal on a Nikon Eclipse Ti Microscope, which is surrounded by a 37°C imaging chamber. All samples were given several minutes to equilibrate before imaging, with each dish imaged for a maximum of one hour. Videos were acquired at 1 frame/second for 5 minutes, 3 frames/second for 15 minutes, or 5 frames/second for 30 minutes. Experiments were imaged on either a Hamamatsu EMCCD C9100-50 camera or a Hamamatsu CMOS ORCA-Fusion (C11440-20UP). The EMCCD camera was used with Volocity Software [Quorom Technologies/PerkinElmer] and the CMOS camera was used with VisiView (Visitron).

DNA-PAINT super-resolution microscopy

Hippocampal neurons were plated in Lab-Tek II 8-well chambered coverglass (ThermoFisher, 155409) at a density of 10,000-15,000 cells per well. Chambers were precoated with poly-L-lysine and neurons were cultured as described above. Neurons in each well were transfected with 125 ng EGFP-FMRP following the above protocol and incubated for 24 hours. Neurons were fixed for 10 min using warm PBS with 4% paraformaldehyde and 4% sucrose. Blocking buffer (PBS containing 10% donkey serum, 0.1% Saponin, and 0.05 mg/mL sonicated salmon sperm single-stranded DNA [Stratagene, La Jolla, California]) was then added for one hour at 25°C before incubation with rabbit anti-Tom20 (see above) in blocking buffer for 1 h at 25°C. Neurons were then washed once with PBS and three times for 5 minutes in 1X Wash Buffer (Massive Photonics, Germany) before incubating with docking-strand-2-conjugated secondary anti-rabbit antibody and docking-strand-3-conjugated GFP nanobody. Neurons were then washed three times for 7 minutes with 1X Wash Buffer and twice with PBS.

Hippocampal neurons were imaged on a Nanoimager microscope (ONI, Oxford, UK) equipped with a 100x oil immersion objective (NA 1.45), 405-, 488-, 561- and 640-nm lasers, 498-551- and 576-620-nm band-pass filters in channel 1, 666-705-839 nm band-pass filters in channel 2, and a 840 Hamamatsu Flash 4 V3 sCMOS camera. Imager strands 2 and 3 conjugated to either Cy3B or ATTO655 were added at a concentration of 0.25 nM in Imaging Buffer (Massive Photonics, Germany). Images were collected at HiLo illumination angle with 100 ms exposure using a laser program alternating between 100 frames collected of the TOM20 channel and 200 frames for the EGFP-FMRP channel, repeated for a total of 25,000 frames. Localizations were generated and drift corrected by Nanoimager operating and analysis software (ONI) and exported as csv files for downstream processing with the following localization filter parameters: 300 photon minimum, 30 nm maximum localization precision in X and Y directions, 10-250 nm sigma in X and Y direction.

Correlative light and electron microscopy and cryo-electron tomography

Cryo-EM grids (Quantifoil 2/2, LF, 200 mesh) were glow-discharged, placed in 35-mm glass-bottom dishes (MatTek, P35G-1.5-20-C), and coated with poly-L lysine as described above. Rat hippocampal

neurons were plated at a density of 70,000-150,000 cells across 3-4 grids and cultured as described above. Cells were transfected with EGFP-FMRP and/or mito-DsRed2 at DIV5. Twenty-four hours post-transfection, grids were supplemented with 10 nm colloid gold beads and blotted from the back side before plunge-freezing using a Leica EM GP2 robot. Cryo-grids were imaged with a Leica EM Cryo-CLEM Cryo Light Microscope or Zeiss LSM900 Airyscan2 cryo-confocal microscope. Z-stack images were collected for individual cells with both bright-field and fluorescence channels, from which maximum intensity projection images were produced for subsequent correlative imaging.

Grids were transferred to a Titan Krios transmission electron microscope (Thermo Fisher) for tomography, which was operated at 300 kV acceleration voltage, equipped with a post-column BioQuantum energy filter and a K3 direct electron detector (Gatan). Full-grid montages were captured at 82× magnification to identify cells of interest. Each cell was further imaged at 470× magnification to obtain maps covering a grid square, which were used for correlation with fluorescence images using CorRelator(J. E. Yang et al., 2021) program. The regions of interest were located by the EGFP fluorescence signal overlaid on cryo-EM maps, and the candidate targets were further imaged at 4800× and 19500× magnifications, at which features of mitochondria could be clearly recognized. The targets for data collection were selected at the interface between the EGFP fluorescence spot and nearby mitochondria. Tilt series were collected at 33000× magnification, with a calibrated pixel size of 2.65 Å, following the dose-symmetric scheme, spanning from -60° to 60° with 3° increment. Images were recorded with an electron dose rate of 40 e^-/pixel/s. Each tilt was exposed for 0.45 s, which was fractionated into 5 movie frames, resulting in an accumulative dose of 105 $e^-/Å^2$ for each tilt series. To boost the contrast of cellular features, the Volta phase plate was used during data collection. The defocus range of the images was -1 to -3 μm.

Immunocytochemistry

Hippocampal neurons and i^3Neurons were fixed for 10 min using warm PBS with 4% paraformaldehyde and 4% sucrose. Cells were washed three times with PBS, permeabilized with 0.2% Triton X-100 in PBS for 15 minutes, and washed three times with PBS. Cells were blocked for 1 hour in blocking solution (5% goat serum and 1% BSA in PBS) and incubated overnight at 4C with primary

antibodies diluted in blocking solution. Cells were then washed three times with PBS, incubated with secondary antibodies diluted in blocking solution, and washed three more times. Neurons were imaged using the spinning disk confocal setup described above, with Z-stacks collected at 200-nm step-size.

Puromycylation assay

Hippocampal neurons were transfected with mito-DsRed2 and EGFP-FMRP following the above protocol. After 24 hours, neurons were treated with 2 µM puromycin for 10 min then fixed and permeabilized according to the immunocytochemistry protocol. Neurons were incubated with anti-puromycin Alexa Fluor 647 conjugate (see above) for 16 hours at 4°C, washed 3 times with PBS, and imaged using a Perkin Elmer UltraView Vox spinning disk confocal, as described above, with Z-stacks collected at 200-nm step-size. Puromycin enrichment for EGFP-FMRP was defined as overlap with a puromycin-positive puncta. For experiments involving translational inhibition with cycloheximide, neurons were treated with 50 µM cycloheximide or equivalent volume DMSO for 30 minutes prior to the addition of puromycin.

Single-molecule RNA FISH

Custom single-molecule RNA-FISH probes with Quasar 670 dye were designed against the human mRNA coding sequences for each gene using the Stellaris Probe Designer (Biosearch Technologies). The pre-designed human GAPDH with Quasar® 670 Dye (Biosearch Technologies, SMF-2019-1) was used as a control. DIV21 i^{3}Neurons were fixed with 4% paraformaldehyde in PBS for 10 min at room temperature and washed three times with PBS. Neurons were stored in 70% ethanol at 4°C for up to two weeks. Neurons were then washed with Wash Buffer (2X SSC [20X SSC (Corning 46-020-CM)] and 10% formamide diluted in Nuclease-free water [ThermoFisher, BP561-1]) for 5 minutes. Pools of Quasar 670-conjugated FISH probes at 250 nM were combined with anti-FMRP and anti-HSP60 antibodies (see above) in Hybridization Buffer (2X SSC solution containing 5% dextran sulfate [Sigma-Aldrich, D8906], and 10% formamide diluted in Nuclease-free water) and hybridized to cells for 16 hours at 37°C. Neurons were then washed in Wash Buffer for 30 min at 37°C to remove unbound probes and incubated in Wash Buffer with secondary antibodies (see above) for 30 min at 37°C. Neurons were then washed 3 times in 2X SSC buffer for 5 minutes and mounted in GLOX Buffer (2X SSC solution containing 10 mM Tris-HCl pH 8.0, 0.4% glucose,

0.5 mg/mL glucose oxidase [Sigma-Aldrich, G0543], and 470 U/mL catalase [Sigma-Aldrich, C3155]). Neurons were imaged using a Perkin Elmer UltraView Vox spinning disk confocal, as described above, with Z-stacks collected at 200-nm step-size.

Proximity Ligation Assay

Hippocampal neurons were transfected with COX8A-BFP and EGFP-FMRP following the above protocol. After 24 hours, neurons were treated with 2 µM puromycin for 10 min, fixed in PBS containing 4% paraformaldehyde and 4% sucrose for 10 min at room temperature, washed 3 times in PBS, permeabilized for 15 minutes in PBS with 0.2% Triton X-100, and washed with PBS. Newly synthesized proteins were detected using Duolink In Situ PLA Mouse/Rabbit kit with red detection reagents (Sigma-Aldrich, DUO92101-1KT) according to manufacturer's protocol with a mouse anti-puromycin antibody in combination with a rabbit anti-MFF antibody (see above for details). Neurons were imaged using a Perkin Elmer UltraView Vox spinning disk confocal, as described above. Z-stacks were collected at 200-nm step-size. PLA puncta were then manually counted and scored for overlap with EGFP-FMRP or COX8A-BFP.

Immunoblotting

Neurons were washed twice with ice-cold PBS and lysed with ice-cold RIPA buffer (50mM Tris-HCl, 150mM NaCl, 0.1% Triton X-100, 0.5% sodium deoxycholate, 0.1% SDS, 2x Halt Protease and Phosphatase inhibitor). Cells were snap frozen in liquid nitrogen and incubated in RIPA buffer for 30 min on ice. Samples were then centrifuged for 10 min at 17,000 x g. The protein concentration of the supernatant was determined by BCA assay, then samples were denatured in sample buffer containing SDS at 95° C. Samples were analyzed by SDS-PAGE and transferred onto PDVF Immobilon FL membranes (Millipore). After drying for 1 hour, membranes were rehydrated in methanol and stained for total protein (LI-COR REVERT Total Protein Stain). Following imaging of total protein, membranes were de-stained with 0.1M NaOH supplemented with 30% Methanol, blocked for 1 hour in EveryBlot Blocking Buffer (Bio-Rad), and incubated overnight at 4 °C with primary antibodies diluted in Blocking Buffer with 0.2% Tween-20. Membranes were washed three times for 5 min in 1xTBS Washing Solution (50 mM Tris-HCl pH 7.4, 274 mM NaCl, 9 mM KCl, 0.1% Tween-20), incubated in secondary antibodies diluted in Blocking Buffer with

0.01% SDS for 1 h, and washed three times for 5 min in Washing Solution. Membranes were imaged using an Odyssey CLx Infrared Imaging System (LI-COR). Band intensities were measured in Image Studio (LI-COR).

Fraction of FMRP on mitochondria

To quantify the number of endogenous FMRP granules contacting mitochondria in i^{3}Neurons and rat hippocampal neurons, we generated max projections of the mitochondria and FMRP channels in ImageJ. Regions containing only neurites were selected from these max projections. We then converted the area for FMRP and mitochondria to binary masks using the Pixel classification module of Ilastik, a machine-learning based image segmentation program (Berg et al., 2019). The masked images of FMRP and mitochondria were then overlayed and scored for overlap in ImageJ. To quantify the number of EGFP-FMRP granules contacting mitochondria, granules were manually counted and scored for overlap with mitochondria. For presentation purposes, sections of individual neurons were “straightened” using the Straighten command in ImageJ.

DNA-PAINT

Mitochondria localizations were Voronoi-segmented and clustered based on a minimum Voronoi area of 5,476 nm^2 and minimum of 15 localizations using a custom-made MATLAB code. Mitochondria clusters with area less than 0.110 µm^2 were considered non-specific background clusters and discarded. FMRP localizations were Voronoi-segmented and clustered based on a minimum Voronoi area of 548 nm^2 and minimum of 10 localizations. FMRP clusters with area less than 0.018 µm^2 were considered non-specific background clusters and discarded. Images surrounding mitochondria in neuronal processes were cropped and used for downstream analysis.

A custom colocalization analysis was performed using MATLAB (Github: https://github.com/LakGroup/Data_Analysis_Software_Fenton_etal) on the Voronoi-segmented data. The mitochondria channel was used as ‘reference’ channel, and the FMRP channel as the ‘colocalization’ channel. The colocalization analysis determined the overlap between the reference and colocalization clusters, and they were considered to colocalize when there is overlap between them. This analysis split

the data of the colocalization (FMRP) channel into two subsets: FMRP that is localized within a mitochondrion, and FMRP that is localized outside mitochondria. In practice, an initial search was performed to find reference clusters with colocalization clusters in their vicinity, without limiting the number of colocalization clusters associated with a reference cluster, and without limiting the number of reference clusters a colocalization cluster was associated with. This was performed to speed up calculations, and achieved by making a low-resolution polygon out of the reference clusters, and then isometrically enlarging them with 5 pixels (i.e., 585 nm). Any colocalization cluster found within this region was then associated to a reference cluster and considered in further steps of the colocalization analysis. The second step in this colocalization analysis described the reference clusters that have colocalization clusters associated to them as high definition alphaShape objects (a polytope that is a subset of the Delaunay Triangulation of the clusters and includes all localizations in the cluster, but also describe holes present in the clusters). The individual localizations of any colocalization cluster that were associated to a reference cluster were then evaluated to be inside or outside that reference cluster. Colocalization clusters with localizations inside a reference cluster were considered colocalized, whereas colocalization clusters without localizations inside a reference cluster were not. This separated the colocalization clusters in two groups on which the different metrics (area, distance to mitochondrion, and circularity) were calculated.

The area of the individual FMRP clusters was calculated from their alphaShape rendering, as well as their perimeter. The circularity of the clusters was then obtained by applying the following formula: $Circularity = \frac{4 \times \pi \times Area}{Perimeter^2}$, which is 1 for a perfect circle and near 0 for highly non-circular shapes. To measure the distance from FMRP to mitochondria for FMRP clusters that do not make mitochondrial contact, we determined which 10 mitochondrial clusters were closest to the FMRP cluster and then calculated the border-to-border distance (FMRP to mitochondrion) between these. The lowest distance between any of these results is reported.

FMRP-mitochondria contact analysis over time

FMRP-mitochondria contacts were determined by manually drawing a line along the length of an axon or dendrite from a confocal video. A kymograph was then generated using the Multiple Kymograph

plugin for ImageJ. Tracks of individual FMRP granules in contact with mitochondria were manually traced in ImageJ to determine contact duration and displacement. Motile FMRP granules (anterograde or retrograde) were defined by a net displacement ≥5 μm while non-motile granules were defined by a net displacement <5 μm.

Normalized position along mitochondria

The positioning of FMRP granules or MFF puncta along mitochondria was measured by manually drawing a line along the length of an axon or dendrite from a confocal video. A kymograph was then generated in ImageJ and used to determine the ends of each mitochondrion. The location of each FMRP granule or MFF puncta in contact or within 1 micron distance from each mitochondrion was recorded and used to determine the distance to both mitochondrial ends. The distance from the proximal mitochondrial end was then divided by the mitochondrial length to determine the relative position along the mitochondrion, with ends normalized to 0 and 1.

Determination of fission events

Mitochondrial fission was defined as any event that showed clear division of a single mitochondrion into two distinct mitochondria that display uncoupled movement following division. A fission event was considered positive for a marker if the relevant marker was within 500 nm distance of the fission location in the frame before fission occurs. To determine when a marker appeared at a fission site before fission, a circular region of interest (ROI) with 1 μm radius was drawn around the fission site. The number of seconds preceding fission while each marker remained within the ROI was reported. Fission events in which both FMRP and DRP1 or MFF puncta are present in the ROI at the beginning of the recording were excluded from analysis. The position of mitochondrial fission was measured by manually drawing a line along the length of the mitochondrion in the frame before fission.

To measure fission rates, regions of rat hippocampal neuron dendrites were selected in which individual mitochondria were easily resolvable and did not leave the focal plane. The dendritic mitochondrial network was then segmented using Ilastik to determine total mitochondrial area. To account for changes in mitochondrial density over time, the final mitochondrial area was determined by averaging the areas in the

region of interest for the first and last frames of the video. Fission rates are indicated as the number of fission events occurring over 30 minutes per square micron of mitochondria.

FISH

To quantify the number of mRNA puncta in contact with FMRP granules and mitochondria we generated max projections of each channel in ImageJ. Regions containing only neurites were selected from these max projections. We then converted each channel to a binary mask using Ilastik, as described above. The masked images for mRNA puncta and FMRP were then overlayed and scored for overlap in ImageJ. For mRNA puncta that overlap with FMRP, the segmented FMRP granule was scored for overlap with mitochondria. For presentation purposes, sections of individual neurons were “straightened” using the Straighten command in ImageJ.

FRAP

The mean fluorescence intensity was measured for each ROI containing an EGFP-FMRP granule. The ROI was moved if/when each granule moved out of the initially determined ROI. The intensities of the ROIs were normalized such that the pre-bleached intensity is 1 and the first photobleached frame is 0.

Tomogram reconstruction and subtomogram averaging

The movie frames of each tilt angle were aligned to correct the beam-induced motion and assembled into tilt-series stacks in Warp (Tegunov et al., 2021). Initial tilt-series alignment was performed with EMAN2 (Chen et al., 2019) software and the tomograms were reconstructed with a binning factor of 4. The ribosome particles were manually picked with e2spt_boxer.py and an initial model was calculated using e2spt_sgd.py which clearly resolved the features of large and small subunits of the ribosome. The particle orientations were refined stepwise using e2spt_refine.py with particles at 4× and 2× binning levels. To achieve the best possible resolution, we made use of the multiparticle refinement approach of Warp-Relion-M pipeline (Burt et al., 2021). The tilt series were re-aligned with autoalign_dynamo using the 10 nm gold beads as fiducials. Tomograms were reconstructed using Warp with deconvolution filter applied to facilitate visualization and particle picking in IMOD (Kremer et al., 1996). A total of 378 particles were picked from 3 tomograms. Subtomograms were first reconstructed with a binning factor of 4. A round of 3D

refinement in Relion-3.1 (Scheres, 2012) produced a reconstruction at 30 Å resolution, estimated by the Fourier shell correlation cut-off of 0.143. The unbinned subtomograms were then reconstructed and fed to M for multiparticle refinement (Tegunov et al., 2021), which resulted in a density map at 27 Å resolution (Fig. 6.4B,F).

Tomogram postprocessing, segmentation, and annotation

Due to multiple steps of transfer, the sample got some surface contamination by crystalline ice. These dense features produced some smeared artifacts in multiple slices of the tomogram. To remove these artifacts, a mask covering the ice density was created in IMOD which was used to reproject the density to tilt-series images for signal subtraction using the Masktorec program(Fernandez et al., 2016). Clean tomograms were reconstructed with the signal-subtracted tilt images and contrast-enhanced with the nonlinear anisotropic diffusion filter in IMOD. The tomogram was segmented manually using IMOD and the density for each feature was cropped out using the imodmop function to facilitate 3D visualization and analysis. The subtomogram average map of the ribosome was placed back into the tomogram according to the original particle position and angular information using ArtiaX(Ermel et al., 2022). The figures were rendered with either IMOD or Chimerax (Goddard et al., 2018).

Postprocessing of correlation

The bright-field light microscopy images were first correlated with the 470× cryo-EM map using the hole centroid as fiducials. The same transformation matrix was applied to the fluorescence channel images. For registration of other cryo-EM images at higher magnifications, the correlation was performed solely between EM images at adjacent magnifications, from which the transformation matrix was derived and applied to fluorescence images for stepwise correlation. The ice contamination served as fiducials for correlating EM images between 470× and 4800× magnifications, and the 10 nm gold colloid beads were used for higher magnifications. The tomogram slices were extracted and correlated with the 19500× EM images using the structural features as fiducials, which allowed the annotation of tomogram features with fluorescence signals.

CHAPTER 7: DISCUSSION

I. Regulation of mitochondrial transport complexes

My finding that TRAK2 links kinesin-1 and dynein-dynactin within a single complex indicates that the regulation of directional transport occurs through the formation of this co-complex. While I was the first to demonstrate the formation of a multi-motor TRAK2 co-complex, this result has been independently validated for both TRAK1 and TRAK2 using purified proteins (Canty et al., 2023). The experiments in Canty et al. align nicely with my key findings that TRAK2 activates kinesin-1 and dynein-dynactin, but there are slight differences between the studies and details that are important to consider. For instance, all TRAK-kinesin-dynein co-complexes examined thus far move exclusively toward the microtubule plus-end (Chapter 2) (Canty et al., 2023). Canty et al. went on to show that adding excess kinesin-1 stalk during *in vitro* motility experiments reduced the amount of TRAK-dynein motility. They concluded that kinesin-1 binding to TRAK prevents dynein from being activated, meaning that dynein is always an inactive passenger within a multi-motor complex, while kinesin is excluded during dynein-mediated transport. This model does not fully agree with my experiments showing that knockdown of kinesin-1, dynein, or dynactin negatively influences TRAK2 transport by the opposing motor.

However, my experiments examined full-length TRAK2 in cell lysate, while Canty et al. examined purified TRAK fragments lacking the C-terminal half of the protein (Canty et al., 2023). I anticipate that the inclusion of the C-terminal half of TRAK2 in my experiments could explain these differences in results. Several dynein activating adaptors contain regions that fold back on the coiled-coil region that binds dynein-dynactin to prevent the formation of active motor complexes (Ali et al., 2023; K. Singh et al., 2023; Terawaki et al., 2015). TRAK2 also folds back on itself in a head-to-tail manner that regulates motor binding (van Spronsen et al., 2013). The association of kinesin-1 or dynein-dynactin could bias TRAK2 to remain in an open conformation that is more likely to interact with the opposing motor. Such a mechanism has recently been demonstrated for HOOK3, a motor adaptor that forms a co-complex with the kinesin KIF1C and dynein-dynactin (Kendrick et al., 2019), and displays co-dependence for these opposing motors (Ali et al., 2023). KIF1C binding to HOOK3 relieves the folded-back autoinhibited state to allow HOOK3 to bind

and activate dynein-dynactin (Ali et al., 2023). Thus, it is possible that assays with full-length TRAK2 display motor co-dependence because they are sensitive to this form of autoinhibition, while experiments with truncated fragments (those ending near the Spindly motif) circumvent this regulatory feature entirely.

Currently, it is not clear how often multi-motor co-complexes form and associate with mitochondria within cells. From my work and others, the fraction of TRAK-motor complexes that form with both kinesin and dynein is considerably lower than those containing a single motor. While this result argues that multi-motor complexes do not occur frequently, additional factors on the mitochondrial surface could favor co-complex formation as a means to control mitochondrial transport. Future super-resolution imaging experiments that map the distribution of TRAKs and motors on mitochondria will be needed to decipher the frequency of co-complex formation. Such experiments could address many critical questions regarding the composition and organization of mitochondrial transport complexes. For example, where do motor complexes reside on mitochondria? A recent study examining mitochondrial transport in *C. elegans* reported that kinesin-1 localizes to the leading edge of axonal mitochondria in order to drive anterograde transport (Y. Wu et al., 2024). In this system, the polarized localization of kinesin-1 is driven by RIC-7, a mitochondria-associated protein that is necessary for mitochondrial transport in *C. elegans* (Rawson et al., 2014). These results suggest that spatial clustering of motor complexes could be an essential part of mitochondrial transport in neurons. However, this polarized localization has not been demonstrated outside of *C. elegans* and RIC-7 has no obvious homolog in vertebrates (Rawson et al., 2014; Y. Wu et al., 2024), making it unclear whether a similar transport mechanism exists in humans.

MIRO proteins are known to oligomerize *in vitro* (Chapter 3) (K. P. Smith et al., 2020) and form nanoclusters on the mitochondrial surface (Modi et al., 2019). The role for MIRO clustering on mitochondria and its relevance for mitochondrial transport remains unexplored. One possibility is that MIRO clusters facilitate the clustering of TRAK proteins together into larger structures that favor efficient transport by recruiting multiple motors. This notion of motor clustering is supported by evidence of dynein clustering on phagosomes to drive retrograde transport (Rai et al., 2016). Additionally, recent structural work has revealed that multiple copies of activating adaptors can scaffold the dynein-dynactin complex (Chaaban &

Carter, 2022). Thus, clustering of MIRO and TRAK proteins has the potential to regulate mitochondrial transport by locally concentrating multiple contact points between the mitochondrial surface and microtubule motors. It will be important to determine how MIRO/TRAK proteins organize into clusters over time, how clustering affects the stoichiometry of motor complexes, and what the impact of clustering is on mitochondrial transport in cells.

Another point of consideration is how motor complexes are coordinated across a whole mitochondrion. While MIRO proteins exist as discrete clusters on mitochondria, each individual mitochondrion contains many clusters spread across its entire surface (Modi et al., 2019), raising the possibility that multiple TRAK-MIRO-motor complexes are active at different locations on a single mitochondrion. Some form of cross-organelle communication is likely at play considering that it would be inefficient to regulate individual motor complexes without also coordinating motor activity across multiple contact points with microtubules. Further, MIRO clusters across mitochondria are dedicated to many mitochondrial functions, such as regulation of Ca^{2+} influx, cristae morphology, ER contacts, and actin-based tethering, as MIRO is a near-ubiquitous regulator of mitochondrial biology (Covill-Cooke et al., 2024; Eberhardt et al., 2020). These different MIRO functions are probably coordinated across distant MIRO clusters for each mitochondrion to synergistically facilitate mitochondrial dynamics. For example, mitochondria-ER contacts and actin-based tethering are thought to simultaneously promote mitochondrial fission (Chakrabarti et al., 2018; Coscia et al., 2023; Kleele et al., 2021; Manor et al., 2015). Cells also seem to tightly control the association of MIRO with TRAK proteins or MYO19 to efficiently coordinate actin- and microtubule-based dynamics (López-Doménech et al., 2018; Oeding et al., 2018). Mechanistically, it is unclear how this sort of cooperation of MIRO complexes across mitochondria would occur. However, one hint is that many MIRO interactors share a common binding interface on MIRO, a conserved hydrophobic pocket on the first ELM (Covill-Cooke et al., 2024). Thus, the availability of this MIRO interface for effector binding is a general feature of MIRO that could be tightly regulated in different clusters across mitochondria to simultaneously drive diverse mitochondrial functions.

Several other proteins deserve mention here for their role in the regulation of mitochondrial transport. Two Metaxin proteins (MTX1 and MTX2) were recently shown to be required for mitochondrial transport in *C. elegans* and human iPSC-derived neurons (Y. Zhao et al., 2021). MTX2 interacts with TRAK, MIRO, kinesin-1, and dynein, suggesting it is a core component of the anterograde and retrograde TRAK/MIRO transport complexes (Y. Zhao et al., 2021). In contrast, MTX1 seems to exclusively mediate mitochondrial transport toward the microtubule plus-end in *C. elegans* neurons by forming a complex with MTX2, MIRO, kinesin-1, and KLC (Y. Zhao et al., 2021). A distinct complex comprising MTX2, MIRO, and TRAK was proposed to mediate dynein-based mitochondrial transport in *C. elegans* neurons (Y. Zhao et al., 2021). These observations suggest that the presence of MTX1 in a mitochondrial transport complex excludes the association of TRAK proteins to specifically enable kinesin-based transport. This notion of distinct complexes containing either MTX1 and KLC or TRAK is intriguing with regard to previous observations that TRAK proteins and KLC do not interact in co-immunoprecipitation experiments (Glater et al., 2006; van Spronsen et al., 2013) and share the same binding site on kinesin-1 (Tan et al., 2023), yet certain KLC isoforms still localize to mitochondria (Khodjakov et al., 1998). I anticipate that binding of MTX1 and KLC to kinesin-1/MIRO/MTX2 physically excludes the binding of TRAK proteins. However, the interaction interface between Metaxins and these other proteins has not been defined, and will need to be investigated more thoroughly with biochemical and structural experiments.

Given the clear evidence for TRAK proteins in kinesin-based mitochondrial transport (Glater et al., 2006; Henrichs et al., 2020; López-Doménech et al., 2018; Stowers et al., 2002; van Spronsen et al., 2013), it is still not fully clear why there would be two separate complexes linking kinesin-1 to mitochondria. One advantage of the TRAK-motor complex is the potential to quickly recruit or activate dynein within the same motor complex, allowing a mitochondrion to rapidly switch between transport in different directions along the microtubule, as seen occasionally for axonal mitochondria (Hollenbeck & Saxton, 2005; Misgeld & Schwarz, 2017). In this way, TRAK-mediated transport could ultimately serve as a means to facilitate bidirectional transport. Conversely, MTX1-mediated mitochondrial transport would likely be biased away from transient dynein activation due to the lack of TRAK proteins in this complex, meaning that this complex could serve as a way to promote kinesin-based transport without any directional switching. The presence

of different adaptor complexes also allows for additional layers of regulation by upstream regulators. For example, the function of TRAK proteins is dictated by post-translational modifications, such as phosphorylation and O-GlcNAcylation (Chung et al., 2016; Pekkurnaz et al., 2014). MTX1 function could also be sensitive to post-translational modification, but in different ways than TRAK proteins, although this possibility remains unexplored. Thus, the combination of these two complexes could fine-tune the placement of mitochondria throughout neurons by ensuring that certain mitochondria move unidirectionally while others move bidirectionally in response to different signals.

II. Mutant kinesin-1 in neurodegeneration

The work described in Chapter 4 demonstrates that ALS-associated mutations in the kinesin-1 isoform KIF5A create a hyperactive motor protein that is toxic to neurons. While our study was the first to establish that these mutations impair KIF5A autoinhibition, cause distal accumulation, alter mitochondrial organization, and decrease neuron survival through a toxic gain of function, several other studies have also characterized the effects of these KIF5A mutations. Importantly, these studies include experiments similar to those described in Chapter 4 and come to the same conclusions that KIF5A$^{\Delta Exon27}$ accumulates distally to form aggregates in cells, undergoes reduced autoinhibition *in vitro*, and has toxic effects on neurons (Nakano et al., 2022; Pant et al., 2022; Soustelle et al., 2023). Further, expression of human KIF5A$^{\Delta Exon27}$ in *Drosophila* results in irregular mitochondrial distribution, altered neuromuscular junction morphology, impaired motor neuron neurotransmission, reduced locomotor function, motor neuron loss, and premature lethality (Pant et al., 2022; Soustelle et al., 2023). Human KIF5A$^{\Delta Exon27}$ also induces neuronal death when expressed in *C. elegans* (Soustelle et al., 2023), confirming the toxicity of the mutation across multiple animal and cell model systems. Together, these studies make a powerful argument for a toxic gain-of-function role of KIF5A$^{\Delta Exon27}$.

Still, many unanswered questions remain as to how the KIF5A$^{\Delta Exon27}$ mutation relates to the pathogenesis of ALS. Foremost among them is the question of which cellular and molecular phenotypes lead to neuron death. Mitochondrial dynamics are disrupted in neurons expressing mutant KIF5A, and

disrupted mitochondrial dynamics are thought to contribute to ALS pathology. However, kinesin-1 is responsible for the transport of many other cellular cargos, suggesting that neuronal dysfunction and death could stem from the combined dysregulation of multiple organelles, not just mitochondria.

Alternatively, intracellular trafficking defects associated with KIF5A$^{\Delta Exon27}$ could have minor consequences compared to other features of this mutant. All studies examining KIF5A$^{\Delta Exon27}$ thus far have reported that the motor accumulates distally in cells and forms large inclusions or aggregates (Nakano et al., 2022; Pant et al., 2022; Soustelle et al., 2023). Such propensity to aggregate may be central to the development of ALS pathology, as protein aggregation is a hallmark characteristic of ALS (Blokhuis et al., 2013). Then again, perhaps the multimerization of KIF5A$^{\Delta Exon27}$ is intrinsically linked to its autoinhibition. Motile KIF5A$^{\Delta Exon27}$ complexes appear brighter than KIF5A^{WT} and KIF5A$^{\Delta C\text{-}term}$ complexes in single-molecule experiments (Fig. 4.3) (Nakano et al., 2022; Pant et al., 2022), suggesting that KIF5A$^{\Delta Exon27}$ complexes contain multiple kinesin-1 dimers. The observation that the ΔExon27 mutation induces longer run lengths without affecting velocity is also consistent with a study showing that artificial scaffolds containing two kinesin-1 dimers produce longer run lengths than single kinesin-1 dimers, but move at the same speed (Rogers et al., 2009). KIF5A multimerization at the C-terminus could favor motor activation by sterically blocking the head-tail interactions that enable kinesin-1 autoinhibition (Coy et al., 1999; D. S. Friedman & Vale, 1999; Tan et al., 2023; Weijman et al., 2022). Thus, the presence of multiple kinesin-1 dimers within a complex could explain the altered motile properties of KIF5A$^{\Delta Exon27}$. Ultimately, a more thorough examination of intracellular transport, protein aggregation, and the links between the two is needed to understand how the properties of KIF5A$^{\Delta Exon27}$ could lead to ALS pathology.

Mutations in KIF5A have been linked to other neurodegenerative diseases, such as hereditary spastic paraplegia and Charcot-Marie-Tooth disease (Crimella et al., 2012; Y.-T. Liu et al., 2014). These diseases are peripheral neuropathies that progressively cause muscle weakness and wasting, similar to ALS. Unlike the mutations examined here, the vast majority of KIF5A mutations associated with HSP and CMT occur in the motor domain (Y.-T. Liu et al., 2014; Nicolas et al., 2018). One study examining the effect of an HSP-associated motor domain mutation on KIF5A-dependent neurofilament transport found

decreased transport flux, suggesting a reduction in KIF5A activity (L. Wang & Brown, 2010). Perhaps the molecular phenotype of KIF5A, either loss- or gain-of-function, correlates with disease pathogenesis. Future studies that systematically assess the effects of each disease-associated KIF5A mutation on motor function and cellular homeostasis will be needed to understand the reason these mutations cause a variety of neurodegenerative diseases.

III. Mitochondrial dysfunction in Fragile X Syndrome

Mitochondrial network abnormalities have repeatedly been observed across numerous animal and cell models of Fragile X Syndrome. Many studies characterizing mitochondrial defects in neurons lacking FMRP utilize therapeutic approaches that specifically target a single mitochondrial function or pathway of interest, such as ATP synthesis, mitochondrial fusion, or insulin signaling; these studies then examine the effectiveness of their strategy by assessing that particular mitochondrial phenotype and a functional readout, such as action potential frequency or behavioral test (Licznerski et al., 2020; Monyak et al., 2017; M. Shen et al., 2019). However, one pressing question is whether treatments that rescue specific phenotypes, such as mitochondrial ultrastructure or respiratory function, are sufficient to rescue all defects arising from a lack of FMRP. For example, is modulation of insulin signaling sufficient to restore mitochondrial DNA homeostasis, mitochondria-ER contacts, rates of fission, and rates of fusion? Is restoration of mitochondrial form and function sufficient to reverse non-mitochondrial phenotypes, such as synaptic defects, in animals lacking FMRP? Our finding that genetic manipulation of insulin signaling or PGC1-α is sufficient to restore both mitochondrial morphology and behavioral deficits in dFMRP mutant flies (Chapter 5), suggests that mitochondrial dysfunction may be upstream of synaptic dysfunction in this model. This notion is supported by prior studies showing that other mitochondria-specific treatments ameliorate behavioral and synaptic phenotypes in animal models of Fragile X Syndrome (Licznerski et al., 2020; M. Shen et al., 2019). However, FMRP binds and regulates the translation of hundreds of RNAs that are not directly related to mitochondria, including many genes that are directly related to synaptic biology (Ascano et al., 2012; Darnell et al., 2011; Jung et al., 2023; Miyashiro et al., 2003; Sawicka et al., 2019),

and the effects of FMRP on these pathways must be thoroughly examined in the context of altered mitochondrial function. Experimental testing of such possibilities would be difficult, time-consuming, and require comprehensive knowledge of the many mitochondrial and non-mitochondrial pathways affected by FMRP.

How then could any approach be sufficient for full phenotypic rescue in Fragile X Syndrome? Such a strategy must address all aspects of FMRP biology, which is likely only accomplishable through restoring the function of FMRP itself. Fortunately, there is some promise for restoring FMRP expression in Fragile X Syndrome. A recent study found that activating DNA repair pathways is sufficient to remove the CGG repeat expansion and restore FMRP expression in stem cells from Fragile X patients (H.-G. Lee et al., 2023). Another recent study shows promise for the use of anti-sense oligonucleotides in restoring FMRP expression (Shah et al., 2023). It will be interesting to see how these kinds of approaches targeting re-expression of FMRP translate to clinical trials in humans, and how advances in gene therapy aid these efforts.

IV. Local translation as a means to control neuronal mitochondria

The findings presented in Chapter 6 reveal a novel mechanism by which local translation is directly linked to the control of mitochondrial dynamics in neurons. This work provides an explanation for the close link between FMRP and mitochondrial morphology, but also raises many new questions about the specifics and generalizability of this mechanism. For example, why might neurons use local protein synthesis for mitochondrial fission? Local translation provides a means to modify the proteome in a way that is both spatially and temporally precise. Generally, it is thought that local translation enhances cellular processes by increasing local protein concentration within a spatially restricted region where a protein will carry out its function (Rangaraju et al., 2017). Over time, however, newly translated proteins will diffuse and spread out, raising the question of how precisely local translation can be matched to a specific cellular function. To my knowledge, the work described in Chapter 6 is the most direct link between local translation and function, as this mechanism: (1) occurs specifically at subregions of individual mitochondria, (2) involves rapid

recruitment of FMRP granules on a timescale of seconds to minutes, and (3) has an immediate functional outcome of mitochondrial fission.

A natural question is whether this kind of mechanism can be generalized to the translation of other proteins and mitochondrial functions. I intentionally selected the mRNAs for KIF5A, TRAK1/2, DHC, and p150^{Glued} in FISH experiments with the idea that components of the mitochondrial transport machinery could be locally translated to efficiently control the transport of mitochondria in neurons. This idea is supported by data showing that dynein cofactors p150^{Glued} and LIS1 are locally translated to promote retrograde transport of other organelles, such as signaling endosomes in distal parts of axons (Villarin et al., 2016). Intriguingly, a recent study examining the spatial organization of RNAs in individual cultured mouse hippocampal neurons found that KIF5A is the most abundant transcript in axons, while TRAK2 is the eleventh most abundant (G. Wang et al., 2020). Another study examining mRNA abundance in mouse retinal ganglion cells *in vivo* classified the mRNAs for KIF5A, DHC, and p150^{Glued} as having high abundance in axons (Jung et al., 2023). The high abundance of these RNAs strongly suggests that axonal functions related to these genes occur through local translation. Given my results that FMRP colocalizes with these RNAs on mitochondria and that reducing FMRP expression in neurons results in mitochondrial transport abnormalities (Yao et al., 2011), I propose that FMRP granules locally control the translation of the mitochondrial transport machinery to facilitate proper mitochondrial network organization in neurons. In theory, mitochondrial transport proteins could be translated at FMRP granules that are stably docked on specific mitochondria to selectively influence the transport of individual mitochondria, similar to how FMRP-associated MFF translation is matched to the fission of single mitochondria. Testing this theory however, will require experiments that directly visualize translation of TRAKs and motors while simultaneously tracking mitochondrial dynamics with high spatiotemporal resolution.

Another mitochondrial process that may utilize a similarly direct form of local translation in neurons is mitophagy, the clearance of damaged mitochondria. Mitophagy depends on PTEN-induced kinase 1 (PINK1), which acts as a molecular sensor for damaged mitochondria (Matsuda et al., 2010; Narendra et al., 2010). The mRNA for PINK1 was recently shown to associate with mitochondria for transport into axons

and dendrites of mouse neurons, where it is then translated locally to support mitophagy (Harbauer et al., 2022). PINK1 genetically interacts with FMRP in pathways affecting mitochondrial morphology in flies (Geng et al., 2023), and we find *PINK1* mRNA in mitochondria-associated FMRP granules (Chapter 6). Together, these findings suggest that FMRP plays a role in the translational control of PINK1 to coordinate the degradation of damaged mitochondria in distal parts of neurons. Even so, it is yet to be seen whether PINK1 translation occurs adjacent to certain mitochondria to initiate a highly localized induction of mitophagy, or whether PINK1 translation occurs throughout neurons as a more general way to maintain PINK1 levels in axons and dendrites.

More recent work from the Harbauer lab indicates that insulin signaling regulates the local translation of PINK1 to control mitophagy in axons (Hees & Harbauer, 2023). In this work, increased insulin signaling decreased the association of PINK1 mRNA to modulate PINK1 translation, and thus PINK1-dependent mitophagy in neurons (Hees & Harbauer, 2023). One takeaway from this study is that insulin signaling feeds into the regulation of local translation. Given our results that insulin signaling modulates mitochondrial abundance and morphology in the absence of FMRP (Chapter 5), and that FMRP granules facilitate local translation to efficiently promote mitochondrial dynamics in neurons (Chapter 6), I anticipate that insulin levels locally regulate translation to more broadly control mitochondrial dynamics in neurons. Protein synthesis, mitochondrial DNA replication, and fission are energetically demanding processes that require the coordinated action of many ATP-consuming enzymes. Thus, a neuron would benefit greatly from the ability to sense metabolites levels and facilitate translation-dependent mitochondrial dynamics only when local energy supply is sufficient. Our results suggest that insulin and FMRP are two major contributors to this form of regulation, but there are likely other factors, such as the local abundance of amino acids, that feed into translation-dependent control of mitochondria in neurons. Further work will be needed to understand how local control of metabolism and signaling cooperate with translation and other pathways to determine the spatiotemporal organization of mitochondria in neurons.

An additional point of consideration for the localized function of FMRP granules is how the composition of each granule relates to its function. FMRP is known to associate with other RNA-binding

proteins, ribosomes, and hundreds of mRNAs, yet studies examining the overlap of these factors in neurons revealed only partial colocalization with FMRP (Antar et al., 2004, 2005; El Fatimy et al., 2016), suggesting that different FMRP granules are compositionally distinct. Similarly, my experiments show that some FMRP granules mark sites of mitochondrial fission in neurons, but many FMRP granules do not exhibit this behavior or associate with mitochondria, indicating that there is some degree of selectivity for which FMRP granules regulate fission. These observations raise the possibility that individual FMRP granules are dedicated to regulating distinct functions within neurons. One appealing idea is that many RNAs related to one particular cellular function could be concentrated together within a granule and synthesized at the same time and place to carry out that function. For example, an FMRP granule that is designated for a role in mitochondrial fission could contain mRNAs for MFF and other fission-related proteins, such as Spire1C (Manor et al., 2015) or INF2 (Korobova et al., 2013), then initiate simultaneous synthesis of these proteins near the mitochondrial midzone to efficiently promote fission. Whether RNAs can be grouped according to function in this manner is not known, but it will be important to determine the contents of each RNA granule and how frequently certain RNAs are contained within the same granule. Future studies performing high-throughput spatial transcriptomics in neurons will be needed to shed light on the spatial association between many RNAs. Recently developed technology such as multiplexed error-robust fluorescence *in situ* hybridization (MERFISH) could address this question, as this technique has already been used to simultaneously examine the localization of thousands of RNA species in cultured neurons (G. Wang et al., 2020; Xia et al., 2019). Combining MERFISH with staining for RNA-binding proteins would provide a wealth of information regarding the composition of RNA granules that could be used to define which RNAs tend to associate in the same granules, providing critical insight into the relationship between RNA granule composition and function.

V. Mitochondrial DNA organization in neurons

One major finding of Chapter 6 is that FMRP granules are critical for the organization of mitochondrial DNA in neurons. Our data suggest that the distribution of mtDNA is facilitated by the precise spatiotemporal

coordination of organelles and local protein synthesis around a mitochondrion during fission. However, it is not clear how mtDNA replication, which happens inside mitochondria, is coordinated with the outer mitochondrial surface and other nearby organelles. Perhaps protein complexes that span both mitochondrial membranes link the organization of the mitochondrial matrix and outer surface to coordinate nucleoid-associated fission. One complex that could potentially perform this role is the MItochondrial contact site and Cristae Organizing System (MICOS), which spans the inner mitochondrial membrane and establishes mitochondrial cristae architecture by forming contacts between the inner and outer mitochondrial membranes (Colina-Tenorio et al., 2020). MICOS clusters are localized to cristae junctions and regions of mitochondria surrounding nucleoids, while depletion of the MICOS complex severely alters mitochondrial DNA organization (H. Li et al., 2016; J. Qin et al., 2020; Stephan et al., 2020). MICOS is also reported to interact with MIRO proteins on the outer mitochondrial membrane to regulate the formation of ER-mitochondria contact sites (Modi et al., 2019; J. Qin et al., 2020). Given these findings and the known role for ER-mitochondria contacts in mitochondrial division, it is conceivable that MICOS and MIRO could facilitate spatial coordination between mitochondrial DNA and other organelles. Another protein that could potentially fill this role is ATAD3A, a AAA-ATPase which resides in the inner mitochondrial membrane and has been shown to bind TFAM within the mitochondrial nucleoid and MFF on the outer mitochondrial membrane (T. Ishihara et al., 2022). Future studies will be required to elucidate the precise signaling by which intramitochondrial DNA organization is matched to mitochondrial contacts with other organelles.

There are still many open questions as to how the amount and distribution of mitochondrial DNA is controlled in neurons. A recent study from the Holzbaur lab used proteomics to characterize the cargos degraded by autophagy in neurons and found that mitochondrial DNA is a major cargo for neuronal autophagy (Goldsmith et al., 2022). This work indicates that autophagic turnover of mitochondria occurs continuously to control levels of mitochondrial DNA. A recent pre-print indicates that levels of mitochondrial DNA are kept low in axons (Hirabayashi et al., 2024). This work shows that most axonal mitochondria lack DNA and suggests that mitochondria lacking DNA are selectively trafficked into, and further along, axons than those with DNA (Hirabayashi et al., 2024). Combined, these results reveal that translational control of mitochondrial fission is just one of many pathways that regulate mitochondrial DNA homeostasis in neurons.

It is not fully clear why neurons would need to have such tight control over the amount and organization of mtDNA in axons and dendrites.

VI. Concluding remarks

The work described in this thesis sheds light on multiple aspects of neuronal homeostasis and points to a model of neuron cell biology in which accurate spatiotemporal regulation of the mitochondrial network is key. I demonstrated new mechanisms by which mitochondrial organization can be fine-tuned at the level of individual mitochondria or single motor-adaptor complexes and showed how this fine control of mitochondrial organization is disrupted in disease states. Defining these mechanisms, however, is just a starting point to decipher mitochondrial biology in neurons, as there are many additional layers of regulation yet to be understood.

I think we should consider the many unanswered questions in neuronal cell biology to be like solving a jigsaw puzzle. Just as each piece of the puzzle reveals a small part of a bigger picture, each study of mitochondrial dynamics, microtubule motors, and neurological disease reveals new pieces of information about how neuronal homeostasis is maintained. Ultimately, as these different avenues of study advance, I believe that they will converge to a single, complete picture of neuronal homeostasis that accurately describes the organization and function of all parts of the neuron. Getting to this endpoint will be extremely difficult, if not impossible, but working toward this goal will continue to reveal interesting and unexpected biology, and will likely lead to the discovery of therapeutic approaches that will help treat individuals affected by many neurological diseases.

APPENDICES

APPENDIX A: SUPPLEMENT TO CHAPTER 2

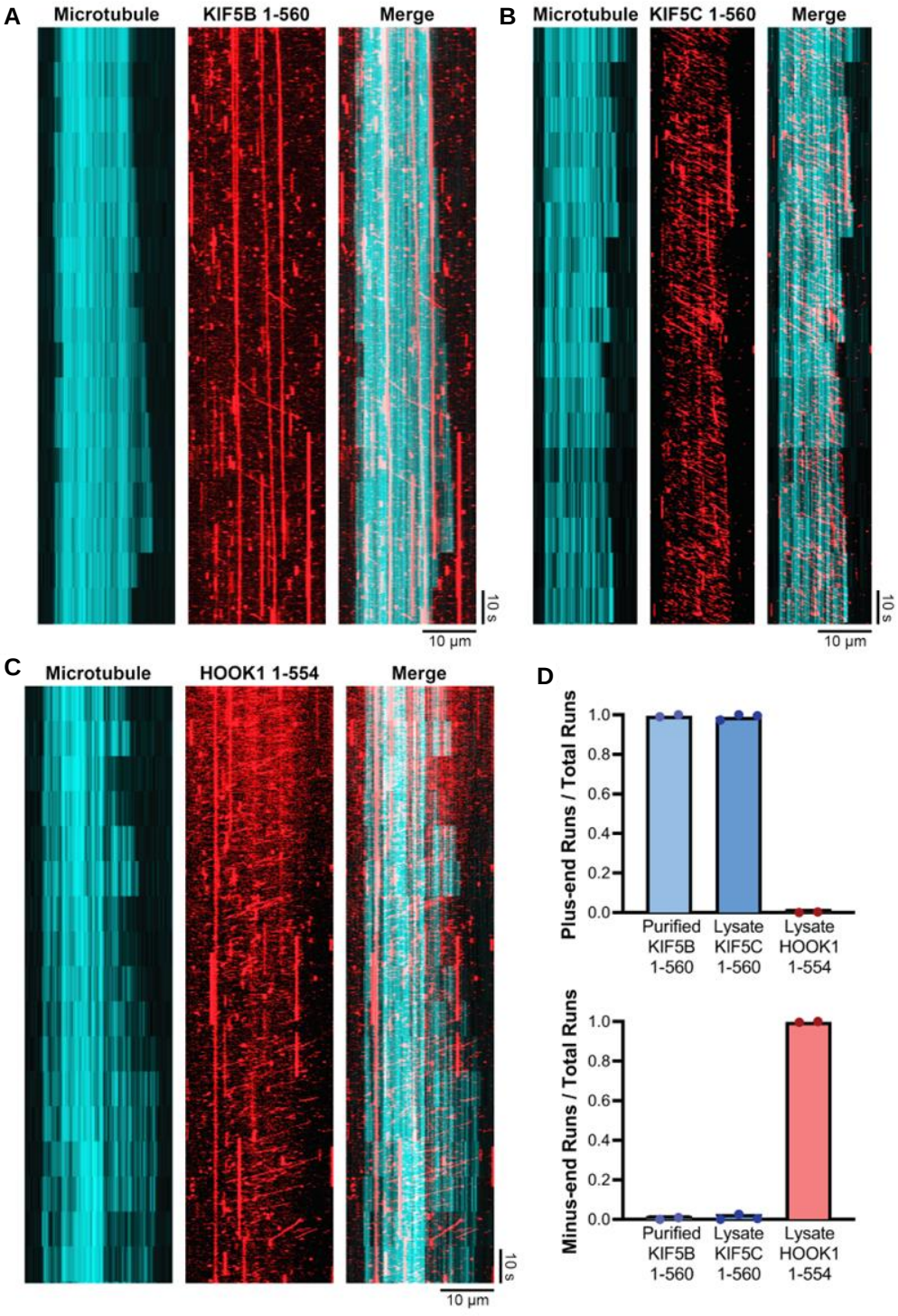

Figure S2.1: Motility of kinesin-1 and dynein on dynamic microtubules. A, Motility of 1 nM purified KIF5B(1–560)-Halo on dynamic microtubules. Left panel shows full kymograph of dynamic microtubule channel. Middle panel shows full kymograph of KIF5B 1-560 channel. **B,** Same as **(A)** but for KIF5C(1-560)-Halo present in COS-7 cell lysate. **C,** Same as **(A)** but for Halo-HOOK1(1-554) present in COS-7 cell lysate. **D,** Quantification of transport direction along dynamic microtubules for KIF5B 1-560, KIF5C 1-560, and HOOK1 1-554 constructs. The bars represent the mean (n = 170 runs from 2 experiments for purified KIF5B 1-560, 1060 runs from 3 experiments for lysate KIF5C 1-560, and 678 runs from 2 experiments for lysate HOOK1 1-554).

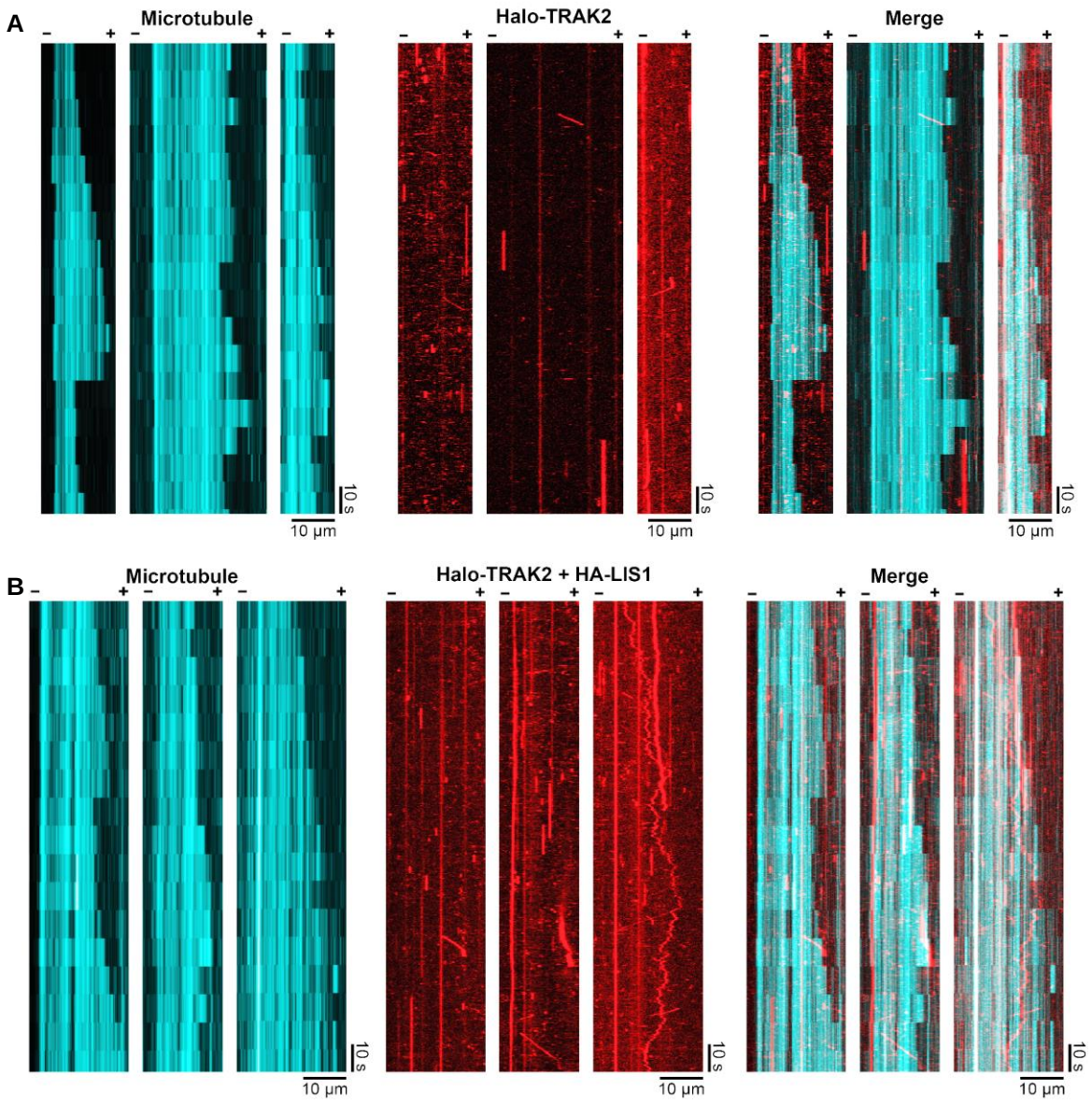

Figure S2.2: Halo-TRAK2 motility on dynamic microtubules. A, Halo-TRAK2 motility on dynamic microtubules. The left panel shows three examples of 3-minute kymographs of the dynamic microtubule channel. The microtubule plus-end is evident from the greater growth and catastrophe rate at the right of each kymograph. The middle panel shows corresponding 3-minute kymographs of the Halo-TRAK2 channel for the same microtubules. The right panel shows a merge of the other two channels. **B,** Same as **(A)** but in the presence of exogenously expressed HA-LIS1.

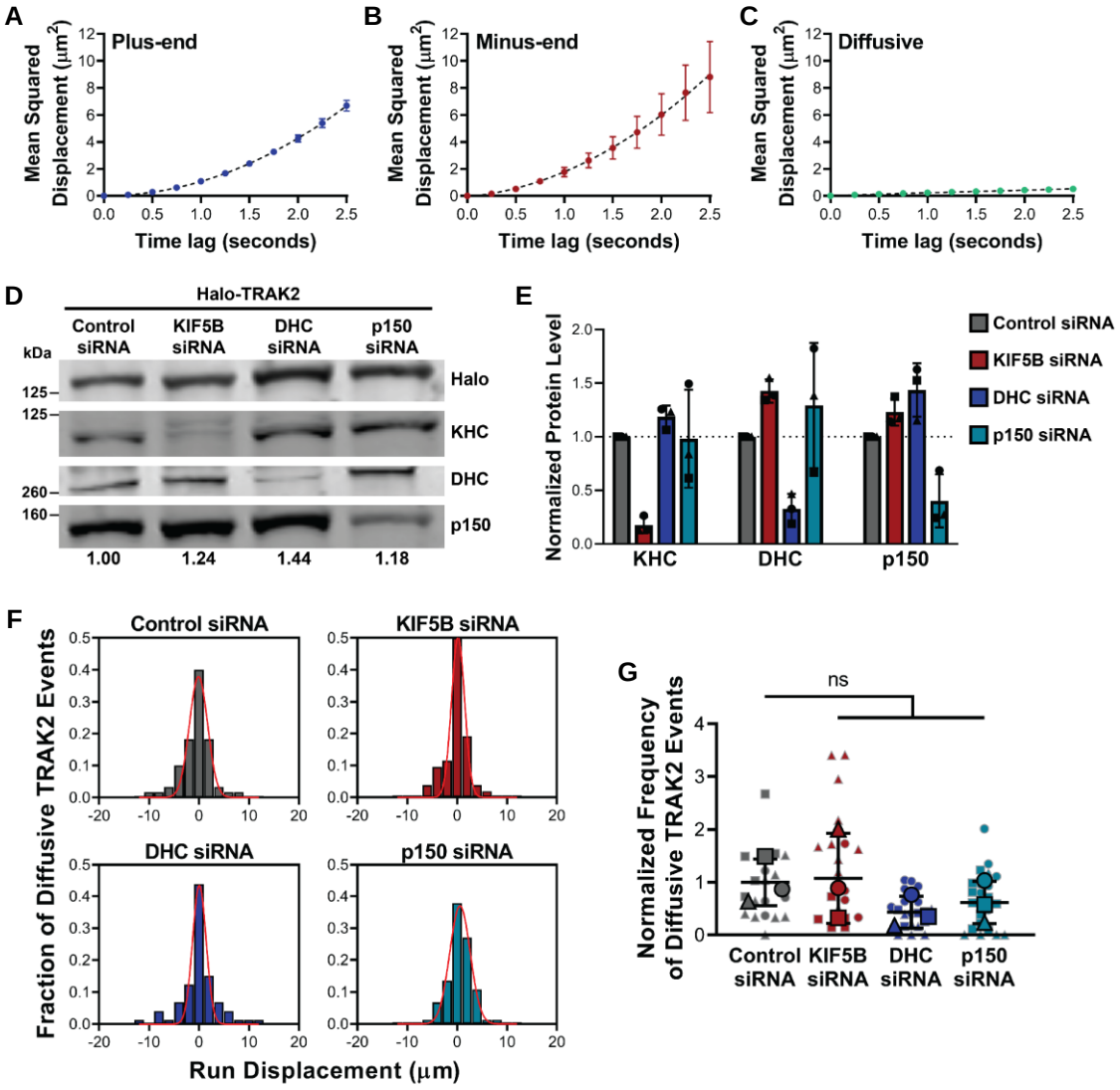

Figure S2.3: The bidirectional motility of TRAK2 is consistent with diffusion. A, Mean-squared displacement (MSD) analysis of unidirectional TRAK2 movement to the microtubule plus-end is processive ($MSD=v^2t^2$). **B,** MSD analysis of unidirectional TRAK2 movement to the microtubule minus-end is processive ($MSD=v^2t^2$). **C,** MSD analysis of TRAK2 bidirectional motility fits a diffusive state ($MSD=2Dt$). Error bars indicate s.e.m. (n = 15 events per condition). **D,** Western blot verification of siRNA knockdown in Halo-TRAK2 cell lysates used for single-molecule experiments. Blots were probed for Halo-TRAK2, kinesin heavy chain (KHC), dynein heavy chain (DHC), and $p150^{Glued}$. Relative protein levels from total protein stain are shown for each condition. **E,** Quantification of protein levels for KHC, DHC, and p150 in siRNA knockdown experiments. The level of each protein is normalized to the level of the control siRNA condition for each replicate. Data are mean ± s.d. with points shaped according to experimental replicate, (n = 3 independent experiments). **F,** Distribution of run displacement for TRAK2 diffusive movement upon knockdown with a control, KIF5B, dynein heavy chain (DHC), or p150 siRNA (n = 60, 52, 70, and 73 events, respectively). Negative displacement indicates movement to the microtubule minus-end. The red line represents a fit to a Gaussian distribution. **G,** Normalized frequency of TRAK2 diffusion upon motor knockdown. Data points represent the frequency of TRAK2 motility per video normalized to the average frequency of control events and are shaped according to experimental replicate, with smaller points representing diffusive frequency per video. The center line and bars represent mean ± s.d., (n = 19 videos for control siRNA, 19 videos for KIF5B siRNA, 21 videos for DHC siRNA, and 23 videos for p150 siRNA, 3 independent experiments). ns, not significant (one-way ANOVA with Dunnett's multiple comparisons test).

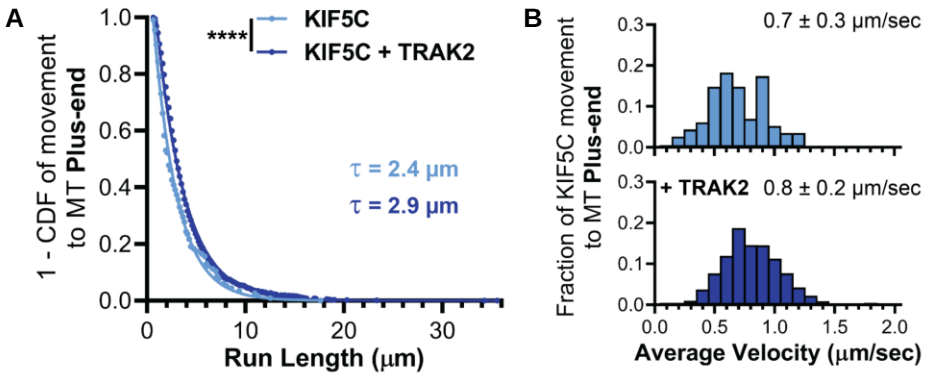

Figure S2.4: TRAK2 increases KIF5C processivity. A, Inverse cumulative distribution functions (CDF) of run lengths for KIF5C transport to the microtubule plus-end in the presence or absence of exogenous TRAK2. The curves represent single exponential decay fits, with the decay constants for each indicated above (n = 115 events without TRAK2 and 1659 events with TRAK2) ****, $p < 0.0001$ (two-tailed Mann-Whitney U test). **B,** Histogram of velocity distributions for KIF5C transport to the microtubule plus-end in the presence or absence of exogenous TRAK2. The values are mean ± s.d.

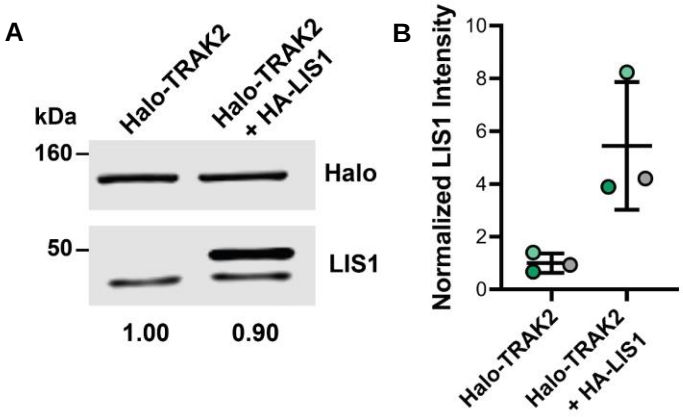

Figure S2.5 Overexpression of LIS1 in samples from single-molecule experiments. A, Representative Western blot showing the expression of Halo-TRAK2 and LIS1 in cell lysates used for single-molecule experiments. Relative protein levels from total protein stain are shown for each condition. **B,** Quantification of LIS1 intensity in cell lysates normalized to total protein levels. Bars represent mean ± s.d. from 3 independent experiments.

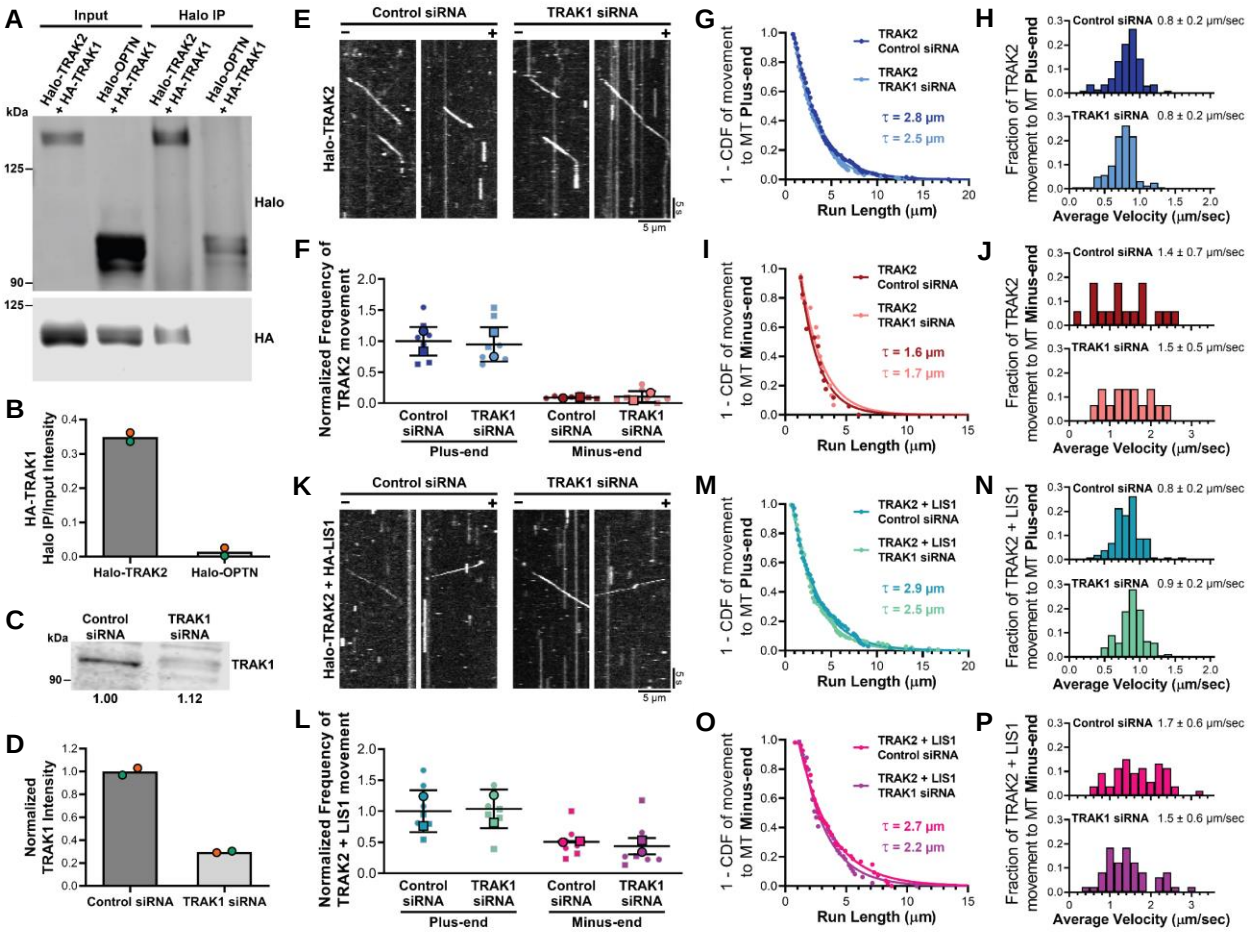

Figure S2.6: TRAK1 interacts with TRAK2, but depletion of endogenous TRAK1 does not alter TRAK2 transport in single-molecule experiments. A, Immunoprecipitation using a Halo antibody of extracts from COS-7 cells transfected with HA-TRAK1 and Halo-tagged TRAK2 or negative control Optineurin (OPTN). **B,** Quantification of co-immunoprecipitation of HA-TRAK1 with Halo-tagged constructs. Bars represent the mean with data points color-coded according to experimental replicate (n = 2 experiments). **C,** Western blot verification for siRNA knockdown of TRAK1. Relative protein levels from total protein stain are shown for each condition. **D,** Quantification of TRAK1 knockdown. Bars represent the mean with data points color-coded according to experimental replicate (n = 2 experiments). **E,** Representative kymographs showing how siRNA knockdown of TRAK1 affects TRAK2 motility along MTs. **F,** Normalized frequency of TRAK2 motile events with control siRNA or TRAK1 siRNA. Data points are shaped according to experimental replicate, with smaller points representing TRAK2 frequency per video. The center line and bars represent the mean ± s.d., (n = 8 videos per condition, 2 experiments). **G-J,** Inverse cumulative distribution functions (CDF) of run length and histogram distributions of velocity for TRAK2 transport to either microtubule end (n = 194 plus-end events with control siRNA, 156 plus-end events with TRAK1 siRNA, 17 minus-end events with control siRNA, and 15 minus-end events with TRAK1 siRNA). The curves in **G,I,** represent single exponential decay fits with decay constants indicated above. In **H,J,** the mean ± s.d. is shown. **K,** Representative kymographs showing how siRNA knockdown of TRAK1 affects TRAK2 motility along MTs when HA-LIS1 is expressed. **L,** Same as **(F)** but with HA-LIS1 expressed (n = 8 videos with control siRNA and 8 videos with TRAK1 siRNA, 2 independent experiments). **M-P,** Same as **(G-J)**, but with HA-LIS1 expressed (n = 103 plus-end events with control siRNA, 153 plus-end events with TRAK1 siRNA, 54 minus-end events with control siRNA, and 49 minus-end events with TRAK1 siRNA).

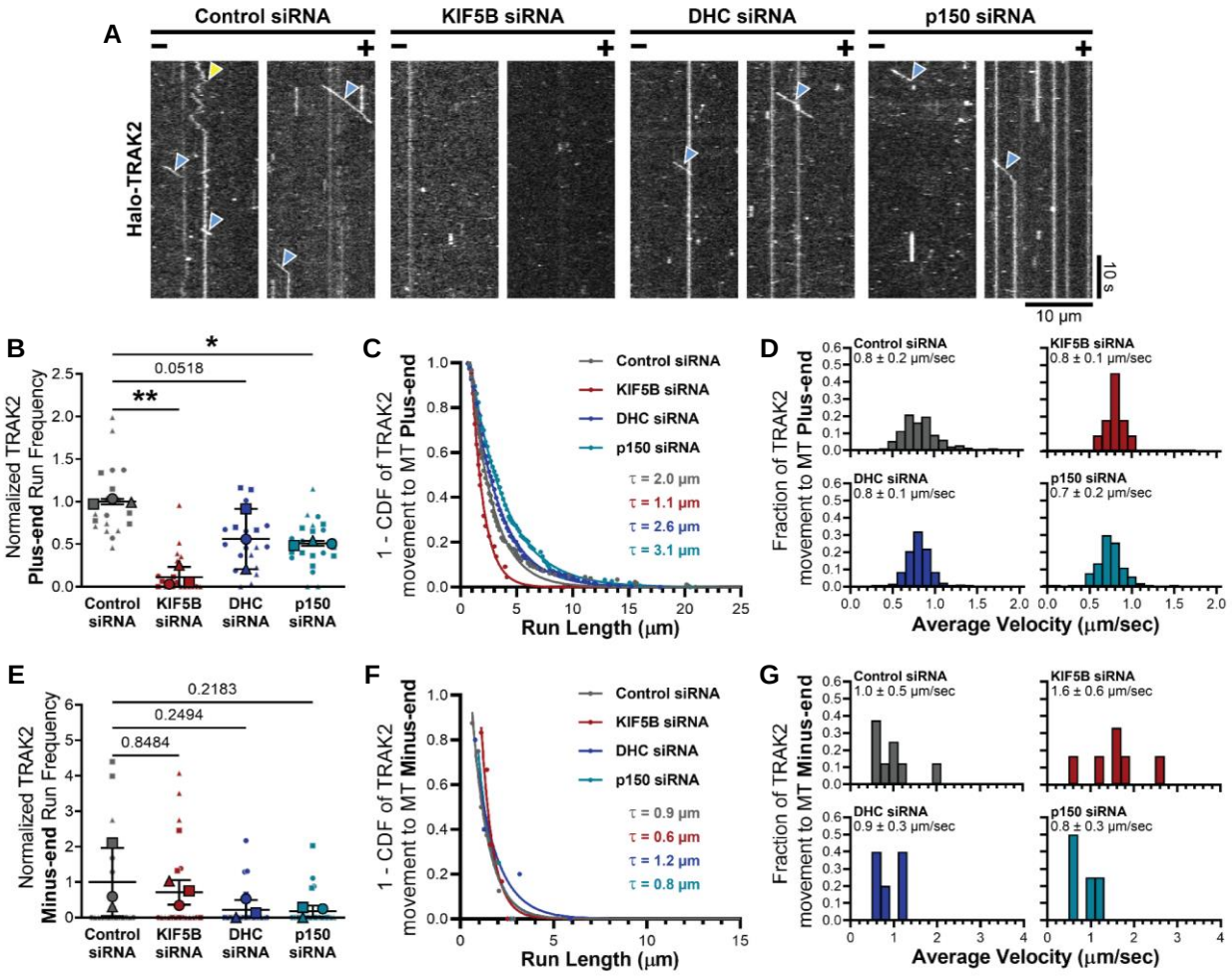

Figure S2.7: Dynein-dynactin promotes plus-end-directed TRAK2 transport in the absence of exogenous LIS1. **A,** Representative kymographs showing how siRNA knockdown of KIF5B, dynein heavy chain (DHC), or p150^{Glued} (p150) affects TRAK2 motility along MTs. Blue and yellow arrows indicate plus-end and diffusive TRAK2 movement, respectively. **B,** Normalized frequency of TRAK2 transport to the MT plus-end upon motor knockdown. Data points represent the frequency of TRAK2 motility per video normalized to the average frequency of control siRNA events. The center line and bars represent mean ± s.d., (n = 19 for control siRNA, 21 for KIF5B siRNA, 25 for DHC siRNA, and 23 for p150 siRNA, 3 independent experiments). Exact p-values are shown when p > 0.05; *, p = 0.0319; **, p = 0.0011 (one-way ANOVA with Dunnett's multiple comparisons test). **C-D,** Inverse cumulative distribution functions (CDF) of run length and histogram distributions of velocity for TRAK2 transport to the microtubule plus-end (n = 177 events for control siRNA, 22 events for KIF5B siRNA, 351 events for DHC siRNA, and 153 events for p150 siRNA). The curves in **(C)** represent single exponential decay fits with decay constants indicated above. The values in **(D)** are mean ± s.d. **E,** Same as **(B)** but for TRAK2 transport to the microtubule minus-end. Exact p-values are shown when p > 0.05 (one-way ANOVA with Dunnett's multiple comparisons test). **F-G,** Same as **(C-D)** but for TRAK2 transport to the microtubule minus-end (n = 8 events for control siRNA, 6 events for KIF5B siRNA, 5 events for DHC siRNA, and 4 events for p150 siRNA).

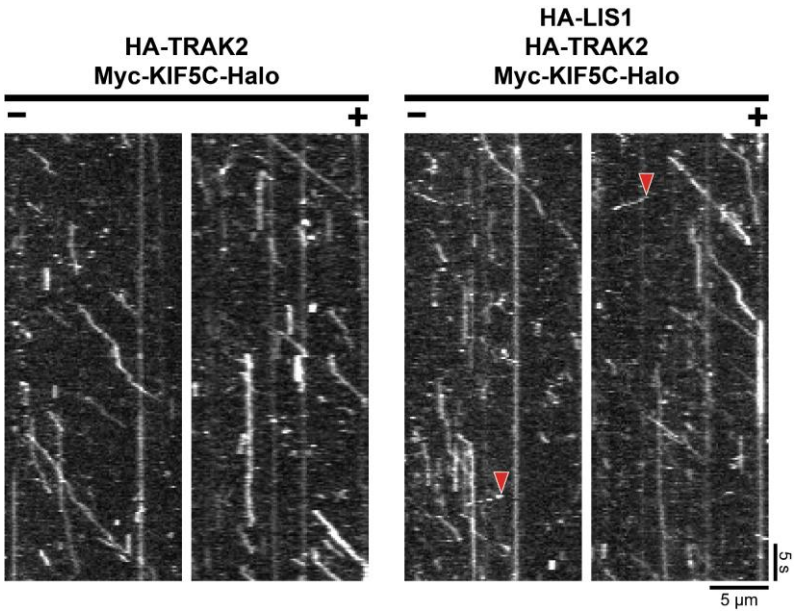

Supplementary Figure S2.8: LIS1 promotes minus-end-directed transport of kinesin-1 in the presence of TRAK2. Representative kymographs show unidirectional KIF5C transport toward the microtubule plus-end in the presence of TRAK2 alone and instances of minus-end-directed KIF5C transport in the presence of TRAK2 and LIS1. Minus-end-directed KIF5C runs are indicated with red arrows.

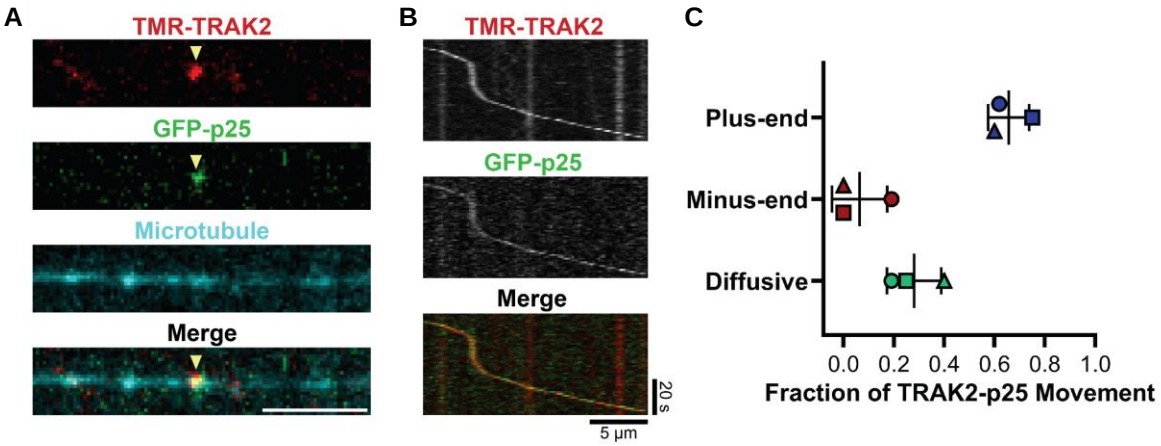

Figure S2.9: TRAK2-p25 co-complexes move processively toward either microtubule end. A, Example still showing co-localization of TRAK2 and the p25 subunit of dynactin on a microtubule. Scale bar is 5 µm. **B,** Representative kymographs showing processive co-migration of TRAK2 with p25. **C,** Fraction of occurrence for plus-end-directed, minus-end-directed, and diffusive movement of TRAK2-p25 co-complexes. Data points are shaped according to experimental replicate. The center line and bars are the mean ± s.d. from 3 independent experiments.

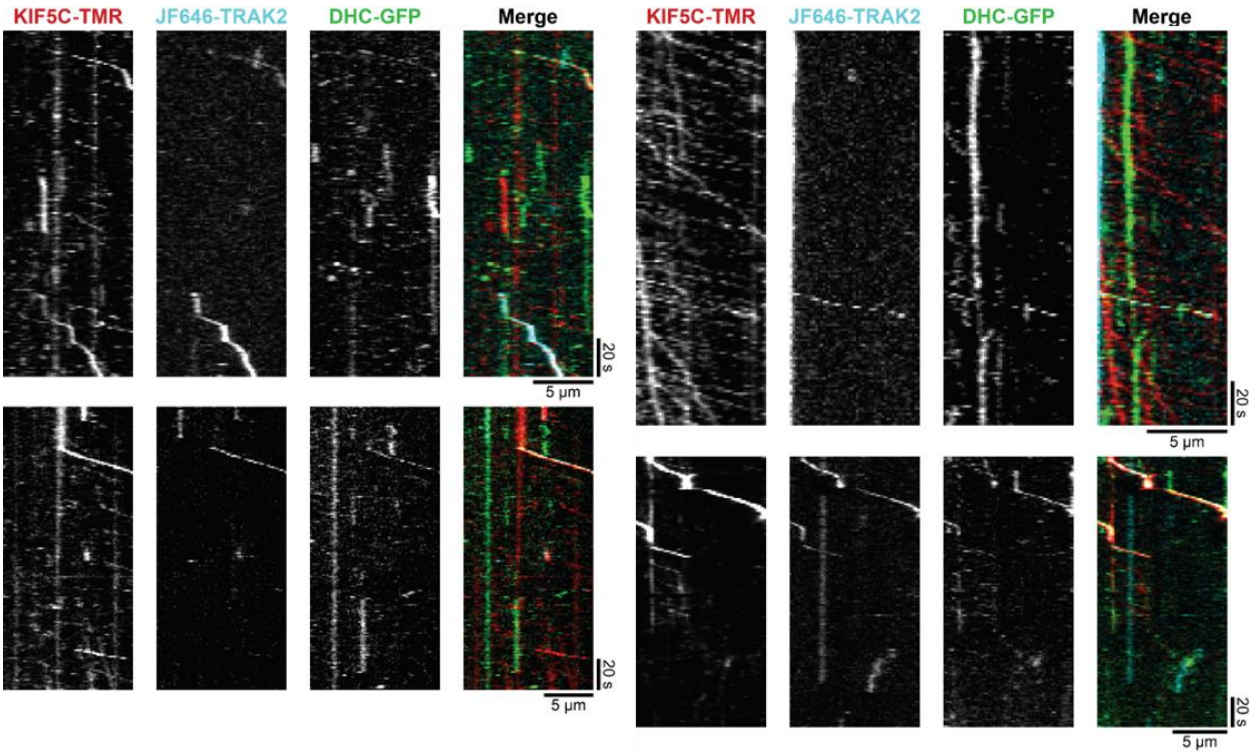

Figure S2.10: TRAK2-KIF5C-DHC co-complexes move processively toward the microtubule plus-end. A panel of representative kymographs show unidirectional co-complex transport toward the microtubule plus-end. Kymographs are oriented with the microtubule plus-end on the right, as shown by the trajectories of complexes containing KIF5C alone.

Supplemental videos for Chapter 2

Video S2.1: TRAK2 moves processively to the microtubule plus-end. Representative video showing a single TMR-Halo-TRAK2 particle (red) moving toward the dynamically growing plus-end of a surface-attached dynamic MT (cyan). The MT plus-end (right) is evident by the faster growth rate. Scale bar is 5 µm. Stopwatch shows time in minutes: seconds.

https://static-content.springer.com/esm/art%3A10.1038%2Fs41467-021-24862-7/MediaObjects/41467_2021_24862_MOESM4_ESM.mov

Video S2.2: KIF5C displays infrequent movement along microtubules when expressed alone. Representative video showing a single Myc-KIF5C-Halo-TMR particle (red) moving along a surface-attached dynamic MT (cyan). Scale bar is 5 µm. Stopwatch shows time in minutes: seconds.

https://static-content.springer.com/esm/art%3A10.1038%2Fs41467-021-24862-7/MediaObjects/41467_2021_24862_MOESM5_ESM.mov

Video S2.3: TRAK2 induces robust KIF5C movement along microtubules. Representative video showing many Myc-KIF5C-Halo-TMR particles (red) moving along a surface-attached dynamic MT (cyan) when HA-TRAK2 is co-expressed. Scale bar is 5 µm. Stopwatch shows time in minutes: seconds.

https://static-content.springer.com/esm/art%3A10.1038%2Fs41467-021-24862-7/MediaObjects/41467_2021_24862_MOESM6_ESM.mov

Video S2.4: TRAK2 moves processively to the microtubule minus-end in the presence of exogenous HA-LIS1. Representative video showing a single TMR-Halo-TRAK2 particle (red) moving toward the minus-end of a surface-attached dynamic MT (cyan) when HA-LIS1 is expressed. The MT plus-end (right) is evident by the faster growth rate. Scale bar is 5 µm. Stopwatch shows time in minutes: seconds.

https://static-content.springer.com/esm/art%3A10.1038%2Fs41467-021-24862-7/MediaObjects/41467_2021_24862_MOESM7_ESM.mov

Video S2.5: TRAK2 switches directions during processive movement. Representative video showing a single TMR-Halo-TRAK2 particle (red) reversing direction while moving processively along a microtubule (cyan). Scale bar is 5 µm. Stopwatch shows time in minutes: seconds.

https://static-content.springer.com/esm/art%3A10.1038%2Fs41467-021-24862-7/MediaObjects/41467_2021_24862_MOESM8_ESM.mov

Video S2.6: TRAK2, kinesin-1, and dynein co-migrate as a complex. Representative video with JF646-SNAP-TRAK2 (top channel, cyan), Myc-KIF5C-Halo-TMR (second channel, red), DHC-GFP (third channel, green), and merge (bottom channel) showing these components comigrating as a single complex along an unlabeled microtubule. Scale bar is 2 µm. The movie is 36 seconds of real time.

https://static-content.springer.com/esm/art%3A10.1038%2Fs41467-021-24862-7/MediaObjects/41467_2021_24862_MOESM9_ESM.mov

APPENDIX B: SUPPLEMENT TO CHAPTER 3

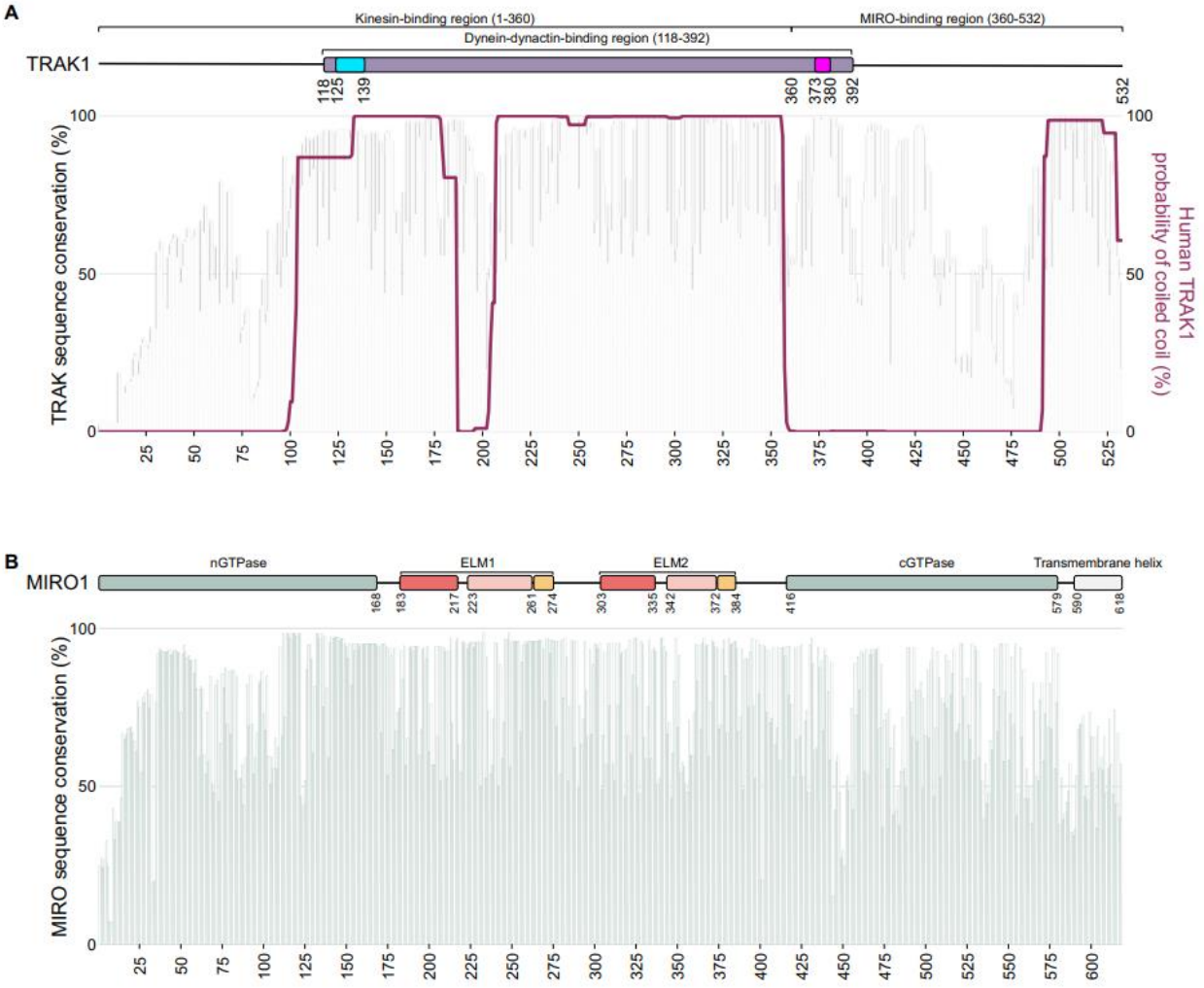

Figure S3.1: Sequence conservation and coiled coil-prediction. A, Per-amino acid sequence conservation and coiled-coil prediction scores for the 1-532 amino acid region of TRAK. Numbering is according to human TRAK1. Insertions or deletions in other sequences relative to human TRAK1 are not shown. A diagram on top shows domains and interactions within this region of TRAK (see also Fig. 3.1A). Sequence conservation scores (calculated with the program Scorecons, see Methods) are based on an alignment of 183 vertebrate TRAK sequences (93 TRAK1 and 90 TRAK2). The coiled-coil prediction (calculated with the program prabi, see Methods) used a 28-amino acid window. **B,** Per-amino acid sequence conservation of MIRO. Numbering is according to human MIRO1. Insertions or deletions in other sequences relative to human MIRO1 are not shown. The diagram on top shows MIRO1's domains (see also Fig. 3.1A). The sequence conservation scores are based on an alignment of 188 vertebrate MIRO sequences (94 MIRO1 and 94 MIRO2).

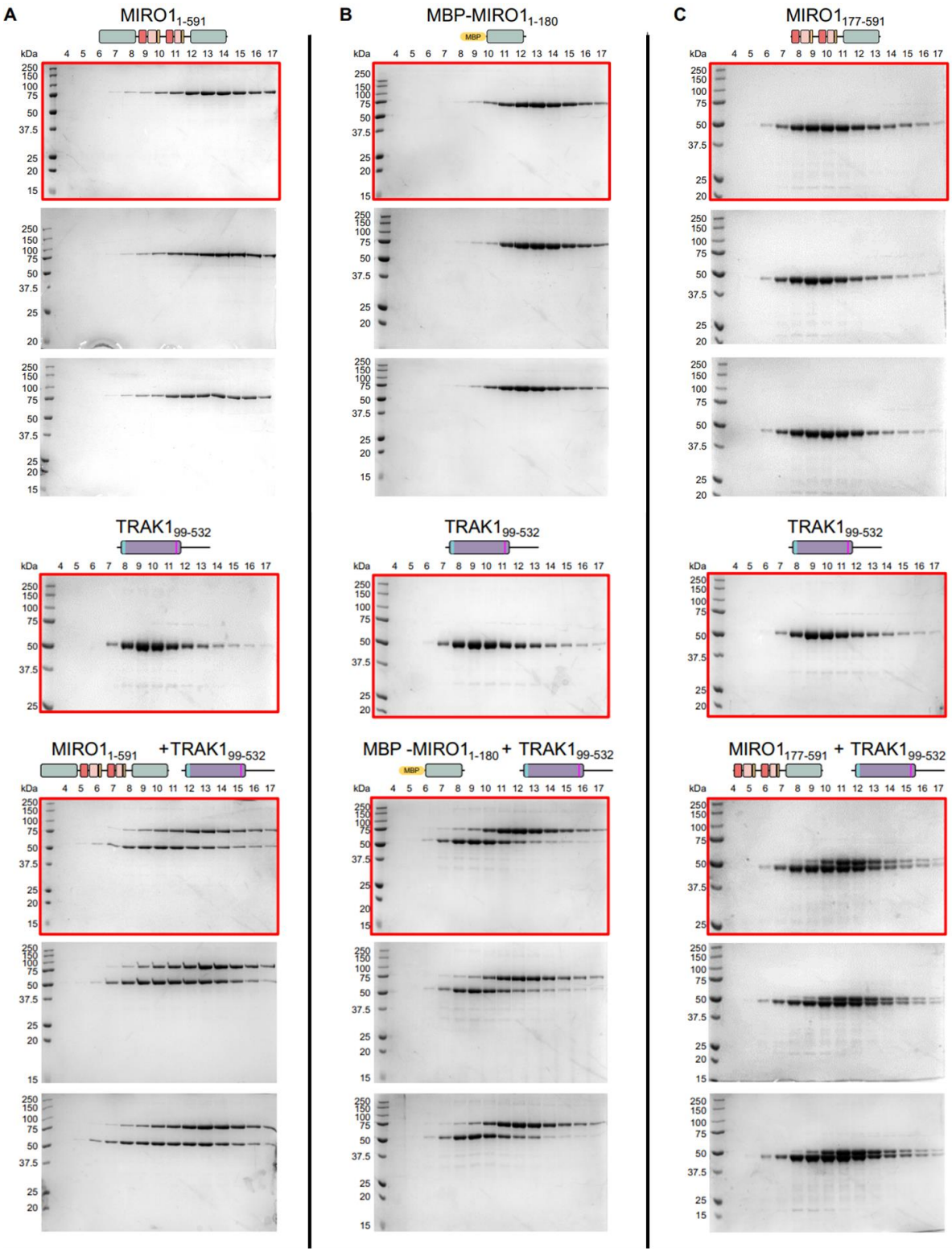

Figure S3.2: Interaction of TRAK1 and MIRO1 by glycerol gradient cosedimentation. SDS-PAGE analysis of glycerol gradient cosedimentation of MIRO1 constructs, TRAK1 constructs, and TRAK1 with MIRO1 constructs (as indicated). Glycerol gradient fractions are indicated above each lane. Gels framed in red are also shown in Fig. 3.1.

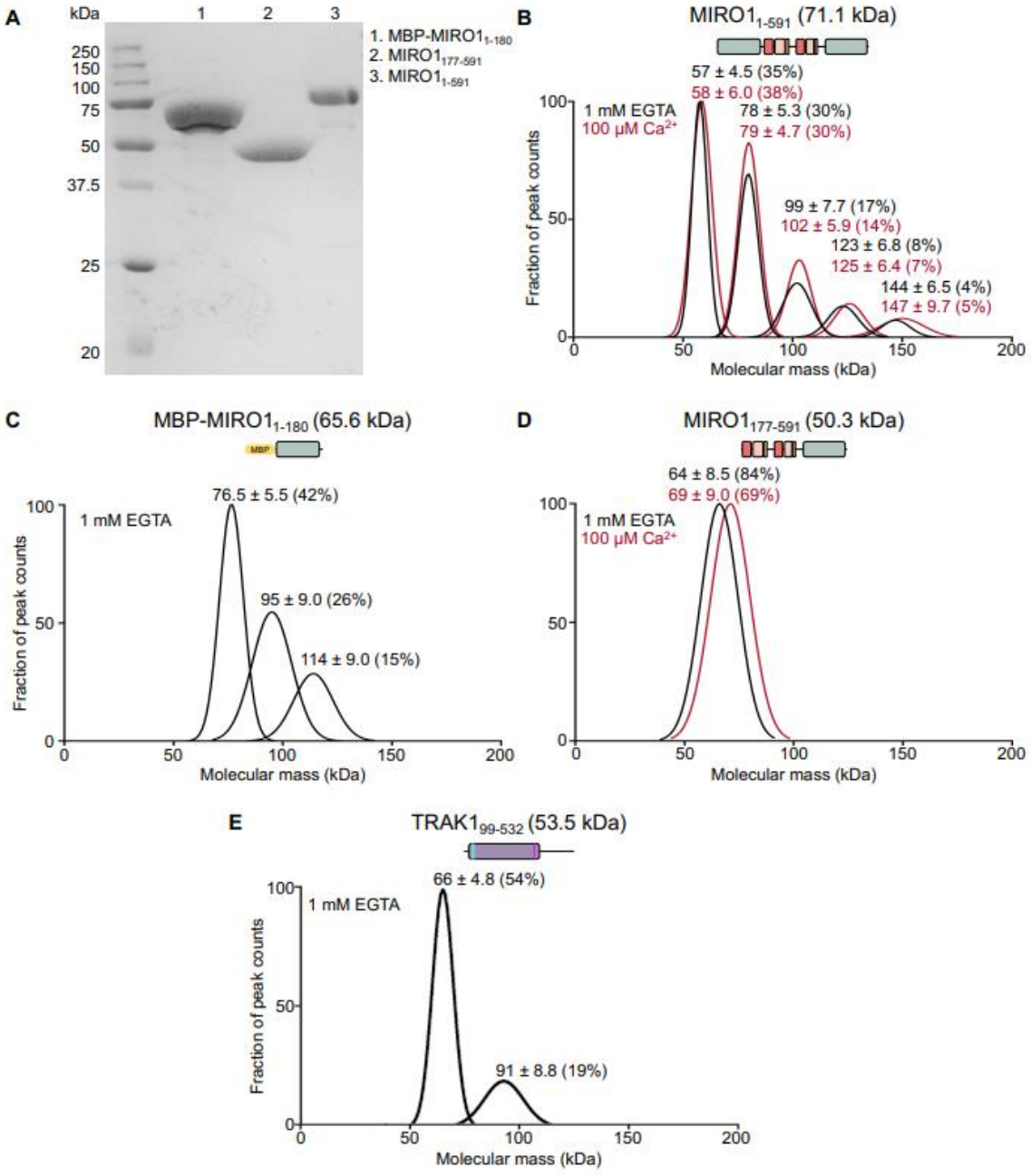

Figure S3.3: Mass photometry analysis of MIRO1 and TRAK1 constructs. A, 12% SDS-PAGE of MIRO1 constructs MIRO1$_{1-591}$, MBP-MIRO1$_{1-180}$, and MIRO1$_{177-591}$ (as indicated). **B-E,** Mass photometry analysis of the MIRO1 constructs and TRAK1$_{99-532}$ (theoretical masses shown in parentheses). MIRO1$_{1-591}$ and MIRO1$_{177-591}$, which include the EF-hands, were analyzed in the presence or the absence of Ca^{2+}. Buffer conditions for the experiments with Ca^{2+} (red curve) are: 20 mM HEPES, 100 mM NaCl, 100 µM $CaCl_2$, 50 µM $MgCl_2$, 50 µM GTP. Buffer conditions for experiments without Ca^{2+} (black curve) are: 20 mM HEPES, 100 mM NaCl, 1 mM EGTA, 50 µM $MgCl_2$, 50 µM GTP. The measured masses were binned (bin width = 1 kDa), and the graphs show the Gaussian fits of the distribution of masses normalized to the bin with the highest number of counts for each experiment. Masses were determined by ratiometric contrast, with calibrations to bovine serum albumin, b-amylase, and thyroglobulin standards (see Methods).

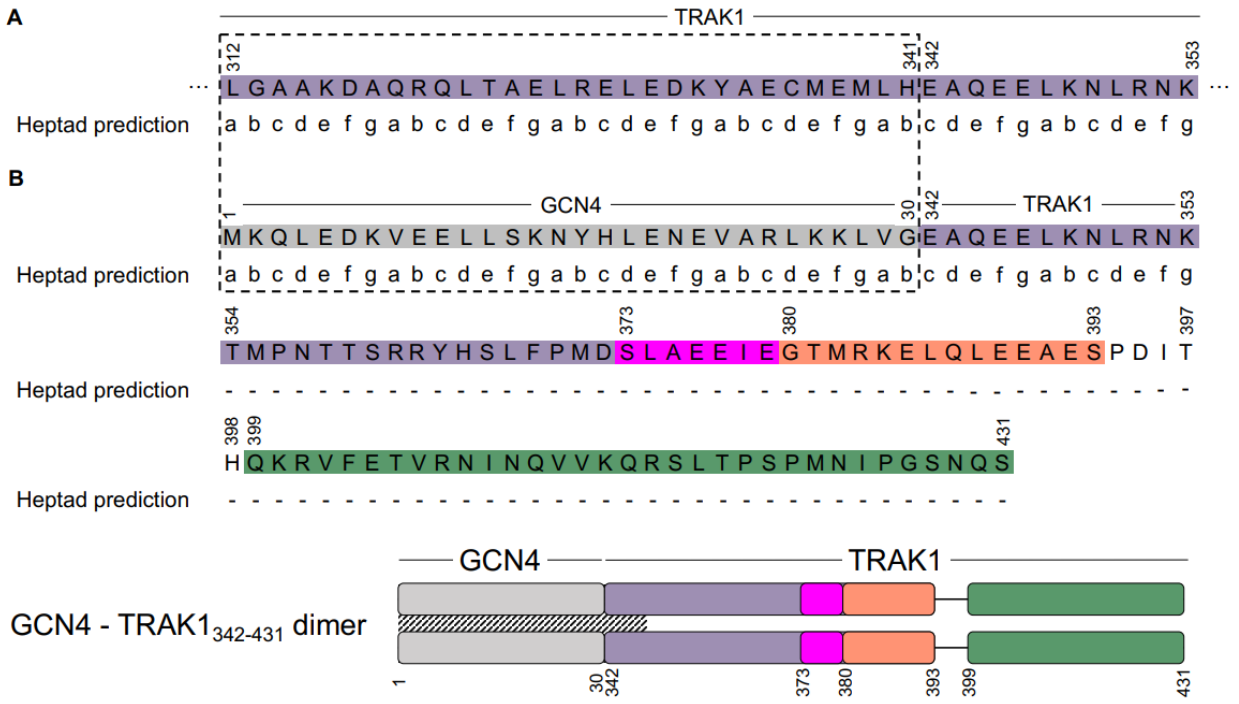

Figure S3.4: Design of GCN4-TRAK1 constructs. A, Coiled-coil heptad prediction (calculated with the program Waggawagga (see Methods)) for the 312-353 region of human TRAK1. **B,** TRAK1 amino acids in the dashed box were replaced with a 30-amino acid GCN4 leucine zipper (gray), ensuring the heptad prediction was in register for both proteins at the point of linkage. A domain diagram of the resulting GCN4-TRAK1$_{342-431}$ dimeric construct is shown at the bottom (domains colored as in Fig. 3.2A, B). Diagonal lines indicate the predicted region of coiled coil, which encompasses GCN4 and a short portion of TRAK1 (342-353). A shorter GCN4-TRAK1$_{342-393}$ construct was also obtained (see Fig. 3.2C).

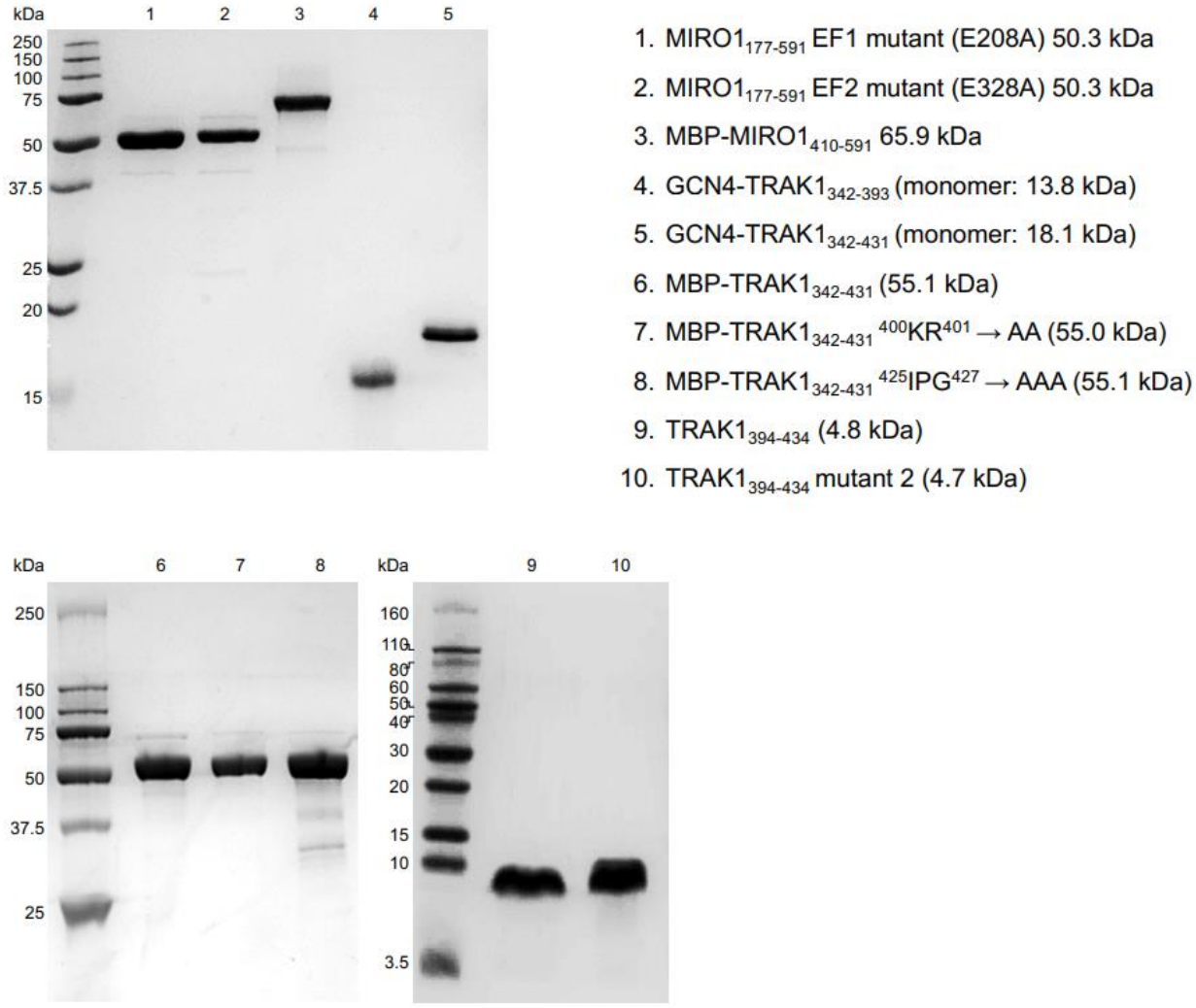

Figure S3.5: SDS-PAGE analysis of proteins used in this study. SDS-PAGE (15%) analysis of MIRO1 and TRAK1 constructs (numbered as indicated, MW in parentheses).

APPENDIX C: SUPPLEMENT TO CHAPTER 4

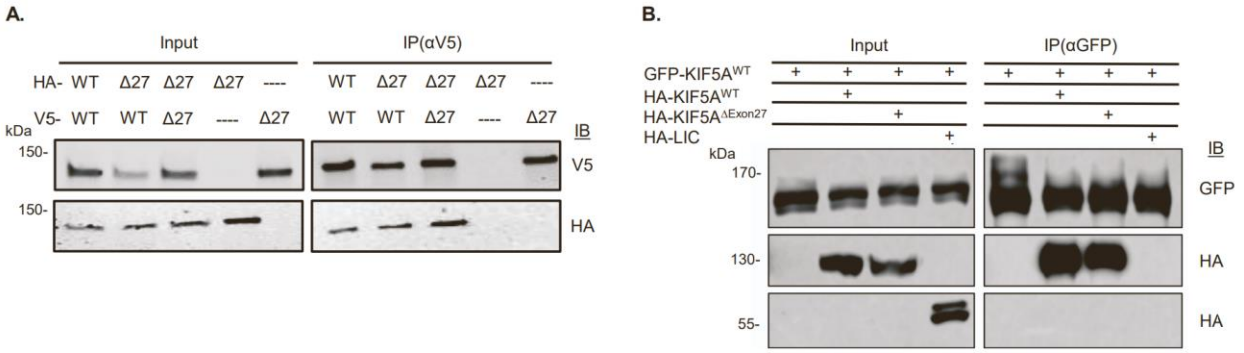

Figure S4.1: Mutant KIF5A can homo/hetero dimerize with other forms of KIF5A suggesting a gain of function toxicity. A, SKNAS were transfected with either V5-KIF5A and HA-KIF5A wild-type or ΔExon27 mutant, then the V5-KIF5A was immunoprecipitated and the lysate probed for V5- and HA-tagged protein. The blot is representative of N=2 biological replicates. **B,** HEK293FT cells were transfected with GFP-KIF5A WT alone or co-transfected with HA-KIF5A Wild-Type, ΔExon27, or Dynein Light Intermediate Chain (LIC, negative control). The GFP-KIF5A was immunoprecipitated and the lysate probed for GFP- and HA-tagged protein.

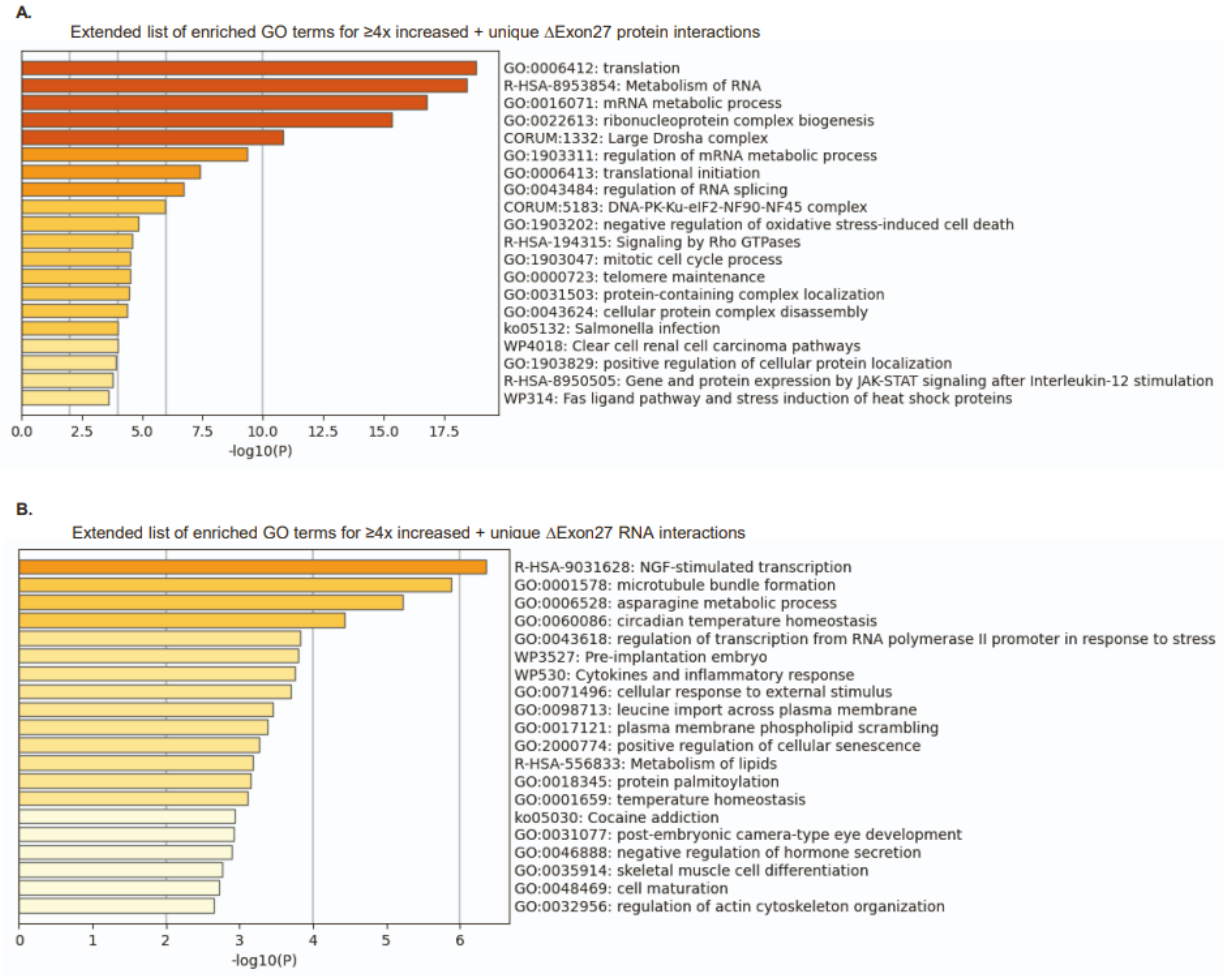

Figure S4.2: Extended pathway analysis information from KIF5A$^{\Delta Exon27}$ interaction experiments. A, Extended list of enriched GO terms for ≥4x increased + unique KIF5A$^{\Delta Exon27}$ protein interactions. **B,** Extended list of enriched GO terms for ≥4x increased + unique KIF5A$^{\Delta Exon27}$ RNA interactions.

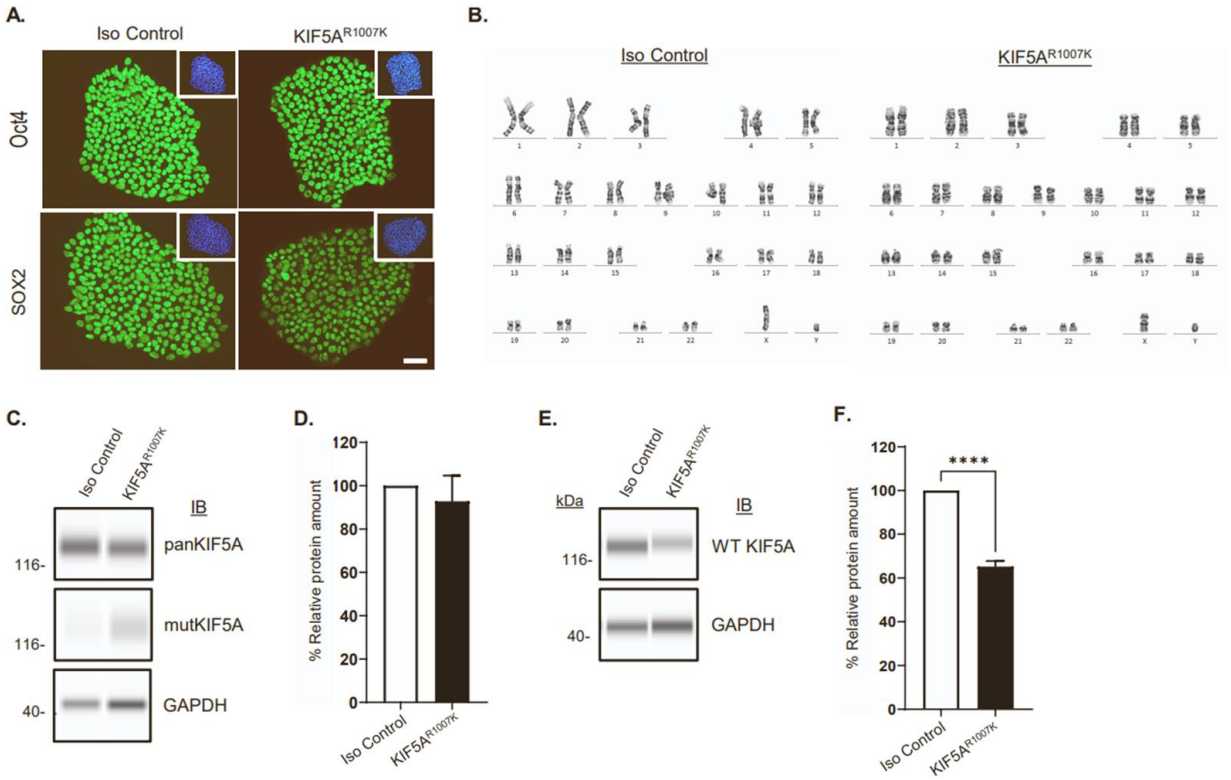

Figure S4.3: KIF5A NIL iPSC characterization. A, KIF5A^{R1007K} mutant and isogenic control iPSC lines stained for the pluripotent markers Oct4 and Sox2. Inset: DAPI staining of iPSC lines. Scale bar = 50µm. **B,** Karyotyping analysis of the lines shown in **(A)**. **C-F,** Expression of wild-type and ALS mutant forms of KIF5A in DIV15 KIF5A^{R1007K} mutant and isogenic control iMNs. Using a pan-KIF5A antibody that recognizes both forms of the protein, capillary western blotting **(C)** shows a non-significant difference in total KIF5A protein levels **(D)**. Blotting the same samples in **(C)** with a lab generated, mutant specific antibody (not shown), raised against the mutant C-terminus of KIF5A, confirms that the mutant protein is present in the KIF5A^{R1007K} cells. Blotting KIF5A^{R1007K} with an antibody for wild-type KIF5A reveals a reduction in wild-type protein levels compared to isogenic controls. Using a lab generated, KIF5A antibody that specifically recognizes the wild-type forms of the protein, capillary western blotting **(E)** shows a significant reduction in wild-type KIF5A protein levels **(F)**.

A.

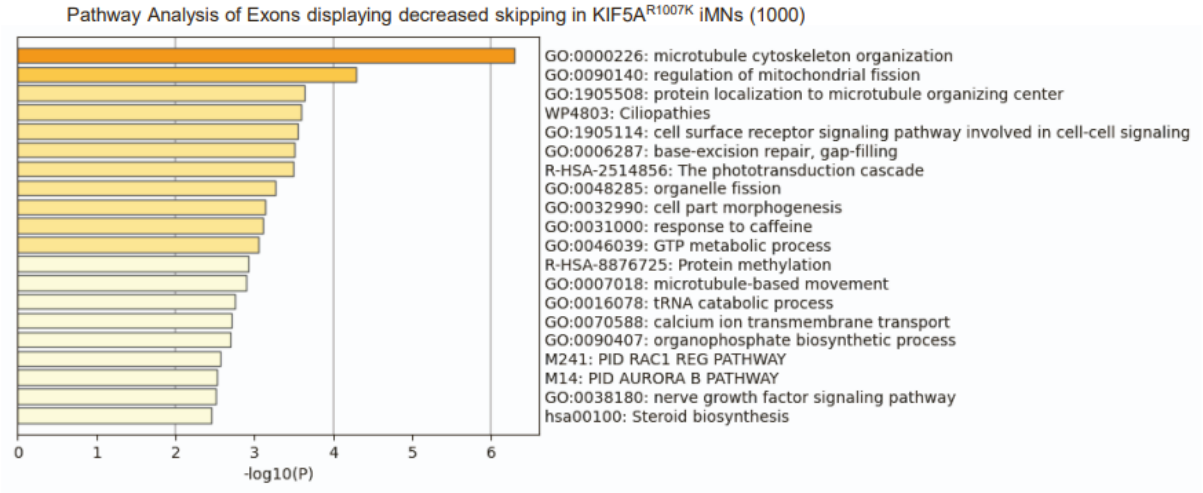

B.

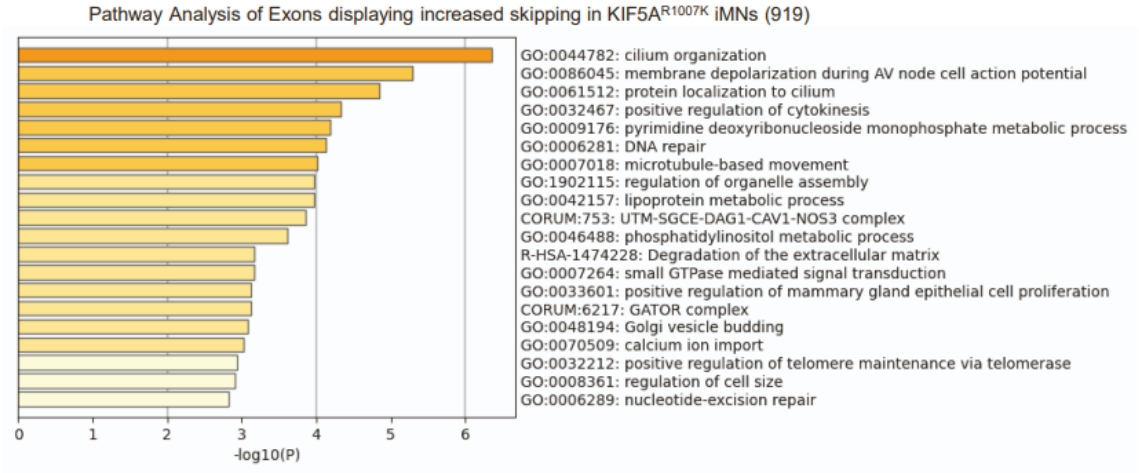

Figure S4.4: Extended pathway analysis information from KIF5A^{R1007K} splicing analysis from RNAseq experiments. A, Extended list of enriched GO terms for genes with decreased exon skipping in KIF5A^{R1007K} iMNs. **B,** Extended list of enriched GO terms for genes with increased exon skipping in KIF5A^{R1007K} iMNs.

Supplemental tables for Chapter 4

Table S4.1: List of protein and RNA interactors identified in this study, related to Figure 4.4.

https://ars.els-cdn.com/content/image/1-s2.0-S2211124722003461-mmc2.xlsx

Table S4.2: List of genes with expression changes identified in KIF5A iMNs, related to Figure 4.5.

https://ars.els-cdn.com/content/image/1-s2.0-S2211124722003461-mmc3.xlsx

Table S4.3: List of genes with splicing changes identified in KIF5A iMNs, related to Figure 4.6.

https://ars.els-cdn.com/content/image/1-s2.0-S2211124722003461-mmc4.xlsx

APPENDIX D: SUPPLEMENT TO CHAPTER 5

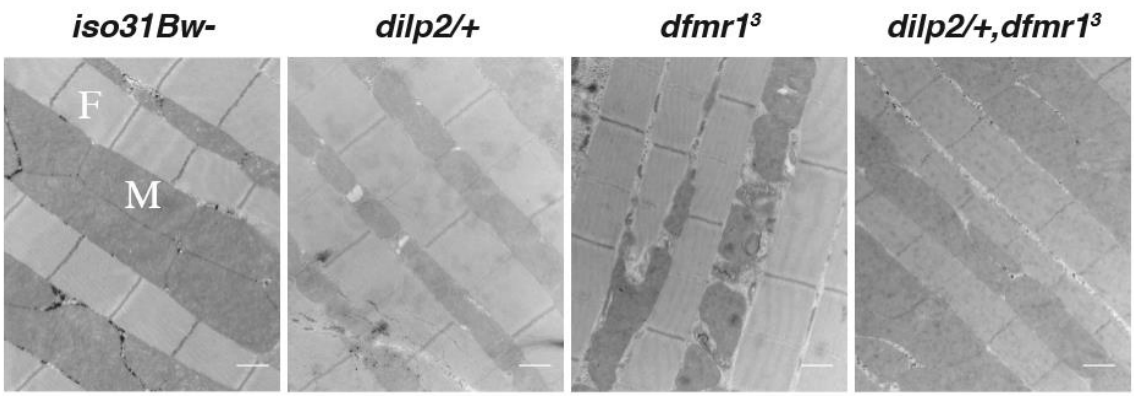

Figure S5.1: Genetic reduction of IS improves mitochondrial ultrastructure in flight muscle of *dfmr1* mutant flies. Longitudinal sections of indirect flight muscle were prepared from isolated thoraces for transmission electron microscopy experiments: Electron micrographs of Drosophila flight muscle at 20,000x magnification. The genotype of each fly is denoted above its corresponding panel, from left to right: *iso31Bw-* control, heterozygous *dilp2/+* single mutant, homozygous *dfmr1* single mutant, and *dilp2/+, dfmr1* double mutant. Scale bar indicates 800 nm. Mitochondria, M, are aligned between rows of myofibrils, F. The mitochondria of the *dfmr1* mutants appear smaller and contain ultrastructural defects, particularly dispersions of cristae compared to *iso31Bw-* controls. In contrast, the mitochondria of the *dilp2/+, dfmr1* double mutants appear larger and have ultrastructure that more closely resembles that of *iso31Bw-* conspecifics than that of *dfmr1* single mutants.

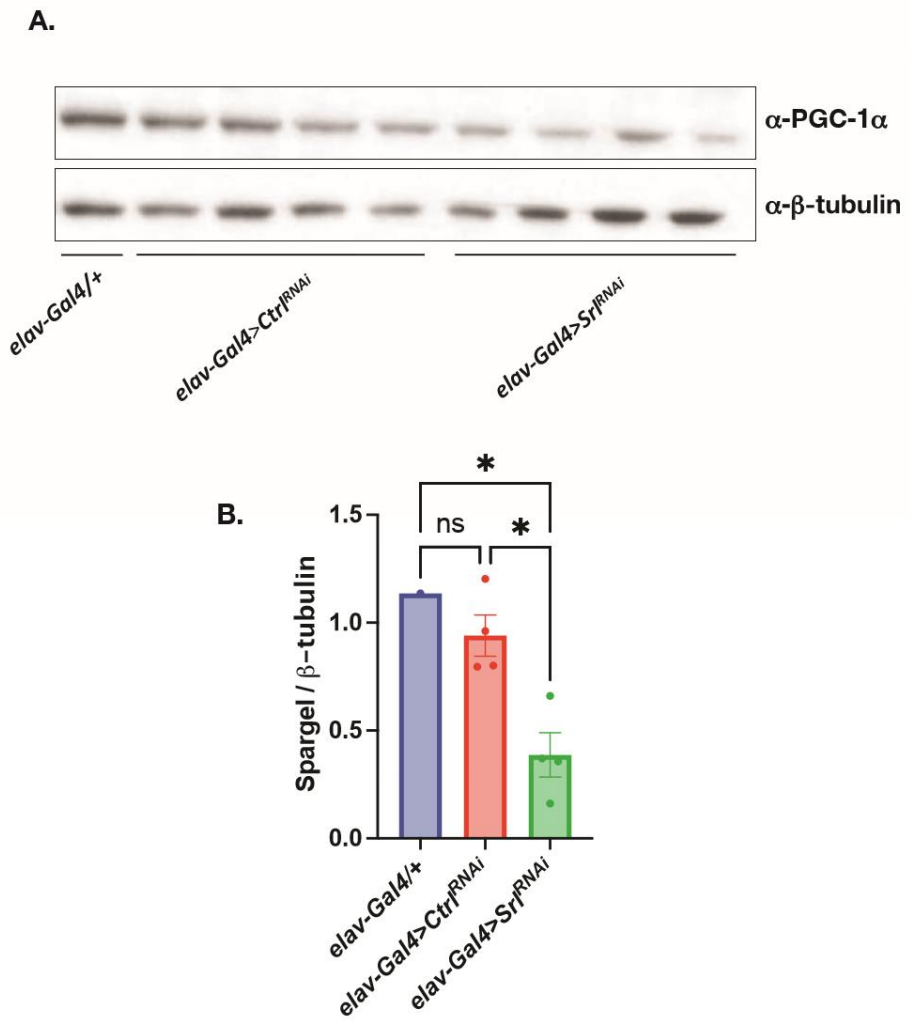

Figure S5.2: *Spargel* antibody validation. A, Western analysis of *Spargel* expression in head extracts from wild type flies that either contained the *elav-Gal4* driver alone (*elav-Gal4/+*); the *elav-Gal4* transgene and a *UAS-Ctrl*^{RNAi} construct (*elav-Gal4 > UAS-Ctrl*^{RNAi}); or the *elav-Gal4* transgene and a *UAS-Srl*^{RNAi} construct (*elav-Gal4 > UAS-Srl* ^{RNAi}). An antibody to PGC-1α was used to detect *Spargel* expression (top). β-Tubulin was used as a loading control (bottom). **B,** Quantification of the intensity of *Spargel* relative to β-Tubulin. A one-way ANOVA revealed a significant group effect for *Spargel* expression relative to β-Tubulin ($p=0.0116$). Post hoc Tukey tests indicated that the *elav-Gal4>UAS-Srl*^{RNAi} flies had significantly lower *Spargel* levels than *elav-Gal4/+* and *elav-Gal4>UAS-Ctrl*^{RNAi} controls. Sample number (N) per genotype: (*elav-Gal4/+*) = 1, (*elav-Gal4>UAS-Ctrl*^{RNAi}) = 4, and (*elav-Gal4>UAS-Srl*^{RNAi}) = 4. Each sample contained 10 fly heads. Values represent mean ± SEM. *p≤0.05. As predicted, we observed a strong band of the correct size whose expression relative to β -Tubulin decreased when we pan-neuronally expressed a *UAS-Srl*^{RNAi} construct (*elav-Gal4>UAS-Srl*^{RNAi}) compared to flies that pan-neuronally expressed the VDRC library control RNAi construct (*elav-Gal4>UAS-Ctrl*^{RNAi}) or *elav-Gal4* driver alone.

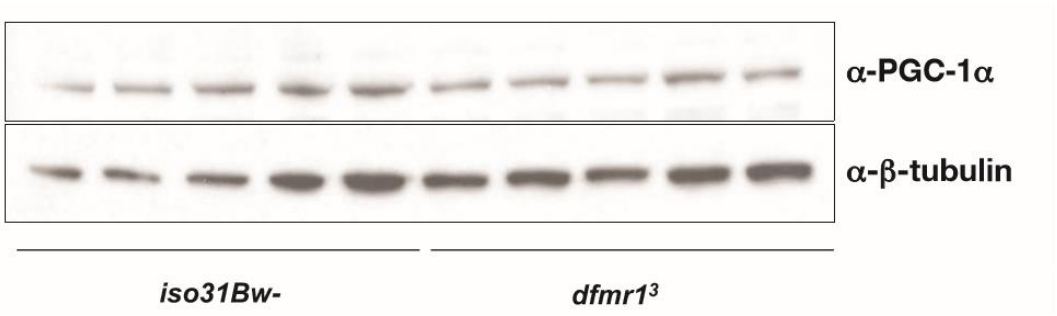

Figure S5.3: Western blot validation of reduced Spargel expression in *dfmr1* mutant flies. Western analysis of Spargel expression in extracts from *iso31Bw-* and dfmr1 mutant fly heads. An antibody to PGC-1α was used to detect Spargel expression (top). β-Tubulin was used as a loading control (bottom).

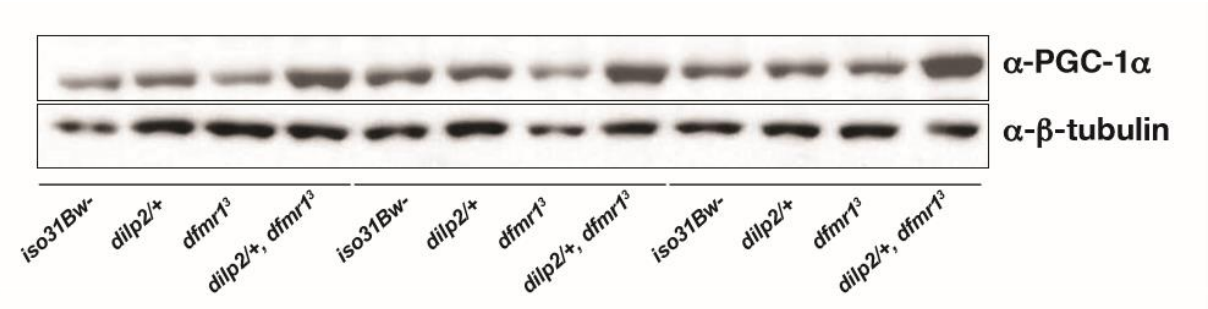

Figure S5.4: Diminished Spargel expression in the heads of dfmr1 mutants is restored by normalization of IS. Western analysis of *Spargel* expression in extracts from *iso31Bw-* wild-type, *dilp2/+* heterozygous mutant, *dfmr1* homozygous mutant, and *dilp2/+, dfmr1* double mutant fly heads.

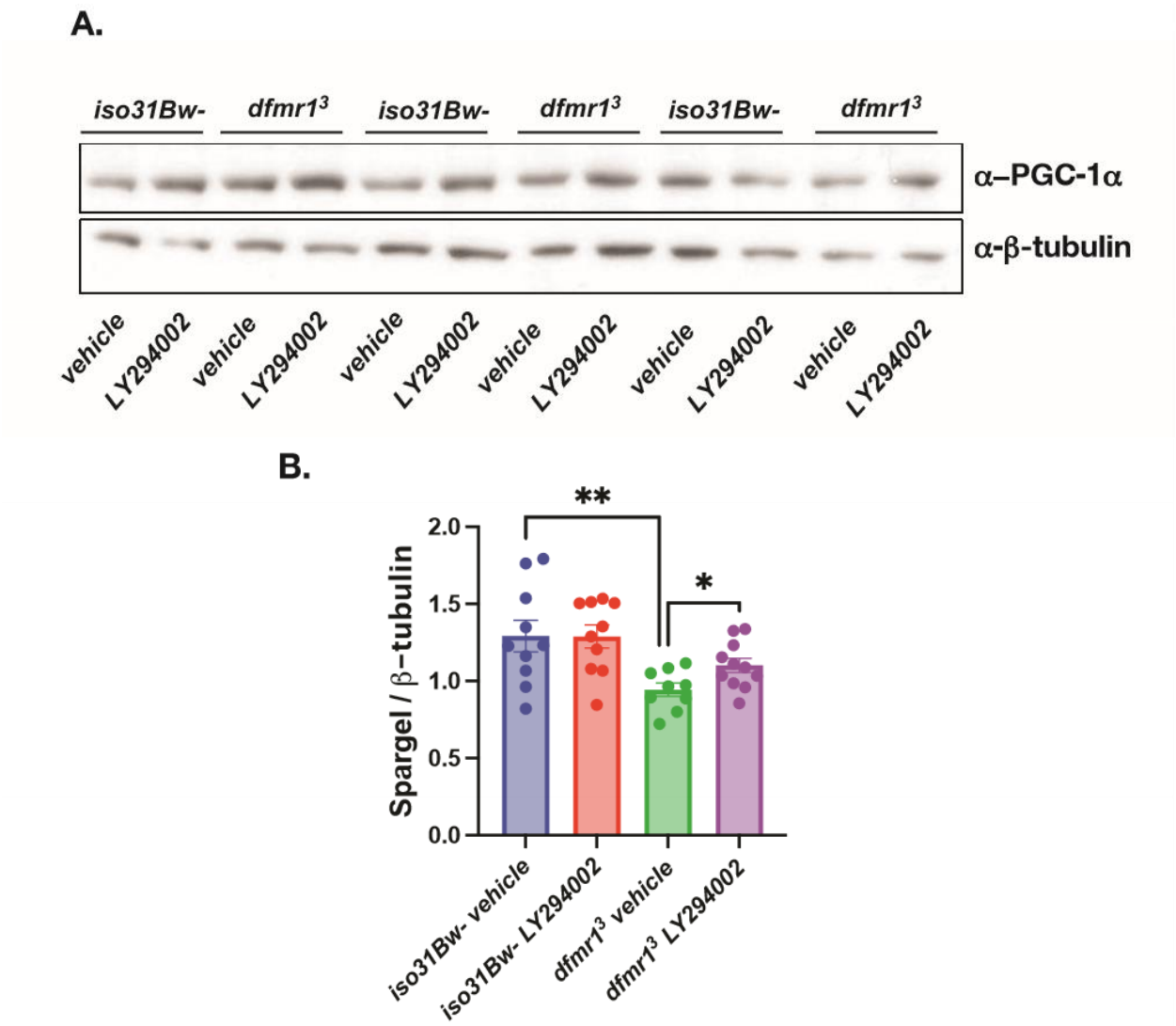

Figure S5.5: Pharmacologic reduction of IS boosts Spargel expression in the heads dfmr1 mutants. A, Representative western analysis of Spargel expression in extracts from *iso31Bw-* and *dfmr1* mutant fly heads that treated with either 5μM LY294002 or ethanol vehicle for 5 days post eclosion. An antibody to PGC-1α was used to detect Spargel expression (top). β-Tubulin was used as a loading control (bottom). **B,** Quantification of the intensity of Spargel relative to β-Tubulin. Results from three independent experiments were pooled together. An unpaired t-test indicated that *dfmr1* mutants treated with vehicle had lower Spargel expression than *iso31Bw-* controls treated with vehicle (p=0.0079). An unpaired t-test indicated that *dfmr1* mutant flies that were treated with LY294002 have higher Spargel expression than *dfmr1* mutants that were treated with vehicle (p=0.0239). Sample number (N) per condition: *iso31Bw-* (vehicle)=10, *iso31Bw-* (LY294002)=10, *dfmr1* (vehicle)=9, *dfmr1* (LY294002)=11. Each sample contained 10 fly heads. Values represent mean ± SEM. *p≤0.05, **p≤0.01.

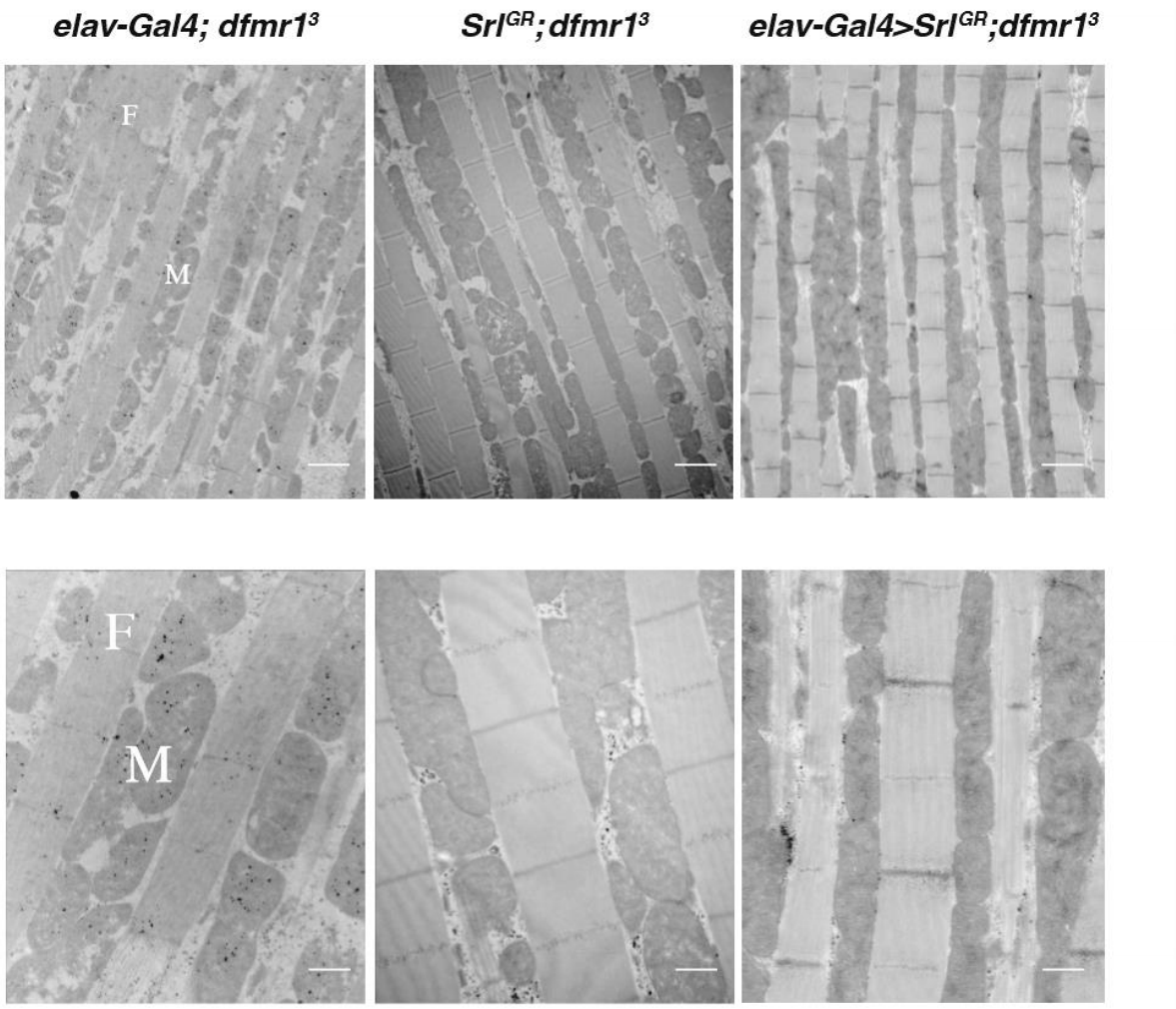

Figure S5.6: Pan-neuronal expression of *Srl^{GR}* in *dfmr1* mutants improves flight muscle mitochondrial ultrastructure. Longitudinal sections of indirect flight muscle were prepared from isolated thoraces for transmission electron microscopy experiments: Electron micrographs of Drosophila flight muscle at 7,500x magnification (top) and 20,000x (bottom). The genotype of each fly is denoted above its corresponding panel, from left to right: (*elav-Gal4; dfmr1^{3}),* (*Srl^{GR}; dfmr1^{3}*), and (*elav-Gal4>Srl^{GR}; dfmr1^{3}*). Scale bar indicates 2 microns for 7,000x magnification panels and 800 nm for 20,000x magnification panels. Mitochondria, M, are aligned between rows of myofibrils, F. The mitochondria of the *dfmr1* mutants that contain the *elav-Gal4* driver alone appear to be small and sparsely distributed along the adjacent myofibrils. These mitochondria also contain ultrastructural defects, particularly dispersions of cristae. In contrast, the mitochondria of the *dfmr1* mutants that contain the *Srl^{GR}* construct in conjunction with the *elav-Gal4* driver appear to be larger and fill the majority of the space between myofibrils. These mitochondria also contain more densely packed cristae that are free of dispersions. The mitochondria of *dfmr1* mutants that contain the *Srl^{GR}* construct alone have an intermediate phenotype, whereby there appears to be some modest improvement in mitochondrial ultrastructure. However, these mitochondria are more variable in size with large gaps between the myofibrils and areas of dispersed cristae. Given that UAS elements are known to have leaky expression even in the absence of a Gal4 driver, we believe that the rescue of mitochondrial ultrastructure by the *Srl^{GR}* construct alone likely results from low levels of leaky expression *Srl^{GR}*. The concordance between the dose-dependent rescue of circadian behavior and that of mitochondrial ultrastructure by *Srl^{GR}* provides further evidence that these phenotypes are mechanistically linked.

APPENDIX E: SUPPLEMENT TO CHAPTER 6

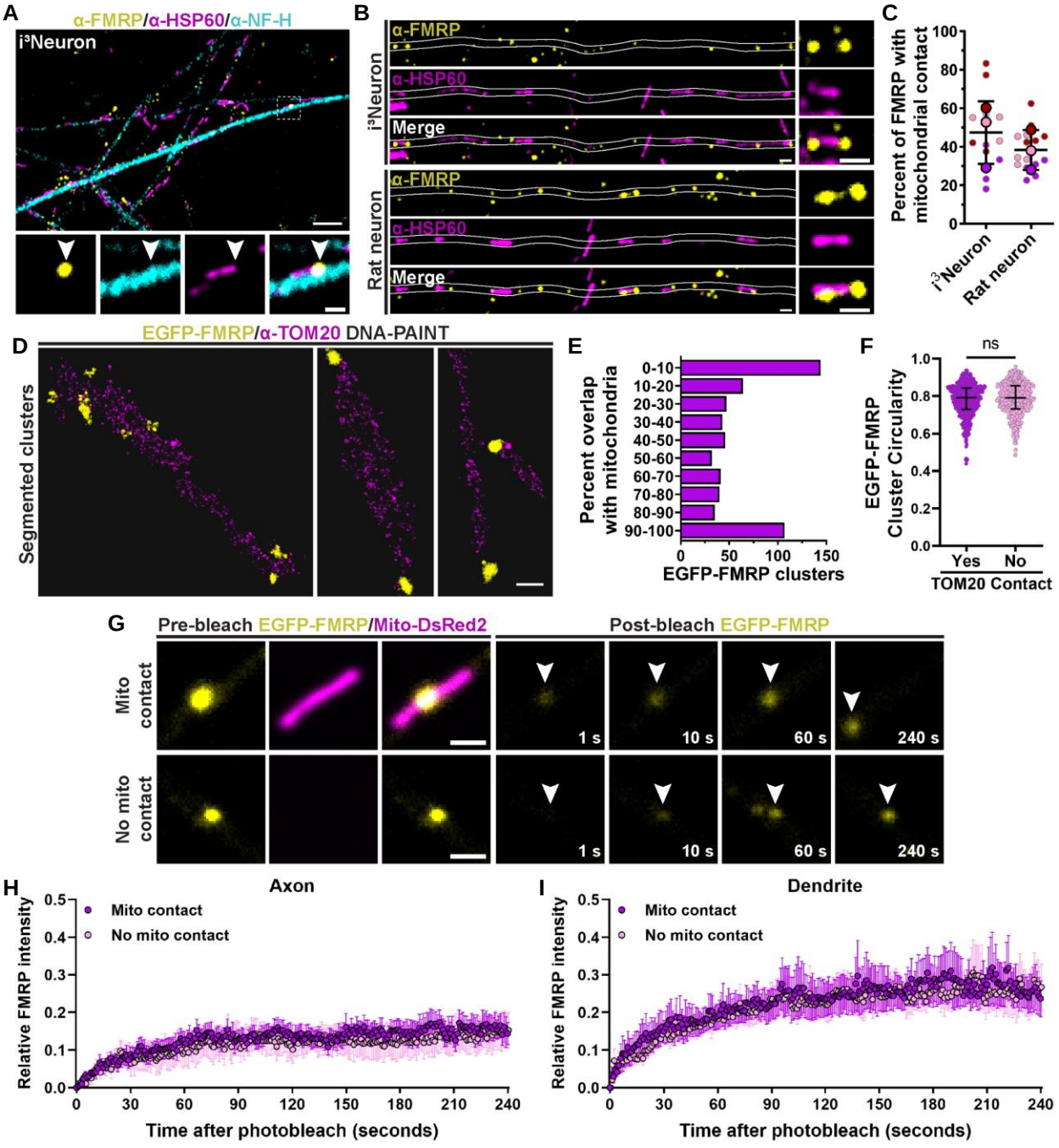

Figure S6.1: Mitochondrial association does not affect the liquid-like properties of FMRP granules. A, Maximum-intensity projection of DIV21 i^{3}Neuron culture stained for FMRP, HSP60, and Neurofilament (NF-H). Arrows indicate FMRP near mitochondria. **B,** Straightened images of DIV21 i^{3}Neuron and DIV8 rat hippocampal neuron cultures stained for FMRP and HSP60. **C,** Percent of FMRP granules contacting mitochondria in neurites. n=3 biological replicates, 15

technical replicates. Line and bars are mean ± s.d. for biological replicates. **D,** Representative images of segmented DNA-PAINT clusters for TOM20-marked mitochondria and EGFP-FMRP in rat hippocampal neurons. **E,** Histogram showing FMRP-mitochondria overlap for EGFP-FMRP clusters contacting mitochondria. n=599 clusters. **F,** Measure of circularity for DNA-PAINT clusters of EGFP-FMRP when contacting or not contacting TOM20 signal. n=599 clusters with contact and 600 clusters without contact. p=0.3322, two-tailed Mann-Whitney test. Circles are individual clusters, line and bars are mean ± s.d. **G,** Representative images showing fluorescence recovery of EGFP-FMRP following photo-bleaching in dendrites of DIV12 rat hippocampal neurons. **H-I,** FRAP quantification for EGFP-FMRP granules in axons or dendrites. n=7 axon granules with contact, 6 axon granules without contact, 9 dendrite granules with contact, and 6 granules without contact. Circles and bars are mean ± s.e.m. Scale bars: 5 µm (**A**); 1 µm (**A** inset**, B**, **G**); 500 nm (**D**).

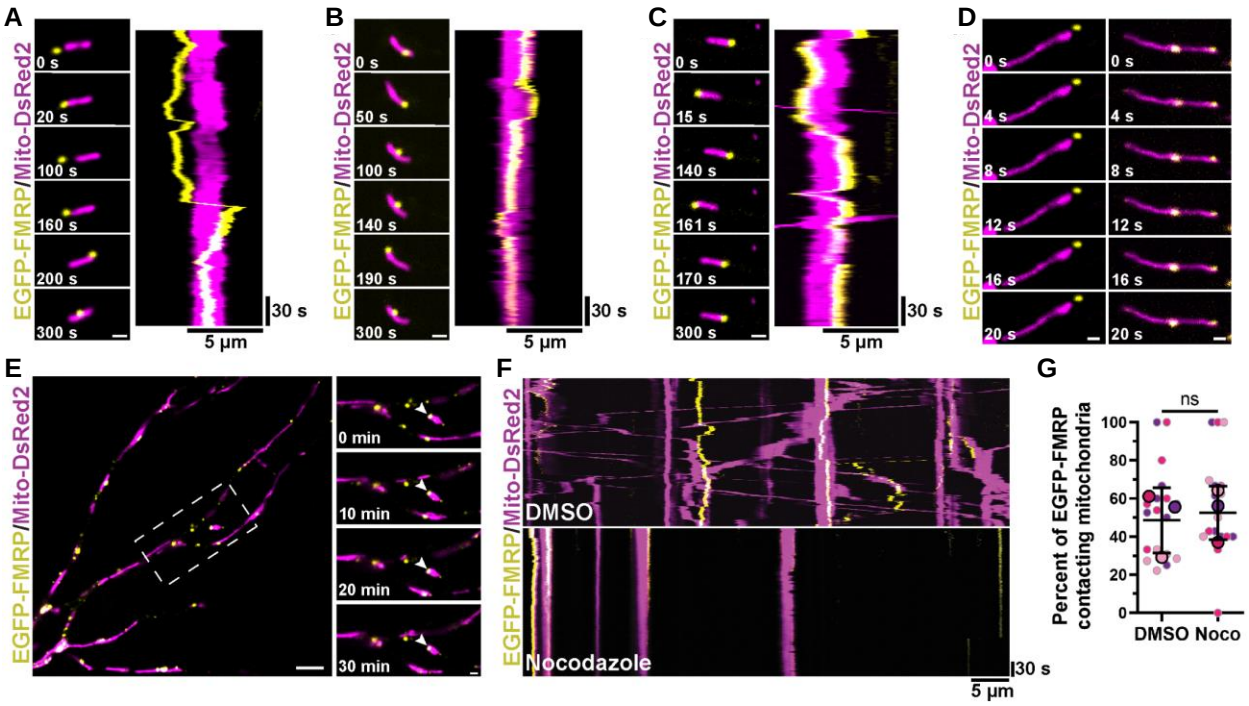

Figure S6.2: Characterization of FMRP-mitochondria dynamics in live neurons. A-C, Representative time series and kymographs depicting the dynamic localization of a FMRP granules along axonal mitochondria in DIV7 mouse cortical neurons **(A,B)** or a DIV10 rat hippocampal neuron **(C)**. **D,** Representative time series depicting stable placement of FMRP at the midzone, end, and near the end of dendritic mitochondria in DIV10 rat hippocampal neurons. **E,** Time series showing an FMRP-mitochondria contact that persists over 30 minutes in the dendrite of a DIV12 rat hippocampal neuron. **F,** Kymographs showing FMRP-mitochondria contacts in axons of DIV8 rat hippocampal neurons upon DMSO or nocodazole treatment. **G,** Percent of EGFP-FMRP granules contacting mitochondria in axons upon DMSO or nocodazole (Noco) treatment. n=18 axons, 3 biological replicates. Line and bars are mean ± s.d. for biological replicates. p=0.7758, two-tailed unpaired t-test. Scale bars: 10 µm (**E**); 1 µm (**A, B, C, D, E** inset).

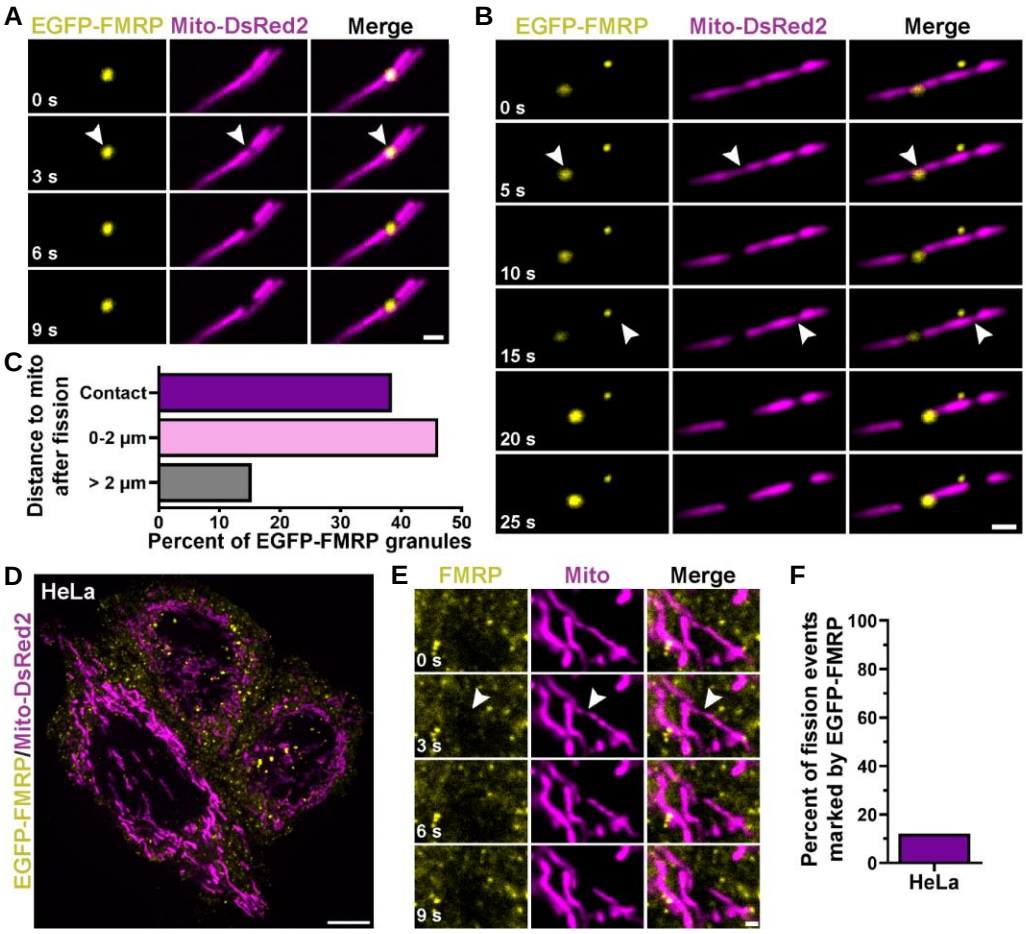

Figure S6.3: Mitochondrial fission sites are marked by FMRP in neurons, but not in HeLa cells. A-B, Representative time series showing EGFP-FMRP granules near sites of mitochondrial fission in dendrites of DIV10 rat hippocampal neurons. Fission sites are indicated by arrowheads. **C,** EGFP-FMRP granules are retained near daughter mitochondria 1 minute after fission has occurred. n=26 fission events. **D,** EGFP-FMRP and Mito-DsRed2 localization in HeLa cells. **E,** Representative time series showing that EGFP-FMRP is not present at a mitochondrial fission event in a HeLa cell. The fission site is indicated by arrowheads. **F,** Percent of mitochondrial fission events marked by EGFP-FMRP in HeLa cells. n=50 fission events from 14 HeLa cells. Scale bars: 10 µm (**A**); 1 µm (**B**, **D**, **E**).

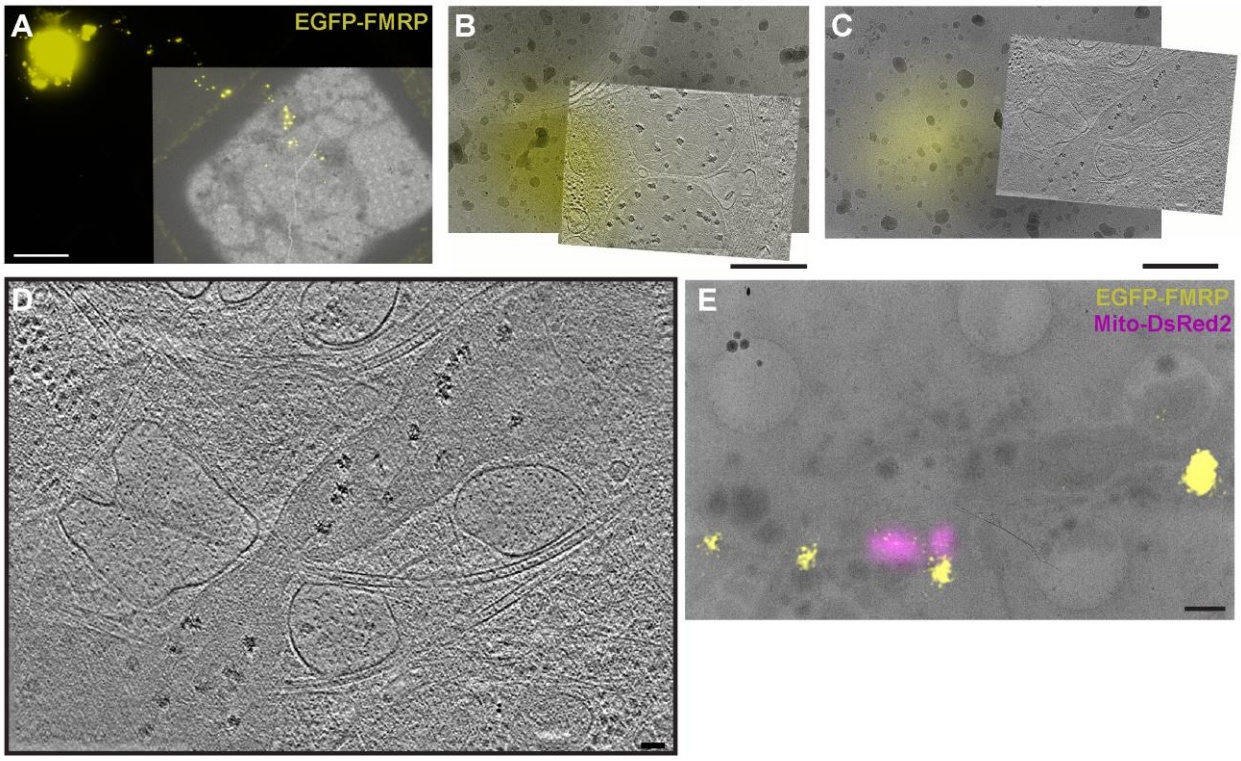

Figure S6.4: Selection of target regions for cryo-ET data collection. A, Overlay of cryogenic fluorescence image (background) and cryo-electron microscopy images (inset) of a DIV6 rat hippocampal neuron expressing EGFP-FMRP cultured on an electron microscopy grid. **B-C,** Low magnification cryo-electron microscopy images (background) and slices from tomograms (inset) with EGFP-FMRP fluorescence (yellow) overlaid. Examples correspond to Fig. 6.4A-B **(B)** and Fig. 6.4F **(C)**. **D,** Tomogram corresponding to Fig. 6.4F. **E,** Low magnification cryo-electron microscopy image corresponding to Fig. 6.4I with EGFP-FMRP and Mito-DsRed2 fluorescence overlaid. Scale bars: 20 µm (**A**); 1 µm (**E**); 500 nm (**B**, **C**); 50 nm (**D**).

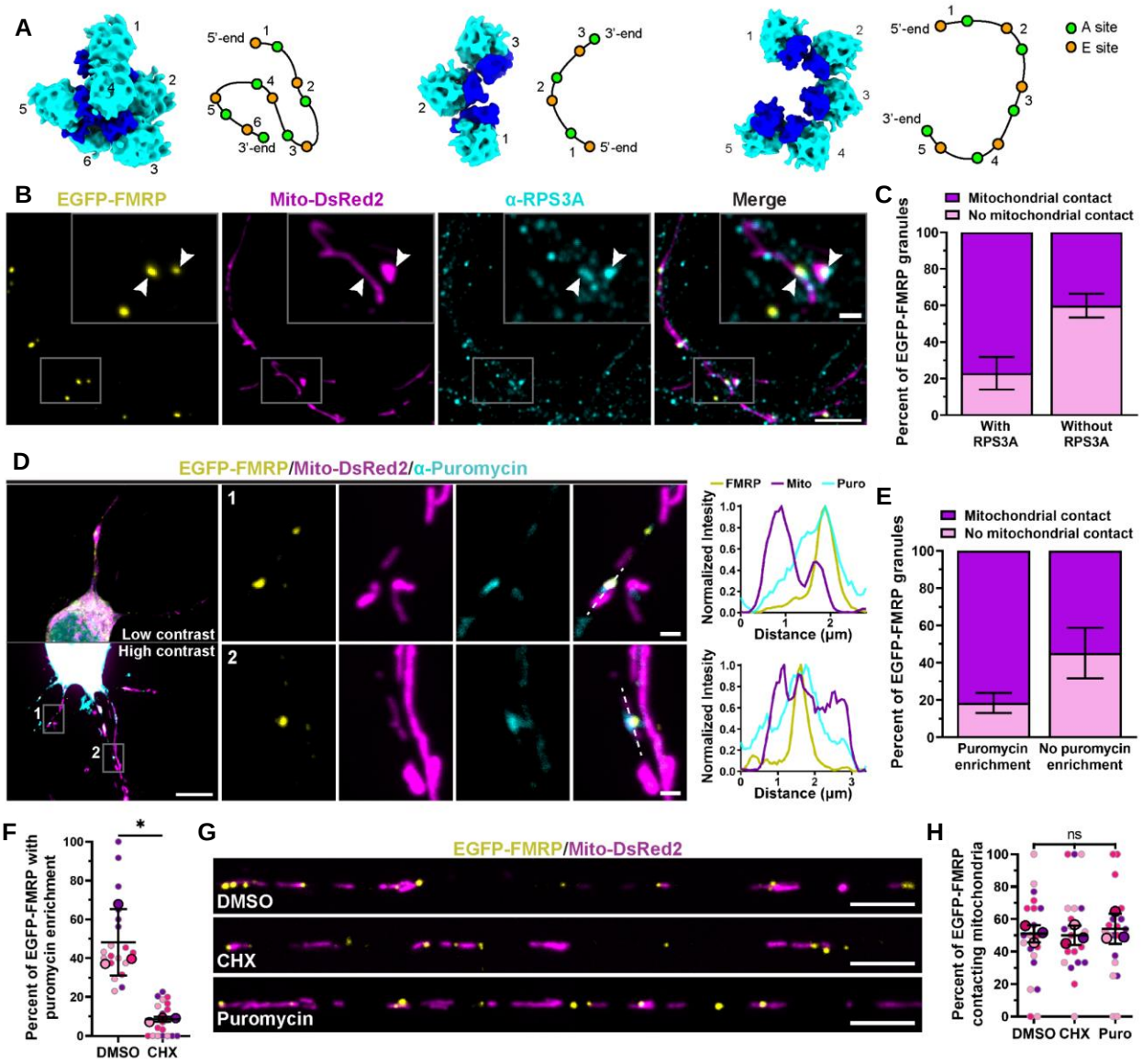

Figure S6.5: Mitochondria-associated FMRP granules are sites of protein synthesis. A, Polysomes found in tomograms with putative mRNA paths depicted to the right of each example. **B,** Maximum-intensity projection of a DIV10 rat hippocampal neuron expressing EGFP-FMRP and Mito-DsRed2, and stained for ribosomal subunit RPS3A. Arrows indicate ribosomal overlap with mitochondria-associated EGFP-FMRP. **C,** Percent of EGFP-FMRP granules contacting mitochondria with or without RPS3A overlap. Line and bars are mean ± s.d. n=3 biological replicates. **D,** Maximum-intensity projection and line scans of a DIV8 rat hippocampal neuron expressing EGFP-FMRP and Mito-DsRed2, and stained for puromycin to label newly synthesized proteins. **E,** Percent of EGFP-FMRP granules contacting mitochondria when there is or is not puromycin enrichment. n=4 biological replicates. Line and bars are mean ± s.d. **F,** Analysis of puromycin enrichment at EGFP-FMRP granules upon inhibition of protein synthesis with cycloheximide (CHX). n=3 biological replicates, 20 neurons. Line and bars are mean ± s.d. for biological replicates. **G,** Straightened images of EGFP-FMRP and Mito-DsRed2 in axons from DIV11 rat hippocampal neurons treated with DMSO, CHX, or puromycin. **H,** Percent of EGFP-FMRP granules contacting mitochondria in axons upon DMSO, CHX, or puromycin treatment. n=20 axons, 3 biological replicates. Line and bars are mean ± s.d. for biological replicates. p values: DMSO vs. CHX, p=0.9845; DMSO vs. Puro, p=0.8644; CHX vs Puro, p=0.7784; ordinary one-way ANOVA with Tukey's multiple comparisons test. Scale bars: 10 µm (**D**), 5 µm (**B, G**), 1 µm (**B** inset, **D** inset).

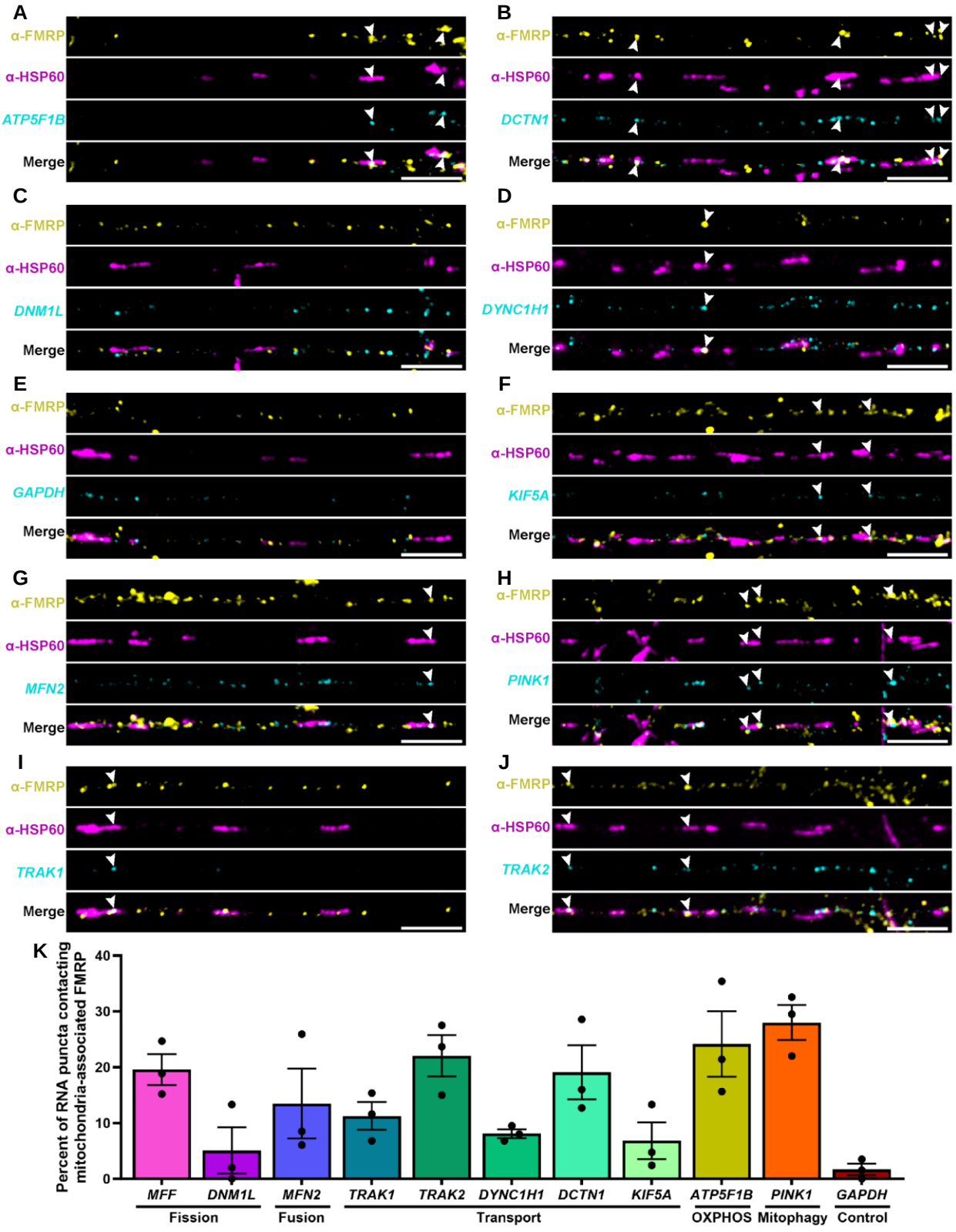
A
α-FMRP
α-HSP60
ATP5F1B
Merge
B
α-FMRP
α-HSP60
DCTN1
Merge
C
α-FMRP
α-HSP60
DNM1L
Merge
D
α-FMRP
α-HSP60
DYNC1H1
Merge
E
α-FMRP
α-HSP60
GAPDH
Merge
F
α-FMRP
α-HSP60
KIF5A
Merge
G
α-FMRP
α-HSP60
MFN2
Merge
H
α-FMRP
α-HSP60
PINK1
Merge
I
α-FMRP
α-HSP60
TRAK1
Merge
J
α-FMRP
α-HSP60
TRAK2
Merge
K
Percent of RNA puncta contacting mitochondria-associated FMRP
0
10
20
30
40
MFF
DNM1L
MFN2
TRAK1
TRAK2
DYNC1H1
DCTN1
KIF5A
ATP5F1B
PINK1
GAPDH
Fission
Fusion
Transport
OXPHOS
Mitophagy
Control

Figure S6.6: FISH analysis of RNA colocalization with mitochondria and FMRP. A-J, Representative images showing RNA FISH combined with immunostaining for FMRP and HSP60 (mitochondria) in DIV21 i^3Neurons. Arrows indicate mRNA puncta that overlap with mitochondria-associated FMRP granules. **K,** Percent of RNA puncta overlapping mitochondria-associated FMRP in DIV21 i^3Neurons. Associated mitochondrial processes are labeled below each gene. Line and bars are mean ± s.d. n=3 biological replicates. Scale bars: 5 µm.

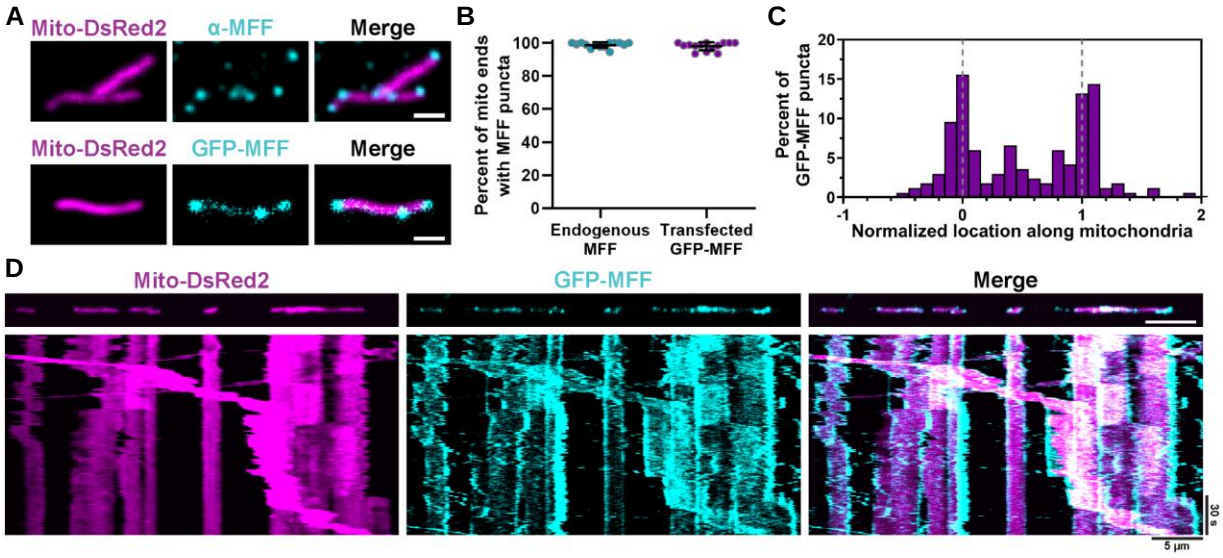

Figure S6.7: MFF marks mitochondrial ends in neurons. A, Representative images showing endogenous MFF and GFP-MFF at the ends of mitochondria in DIV9 rat hippocampal neurons. Scale bars are 1 micron. **B,** Quantification of MFF presence at mitochondrial ends. n=14 neurons. Line and bars are mean ± s.d. **C,** Normalized quantification of GFP-MFF location along mitochondria, where the length of the mitochondria is normalized from 0 to 1. n=168 puncta from 11 rat hippocampal neurons. **D,** Images and corresponding kymographs showing GFP-MFF co-trafficking with mitochondrial ends in a DIV10 rat hipp ocampal neuron. Scale bars: 1 µm (**A**); 5 µm (**D**).

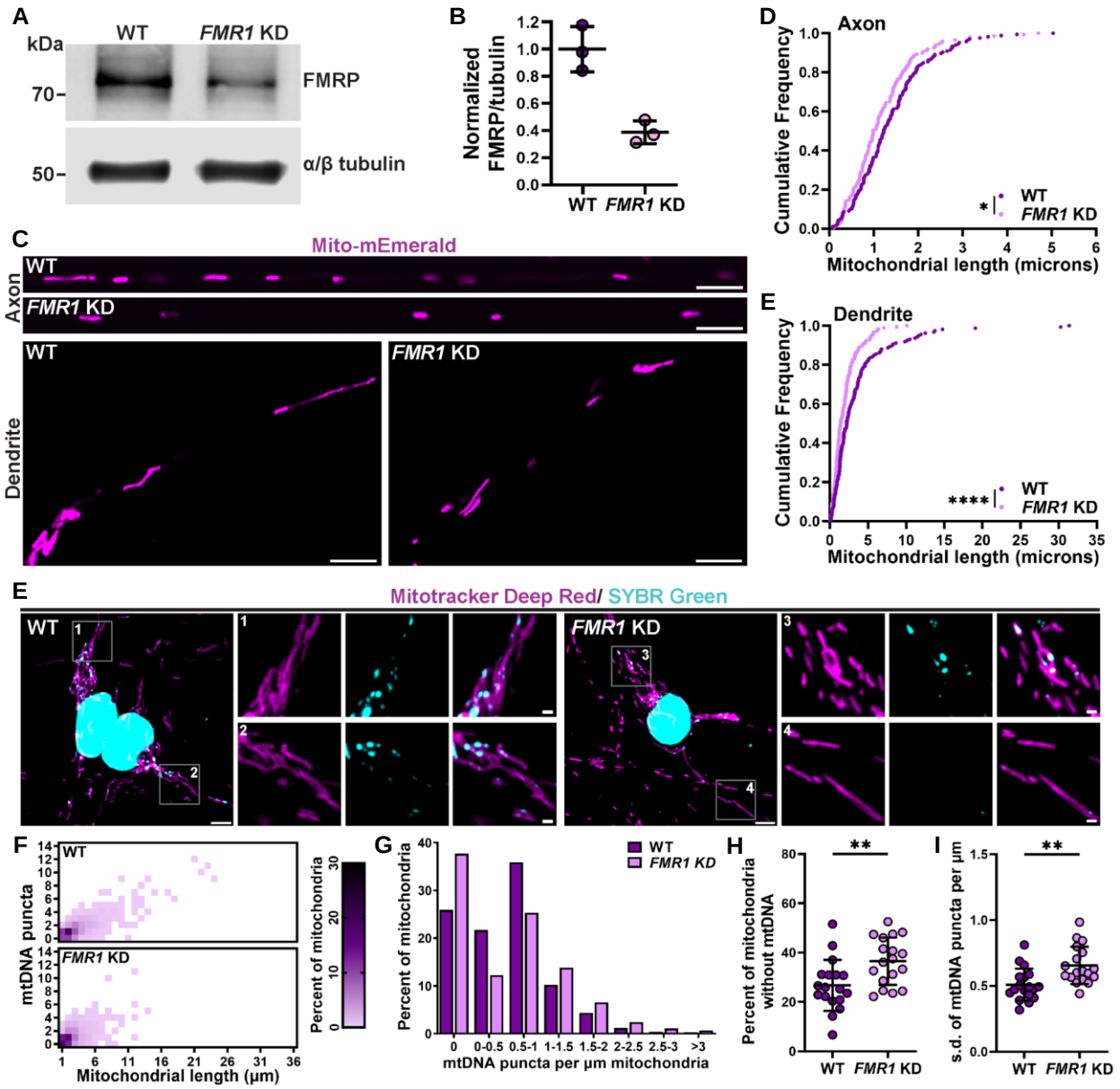

Figure S6.8: FMRP knockdown in i^{3}Neurons produces shortened mitochondrial networks with disorganized mitochondrial DNA. A, Representative western blot showing levels of FMRP in wild-type (WT) or *FMR1* KD i^{3}Neurons. **B,** Quantification of FMRP knockdown in i^{3}Neurons. Bars represent mean ± s.d. from three independent experiments. **C,** Representative images showing Mito-mEmerald-labelled mitochondria in straightened axons or dendrites of DIV21 WT or *FMR1* KD neurons. **D,** Cumulative frequency of mitochondrial length in axons of WT or *FMR1* KD neurons. n=165 mitochondria from 16 WT axons and 149 mitochondria from 16 *FMR1* KD axons. *p < 0.05, two-tailed Mann-Whitney test. **E,** Cumulative frequency of mitochondrial length in DIV21 dendrites of WT or *FMR1* KD neurons. n=159 mitochondria from 9 WT dendrites and 183 mitochondria from 8 *FMR1* KD dendrites. ****p < 0.0001, two-tailed Mann-Whitney test. **F,** Representative maximum-intensity projections with insets of mitochondria labeled with Mitotracker Deep Red and DNA labeled with SYBR green in DIV21 wild-type (WT) or *Fmr1* KD i^{3}Neurons. **G-H,** Heatmap of mitochondrial DNA (mtDNA) puncta per mitochondrion vs mitochondrial length **(G)** and distribution of mtDNA puncta

density **(H)** in WT and *Fmr1* KD i^{3}Neurons. n=1006 WT mitochondria and 1154 *Fmr1* KO mitochondria. **I-J,** Percent of mitochondria lacking mtDNA **(I)** and standard deviation of mtDNA puncta per micron mitochondria **(J)** for 18 WT and *Fmr1* KD i^{3}Neurons. Line and bars are mean ± s.d. **p < 0.01, two-tailed unpaired t-test. Scale bars: 5 µm (**C**, **F**); 1 µm (**F** inset).

Supplemental videos for Chapter 6

Video S6.1: FMRP-mitochondria dynamics in a mouse axon. Dynamics of EGFP-FMRP (yellow) and Mito-DsRed2-labelled mitochondria (magenta) in the axon (top) of a mouse cortical neuron. Time = min:sec. Scale bar: 5 µm.

https://upenn.box.com/s/kmnk3xvvx0t3jli9qh01k3yvq40flw4g

Video S6.2: FMRP-mitochondria dynamics in a rat axon. Dynamics of EGFP-FMRP (yellow) and Mito-DsRed2-labelled mitochondria (magenta) in the axon of a rat hippocampal neuron. Time = min:sec.

https://upenn.box.com/s/wlnpc3ubhszh6ox7bnkysyc0y4yyk8ih

Video S6.3: FMRP-mitochondria co-transport. Co-transport of EGFP-FMRP (yellow) and Mito-DsRed2-labelled mitochondria (magenta) in the axon of a rat hippocampal neuron. Time = min:sec. Scale bar: 5 µm.

https://upenn.box.com/s/fbsutu3wqr18ahv1owwzdt3zij24w814

Video S6.4: FMRP granules mark sites of mitochondrial fission. An EGFP-FMRP granule (yellow) is recruited to the midzone of a Mito-DsRed2-labelled mitochondria (magenta), where it marks a site of fission in the axon of a mouse cortical neuron. Time = min:sec. Scale bar: 1 µm.

https://upenn.box.com/s/6wr5ztljfldrvq4fli0d4p2bf5o45o6u

Video S6.5: Lysosome-FMRP-mitochondria contacts. A LAMP1-Halo vesicle (cyan) forms stable contacts with a Halo-FMRP granule (yellow) and the end of a Mito-DsRed2-labelled mitochondria (magenta) in the dendrite of a rat hippocampal neuron. Left (mitochondria and FMRP), middle (mitochondria and LAMP1), right (merge). Time = min:sec. Scale bars: 1 µm.

https://upenn.box.com/s/1vqk4sahlo2rpiz67mg43gjsl9o93hqm

Video S6.6: Lysosome-associated FMRP granules mark sites of mitochondrial fission. Halo-FMRP (yellow) and LAMP1-Halo (cyan) mark a site of fission for Mito-DsRed2-labelled mitochondria (magenta) in the dendrite of a rat hippocampal neuron. Left (mitochondria and FMRP), middle (mitochondria and LAMP1), right (merge). Time = min:sec. Scale bars: 1 µm.

https://upenn.box.com/s/k053al3v3hrdrxagdpmyjrpmiwi7vda9

Video S6.7: Lysosome-associated FMRP granules mark sites of mitochondrial fission. Halo Tomogram and segmented reconstruction of an EGFP-FMRP target in a rat hippocampal neuron.

https://upenn.box.com/s/1a41ig450shx6vslh2ntqbkfegngx3w2

Video S6.8: Lysosome-associated FMRP granules mark sites of mitochondrial fission. Halo Tomogram and segmented reconstruction near an EGFP-FMRP target in a rat hippocampal neuron.

https://upenn.box.com/s/2732m3hajeanlxcumhw9yzm1thrv5xt9

Video S6.9: Lysosome-associated FMRP granules mark sites of mitochondrial fission. Halo Halo-FMRP (yellow) and GFP-MFF (cyan) mark a site of fission for Mito-DsRed2-labelled mitochondria (magenta) in the dendrite of a rat hippocampal neuron. Left (mitochondria and FMRP), middle (mitochondria and MFF), right (merge). Time = min:sec.

https://upenn.box.com/s/k1h9vnn6g7bpz9tcm07dehggmvbvacx3

BIBLIOGRAPHY

Abrisch, R. G., Gumbin, S. C., Wisniewski, B. T., Lackner, L. L., & Voeltz, G. K. (2020). Fission and fusion machineries converge at ER contact sites to regulate mitochondrial morphology. *Journal of Cell Biology*, *219*(4), e201911122. https://doi.org/10.1083/jcb.201911122

Aiken, J., & Holzbaur, E. L. F. (2021). Cytoskeletal regulation guides neuronal trafficking to effectively supply the synapse. *Current Biology*, *31*(10), R633–R650. https://doi.org/10.1016/j.cub.2021.02.024

Aiken, J., & Holzbaur, E. L. F. (2023). *Spastin locally amplifies microtubule dynamics to pattern the axon for presynaptic cargo delivery* [Preprint]. Cell Biology. https://doi.org/10.1101/2023.08.08.552320

Akiyama, T., Suzuki, N., Ishikawa, M., Fujimori, K., Sone, T., Kawada, J., Funayama, R., Fujishima, F., Mitsuzawa, S., Ikeda, K., Ono, H., Shijo, T., Osana, S., Shirota, M., Nakagawa, T., Kitajima, Y., Nishiyama, A., Izumi, R., Morimoto, S., … Aoki, M. (2019). Aberrant axon branching via Fos-B dysregulation in FUS-ALS motor neurons. *EBioMedicine*, *45*, 362–378. https://doi.org/10.1016/j.ebiom.2019.06.013

Ali, F. A., Zwetsloot, A. J., Stone, C. E., Morgan, T. E., Wademan, R. F., Carter, A. P., & Straube, A. (2023). *KIF1C activates and extends dynein movement through the FHF cargo adaptor* (p. 2023.10.26.564242). bioRxiv. https://doi.org/10.1101/2023.10.26.564242

Amin, A., Perera, N. D., Beart, P. M., Turner, B. J., & Shabanpoor, F. (2020). Amyotrophic Lateral Sclerosis and Autophagy: Dysfunction and Therapeutic Targeting. *Cells*, *9*(11), Article 11. https://doi.org/10.3390/cells9112413

Anand, R., Wai, T., Baker, M. J., Kladt, N., Schauss, A. C., Rugarli, E., & Langer, T. (2014). The i-AAA protease YME1L and OMA1 cleave OPA1 to balance mitochondrial fusion and fission. *The Journal of Cell Biology*, *204*(6), 919–929. https://doi.org/10.1083/jcb.201308006

Anders, S., Pyl, P. T., & Huber, W. (2015). HTSeq—A Python framework to work with high-throughput sequencing data. *Bioinformatics*, *31*(2), 166–169. https://doi.org/10.1093/bioinformatics/btu638

Antar, L. N., Afroz, R., Dictenberg, J. B., Carroll, R. C., & Bassell, G. J. (2004). Metabotropic Glutamate Receptor Activation Regulates Fragile X Mental Retardation Protein and Fmr1 mRNA Localization Differentially in Dendrites and at Synapses. *Journal of Neuroscience*, *24*(11), 2648–2655. https://doi.org/10.1523/JNEUROSCI.0099-04.2004

Antar, L. N., Dictenberg, J. B., Plociniak, M., Afroz, R., & Bassell, G. J. (2005). Localization of FMRP-associated mRNA granules and requirement of microtubules for activity-dependent trafficking in hippocampal neurons. *Genes, Brain and Behavior*, *4*(6), 350–359. https://doi.org/10.1111/j.1601-183X.2005.00128.x

Antar, L. N., Li, C., Zhang, H., Carroll, R. C., & Bassell, G. J. (2006). Local functions for FMRP in axon growth cone motility and activity-dependent regulation of filopodia and spine synapses. *Molecular and Cellular Neuroscience*, *32*(1), 37–48. https://doi.org/10.1016/j.mcn.2006.02.001

Antrobus, R., & Borner, G. H. H. (2011). Improved Elution Conditions for Native Co-Immunoprecipitation. *PLOS ONE*, *6*(3), e18218. https://doi.org/10.1371/journal.pone.0018218

Arrasate, M., & Finkbeiner, S. (2005). Automated microscope system for determining factors that predict neuronal fate. *Proceedings of the National Academy of Sciences*, *102*(10), 3840–3845. https://doi.org/10.1073/pnas.0409777102

Ascano, M., Mukherjee, N., Bandaru, P., Miller, J. B., Nusbaum, J. D., Corcoran, D. L., Langlois, C., Munschauer, M., Dewell, S., Hafner, M., Williams, Z., Ohler, U., & Tuschl, T. (2012). FMRP targets distinct mRNA sequence elements to regulate protein expression. *Nature*, *492*(7429), 382–386. https://doi.org/10.1038/nature11737

Ashley, C. T., Wilkinson, K. D., Reines, D., & Warren, S. T. (1993). FMR1 Protein: Conserved RNP Family Domains and Selective RNA Binding. *Science*, *262*(5133), 563–566. https://doi.org/10.1126/science.7692601

Asselin, L., Rivera Alvarez, J., Heide, S., Bonnet, C. S., Tilly, P., Vitet, H., Weber, C., Bacino, C. A., Baranaño, K., Chassevent, A., Dameron, A., Faivre, L., Hanchard, N. A., Mahida, S., McWalter, K., Mignot, C., Nava, C., Rastetter, A., Streff, H., … Godin, J. D. (2020). Mutations in the KIF21B kinesin gene cause neurodevelopmental disorders through imbalanced canonical motor activity. *Nature Communications*, *11*(1), Article 1. https://doi.org/10.1038/s41467-020-16294-6

Ayloo, S., Lazarus, J. E., Dodda, A., Tokito, M., Ostap, E. M., & Holzbaur, E. L. F. (2014). Dynactin functions as both a dynamic tether and brake during dynein-driven motility. *Nature Communications*, *5*(1), 4807. https://doi.org/10.1038/ncomms5807

Baas, P. W., Deitch, J. S., Black, M. M., & Banker, G. A. (1988). Polarity orientation of microtubules in hippocampal neurons: Uniformity in the axon and nonuniformity in the dendrite. *Proceedings of the National Academy of Sciences*, *85*(21), 8335–8339. https://doi.org/10.1073/pnas.85.21.8335

Babic, M., Russo, G. J., Wellington, A. J., Sangston, R. M., Gonzalez, M., & Zinsmaier, K. E. (2015). Miro's N-Terminal GTPase Domain Is Required for Transport of Mitochondria into Axons and Dendrites. *Journal of Neuroscience*, *35*(14), 5754–5771. https://doi.org/10.1523/JNEUROSCI.1035-14.2015

Bailey, D. B., Raspa, M., & Olmsted, M. G. (2010). Using a Parent Survey to Advance Knowledge About the Nature and Consequences of Fragile X Syndrome. *American Journal on Intellectual and Developmental Disabilities*, *115*(6), 447–460. https://doi.org/10.1352/1944-7558-115.6.447

Bakker, C. E., & Oostra, B. A. (2003). Understanding fragile X syndrome: Insights from animal models. *Cytogenetic and Genome Research*, *100*(1–4), 111–123. https://doi.org/10.1159/000072845

Balan, V., Miller, G. S., Kaplun, L., Balan, K., Chong, Z.-Z., Li, F., Kaplun, A., VanBerkum, M. F. A., Arking, R., Freeman, D. C., Maiese, K., & Tzivion, G. (2008). Life Span Extension and Neuronal Cell Protection by *Drosophila* Nicotinamidase*. *Journal of Biological Chemistry*, *283*(41), 27810–27819. https://doi.org/10.1074/jbc.M804681200

Baldwin, K. R., Godena, V. K., Hewitt, V. L., & Whitworth, A. J. (2016). Axonal transport defects are a common phenotype in *Drosophila* models of ALS. *Human Molecular Genetics*, ddw105. https://doi.org/10.1093/hmg/ddw105

Ban, T., Ishihara, T., Kohno, H., Saita, S., Ichimura, A., Maenaka, K., Oka, T., Mihara, K., & Ishihara, N. (2017). Molecular basis of selective mitochondrial fusion by heterotypic action between OPA1 and cardiolipin. *Nature Cell Biology*, *19*(7), 856–863. https://doi.org/10.1038/ncb3560

Bardoni, B., & Mandel, J.-L. (2002). Advances in understanding of fragile X pathogenesis and FMRP function, and in identification of X linked mental retardation genes. *Current Opinion in Genetics & Development*, *12*(3), 284–293. https://doi.org/10.1016/S0959-437X(02)00300-3

Barmada, S. J., Ju, S., Arjun, A., Batarse, A., Archbold, H. C., Peisach, D., Li, X., Zhang, Y., Tank, E. M. H., Qiu, H., Huang, E. J., Ringe, D., Petsko, G. A., & Finkbeiner, S. (2015). Amelioration of toxicity in neuronal models of amyotrophic lateral sclerosis by hUPF1. *Proceedings of the National Academy of Sciences*, *112*(25), 7821–7826. https://doi.org/10.1073/pnas.1509744112

Barmada, S. J., Serio, A., Arjun, A., Bilican, B., Daub, A., Ando, D. M., Tsvetkov, A., Pleiss, M., Li, X., Peisach, D., Shaw, C., Chandran, S., & Finkbeiner, S. (2014). Autophagy induction enhances TDP43 turnover and survival in neuronal ALS models. *Nature Chemical Biology*, *10*(8), Article 8. https://doi.org/10.1038/nchembio.1563

Barmada, S. J., Skibinski, G., Korb, E., Rao, E. J., Wu, J. Y., & Finkbeiner, S. (2010). Cytoplasmic Mislocalization of TDP-43 Is Toxic to Neurons and Enhanced by a Mutation Associated with

Familial Amyotrophic Lateral Sclerosis. *Journal of Neuroscience*, *30*(2), 639–649. https://doi.org/10.1523/JNEUROSCI.4988-09.2010

Baumbach, J., Murthy, A., McClintock, M. A., Dix, C. I., Zalyte, R., Hoang, H. T., & Bullock, S. L. (2017). Lissencephaly-1 is a context-dependent regulator of the human dynein complex. *eLife*, *6*, e21768. https://doi.org/10.7554/eLife.21768

Bechara, E. G., Didiot, M. C., Melko, M., Davidovic, L., Bensaid, M., Martin, P., Castets, M., Pognonec, P., Khandjian, E. W., Moine, H., & Bardoni, B. (2009). A Novel Function for Fragile X Mental Retardation Protein in Translational Activation. *PLOS Biology*, *7*(1), e1000016. https://doi.org/10.1371/journal.pbio.1000016

Becker, L.-L., Dafsari, H. S., Schallner, J., Abdin, D., Seifert, M., Petit, F., Smol, T., Bok, L., Rodan, L., Krapels, I., Spranger, S., Weschke, B., Johnson, K., Straub, V., Kaindl, A. M., Di Donato, N., von der Hagen, M., & Cirak, S. (2020). The clinical-phenotype continuum in DYNC1H1-related disorders—Genomic profiling and proposal for a novel classification. *Journal of Human Genetics*, *65*(11), 1003–1017. https://doi.org/10.1038/s10038-020-0803-1

Bell, M. V., Hirst, M. C., Nakahori, Y., MacKinnon, R. N., Roche, A., Flint, T. J., Jacobs, P. A., Tommerup, N., Tranebjaerg, L., Froster-Iskenius, U., Kerr, B., Turner, G., Lindenbaum, R. H., Winter, R., Prembrey, M., Thibodeau, S., & Davies, K. E. (1991). Physical mapping across the fragile X: Hypermethylation and clinical expression of the fragile X syndrome. *Cell*, *64*(4), 861–866. https://doi.org/10.1016/0092-8674(91)90514-Y

Berg, S., Kutra, D., Kroeger, T., Straehle, C. N., Kausler, B. X., Haubold, C., Schiegg, M., Ales, J., Beier, T., Rudy, M., Eren, K., Cervantes, J. I., Xu, B., Beuttenmueller, F., Wolny, A., Zhang, C., Koethe, U., Hamprecht, F. A., & Kreshuk, A. (2019). ilastik: Interactive machine learning for (bio)image analysis. *Nature Methods*, *16*(12), 1226–1232. https://doi.org/10.1038/s41592-019-0582-9

Berridge, M. J., Bootman, M. D., & Lipp, P. (1998). Calcium—A life and death signal. *Nature*, *395*(6703), Article 6703. https://doi.org/10.1038/27094

Berridge, M. J., Lipp, P., & Bootman, M. D. (2000). The versatility and universality of calcium signalling. *Nature Reviews Molecular Cell Biology*, *1*(1), Article 1. https://doi.org/10.1038/35036035

Berth, S. H., & Lloyd, T. E. (2023). Disruption of axonal transport in neurodegeneration. *The Journal of Clinical Investigation*, *133*(11). https://doi.org/10.1172/JCI168554

Bhogal, B., & Jongens, T. A. (2010). Fragile X syndrome and model organisms: Identifying potential routes of therapeutic intervention. *Disease Models & Mechanisms*, *3*(11–12), 693–700. https://doi.org/10.1242/dmm.002006

Bilican, B., Serio, A., Barmada, S. J., Nishimura, A. L., Sullivan, G. J., Carrasco, M., Phatnani, H. P., Puddifoot, C. A., Story, D., Fletcher, J., Park, I.-H., Friedman, B. A., Daley, G. Q., Wyllie, D. J. A., Hardingham, G. E., Wilmut, I., Finkbeiner, S., Maniatis, T., Shaw, C. E., & Chandran, S. (2012). Mutant induced pluripotent stem cell lines recapitulate aspects of TDP-43 proteinopathies and reveal cell-specific vulnerability. *Proceedings of the National Academy of Sciences*, *109*(15), 5803–5808. https://doi.org/10.1073/pnas.1202922109

Birsa, N., Norkett, R., Higgs, N., Lopez-Domenech, G., & Kittler, J. T. (2013). Mitochondrial trafficking in neurons and the role of the Miro family of GTPase proteins. *Biochemical Society Transactions*, *41*(6), 1525–1531. https://doi.org/10.1042/BST20130234

Blasius, T. L., Cai, D., Jih, G. T., Toret, C. P., & Verhey, K. J. (2007). Two binding partners cooperate to activate the molecular motor Kinesin-1. *Journal of Cell Biology*, *176*(1), 11–17. https://doi.org/10.1083/jcb.200605099

Blasius, T. L., Yue, Y., Prasad, R., Liu, X., Gennerich, A., & Verhey, K. J. (2021). Sequences in the stalk domain regulate auto-inhibition and ciliary tip localization of the immotile kinesin-4 KIF7. *Journal of Cell Science*, *134*(13), jcs258464. https://doi.org/10.1242/jcs.258464

Blokhuis, A. M., Groen, E. J. N., Koppers, M., van den Berg, L. H., & Pasterkamp, R. J. (2013). Protein aggregation in amyotrophic lateral sclerosis. *Acta Neuropathologica*, *125*(6), 777–794. https://doi.org/10.1007/s00401-013-1125-6

Bocanegra, J. L., Fujita, B. M., Melton, N. R., Cowan, J. M., Schinski, E. L., Tamir, T. Y., Major, M. B., & Quintero, O. A. (2020). The MyMOMA domain of MYO19 encodes for distinct Miro-dependent and Miro-independent mechanisms of interaction with mitochondrial membranes. *Cytoskeleton*, *77*(3–4), 149–166. https://doi.org/10.1002/cm.21560

Bolduc, F. V., Bell, K., Cox, H., Broadie, K. S., & Tully, T. (2008). Excess protein synthesis in Drosophila Fragile X mutants impairs long-term memory. *Nature Neuroscience*, *11*(10), Article 10. https://doi.org/10.1038/nn.2175

Boyden, E. D., Campos-Xavier, A. B., Kalamajski, S., Cameron, T. L., Suarez, P., Tanackovich, G., Andria, G., Ballhausen, D., Briggs, M. D., Hartley, C., Cohn, D. H., Davidson, H. R., Hall, C., Ikegawa, S., Jouk, P.-S., König, R., Megarbané, A., Nishimura, G., Lachman, R. S., … Bonafé, L. (2011).

Recurrent Dominant Mutations Affecting Two Adjacent Residues in the Motor Domain of the Monomeric Kinesin KIF22 Result in Skeletal Dysplasia and Joint Laxity. *The American Journal of Human Genetics*, *89*(6), 767–772. https://doi.org/10.1016/j.ajhg.2011.10.016

Brandt, F., Carlson, L.-A., Hartl, F. U., Baumeister, W., & Grünewald, K. (2010). The Three-Dimensional Organization of Polyribosomes in Intact Human Cells. *Molecular Cell*, *39*(4), 560–569. https://doi.org/10.1016/j.molcel.2010.08.003

Brickley, K., & Stephenson, F. A. (2011). Trafficking Kinesin Protein (TRAK)-mediated Transport of Mitochondria in Axons of Hippocampal Neurons. *Journal of Biological Chemistry*, *286*(20), 18079–18092. https://doi.org/10.1074/jbc.M111.236018

Broix, L., Turchetto, S., & Nguyen, L. (2021). Coordination between Transport and Local Translation in Neurons. *Trends in Cell Biology*, *31*(5), 372–386. https://doi.org/10.1016/j.tcb.2021.01.001

Brough, D., Schell, M. J., & Irvine, R. F. (2005). Agonist-induced regulation of mitochondrial and endoplasmic reticulum motility. *Biochemical Journal*, *392*(2), 291–297. https://doi.org/10.1042/BJ20050738

Brown, V., Jin, P., Ceman, S., Darnell, J. C., O'Donnell, W. T., Tenenbaum, S. A., Jin, X., Feng, Y., Wilkinson, K. D., Keene, J. D., Darnell, R. B., & Warren, S. T. (2001). Microarray Identification of FMRP-Associated Brain mRNAs and Altered mRNA Translational Profiles in Fragile X Syndrome. *Cell*, *107*(4), 477–487. https://doi.org/10.1016/S0092-8674(01)00568-2

Bryan, J., & Wilson, L. (1971). Are Cytoplasmic Microtubules Heteropolymers? *Proceedings of the National Academy of Sciences*, *68*(8), 1762–1766. https://doi.org/10.1073/pnas.68.8.1762

Bülow, P., Wenner, P. A., Faundez, V., & Bassell, G. J. (2021). Mitochondrial Structure and Polarity in Dendrites and the Axon Initial Segment Are Regulated by Homeostatic Plasticity and Dysregulated in Fragile X Syndrome. *Frontiers in Cell and Developmental Biology*, *9*, 702020. https://doi.org/10.3389/fcell.2021.702020

Bülow, P., Zlatic, S. A., Wenner, P. A., Bassell, G. J., & Faundez, V. (2021). FMRP attenuates activity dependent modifications in the mitochondrial proteome. *Molecular Brain*, *14*(1), 75. https://doi.org/10.1186/s13041-021-00783-w

Burt, A., Gaifas, L., Dendooven, T., & Gutsche, I. (2021). A flexible framework for multi-particle refinement in cryo-electron tomography. *PLOS Biology*, *19*(8), e3001319. https://doi.org/10.1371/journal.pbio.3001319

Butti, Z., & Patten, S. A. (2019). RNA Dysregulation in Amyotrophic Lateral Sclerosis. *Frontiers in Genetics*, *9*. https://www.frontiersin.org/articles/10.3389/fgene.2018.00712

Cai, D., Hoppe, A. D., Swanson, J. A., & Verhey, K. J. (2007). Kinesin-1 structural organization and conformational changes revealed by FRET stoichiometry in live cells. *Journal of Cell Biology*, *176*(1), 51–63. https://doi.org/10.1083/jcb.200605097

Callan, M. A., Clements, N., Ahrendt, N., & Zarnescu, D. C. (2012). Fragile X Protein is required for inhibition of insulin signaling and regulates glial-dependent neuroblast reactivation in the developing brain. *Brain Research*, *1462*, 151–161. https://doi.org/10.1016/j.brainres.2012.03.042

Canty, J. T., Hensley, A., Aslan, M., Jack, A., & Yildiz, A. (2023). TRAK adaptors regulate the recruitment and activation of dynein and kinesin in mitochondrial transport. *Nature Communications*, *14*(1), Article 1. https://doi.org/10.1038/s41467-023-36945-8

Canty, J. T., & Yildiz, A. (2020). Activation and Regulation of Cytoplasmic Dynein. *Trends in Biochemical Sciences*, *45*(5), 440–453. https://doi.org/10.1016/j.tibs.2020.02.002

Carrington, G., Fatima, U., Caramujo, I., Lewis, T., Casas-Mao, D., & Peckham, M. (2024). A multiscale approach reveals the molecular architecture of the autoinhibited kinesin KIF5A. *Journal of Biological Chemistry*, *300*(3), 105713. https://doi.org/10.1016/j.jbc.2024.105713

Cartoni, R., Norsworthy, M. W., Bei, F., Wang, C., Li, S., Zhang, Y., Gabel, C. V., Schwarz, T. L., & He, Z. (2016). The Mammalian-Specific Protein Armcx1 Regulates Mitochondrial Transport during Axon Regeneration. *Neuron*, *92*(6), 1294–1307. https://doi.org/10.1016/j.neuron.2016.10.060

Cason, S. E., Carman, P. J., Van Duyne, C., Goldsmith, J., Dominguez, R., & Holzbaur, E. L. F. (2021). Sequential dynein effectors regulate axonal autophagosome motility in a maturation-dependent pathway. *Journal of Cell Biology*, *220*(7), e202010179. https://doi.org/10.1083/jcb.202010179

Cason, S. E., & Holzbaur, E. L. F. (2023). Axonal transport of autophagosomes is regulated by dynein activators JIP3/JIP4 and ARF/RAB GTPases. *Journal of Cell Biology*, *222*(12), e202301084. https://doi.org/10.1083/jcb.202301084

Celestino, R., Gama, J. B., Castro-Rodrigues, A. F., Barbosa, D. J., Rocha, H., d'Amico, E. A., Musacchio, A., Carvalho, A. X., Morais-Cabral, J. H., & Gassmann, R. (2022). JIP3 interacts with dynein and kinesin-1 to regulate bidirectional organelle transport. *Journal of Cell Biology*, *221*(8), e202110057. https://doi.org/10.1083/jcb.202110057

Celestino, R., Henen, M. A., Gama, J. B., Carvalho, C., McCabe, M., Barbosa, D. J., Born, A., Nichols, P. J., Carvalho, A. X., Gassmann, R., & Vögeli, B. (2019). A transient helix in the disordered region of dynein light intermediate chain links the motor to structurally diverse adaptors for cargo transport. *PLOS Biology*, *17*(1), e3000100. https://doi.org/10.1371/journal.pbio.3000100

Ceman, S., O'Donnell, W. T., Reed, M., Patton, S., Pohl, J., & Warren, S. T. (2003). Phosphorylation influences the translation state of FMRP-associated polyribosomes. *Human Molecular Genetics*, *12*(24), 3295–3305. https://doi.org/10.1093/hmg/ddg350

Chaaban, S., & Carter, A. P. (2022). Structure of dynein–dynactin on microtubules shows tandem adaptor binding. *Nature*, *610*(7930), Article 7930. https://doi.org/10.1038/s41586-022-05186-y

Chakrabarti, R., Ji, W.-K., Stan, R. V., de Juan Sanz, J., Ryan, T. A., & Higgs, H. N. (2018). INF2-mediated actin polymerization at the ER stimulates mitochondrial calcium uptake, inner membrane constriction, and division. *Journal of Cell Biology*, *217*(1), 251–268. https://doi.org/10.1083/jcb.201709111

Chang, K. T., Niescier, R. F., & Min, K.-T. (2011). Mitochondrial matrix Ca2+ as an intrinsic signal regulating mitochondrial motility in axons. *Proceedings of the National Academy of Sciences*, *108*(37), 15456–15461. https://doi.org/10.1073/pnas.1106862108

Chen, M., Bell, J. M., Shi, X., Sun, S. Y., Wang, Z., & Ludtke, S. J. (2019). A complete data processing workflow for cryo-ET and subtomogram averaging. *Nature Methods*, *16*(11), 1161–1168. https://doi.org/10.1038/s41592-019-0591-8

Chevalier-Larsen, E., & Holzbaur, E. L. F. (2006). Axonal transport and neurodegenerative disease. *Biochimica et Biophysica Acta (BBA) - Molecular Basis of Disease*, *1762*(11), 1094–1108. https://doi.org/10.1016/j.bbadis.2006.04.002

Chiba, K., Takahashi, H., Chen, M., Obinata, H., Arai, S., Hashimoto, K., Oda, T., McKenney, R. J., & Niwa, S. (2019). Disease-associated mutations hyperactivate KIF1A motility and anterograde axonal transport of synaptic vesicle precursors. *Proceedings of the National Academy of Sciences*, *116*(37), 18429–18434. https://doi.org/10.1073/pnas.1905690116

Chin, D., & Means, A. R. (2000). Calmodulin: A prototypical calcium sensor. *Trends in Cell Biology*, *10*(8), 322–328. https://doi.org/10.1016/S0962-8924(00)01800-6

Cho, B., Cho, H. M., Jo, Y., Kim, H. D., Song, M., Moon, C., Kim, H., Kim, K., Sesaki, H., Rhyu, I. J., Kim, H., & Sun, W. (2017). Constriction of the mitochondrial inner compartment is a priming event for

mitochondrial division. *Nature Communications*, *8*(1), 15754. https://doi.org/10.1038/ncomms15754

Chonchaiya, W., Schneider, A., & Hagerman, R. J. (2009). Fragile X: A Family of Disorders. *Advances in Pediatrics*, *56*(1), 165–186. https://doi.org/10.1016/j.yapd.2009.08.008

Chowdhury, S., Ketcham, S. A., Schroer, T. A., & Lander, G. C. (2015). Structural organization of the dynein–dynactin complex bound to microtubules. *Nature Structural & Molecular Biology*, *22*(4), 345–347. https://doi.org/10.1038/nsmb.2996

Chung, J. Y.-M., Steen, J. A., & Schwarz, T. L. (2016). Phosphorylation-Induced Motor Shedding Is Required at Mitosis for Proper Distribution and Passive Inheritance of Mitochondria. *Cell Reports*, *16*(8), 2142–2155. https://doi.org/10.1016/j.celrep.2016.07.055

Cioni, J.-M., Lin, J. Q., Holtermann, A. V., Koppers, M., Jakobs, M. A. H., Azizi, A., Turner-Bridger, B., Shigeoka, T., Franze, K., Harris, W. A., & Holt, C. E. (2019). Late Endosomes Act as mRNA Translation Platforms and Sustain Mitochondria in Axons. *Cell*, *176*(1–2), 56-72.e15. https://doi.org/10.1016/j.cell.2018.11.030

Cipolat, S., de Brito, O. M., Dal Zilio, B., & Scorrano, L. (2004). OPA1 requires mitofusin 1 to promote mitochondrial fusion. *Proceedings of the National Academy of Sciences*, *101*(45), 15927–15932. https://doi.org/10.1073/pnas.0407043101

Clark, I. E., Dodson, M. W., Jiang, C., Cao, J. H., Huh, J. R., Seol, J. H., Yoo, S. J., Hay, B. A., & Guo, M. (2006). Drosophila pink1 is required for mitochondrial function and interacts genetically with parkin. *Nature*, *441*(7097), Article 7097. https://doi.org/10.1038/nature04779

Claussnitzer, M., Cho, J. H., Collins, R., Cox, N. J., Dermitzakis, E. T., Hurles, M. E., Kathiresan, S., Kenny, E. E., Lindgren, C. M., MacArthur, D. G., North, K. N., Plon, S. E., Rehm, H. L., Risch, N., Rotimi, C. N., Shendure, J., Soranzo, N., & McCarthy, M. I. (2020). A brief history of human disease genetics. *Nature*, *577*(7789), 179–189. https://doi.org/10.1038/s41586-019-1879-7

Colina-Tenorio, L., Horten, P., Pfanner, N., & Rampelt, H. (2020). Shaping the mitochondrial inner membrane in health and disease. *Journal of Internal Medicine*, *287*(6), 645–664. https://doi.org/10.1111/joim.13031

Combet, C., Blanchet, C., Geourjon, C., & Deléage, G. (2000). NPS@: Network Protein Sequence Analysis. *Trends in Biochemical Sciences*, *25*(3), 147–150. https://doi.org/10.1016/S0968-0004(99)01540-6

Coscia, S. M., Thompson, C. P., Tang, Q., Baltrusaitis, E. E., Rhodenhiser, J. A., Quintero-Carmona, O. A., Ostap, E. M., Lakadamyali, M., & Holzbaur, E. L. F. (2023). Myo19 tethers mitochondria to endoplasmic reticulum-associated actin to promote mitochondrial fission. *Journal of Cell Science*, *136*(5), jcs260612. https://doi.org/10.1242/jcs.260612

Covill-Cooke, C., Kwizera, B., López-Doménech, G., Thompson, C. O., Cheung, N. J., Cerezo, E., Peterka, M., Kittler, J. T., & Kornmann, B. (2024). Shared structural features of Miro binding control mitochondrial homeostasis. *The EMBO Journal*, 1–20. https://doi.org/10.1038/s44318-024-00028-1

Coy, D. L., Hancock, W. O., Wagenbach, M., & Howard, J. (1999). Kinesin's tail domain is an inhibitory regulator of the motor domain. *Nature Cell Biology*, *1*(5), Article 5. https://doi.org/10.1038/13001

Crawford, D. C., Acuña, J. M., & Sherman, S. L. (2001). *FMR1* and the fragile X syndrome: Human genome epidemiology review. *Genetics in Medicine*, *3*(5), 359–371. https://doi.org/10.1097/00125817-200109000-00006

Crimella, C., Baschirotto, C., Arnoldi, A., Tonelli, A., Tenderini, E., Airoldi, G., Martinuzzi, A., Trabacca, A., Losito, L., Scarlato, M., Benedetti, S., Scarpini, E., Spinicci, G., Bresolin, N., & Bassi, M. (2012). Mutations in the motor and stalk domains of KIF5A in spastic paraplegia type 10 and in axonal Charcot–Marie–Tooth type 2. *Clinical Genetics*, *82*(2), 157–164. https://doi.org/10.1111/j.1399-0004.2011.01717.x

Cross, J. A., & Dodding, M. P. (2019). Motor–cargo adaptors at the organelle–cytoskeleton interface. *Current Opinion in Cell Biology*, *59*, 16–23. https://doi.org/10.1016/j.ceb.2019.02.010

D'Antoni, S., de Bari, L., Valenti, D., Borro, M., Bonaccorso, C. M., Simmaco, M., Vacca, R. A., & Catania, M. V. (2020). Aberrant mitochondrial bioenergetics in the cerebral cortex of the Fmr1 knockout mouse model of fragile X syndrome. *Biological Chemistry*, *401*(4), 497–503. https://doi.org/10.1515/hsz-2019-0221

Darnell, J. C. (2005). Kissing complex RNAs mediate interaction between the Fragile-X mental retardation protein KH2 domain and brain polyribosomes. *Genes & Development*, *19*(8), 903–918. https://doi.org/10.1101/gad.1276805

Darnell, J. C., Jensen, K. B., Jin, P., Brown, V., Warren, S. T., & Darnell, R. B. (2001). Fragile X Mental Retardation Protein Targets G Quartet mRNAs Important for Neuronal Function. *Cell*, *107*(4), 489–499. https://doi.org/10.1016/S0092-8674(01)00566-9

Darnell, J. C., & Klann, E. (2013). The translation of translational control by FMRP: Therapeutic targets for FXS. *Nature Neuroscience*, *16*(11), Article 11. https://doi.org/10.1038/nn.3379

Darnell, J. C., Van Driesche, S. J., Zhang, C., Hung, K. Y. S., Mele, A., Fraser, C. E., Stone, E. F., Chen, C., Fak, J. J., Chi, S. W., Licatalosi, D. D., Richter, J. D., & Darnell, R. B. (2011). FMRP Stalls Ribosomal Translocation on mRNAs Linked to Synaptic Function and Autism. *Cell*, *146*(2), 247–261. https://doi.org/10.1016/j.cell.2011.06.013

Davis, K., Basu, H., Izquierdo-Villalba, I., Shurberg, E., & Schwarz, T. L. (2023). Miro GTPase domains regulate the assembly of the mitochondrial motor–adaptor complex. *Life Science Alliance*, *6*(1). https://doi.org/10.26508/lsa.202201406

De Boulle, K., Verkerk, A. J. M. H., Reyniers, E., Vits, L., Hendrickx, J., Van Roy, B., Van Den Bos, F., de Graaff, E., Oostra, B. A., & Willems, P. J. (1993). A point mutation in the FMR-1 gene associated with fragile X mental retardation. *Nature Genetics*, *3*(1), 31–35. https://doi.org/10.1038/ng0193-31

De Vos, K. J., Allan, V. J., Grierson, A. J., & Sheetz, M. P. (2005). Mitochondrial Function and Actin Regulate Dynamin-Related Protein 1-Dependent Mitochondrial Fission. *Current Biology*, *15*(7), 678–683. https://doi.org/10.1016/j.cub.2005.02.064

de Vries, B. B., Halley, D. J., Oostra, B. A., & Niermeijer, M. F. (1998). The fragile X syndrome. *Journal of Medical Genetics*, *35*(7), 579–589.

DeBoer, S. R., You, Y., Szodorai, A., Kaminska, A., Pigino, G., Nwabuisi, E., Wang, B., Estrada-Hernandez, T., Kins, S., Brady, S. T., & Morfini, G. (2008). Conventional Kinesin Holoenzymes Are Composed of Heavy and Light Chain Homodimers. *Biochemistry*, *47*(15), 4535–4543. https://doi.org/10.1021/bi702445j

del Castillo, U., Winding, M., Lu, W., & Gelfand, V. I. (2015). Interplay between kinesin-1 and cortical dynein during axonal outgrowth and microtubule organization in Drosophila neurons. *eLife*, *4*, e10140. https://doi.org/10.7554/eLife.10140

DeSantis, M. E., Cianfrocco, M. A., Htet, Z. M., Tran, P. T., Reck-Peterson, S. L., & Leschziner, A. E. (2017). Lis1 Has Two Opposing Modes of Regulating Cytoplasmic Dynein. *Cell*, *170*(6), 1197-1208.e12. https://doi.org/10.1016/j.cell.2017.08.037

Dictenberg, J. B., Swanger, S. A., Antar, L. N., Singer, R. H., & Bassell, G. J. (2008). A Direct Role for FMRP in Activity-Dependent Dendritic mRNA Transport Links Filopodial-Spine Morphogenesis to

Fragile X Syndrome. *Developmental Cell*, *14*(6), 926–939. https://doi.org/10.1016/j.devcel.2008.04.003

Dietrich, K. A., Sindelar, C. V., Brewer, P. D., Downing, K. H., Cremo, C. R., & Rice, S. E. (2008). The kinesin-1 motor protein is regulated by a direct interaction of its head and tail. *Proceedings of the National Academy of Sciences*, *105*(26), 8938–8943. https://doi.org/10.1073/pnas.0803575105

Ding, B., & Sepehrimanesh, M. (2021). Nucleocytoplasmic Transport: Regulatory Mechanisms and the Implications in Neurodegeneration. *International Journal of Molecular Sciences*, *22*(8), Article 8. https://doi.org/10.3390/ijms22084165

Dobin, A., Davis, C. A., Schlesinger, F., Drenkow, J., Zaleski, C., Jha, S., Batut, P., Chaisson, M., & Gingeras, T. R. (2013). STAR: Ultrafast universal RNA-seq aligner. *Bioinformatics*, *29*(1), 15–21. https://doi.org/10.1093/bioinformatics/bts635

Dockendorff, T. C., Su, H. S., McBride, S. M. J., Yang, Z., Choi, C. H., Siwicki, K. K., Sehgal, A., & Jongens, T. A. (2002). Drosophila Lacking dfmr1 Activity Show Defects in Circadian Output and Fail to Maintain Courtship Interest. *Neuron*, *34*(6), 973–984. https://doi.org/10.1016/S0896-6273(02)00724-9

Duran, A., Amanchy, R., Linares, J. F., Joshi, J., Abu-Baker, S., Porollo, A., Hansen, M., Moscat, J., & Diaz-Meco, M. T. (2011). P62 Is a Key Regulator of Nutrient Sensing in the mTORC1 Pathway. *Molecular Cell*, *44*(1), 134–146. https://doi.org/10.1016/j.molcel.2011.06.038

Eberhardt, E. L., Ludlam, A. V., Tan, Z., & Cianfrocco, M. A. (2020). Miro: A molecular switch at the center of mitochondrial regulation. *Protein Science*, *29*(6), 1269–1284. https://doi.org/10.1002/pro.3839

Eira, J., Silva, C. S., Sousa, M. M., & Liz, M. A. (2016). The cytoskeleton as a novel therapeutic target for old neurodegenerative disorders. *Progress in Neurobiology*, *141*, 61–82. https://doi.org/10.1016/j.pneurobio.2016.04.007

El Fatimy, R., Davidovic, L., Tremblay, S., Jaglin, X., Dury, A., Robert, C., De Koninck, P., & Khandjian, E. W. (2016). Tracking the Fragile X Mental Retardation Protein in a Highly Ordered Neuronal RiboNucleoParticles Population: A Link between Stalled Polyribosomes and RNA Granules. *PLOS Genetics*, *12*(7), e1006192. https://doi.org/10.1371/journal.pgen.1006192

Elshenawy, M. M., Kusakci, E., Volz, S., Baumbach, J., Bullock, S. L., & Yildiz, A. (2020). Lis1 activates dynein motility by modulating its pairing with dynactin. *Nature Cell Biology*, *22*(5), 570–578. https://doi.org/10.1038/s41556-020-0501-4

Ermel, U. H., Arghittu, S. M., & Frangakis, A. S. (2022). ArtiaX: An electron tomography toolbox for the interactive handling of sub-tomograms in UCSF ChimeraX. *Protein Science*, *31*(12), e4472. https://doi.org/10.1002/pro.4472

Ewels, P., Magnusson, M., Lundin, S., & Käller, M. (2016). MultiQC: Summarize analysis results for multiple tools and samples in a single report. *Bioinformatics*, *32*(19), 3047–3048. https://doi.org/10.1093/bioinformatics/btw354

Falchetti, A., Di Stefano, M., Marini, F., Del Monte, F., Mavilia, C., Strigoli, D., De Feo, M. L., Isaia, G., Masi, L., Amedei, A., Cioppi, F., Ghinoi, V., Bongi, S. M., Di Fede, G., Sferrazza, C., Rini, G. B., Melchiorre, D., Matucci-Cerinic, M., & Brandi, M. L. (2004). Two Novel Mutations at Exon 8 of the Sequestosome 1 (SQSTM1) Gene in an Italian Series of Patients Affected by Paget's Disease of Bone (PDB). *Journal of Bone and Mineral Research*, *19*(6), 1013–1017. https://doi.org/10.1359/JBMR.040203

Fallini, C., Bassell, G. J., & Rossoll, W. (2010). High-efficiency transfection of cultured primary motor neurons to study protein localization, trafficking, and function. *Molecular Neurodegeneration*, *5*(1), 17. https://doi.org/10.1186/1750-1326-5-17

Farrer, M. J., Hulihan, M. M., Kachergus, J. M., Dächsel, J. C., Stoessl, A. J., Grantier, L. L., Calne, S., Calne, D. B., Lechevalier, B., Chapon, F., Tsuboi, Y., Yamada, T., Gutmann, L., Elibol, B., Bhatia, K. P., Wider, C., Vilariño-Güell, C., Ross, O. A., Brown, L. A., … Wszolek, Z. K. (2009). DCTN1 mutations in Perry syndrome. *Nature Genetics*, *41*(2), 163–165. https://doi.org/10.1038/ng.293

Fatiga, F. F., Wang, L., Hsu, T., Capuno, J. I., & Fu, C. (2021). Miro1 functions as an inhibitory regulator of MFN at elevated mitochondrial Ca2+ levels. *Journal of Cellular Biochemistry*, *122*(12), 1848–1862. https://doi.org/10.1002/jcb.30138

Fecto, F., Yan, J., Vemula, S. P., Liu, E., Yang, Y., Chen, W., Zheng, J. G., Shi, Y., Siddique, N., Arrat, H., Donkervoort, S., Ajroud-Driss, S., Sufit, R. L., Heller, S. L., Deng, H.-X., & Siddique, T. (2011). SQSTM1 Mutations in Familial and Sporadic Amyotrophic Lateral Sclerosis. *Archives of Neurology*, *68*(11), 1440–1446. https://doi.org/10.1001/archneurol.2011.250

Feit, H., Slusarek, L., & Shelanski, M. L. (1971). Heterogeneity of Tubulin Subunits. *Proceedings of the National Academy of Sciences*, *68*(9), 2028–2031. https://doi.org/10.1073/pnas.68.9.2028

Feng, Q., Gicking, A. M., & Hancock, W. O. (2020). Dynactin p150 promotes processive motility of DDB complexes by minimizing diffusional behavior of dynein. *Molecular Biology of the Cell*, *31*(8), 782–792. https://doi.org/10.1091/mbc.E19-09-0495

Feng, Y., Gutekunst, C.-A., Eberhart, D. E., Yi, H., Warren, S. T., & Hersch, S. M. (1997). Fragile X Mental Retardation Protein: Nucleocytoplasmic Shuttling and Association with Somatodendritic Ribosomes. *Journal of Neuroscience*, *17*(5), 1539–1547. https://doi.org/10.1523/JNEUROSCI.17-05-01539.1997

Fenton, A. R., Jongens, T. A., & Holzbaur, E. L. F. (2021a). Mitochondrial adaptor TRAK2 activates and functionally links opposing kinesin and dynein motors. *Nature Communications*, *12*(1), 4578. https://doi.org/10.1038/s41467-021-24862-7

Fenton, A. R., Jongens, T. A., & Holzbaur, E. L. F. (2021b). Mitochondrial dynamics: Shaping and remodeling an organelle network. *Current Opinion in Cell Biology*, *68*, 28–36. https://doi.org/10.1016/j.ceb.2020.08.014

Fernandez, J.-J., Laugks, U., Schaffer, M., Bäuerlein, F. J. B., Khoshouei, M., Baumeister, W., & Lucic, V. (2016). Removing Contamination-Induced Reconstruction Artifacts from Cryo-electron Tomograms. *Biophysical Journal*, *110*(4), 850–859. https://doi.org/10.1016/j.bpj.2015.10.043

Fernandopulle, M. S. (2021). RNA transport and local translation in neurodevelopmental and neurodegenerative disease. *Nature Neuroscience*, *24*, 11.

Fernandopulle, M. S., Prestil, R., Grunseich, C., Wang, C., Gan, L., & Ward, M. E. (2018). Transcription Factor-Mediated Differentiation of Human iPSCs into Neurons: Rapid differentiation of iPSCs into neurons. *Current Protocols in Cell Biology*, *79*(1), e51. https://doi.org/10.1002/cpcb.51

Fonseca, T. B., Sánchez-Guerrero, Á., Milosevic, I., & Raimundo, N. (2019). Mitochondrial fission requires DRP1 but not dynamins. *Nature*, *570*(7761), E34–E42. https://doi.org/10.1038/s41586-019-1296-y

Fransson, Å., Ruusala, A., & Aspenström, P. (2003). Atypical Rho GTPases Have Roles in Mitochondrial Homeostasis and Apoptosis. *Journal of Biological Chemistry*, *278*(8), 6495–6502. https://doi.org/10.1074/jbc.M208609200

Fransson, Å., Ruusala, A., & Aspenström, P. (2006). The atypical Rho GTPases Miro-1 and Miro-2 have essential roles in mitochondrial trafficking. *Biochemical and Biophysical Research Communications*, *344*(2), 500–510. https://doi.org/10.1016/j.bbrc.2006.03.163

Friedman, D. S., & Vale, R. D. (1999). Single-molecule analysis of kinesin motility reveals regulation by the cargo-binding tail domain. *Nature Cell Biology*, *1*(5), 293–297. https://doi.org/10.1038/13008

Friedman, J. R., Lackner, L. L., West, M., DiBenedetto, J. R., Nunnari, J., & Voeltz, G. K. (2011). ER Tubules Mark Sites of Mitochondrial Division. *Science*, *334*(6054), 358–362. https://doi.org/10.1126/science.1207385

Friedman, J. R., & Nunnari, J. (2014). Mitochondrial form and function. *Nature*, *505*(7483), 335–343. https://doi.org/10.1038/nature12985

Fritzsche, R., Karra, D., Bennett, K. L., Ang, F. yee, Heraud-Farlow, J. E., Tolino, M., Doyle, M., Bauer, K. E., Thomas, S., Planyavsky, M., Arn, E., Bakosova, A., Jungwirth, K., Hörmann, A., Palfi, Z., Sandholzer, J., Schwarz, M., Macchi, P., Colinge, J., … Kiebler, M. A. (2013). Interactome of Two Diverse RNA Granules Links mRNA Localization to Translational Repression in Neurons. *Cell Reports*, *5*(6), 1749–1762. https://doi.org/10.1016/j.celrep.2013.11.023

Fu, M., & Holzbaur, E. L. F. (2013). JIP1 regulates the directionality of APP axonal transport by coordinating kinesin and dynein motors. *The Journal of Cell Biology*, *202*(3), 495–508. https://doi.org/10.1083/jcb.201302078

Fu, M., Nirschl, J. J., & Holzbaur, E. L. F. (2014). LC3 Binding to the Scaffolding Protein JIP1 Regulates Processive Dynein-Driven Transport of Autophagosomes. *Developmental Cell*, *29*(5), 577–590. https://doi.org/10.1016/j.devcel.2014.04.015

Fu, X., Rao, L., Li, P., Liu, X., Wang, Q., Son, A. I., Gennerich, A., & Liu, J. S.-H. (2022). Doublecortin and JIP3 are neural-specific counteracting regulators of dynein-mediated retrograde trafficking. *eLife*, *11*, e82218. https://doi.org/10.7554/eLife.82218

Fumagalli, L., Young, F. L., Boeynaems, S., De Decker, M., Mehta, A. R., Swijsen, A., Fazal, R., Guo, W., Moisse, M., Beckers, J., Dedeene, L., Selvaraj, B. T., Vandoorne, T., Madan, V., van Blitterswijk, M., Raitcheva, D., McCampbell, A., Poesen, K., Gitler, A. D., … Van Damme, P. (2021). C9orf72-derived arginine-containing dipeptide repeats associate with axonal transport machinery and impede microtubule-based motility. *Science Advances*, *7*(15), eabg3013. https://doi.org/10.1126/sciadv.abg3013

Gallagher, E. R., & Holzbaur, E. L. F. (2023). The selective autophagy adaptor p62/SQSTM1 forms phase condensates regulated by HSP27 that facilitate the clearance of damaged lysosomes via lysophagy. *Cell Reports*, *42*(2), 112037. https://doi.org/10.1016/j.celrep.2023.112037

Gama, J. B., Pereira, C., Simões, P. A., Celestino, R., Reis, R. M., Barbosa, D. J., Pires, H. R., Carvalho, C., Amorim, J., Carvalho, A. X., Cheerambathur, D. K., & Gassmann, R. (2017). Molecular mechanism of dynein recruitment to kinetochores by the Rod–Zw10–Zwilch complex and Spindly. *The Journal of Cell Biology*, *216*(4), 943–960. https://doi.org/10.1083/jcb.201610108

Ge, Y., Shi, X., Boopathy, S., McDonald, J., Smith, A. W., & Chao, L. H. (2020). Two forms of Opa1 cooperate to complete fusion of the mitochondrial inner-membrane. *eLife*, *9*, e50973. https://doi.org/10.7554/eLife.50973

Geng, J., Khaket, T. P., Pan, J., Li, W., Zhang, Y., Ping, Y., Cobos Sillero, M. I., & Lu, B. (2023). Deregulation of ER-mitochondria contact formation and mitochondrial calcium homeostasis mediated by VDAC in fragile X syndrome. *Developmental Cell*, *58*(7), 597-615.e10. https://doi.org/10.1016/j.devcel.2023.03.002

Giampetruzzi, A., Danielson, E. W., Gumina, V., Jeon, M., Boopathy, S., Brown, R. H., Ratti, A., Landers, J. E., & Fallini, C. (2019). Modulation of actin polymerization affects nucleocytoplasmic transport in multiple forms of amyotrophic lateral sclerosis. *Nature Communications*, *10*(1), Article 1. https://doi.org/10.1038/s41467-019-11837-y

Gill, S. R., Schroer, T. A., Szilak, I., Steuer, E. R., Sheetz, M. P., & Cleveland, D. W. (1991). Dynactin, a conserved, ubiquitously expressed component of an activator of vesicle motility mediated by cytoplasmic dynein. *Journal of Cell Biology*, *115*(6), 1639–1650. https://doi.org/10.1083/jcb.115.6.1639

Glater, E. E., Megeath, L. J., Stowers, R. S., & Schwarz, T. L. (2006). Axonal transport of mitochondria requires milton to recruit kinesin heavy chain and is light chain independent. *The Journal of Cell Biology*, *173*(4), 545–557. https://doi.org/10.1083/jcb.200601067

Goddard, T. D., Huang, C. C., Meng, E. C., Pettersen, E. F., Couch, G. S., Morris, J. H., & Ferrin, T. E. (2018). UCSF ChimeraX: Meeting modern challenges in visualization and analysis: UCSF ChimeraX Visualization System. *Protein Science*, *27*(1), 14–25. https://doi.org/10.1002/pro.3235

Goering, R., Hudish, L. I., Guzman, B. B., Raj, N., Bassell, G. J., Russ, H. A., Dominguez, D., & Taliaferro, J. M. (2020). FMRP promotes RNA localization to neuronal projections through interactions between its RGG domain and G-quadruplex RNA sequences. *eLife*, *9*, e52621. https://doi.org/10.7554/eLife.52621

Goldsmith, J., Ordureau, A., Harper, J. W., & Holzbaur, E. L. F. (2022). Brain-derived autophagosome profiling reveals the engulfment of nucleoid-enriched mitochondrial fragments by basal

autophagy in neurons. *Neuron*, *110*(6), 967-976.e8. https://doi.org/10.1016/j.neuron.2021.12.029

Görlich, D., & Mattaj, I. W. (1996). Nucleocytoplasmic Transport. *Science*, *271*(5255), 1513–1519. https://doi.org/10.1126/science.271.5255.1513

Gould, E. L., Loesch, D. Z., Martin, M. J., Hagerman, R. J., Armstrong, S. M., & Huggins, R. M. (2000). Melatonin profiles and sleep characteristics in boys with fragile X syndrome: A preliminary study. *American Journal of Medical Genetics*, *95*(4), 307–315. https://doi.org/10.1002/1096-8628(20001211)95:4<307::AID-AJMG3>3.0.CO;2-3

Gowrishankar, S., Wu, Y., & Ferguson, S. M. (2017). Impaired JIP3-dependent axonal lysosome transport promotes amyloid plaque pathology. *Journal of Cell Biology*, *216*(10), 3291–3305. https://doi.org/10.1083/jcb.201612148

Grabarek, Z. (2011). Insights into modulation of calcium signaling by magnesium in calmodulin, troponin C and related EF-hand proteins. *Biochimica et Biophysica Acta (BBA) - Molecular Cell Research*, *1813*(5), 913–921. https://doi.org/10.1016/j.bbamcr.2011.01.017

Greenblatt, E. J., & Spradling, A. C. (2018). Fragile X mental retardation 1 gene enhances the translation of large autism-related proteins. *Science*, *361*(6403), 709–712. https://doi.org/10.1126/science.aas9963

Griffiths, K. K., Wang, A., Wang, L., Tracey, M., Kleiner, G., Quinzii, C. M., Sun, L., Yang, G., Perez-Zoghbi, J. F., Licznerski, P., Yang, M., Jonas, E. A., & Levy, R. J. (2020). Inefficient thermogenic mitochondrial respiration due to futile proton leak in a mouse model of fragile X syndrome. *The FASEB Journal*, *34*(6), 7404–7426. https://doi.org/10.1096/fj.202000283RR

Grønskov, K., Brøndum-Nielsen, K., Dedic, A., & Hjalgrim, H. (2011). A nonsense mutation in FMR1 causing fragile X syndrome. *European Journal of Human Genetics*, *19*(4), 489–491. https://doi.org/10.1038/ejhg.2010.223

Gross, C., & Bassell, G. (2014). Neuron-specific regulation of class I PI3K catalytic subunits and their dysfunction in brain disorders. *Frontiers in Molecular Neuroscience*, *7*. https://www.frontiersin.org/articles/10.3389/fnmol.2014.00012

Gross, C., & Bassell, G. J. (2012). Excess Protein Synthesis in FXS Patient Lymphoblastoid Cells Can Be Rescued with a p110β-Selective Inhibitor. *Molecular Medicine*, *18*(3), Article 3. https://doi.org/10.2119/molmed.2011.00363

Gross, C., Chang, C.-W., Kelly, S. M., Bhattacharya, A., McBride, S. M. J., Danielson, S. W., Jiang, M. Q., Chan, C. B., Ye, K., Gibson, J. R., Klann, E., Jongens, T. A., Moberg, K. H., Huber, K. M., & Bassell, G. J. (2015). Increased Expression of the PI3K Enhancer PIKE Mediates Deficits in Synaptic Plasticity and Behavior in Fragile X Syndrome. *Cell Reports*, *11*(5), 727–736. https://doi.org/10.1016/j.celrep.2015.03.060

Gross, C., Nakamoto, M., Yao, X., Chan, C.-B., Yim, S. Y., Ye, K., Warren, S. T., & Bassell, G. J. (2010). Excess Phosphoinositide 3-Kinase Subunit Synthesis and Activity as a Novel Therapeutic Target in Fragile X Syndrome. *Journal of Neuroscience*, *30*(32), 10624–10638. https://doi.org/10.1523/JNEUROSCI.0402-10.2010

Gross, C., Raj, N., Molinaro, G., Allen, A. G., Whyte, A. J., Gibson, J. R., Huber, K. M., Gourley, S. L., & Bassell, G. J. (2015). Selective Role of the Catalytic PI3K Subunit p110β in Impaired Higher Order Cognition in Fragile X Syndrome. *Cell Reports*, *11*(5), 681–688. https://doi.org/10.1016/j.celrep.2015.03.065

Grotjahn, D. A., Chowdhury, S., Xu, Y., McKenney, R. J., Schroer, T. A., & Lander, G. C. (2018). Cryo-electron tomography reveals that dynactin recruits a team of dyneins for processive motility. *Nature Structural & Molecular Biology*, *25*(3), 203–207. https://doi.org/10.1038/s41594-018-0027-7

Guardia, C. M., Farías, G. G., Jia, R., Pu, J., & Bonifacino, J. S. (2016). BORC Functions Upstream of Kinesins 1 and 3 to Coordinate Regional Movement of Lysosomes along Different Microtubule Tracks. *Cell Reports*, *17*(8), 1950–1961. https://doi.org/10.1016/j.celrep.2016.10.062

Guedes-Dias, P., Nirschl, J. J., Abreu, N., Tokito, M. K., Janke, C., Magiera, M. M., & Holzbaur, E. L. F. (2019). Kinesin-3 Responds to Local Microtubule Dynamics to Target Synaptic Cargo Delivery to the Presynapse. *Current Biology*, *29*(2), 268-282.e8. https://doi.org/10.1016/j.cub.2018.11.065

Guo, W., Stoklund Dittlau, K., & Van Den Bosch, L. (2020). Axonal transport defects and neurodegeneration: Molecular mechanisms and therapeutic implications. *Seminars in Cell & Developmental Biology*, *99*, 133–150. https://doi.org/10.1016/j.semcdb.2019.07.010

Guo, X., Macleod, G. T., Wellington, A., Hu, F., Panchumarthi, S., Schoenfield, M., Marin, L., Charlton, M. P., Atwood, H. L., & Zinsmaier, K. E. (2005). The GTPase dMiro Is Required for Axonal Transport of Mitochondria to Drosophila Synapses. *Neuron*, *47*(3), 379–393. https://doi.org/10.1016/j.neuron.2005.06.027

Guo, Y., Li, D., Zhang, S., Yang, Y., Liu, J.-J., Wang, X., Liu, C., Milkie, D. E., Moore, R. P., Tulu, U. S., Kiehart, D. P., Hu, J., Lippincott-Schwartz, J., Betzig, E., & Li, D. (2018). Visualizing Intracellular Organelle and Cytoskeletal Interactions at Nanoscale Resolution on Millisecond Timescales. *Cell*, *175*(5), 1430-1442.e17. https://doi.org/10.1016/j.cell.2018.09.057

Hackney, D. D., Baek, N., & Snyder, A. C. (2009). Half-Site Inhibition of Dimeric Kinesin Head Domains by Monomeric Tail Domains. *Biochemistry*, *48*(15), 3448–3456. https://doi.org/10.1021/bi8022575

Hackney, D. D., & Stock, M. F. (2000). Kinesin's IAK tail domain inhibits initial microtubule-stimulated ADP release. *Nature Cell Biology*, *2*(5), Article 5. https://doi.org/10.1038/35010525

Hagerman, R. J., Berry-Kravis, E., Kaufmann, W. E., Ono, M. Y., Tartaglia, N., Lachiewicz, A., Kronk, R., Delahunty, C., Hessl, D., Visootsak, J., Picker, J., Gane, L., & Tranfaglia, M. (2009). Advances in the Treatment of Fragile X Syndrome. *Pediatrics*, *123*(1), 378–390. https://doi.org/10.1542/peds.2008-0317

Hale, C. R., Sawicka, K., Mora, K., Fak, J. J., Kang, J. J., Cutrim, P., Cialowicz, K., Carroll, T. S., & Darnell, R. B. (2021). FMRP regulates mRNAs encoding distinct functions in the cell body and dendrites of CA1 pyramidal neurons. *eLife*, *10*, e71892. https://doi.org/10.7554/eLife.71892

Hancock, W. O. (2014). Bidirectional cargo transport: Moving beyond tug of war. *Nature Reviews Molecular Cell Biology*, *15*(9), 615–628. https://doi.org/10.1038/nrm3853

Harbauer, A. B., Hees, J. T., Wanderoy, S., Segura, I., Gibbs, W., Cheng, Y., Ordonez, M., Cai, Z., Cartoni, R., Ashrafi, G., Wang, C., Perocchi, F., He, Z., & Schwarz, T. L. (2022). Neuronal mitochondria transport Pink1 mRNA via synaptojanin 2 to support local mitophagy. *Neuron*. https://linkinghub.elsevier.com/retrieve/pii/S0896627322001052

Hardiman, O., Al-Chalabi, A., Chio, A., Corr, E. M., Logroscino, G., Robberecht, W., Shaw, P. J., Simmons, Z., & van den Berg, L. H. (2017). Amyotrophic lateral sclerosis. *Nature Reviews Disease Primers*, *3*(1), 1–19. https://doi.org/10.1038/nrdp.2017.71

Hees, J. T., & Harbauer, A. B. (2023). *Insulin signaling regulates Pink1 mRNA localization via modulation of AMPK activity to support PINK1 function in neurons* (p. 2023.02.06.527276). bioRxiv. https://doi.org/10.1101/2023.02.06.527276

Heidemann, S. R., Landers, J. M., & Hamborg, M. A. (1981). Polarity orientation of axonal microtubules. *Journal of Cell Biology*, *91*(3), 661–665. https://doi.org/10.1083/jcb.91.3.661

Henrichs, V., Grycova, L., Barinka, C., Nahacka, Z., Neuzil, J., Diez, S., Rohlena, J., Braun, M., & Lansky, Z. (2020). Mitochondria-adaptor TRAK1 promotes kinesin-1 driven transport in crowded

environments. *Nature Communications*, *11*(1), 3123. https://doi.org/10.1038/s41467-020-16972-5

Hirabayashi, Y., Lewis, T. L., Du, Y., Virga, D. M., Decker, A. M., Coceano, G., Alvelid, J., Paul, M. A., Hamilton, S., Kneis, P., Takahashi, Y., Gaublomme, J. T., Testa, I., & Polleux, F. (2024). *Most axonal mitochondria in cortical pyramidal neurons lack mitochondrial DNA and consume ATP* (p. 2024.02.12.579972). bioRxiv. https://doi.org/10.1101/2024.02.12.579972

Hirokawa, N., & Takemura, R. (2005a). Molecular motors and mechanisms of directional transport in neurons. *Nature Reviews Neuroscience*, *6*(3), Article 3. https://doi.org/10.1038/nrn1624

Hirokawa, N., & Takemura, R. (2005b). Molecular motors and mechanisms of directional transport in neurons. *Nature Reviews. Neuroscience*, *6*(3), 201–214. https://doi.org/10.1038/nrn1624

Hirokawa, N., & Tanaka, Y. (2015). Kinesin superfamily proteins (KIFs): Various functions and their relevance for important phenomena in life and diseases. *Experimental Cell Research*, *334*(1), 16–25. https://doi.org/10.1016/j.yexcr.2015.02.016

Hirtz, D., Thurman, D. J., Gwinn-Hardy, K., Mohamed, M., Chaudhuri, A. R., & Zalutsky, R. (2007). How common are the "common" neurologic disorders? *Neurology*, *68*(5), 326–337. https://doi.org/10.1212/01.wnl.0000252807.38124.a3

Hocking, L. J., Lucas, G. J., Daroszewska, A., Cundy, T., Nicholson, G. C., Donath, J., Walsh, J. P., Finlayson, C., Cavey, J. R., Ciani, B., Sheppard, P. W., Searle, M. S., Layfield, R., & Ralston, S. H. (2004). Novel UBA Domain Mutations of SQSTM1 in Paget's Disease of Bone: Genotype Phenotype Correlation, Functional Analysis, and Structural Consequences. *Journal of Bone and Mineral Research*, *19*(7), 1122–1127. https://doi.org/10.1359/JBMR.0403015

Hollenbeck, P. J., & Saxton, W. M. (2005). The axonal transport of mitochondria. *Journal of Cell Science*, *118*(23), 5411–5419. https://doi.org/10.1242/jcs.02745

Horlbeck, M. A., Gilbert, L. A., Villalta, J. E., Adamson, B., Pak, R. A., Chen, Y., Fields, A. P., Park, C. Y., Corn, J. E., Kampmann, M., & Weissman, J. S. (2016). Compact and highly active next-generation libraries for CRISPR-mediated gene repression and activation. *eLife*, *5*, e19760. https://doi.org/10.7554/eLife.19760

Htet, Z. M., Gillies, J. P., Baker, R. W., Leschziner, A. E., DeSantis, M. E., & Reck-Peterson, S. L. (2020). LIS1 promotes the formation of activated cytoplasmic dynein-1 complexes. *Nature Cell Biology*, *22*(5), 518–525. https://doi.org/10.1038/s41556-020-0506-z

Huang, J., Roberts, A. J., Leschziner, A. E., & Reck-Peterson, S. L. (2012). Lis1 Acts as a "Clutch" between the ATPase and Microtubule-Binding Domains of the Dynein Motor. *Cell*, *150*(5), 975–986. https://doi.org/10.1016/j.cell.2012.07.022

Hutten, S., & Dormann, D. (2020). Nucleocytoplasmic transport defects in neurodegeneration—Cause or consequence? *Seminars in Cell & Developmental Biology*, *99*, 151–162. https://doi.org/10.1016/j.semcdb.2019.05.020

Hwang, J. Y., Jung, S., Kook, T. L., Rouchka, E. C., Bok, J., & Park, J. W. (2020). rMAPS2: An update of the RNA map analysis and plotting server for alternative splicing regulation. *Nucleic Acids Research*, *48*(W1), W300–W306. https://doi.org/10.1093/nar/gkaa237

Inoue, S. B., Shimoda, M., Nishinokubi, I., Siomi, M. C., Okamura, M., Nakamura, A., Kobayashi, S., Ishida, N., & Siomi, H. (2002). A Role for the *Drosophila* Fragile X-Related Gene in Circadian Output. *Current Biology*, *12*(15), 1331–1335. https://doi.org/10.1016/S0960-9822(02)01036-9

Ishihara, N. (2004). Mitofusin 1 and 2 play distinct roles in mitochondrial fusion reactions via GTPase activity. *Journal of Cell Science*, *117*(26), 6535–6546. https://doi.org/10.1242/jcs.01565

Ishihara, T., Ban-Ishihara, R., Ota, A., & Ishihara, N. (2022). Mitochondrial nucleoid trafficking regulated by the inner-membrane AAA-ATPase ATAD3A modulates respiratory complex formation. *Proceedings of the National Academy of Sciences*, *119*(47), e2210730119. https://doi.org/10.1073/pnas.2210730119

Ji, W., Hatch, A. L., Merrill, R. A., Strack, S., & Higgs, H. N. (2015). Actin filaments target the oligomeric maturation of the dynamin GTPase Drp1 to mitochondrial fission sites. *eLife*, *4*, e11553. https://doi.org/10.7554/eLife.11553

Ji, W.-K., Chakrabarti, R., Fan, X., Schoenfeld, L., Strack, S., & Higgs, H. N. (2017). Receptor-mediated Drp1 oligomerization on endoplasmic reticulum. *Journal of Cell Biology*, *216*(12), 4123–4139. https://doi.org/10.1083/jcb.201610057

Jin, D., Hidaka, K., Shirai, M., & Morisaki, T. (2010). RNA-binding motif protein 24 regulates myogenin expression and promotes myogenic differentiation. *Genes to Cells*, *15*(11), 1158–1167. https://doi.org/10.1111/j.1365-2443.2010.01446.x

Jones, M. W., Errington, M. L., French, P. J., Fine, A., Bliss, T. V. P., Garel, S., Charnay, P., Bozon, B., Laroche, S., & Davis, S. (2001). A requirement for the immediate early gene Zif268 in the expression of late LTP and long-term memories. *Nature Neuroscience*, *4*(3), Article 3. https://doi.org/10.1038/85138

Jumper, J., Evans, R., Pritzel, A., Green, T., Figurnov, M., Ronneberger, O., Tunyasuvunakool, K., Bates, R., Žídek, A., Potapenko, A., Bridgland, A., Meyer, C., Kohl, S. A. A., Ballard, A. J., Cowie, A., Romera-Paredes, B., Nikolov, S., Jain, R., Adler, J., … Hassabis, D. (2021). Highly accurate protein structure prediction with AlphaFold. *Nature*, *596*(7873), Article 7873. https://doi.org/10.1038/s41586-021-03819-2

Jung, J., Ohk, J., Kim, H., Holt, C. E., Park, H. J., & Jung, H. (2023). mRNA transport, translation, and decay in adult mammalian central nervous system axons. *Neuron*, *111*(5), 650-668.e4. https://doi.org/10.1016/j.neuron.2022.12.015

Jungmann, R., Avendaño, M. S., Woehrstein, J. B., Dai, M., Shih, W. M., & Yin, P. (2014). Multiplexed 3D cellular super-resolution imaging with DNA-PAINT and Exchange-PAINT. *Nature Methods*, *11*(3), 313–318. https://doi.org/10.1038/nmeth.2835

Kaan, H. Y. K., Hackney, D. D., & Kozielski, F. (2011). The Structure of the Kinesin-1 Motor-Tail Complex Reveals the Mechanism of Autoinhibition. *Science*, *333*(6044), 883–885. https://doi.org/10.1126/science.1204824

Kalia, R., Wang, R. Y.-R., Yusuf, A., Thomas, P. V., Agard, D. A., Shaw, J. M., & Frost, A. (2018). Structural basis of mitochondrial receptor binding and constriction by DRP1. *Nature*, *558*(7710), 401–405. https://doi.org/10.1038/s41586-018-0211-2

Kamerkar, S. C., Kraus, F., Sharpe, A. J., Pucadyil, T. J., & Ryan, M. T. (2018). Dynamin-related protein 1 has membrane constricting and severing abilities sufficient for mitochondrial and peroxisomal fission. *Nature Communications*, *9*(1), 5239. https://doi.org/10.1038/s41467-018-07543-w

Kanai, Y., Okada, Y., Tanaka, Y., Harada, A., Terada, S., & Hirokawa, N. (2000). KIF5C, a Novel Neuronal Kinesin Enriched in Motor Neurons. *Journal of Neuroscience*, *20*(17), 6374–6384. https://doi.org/10.1523/JNEUROSCI.20-17-06374.2000

Kanfer, G., Courthéoux, T., Peterka, M., Meier, S., Soste, M., Melnik, A., Reis, K., Aspenström, P., Peter, M., Picotti, P., & Kornmann, B. (2015). Mitotic redistribution of the mitochondrial network by Miro and Cenp-F. *Nature Communications*, *6*(1), Article 1. https://doi.org/10.1038/ncomms9015

Kaufmann, W. E., Abrams, M. T., Chen, W., & Reiss, A. L. (1999). Genotype, molecular phenotype, and cognitive phenotype: Correlations in fragile X syndrome. *American Journal of Medical Genetics*, *83*(4), 286–295. https://doi.org/10.1002/(SICI)1096-8628(19990402)83:4<286::AID-AJMG10>3.0.CO;2-H

Kaufmann, W. E., Cortell, R., Kau, A. S. M., Bukelis, I., Tierney, E., Gray, R. M., Cox, C., Capone, G. T., & Stanard, P. (2004). Autism spectrum disorder in fragile X syndrome: Communication, social interaction, and specific behaviors. *American Journal of Medical Genetics Part A*, *129A*(3), 225–234. https://doi.org/10.1002/ajmg.a.30229

Kaufmann, W. E., Kidd, S. A., Andrews, H. F., Budimirovic, D. B., Esler, A., Haas-Givler, B., Stackhouse, T., Riley, C., Peacock, G., Sherman, S. L., Brown, W. T., & Berry-Kravis, E. (2017). Autism Spectrum Disorder in Fragile X Syndrome: Cooccurring Conditions and Current Treatment. *Pediatrics*, *139*(Supplement_3), S194–S206. https://doi.org/10.1542/peds.2016-1159F

Kawasaki, H., & Kretsinger, R. H. (2017). Structural and functional diversity of EF-hand proteins: Evolutionary perspectives. *Protein Science*, *26*(10), 1898–1920. https://doi.org/10.1002/pro.3233

Keller, A., Nesvizhskii, A. I., Kolker, E., & Aebersold, R. (2002). Empirical Statistical Model To Estimate the Accuracy of Peptide Identifications Made by MS/MS and Database Search. *Analytical Chemistry*, *74*(20), 5383–5392. https://doi.org/10.1021/ac025747h

Kendrick, A. A., Dickey, A. M., Redwine, W. B., Tran, P. T., Vaites, L. P., Dzieciatkowska, M., Harper, J. W., & Reck-Peterson, S. L. (2019). Hook3 is a scaffold for the opposite-polarity microtubule-based motors cytoplasmic dynein-1 and KIF1C. *Journal of Cell Biology*, *218*(9), 2982–3001. https://doi.org/10.1083/jcb.201812170

Khodjakov, A., Lizunova, E. M., Minin, A. A., Koonce, M. P., & Gyoeva, F. K. (1998). A Specific Light Chain of Kinesin Associates with Mitochondria in Cultured Cells. *Molecular Biology of the Cell*, *9*(2), 333–343. https://doi.org/10.1091/mbc.9.2.333

Kidd, S. A., Lachiewicz, A., Barbouth, D., Blitz, R. K., Delahunty, C., McBrien, D., Visootsak, J., & Berry-Kravis, E. (2014). Fragile X Syndrome: A Review of Associated Medical Problems. *Pediatrics*, *134*(5), 995–1005. https://doi.org/10.1542/peds.2013-4301

Kleele, T., Rey, T., Winter, J., Zaganelli, S., Mahecic, D., Perreten Lambert, H., Ruberto, F. P., Nemir, M., Wai, T., Pedrazzini, T., & Manley, S. (2021). Distinct fission signatures predict mitochondrial degradation or biogenesis. *Nature*, *593*(7859), 435–439. https://doi.org/10.1038/s41586-021-03510-6

Klosowiak, J. L., Focia, P. J., Chakravarthy, S., Landahl, E. C., Freymann, D. M., & Rice, S. E. (2013). Structural coupling of the EF hand and C-terminal GTPase domains in the mitochondrial protein Miro. *EMBO Reports*, *14*(11), 968–974. https://doi.org/10.1038/embor.2013.151

Klosowiak, J. L., Park, S., Smith, K. P., French, M. E., Focia, P. J., Freymann, D. M., & Rice, S. E. (2016). Structural insights into Parkin substrate lysine targeting from minimal Miro substrates. *Scientific Reports*, *6*(1), Article 1. https://doi.org/10.1038/srep33019

Kodiha, M., Chu, A., Matusiewicz, N., & Stochaj, U. (2004). Multiple mechanisms promote the inhibition of classical nuclear import upon exposure to severe oxidative stress. *Cell Death & Differentiation*, *11*(8), Article 8. https://doi.org/10.1038/sj.cdd.4401432

Korobova, F., Gauvin, T. J., & Higgs, H. N. (2014). A Role for Myosin II in Mammalian Mitochondrial Fission. *Current Biology*, *24*(4), 409–414. https://doi.org/10.1016/j.cub.2013.12.032

Korobova, F., Ramabhadran, V., & Higgs, H. N. (2013). An Actin-Dependent Step in Mitochondrial Fission Mediated by the ER-Associated Formin INF2. *Science*, *339*(6118), 464–467. https://doi.org/10.1126/science.1228360

Koshiba, T., Holman, H. A., Kubara, K., Yasukawa, K., Kawabata, S., Okamoto, K., Macfarlane, J., & Shaw, J. M. (2011). Structure-Function Analysis of the Yeast Mitochondrial Rho GTPase, Gem1p: IMPLICATIONS FOR MITOCHONDRIAL INHERITANCE*. *Journal of Biological Chemistry*, *286*(1), 354–362. https://doi.org/10.1074/jbc.M110.180034

Kremer, J. R., Mastronarde, D. N., & McIntosh, J. R. (1996). Computer Visualization of Three-Dimensional Image Data Using IMOD. *Journal of Structural Biology*, *116*(1), 71–76. https://doi.org/10.1006/jsbi.1996.0013

Kuzniewska, B., Cysewski, D., Wasilewski, M., Sakowska, P., Milek, J., Kulinski, T. M., Winiarski, M., Kozielewicz, P., Knapska, E., Dadlez, M., Chacinska, A., Dziembowski, A., & Dziembowska, M. (2020). Mitochondrial protein biogenesis in the synapse is supported by local translation. *EMBO Reports*, *21*(8). https://doi.org/10.15252/embr.201948882

Laggerbauer, B., Ostareck, D., Keidel, E.-M., Ostareck-Lederer, A., & Fischer, U. (2001). Evidence that fragile X mental retardation protein is a negative regulator of translation. *Human Molecular Genetics*, *10*(4), 329–338. https://doi.org/10.1093/hmg/10.4.329

LaMonte, B. H., Wallace, K. E., Holloway, B. A., Shelly, S. S., Ascaño, J., Tokito, M., Van Winkle, T., Howland, D. S., & Holzbaur, E. L. F. (2002). Disruption of Dynein/Dynactin Inhibits Axonal Transport in Motor Neurons Causing Late-Onset Progressive Degeneration. *Neuron*, *34*(5), 715–727. https://doi.org/10.1016/S0896-6273(02)00696-7

Lattante, S., de Calbiac, H., Le Ber, I., Brice, A., Ciura, S., & Kabashi, E. (2015). Sqstm1 knock-down causes a locomotor phenotype ameliorated by rapamycin in a zebrafish model of ALS/FTLD. *Human Molecular Genetics*, *24*(6), 1682–1690. https://doi.org/10.1093/hmg/ddu580

Laurin, N., Brown, J. P., Morissette, J., & Raymond, V. (2002). Recurrent Mutation of the Gene Encoding sequestosome 1 (SQSTM1/p62) in Paget Disease of Bone. *The American Journal of Human Genetics*, *70*(6), 1582–1588. https://doi.org/10.1086/340731

Lee, C. A., Chin, L.-S., & Li, L. (2018). Hypertonia-linked protein Trak1 functions with mitofusins to promote mitochondrial tethering and fusion. *Protein & Cell*, *9*(8), 693–716. https://doi.org/10.1007/s13238-017-0469-4

Lee, H.-G., Imaichi, S., Kraeutler, E., Aguilar, R., Lee, Y.-W., Sheridan, S. D., & Lee, J. T. (2023). Site-specific R-loops induce CGG repeat contraction and fragile X gene reactivation. *Cell*, *186*(12), 2593-2609.e18. https://doi.org/10.1016/j.cell.2023.04.035

Lee, I.-G., Cason, S. E., Alqassim, S. S., Holzbaur, E. L. F., & Dominguez, R. (2020). A tunable LIC1-adaptor interaction modulates dynein activity in a cargo-specific manner. *Nature Communications*, *11*(1), 5695. https://doi.org/10.1038/s41467-020-19538-7

Lee, I.-G., Olenick, M. A., Boczkowska, M., Franzini-Armstrong, C., Holzbaur, E. L. F., & Dominguez, R. (2018). A conserved interaction of the dynein light intermediate chain with dynein-dynactin effectors necessary for processivity. *Nature Communications*, *9*(1), 986. https://doi.org/10.1038/s41467-018-03412-8

Lee, J. E., Westrate, L. M., Wu, H., Page, C., & Voeltz, G. K. (2016). Multiple dynamin family members collaborate to drive mitochondrial division. *Nature*, *540*(7631), 139–143. https://doi.org/10.1038/nature20555

Lee, S., Lee, K.-S., Huh, S., Liu, S., Lee, D.-Y., Hong, S. H., Yu, K., & Lu, B. (2016). Polo Kinase Phosphorylates Miro to Control ER-Mitochondria Contact Sites and Mitochondrial Ca 2+ Homeostasis in Neural Stem Cell Development. *Developmental Cell*, *37*(2), 174–189. https://doi.org/10.1016/j.devcel.2016.03.023

Lenzen, C., Cool, R. H., Prinz, H., Kuhlmann, J., & Wittinghofer, A. (1998). Kinetic Analysis by Fluorescence of the Interaction between Ras and the Catalytic Domain of the Guanine Nucleotide Exchange Factor Cdc25Mm. *Biochemistry*, *37*(20), 7420–7430. https://doi.org/10.1021/bi972621j

Lewis, S. C., Uchiyama, L. F., & Nunnari, J. (2016). ER-mitochondria contacts couple mtDNA synthesis with mitochondrial division in human cells. *Science*, *353*(6296), aaf5549. https://doi.org/10.1126/science.aaf5549

Li, H., Ruan, Y., Zhang, K., Jian, F., Hu, C., Miao, L., Gong, L., Sun, L., Zhang, X., Chen, S., Chen, H., Liu, D., & Song, Z. (2016). Mic60/Mitofilin determines MICOS assembly essential for mitochondrial dynamics and mtDNA nucleoid organization. *Cell Death & Differentiation*, *23*(3), Article 3. https://doi.org/10.1038/cdd.2015.102

Li, X., Wang, W., Wang, J., Malovannaya, A., Xi, Y., Li, W., Guerra, R., Hawke, D. H., Qin, J., & Chen, J. (2015). Proteomic analyses reveal distinct chromatin-associated and soluble transcription factor complexes. *Molecular Systems Biology*, *11*(1), 775. https://doi.org/10.15252/msb.20145504

Li, Z., Zhang, Y., Ku, L., Wilkinson, K. D., Warren, S. T., & Feng, Y. (2001). The fragile X mental retardation protein inhibits translation via interacting with mRNA. *Nucleic Acids Research*, *29*(11), 2276–2283. https://doi.org/10.1093/nar/29.11.2276

Liao, Y.-C., Fernandopulle, M. S., Wang, G., Choi, H., Hao, L., Drerup, C. M., Patel, R., Qamar, S., Nixon-Abell, J., Shen, Y., Meadows, W., Vendruscolo, M., Knowles, T. P. J., Nelson, M., Czekalska, M. A., Musteikyte, G., Gachechiladze, M. A., Stephens, C. A., Pasolli, H. A., … Ward, M. E. (2019). RNA Granules Hitchhike on Lysosomes for Long-Distance Transport, Using Annexin A11 as a Molecular Tether. *Cell*, *179*(1), 147-164.e20. https://doi.org/10.1016/j.cell.2019.08.050

Licznerski, P., Park, H.-A., Rolyan, H., Chen, R., Mnatsakanyan, N., Miranda, P., Graham, M., Wu, J., Cruz-Reyes, N., Mehta, N., Sohail, S., Salcedo, J., Song, E., Effman, C., Effman, S., Brandao, L., Xu, G. N., Braker, A., Gribkoff, V. K., … Jonas, E. A. (2020). ATP Synthase c-Subunit Leak Causes Aberrant Cellular Metabolism in Fragile X Syndrome. *Cell*, *182*(5), 1170-1185.e9. https://doi.org/10.1016/j.cell.2020.07.008

Lin, Y., Tan, K. T., Liu, J., Kong, X., Huang, Z., & Xu, X. Q. (2018). Global profiling of Rbm24 bound RNAs uncovers a multi-tasking RNA binding protein. *The International Journal of Biochemistry & Cell Biology*, *94*, 10–21. https://doi.org/10.1016/j.biocel.2017.11.002

Linsley, J. W., Tripathi, A., Epstein, I., Schmunk, G., Mount, E., Campioni, M., Oza, V., Barch, M., Javaherian, A., Nowakowski, T. J., Samsi, S., & Finkbeiner, S. (2019). Automated four-dimensional long term imaging enables single cell tracking within organotypic brain slices to study neurodevelopment and degeneration. *Communications Biology*, *2*(1), Article 1. https://doi.org/10.1038/s42003-019-0411-9

Liu, J., Lamb, D., Chou, M. M., Liu, Y.-J., & Li, G. (2007). Nerve Growth Factor-mediated Neurite Outgrowth via Regulation of Rab5. *Molecular Biology of the Cell*, *18*(4), 1375–1384. https://doi.org/10.1091/mbc.e06-08-0725

Liu, Y.-T., Laurá, M., Hersheson, J., Horga, A., Jaunmuktane, Z., Brandner, S., Pittman, A., Hughes, D., Polke, J. M., Sweeney, M. G., Proukakis, C., Janssen, J. C., Auer-Grumbach, M., Zuchner, S., Shields, K. G., Reilly, M. M., & Houlden, H. (2014). Extended phenotypic spectrum of KIF5A mutations. *Neurology*, *83*(7), 612–619. https://doi.org/10.1212/WNL.0000000000000691

López-Doménech, G., Covill-Cooke, C., Ivankovic, D., Halff, E. F., Sheehan, D. F., Norkett, R., Birsa, N., & Kittler, J. T. (2018). Miro proteins coordinate microtubule- and actin-dependent mitochondrial transport and distribution. *The EMBO Journal*, *37*(3), 321–336. https://doi.org/10.15252/embj.201696380

López-Doménech, G., Higgs, N. F., Vaccaro, V., Roš, H., Arancibia-Cárcamo, I. L., MacAskill, A. F., & Kittler, J. T. (2016). Loss of Dendritic Complexity Precedes Neurodegeneration in a Mouse Model with Disrupted Mitochondrial Distribution in Mature Dendrites. *Cell Reports*, *17*(2), 317–327. https://doi.org/10.1016/j.celrep.2016.09.004

López-Doménech, G., Serrat, R., Mirra, S., D'Aniello, S., Somorjai, I., Abad, A., Vitureira, N., García-Arumí, E., Alonso, M. T., Rodriguez-Prados, M., Burgaya, F., Andreu, A. L., García-Sancho, J., Trullas, R., Garcia-Fernàndez, J., & Soriano, E. (2012). The Eutherian Armcx genes regulate mitochondrial trafficking in neurons and interact with Miro and Trak2. *Nature Communications*, *3*(1), Article 1. https://doi.org/10.1038/ncomms1829

LoRusso, E., Hickman, J. J., & Guo, X. (2019). Ion channel dysfunction and altered motoneuron excitability in ALS. *Neurological Disorders & Epilepsy Journal*, *3*(2), 124.

Loss, O., & Stephenson, F. A. (2017). Developmental changes in trak-mediated mitochondrial transport in neurons. *Molecular and Cellular Neuroscience*, *80*, 134–147. https://doi.org/10.1016/j.mcn.2017.03.006

Love, M. I., Huber, W., & Anders, S. (2014). Moderated estimation of fold change and dispersion for RNA-seq data with DESeq2. *Genome Biology*, *15*(12), 550. https://doi.org/10.1186/s13059-014-0550-8

Lu, W., Lakonishok, M., Liu, R., Billington, N., Rich, A., Glotzer, M., Sellers, J. R., & Gelfand, V. I. (2020). Competition between kinesin-1 and myosin-V defines Drosophila posterior determination. *eLife*, *9*, e54216. https://doi.org/10.7554/eLife.54216

Lu, W., Lakonishok, M., Serpinskaya, A. S., Kirchenbüechler, D., Ling, S.-C., & Gelfand, V. I. (2018). Ooplasmic flow cooperates with transport and anchorage in Drosophila oocyte posterior determination. *Journal of Cell Biology*, *217*(10), 3497–3511. https://doi.org/10.1083/jcb.201709174

Luhur, A., Buddika, K., Ariyapala, I. S., Chen, S., & Sokol, N. S. (2017). Opposing Post-transcriptional Control of InR by FMRP and LIN-28 Adjusts Stem Cell-Based Tissue Growth. *Cell Reports*, *21*(10), 2671–2677. https://doi.org/10.1016/j.celrep.2017.11.039

MacAskill, A. F., Brickley, K., Stephenson, F. A., & Kittler, J. T. (2009). GTPase dependent recruitment of Grif-1 by Miro1 regulates mitochondrial trafficking in hippocampal neurons. *Molecular and Cellular Neuroscience*, *40*(3), 301–312. https://doi.org/10.1016/j.mcn.2008.10.016

MacAskill, A. F., Rinholm, J. E., Twelvetrees, A. E., Arancibia-Carcamo, I. L., Muir, J., Fransson, A., Aspenstrom, P., Attwell, D., & Kittler, J. T. (2009). Miro1 Is a Calcium Sensor for Glutamate Receptor-Dependent Localization of Mitochondria at Synapses. *Neuron*, *61*(4), 541–555. https://doi.org/10.1016/j.neuron.2009.01.030

MacDonald, R., Barbat-Artigas, S., Cho, C., Peng, H., Shang, J., Moustaine, A., Carbonetto, S., Robitaille, R., Chalifour, L. E., & Paudel, H. (2017). A Novel Egr-1-Agrin Pathway and Potential Implications for Regulation of Synaptic Physiology and Homeostasis at the Neuromuscular Junction. *Frontiers in Aging Neuroscience*, *9*. https://www.frontiersin.org/articles/10.3389/fnagi.2017.00258

Manor, U., Bartholomew, S., Golani, G., Christenson, E., Kozlov, M., Higgs, H., Spudich, J., & Lippincott-Schwartz, J. (2015). A mitochondria-anchored isoform of the actin-nucleating spire protein regulates mitochondrial division. *eLife*, *4*, e08828. https://doi.org/10.7554/eLife.08828

Markus, S. M., Marzo, M. G., & McKenney, R. J. (2020). New insights into the mechanism of dynein motor regulation by lissencephaly-1. *eLife*, *9*, e59737. https://doi.org/10.7554/eLife.59737

Martin, M., Iyadurai, S. J., Gassman, A., Gindhart, J. G., Hays, T. S., & Saxton, W. M. (1999). Cytoplasmic Dynein, the Dynactin Complex, and Kinesin Are Interdependent and Essential for Fast Axonal Transport. *Molecular Biology of the Cell*, *10*(11), 3717–3728. https://doi.org/10.1091/mbc.10.11.3717

Marzo, M. G., Griswold, J. M., & Markus, S. M. (2020). Pac1/LIS1 stabilizes an uninhibited conformation of dynein to coordinate its localization and activity. *Nature Cell Biology*, *22*(5), 559–569. https://doi.org/10.1038/s41556-020-0492-1

Masucci, E. M., Relich, P. K., Lakadamyali, M., Ostap, E. M., & Holzbaur, E. L. F. (2021). Kinesin-4 Motor Teams Effectively Navigate Dendritic Microtubule Arrays Through Track Switching and Regulation of Microtubule Dynamics. *bioRxiv*, 2021.02.28.433181. https://doi.org/10.1101/2021.02.28.433181

Matsuda, N., Sato, S., Shiba, K., Okatsu, K., Saisho, K., Gautier, C. A., Sou, Y., Saiki, S., Kawajiri, S., Sato, F., Kimura, M., Komatsu, M., Hattori, N., & Tanaka, K. (2010). PINK1 stabilized by mitochondrial depolarization recruits Parkin to damaged mitochondria and activates latent Parkin for mitophagy. *Journal of Cell Biology*, *189*(2), 211–221. https://doi.org/10.1083/jcb.200910140

Matsuura, Y. (2016). Mechanistic Insights from Structural Analyses of Ran-GTPase-Driven Nuclear Export of Proteins and RNAs. *Journal of Molecular Biology*, *428*(10, Part A), 2025–2039. https://doi.org/10.1016/j.jmb.2015.09.025

Mattson, M. P., Gleichmann, M., & Cheng, A. (2008). Mitochondria in Neuroplasticity and Neurological Disorders. *Neuron*, *60*(5), 748–766. https://doi.org/10.1016/j.neuron.2008.10.010

Maurin, T., Lebrigand, K., Castagnola, S., Paquet, A., Jarjat, M., Popa, A., Grossi, M., Rage, F., & Bardoni, B. (2018). HITS-CLIP in various brain areas reveals new targets and new modalities of RNA binding by fragile X mental retardation protein. *Nucleic Acids Research*, *46*(12), 6344–6355. https://doi.org/10.1093/nar/gky267

McBride, S. M. J., Choi, C. H., Wang, Y., Liebelt, D., Braunstein, E., Ferreiro, D., Sehgal, A., Siwicki, K. K., Dockendorff, T. C., Nguyen, H. T., McDonald, T. V., & Jongens, T. A. (2005). Pharmacological Rescue of Synaptic Plasticity, Courtship Behavior, and Mushroom Body Defects in a Drosophila Model of Fragile X Syndrome. *Neuron*, *45*(5), 753–764. https://doi.org/10.1016/j.neuron.2005.01.038

McKenney, R. J., Huynh, W., Tanenbaum, M. E., Bhabha, G., & Vale, R. D. (2014). Activation of cytoplasmic dynein motility by dynactin-cargo adapter complexes. *Science*, *345*(6194), 337–341. https://doi.org/10.1126/science.1254198

McLelland, G., Soubannier, V., Chen, C. X., McBride, H. M., & Fon, E. A. (2014). Parkin and PINK1 function in a vesicular trafficking pathway regulating mitochondrial quality control. *The EMBO Journal*, *33*(4), 282–295. https://doi.org/10.1002/embj.201385902

McMurray, C. T. (2000). Neurodegeneration: Diseases of the cytoskeleton? *Cell Death & Differentiation*, *7*(10), Article 10. https://doi.org/10.1038/sj.cdd.4400764

Mehta, P., Kaye, W., Raymond, J., Wu, R., Larson, T., Punjani, R., Heller, D., Cohen, J., Peters, T., Muravov, O., & Horton, K. (2018). *Prevalence of Amyotrophic Lateral Sclerosis—United States, 2014*. *67*(7).

Meijering, E., Dzyubachyk, O., & Smal, I. (2012). Chapter nine—Methods for Cell and Particle Tracking. In P. M. conn (Ed.), *Methods in Enzymology* (Vol. 504, pp. 183–200). Academic Press. https://doi.org/10.1016/B978-0-12-391857-4.00009-4

Meister, G., Landthaler, M., Peters, L., Chen, P. Y., Urlaub, H., Lührmann, R., & Tuschl, T. (2005). Identification of Novel Argonaute-Associated Proteins. *Current Biology*, *15*(23), 2149–2155. https://doi.org/10.1016/j.cub.2005.10.048

Merzetti, E. M., & Staveley, B. E. (2015). Spargel, the PGC-1α homologue, in models of Parkinson disease in Drosophila melanogaster. *BMC Neuroscience*, *16*(1), 70. https://doi.org/10.1186/s12868-015-0210-2

Miki, H., Setou, M., Kaneshiro, K., & Hirokawa, N. (2001). All kinesin superfamily protein, KIF, genes in mouse and human. *Proceedings of the National Academy of Sciences*, *98*(13), 7004–7011. https://doi.org/10.1073/pnas.111145398

Millecamps, S., & Julien, J.-P. (2013). Axonal transport deficits and neurodegenerative diseases. *Nature Reviews Neuroscience*, *14*(3), Article 3. https://doi.org/10.1038/nrn3380

Min, B.-J., Kim, N., Chung, T., Kim, O.-H., Nishimura, G., Chung, C. Y., Song, H. R., Kim, H. W., Lee, H. R., Kim, J., Kang, T.-H., Seo, M.-E., Yang, S.-D., Kim, D.-H., Lee, S.-B., Kim, J.-I., Seo, J.-S., Choi, J.-Y., Kang, D., … Cho, T.-J. (2011). Whole-Exome Sequencing Identifies Mutations of KIF22 in Spondyloepimetaphyseal Dysplasia with Joint Laxity, Leptodactylic Type. *The American Journal of Human Genetics*, *89*(6), 760–766. https://doi.org/10.1016/j.ajhg.2011.10.015

Misgeld, T., & Schwarz, T. L. (2017). Mitostasis in Neurons: Maintaining Mitochondria in an Extended Cellular Architecture. *Neuron*, *96*(3), 651–666. https://doi.org/10.1016/j.neuron.2017.09.055

Mishra, P., Carelli, V., Manfredi, G., & Chan, D. C. (2014). Proteolytic Cleavage of Opa1 Stimulates Mitochondrial Inner Membrane Fusion and Couples Fusion to Oxidative Phosphorylation. *Cell Metabolism*, *19*(4), 630–641. https://doi.org/10.1016/j.cmet.2014.03.011

Misko, A., Jiang, S., Wegorzewska, I., Milbrandt, J., & Baloh, R. H. (2010). Mitofusin 2 Is Necessary for Transport of Axonal Mitochondria and Interacts with the Miro/Milton Complex. *Journal of Neuroscience*, *30*(12), 4232–4240. https://doi.org/10.1523/JNEUROSCI.6248-09.2010

Miyashiro, K. Y., Beckel-Mitchener, A., Purk, T. P., Becker, K. G., Barret, T., Liu, L., Carbonetto, S., Weiler, I. J., Greenough, W. T., & Eberwine, J. (2003). RNA Cargoes Associating with FMRP Reveal Deficits in Cellular Functioning in Fmr1 Null Mice. *Neuron*, *37*(3), 417–431. https://doi.org/10.1016/S0896-6273(03)00034-5

Modi, S., López-Doménech, G., Halff, E. F., Covill-Cooke, C., Ivankovic, D., Melandri, D., Arancibia-Cárcamo, I. L., Burden, J. J., Lowe, A. R., & Kittler, J. T. (2019). Miro clusters regulate ER-mitochondria contact sites and link cristae organization to the mitochondrial transport machinery. *Nature Communications*, *10*(1), 4399. https://doi.org/10.1038/s41467-019-12382-4

Monyak, R. E., Emerson, D., Schoenfeld, B. P., Zheng, X., Chambers, D. B., Rosenfelt, C., Langer, S., Hinchey, P., Choi, C. H., McDonald, T. V., Bolduc, F. V., Sehgal, A., McBride, S. M. J., & Jongens, T. A. (2017). Insulin signaling misregulation underlies circadian and cognitive deficits in a Drosophila fragile X model. *Molecular Psychiatry*, *22*(8), 1140–1148. https://doi.org/10.1038/mp.2016.51

Monzel, A. S., Enríquez, J. A., & Picard, M. (2023). Multifaceted mitochondria: Moving mitochondrial science beyond function and dysfunction. *Nature Metabolism*, *5*(4), 546–562. https://doi.org/10.1038/s42255-023-00783-1

Mooney, C. M., Jimenez-Mateos, E. M., Engel, T., Mooney, C., Diviney, M., Venø, M. T., Kjems, J., Farrell, M. A., O'Brien, D. F., Delanty, N., & Henshall, D. C. (2017). RNA sequencing of synaptic and cytoplasmic Upf1-bound transcripts supports contribution of nonsense-mediated decay to epileptogenesis. *Scientific Reports*, *7*(1), Article 1. https://doi.org/10.1038/srep41517

Moore, A. S., Wong, Y. C., Simpson, C. L., & Holzbaur, E. L. F. (2016). Dynamic actin cycling through mitochondrial subpopulations locally regulates the fission–fusion balance within mitochondrial networks. *Nature Communications*, *7*(1), 12886. https://doi.org/10.1038/ncomms12886

Morales, J., Hiesinger, P. R., Schroeder, A. J., Kume, K., Verstreken, P., Jackson, F. R., Nelson, D. L., & Hassan, B. A. (2002). *Drosophila* Fragile X Protein, DFXR, Regulates Neuronal Morphology and Function in the Brain. *Neuron*, *34*(6), 961–972. https://doi.org/10.1016/S0896-6273(02)00731-6

Moughamian, A. J., & Holzbaur, E. L. F. (2012). Dynactin Is Required for Transport Initiation from the Distal Axon. *Neuron*, *74*(2), 331–343. https://doi.org/10.1016/j.neuron.2012.02.025

Moughamian, A. J., Osborn, G. E., Lazarus, J. E., Maday, S., & Holzbaur, E. L. F. (2013). Ordered Recruitment of Dynactin to the Microtubule Plus-End is Required for Efficient Initiation of

Retrograde Axonal Transport. *Journal of Neuroscience*, *33*(32), 13190–13203. https://doi.org/10.1523/JNEUROSCI.0935-13.2013

Mukherjee, S., Basar, M. A., Davis, C., & Duttaroy, A. (2014). Emerging functional similarities and divergences between Drosophila Spargel/dPGC-1 and mammalian PGC-1 protein. *Frontiers in Genetics*, *5*. https://doi.org/10.3389/fgene.2014.00216

Nagashima, S., Tábara, L.-C., Tilokani, L., Paupe, V., Anand, H., Pogson, J. H., Zunino, R., McBride, H. M., & Prudent, J. (2020). Golgi-derived PI **(** 4 **)** P-containing vesicles drive late steps of mitochondrial division. *Science*, *367*(6484), 1366–1371. https://doi.org/10.1126/science.aax6089

Nakano, J., Chiba, K., & Niwa, S. (2022). An ALS-associated KIF5A mutant forms oligomers and aggregates and induces neuronal toxicity. *Genes to Cells*, *27*(6), 421–435. https://doi.org/10.1111/gtc.12936

Narendra, D. P., Jin, S. M., Tanaka, A., Suen, D.-F., Gautier, C. A., Shen, J., Cookson, M. R., & Youle, R. J. (2010). PINK1 Is Selectively Stabilized on Impaired Mitochondria to Activate Parkin. *PLOS Biology*, *8*(1), e1000298. https://doi.org/10.1371/journal.pbio.1000298

Naruse, H., Ishiura, H., Mitsui, J., Takahashi, Y., Matsukawa, T., Sakuishi, K., Nakamagoe, K., Miyake, Z., Tamaoka, A., Goto, J., Yoshimura, J., Doi, K., Morishita, S., Toda, T., & Tsuji, S. (2021). Splice-site mutations in KIF5A in the Japanese case series of amyotrophic lateral sclerosis. *Neurogenetics*, *22*(1), 11–17. https://doi.org/10.1007/s10048-020-00626-1

Nawaz, A., Shilikbay, T., Skariah, G., & Ceman, S. (2022). Unwinding the roles of RNA helicase MOV10. *WIREs RNA*, *13*(2), e1682. https://doi.org/10.1002/wrna.1682

Nedozralova, H., Basnet, N., Ibiricu, I., Bodakuntla, S., Biertümpfel, C., & Mizuno, N. (2022). In situ cryo-electron tomography reveals local cellular machineries for axon branch development. *Journal of Cell Biology*, *221*(4), e202106086. https://doi.org/10.1083/jcb.202106086

Nesvizhskii, A. I., Keller, A., Kolker, E., & Aebersold, R. (2003). A Statistical Model for Identifying Proteins by Tandem Mass Spectrometry. *Analytical Chemistry*, *75*(17), 4646–4658. https://doi.org/10.1021/ac0341261

Ng, C.-H., Basil, A. H., Hang, L., Tan, R., Goh, K.-L., O'Neill, S., Zhang, X., Yu, F., & Lim, K.-L. (2017). Genetic or pharmacological activation of the *Drosophila* PGC-1α ortholog *spargel* rescues the disease phenotypes of genetic models of Parkinson's disease. *Neurobiology of Aging*, *55*, 33–37. https://doi.org/10.1016/j.neurobiolaging.2017.03.017

Nguyen, T. T., Oh, S. S., Weaver, D., Lewandowska, A., Maxfield, D., Schuler, M.-H., Smith, N. K., Macfarlane, J., Saunders, G., Palmer, C. A., Debattisti, V., Koshiba, T., Pulst, S., Feldman, E. L., Hajnoczky, G., & Shaw, J. M. (2014). Loss of Miro1-directed mitochondrial movement results in a novel murine model for neuron disease. *Proceedings of the National Academy of Sciences*, *111*(35), E3631–E3640. https://doi.org/10.1073/pnas.1402449111

Nicolas, A., Kenna, K. P., Renton, A. E., Ticozzi, N., Faghri, F., Chia, R., Dominov, J. A., Kenna, B. J., Nalls, M. A., Keagle, P., Rivera, A. M., van Rheenen, W., Murphy, N. A., van Vugt, J. J. F. A., Geiger, J. T., Van der Spek, R. A., Pliner, H. A., Shankaracharya, Smith, B. N., … Twine, N. A. (2018). Genome-wide Analyses Identify KIF5A as a Novel ALS Gene. *Neuron*, *97*(6), 1268-1283.e6. https://doi.org/10.1016/j.neuron.2018.02.027

Nirschl, J. J., Magiera, M. M., Lazarus, J. E., Janke, C., & Holzbaur, E. L. F. (2016). α-Tubulin Tyrosination and CLIP-170 Phosphorylation Regulate the Initiation of Dynein-Driven Transport in Neurons. *Cell Reports*, *14*(11), 2637–2652. https://doi.org/10.1016/j.celrep.2016.02.046

Nogales, E. (2000). Structural Insights into Microtubule Function. *Annual Review of Biochemistry*, *69*(1), 277–302. https://doi.org/10.1146/annurev.biochem.69.1.277

Oberlé, I., Rousseau, F., Heitz, D., Kretz, C., Devys, D., Hanauer, A., Boué, J., Bertheas, M. F., & Mandel, J. L. (1991). Instability of a 550-Base Pair DNA Segment and Abnormal Methylation in Fragile X Syndrome. *Science*, *252*(5009), 1097–1102. https://doi.org/10.1126/science.252.5009.1097

Oeding, S. J., Majstrowicz, K., Hu, X.-P., Schwarz, V., Freitag, A., Honnert, U., Nikolaus, P., & Bähler, M. (2018). Identification of Miro1 and Miro2 as mitochondrial receptors for myosin XIX. *Journal of Cell Science*, *131*(17), jcs219469. https://doi.org/10.1242/jcs.219469

Ogawa, F., Malavasi, E. L. V., Crummie, D. K., Eykelenboom, J. E., Soares, D. C., Mackie, S., Porteous, D. J., & Millar, J. K. (2014). DISC1 complexes with TRAK1 and Miro1 to modulate anterograde axonal mitochondrial trafficking. *Human Molecular Genetics*, *23*(4), 906–919. https://doi.org/10.1093/hmg/ddt485

Ogawa, F., Murphy, L. C., Malavasi, E. L. V., O'Sullivan, S. T., Torrance, H. S., Porteous, D. J., & Millar, J. K. (2016). NDE1 and GSK3β Associate with TRAK1 and Regulate Axonal Mitochondrial Motility: Identification of Cyclic AMP as a Novel Modulator of Axonal Mitochondrial Trafficking. *ACS Chemical Neuroscience*, *7*(5), 553–564. https://doi.org/10.1021/acschemneuro.5b00255

Olenick, M. A., & Holzbaur, E. L. F. (2019). Dynein activators and adaptors at a glance. *Journal of Cell Science*, *132*(6), jcs227132. https://doi.org/10.1242/jcs.227132

Olenick, M. A., Tokito, M., Boczkowska, M., Dominguez, R., & Holzbaur, E. L. F. (2016). Hook Adaptors Induce Unidirectional Processive Motility by Enhancing the Dynein-Dynactin Interaction. *Journal of Biological Chemistry*, *291*(35), 18239–18251. https://doi.org/10.1074/jbc.M116.738211

Ortiz-González, X. R. (2021). Mitochondrial Dysfunction: A Common Denominator in Neurodevelopmental Disorders? *Developmental Neuroscience*, *43*(3–4), 222–229. https://doi.org/10.1159/000517870

Osellame, L. D., Singh, A. P., Stroud, D. A., Palmer, C. S., Stojanovski, D., Ramachandran, R., & Ryan, M. T. (2016). Cooperative and independent roles of the Drp1 adaptors Mff, MiD49 and MiD51 in mitochondrial fission. *Journal of Cell Science*, *129*(11), 2170–2181. https://doi.org/10.1242/jcs.185165

O'Shea, E. K., Klemm, J. D., Kim, P. S., & Alber, T. (1991). X-Ray Structure of the GCN4 Leucine Zipper, a Two-Stranded, Parallel Coiled Coil. *Science*, *254*(5031), 539–544. https://doi.org/10.1126/science.1948029

Otera, H., Wang, C., Cleland, M. M., Setoguchi, K., Yokota, S., Youle, R. J., & Mihara, K. (2010). Mff is an essential factor for mitochondrial recruitment of Drp1 during mitochondrial fission in mammalian cells. *The Journal of Cell Biology*, *191*(6), 1141–1158. https://doi.org/10.1083/jcb.201007152

Palmer, C. S., Elgass, K. D., Parton, R. G., Osellame, L. D., Stojanovski, D., & Ryan, M. T. (2013). Adaptor Proteins MiD49 and MiD51 Can Act Independently of Mff and Fis1 in Drp1 Recruitment and Are Specific for Mitochondrial Fission. *Journal of Biological Chemistry*, *288*(38), 27584–27593. https://doi.org/10.1074/jbc.M113.479873

Pant, D. C., Parameswaran, J., Rao, L., Loss, I., Chilukuri, G., Parlato, R., Shi, L., Glass, J. D., Bassell, G. J., Koch, P., Yilmaz, R., Weishaupt, J. H., Gennerich, A., & Jiang, J. (2022). ALS-linked KIF5A ΔExon27 mutant causes neuronal toxicity through gain-of-function. *EMBO Reports*. https://doi.org/10.15252/embr.202154234

Parakh, S., & Atkin, J. D. (2016). Protein folding alterations in amyotrophic lateral sclerosis. *Brain Research*, *1648*, 633–649. https://doi.org/10.1016/j.brainres.2016.04.010

Paschal, B. M., & Vallee, R. B. (1987). Retrograde transport by the microtubule-associated protein MAP 1C. *Nature*, *330*(6144), 181–183. https://doi.org/10.1038/330181a0

Pekkurnaz, G., Trinidad, J. C., Wang, X., Kong, D., & Schwarz, T. L. (2014). Glucose Regulates Mitochondrial Motility via Milton Modification by O-GlcNAc Transferase. *Cell*, *158*(1), 54–68. https://doi.org/10.1016/j.cell.2014.06.007

Perez-Riverol, Y., Bai, J., Bandla, C., García-Seisdedos, D., Hewapathirana, S., Kamatchinathan, S., Kundu, D. J., Prakash, A., Frericks-Zipper, A., Eisenacher, M., Walzer, M., Wang, S., Brazma, A., & Vizcaíno, J. A. (2022). The PRIDE database resources in 2022: A hub for mass spectrometry-based proteomics evidences. *Nucleic Acids Research*, *50*(D1), D543–D552. https://doi.org/10.1093/nar/gkab1038

Peters, D. T., Kay, L., Eswaran, J., Lakey, J. H., & Soundararajan, M. (2018). Human Miro Proteins Act as NTP Hydrolases through a Novel, Non-Canonical Catalytic Mechanism. *International Journal of Molecular Sciences*, *19*(12), Article 12. https://doi.org/10.3390/ijms19123839

Pieretti, M., Zhang, F., Fu, Y.-H., Warren, S. T., Oostra, B. A., Caskey, C. T., & Nelson, D. L. (1991). Absence of expression of the FMR-1 gene in fragile X syndrome. *Cell*, *66*(4), 817–822. https://doi.org/10.1016/0092-8674(91)90125-I

Pilling, A. D., Horiuchi, D., Lively, C. M., & Saxton, W. M. (2006). Kinesin-1 and Dynein Are the Primary Motors for Fast Transport of Mitochondria in Drosophila Motor Axons. *Molecular Biology of the Cell*, *17*, 12.

Poirier, K., Lebrun, N., Broix, L., Tian, G., Saillour, Y., Boscheron, C., Parrini, E., Valence, S., Pierre, B. S., Oger, M., Lacombe, D., Geneviève, D., Fontana, E., Darra, F., Cances, C., Barth, M., Bonneau, D., Bernadina, B. D., N'Guyen, S., … Chelly, J. (2013). Mutations in TUBG1, DYNC1H1, KIF5C and KIF2A cause malformations of cortical development and microcephaly. *Nature Genetics*, *45*(6), 639–647. https://doi.org/10.1038/ng.2613

Poser, I., Sarov, M., Hutchins, J. R. A., Hériché, J.-K., Toyoda, Y., Pozniakovsky, A., Weigl, D., Nitzsche, A., Hegemann, B., Bird, A. W., Pelletier, L., Kittler, R., Hua, S., Naumann, R., Augsburg, M., Sykora, M. M., Hofemeister, H., Zhang, Y., Nasmyth, K., … Hyman, A. A. (2008). BAC TransgeneOmics: A high-throughput method for exploration of protein function in mammals. *Nature Methods*, *5*(5), 409–415. https://doi.org/10.1038/nmeth.1199

Puls, I., Jonnakuty, C., LaMonte, B. H., Holzbaur, E. L. F., Tokito, M., Mann, E., Floeter, M. K., Bidus, K., Drayna, D., Oh, S. J., Brown, R. H., Ludlow, C. L., & Fischbeck, K. H. (2003). Mutant dynactin in motor neuron disease. *Nature Genetics*, *33*(4), Article 4. https://doi.org/10.1038/ng1123

Qin, J., Guo, Y., Xue, B., Shi, P., Chen, Y., Su, Q. P., Hao, H., Zhao, S., Wu, C., Yu, L., Li, D., & Sun, Y. (2020). ER-mitochondria contacts promote mtDNA nucleoids active transportation via mitochondrial dynamic tubulation. *Nature Communications*, *11*(1), 4471. https://doi.org/10.1038/s41467-020-18202-4

Qin, M., Kang, J., Burlin, T. V., Jiang, C., & Smith, C. B. (2005). Postadolescent Changes in Regional Cerebral Protein Synthesis: An In Vivo Study in the Fmr1 Null Mouse. *Journal of Neuroscience*, *25*(20), 5087–5095. https://doi.org/10.1523/JNEUROSCI.0093-05.2005

Qiu, R., Zhang, J., & Xiang, X. (2019). LIS1 regulates cargo-adapter–mediated activation of dynein by overcoming its autoinhibition in vivo. *The Journal of Cell Biology*, jcb.201905178. https://doi.org/10.1083/jcb.201905178

Quan, F., Zonana, J., Gunter, K., Peterson, K. L., & Magenis, R. E., Popovich, B. W. (1995). An atypical case of fragile X syndrome caused by a deletion that includes FMRI gene. *American Journal of Human Genetics*, *56*. https://www.osti.gov/biblio/75444

Quintana, A., Schwarz, E. C., Schwindling, C., Lipp, P., Kaestner, L., & Hoth, M. (2006). Sustained Activity of Calcium Release-activated Calcium Channels Requires Translocation of Mitochondria to the Plasma Membrane*. *Journal of Biological Chemistry*, *281*(52), 40302–40309. https://doi.org/10.1074/jbc.M607896200

Quintero, O. A., DiVito, M. M., Adikes, R. C., Kortan, M. B., Case, L. B., Lier, A. J., Panaretos, N. S., Slater, S. Q., Rengarajan, M., Feliu, M., & Cheney, R. E. (2009). Human Myo19 Is a Novel Myosin that Associates with Mitochondria. *Current Biology*, *19*(23), 2008–2013. https://doi.org/10.1016/j.cub.2009.10.026

Rai, A., Pathak, D., Thakur, S., Singh, S., Dubey, A. K., & Mallik, R. (2016). Dynein Clusters into Lipid Microdomains on Phagosomes to Drive Rapid Transport toward Lysosomes. *Cell*, *164*(4), 722–734. https://doi.org/10.1016/j.cell.2015.12.054

Raj, A., van den Bogaard, P., Rifkin, S. A., van Oudenaarden, A., & Tyagi, S. (2008). Imaging individual mRNA molecules using multiple singly labeled probes. *Nature Methods*, *5*(10), 877–879. https://doi.org/10.1038/nmeth.1253

Raj, N., McEachin, Z. T., Harousseau, W., Zhou, Y., Zhang, F., Merritt-Garza, M. E., Taliaferro, J. M., Kalinowska, M., Marro, S. G., Hales, C. M., Berry-Kravis, E., Wolf-Ochoa, M. W., Martinez-Cerdeño, V., Wernig, M., Chen, L., Klann, E., Warren, S. T., Jin, P., Wen, Z., & Bassell, G. J. (2021). Cell-type-specific profiling of human cellular models of fragile X syndrome reveal PI3K-

dependent defects in translation and neurogenesis. *Cell Reports*, *35*(2), 108991. https://doi.org/10.1016/j.celrep.2021.108991

Ramesh Babu, J., Lamar Seibenhener, M., Peng, J., Strom, A.-L., Kemppainen, R., Cox, N., Zhu, H., Wooten, M. C., Diaz-Meco, M. T., Moscat, J., & Wooten, M. W. (2008). Genetic inactivation of p62 leads to accumulation of hyperphosphorylated tau and neurodegeneration. *Journal of Neurochemistry*, *106*(1), 107–120. https://doi.org/10.1111/j.1471-4159.2008.05340.x

Randall, T. S., Moores, C., & Stephenson, F. A. (2013). Delineation of the TRAK binding regions of the kinesin-1 motor proteins. *FEBS Letters*, *587*(23), 3763–3769. https://doi.org/10.1016/j.febslet.2013.09.049

Randall, T. S., Yip, Y. Y., Wallock-Richards, D. J., Pfisterer, K., Sanger, A., Ficek, W., Steiner, R. A., Beavil, A. J., Parsons, M., & Dodding, M. P. (2017). A small-molecule activator of kinesin-1 drives remodeling of the microtubule network. *Proceedings of the National Academy of Sciences*, *114*(52), 13738–13743. https://doi.org/10.1073/pnas.1715115115

Rangaraju, V., tom Dieck, S., & Schuman, E. M. (2017). Local translation in neuronal compartments: How local is local? *EMBO Reports*, *18*(5), 693–711. https://doi.org/10.15252/embr.201744045

Rawson, R. L., Yam, L., Weimer, R. M., Bend, E. G., Hartwieg, E., Horvitz, H. R., Clark, S. G., & Jorgensen, E. M. (2014). Axons Degenerate in the Absence of Mitochondria in C. elegans. *Current Biology*, *24*(7), 760–765. https://doi.org/10.1016/j.cub.2014.02.025

Reck-Peterson, S. L., Redwine, W. B., Vale, R. D., & Carter, A. P. (2018). The cytoplasmic dynein transport machinery and its many cargoes. *Nature Reviews Molecular Cell Biology*, *19*(6), 382–398. https://doi.org/10.1038/s41580-018-0004-3

Renton, A. E., Chiò, A., & Traynor, B. J. (2014). State of play in amyotrophic lateral sclerosis genetics. *Nature Neuroscience*, *17*(1), 17–23. https://doi.org/10.1038/nn.3584

Richter, J. D., & Zhao, X. (2021). The molecular biology of FMRP: New insights into fragile X syndrome. *Nature Reviews Neuroscience*, *22*(4), 209–222. https://doi.org/10.1038/s41583-021-00432-0

Rizzuto, R., Brini, M., Giorgi, F. D., Rossi, R., Heim, R., Tsien, R. Y., & Pozzan, T. (1996). Double labelling of subcellular structures with organelle-targeted GFP mutants *in vivo*. *Current Biology*, *6*(2), 183–188. https://doi.org/10.1016/S0960-9822(02)00451-7

Rogers, A. R., Driver, J. W., Constantinou, P. E., Jamison, D. K., & Diehl, M. R. (2009). Negative interference dominates collective transport of kinesin motors in the absence of load. *Physical Chemistry Chemical Physics*, *11*(24), 4882–4889. https://doi.org/10.1039/B900964G

Romani, A., & Scarpa, A. (1992). Regulation of cell magnesium. *Archives of Biochemistry and Biophysics*, *298*(1), 1–12. https://doi.org/10.1016/0003-9861(92)90086-C

Roy, A., Kucukural, A., & Zhang, Y. (2010). I-TASSER: A unified platform for automated protein structure and function prediction. *Nature Protocols*, *5*(4), Article 4. https://doi.org/10.1038/nprot.2010.5

Russo, A., & DiAntonio, A. (2019). Wnd/DLK Is a Critical Target of FMRP Responsible for Neurodevelopmental and Behavior Defects in the Drosophila Model of Fragile X Syndrome. *Cell Reports*, *28*(10), 2581-2593.e5. https://doi.org/10.1016/j.celrep.2019.08.001

Russo, G. J., Louie, K., Wellington, A., Macleod, G. T., Hu, F., Panchumarthi, S., & Zinsmaier, K. E. (2009). Drosophila Miro Is Required for Both Anterograde and Retrograde Axonal Mitochondrial Transport. *Journal of Neuroscience*, *29*(17), 5443–5455. https://doi.org/10.1523/JNEUROSCI.5417-08.2009

Saez-Atienzar, S., Dalgard, C. L., Ding, J., Chiò, A., Alba, C., Hupalo, D. N., Wilkerson, M. D., Bowser, R., Pioro, E. P., Bedlack, R., & Traynor, B. J. (2020). Identification of a pathogenic intronic KIF5A mutation in an ALS-FTD kindred. *Neurology*, *95*(22), 1015–1018. https://doi.org/10.1212/WNL.0000000000011064

Sainath, R., & Gallo, G. (2015). The dynein inhibitor Ciliobrevin D inhibits the bidirectional transport of organelles along sensory axons and impairs NGF-mediated regulation of growth cones and axon branches: Ciliobrevin D Inhibits Axon Transport. *Developmental Neurobiology*, *75*(7), 757–777. https://doi.org/10.1002/dneu.22246

Saotome, M., Safiulina, D., Szabadkai, G., Das, S., Fransson, A., Aspenstrom, P., Rizzuto, R., & Hajnoczky, G. (2008). Bidirectional Ca2+-dependent control of mitochondrial dynamics by the Miro GTPase. *Proceedings of the National Academy of Sciences*, *105*(52), 20728–20733. https://doi.org/10.1073/pnas.0808953105

Sawicka, K., Hale, C. R., Park, C. Y., Fak, J. J., Gresack, J. E., Van Driesche, S. J., Kang, J. J., Darnell, J. C., & Darnell, R. B. (2019). FMRP has a cell-type-specific role in CA1 pyramidal neurons to regulate autism-related transcripts and circadian memory. *eLife*, *8*, e46919. https://doi.org/10.7554/eLife.46919

Scheres, S. H. W. (2012). RELION: Implementation of a Bayesian approach to cryo-EM structure determination. *Journal of Structural Biology*, *180*(3), 519–530. https://doi.org/10.1016/j.jsb.2012.09.006

Schlager, M. A., Hoang, H. T., Urnavicius, L., Bullock, S. L., & Carter, A. P. (2014). *In vitro* reconstitution of a highly processive recombinant human dynein complex. *The EMBO Journal*, *33*(17), 1855–1868. https://doi.org/10.15252/embj.201488792

Schlager, M. A., Serra-Marques, A., Grigoriev, I., Gumy, L. F., Esteves da Silva, M., Wulf, P. S., Akhmanova, A., & Hoogenraad, C. C. (2014). Bicaudal D Family Adaptor Proteins Control the Velocity of Dynein-Based Movements. *Cell Reports*, *8*(5), 1248–1256. https://doi.org/10.1016/j.celrep.2014.07.052

Schroer, T. A. (2004). Dynactin. *Annual Review of Cell and Developmental Biology*, *20*(1), 759–779. https://doi.org/10.1146/annurev.cellbio.20.012103.094623

Schroer, T. A., & Sheetz, M. P. (1991). Two activators of microtubule-based vesicle transport. *Journal of Cell Biology*, *115*(5), 1309–1318. https://doi.org/10.1083/jcb.115.5.1309

Schuhmacher, J. S., Tom Dieck, S., Christoforidis, S., Landerer, C., Davila Gallesio, J., Hersemann, L., Seifert, S., Schäfer, R., Giner, A., Toth-Petroczy, A., Kalaidzidis, Y., Bohnsack, K. E., Bohnsack, M. T., Schuman, E. M., & Zerial, M. (2023). The Rab5 effector FERRY links early endosomes with mRNA localization. *Molecular Cell*, *83*(11), 1839-1855.e13. https://doi.org/10.1016/j.molcel.2023.05.012

Schwanhäusser, B., Busse, D., Li, N., Dittmar, G., Schuchhardt, J., Wolf, J., Chen, W., & Selbach, M. (2011). Global quantification of mammalian gene expression control. *Nature*, *473*(7347), Article 7347. https://doi.org/10.1038/nature10098

Schwarz, T. L. (2013). Mitochondrial Trafficking in Neurons. *Cold Spring Harbor Perspectives in Biology*, *5*(6), a011304–a011304. https://doi.org/10.1101/cshperspect.a011304

Seiler, S., Kirchner, J., Horn, C., Kallipolitou, A., Woehlke, G., & Schliwa, M. (2000). Cargo binding and regulatory sites in the tail of fungal conventional kinesin. *Nature Cell Biology*, *2*(6), Article 6. https://doi.org/10.1038/35014022

Senguen, F. T., & Grabarek, Z. (2012). X-ray Structures of Magnesium and Manganese Complexes with the N-Terminal Domain of Calmodulin: Insights into the Mechanism and Specificity of Metal Ion Binding to an EF-Hand. *Biochemistry*, *51*(31), 6182–6194. https://doi.org/10.1021/bi300698h

Shah, S., Molinaro, G., Liu, B., Wang, R., Huber, K. M., & Richter, J. D. (2020). FMRP Control of Ribosome Translocation Promotes Chromatin Modifications and Alternative Splicing of Neuronal Genes Linked to Autism. *Cell Reports*, *30*(13), 4459-4472.e6. https://doi.org/10.1016/j.celrep.2020.02.076

Shah, S., Sharp, K. J., Raju Ponny, S., Lee, J., Watts, J. K., Berry-Kravis, E., & Richter, J. D. (2023). Antisense oligonucleotide rescue of CGG expansion–dependent FMR1 mis-splicing in fragile X syndrome restores FMRP. *Proceedings of the National Academy of Sciences*, *120*(27), e2302534120. https://doi.org/10.1073/pnas.2302534120

Shao, C.-Y., Zhu, J., Xie, Y.-J., Wang, Z., Wang, Y.-N., Wang, Y., Su, L.-D., Zhou, L., Zhou, T.-H., & Shen, Y. (2013). Distinct Functions of Nuclear Distribution Proteins LIS1, Ndel1 and NudCL in Regulating Axonal Mitochondrial Transport: Nud Proteins Regulate Mitochondrial Transport. *Traffic*, *14*(7), 785–797. https://doi.org/10.1111/tra.12070

Shen, M., Wang, F., Li, M., Sah, N., Stockton, M. E., Tidei, J. J., Gao, Y., Korabelnikov, T., Kannan, S., Vevea, J. D., Chapman, E. R., Bhattacharyya, A., van Praag, H., & Zhao, X. (2019). Reduced mitochondrial fusion and Huntingtin levels contribute to impaired dendritic maturation and behavioral deficits in Fmr1-mutant mice. *Nature Neuroscience*, *22*(3), 386–400. https://doi.org/10.1038/s41593-019-0338-y

Shen, S., Park, J. W., Lu, Z., Lin, L., Henry, M. D., Wu, Y. N., Zhou, Q., & Xing, Y. (2014). rMATS: Robust and flexible detection of differential alternative splicing from replicate RNA-Seq data. *Proceedings of the National Academy of Sciences*, *111*(51), E5593–E5601. https://doi.org/10.1073/pnas.1419161111

Sievers, F., & Higgins, D. G. (2021). The Clustal Omega Multiple Alignment Package. In K. Katoh (Ed.), *Multiple Sequence Alignment: Methods and Protocols* (pp. 3–16). Springer US. https://doi.org/10.1007/978-1-0716-1036-7_1

Silva Ramos, E., Motori, E., Brüser, C., Kühl, I., Yeroslaviz, A., Ruzzenente, B., Kauppila, J. H. K., Busch, J. D., Hultenby, K., Habermann, B. H., Jakobs, S., Larsson, N.-G., & Mourier, A. (2019). Mitochondrial fusion is required for regulation of mitochondrial DNA replication. *PLOS Genetics*, *15*(6), e1008085. https://doi.org/10.1371/journal.pgen.1008085

Simm, D., Hatje, K., & Kollmar, M. (2015). Waggawagga: Comparative visualization of coiled-coil predictions and detection of stable single α-helices (SAH domains). *Bioinformatics*, *31*(5), 767–769. https://doi.org/10.1093/bioinformatics/btu700

Singh, G., Rebbapragada, I., & Lykke-Andersen, J. (2008). A Competition between Stimulators and Antagonists of Upf Complex Recruitment Governs Human Nonsense-Mediated mRNA Decay. *PLOS Biology*, *6*(4), e111. https://doi.org/10.1371/journal.pbio.0060111

Singh, G., Ricci, E. P., & Moore, M. J. (2014). RIPiT-Seq: A high-throughput approach for footprinting RNA:protein complexes. *Methods*, *65*(3), 320–332. https://doi.org/10.1016/j.ymeth.2013.09.013

Singh, K., Lau, C. K., Manigrasso, G., Gama, J. B., Gassmann, R., & Carter, A. P. (2023). *Molecular mechanism of dynein-dynactin activation by JIP3 and LIS1* (p. 2022.08.17.504273). bioRxiv. https://doi.org/10.1101/2022.08.17.504273

Siomi, H., Siomi, M. C., Nussbaum, R. L., & Dreyfuss, G. (1993). The protein product of the fragile X gene, *FMR1*, has characteristics of an RNA-binding protein. *Cell*, *74*(2), 291–298. https://doi.org/10.1016/0092-8674(93)90420-U

Skibinski, G., Nakamura, K., Cookson, M. R., & Finkbeiner, S. (2014). Mutant LRRK2 Toxicity in Neurons Depends on LRRK2 Levels and Synuclein But Not Kinase Activity or Inclusion Bodies. *Journal of Neuroscience*, *34*(2), 418–433. https://doi.org/10.1523/JNEUROSCI.2712-13.2014

Skowronek, K. J., Kocik, E., & Kasprzak, A. A. (2007). Subunits interactions in kinesin motors. *European Journal of Cell Biology*, *86*(9), 559–568. https://doi.org/10.1016/j.ejcb.2007.05.008

Smirnova, E., Griparic, L., Shurland, D.-L., & van der Bliek, A. M. (2001). Dynamin-related Protein Drp1 Is Required for Mitochondrial Division in Mammalian Cells. *Molecular Biology of the Cell*, *12*(8), 2245–2256. https://doi.org/10.1091/mbc.12.8.2245

Smith, E. F., Shaw, P. J., & De Vos, K. J. (2019). The role of mitochondria in amyotrophic lateral sclerosis. *Neuroscience Letters*, *710*, 132933. https://doi.org/10.1016/j.neulet.2017.06.052

Smith, K. P., Focia, P. J., Chakravarthy, S., Landahl, E. C., Klosowiak, J. L., Rice, S. E., & Freymann, D. M. (2020). Insight into human Miro1/2 domain organization based on the structure of its N-terminal GTPase. *Journal of Structural Biology*, *212*(3), 107656. https://doi.org/10.1016/j.jsb.2020.107656

Smith, M. J., Pozo, K., Brickley, K., & Stephenson, F. A. (2006). Mapping the GRIF-1 Binding Domain of the Kinesin, KIF5C, Substantiates a Role for GRIF-1 as an Adaptor Protein in the Anterograde Trafficking of Cargoes. *Journal of Biological Chemistry*, *281*(37), 27216–27228. https://doi.org/10.1074/jbc.M600522200

Sonn-Segev, A., Belacic, K., Bodrug, T., Young, G., VanderLinden, R. T., Schulman, B. A., Schimpf, J., Friedrich, T., Dip, P. V., Schwartz, T. U., Bauer, B., Peters, J.-M., Struwe, W. B., Benesch, J. L. P., Brown, N. G., Haselbach, D., & Kukura, P. (2020). Quantifying the heterogeneity of macromolecular machines by mass photometry. *Nature Communications*, *11*(1), Article 1. https://doi.org/10.1038/s41467-020-15642-w

Soria-Valles, C., Gutiérrez-Fernández, A., Osorio, F. G., Carrero, D., Ferrando, A. A., Colado, E., Fernández-García, M. S., Bonzon-Kulichenko, E., Vázquez, J., Fueyo, A., & López-Otín, C. (2016). MMP-25 Metalloprotease Regulates Innate Immune Response through NF-κB Signaling. *The Journal of Immunology*, *197*(1), 296–302. https://doi.org/10.4049/jimmunol.1600094

Soustelle, L., Aimond, F., López-Andrés, C., Brugioti, V., Raoul, C., & Layalle, S. (2023). ALS-Associated KIF5A Mutation Causes Locomotor Deficits Associated with Cytoplasmic Inclusions, Alterations of Neuromuscular Junctions, and Motor Neuron Loss. *Journal of Neuroscience*, *43*(47), 8058–8072. https://doi.org/10.1523/JNEUROSCI.0562-23.2023

Splinter, D., Razafsky, D. S., Schlager, M. A., Serra-Marques, A., Grigoriev, I., Demmers, J., Keijzer, N., Jiang, K., Poser, I., Hyman, A. A., Hoogenraad, C. C., King, S. J., & Akhmanova, A. (2012). BICD2, dynactin, and LIS1 cooperate in regulating dynein recruitment to cellular structures. *Molecular Biology of the Cell*, *23*(21), 4226–4241. https://doi.org/10.1091/mbc.e12-03-0210

Stathopulos, P. B., Zheng, L., Li, G.-Y., Plevin, M. J., & Ikura, M. (2008). Structural and Mechanistic Insights into STIM1-Mediated Initiation of Store-Operated Calcium Entry. *Cell*, *135*(1), 110–122. https://doi.org/10.1016/j.cell.2008.08.006

Steggerda, S. M., & Paschal, B. M. (2002). Regulation of nuclear import and export by the GTPase Ran. *International Review of Cytology*, *217*, 41–91. https://doi.org/10.1016/s0074-7696(02)17012-4

Stephan, T., Brüser, C., Deckers, M., Steyer, A. M., Balzarotti, F., Barbot, M., Behr, T. S., Heim, G., Hübner, W., Ilgen, P., Lange, F., Pacheu-Grau, D., Pape, J. K., Stoldt, S., Huser, T., Hell, S. W., Möbius, W., Rehling, P., Riedel, D., & Jakobs, S. (2020). MICOS assembly controls mitochondrial inner membrane remodeling and crista junction redistribution to mediate cristae formation. *The EMBO Journal*, *39*(14), e104105. https://doi.org/10.15252/embj.2019104105

Stowers, R. S., Megeath, L. J., Górska-Andrzejak, J., Meinertzhagen, I. A., & Schwarz, T. L. (2002). Axonal Transport of Mitochondria to Synapses Depends on Milton, a Novel Drosophila Protein. *Neuron*, *36*(6), 1063–1077. https://doi.org/10.1016/S0896-6273(02)01094-2

Su, T., Yan, Y., Hu, Q., Liu, Y., & Xu, S. (2022). De novo DYNC1H1 mutation causes infantile developmental and epileptic encephalopathy with brain malformations. *Molecular Genetics & Genomic Medicine*, *10*(3), e1874. https://doi.org/10.1002/mgg3.1874

Sutcliffe, J. S., Nelson, D. L., Zhang, F., Pieretti, M., Caskey, C. T., Saxe, D., & Warren, S. T. (1992). DNA methylation represses FMR-1 transcription in fragile X syndrome. *Human Molecular Genetics*, *1*(6), 397–400. https://doi.org/10.1093/hmg/1.6.397

Suzuki, M., Danilchanka, O., & Mekalanos, J. J. (2014). Vibrio cholerae T3SS Effector VopE Modulates Mitochondrial Dynamics and Innate Immune Signaling by Targeting Miro GTPases. *Cell Host & Microbe*, *16*(5), 581–591. https://doi.org/10.1016/j.chom.2014.09.015

Suzuki, M., Jeong, S.-Y., Karbowski, M., Youle, R. J., & Tjandra, N. (2003). The Solution Structure of Human Mitochondria Fission Protein Fis1 Reveals a Novel TPR-like Helix Bundle. *Journal of Molecular Biology*, *334*(3), 445–458. https://doi.org/10.1016/j.jmb.2003.09.064

Tan, Z., Yue, Y., Leprevost, F. da V., Haynes, S. E., Basrur, V., Nesvizhskii, A. I., Verhey, K. J., & Cianfrocco, M. A. (2023). Autoinhibited kinesin-1 adopts a hierarchical folding pattern. *eLife*, *12*. https://doi.org/10.7554/eLife.86776

Tanenbaum, M. E., Gilbert, L. A., Qi, L. S., Weissman, J. S., & Vale, R. D. (2014). A Protein-Tagging System for Signal Amplification in Gene Expression and Fluorescence Imaging. *Cell*, *159*(3), 635–646. https://doi.org/10.1016/j.cell.2014.09.039

Tauber, J. M., Vanlandingham, P. A., & Zhang, B. (2011). Elevated Levels of the Vesicular Monoamine Transporter and a Novel Repetitive Behavior in the Drosophila Model of Fragile X Syndrome. *PLOS ONE*, *6*(11), e27100. https://doi.org/10.1371/journal.pone.0027100

Taylor, J. P., Brown, R. H., & Cleveland, D. W. (2016). Decoding ALS: From genes to mechanism. *Nature*, *539*(7628), 197–206. https://doi.org/10.1038/nature20413

Tegunov, D., Xue, L., Dienemann, C., Cramer, P., & Mahamid, J. (2021). Multi-particle cryo-EM refinement with M visualizes ribosome-antibiotic complex at 3.5 Å in cells. *Nature Methods*, *18*(2), 186–193. https://doi.org/10.1038/s41592-020-01054-7

Tennessen, J. M., Barry, W. E., Cox, J., & Thummel, C. S. (2014). Methods for studying metabolism in *Drosophila*. *Methods*, *68*(1), 105–115. https://doi.org/10.1016/j.ymeth.2014.02.034

Terawaki, S., Yoshikane, A., Higuchi, Y., & Wakamatsu, K. (2015). Structural basis for cargo binding and autoinhibition of Bicaudal-D1 by a parallel coiled-coil with homotypic registry. *Biochemical and Biophysical Research Communications*, *460*(2), 451–456. https://doi.org/10.1016/j.bbrc.2015.03.054

The HD iPSC Consortium. (2012). Induced Pluripotent Stem Cells from Patients with Huntington's Disease Show CAG-Repeat-Expansion-Associated Phenotypes. *Cell Stem Cell*, *11*(2), 264–278. https://doi.org/10.1016/j.stem.2012.04.027

Tian, R., Gachechiladze, M. A., Ludwig, C. H., Laurie, M. T., Hong, J. Y., Nathaniel, D., Prabhu, A. V., Fernandopulle, M. S., Patel, R., Abshari, M., Ward, M. E., & Kampmann, M. (2019). CRISPR

Interference-Based Platform for Multimodal Genetic Screens in Human iPSC-Derived Neurons. *Neuron*, *104*(2), 239-255.e12. https://doi.org/10.1016/j.neuron.2019.07.014

Tiefenböck, S. K., Baltzer, C., Egli, N. A., & Frei, C. (2010). The Drosophila PGC-1 homologue Spargel coordinates mitochondrial activity to insulin signalling. *The EMBO Journal*, *29*(1), 171–183. https://doi.org/10.1038/emboj.2009.330

Tilney, L. G., Bryan, J., Bush, D. J., Fujiwara, K., Mooseker, M. S., Murphy, D. B., & Snyder, D. H. (1973). MICROTUBULES: EVIDENCE FOR 13 PROTOFILAMENTS. *Journal of Cell Biology*, *59*(2), 267–275. https://doi.org/10.1083/jcb.59.2.267

Tokito, M. K., Howland, D. S., Lee, V. M., & Holzbaur, E. L. (1996). Functionally distinct isoforms of dynactin are expressed in human neurons. *Molecular Biology of the Cell*, *7*(8), 1167–1180. https://doi.org/10.1091/mbc.7.8.1167

tom Dieck, S., Kochen, L., Hanus, C., Heumüller, M., Bartnik, I., Nassim-Assir, B., Merk, K., Mosler, T., Garg, S., Bunse, S., Tirrell, D. A., & Schuman, E. M. (2015). Direct visualization of newly synthesized target proteins in situ. *Nature Methods*, *12*(5), 411–414. https://doi.org/10.1038/nmeth.3319

Traut, T. W. (1994). Physiological concentrations of purines and pyrimidines. *Molecular and Cellular Biochemistry*, *140*(1), 1–22. https://doi.org/10.1007/BF00928361

Tsang, B., Arsenault, J., Vernon, R. M., Lin, H., Sonenberg, N., Wang, L.-Y., Bah, A., & Forman-Kay, J. D. (2019). Phosphoregulated FMRP phase separation models activity-dependent translation through bidirectional control of mRNA granule formation. *Proceedings of the National Academy of Sciences*, *116*(10), 4218–4227. https://doi.org/10.1073/pnas.1814385116

Urnavicius, L., Lau, C. K., Elshenawy, M. M., Morales-Rios, E., Motz, C., Yildiz, A., & Carter, A. P. (2018). Cryo-EM shows how dynactin recruits two dyneins for faster movement. *Nature*, *554*(7691), 202–206. https://doi.org/10.1038/nature25462

Urnavicius, L., Zhang, K., Diamant, A. G., Motz, C., Schlager, M. A., Yu, M., Patel, N. A., Robinson, C. V., & Carter, A. P. (2015). The structure of the dynactin complex and its interaction with dynein. *Science*, *347*(6229), 1441–1446. https://doi.org/10.1126/science.aaa4080

Vagnoni, A., & Bullock, S. L. (2016). A simple method for imaging axonal transport in aging neurons using the adult Drosophila wing. *Nature Protocols*, *11*(9), 1711–1723. https://doi.org/10.1038/nprot.2016.112

Valdar, W. S. J. (2002). Scoring residue conservation. *Proteins: Structure, Function, and Bioinformatics*, *48*(2), 227–241. https://doi.org/10.1002/prot.10146

Vale, R. D., Reese, T. S., & Sheetz, M. P. (1985). Identification of a novel force-generating protein, kinesin, involved in microtubule-based motility. *Cell*, *42*(1), 39–50. https://doi.org/10.1016/S0092-8674(85)80099-4

Vale, R. D., Schnapp, B. J., Mitchison, T., Steuer, E., Reese, T. S., & Sheetz, M. P. (1985). Different axoplasmic proteins generate movement in opposite directions along microtubules in vitro. *Cell*, *43*(3, Part 2), 623–632. https://doi.org/10.1016/0092-8674(85)90234-X

Valenti, D., de Bari, L., De Filippis, B., Henrion-Caude, A., & Vacca, R. A. (2014). Mitochondrial dysfunction as a central actor in intellectual disability-related diseases: An overview of Down syndrome, autism, Fragile X and Rett syndrome. *Neuroscience & Biobehavioral Reviews*, *46*, 202–217. https://doi.org/10.1016/j.neubiorev.2014.01.012

Valenti, D., & Vacca, R. A. (2023). Brain Mitochondrial Bioenergetics in Genetic Neurodevelopmental Disorders: Focus on Down, Rett and Fragile X Syndromes. *International Journal of Molecular Sciences*, *24*(15), Article 15. https://doi.org/10.3390/ijms241512488

van Riel, W. E., Rai, A., Bianchi, S., Katrukha, E. A., Liu, Q., Heck, A. J., Hoogenraad, C. C., Steinmetz, M. O., Kapitein, L. C., & Akhmanova, A. (2017). Kinesin-4 KIF21B is a potent microtubule pausing factor. *eLife*, *6*, e24746. https://doi.org/10.7554/eLife.24746

van Spronsen, M., Mikhaylova, M., Lipka, J., Schlager, M. A., van den Heuvel, D. J., Kuijpers, M., Wulf, P. S., Keijzer, N., Demmers, J., Kapitein, L. C., Jaarsma, D., Gerritsen, H. C., Akhmanova, A., & Hoogenraad, C. C. (2013). TRAK/Milton Motor-Adaptor Proteins Steer Mitochondrial Trafficking to Axons and Dendrites. *Neuron*, *77*(3), 485–502. https://doi.org/10.1016/j.neuron.2012.11.027

Verhey, K. J., & Hammond, J. W. (2009). Traffic control: Regulation of kinesin motors. *Nature Reviews Molecular Cell Biology*, *10*(11), 765–777. https://doi.org/10.1038/nrm2782

Verkerk, A. J. M. H., Pieretti, M., Sutcliffe, J. S., Fu, Y.-H., Kuhl, D. P. A., Pizzuti, A., Reiner, O., Richards, S., Victoria, M. F., Zhang, F., Eussen, B. E., van Ommen, G.-J. B., Blonden, L. A. J., Riggins, G. J., Chastain, J. L., Kunst, C. B., Galjaard, H., Thomas Caskey, C., Nelson, D. L., … Warren, S. T. (1991). Identification of a gene (FMR-1) containing a CGG repeat coincident with a breakpoint cluster region exhibiting length variation in fragile X syndrome. *Cell*, *65*(5), 905–914. https://doi.org/10.1016/0092-8674(91)90397-H

Villarin, J. M., McCurdy, E. P., Martínez, J. C., & Hengst, U. (2016). Local synthesis of dynein cofactors matches retrograde transport to acutely changing demands. *Nature Communications*, *7*(1), 13865. https://doi.org/10.1038/ncomms13865

Wallace, D. C. (2011). Bioenergetic Origins of Complexity and Disease. *Cold Spring Harbor Symposia on Quantitative Biology*, *76*, 1–16. https://doi.org/10.1101/sqb.2011.76.010462

Wallace, D. C., Fan, W., & Procaccio, V. (2010). Mitochondrial Energetics and Therapeutics. *Annual Review of Pathology: Mechanisms of Disease*, *5*(1), 297–348. https://doi.org/10.1146/annurev.pathol.4.110807.092314

Wan, L., Dockendorff, T. C., Jongens, T. A., & Dreyfuss, G. (2000). Characterization of dFMR1, a Drosophila melanogaster Homolog of the Fragile X Mental Retardation Protein. *Molecular and Cellular Biology*, *20*(22), 8536–8547. https://doi.org/10.1128/MCB.20.22.8536-8547.2000

Wang, C., Ward, M. E., Chen, R., Liu, K., Tracy, T. E., Chen, X., Xie, M., Sohn, P. D., Ludwig, C., Meyer-Franke, A., Karch, C. M., Ding, S., & Gan, L. (2017). Scalable Production of iPSC-Derived Human Neurons to Identify Tau-Lowering Compounds by High-Content Screening. *Stem Cell Reports*, *9*(4), 1221–1233. https://doi.org/10.1016/j.stemcr.2017.08.019

Wang, G., Ang, C.-E., Fan, J., Wang, A., Moffitt, J. R., & Zhuang, X. (2020). *Spatial organization of the transcriptome in individual neurons* (p. 2020.12.07.414060). bioRxiv. https://doi.org/10.1101/2020.12.07.414060

Wang, L., & Brown, A. (2010). A hereditary spastic paraplegia mutation in kinesin-1A/KIF5A disrupts neurofilament transport. *Molecular Neurodegeneration*, *5*(1), 52. https://doi.org/10.1186/1750-1326-5-52

Wang, Q., Tian, J., Chen, H., Du, H., & Guo, L. (2019). Amyloid beta-mediated KIF5A deficiency disrupts anterograde axonal mitochondrial movement. *Neurobiology of Disease*, *127*, 410–418. https://doi.org/10.1016/j.nbd.2019.03.021

Wang, X., Perry, G., Smith, M. A., & Zhu, X. (2010). Amyloid-β-Derived Diffusible Ligands Cause Impaired Axonal Transport of Mitochondria in Neurons. *Neurodegenerative Diseases*, *7*(1–3), 56–59. https://doi.org/10.1159/000283484

Wang, X., & Schwarz, T. L. (2009). The Mechanism of Ca2+-Dependent Regulation of Kinesin-Mediated Mitochondrial Motility. *Cell*, *136*(1), 163–174. https://doi.org/10.1016/j.cell.2008.11.046

Wang, X., Winter, D., Ashrafi, G., Schlehe, J., Wong, Y. L., Selkoe, D., Rice, S., Steen, J., LaVoie, M. J., & Schwarz, T. L. (2011). PINK1 and Parkin Target Miro for Phosphorylation and Degradation to Arrest Mitochondrial Motility. *Cell*, *147*(4), 893–906. https://doi.org/10.1016/j.cell.2011.10.018

Waterman-Storer, C. M., Karki, S., & Holzbaur, E. L. F. (1995). The p150Glued Component of the Dynactin Complex Binds to Both Microtubules and the Actin-Related Protein Centractin (Arp-1). *Proceedings of the National Academy of Sciences of the United States of America*, *92*(5), 1634–1638.

Weihofen, A., Thomas, K. J., Ostaszewski, B. L., Cookson, M. R., & Selkoe, D. J. (2009). Pink1 Forms a Multiprotein Complex with Miro and Milton, Linking Pink1 Function to Mitochondrial Trafficking. *Biochemistry*, *48*(9), 2045–2052. https://doi.org/10.1021/bi8019178

Weijman, J. F., Yadav, S. K. N., Surridge, K. J., Cross, J. A., Borucu, U., Mantell, J., Woolfson, D. N., Schaffitzel, C., & Dodding, M. P. (2022). Molecular architecture of the autoinhibited kinesin-1 lambda particle. *Science Advances*, *8*(37), eabp9660. https://doi.org/10.1126/sciadv.abp9660

Weisz, E. D., Monyak, R. E., & Jongens, T. A. (2015). Deciphering discord: How Drosophila research has enhanced our understanding of the importance of FMRP in different spatial and temporal contexts. *Experimental Neurology*, *274*, 14–24. https://doi.org/10.1016/j.expneurol.2015.05.015

Weisz, E. D., Towheed, A., Monyak, R. E., Toth, M. S., Wallace, D. C., & Jongens, T. A. (2018). Loss of Drosophila FMRP leads to alterations in energy metabolism and mitochondrial function. *Human Molecular Genetics*, *27*(1), 95–106. https://doi.org/10.1093/hmg/ddx387

Wong, Y. C., & Holzbaur, E. L. F. (2015). Temporal dynamics of PARK2/parkin and OPTN/optineurin recruitment during the mitophagy of damaged mitochondria. *Autophagy*, *11*(2), 422–424. https://doi.org/10.1080/15548627.2015.1009792

Wong, Y. C., Peng, W., & Krainc, D. (2019). Lysosomal Regulation of Inter-mitochondrial Contact Fate and Motility in Charcot-Marie-Tooth Type 2. *Developmental Cell*, *50*(3), 339-354.e4. https://doi.org/10.1016/j.devcel.2019.05.033

Wong, Y. C., Ysselstein, D., & Krainc, D. (2018). Mitochondria–lysosome contacts regulate mitochondrial fission via RAB7 GTP hydrolysis. *Nature*, *554*(7692), 382–386. https://doi.org/10.1038/nature25486

Wong, Y. L., & Rice, S. E. (2010). Kinesin's light chains inhibit the head- and microtubule-binding activity of its tail. *Proceedings of the National Academy of Sciences*, *107*(26), 11781–11786. https://doi.org/10.1073/pnas.1005854107

Wu, B., Eliscovich, C., Yoon, Y. J., & Singer, R. H. (2016). Translation dynamics of single mRNAs in live cells and neurons. *Science*, *352*(6292), 1430–1435. https://doi.org/10.1126/science.aaf1084

Wu, Y., Ding, C., Sharif, B., Weinreb, A., Swaim, G., Hao, H., Yogev, S., Watanabe, S., & Hammarlund, M. (2024). Polarized localization of kinesin-1 and RIC-7 drives axonal mitochondria anterograde transport. *Journal of Cell Biology*, *223*(5), e202305105. https://doi.org/10.1083/jcb.202305105

Xia, C., Babcock, H. P., Moffitt, J. R., & Zhuang, X. (2019). Multiplexed detection of RNA using MERFISH and branched DNA amplification. *Scientific Reports*, *9*(1), Article 1. https://doi.org/10.1038/s41598-019-43943-8

Xu, E., Zhang, J., Zhang, M., Jiang, Y., Cho, S.-J., & Chen, X. (2014). RNA-Binding Protein RBM24 Regulates p63 Expression via mRNA Stability. *Molecular Cancer Research*, *12*(3), 359–369. https://doi.org/10.1158/1541-7786.MCR-13-0526

Yamada, K., Andrews, C., Chan, W.-M., McKeown, C. A., Magli, A., de Berardinis, T., Loewenstein, A., Lazar, M., O'Keefe, M., Letson, R., London, A., Ruttum, M., Matsumoto, N., Saito, N., Morris, L., Monte, M. D., Johnson, R. H., Uyama, E., Houtman, W. A., … Engle, E. C. (2003). Heterozygous mutations of the kinesin KIF21A in congenital fibrosis of the extraocular muscles type 1 (CFEOM1). *Nature Genetics*, *35*(4), Article 4. https://doi.org/10.1038/ng1261

Yang, C., & Svitkina, T. M. (2019). Ultrastructure and dynamics of the actin–myosin II cytoskeleton during mitochondrial fission. *Nature Cell Biology*, *21*(5), 603–613. https://doi.org/10.1038/s41556-019-0313-6

Yang, H., Sibilla, C., Liu, R., Yun, J., Hay, B. A., Blackstone, C., Chan, D. C., Harvey, R. J., & Guo, M. (2022). Clueless/CLUH regulates mitochondrial fission by promoting recruitment of Drp1 to mitochondria. *Nature Communications*, *13*(1), 1582. https://doi.org/10.1038/s41467-022-29071-4

Yang, J. E., Larson, M. R., Sibert, B. S., Shrum, S., & Wright, E. R. (2021). CorRelator: Interactive software for real-time high precision cryo-correlative light and electron microscopy. *Journal of Structural Biology*, *213*(2), 107709. https://doi.org/10.1016/j.jsb.2021.107709

Yang, J., Yan, R., Roy, A., Xu, D., Poisson, J., & Zhang, Y. (2015). The I-TASSER Suite: Protein structure and function prediction. *Nature Methods*, *12*(1), Article 1. https://doi.org/10.1038/nmeth.3213

Yang, R., Bentley, M., Huang, C.-F., & Banker, G. (2016). Analyzing kinesin motor domain translocation in cultured hippocampal neurons. *Methods in Cell Biology*, *131*, 217–232. https://doi.org/10.1016/bs.mcb.2015.06.021

Yao, A., Jin, S., Li, X., Liu, Z., Ma, X., Tang, J., & Zhang, Y. Q. (2011). Drosophila FMRP regulates microtubule network formation and axonal transport of mitochondria. *Human Molecular Genetics*, *20*(1), 51–63. https://doi.org/10.1093/hmg/ddq431

Yi, M., Weaver, D., & Hajnóczky, G. (2004). Control of mitochondrial motility and distribution by the calcium signal: A homeostatic circuit. *The Journal of Cell Biology*, *167*(4), 661–672. https://doi.org/10.1083/jcb.200406038

Yip, Y. Y., Pernigo, S., Sanger, A., Xu, M., Parsons, M., Steiner, R. A., & Dodding, M. P. (2016). The light chains of kinesin-1 are autoinhibited. *Proceedings of the National Academy of Sciences*, *113*(9), 2418–2423. https://doi.org/10.1073/pnas.1520817113

Yoon, Y., Krueger, E. W., Oswald, B. J., & McNiven, M. A. (2003). The Mitochondrial Protein hFis1 Regulates Mitochondrial Fission in Mammalian Cells through an Interaction with the Dynamin-Like Protein DLP1. *Molecular and Cellular Biology*, *23*(15), 5409–5420. https://doi.org/10.1128/MCB.23.15.5409-5420.2003

Young, G., Hundt, N., Cole, D., Fineberg, A., Andrecka, J., Tyler, A., Olerinyova, A., Ansari, A., Marklund, E. G., Collier, M. P., Chandler, S. A., Tkachenko, O., Allen, J., Crispin, M., Billington, N., Takagi, Y., Sellers, J. R., Eichmann, C., Selenko, P., … Kukura, P. (2018). Quantitative mass imaging of single biological macromolecules. *Science*, *360*(6387), 423–427. https://doi.org/10.1126/science.aar5839

Yu, R., Jin, S., Lendahl, U., Nistér, M., & Zhao, J. (2019). Human Fis1 regulates mitochondrial dynamics through inhibition of the fusion machinery. *The EMBO Journal*, *38*(8). https://doi.org/10.15252/embj.201899748

Yu, R., Liu, T., Jin, S.-B., Ning, C., Lendahl, U., Nistér, M., & Zhao, J. (2017). MIEF1/2 function as adaptors to recruit Drp1 to mitochondria and regulate the association of Drp1 with Mff. *Scientific Reports*, *7*(1), 880. https://doi.org/10.1038/s41598-017-00853-x

Zhang, K., Foster, H. E., Rondelet, A., Lacey, S. E., Bahi-Buisson, N., Bird, A. W., & Carter, A. P. (2017). Cryo-EM Reveals How Human Cytoplasmic Dynein Is Auto-inhibited and Activated. *Cell*, *169*(7), 1303-1314.e18. https://doi.org/10.1016/j.cell.2017.05.025

Zhang, M., Zhang, Y., Xu, E., Mohibi, S., de Anda, D. M., Jiang, Y., Zhang, J., & Chen, X. (2018). Rbm24, a target of p53, is necessary for proper expression of p53 and heart development. *Cell Death & Differentiation*, *25*(6), Article 6. https://doi.org/10.1038/s41418-017-0029-8

Zhang, Y. (2008). I-TASSER server for protein 3D structure prediction. *BMC Bioinformatics*, *9*(1), 40. https://doi.org/10.1186/1471-2105-9-40

Zhang, Y. Q., Bailey, A. M., Matthies, H. J. G., Renden, R. B., Smith, M. A., Speese, S. D., Rubin, G. M., & Broadie, K. (2001). Drosophila Fragile X-Related Gene Regulates the MAP1B Homolog Futsch to Control Synaptic Structure and Function. *Cell*, *107*(5), 591–603. https://doi.org/10.1016/S0092-8674(01)00589-X

Zhao, X.-L., Wang, W.-A., Tan, J.-X., Huang, J.-K., Zhang, X., Zhang, B.-Z., Wang, Y.-H., YangCheng, H.-Y., Zhu, H.-L., Sun, X.-J., & Huang, F.-D. (2010). Expression of -Amyloid Induced Age-Dependent Presynaptic and Axonal Changes in Drosophila. *Journal of Neuroscience*, *30*(4), 1512–1522. https://doi.org/10.1523/JNEUROSCI.3699-09.2010

Zhao, Y., Song, E., Wang, W., Hsieh, C.-H., Wang, X., Feng, W., Wang, X., & Shen, K. (2021). Metaxins are core components of mitochondrial transport adaptor complexes. *Nature Communications*, *12*(1), 83. https://doi.org/10.1038/s41467-020-20346-2

Zhou, Y., Zhou, B., Pache, L., Chang, M., Khodabakhshi, A. H., Tanaseichuk, O., Benner, C., & Chanda, S. K. (2019). Metascape provides a biologist-oriented resource for the analysis of systems-level datasets. *Nature Communications*, *10*(1), Article 1. https://doi.org/10.1038/s41467-019-09234-6